ADVANCES IN GLOBAL WARMING OBSERVATIONS AND THEIR UNCERTAINTIES

EDITED BY: Qingxiang Li, Boyin Huang and Xiaolan L. Wang
PUBLISHED IN: Frontiers in Environmental Science and
Frontiers in Earth Science

frontiers Research Topics

ISSN 1664-8714
ISBN 978-2-83250-417-8
DOI 10.3389/978-2-83250-417-8

About Frontiers

Frontiers is more than just an open-access publisher of scholarly articles: it is a pioneering approach to the world of academia, radically improving the way scholarly research is managed. The grand vision of Frontiers is a world where all people have an equal opportunity to seek, share and generate knowledge. Frontiers provides immediate and permanent online open access to all its publications, but this alone is not enough to realize our grand goals.

Frontiers Journal Series

The Frontiers Journal Series is a multi-tier and interdisciplinary set of open-access, online journals, promising a paradigm shift from the current review, selection and dissemination processes in academic publishing. All Frontiers journals are driven by researchers for researchers; therefore, they constitute a service to the scholarly community. At the same time, the Frontiers Journal Series operates on a revolutionary invention, the tiered publishing system, initially addressing specific communities of scholars, and gradually climbing up to broader public understanding, thus serving the interests of the lay society, too.

Dedication to Quality

Each Frontiers article is a landmark of the highest quality, thanks to genuinely collaborative interactions between authors and review editors, who include some of the world's best academicians. Research must be certified by peers before entering a stream of knowledge that may eventually reach the public - and shape society; therefore, Frontiers only applies the most rigorous and unbiased reviews.
Frontiers revolutionizes research publishing by freely delivering the most outstanding research, evaluated with no bias from both the academic and social point of view. By applying the most advanced information technologies, Frontiers is catapulting scholarly publishing into a new generation.

What are Frontiers Research Topics?

Frontiers Research Topics are very popular trademarks of the Frontiers Journals Series: they are collections of at least ten articles, all centered on a particular subject. With their unique mix of varied contributions from Original Research to Review Articles, Frontiers Research Topics unify the most influential researchers, the latest key findings and historical advances in a hot research area! Find out more on how to host your own Frontiers Research Topic or contribute to one as an author by contacting the Frontiers Editorial Office: frontiersin.org/about/contact

ADVANCES IN GLOBAL WARMING OBSERVATIONS AND THEIR UNCERTAINTIES

Topic Editors:
Qingxiang Li, Sun Yat-sen University, Zhuhai Campus, China
Boyin Huang, National Centers for Environmental Information, National Oceanic and Atmospheric Administration (NOAA), United States
Xiaolan L. Wang, Environment and Climate Change Canada (ECCC), Canada

Citation: Li, Q., Huang, B., Wang, X. L., eds. (2022). Advances in Global Warming Observations and Their Uncertainties. Lausanne: Frontiers Media SA.
doi: 10.3389/978-2-83250-417-8

Table of Contents

frontiers in Environmental Science

ORIGINAL RESEARCH
published: 09 September 2020
doi: 10.3389/fenvs.2020.581536

Trend in Short-Duration Extreme Precipitation in Hong Kong

Lejiang Yu[1,2], Shiyuan Zhong[3], Yubao Qiu[4] and Xi Liang[5]*

[1] SOA Key Laboratory for Polar Science, Polar Research Institute of China, Shanghai, China, [2] Southern Marine Science and Engineering Guangdong Laboratory, Zhuhai, China, [3] Department of Geography, Environment, and Spatial Sciences, Michigan State University, East Lansing, MI, United States, [4] Aerospace Information Research Institute, Chinese Academy of Sciences, Beijing, China, [5] National Marine Environmental Forecasting Center, Beijing, China

This study examines trends in the intensity and frequency of short-duration (5 min to 3 h) rainfall extremes in Hong Kong for the period of 1984 to 2010 and the drivers for the trends using gauge observations and gridded reanalysis. Both the intensity and frequency of rainfall extremes exhibit an upward trend, with the slope for the intensity (frequency) trend increasing (decreasing) as duration lengthens from 5 min to 3 h. The upward intensity (frequency) trends appear to be a manifestation of an abrupt change around 1991/1992 (1992/1993) that separates a period of lower and fewer rainfall extremes before from a period of higher and more extremes after. The increase in Hong Kong's extreme rainfall after the early 1990s is likely caused by a combination of stronger rising motion along Southeast China Coasts and enhanced moisture transport into South China Sea resulting from the strengthening and westward shift of the western Pacific subtropical high associated with anomalous convective activities over the tropical western Indian Ocean and a positive phase circumglobal teleconnection wavetrain.

Keywords: extreme rainfall, climate analysis, climate extremes, monsoon, climate of Hong Kong

OPEN ACCESS

Edited by:
Qingxiang Li,
Sun Yat-sen University, China

Reviewed by:
Zengyun Hu,
Chinese Academy of Sciences (CAS), China
Fangxing Tian,
University of Reading, United Kingdom

****Correspondence:***
Lejiang Yu
yulejiang@sina.com.cn

Specialty section:
This article was submitted to Interdisciplinary Climate Studies, a section of the journal Frontiers in Environmental Science

Received: *09 July 2020*
Accepted: *18 August 2020*
Published: *09 September 2020*

Citation:
Yu L, Zhong S, Qiu Y and Liang X (2020) Trend in Short-Duration Extreme Precipitation in Hong Kong. Front. Environ. Sci. 8:581536. doi: 10.3389/fenvs.2020.581536

INTRODUCTION

It has been widely recognized that heavy precipitation and the associated flooding events have serious socioeconomical consequences. For example, the 1993 summer floods in the upper Mississippi River Basin of the United States devastated many low-lying communities in the basin and cost the economy nearly $20 billion (Kunkel et al., 1994). Most recently in winter 2019–2020, extremely heavy rainfall associated with three powerful extra tropical cyclones caused widespread flooding across the United Kingdom, resulting in loss of lives and at least €150 million property damages. Understand the trends and variability as well as the drivers of these high impact extreme precipitation events is, therefore, vital for economical and societal activities.

In recent decades, extreme precipitation events have been on the rise in some parts of the world while decreasing in other parts, depending on various factors such as season, period, and geographical location (Easterling et al., 2000; Ghosh et al., 2012). For example, several studies have documented an upward trend of extreme precipitation events across much of the United States and Canada (e.g., Karl et al., 1996; Kunkel et al., 1994; Easterling et al., 2000), Japan (Iwashima and Yamamoto, 1993), Indian (Mukherjee et al., 2018), and Australia (Suppiah and Hennessy, 1998). However, in the United Kingdom (UK) heavy rainfall events have been increasing in winter, but decreasing in summer (Osborn et al., 1999) with substantial interannual variability (Jones et al., 2013; Simpson and Jones, 2014; Brown, 2018). Decreases in extreme precipitation events have been

documented for the Sahel region of Nigeria (Tarhule and Woo, 1998) and across most stations in Southeast Asia and the South Pacific (Manton et al., 2001). In addition to changing frequency, the intensity of extreme precipitation events have also been changing and majority of observational evidence has suggested an increasing trend in the intensity, but the slope of the increasing trends vary substantially by region (Donat et al., 2016).

Previous studies have linked the changes in extreme precipitation frequency and intensity to increases in temperature and moisture under global warming caused by increases in anthropogenic greenhouse gas emissions (Min et al., 2011; Ghosh et al., 2012; Mishra et al., 2012; Mukherjee et al., 2018). Atmospheric circulation anomalies also play an important role. For example, the increase frequency of extreme precipitation events in the United States has been linked to the Pacific Decadal Oscillation (PDO) and Atlantic Multidecadal Oscillation (AMO) (Yu et al., 2016). A review of the recent progress toward understanding global observed long-term changes in extreme precipitation is provided by Alexander (2016).

Extreme precipitation events occur on time scales of minutes, days to weeks and among them short-duration (less than one day) events, which are mostly responsible for occurrence of flash floods, is most difficult to forecast in advance (Ahern et al., 2005). Westra et al. (2014) noted that intensity and frequency of sub-daily rainfall extremes have been increasing more rapidly than daily rainfall extremes. The change in sub-daily rainfall extremes have been attributed to local temperature change according to the Clausius-Clapeyron (CC) relation (Pall et al., 2007) and to large-scale atmosphere-ocean variability modes, such as the El Niño–Southern Oscillation (ENSO) and the monsoon systems (Blenkinsop et al., 2018). It is therefore necessary to examine the changes in sub-daily extreme precipitation in the context of internal (atmospheric circulation) and external (e.g., anthropogenic) factors. To this end, the INTElligent use of climate models for adaptation to non-Stationary hydrological Extremes (INTENSE) project sought to understand the past, present and future of sub-daily rainfall extremes using observations and models (Blenkinsop et al., 2018).

The current study focuses on trends in short-duration ($\leq$3 h) extreme rainfall events in Hong Kong. Located in China's southeast coast surrounded by the South China Sea by all sides except the north side, Hong Kong is subject to extreme rainfall related to the East Asian summer monsoon. The hilly and mountainous terrain makes rainfall patterns highly heterogeneous across the main peninsula and the numerous islands. As a global business and commercial center and one of the most densely populated regions in the world, heavy flooding caused by short-duration extreme precipitation can have a profound socioeconomic impact (Peterson and Kwong, 1981; Lam and Leung, 1994). Hence, understanding the trends and interannual variability of short-duration extreme rainfall events in Hong Kong is becoming increasingly important in the context of global warming and local/regional atmospheric circulation change noted above as potential drivers.

Previous studies have documented an increase in extreme precipitation in Hong Kong in the past. For example, Ginn et al. (2010) reported an increase in the annual number of days with hourly rainfall greater than 30 mm from 1947 to 2008. Wong et al. (2011) found an increase in the frequency of occurrence of extreme 1-, 2-, and 3-hourly rainfall amounts from 1885 to 2008 and a shortened return period of hourly rainfall of more than 100 mm from 37 years in 1900 to 18 years in 2000. Extreme rainfall in Hong Kong in the 21st century is projected to become more frequent. For example, Wu et al. (2006) indicated that the number of days with hourly rainfall of greater than 30 mm will increase from 5.6 days during 1961–1990 to 6.5 days for the period of 2070–2099. However, the changes in the frequency of future hourly extreme rainfall have been based primarily on projections using General Circulation Models (GCMs) with spatial resolutions too coarse to represent convection, the major driver for sub-daily extreme precipitation events (Kendon et al., 2014; Prein et al., 2015). As such, the changes between current and future sub-daily extreme precipitation events projected by coarse resolution models are associated with great uncertainty.

Although aforementioned studies have investigated the trends in extreme rainfall in Hong Kong, few have, to our knowledge, examined trends in and cause for short-duration extreme rainfall events that last from a few minutes to several hours. The relative role of atmospheric circulation and the increased greenhouse gas emissions play in the trends of extreme rainfall needs to be assessed further. The current study will examine trends in short-duration (from 5 min to 3 h) rainfall extremes in Hong Kong with a focus on their relationship to large-scale circulations.

The rest of the paper is organized as follows: the data sets and methods used in the study are described in Section "Data and Methods." Section "Results" presents the trends of extreme rainfall in Hong Kong and their potential drivers. A summary of the results and discussion are presented in Section "Summary and Discussion."

DATA AND METHODS

The Geotechnical Engineering Office (GEO) of Civil Engineering and Development Department in Hong Kong has been operating a network of automated rain gauges to collect rainfall data at 5-min time interval since 1984. The number of gauges varied with time, ranging from 42 gauges in the early half of 1984 to 111 gauges in 1999. The data were missing at some gauges for December 30 and 31, 1984 and January 1-June 1, 1985. This study selected 39 GEO rain gauges for the period of 1984 to 2010, when there were no missing data records from these gauges. The locations of the 39 rain gauges are shown in **Figure 1** and their coordinates and elevations are given in **Table 1**. Some quality control procedures were performed to identify and remove suspiciously high rainfall values, determine and remove erroneous values by comparing with other datasets and supplement missing values according to spatial and temporal continuity. More details on the data and quality control can be found in Tang and Cheung (2011).

In this study, we focus on the annual maxima of sub-daily rainfall extremes. Sub-daily rainfall accumulation is an important factor for flood control. The calculation of annual maxima is based on 5-min rainfall data for the 1984–2010

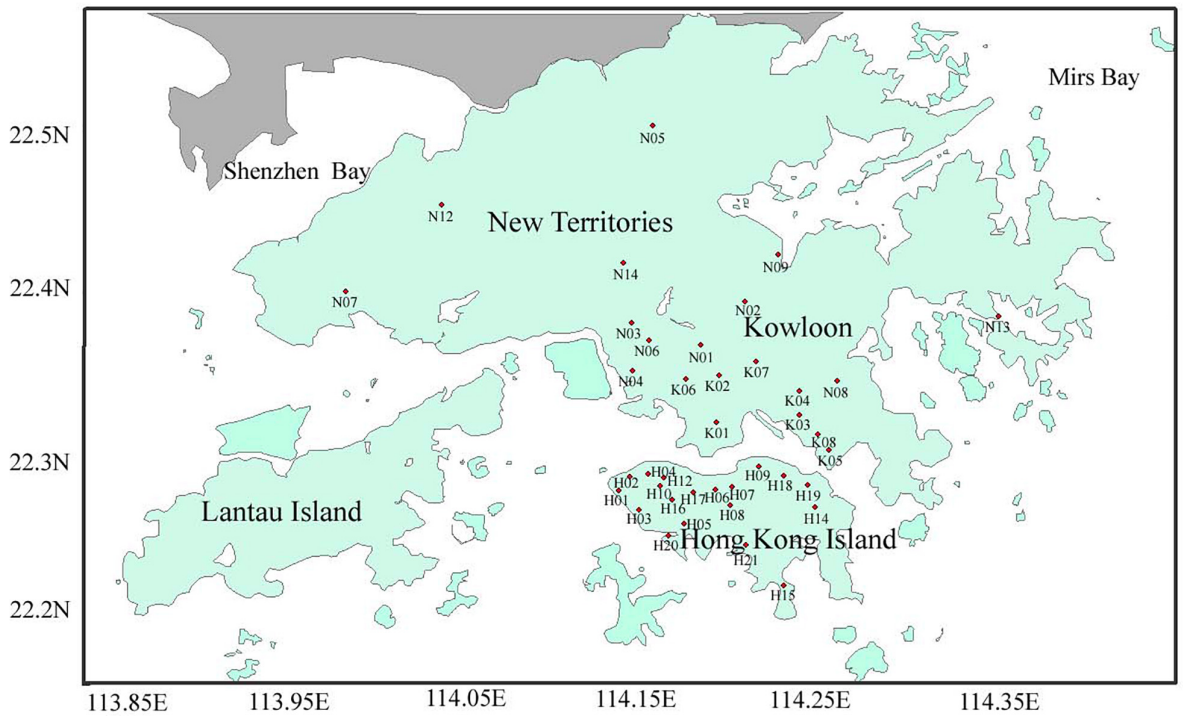

FIGURE 1 | Locations of the 39 GEO rain gauges in Hong Kong. Refer to **Table 1** for gauge latitude, longitude, and elevation.

period. Although the analysis period is only 27 (1984–2010) years because of data availability, Evans and Yu (2001) recommended a minimum of 20 years as an adequate length of data records for examining extreme rainfall intensity. The durations of rainfall accumulations considered in the present analysis include 5, 10, and 30 min and 1, 2, and 3 h. Apart from intensity of annual maximum precipitation accumulation over the 6 durations, the frequency of extreme precipitation events defined using the 99th percentile threshold of all data over all years for each gauge is also examined.

We examine the trends and interannual variability of the extreme precipitation in Hong Kong in the context of large-scale atmospheric circulation and sea surface temperature (SST) anomalies. Large-scale atmospheric circulations are described by the anomalous fields of 500-hPa geopotential height and vertical velocity, 850-hPa wind and 1000–700 hPa specific humidity, all of which are derived from the U.S. National Centers for Environmental Prediction (NCEP) and Department of Energy (DOE) global reanalysis with a horizontal resolution of T62 (∼209 km) and 28 vertical levels and a temporal coverage of four times per day (Kalnay et al., 1996; Kistler et al., 2001; Kanamitsu et al., 2002). SST anomalies are described using the US National Oceanic and Atmospheric Administration (NOAA) Extended Reconstructed Sea Surface Temperature (Smith et al., 2008). Finally, NOAA's Outgoing Longwave Radiation (OLR) (Liebmann and Smith, 1996) data are also analyzed as a proxy for convection[1].

[1]ftp://ftp.cdc.noaa.gov/Datasets/

Since more than half of Hong Kong's annual maxima rainfall occur in summer (June, July August), followed by nearly one third in spring (March, April, and May), we focus our analyses on the relations between summertime anomalous large-scale circulation patterns and the changes in annual maxima of extreme rainfall in Hong Kong using the composite analysis method. Mann-Kendall (MK) test (Mann, 1945) is utilized to detect significant trend and abrupt change point in the time series.

RESULTS

The annual maxima of short-duration (5, 10, 30 min and 1, 2 3 h) rainfall extremes are estimated using 39 automated rain gauges during the 27-year period from 1984 to 2010. The values are then averaged over the 39 rain gauges to obtain domain-averaged annual maxima of rainfall extremes for the respective duration. The median of domain-averaged annual maxima of rainfall extremes over the 27 year period for the 6 gradually increasing durations are 12.5, 22.0, 46.8, 68.4, 94.3, and 110.7 mm, respectively.

The time series and trends of domain-averaged annual maxima of rainfall accumulations over the 6 durations are shown in **Figure 2**. The 27-year time series is characterized by a remarkable interdecadal variability and this is true for all 6 accumulation durations. Based on the Mann-Kendall (MK) (Mann, 1945) abrupt change test, an abrupt change point occurred in 1991/1992 regardless of duration (**Figure 3**).

TABLE 1 | Locations and elevations of the 39 GEO rain gauges.

No.	Latitude (°)	Longitude (°)	Elevation (m)
H01	114.1219	22.27278	107
H02	114.1280	22.28060	95
H03	114.1334	22.26113	132
H04	114.1384	22.28309	123
H05	114.1589	22.25283	103
H06	114.1763	22.27330	88
H07	114.1869	22.27579	94
H08	114.1852	22.26408	129
H09	114.2009	22.28720	160
H10	114.1452	22.27552	530
H12	114.1478	22.28072	188
H14	114.2333	22.26277	141
H15	114.2158	22.21531	50
H16	114.1526	22.26755	439
H17	114.1641	22.27173	200
H18	114.2155	22.28177	77
H19	114.2291	22.27590	53
H20	114.1502	22.24462	104
H21	114.1943	22.23951	139
K01	114.1776	22.31471	91
K02	114.1789	22.34299	92
K03	114.2246	22.31861	91
K04	114.2251	22.33298	178
K05	114.2414	22.29726	117
K06	114.1600	22.34041	35
K07	114.2001	22.35117	197
K08	114.235	22.30637	77
N01	114.1292	22.37400	38
N02	114.1300	22.34530	73
N03	114.1412	22.49433	113
N04	114.1392	22.36377	96
N05	113.9664	22.39309	111
N06	114.2456	22.33943	106
N07	114.2124	22.41540	41
N08	114.0602	22.36858	256
N09	114.0937	22.33686	6
N12	114.0210	22.44615	79
N13	114.3385	22.37786	87
N14	114.1243	22.41093	944

Corresponding to this abrupt change, the domain-averaged annual maxima are significantly smaller during 1984 – 1991 than those from 1992 to 2010.

The systematic differences in the values before and after the abrupt change point yields an upward trend in the domain-averaged annual maxima of rainfall extremes. The slope of the upward trend increases as the accumulation duration lengthens, from 0.1, 0.2, and 0.5 mm yr^{-1} for 5-, 10-, and 30- min durations, to 0.8, 1.2, and 1.3 mm yr^{-1} for the 1-, 2-, and 3-h durations, respectively. The trends are statistically significant ($p \leq 0.05$) for all but the two longest (2- and 3-h) durations. The increasing trends in extreme rainfall intensity are consistent with the increasing trends in frequency of extreme rainfall in Hong Kong (Ginn et al., 2010; Wong et al., 2011). The increasing trend is mostly due to the abrupt change in 1991/1992. The 39 gauges are unevenly distributed with more than half located in Hong Kong Island while none in Lanton Island. As a result, the 39-gauge unweighted means may be skewed by those on Hong Kong Island. **Figure 2** shows considerable differences among the values at different gauges, which suggests large spatial variability in the annual maximum rainfall values. As expected, the spatial standard deviations are proportional to the mean values that increases with the length of accumulation duration.

To access the domain averaged results, Empirical Orthogonal Function (EOF) analysis is performed and the results are shown in **Figure 4** for the 5-min accumulation duration. The total variances explained by the first EOF mode (EOF1) range from 32.8% for the 5-min accumulation to 55.0% for the 3-h accumulation. Although the values are all positive across the entire domain, there are several localized maxima and the largest one is in the New Territories near gauge N14 (**Figure 4A**). An abrupt change of the EOF1 time series also occurred in 1991/1992 (**Figure 4B**). As such, the above domain-averaged results can reflect the common feature of annual maxima of rainfall at the 39 gauges. To further determine the abrupt change signal, we examine the time series of annual maxima of 5-min accumulated rainfall for each gauge. More than half (22) of the 39 gauges, which are scattered in different regions, show a similar abrupt change point in the early 1990s. Similar results from EOF analysis and analysis of individual gauge data are found for other 5 durations. It is, therefore, certain that there exists an abrupt change in the annual maxima of rainfall with accumulation duration up to 3 h in Hong Kong. Although the analysis here is limited to accumulation durations up to 3 h, it is highly likely that this finding can be extended to longer durations.

While changes in the intensity of extreme precipitation described by the annual maxima of rainfall accumulation over the respective period is an important factor to consider for flood control, changes in the frequency of extreme precipitation is equally important for such application. **Figure 5** shows the time series of domain-averaged occurrence of extreme events when rainfall amount accumulated over a given duration is above the 99th percentile of all events for the given duration over the 27-year period. The frequency time series (**Figure 5**) are significantly correlated with their respective intensity time series (**Figure 2**), with correlation coefficients varying in a narrow range from 0.59 for the 2-h accumulation to 0.68 for the 10-min accumulation ($p \leq 0.05$). An abrupt change occurred in 1992/1993 based on the MK test (Not shown). Similar to the intensity time series, the frequency time series also have upward trends with slopes of 11.1, 6.1, 2.5 yr^{-1} for 5-, 10-, and 30-min accumulations, and 1.4, 0.8, and 0.6 yr^{-1} for 1-, 2-, and 3-h accumulations, respectively. But different from the intensity trends that are statistically significant for all but the two longest durations (2 and 3 h), the frequency trends are significant for all but the two shortest durations (5 and 10 min). An increasing trend in the occurrence of extreme precipitation is also found in previous studies (Ginn et al., 2010; Wong et al., 2011) that only included 1-h accumulation. Similarly to the intensity trends, the frequency trends also result from a manifestation of an abrupt change point.

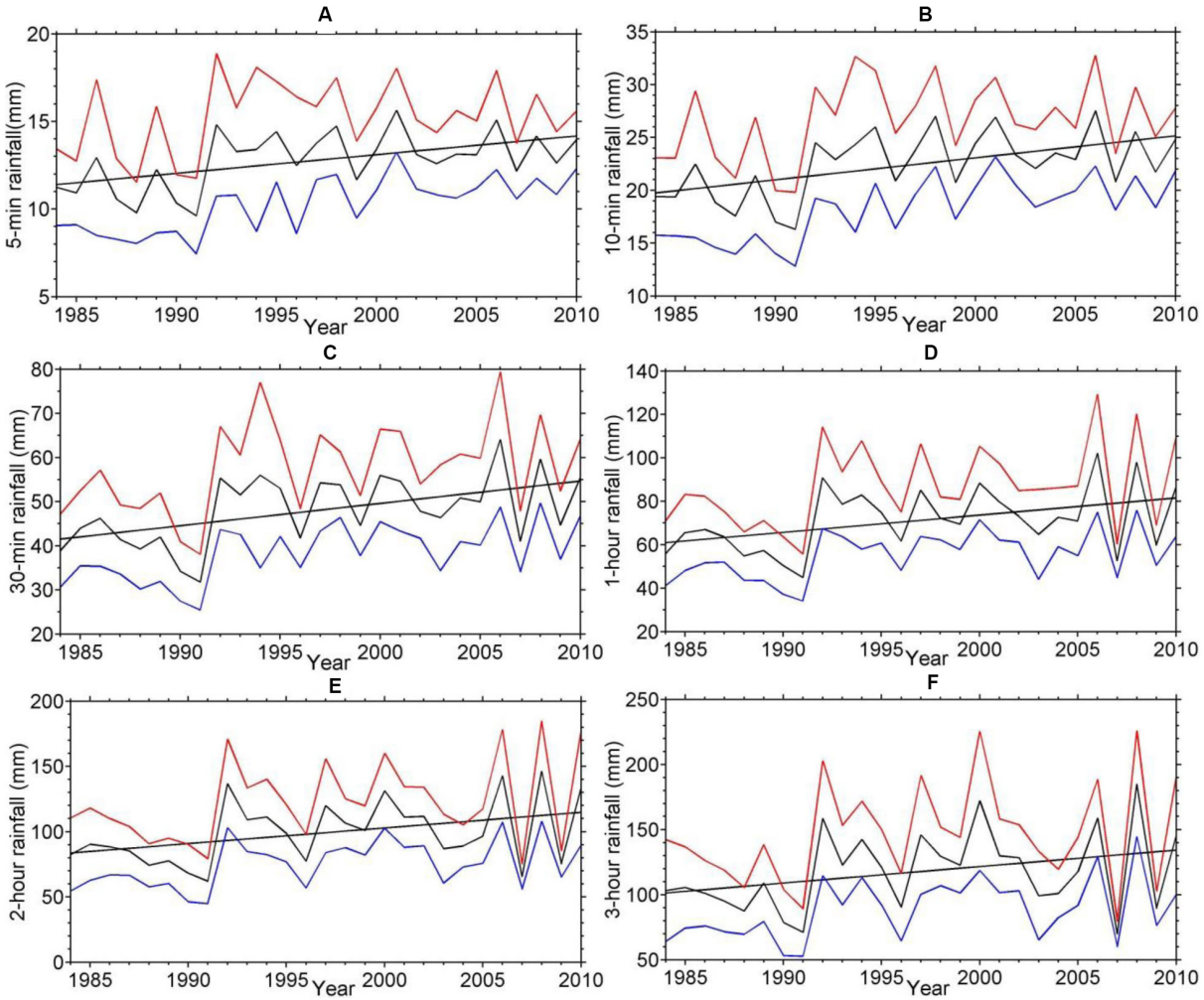

FIGURE 2 | Time series (black lines) and trends (straight black lines) of domain-averaged annual maxima of rainfall accumulations over 5 min **(A)**, 10 min **(B)**, 30 min **(C)**, 1 h **(D)**, 2 h **(E)**, and 3 h **(F)** for the period of 1984 to 2010. The red and blue lines denote the 39-station mean value plus and minus one 39-station standard deviation, respectively.

The aforementioned results indicate that an abrupt change in both the intensity and frequency of occurrences of short-duration (<3 h) extreme precipitation events in Hong Kong occurred in the early 1990's, with more frequent and stronger extreme precipitation following the change.

Because annual rainfall in Hong Kong usually peaks in summer, a composite analysis of summertime (JJA) atmospheric variables is performed to explore the cause for the abrupt change in the early 1990s. The 27 years in the study period are separated into two groups, the years prior to 1992 and the years afterward, which correspond to weak and less frequent extreme precipitation events and stronger and more frequent extreme precipitation events, respectively. At each grid point in the study domain, a mean value is calculated for each of the two groups and the differences between the means are examined. Similar composite analysis method was also utilized to examine an inter-decadal change of the East Asian summer monsoon (EASM) for which the abrupt changing point is 1993/1994 (Zhang et al., 2017; Zhu et al., 2018).

The western Pacific subtropical high (WPSH) is one important component of the EASM system (Tao and Chen, 1987; Ding, 1994) and its intensity and location dominates the distribution and strength of summer rainfall in southeast China (Tao and Xu, 1962; Huang, 1963) including Hong Kong. A comparison of the WPSH strengths between the two groups (**Figure 6A**) shows that WPSH is stronger and extends more westwards for 1992–2010 than for 1984–1991 (**Figure 6A**). Consistent with the westward extension of the summertime WPSH is an anomalous 850 hPa anticyclonic circulation over the western Pacific Ocean and South China Sea (**Figure 7A**). The anomalous southwesterly winds from the South China Sea brings moisture-laden air to Hong Kong (**Figure 6B**), providing an environment favorable for the occurrence of intense extreme rainfall.

In addition to ample moisture, strong dynamical lifting is also necessary for extreme rainfall. The difference in the 500-hPa

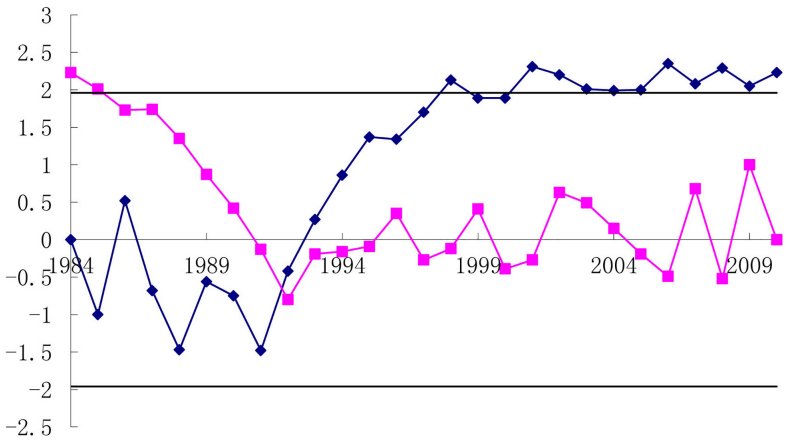

FIGURE 3 | The statistical lines of the Mann-Kendall (MK) (Mann, 1945) abrupt change test for the time series of domain-averaged annual maxima of rainfall with 5-min accumulation in **Figure 2A**. The black solid straight lines denote 95% confidence levels. The vertical axis is the statistical value calculated by the statistical variables of UB (pink lines) and UF (blue lines) according to MK method.

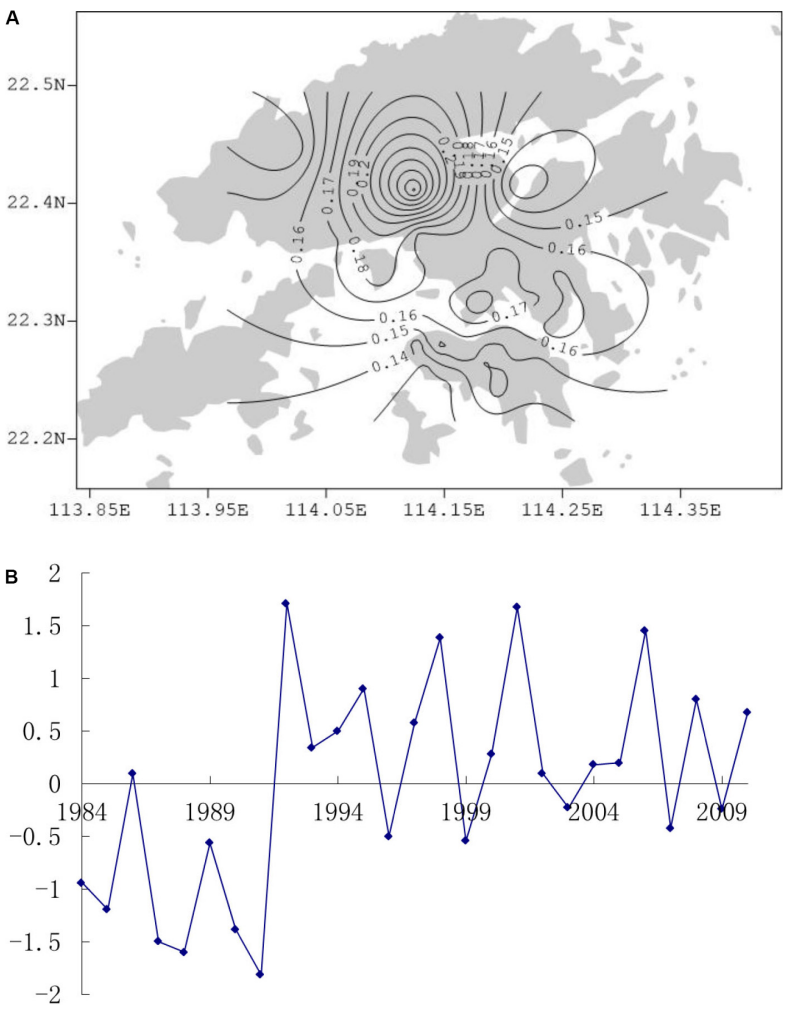

FIGURE 4 | The spatial pattern **(A)** and normalized time series **(B)** of the first EOF mode for annual maxima of 5-min rainfall. The values in **(A)** (unit: decimeter) shows the response of annual maxima for each station to the change of one standard variation of the normalized time series **(B).**

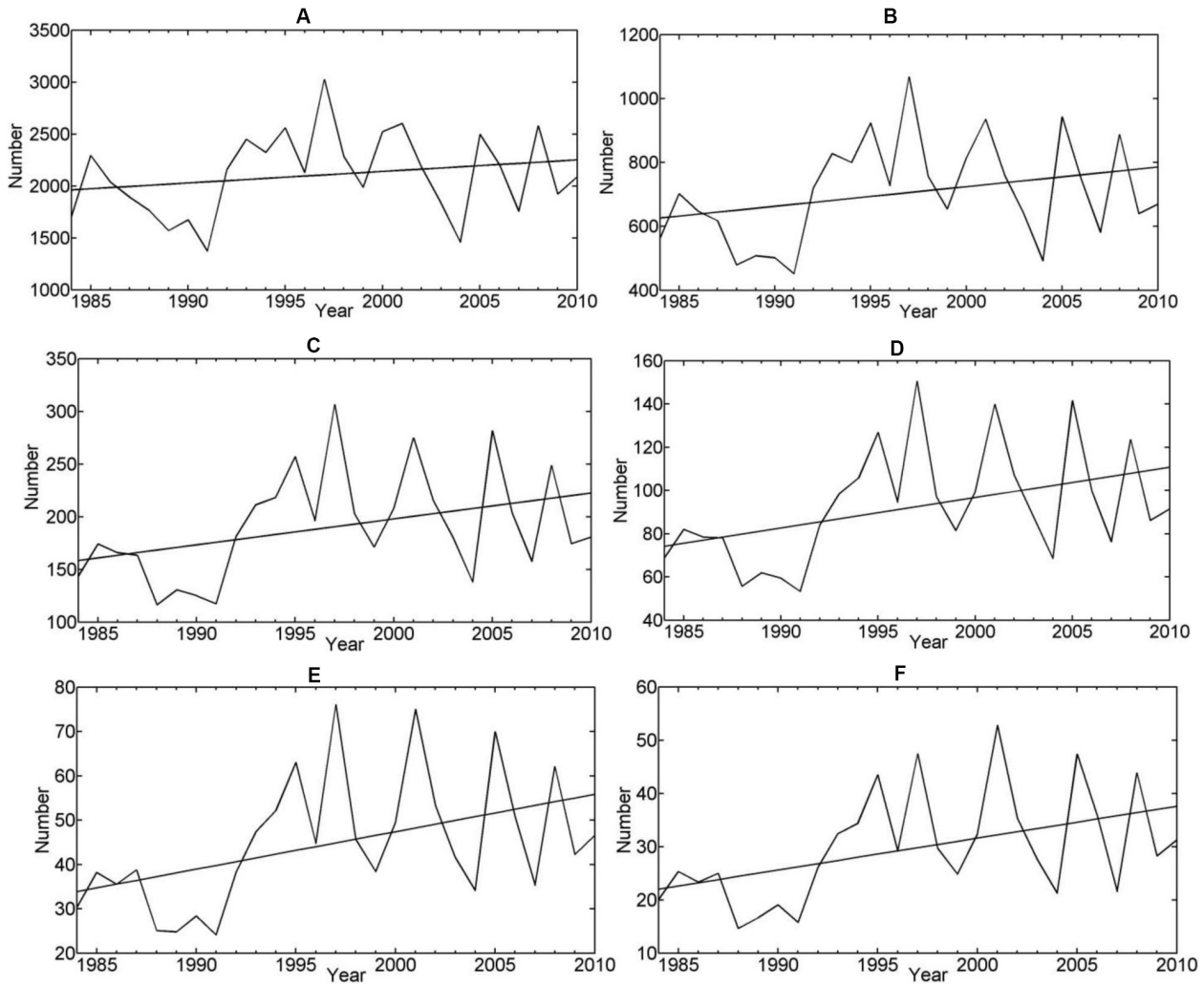

FIGURE 5 | Time series and trends of domain-averaged number of extreme rainfall accumulations over 5 min **(A)**, 10 min **(B)**, 30 min **(C)**, 1 h **(D),** 2 h **(E),** and 3 h **(F)** using the 99th percentile threshold for the period of 1984 to 2010.

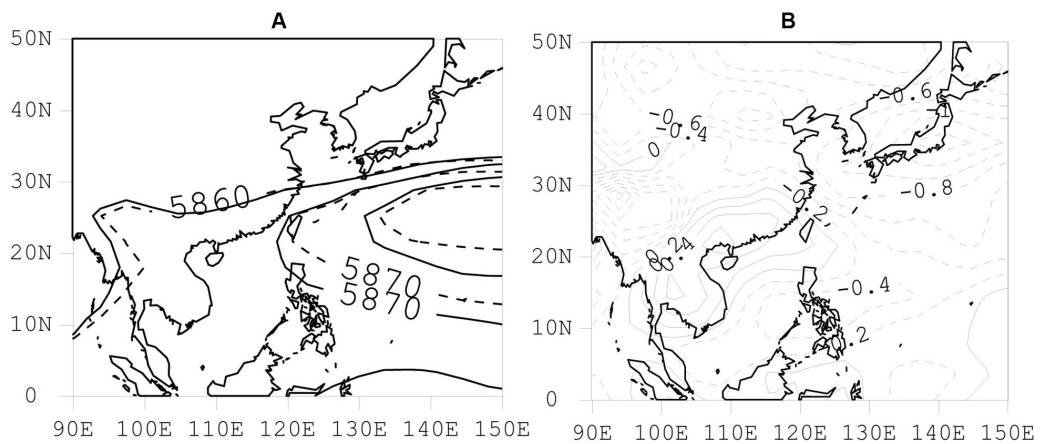

FIGURE 6 | Locations of summertime mean 5870-gpm isoline at 500 hPa for the period of 1984–1991 (dash line) and 1992–2010 (solid line) **(A)**, and the difference of low-level (1000–700 hPa) specific humidity (g/kg) between 1992–2010 and 1984–1991 **(B)**.

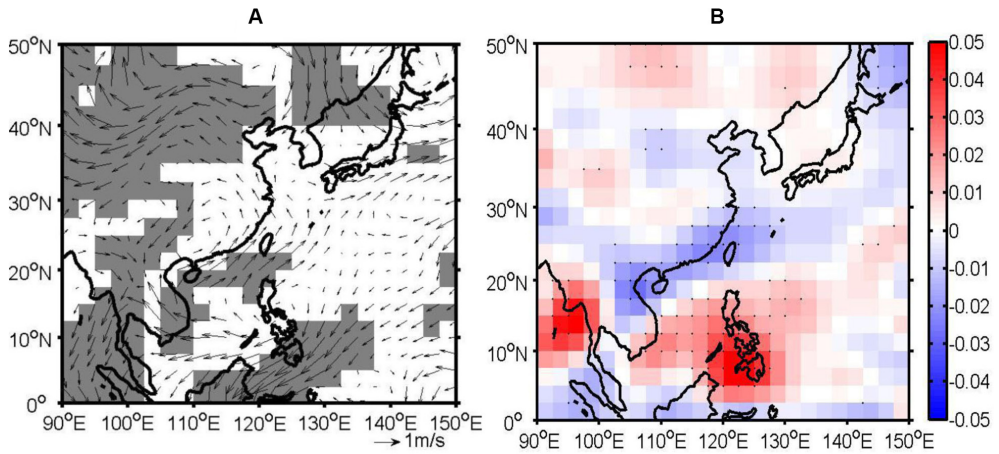

FIGURE 7 | Differences between the 1992–2014 and 1984–1991 means of 850-hPa wind **(A)** and 500-hPa vertical velocity (Pa/s) **(B)**. The shaded and dotted regions indicate the regions with above 95% confidence level using the Student' *t*-test.

omega field between the two groups are negative along Southeast China coasts (**Figure 7B**), which indicates stronger rising motion during 1992–2010 than during 1984–1991. The stronger lifting of moisture-laden air contributes to the increase in the frequency and intensity of extreme precipitation over Hong Kong. Over the South China Sea and the Philippines, positive difference in the omega field indicates stronger sinking motion associated with the stronger WPSH in these regions.

The above results suggest that the changes in the intensity and frequency of extreme precipitation in Hong Kong between the earlier (1984–1991) and later (1992–2010) periods are consistent with the changes in atmospheric conditions resulting from the westward extension along with a slight intensification of the summertime WPSH. Hu (1997) and Zhou et al. (2009) found the westward extension of WPSH on an interdecadal time scale may be related to the Indian Ocean-western Pacific warming. Although positive SST differences occur over the tropical Indian Ocean and tropical western Pacific Ocean (**Figure 8A**), there is no significant negative OLR, a proxy for convection in tropical and subtropical oceans, over the tropical eastern Indian Ocean and western Pacific Ocean, indicating few convective activities there (**Figure 8B**). The positive SST differences over the tropical eastern Indian Ocean and western Pacific Ocean may result from the changes in radiation related to significant downward motion (**Figure 7B**) induced by the westward extension of WPSH. Rodwell and Hoskins (2001) found that diabatic heating related to the South-Asian-summer-monsoon rainfall could increase the strength of the WPSH. The convective activities over the tropical western Indian Ocean (**Figure 8A**) may help westward extension of WPSH. In summer season, there are three monsoon circulations: the transverse monsoon, the lateral monsoon and the Walker circulation (Webster et al., 1998). The transverse monsoon circulation over the Indian Ocean is associated with a subsidence (ascent) over the western (eastern) tropical Indian Ocean and East Africa (the Maritime Continent). The increased (weakened) convective activities over the western Indian Ocean (the eastern Indian Ocean and the western Pacific Ocean) (**Figures 7B**, **8B**) can decrease the strength of the transverse circulation over the Indian Ocean, thus leading to the positive WPSH anomalies (Wu and Zhou, 2008). In addition, the large negative OLR differences over the southeastern China and northern South China Sea indicate stronger convective development and positive rainfall there after 1991 than before 1991, which also help the occurrence of stronger annual extreme rainfall.

Finally, putting the regional changes between the two periods into the perspective of changes in large-scale circulations, the differences in the 500-hPa geopotential height field are characterized by a Rossby wavetrain with positive values over Europe, northern China, western and eastern North Pacific Ocean, southern and northeastern North America and southern North Atlantic Ocean and negative anomalies over western Asia, Japan, central North Pacific Ocean, central North America and eastern North Atlantic Ocean (**Figure 9**). Similar pattern is also found in the 200 hPa geopotential height difference map (not shown). The wavetrain is similar to the positive phase of the circumglobal teleconnection (CGT) pattern in the northern hemisphere summer (Ding and Wang, 2005; Ding et al., 2011). The positive height difference over the western Pacific Ocean strengthens the WPSH. The negative height difference over western India indicates more convective activities and monsoon rainfall. Ding and Wang (2005) and Ding et al. (2011) related the CGT pattern in summer to Indian monsoon rainfall anomalies. As such, the positive phase of the CGT related to stronger Indian monsoon also helps strengthen the WPSH and extend it more westward.

SUMMARY AND DISCUSSION

Using data from a 39-gauge network across Hong Kong, we examined the trends in both the intensity and frequency of short-duration (5, 10, 30 min and 1, 2, 3 h) rainfall extremes over the period 1984–2010.

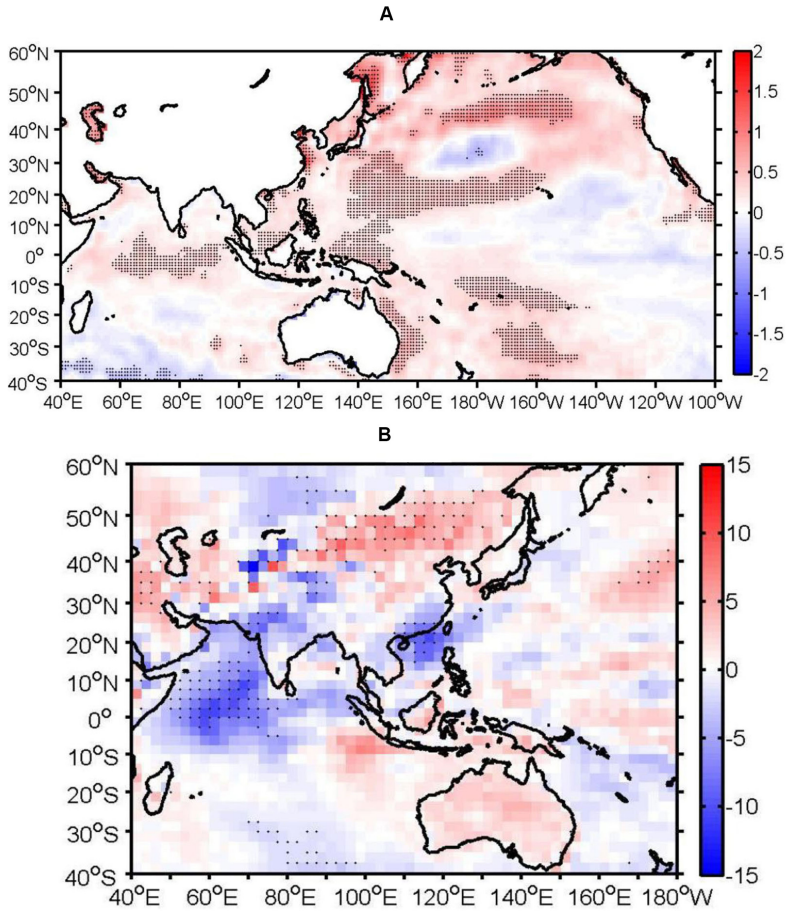

FIGURE 8 | Differences between the 1992–2014 and 1984–1991 means of sea surface temperature (SST) (°C) **(A)** and Outgoing Longwave Radiation (OLR) (W/m^2) **(B)**. The dotted regions indicate the regions with above 95% confidence level using the Student' *t*-test.

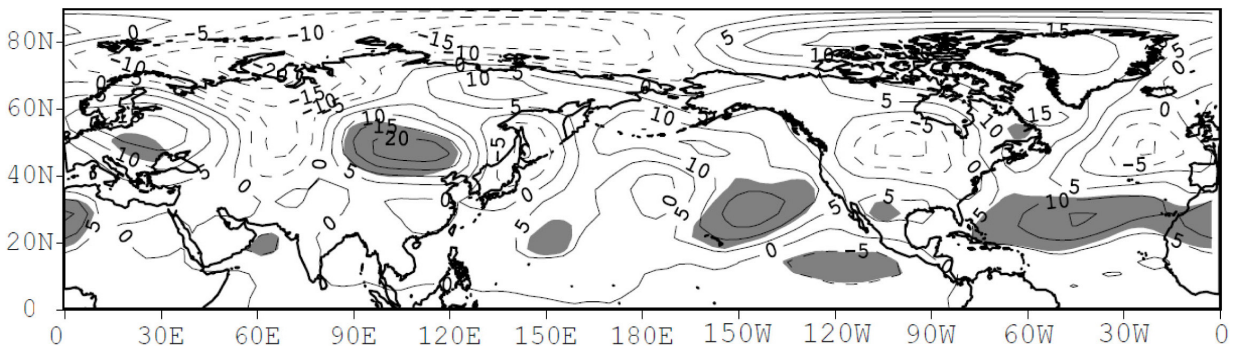

FIGURE 9 | Differences between the 1992–2014 and 1984–1991 means of summertime 500-hPa geopotential height (gpm). The shaded regions indicate the regions with above 95% confidence level using the Student' *t*-test.

Averaging across the gauge network, the intensity and frequency of precipitation extremes exhibit an upward trend. The intensity trend is statistically significant for all but the two longest durations (2 and 3 h) and the slope of the trend increases as the duration increases. An opposite relation is seen between the frequency trend and the length of the duration. The upward trend over the 27-year period appears to be a manifestation of an abrupt change near the beginning of 1990s that separates a period of lower and fewer precipitation extremes before, from a period of higher and more extremes after, which suggests that the use of linear trend analysis may not be appropriate.

The increases in the intensity and frequency of extreme precipitation in Hong Kong after the early 1990s is linked, through composite analyses, to strengthening and westward shift of the western Pacific subtropical high and the associated anticyclonic motion that enhances the transport of moisture-laden air as well as rising motion over Hong Kong – the two ingredients for strong convective activities responsible for extreme precipitation. The westward shift of the western Pacific subtropical high is related to the anomalous convective activities over the tropical western Indian Ocean and a positive phase circumglobal teleconnection 500 hPa wavetrain. The inter-decadal variability of extreme precipitation in Hong Kong is consistent with the inter-decadal change of the East Asian summer monsoon (EASM) (Zhang et al., 2017; Zhu et al., 2018), but the exact change point is different. The abrupt change point for EASM is 1993/1994, the same change point for the mean summer rainfall in Hong Kong (not shown), but the changes in extreme precipitation in Hong Kong occurred 2 years earlier round 1991/1992 for intensity and 1 year earlier around 1992/1993 for frequency. It is unclear what caused these small shifts in the exact year of change, which can be a topic of future investigation. Despite the small differences in the exact change point, the similar inter-decadal variability between the extreme precipitation and EASM suggests that extreme precipitation in Hong Kong is strongly linked to monsoon precipitation, not to typhoon precipitation that, according to Chang et al. (2012), did not exhibit a similar pattern of inter-decadal variability. Kajikawa and Wang (2012) and Xiang and Wang (2013) documented an abrupt change of South China Sea summer onset in 1993/1994. The summertime rainfall in Hong Kong also performs an abrupt change in 1993/1994 (not shown). The reason of the difference between the two abrupt years also needs to be further investigated.

Previous studies usually presumed the role of anthropogenic global warming in increasing extreme precipitation. For example, Wong et al. (2011) also noted the increasing trends in the frequency of occurrence of extreme 1-, 2-, and 3-h rainfall amounts from 1885 to 2008. They simply attributed the increasing trends to global warming and did not consider the impact from the natural factors. Our results suggest that natural variability could potentially be a significant driver for the increasing intensity and frequency of extreme precipitation in recent decades. Another active debate is on the relative role atmospheric thermodynamic and dynamic processes play in the changes of extreme rainfall. Pfahl et al. (2017) noted that an increase in atmospheric upward vertical motion, a dynamic process, makes the most contribution to annual daily maximum precipitation in the Asian monsoon region. Their results agree with our conclusion, though they focused on daily rainfall amount. Our conclusions offer some insights into processes that could subsequently be used to develop a predictive tool for occurrence of sub-daily extreme precipitation, especially those of less than 3 h that are mostly responsible for flash floods.

DATA AVAILABILITY STATEMENT

The original contributions presented in the study are included in the article/supplementary materials, further inquiries can be directed to the corresponding author.

AUTHOR CONTRIBUTIONS

LY analyzed the data and wrote the manuscript. SZ revised the manuscript. YQ and XL offered the suggestion.

FUNDING

This study was supported by the National Key R&D Program of China (Nos. 2017YFE0111700 and 2019YFC1509102).

ACKNOWLEDGMENTS

The authors thank the Geotechnical Engineering Office (GEO) of Civil Engineering and Development Department in Hong Kong for 5-min rainfall data at 39 rain gauges and NCEP for the global reanalysis data.

REFERENCES

Ahern, M., Kovats, R. S., Wilkinson, P., Few, R., and Matthies, F. (2005). Global health impacts of floods: epidemiologic evidence. *Epidemiol. Rev.* 27, 36–46. doi: 10.1093/epirev/mxi004

Alexander, L. V. (2016). Global observed long-term changes in temperature and precipitation extremes: a review of progress and limitations in IPCC assessments and beyond. *Weather Clim. Extre.* 11, 4–46. doi: 10.1016/j.wace.2015.10.007

Blenkinsop, S., Fowler, H. J., Barbero, R., Chan, S. C., Guerreiro, S. B., Kendon, E., et al. (2018). The INTENSE project: using observations and models to understand the past, present and future of sub-daily rainfall extremes. *Adv. Sci. Res.* 15, 117–126. doi: 10.5194/asr-15-117-2018

Brown, S. J. (2018). The drivers of variability in UK extreme rainfall. *Int. J. Climatol.* 38, e119–e130. doi: 10.1002/joc.5356

Chang, C.-P., Lei, Y., Sui, C.-H., Lin, X., and Ren, F. (2012). Tropical cyclone and extreme rainfall trends in East Asian summer monsoon since mid-20th century. *Geophys. Res. Lett.* 39:L18702.

Ding, Q., and Wang, B. (2005). Circumglobal teleconnection in the Northern Hemisphere summer. *J. Clim.* 18, 3483–3505. doi: 10.1175/jcli3473.1

Ding, Q., Wang, B., Wallace, J. M., and Branstator, G. (2011). Tropical-extratropical teleconnections in boreal summer: observed interanual variability. *J. Clim.* 24, 1878–1896. doi: 10.1175/2011jcli3621.1

Ding, Y. H. (1994). *Monsoons Over China*. Dordrecht: Kluwer Academic.

Donat, M. G., Alexander, L. V., Herold, N., and Dittus, A. J. (2016). Temperature abd precipitation extremes in century-long gridded observations, reanalyses, and atmospheric model simulations. *J. Geophys. Res. Atmos.* 121, 11174–11189. doi: 10.1002/2016JD025480

Easterling, D. R., Evans, J. L., Groisman, P. Y., Karl, T. R., Kunkel, K. E., and Ambenje, P. (2000). Observed variability and trends in extreme climate events: a brief review. *Bull. Am. Meteorol. Soc.* 81, 417–425. doi: 10.1175/1520-0477(2000)081<0417:ovatie>2.3.co;2

Evans, N. C., and Yu, Y. F. (2001). *Regional Variation in Extreme Rainfall Values, GEO Report No.115*. Hong Kong: Geotechnical Engineering Office.

Ghosh, S., Das, D., Kao, S. C., and Ganguly, A. R. (2012). Lack of uniform trends but increasingspatial variability in observed Indian rainfall extremes. *Nat. Clim. Change* 2, 86–91. doi: 10.1038/nclimate1327

Ginn, W.-L., Lee, T.-C., and Chan, K.-Y. (2010). Past and future changes in the climate of Hong Kong. *Acta Meteor. Sinica* 24, 163–175.

Hu, Z.-Z. (1997). Interdecadal variability of summer climate over East Asia and its association with 500 hPa height and global sea surface temperature. *J. Geophys. Res.* 102, 19403–19412. doi: 10.1029/97jd01052

Huang, S. S. (1963). Longitudinal movement of the subtropical anticyclone and its prediction (in Chinese). *Acta Meteorol. Sin.* 33, 320–332.

Iwashima, T., and Yamamoto, R. (1993). A statistical analysis of the extreme events: long-term trend ofheavy precipitation. *J. Meteor. Soc. Japan* 71, 637–640. doi: 10.2151/jmsj1965.71.5_637

Jones, M. R., Fowler, H. J., Kilsby, C. G., and Blenkinsop, S. (2013). An assessment of changes in seasonal and annual extreme rainfall in the UK between 1961 and 2009. *Int. J. Climatol.* 33, 1178–1194. doi: 10.1002/joc.3503

Kajikawa, Y., and Wang, B. (2012). Interdecadal change of the South China Sea summer monsoon onset. *J. Clim.* 25, 3207–3218. doi: 10.1175/jcli-d-11-00207.1

Kalnay, E., Kanamitsu, M., Kistler, R., Collins, W., Deaven, D., Gandin, L., et al. (1996). The NCEP/NCAR 40-year reanalysis project. *Bull. Am. Meteorol. Soc.* 77, 437–471.

Kanamitsu, M., Ebisuzaki, W., Woollen, J., Yang, S.-K., Hnilo, J. J., Fiorino, M., et al. (2002). NCEP/DOE AMIP-Reanalysis (R-2). *Bull. Am. Meteorol. Soc.* 83, 1631–1643. doi: 10.1175/bams-83-11-1631(2002)083<1631:nar>2.3.co;2

Karl, T. R., Knight, R. W., Easterling, D. R., and Quayle, R. G. (1996). Indices of climate change for the United States. *Bull. Am. Meteorol. Soc.* 77, 279–291.

Kendon, E. J., Roberts, N. M., Fowler, H. J., Roberts, M. J., Chan, S. C., and Senior, C. A. (2014). Heavier summer downpours with climate changerevealed by weather forecast resolution model. *Nat. Clim. Change* 4, 570–576. doi: 10.1038/nclimate2258

Kistler, R., Kalnay, E., Collins, W., Saha, S., White, G., Woollen, J., et al. (2001). The NCEP-NCAR 50-year reanalysis: monthly means CD-ROM and documentation. *Bull. Am. Meteorol. Soc.* 82, 247–267. doi: 10.1175/1520-0477(2001)082<0247:tnnyrm>2.3.co;2

Kunkel, K. E., Changnon, S. A., and Angel, J. R. (1994). Climatic aspects of the 1993 upper Mississippi River basin flood. *Bull. Am. Meteorol. Soc.* 75, 811–822. doi: 10.1175/1520-0477(1994)075<0811:caotum>2.0.co;2

Lam, C. C., and Leung, Y. K. (1994). *Extreme Rainfall Statistics and Design Rainstorm Profiles at Selected Locations in Hong Kong. Hong Kong Observatory Technical Note* 86. Kowloon: Royal Observatory.

Liebmann, B., and Smith, C. A. (1996). Description of a complete (interpolated) outgoing longwave radiation dataset. *Bull. Am. Meteorol. Soc.* 77, 1275–1277.

Mann, H. B. (1945). Non-parametric test against trend. *Econometrika* 13, 245–259.

Manton, M. J., Della-Marta, P. M., Haylock, M. R., Hennessy, K. J., Nicholls, N., Chambers, L. E., et al. (2001). Trends in extreme daily rainfall and temperature in Southeast Asia and the South Pacific:1961-1998. *Int. J. Clim.* 21, 269–284. doi: 10.1002/joc.610

Min, S.-K., Zhang, Z., Zwiers, F. W., and Hegerl, G. C. (2011). Human contribution to more-intense precipitation extremes. *Nature* 470, 378–381. doi: 10.1038/nature09763

Mishra, V., Wallace, J. M., and Lettenmaier, D. P. (2012). Relationship between hourly extreme precipitation and local air temperature in the United States. *Geophys. Res. Lett.* 39:L16403. doi: 10.1029/2012GL052790

Mukherjee, S., Aadhar, S., Stone, D., and Mishra, V. (2018). Increase in extreme precipitation events under anthropogenic warming in India. *Weather Clim. Extre.* 20, 45–53. doi: 10.1016/j.wace.2018.03.005

Osborn, T. J., Hulme, M., Jones, P. D., and Basnett, T. A. (1999). Observed trends in the daily intensity of United Kingdom precipitation. *Int. J. Clim.* 20, 347–364. doi: 10.1002/(sici)1097-0088(20000330)20:4<347::aid-joc475>3.0.co;2-c

Pall, P., Allen, M. R., and Stone, D. A. (2007). Testing the Clausius-Clapeyron constraint on changes in extreme precipitation under CO2 warming. *Clim. Dynam.* 28, 351–363. doi: 10.1007/s00382-006-0180-2

Peterson, P., and Kwong, H. (1981). *A Design Rain Storm Profile for Hong Kong.* London: Royal Observatory.

Pfahl, S., O'Gorman, P. A., and Fischer, E. M. (2017). Understanding the regional pattern of projected future changes in extreme precipitation. *Nat. Clim. Change* 7, 423–427. doi: 10.1038/nclimate3287

Prein, A. F., Langhans, W., Fosser, G., Ferrone, A., Ban, N., Goergen, K., et al. (2015). A review on regional convection-permitting climate modeling: demonstrations, prospects, and challenges. *Rev. Geophys.* 53, 323–361. doi: 10.1002/2014RG000475

Rodwell, M. J., and Hoskins, B. J. (2001). Subtropical anticyclones and summer monsoons. *J. Clim.* 14, 3192–3211. doi: 10.1175/1520-0442(2001)014<3192:saasm>2.0.co;2

Simpson, I. R., and Jones, P. D. (2014). Analysis of UK precipitation extremes derived from met office gridded data. *Int. J. Climatol.* 34, 2438–2449. doi: 10.1002/joc.3850

Smith, T. M., Reynolds, R. W., Peterson, T. C., and Lawrimore, J. (2008). Improvements NOAAs historical merged land-ocean temp analysis (1880-2006). *J. Clim.* 21, 2283–2296. doi: 10.1175/2007jcli2100.1

Suppiah, R., and Hennessy, K. (1998). Trends in seasonal rainfall, heavy rain-days, and number if dry days in Australian 1910-1990. *Int. J. Climatol.* 18, 1141–1151.

Tang, C. S. C., and Cheung, S. P. Y. (2011). *Frequency Analysis of Extreme Rainfall Values. GEO Report No.* 261. Kowloon: Geotechnical Engineering Office, Civil Engineering and Development Department, 209.

Tao, S. Y., and Chen, L. X. (1987). "A review of recent research on the East Asian summer monsoon in China," in *Monsoon Meteorology, Oxford Monogr. On Geology and Geophysics*, Vol. 7, eds P. Chang and T. N. Krishnamurti (Oxford: Oxford University Press).

Tao, S. Y., and Xu, S. Y. (1962). Circulation characteristics in association with persistent summer drought and flood in the Yangtze-Huaihe River reaches. *Acta Meteorol. Sin.* 32, 1–18.

Tarhule, S., and Woo, M. (1998). Changes in rainfall characteristics in northern Nigeria. *Int. J. Climatol.* 18, 1261–1272.

Webster, P. J., Magaña, V. O., Palmer, T. N., Shukla, J., Tomas, R. A., Yanai, M., et al. (1998). Monsoons: processes, predictability, and the prospects for prediction. *J. Geophys. Res.* 103, 14451–14510.

Westra, S., Fowler, H. J., Evans, J. P., Alexander, L. V., Berg, P., Johnson, F., et al. (2014). Future changes to the intensity and frequency of short-duration extreme rainfall. *Rev. Geophys.* 52, 522–555. doi: 10.1002/2014RG000464

Wong, M. C., Mok, H. Y., and Lee, T. C. (2011). Observed changes in extreme weather indices in Hong Kong. *Int. J. Climatol.* 31, 2300–2311.

Wu, B., and Zhou, T. (2008). Oceanic origin of the interannual and interdecadal variability of the summertime western Pacific subtropical High. *Geophys. Res. Lett.* 35:L13701. doi: 10.1029/2008GL034584

Wu, M. C., Leung, Y. K., and Yeung, K. H. (2006). Projected change in Hong Kong's Rainfall in the 21st century. *Hong Kong Meterorl. Soc. Bull.* 15:644.

Xiang, B., and Wang, B. (2013). Mechanisms for the advanced Asian summer monsoon onset since the mid-to-late 1990s. *J. Clim.* 26, 1993–2009.

Yu, L., Zhong, S., Pei, L., Bian, X., and Heilman, W. E. (2016). Contribution of large-scale circulation anomalies to changes in extreme precipitation frequency in the United States. *Environ. Res. Lett.* 11:044003. doi: 10.1088/1748-9326/11/4/044003

Zhang, H., Wen, Z., Wu, R., Chen, Z., and Guo, Y. (2017). Inter-decadal changes in the East Asian summer monsoon and associations with sea surface temperature anomaly in the South Indian Ocean. *Clim. Dyn.* 48, 1125–1139. doi: 10.1007/s00382-016-3131-6

Zhou, T., Yu, R., Zhang, J., Drange, H., Cassou, C., Deser, C., et al. (2009). Why the western Pacific subtropical high has extended westward since the late 1970s. *J. Clim.* 22, 2199–2215.

Zhu, X.-C., Guo, Y.-Y., Zhang, H.-Y., Li, X.-Z., Chen, R.-D., and Wen, Z.-P. (2018). A southward withdrawal of the northern edge of the East Asian summer monsoon around the early 1990s. *Atmos. Oceanic Sci. Lett.* 11, 136–142. doi: 10.1080/16742834.2018.1410058

Conflict of Interest: The authors declare that the research was conducted in the absence of any commercial or financial relationships that could be construed as a potential conflict of interest.

frontiers in Environmental Science

ORIGINAL RESEARCH
published: 29 October 2020
doi: 10.3389/fenvs.2020.588570

Development of High Resolution and Homogenized Gridded Land Surface Air Temperature Data: A Case Study Over Pan-East Asia

Jiayi Cheng[1], Qingxiang Li[1]†, Liya Chao[1], Suman Maity[1], Boyin Huang[2] and Phil Jones[3]*

[1] Guangdong Province Key Laboratory for Climate Change and Natural Disasters, School of Atmospheric Sciences, Sun Yat-sen University, Guangzhou, China, [2] National Centers for Environmental Information, National Oceanic and Atmospheric Administration (NOAA), Asheville, NC, United States, [3] Climatic Research Unit, School of Environmental Sciences, University of East Anglia, Norwich, United Kingdom

OPEN ACCESS

Edited by:
Folco Giomi, University of Padua, Italy

Reviewed by:
Xander Wang, University of Prince Edward Island, Canada
Xuejie Gao, Institute of Atmospheric Physics (CAS), China

***Correspondence:**
Qingxiang Li
liqingx5@mail.sysu.edu.cn

†Present address:
Qingxiang Li, Southern Laboratory of Ocean Science and Engineering (Guangdong Zhuhai), Zhuhai, China

Specialty section:
This article was submitted to Interdisciplinary Climate Studies, a section of the journal Frontiers in Environmental Science

Received: *29 July 2020*
Accepted: *18 September 2020*
Published: *29 October 2020*

Citation:
Cheng J, Li Q, Chao L, Maity S, Huang B and Jones P (2020) Development of High Resolution and Homogenized Gridded Land Surface Air Temperature Data: A Case Study Over Pan-East Asia. Front. Environ. Sci. 8:588570. doi: 10.3389/fenvs.2020.588570

The Land Surface Air Temperature (LSAT) climatology during the period of 1961–1990 and the anomalies (relative to the 1961–1990 climatology) have been developed over Pan-East Asian region at a (monthly) 0.5° × 0.5° resolution. The development of these LSAT data sets are based on the recently released C-LSAT station datasets and the high resolution Digital Elevation Model (DEM), and interpolated by the Thin Plate Spline (TPS) method (through ANUSPLIN software) and the Adjusted Inverse Distance Weighting (AIDW) method. Then they are combined into the high resolution gridded LSAT datasets (including the monthly mean, maximum, and minimum temperature). Considering the mean LSAT for example, the Cross Validation (CV) of the datasets indicates that the regional average of the Root Mean Square Error (RMSE) for the climatology is about 0.62°C, and the average RMSE and Mean Absolute Error (MAE) for the anomalies are between 0.47–0.90°C and 0.32–0.63°C during the study period. The analysis also demonstrate that the gridded anomalies describe the spatial pattern fairly well for the coldest (1912, 1969) and the warmest (1948, 2007) years during the first and second half of the 20th century. Further analysis reveals that the high resolution dataset also performs well in the estimation of long-term LSAT change trend. Thus it can be concluded that this newly constructed datasets is a useful tool for regional climate monitoring, climate change research as well as climate model verification.

Keywords: land surface air temperature (LSAT), thin plate spline (TPS), adjusted inverse distance weight (AIDW), high resolution, gridded dataset

INTRODUCTION

Land Surface Air Temperature (LSAT) is considered one of the important indicators of the global and regional climate change. Many studies have shown that the global LSAT change can greatly impact on human being as well as the social and economic society (Köppen, 1931; Callendar, 1938, 1961; Hawkins and Jones, 2013). Major issues in studying the LSAT variations and change are associated with the inconsistency in observing times, uneven spatial distribution of LSAT stations, differences in statistical methods, and the quality of the observational data over global

or continental regions at century scale. To resolve these issues, scientists developed homogenized station datasets and converted them into gridded datasets for the convenience of applications (Hutchinson, 1991; Daly et al., 1994; Li and Li, 2007; Xu et al., 2009). For global large-scale climate temperature trend estimation using low-resolution datasets (normally in 5° × 5° resolution to avoid changes at small scales) (Jones and Briffa, 1992; Peterson and Vose, 1997; Hansen et al., 1999; Li et al., 2017; Xu C. et al., 2018; Yun et al., 2019) can basically meet the accuracy requirements. For example, a consistent outcome from available low-resolution data sets is that the global land temperature trend since 1880 has become more and more significant (Li et al., 2020).

In contrast, high-resolution datasets (both the climatology and the anomaly time series) are widely and urgently needed (Huang et al., 2020; Xu et al., 2020) for research in climate change monitoring and climate model validation and development in regional/local scales. However, it is not easy to develop a high-resolution global and regional datasets due to the problems such as the uneven distribution and difference in the length of observation records. New et al. (1999a,b) used the Thin Plate Spline (TPS) method and angular weighting method to develop the first relatively high-resolution (0.5° × 0.5°) global LSAT climatology and anomaly dataset based on the CRU (Climatic Research Unit) LSAT station dataset, and the Climate Research Unit gridded Time series (CRU TS) has been produced and shared openly to facilitate research and analysis in all areas related to climate and climate change since the first version was released in 2000. CRU TS Version 4 (CRU TS4) is the first major update since version 3 was published in 2013 (Harris et al., 2020). The US Berkeley Earth Program team developed LSAT climatology and anomaly dataset at high-resolution (1.0° × 1.0°) – Berkeley Earth Surface Temperature (BEST) using Kriging and Inverse Distance Weighting (IDW) methods (Rohde et al., 2013). Besides, Hijmans et al. (2005) developed a global (excluding the Antarctic) high resolution climatology datasets of 1 km × 1 km resolution from 1950 to 2000, and they concluded that the use of the digital elevation model (DEM) is necessary when developing high-resolution grid data; and Fick and Hijmans (2017) further updated the datasets from 1970 to 2000 in some regions by using satellite observations and elevation data as covariates, and upgraded a new high-resolution datasets (also in 1 km × 1 km resolution). In addition, observational stations are relatively sparse in some regions in Asia (Tibet Mountains), South America, Africa, etc., and data before 1950 is relatively limited. The records in these regions are very precious for global climate change studies, while the sparse observations sometimes resulted in deficiencies in describing regional climate and climate change with the global high-resolution datasets (Li et al., 2007). Therefore, with the continuous improvement of data collection and data quality, it is inevitable to develop new high-quality global climate datasets.

Various high-resolution climate datasets at the regional scale have been developed in many countries in recent years. These countries include China (Hong et al., 2005; Xie et al., 2007; Yatagai et al., 2009; Wu and Gao, 2013; Peng et al., 2019; Huang et al., 2020; Xu et al., 2020), India (Sinha et al., 2006), Southeast Asia (Van den Besselaar et al., 2017), Europe (Nynke et al., 2009), the United States (Price et al., 2004), Australia (Hutchinson, 1991), etc., which provide good supports to climate change research at regional scales. However, there exist some obvious difference in accuracy due to the different station number, data quality control and homogenization processing in the basic dataset used by each developer. Moreover, the high-resolution datasets are sometimes difficult to be developed at the continental or global scales due to different processing methods or parameterization schemes. Some high-resolution datasets emphasized the improvement of the spatial distribution of stations but did not make the necessary assessments for the inhomogeneity due to the station number changes, which will have problems in long-term climate change trend detection (Li et al., 2007). Therefore, it is of vital importance to enhance the collection of the station data and the in-depth evaluation of the data accuracy in some regions with few observations, such as South America, Antarctica and Africa for the existing global dataset; and it is also important to develop new high quality, global, high-resolution climate datasets.

The ultimate goal of this study is to develop a global high-resolution gridded LSAT data set based on C-LSAT, a monthly global LSAT dataset developed by Chinese scientists recently (Xu W. et al., 2018; Li et al., 2020). However, C-LSAT is only a 5° × 5° anomaly dataset used to determine the long-term changes of large-scale land surface air temperature. It is necessary to develop a new higher resolution (0.5° × 0.5°) dataset, which can describe the spatial details of LSAT change at smaller scales. In this manuscript, we take the pan-East Asian region as the research region, which has numerous stations and complex terrains (including coasts, large plateaus, basins, plains and undulating areas), to test our high-resolution gridding model, so as to provide a basis for the subsequent high-resolution gridding for global area.

The remainder of this paper is arranged as follows: Section "Data Sources and Methods" introduces the main data sources, interpolation methods and validation methods used to develop high resolution gridded LSAT datasets in this paper. The interpolation and validation results of climatology and anomaly data are presented in Sections "Climatology Interpolation" and "Interpolation and Validation of LSAT Anomaly," respectively. Section "Regional LSAT Warming Trends Analysis" discusses the regional warming trend with the newly interpolated LSAT anomaly data and the comparison with new CRU TS4 dataset. Section "Conclusion" provides final discussion and conclusions.

DATA SOURCES AND METHODS

Data Sources

In this study, the observational station data is derived from C-LSAT, a monthly global LSAT dataset developed by Chinese scientists recently (Xu W. et al., 2018). This dataset has been systematically homogenized and updated by Yun et al. (2019) and Li et al. (2020). The advantage of this dataset is that it has used more observational stations compared to other similar global datasets, and the elements include monthly mean 2 m air temperature (Tavg), daily maximum (Tmax), and

minimum (Tmin) temperature for the period from 1850 to 2019 (however, we only intercepts the data from 1901 to 2018 in this paper for analysis).

A rectangular region (10–60°N, 60–150°E, see **Figure 1** below) was selected to test interpolation methods used in this paper. The region encompasses the key areas affected by both the Indian and East Asian monsoon. From the topographic perspective, the region contains high-altitude areas of the Qinghai-Tibet Plateau, low-altitude plain areas of the middle and lower reaches of the Yangtze River, undulating terrain areas of southwest China and central Asia, and ocean areas of western Pacific and Indian Ocean. There are a total of about 2800 observational stations in this region, and the distribution of the stations is very uneven with few stations in some parts and dense coverage in others. The region is referred to as "Pan-East Asia" henceforth for interpolation experiments and validation.

Figure 1 shows the spatial distribution of the observational stations in the C-LSAT2.0 dataset in Pan-East Asia regions, and classifies the start year (SY) of the data series for each station. Many weather stations were established in India, Japan and other countries before 1930. The observation stations established in China before 1930 were mainly located in the eastern parts of the country, and most of them were built by meteorological enthusiasts or foreign missionaries (Li et al., 2020). A large number of basic and standard meteorological stations (currently about 825 stations) were set up after 1949. The Indochina peninsula has a relatively sparse density station network, and the stations with long data series are mainly located in coastal regions. Many stations have been built in Indochina peninsula and Korean peninsula after 1960, and the record length is relatively short.

Figure 2 shows the change of the station numbers in the Pan-East Asia regions during the period from 1901 to 2018 for the monthly LSAT, maximum and minimum temperature. Obviously, the station numbers of maximum and minimum temperature were less than those of average LSAT, but the overall change shape is similar.

Taking the average LSAT as an example, before the 1930s, the number of stations in Pan-East Asia was less than 500. From the 1930s to the 1960s, the number of stations gradually increased, especially from less than 800 stations in the 1950s to nearly 2,000 stations in the 1960s. The number of stations with records reached the peak and remains stable during the 1960s–1990s. In this period, the number of stations with observed data is the greatest, and the number of stations that can calculate the climatology and LSAT anomaly is also the greatest. This is why we choose 1961–1990 as the base period for calculating the climatology. Further decrease of the station number in recent years may be related to the lagging of data collection and sharing.

Altitude has a significant influence on the LSAT distribution at local scales, so the digital elevation model (DEM) is usually one of the most important factors to be considered in the interpolation of LSAT, especially climatological LSAT. Previous comparison (Ma and Li, 2006) showed that although the Shuttle Radar Topography Mission (SRTM) DEM30 (which is generally recognized as having higher global average accuracy) (Farr et al., 2007) has some advantages globally, there are a little more missing areas of SRTM DEM30 based on the radar mapping of the space shuttle in complex terrain areas such as the Tibet Plateau, resulting in lower accuracy than GTOPO30 (a global 30 arc-second elevation data) in these areas; In addition, it only includes the DEM between 60°N and 60°S. So in this

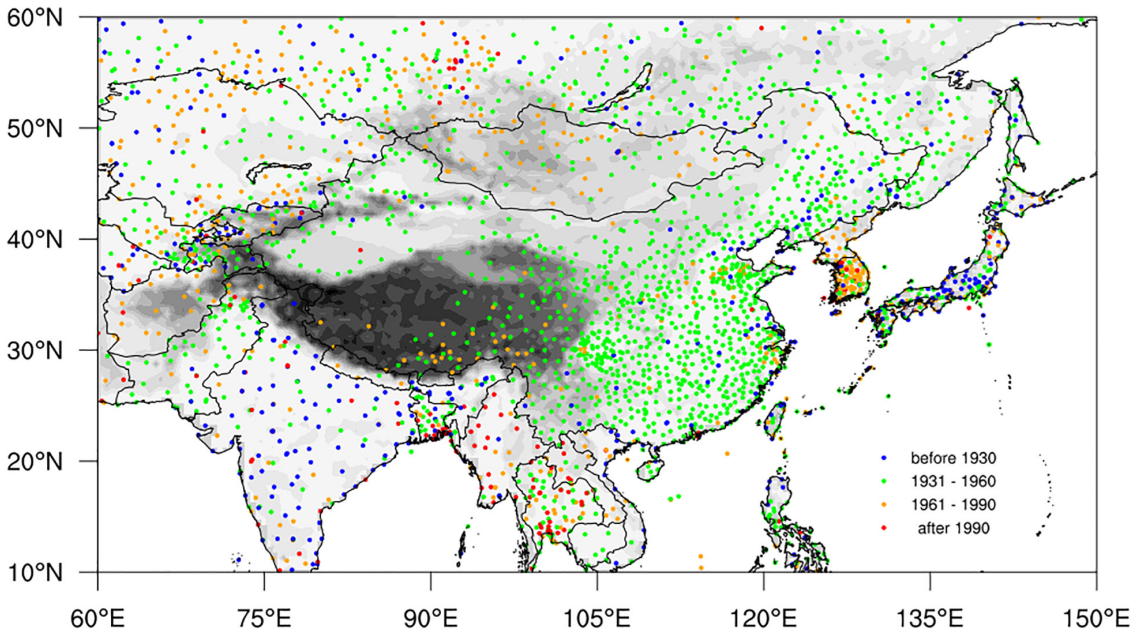

FIGURE 1 | Spatial distribution of the observational stations in the C-LSAT2.0 dataset in the Pan-East Asia regions. The different colored dots represent stations with different starting years (SY) of observations.

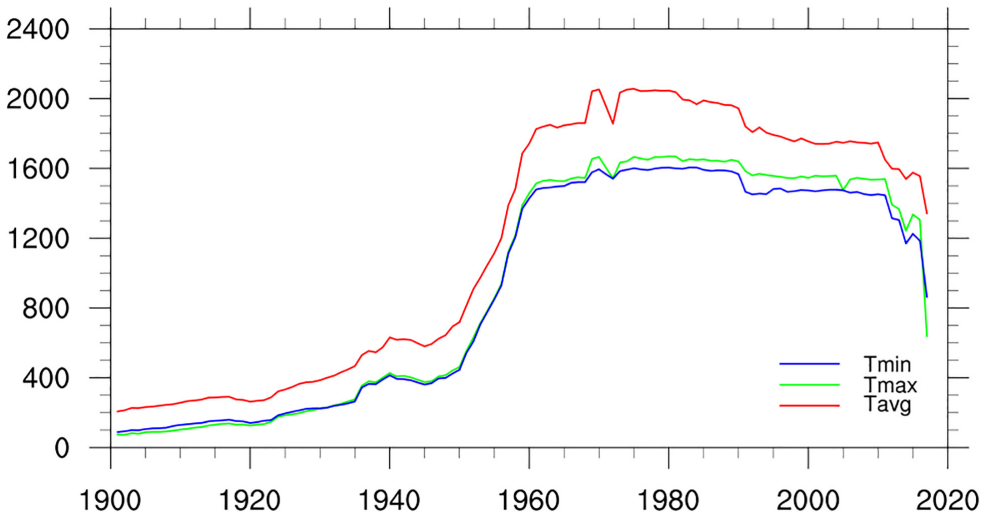

FIGURE 2 | The number of stations in gridding region over time.

paper, the GTOPO30 is still used for the interpolation of the LSAT including average, maximum, and minimum LSATs similar to Xu et al. (2020).

Interpolation Schemes and Methods

In the interpolation process, the spatial density and distribution of the observational stations have great influence on the results. Studies indicated that the direct use of absolute temperature data for long term and large area interpolation are not desirable (Li et al., 2007). A common method is first to interpolate climatology and anomaly separately, and then to merge the interpolated climatology and anomaly (New et al., 1999b; Haylock et al., 2008; Rohde et al., 2013).

Based on the above procedure, the LSAT data are divided into two parts: climatology (1961–1990 average) and anomaly. A three-step procedure was adopted to grid the LSAT data: (1) the effective station data are used for interpolation of the LSAT climatology field; (2) the interpolation of LSAT anomaly field using effective station anomaly series; and (3) the final grid dataset by adding up the climatology and the anomaly gridded dataset. This gridding approach is widely used by many climate data research groups to build global and regional dataset products. For example, the CRU TS1, TS2 and the Berkeley earth surface temperature (Berkeley Earth) used a similar approach to construct the LSAT grid datasets (New et al., 1999b; Rohde et al., 2013). In this study, we calculated the 1961–1990 averages of the stations for climatology where the effective data covers temporally no less than 20 years. Then the anomalies for the whole period are computed relative to this baseline period.

Thin-Plate Spline (TPS) Interpolation for Climatology

Using the stations during the climatological period, we interpolated them onto 0.5° × 0.5° grids with the elevation information data (GTOPO30) over Pan-East Asia as the covariates. The ANUSPLIN software package version 4.4 (Hutchinson and Xu, 2013) is used to interpolate the climatology in this paper. It is an efficient and useful tool for data transparent analysis and interpolation of multivariate data using the TPS method. It completes the process by providing comprehensive statistical analysis, data diagnostics, and spatial distribution standard errors, as well as support for multiple data inputs and multiple fitting surface outputs. The TPS method used in ANUSPLIN is a reliable way to develop the spatial interpolation of climate elements, which is widely used around the world (New et al., 1999a; Hijmans et al., 2005; Haylock et al., 2008). The partial TPS method is the core algorithm of ANUSPLIN, which was originally proposed by Wahba and Wendelberger (1980). Hutchinson applied the partial TPS to the spatial interpolation of the monthly mean climate variables (Hutchinson, 1991), and its theoretical statistical model is given as follows:

$$Z_i = f(x_i) + b^T y_i + e_i (i = 1, ..., N) \quad (1)$$

Where Z_i is the dependent variable with N observed data values; x_i is the spline independent variable as a multi-dimensional vector, and f is the unknown smooth function for the x_i; y_i is the independent covariate as a multidimensional vector, and b is the unknown coefficients for the y_i. Each e_i is an independent, zero mean error term with variance $w_i\sigma^2$, where w_i is termed the relative error variance and σ^2 is the error variance which is constant across all data points. It can be seen from equation (1) that: when there is no covariate, the second covariate item is ignored and the model turns back to an ordinary TPS model; on the other hand, when $f(x_i)$ is absent, the first independent item is removed and the model reduces to a simple multivariate linear regression model. In fact, the partial thin plate smoothing spline function can be understood as a generalized standard multivariate linear regression model, while its parameters are replaced by a suitable non-parameterized smooth function (Hutchinson, 1991).

The function f and the coefficient vector b are determined by minimizing

$$\sum_{i=1}^{N}\left(\frac{z_{\mathrm{i}}-f(x_{\mathrm{i}})-b^{\mathrm{T}}y_{\mathrm{i}}}{w_{\mathrm{i}}}\right)^{2}+\rho J_{\mathrm{m}}(f) \tag{2}$$

Where $J_m(f)$ is a measure of the complexity of f, the "roughness penalty" defined in terms of an integral of m'th order partial derivatives of f, and the smoothing parameter ρ is a positive number. As ρ approaches to zero, the fitted function approaches an exact interpolation. As ρ approaches to infinity, the function f approaches a least squares polynomial, with order depending on the order m of the roughness penalty. The value of the smoothing parameter is normally determined by minimizing a measure of predictive error of the fitted surface given by the generalized cross validation (GCV; Hutchinson, 1991). The GCV is provided as a predictive error estimate of interpolation by removing each data point and summing the square of deviation between each omitted value and the corresponding interpolation value (Xu et al., 2020). The Root Square of GCV (RGCV) is used to determine the optimum parameters for ANUSPLIN.

The TPS method is very popular because of its high efficiency and its ability to generate accurate predictions with a minimum of guiding covariates (Hutchinson, 1991; New et al., 1999a; Price et al., 2004; Hijmans et al., 2005; Hong et al., 2005; Xu et al., 2009). It is observed from the comparison with other methods such as Kriging (Rohde et al., 2013) and Prism (Daly et al., 2008) that TPS is more suitable for the interpolation of the LSAT for the selected region in and hence preferred for this study.

Interpolating Method for Anomaly

In this paper, a kind of Adjusted Inverse Distance Weighted (AIDW) method was used to interpolate the anomaly data of LSAT during the period of 1900–2018. Inverse Distance Weighted (IDW) is a common and simple spatial interpolation method, based on similarity principle which describes that if two objects are nearer (farther), their properties will be similar (different). IDW sets the distance between interpolation point and sample point as the weight to achieve the weighted average. In a specific application, a higher weight is given in the LSAT interpolation when the observation station is more close to the grid point. The principle of this method is simple and easy to understand and operate. It is suitable for the case that there are many observation stations in uniform distribution.

The general formula of the IDW is:

$$T=\sum_{i=1}^{n}w_{\mathrm{i}}T_{\mathrm{i}} \tag{3}$$

$$w_{\mathrm{i}}=\frac{d_{\mathrm{i}}^{-\alpha}}{\sum_{i=1}^{n}d_{\mathrm{i}}^{-\alpha}} \tag{4}$$

Where, T means the temperature of the grid point to be estimated; n stands for the number of observation stations participating in the interpolation for the finite region; T_i means the temperature of each station; w_i means the distance weighting of each stations; d_i means the spatial distance from each stations to the grid point to be estimated; α is a control parameter, generally assumed to be 2. Importantly, after calculation we found that the temperature anomaly field interpolated using the equations above produces "bull eyes" (Duan et al., 2014), thus we modified the formula (3) for the specific adjustment (AIDW) as follows:

$$w_{\mathrm{i}}=\frac{(e^{d_i/d_0})^{-\alpha}}{\sum_{i=1}^{n}(e^{d_i/d_0})^{-\alpha}} \tag{5}$$

The cross validation indicate that the anomaly temperature interpolation result is better when assuming α as 4 and d_0 as 1,200 km.

Validation Methods

Cross Validation (CV) is one of the most effective tool to evaluate the performance of the interpolation method. First, the *in situ* observations are the most precise data and are always used as the baseline data for the validation of other data types. So it is very difficult to find other different subsets of the data for validation of the gridded dataset; second, the gridded data set is derived from the *in situ* observations, so we cannot use the gridded data to assess the errors of the gridded data directly, thus Cross Validation (CV) is used. CV is widely used to validate the gridded observations dataset. In our manuscript, Leave One Out CV is used, which refers to taking out one station as the test station each time, and then interpolating the estimated value from the corresponding observed values of the other remaining stations. The advantage of this method is (1) nearly all the samples will be used to train the model in any round, thus the evaluation will be more reliable; (2) no random factor affects the experimental data, thus we make sure the experiment can be duplicated. Based on the results of CV, we adopted the statistical indices of Root Mean Square Error (RMSE) and Mean Absolute Error (MAE) to evaluate the interpolation errors between the estimated and observational values. The calculation formulas of RMSE and MAE are shown as follows:

$$RMSE=\sqrt{\frac{1}{\mathrm{n}}\sum_{i=1}^{n}(X_{\mathrm{i}}-Y_{\mathrm{i}})^{2}} \tag{6}$$

$$MAE=\frac{1}{\mathrm{n}}\sum_{i=1}^{n}|X_{\mathrm{i}}-Y_{\mathrm{i}}| \tag{7}$$

TABLE 1 | The annual average RGCV and RMSE of the six test experiments [Ax (Bx) is the *x*th experiment for Group A (B)].

Experiments	Model parameters			Interpolation error	
	Independent variables	Covariates	Spline order	RGCV(°C)	RMSE(°C)
A1	Lon, Lat, Elev	No	2	0.850	0.628
A2	Lon, Lat, Elev	No	3	0.835	0.619
A3	Lon, Lat, Elev	No	4	0.848	0.633
B1	Lon, Lat	Elev	2	0.966	0.745
B2	Lon, Lat	Elev	3	0.982	0.749
B3	Lon, Lat	Elev	4	0.997	0.751

Where, X_i, Y_i are the estimated value and the original observational value at each station, respectively, while n is the sample number. RMSE reflects the random error between the estimated value and the actual observed value. Moreover, it estimates the degree of dispersion for the interpolation errors. MAE reflects the systematic error and estimate the average deviation between the interpolation results and the actual observed values.

CLIMATOLOGY INTERPOLATION

Selection of Model Parameters

It is well known that ANUSPLIN can form different interpolation models based on various input parameters such as independent variables, covariates and spline orders. Many studies on meteorological data interpolation treat longitude and latitude as independent variables, and elevation as independent variables or

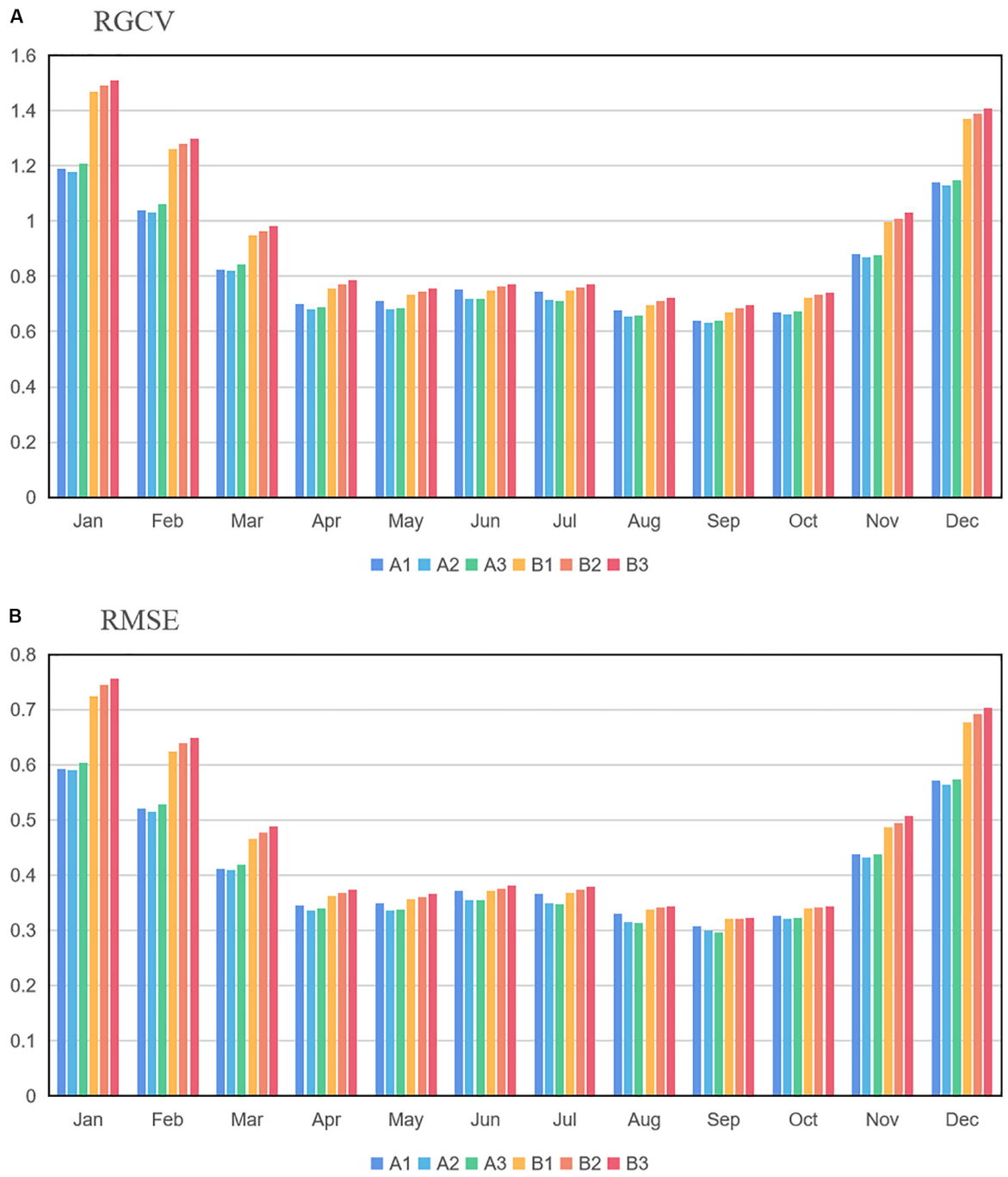

FIGURE 3 | Monthly RGCV **(A)** and RMSE **(B)** of the six test experiments (°C).

covariates in the model (Hutchinson and Xu, 2013). Different interpolation model parameters may lead to different results. For example, Hong et al. (2005) used the longitude and latitude as independent variables and elevation as a covariate, while Xu et al. (2020) argued toward use of elevation as an independent variable rather than as covariate in TPS model because of its better performance.

However, since the data used in the above studies are different in terms of data volume and coverage, we first want to determine which model parameter scheme is the most preferable one according to our own data and actual situation. We use the RGCV and RMSE to determine the proper model parameter scheme. Based on the input treatment of elevation as independent variables or covariate parameters, the test groups were divided into two large groups: altitude as independent variable in group A and as covariates parameter in group B. Then according to the order of splines 2–4, both groups were subdivided again into three experiments. Therefore, a total of six experiments were taken to be tested (see **Table 1**). The statistical indices of RGCV and RMSE are used to analyze the errors of 6 test experiments.

RGCV is one of the efficient measures of the interpolation error of the fitted surfaces provided by the ANUSPLIN software.

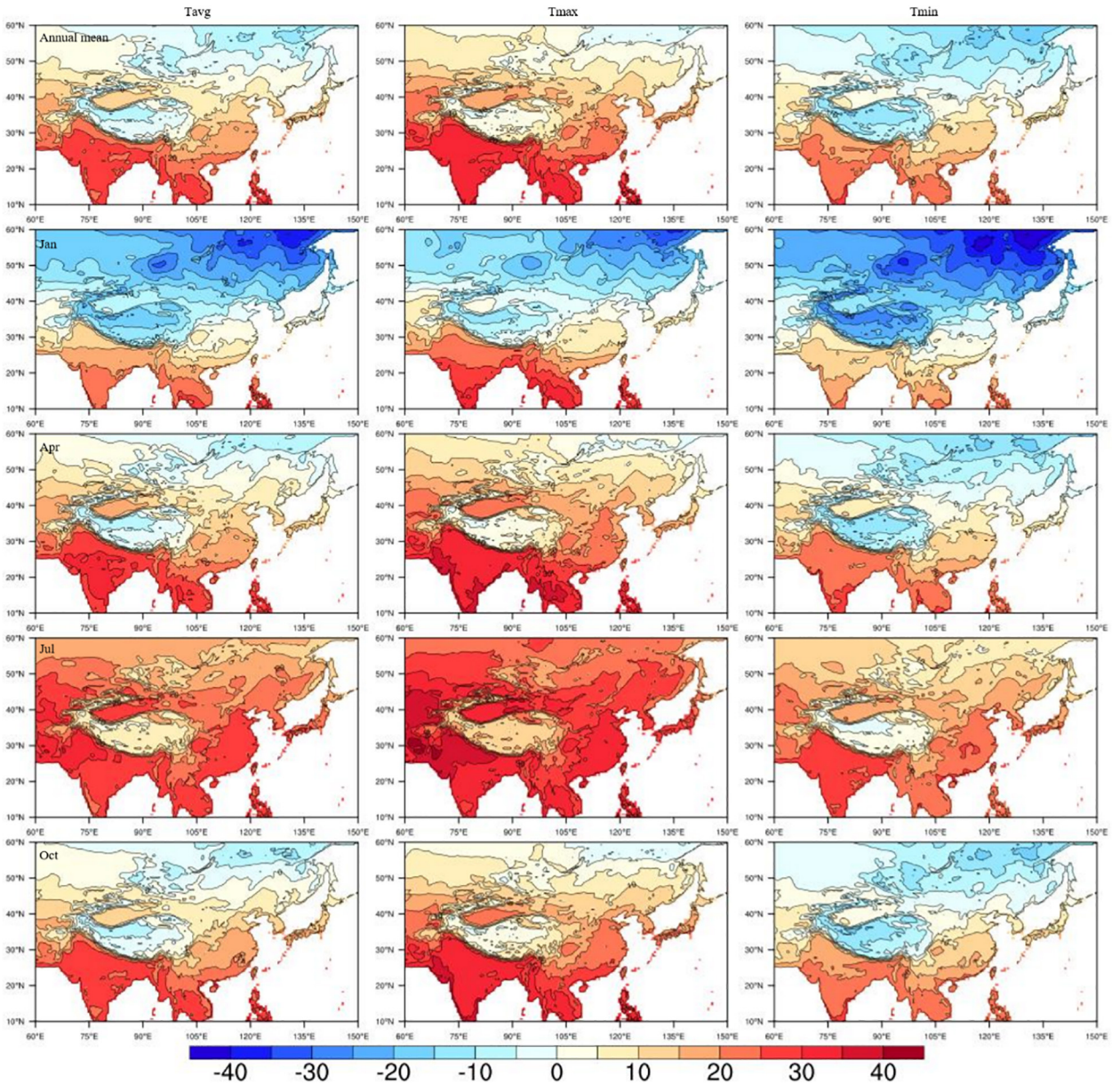

FIGURE 4 | Gridded climatology (°C) of LSAT over eastern Asia for (top to bottom) annual mean and different seasons (presented by January, April, July, and October) of mean, maximum and minimum temperature (left to right).

Figure 3A shows the RGCV of the six experiments. As seen from the picture, seasonally, the RGCV in winter (December to February) is much higher than that in other seasons, and the RGCVs of group B are higher than those of group A, especially in winter.

RMSE is another statistical measure to estimate the degree of dispersion of interpolation errors. **Figure 3B** shows the RMSE of the six experiments. As seen from the figure, the lowest RMSE occurs in spring and autumn, slightly higher in summer, and highest in winter.

Table 1 shows the annual average RGCV and RMSE for the six test experiments. It is found that both the RGCV and RMSE are lower in group A than that in group B, and the smallest RGCV (0.835°C) and RMSE (0.619°C) appear in experiment A2.

After taking into account the above statistical indices, we decided to take experiment A2 as the preferred scheme to interpolate the climatology temperature, which means to treat the longitude, latitude as well as the elevation as independent variables, and the spline order as 3. It is worth noting that this scheme is just applicable to the data in this study. There may be other better schemes for data from different regions or scales, which need to be analyzed according to the actual situation.

Climatology Interpolation

After the preparation for the input data and model parameter setting, we adopted the ANUSPLIN software to interpolate the gridded temperature climatology over Pan-East Asia. **Figure 4** shows the gridded result of the LSAT climatology over the region. The spatial distribution of LSAT climatology is obviously affected by the terrain and latitude. Naturally, the climatological temperature is higher at lower latitudes. The lowest temperature was found at high latitudes in eastern Siberia while the

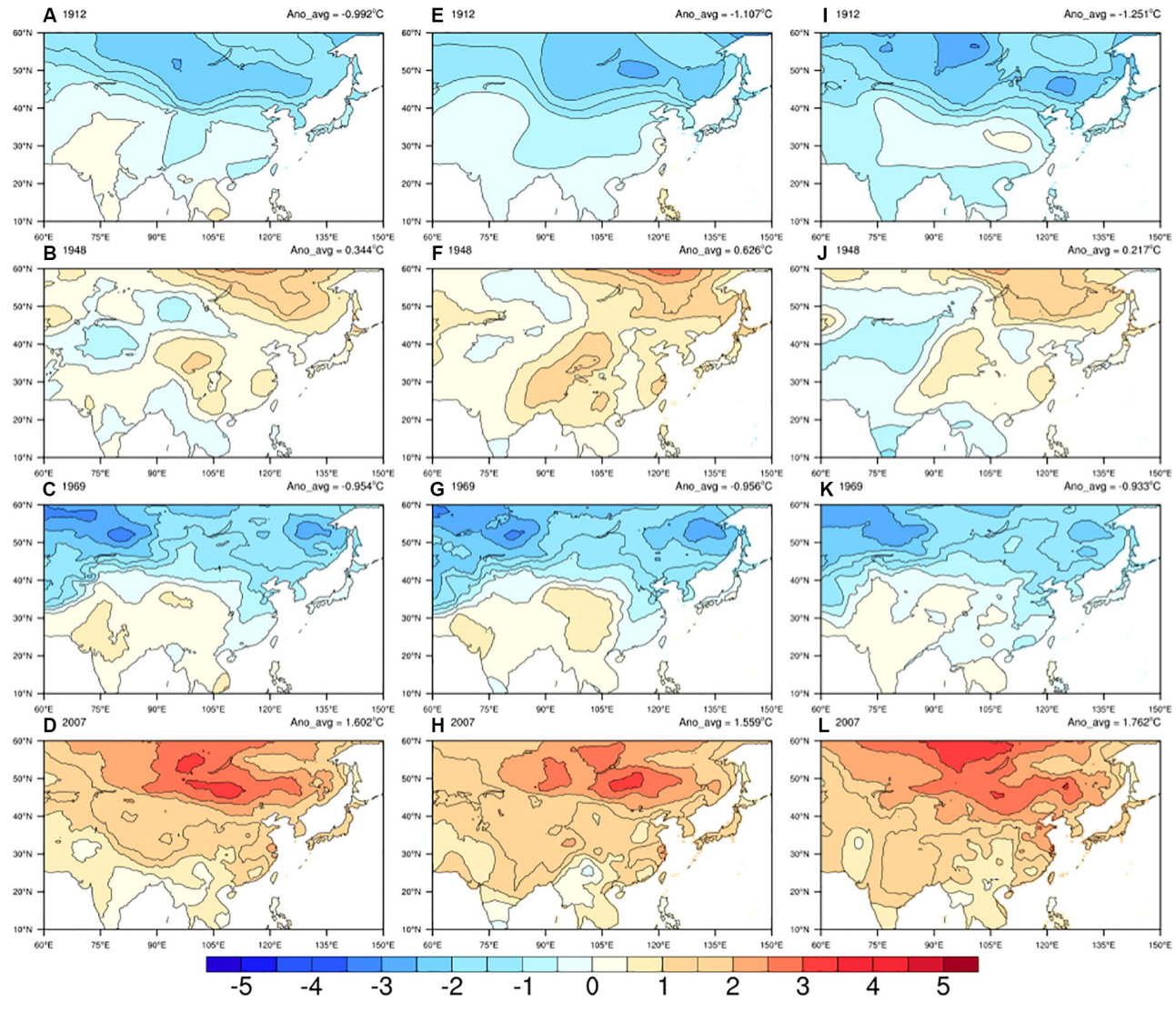

FIGURE 5 | The spatial distribution of the annual anomalies of mean **(A–D)**, maximum **(E–H)** and minimum **(I–L)** LSAT (left to right) of the coldest (1912) and warmest (1948) year before 1950s and the coldest (1969) and warmest (2007) year after 1950s.

highest temperature was found at low latitudes in India and Indochina. In addition, the temperature climatology decreases with the increasing elevation. The climatological temperature at high altitude areas, such as the Tibet plateau and Mount Tianshan, is significantly lower than that at low altitude areas at the same latitude.

INTERPOLATION AND VALIDATION OF LSAT ANOMALY

Anomaly Interpolation

In this section, we used the AIDW method to interpolate the monthly anomaly of LSAT over Pan-East Asia during 1900–2018. In order to demonstrate the interpolation effect, four representative years are selected to display the spatial distributions of temperature anomalies (**Figure 5**): the spatial distribution of the LSAT anomalies of the coldest (1912) and warmest (1948) year before 1950 and the coldest (1969) and warmest (2007) year after 1950.

In the two coldest years (1912 and 1969), the temperature anomalies (relative to 1961–1990 averages) in the high latitude region north of 40°N is generally lower than those in the lower latitude region, and there is very little change before and after 1950s. Differences exist in the detailed distribution of the anomaly in warmest years, in the first half of the 20th century, the LSAT anomaly was not so high (0.34°C) relative to 1961–1990 average even in the warmest year (1948), and the warming center happened at higher latitude (55–60°N). The regional LSAT anomaly increased significantly after entering the second half of the 20th century. It reaches the highest LSAT anomaly (1.6°C) in 2007, and the warming center moved to the lower latitude and was significantly expanded. The annual anomalies of maximum and minimum LSAT perform similarly to those of mean LSAT.

Anomaly Validation

In this case, we used the leave-one-out CV to evaluate the interpolation performance. The RMSE, MAE, and MBE have been calculated to evaluate and analyze the interpolation errors between the estimated and observational LSAT.

Figures 6A–D show the distribution of the RMSE of the LSAT anomaly at each station in four seasons (presented by January, April, July, and October) over Pan-East Asia from 1900 to 2018. Inset figures in the lower right corner is the probability density distribution diagram of RMSE for all stations. The stations with RMSE in the range of below 0.75°C are in the majority, accounting for 67.5, 88.5, 90.1, and 88.7% in each month (January, April, July, and October), respectively. **Figures 6B–D** show that the spatial distribution and the average of the RMSE is mostly similar between spring, summer, and autumn. The stations with lowest RMSE mainly located in

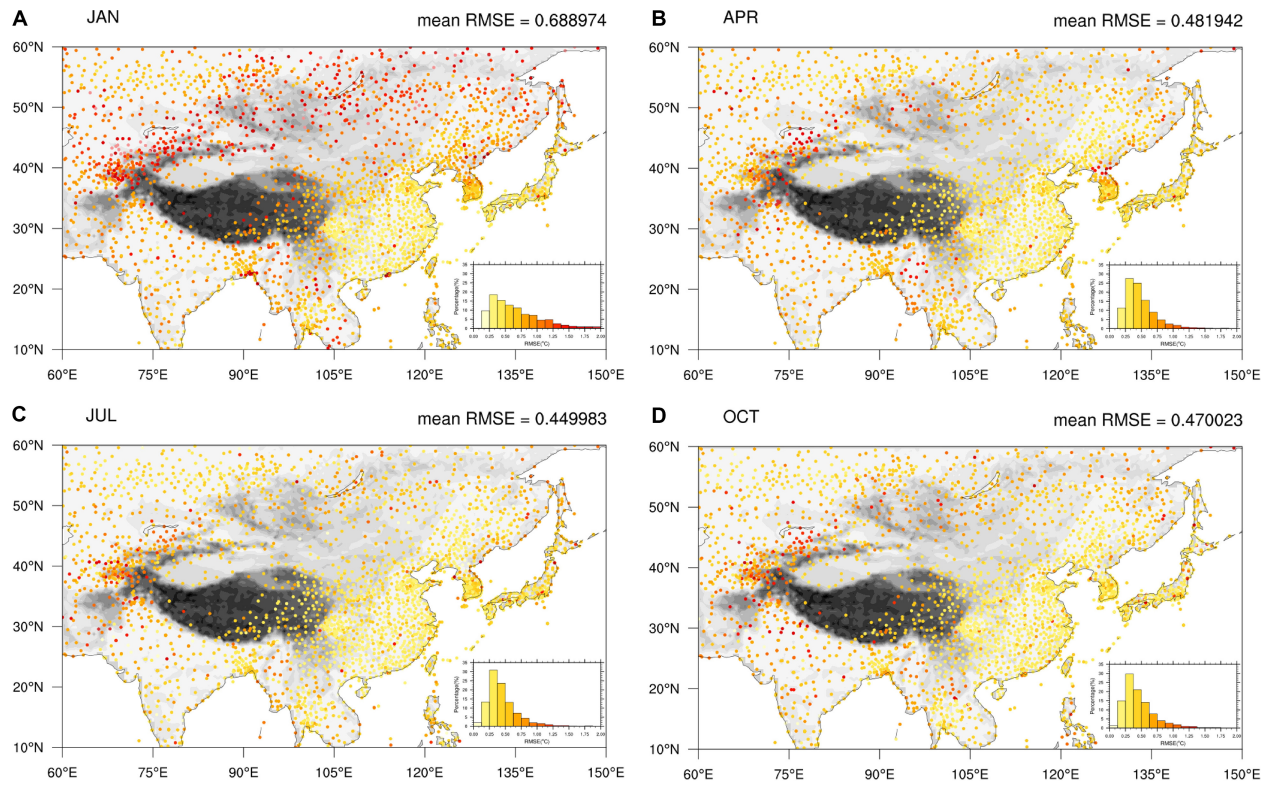

FIGURE 6 | RMSEs of the LSAT anomaly over Pan-East Asian from 1900 to 2018 at each station in 4 months [January **(A)**, April **(B)**, July **(C)**, and October **(D)**] calculated by leave-one-out cross validation.

the regions with high station density in eastern China, Japan, and South Korea. Those with higher RMSE are in regions of relatively sparse station density in India, Indo-China Peninsula and Mongolia. The stations with largest RMSE exist mainly in high latitude mountain areas such as Mount Tianshan (around 40–45°N, 75–80°E). The RMSE over the Tibetan Plateau is hard to determine due to the lack of observational station data. The RMSE in winter is larger than those in other seasons, especially on the Tibetan Plateau and regions north of 40°N. The RMSE in winter (January) is about 0.4°C higher than that in other

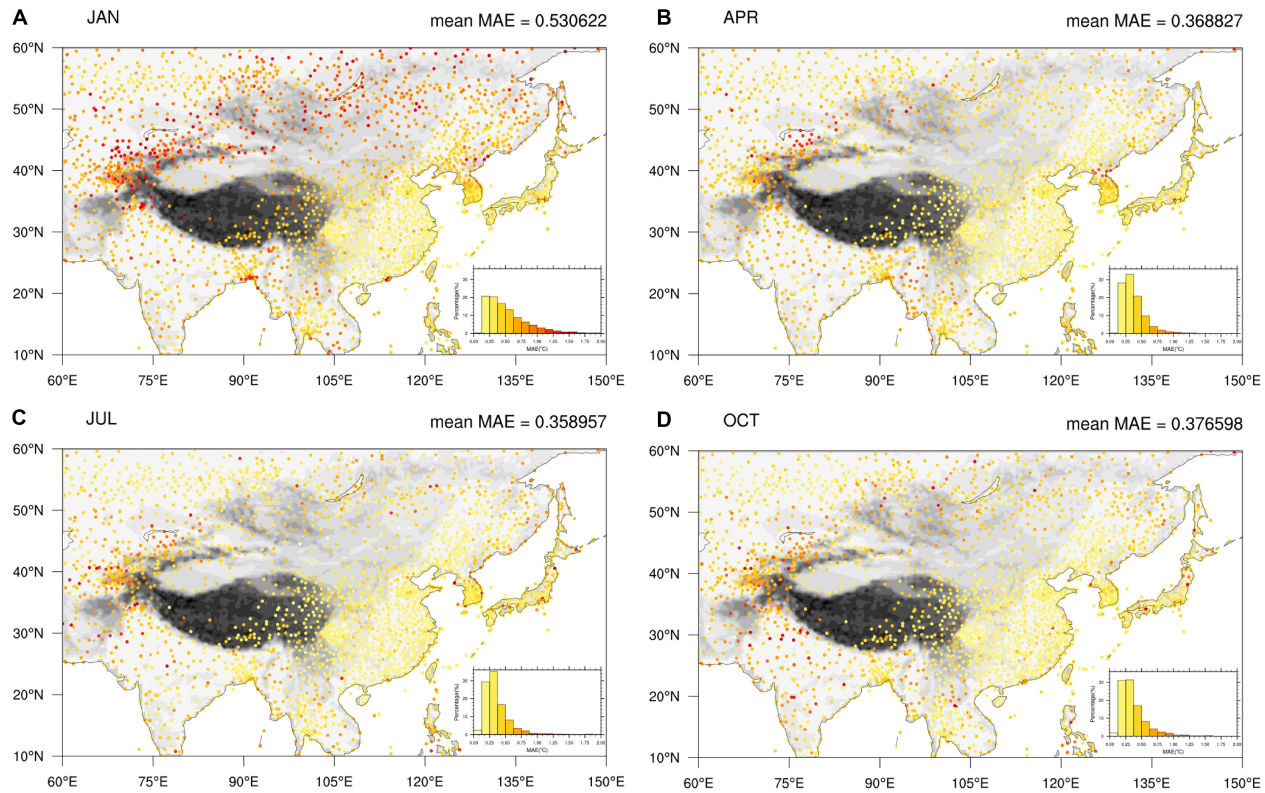

FIGURE 7 | MAEs of the LSAT anomaly over Pan-East Asian from 1900 to 2018 at each station in 4 months [January **(A)**, April **(B)**, July **(C)**, and October **(D)**] calculated by leave-one-out cross validation.

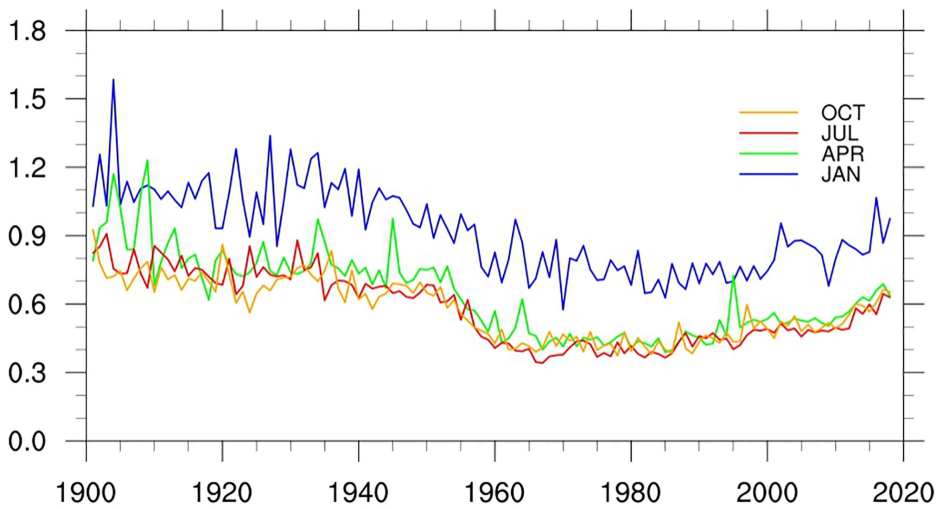

FIGURE 8 | Mean RMSEs of the LSAT anomaly from 1900 to 2018 for 4 months (January, April, July, and October).

seasons on average. In contrast, the RMSE in the plain regions south of 40°N is just about 0.08°C higher in winter than in other seasons on average. We suspect that this higher noise level may be related to the circulation and front activities in high latitude regions in winter.

Figures 7A–D show the MAEs of the anomaly of LSAT at each station in 4 months (January, April, July, and October) over Pan-East Asia from 1900 to 2018. The magnitude of MAE is smaller than RMSE, but its spatial distribution is very similar to RMSE. In addition, **Figure 7** also shows that the MAE is relatively low in general, which means that the systematic error of anomaly temperature generated by the AIDW interpolation model used in this paper is relatively small.

Figures 8, **9** show the changes of RMSE and MAE of LSAT anomaly during 1900 to 2018 for the 4 months (January, April, July, and October), respectively. Although the 4 months exhibit short-term fluctuations, their long term variations are very similar. Before the 1950s, both of RMSE and MAE are relatively larger and gradually decrease with time. They decreased rapidly and then rose slowly after 1950s (with the change of the stations number), but basically remained lower than those before 1950s. The evolution of RMSE and MAE is strongly related to the change in the station numbers: more station observations correspond to a denser station distribution and hence lower error RMSE and MAE. Similarly, both of the RMSE and MAE in winter are larger than those in other seasons. This also shows that we need more stations in January to reduce the error to that of the other times of the year.

REGIONAL LSAT WARMING TRENDS ANALYSIS

In order to investigate the long-term climate change trend reflected by the new interpolation high resolution dataset, we calculated the long term regional C-LSAT high resolution (C-LSAT HR) anomaly time series over the Pan-East Asia and compared it with the newly released high resolution CRU TS4 (Harris et al., 2020) dataset. **Table 2** shows the difference of the high resolution gridded dataset between CRU TS and C-LSAT HR over Pan East Asia.

Figure 10 shows the time series of the annual surface air temperature anomaly over Pan-East Asia from the high-resolution dataset obtained by AIDW (C-LSAT HR) and the high-resolution estimation of CRU data (CRU TS) in the same region, respectively. The linear trends with 5% significant range are listed in **Table 3**.

From **Table 3** and **Figure 10**, it is noticed that the variations of the two annual mean LSAT anomalies are overall close to each other, except for slight difference in the warming trends between two datasets. The trend derived from the C-LSAT HR (0.5 × 0.5) (0.155 ± 0.019°C/10 years) is slightly larger than that of CRU TS4 (0.126 ± 0.019°C/10 years) for the whole period of 1901–2018. It is similar for the linear trends comparison during different periods. From the early 20th century to the early 1960s, the trend of annual average temperature is relatively low (0.076 ± 0.041°C/10 years for AIDW and 0.044 ± 0.041°C/10 years for CRU TS4). The linear trend of annual LSAT anomaly rose rapidly after the mid-1960s (0.289 ± 0.054°C/10 years for AIDW and 0.261 ± 0.052°C/10 years for CRU TS4). Further comparison indicates that this agrees well with the result calculated by the arithmetic average trend of all the stations, which also shows the interpolation process performs well.

Finally, from **Table 3**, no matter for C-LSAT or CRU TS gridded datasets (both 0.5° × 0.5° and 5° × 5° resolution), the trends calculated by low resolution datasets (5° × 5° resolution, Yun et al., 2019) are lower than those by higher resolution datasets (0.5° × 0.5° resolution). This may be due to the fact that the high-resolution data sets emphasize more on the amplification effect of local warming in some areas in high altitudes (Li et al., 2009; Pepin et al., 2015) or in

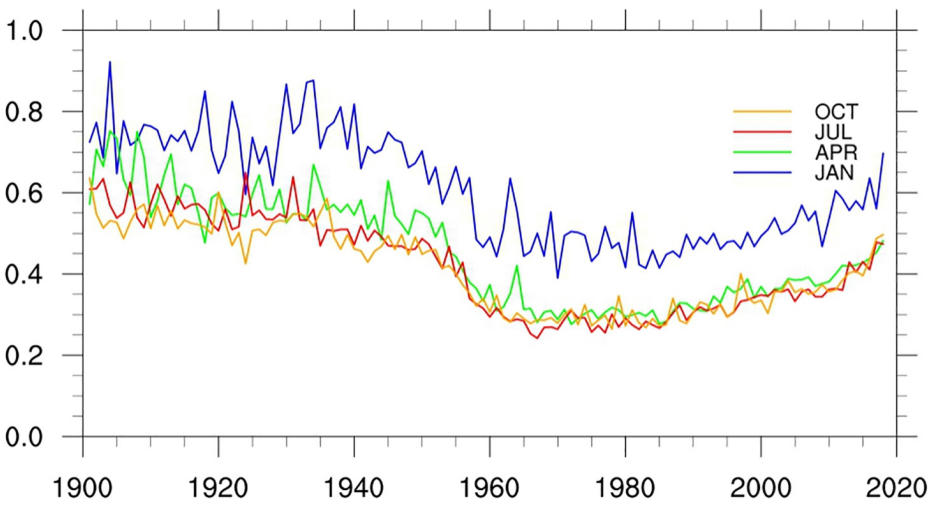

FIGURE 9 | Mean MAEs of the LSAT anomaly from 1900 to 2018 for 4 months (January, April, July, and October).

TABLE 2 | The comparison of the high resolution gridded dataset derived from CRU TS and C-LSAT HR.

Station numbers in research region	Methodology of gridding		DEM
	Climatology	Anomaly	
CRU TS			
2179	TPS(thin-plate splines)	ADW (angular-distance weighting)	TBASE5-min lat-long global DEM
C-LSAT HR			
2890	TPS(thin-plate splines)	AIDW(adjusted inverse-distance weighting)	GTOPO30

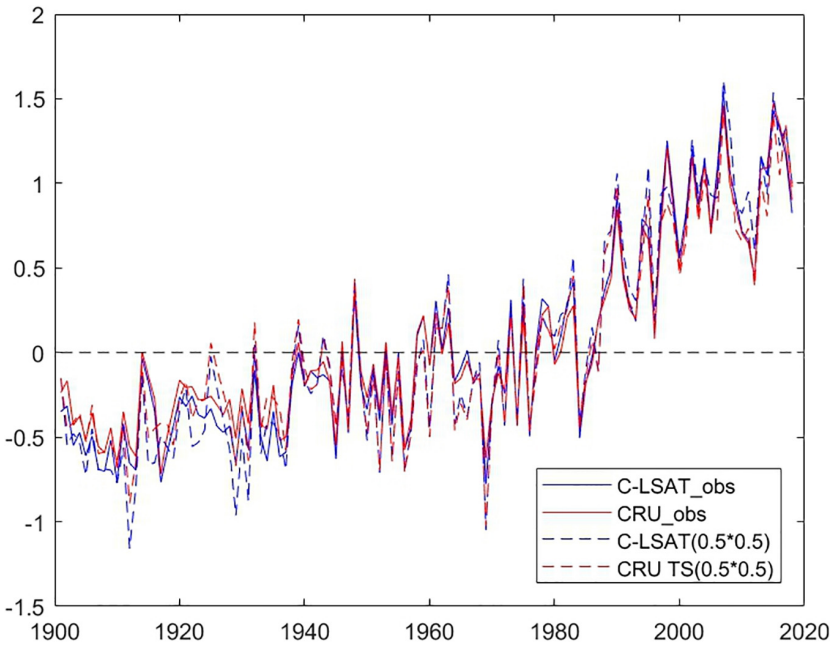

FIGURE 10 | The time series of the annual LAST anomaly in Pan-East Asian area from C-LSAT HR (blue) and CRU TS4 (red), including observed (dashed), and estimated (solid) data.

TABLE 3 | Warming trends (°C $10a^{-1}$) and their uncertainty at 95% confidence level of annual LSAT anomaly from observation and gridded datasets over Pan-East Asian.

Dataset	Forms	1901–2018	1901–1960	1961–2018
C-LSAT HR	C-LSAT_obs	0.141 ± 0.017	0.075 ± 0.032	0.262 ± 0.052
	C-LSAT (0.5° × 0.5°)	0.155 ± 0.019	0.076 ± 0.041	0.289 ± 0.054
	C-LSAT(5° × 5°)	0.118 ± 0.016	0.041 ± 0.029	0.249 ± 0.041
CRUTEM	CRU_obs	0.126 ± 0.017	0.059 ± 0.031	0.264 ± 0.047
	CRU TS4 (0.5° × 0.5°)	0.126 ± 0.019	0.045 ± 0.041	0.261 ± 0.052
	CRUTEM4 (5° × 5°)	0.105 ± 0.017	0.019 ± 0.029	0.255 ± 0.042

regions with severe drought (Huang et al., 2016) where there are no actual observation stations especially when the stations are relatively scarce (mostly in the Tibet Plateau and large desert areas) before 1960.

CONCLUSION

In this paper, we first split the land surface air temperature from C-LSAT2.0 into climatology and anomaly data, and then interpolate them into a 0.5° × 0.5° grid datasets, respectively. Finally they are combined into a new monthly high-resolution LSAT grid data set for the period of 1900–2018 over Pan-East Asia. The validation of the dataset shows that the interpolated dataset is of good accuracy in both climatology and the LSAT anomaly variations.

The climatology data is interpolated by thin-plate splines (TPS) method using station LSAT data from C-LSAT2.0 and elevation information (DEM) from GTOPO30 as the input data

to the ANUSPLIN software. We found that the interpolation scheme performs best when the longitude, latitude and elevation are all used as independent variables, and the spline order is set to 3. Under this situation, the lowest RGCV and RMSE are achieved.

The LSAT anomaly data is interpolated by an AIDW method. The gridded LSAT anomaly data errors are evaluated by leave-one-out CV. The spatial distribution characteristic of RMSE and MAE are closely correlated with the station density in both temporal and special perspective. The low RMSE mainly occurs in the regions with high station density areas in eastern China, Japan, and South Korea. The RMSE further decreases with the increase of the station numbers during the period of 1900–2018. In addition, the RMSE and MAE in winter are much larger than those in other seasons, which indicate a clear seasonal difference. This may be related to the more active cold air activities in the high latitudes regions in winter and the temperature anomalies in winter being more controlled by advection when the winds are strong than the other seasons.

In addition, we evaluated the long term LSAT change trend during the period of 1901–2018, 1901–1960, and 1961–2018, respectively with the newly interpolated high resolution dataset, and compared the results with those derived from CRU TS4 dataset. The LSAT anomaly series during 1900–2018 derived in this paper and from CRU TS4 are generally consistent with each other, while the linear warming trends have slight differences. The trend derived from newly dataset is a bit larger than those from the latter dataset in different time periods of 1901–2018, 1901–1960, and 1961–2018, respectively. Based on above analysis, the dataset developed in this paper is proved to be a useful tool in the regional climate and climate change detection, monitoring and validation of model output.

The future plan is developing a global higher resolution LSAT dataset based on the whole C-LSAT (C-LSAT HR). This is a part of global dataset, we found it is relatively mature in pan East Asia. We are going to apply this gridding and validation method to other sub-regions over the world, and focus on the gridded data integration of regions and the overall quality of the global gridded dataset. Once the development of this global high-resolution LSAT dataset is completed, the dataset will be available to the public (for free) in near future. The gridding and validation method used in this study is also helpful for other similar research, such as gridding of precipitation, wind speed or other meteorological elements in monthly, daily or even higher temporal scale, which is also another part of our future research direction.

DATA AVAILABILITY STATEMENT

The raw data supporting the conclusions of this article will be made available by the authors, without undue reservation, to any qualified researcher.

AUTHOR CONTRIBUTIONS

JC analyzed the data. QL put forward the idea. QL and JC wrote the manuscript. All authors revised the manuscript.

FUNDING

This study was supported by the National Key R&D Program of China (Grant: 2017YFC1502301 and 2018YFC1507705) and the Natural Science Foundation of China (Grant: 41975105).

ACKNOWLEDGMENTS

The authors thank the editor and the reviewers for their constructive suggestions/comments in the initial reviews.

REFERENCES

Callendar, G. S. (1938). The artificial production of carbon dioxide and its influence on temperature. *Q. J. R. Meteorol. Soc.* 64, 223–240. doi: 10.1002/qj.49706427503

Callendar, G. S. (1961). Temperature fluctuations and trends over the Earth. *Q. J.R. Meteorol. Soc.* 87, 1–12. doi: 10.1002/qj.49708737102

Daly, C., Halbleib, M., Smith, J. I., Gibson, W. P., Doggett, M. K., Taylor, G. H., et al. (2008). Physiographically sensitive mapping of climatological temperature and precipitation across the conterminous united states. *Int. J. Climatol.* 28, 2031–2064. doi: 10.1002/joc.1688

Daly, C., Neilson, R. P., and Phillips, D. L. (1994). A statistical-topographic model for mapping climatological precipitation over mountainous terrain. *J. Appl. Meteor.* 33, 140–158. doi: 10.1175/1520-0450(1994)033<0140:astmfm>2.0.co;2

Duan, P., Sheng, Y., Li, J., Lv, H., and Zhang, S. (2014). Adaptive idw interpolation method and its application in the temperature field. *Geograph. Res.* 196, 31–38.

Farr, T. G., Rosen, P. A., Caro, E., Crippen, R., Duren, R., Hensley, S., et al. (2007). The shuttle radar topography mission. *Rev. Geophys.* 45:RG2004. doi: 10.1029/2005RG000183

Fick, S. E., and Hijmans, R. J. (2017). WorldClim 2: new 1-km spatial resolution climate surfaces for global land areas. *Int. J. Climatol.* 37, 4302–4315. doi: 10.1002/joc.5086

Hansen, J., Ruedy, R., Glascoe, J., and Sato, M. (1999). GISS analysis of surface temperature change. *J. Geophys. Res.* 104, 30997–31022. doi: 10.1029/1999jd900835

Harris, I., Osborn, T. J., Jones, P., and Lister, D. (2020). Version 4 of the CRU TS monthly high-resolution gridded multivariate climate dataset. *Sci. Data* 7:109.

Hawkins, E. D., and Jones, P. D. (2013). Notes and Correspondence On increasing global temperatures: 75 years after Callendar. *Q. J. R. Meteorol. Soc.* 139, 1961–1963. doi: 10.1002/qj.2178

Haylock, M. R., Hofstra, N., Klein Tank, A. M. G., Klok, E. J., Jones, P. D., and New, M. (2008). A European daily high-resolution gridded data set of surface temperature and precipitation for 1950–2006. *J. Geophys. Res.* 113: D20119.

Hijmans, R. J., Cameron, S. E., Parra, J. L., Jones, P. G., and Jarvis, A. (2005). Very high resolution interpolated climate surfaces for global land areas. *Int. J. Climatol.* 25, 1965–1978. doi: 10.1002/joc.1276

Hong, Y., Nix, H. A., Hutchinsonb, M. F., and Booth, T. H. (2005). Spatial interpolation of monthly mean climate data for china. *Int. J. Climatol.* 25, 1369–1379. doi: 10.1002/joc.1187

Huang, J., Yu, H., Guan, X., Wang, G., and Guo, R. (2016). Accelerated dryland expansion under climate change. *Nat. Clim. Change* 6, 166–171. doi: 10.1038/nclimate2837

Huang, W., Liu, C., Cao, J., Chen, J., and Feng, S. (2020). Changes of hydroclimatic patterns in China in the present day and future. *Sci. Bull.* 65, 1061–1063. doi: 10.1016/j.scib.2020.03.033

Hutchinson, M. F. (1991). The application of thin plate smoothing splines to continent-wide data assimilation. *Melbourne Bureau Meteorol. Res. Rep.* 01, 104–113.

Hutchinson, M. F., and Xu, T. (2013). *Anusplin version 4.4 user guide*.

Jones, P. D., and Briffa, K. R. (1992). Global surface air temperature variations during the twentieth century: part I, spatial temporal and seasonal details. *Holocene* 2, 165–179. doi: 10.1177/095968369200200208

Köppen, W. (1931). *Grundriss der Klimakunde. (Zweite, verbesserte Auflage der Klimate der Erde.)*. Berlin: Walter de Gruyter & Co.

Li, Q., and Li, W. (2007). Construction of the gridded historic temperature dataset over china during the recent half century. *Acta Meteorol. Sin.* 65, 293–300.

Li, Q., Li, W., Si, P., Gao, X., Dong, W., Jones, P., et al. (2009). Assessment of surface air warming in northeast China, with emphasis on the impacts of urbanization. *Theor. Appl. Climatol.* 99, 469–478. doi: 10.1007/s00704-009-0155-4

Li, Q., Sun, W., Huang, B., Dong, W., Wang, X., Zhai, P., et al. (2020). Consistence of global warming trends strengthened since 1880s. *Sci. Bull.* 65, 1709–1712. doi: 10.1016/j.scib.2020.06.009

Li, Q., Zhang, L., Xu, W., Zhou, T., Wang, J., Zhai, P., et al. (2017). Comparisons of time series of annual mean surface air temperature for China since the 1900s:Observation, Model simulation and extended reanalysis. *Bull. Am. Meteor. Soc.* 98, 699–711. doi: 10.1175/BAMS-D-16-0092.1

Li, W., Li, Q., and Jiang, Z. (2007). Discussion on feasibility of gridding the historic temperature data in China with kriging method. *J. Nanjing Instit. Meteorol.* 30, 246–252.

Ma, L., and Li, Y. (2006). Study on accuracy of GTOP030 and srtm dem - a case study of tibet. *Bull. Soil Water Conserv.* 5, 71–74. doi: 10.2747/1548-1603.49.1.71

New, M., Hulme, M., and Jones, P. (1999a). Representing twentieth-century space-time climate variability. Part I: development of a 1961-90 mean monthly terrestrial climatology. *J. Clim.* 12, 829–856. doi: 10.1175/1520-0442(1999)012<0829:rtcstc>2.0.co;2

New, M., Hulme, M., and Jones, P. (1999b). Representing twentieth-century space-time climate variability. Part II: development of 1901-96 monthly grids of terrestrial surface climate. *J. Clim.* 13, 2217–2238. doi: 10.1175/1520-0442(2000)013<2217:rtcstc>2.0.co;2

Nynke, H., Malcolm, H., Mark, N., and Phil, J. (2009). Testing E-OBS European high-resolution gridded dataset of daily precipitation and surface temperature. *J. Geophys. Res.* 114:D21101.

Peng, S., Ding, Y., Liu, W., and Li, Z. (2019). 1km monthly temperature and precipitation dataset for China from 1901 to 2017. *Earth Syst. Sci. Data* 11, 1931–1946. doi: 10.5194/essd-11-1931-2019

Pepin, N. C., Bradly, R. S., Diaz, H. F., Baraer, M., Caceres, E. B., Forsythe, N., et al. (2015). Elevation-dependent warming in mountain regions of the world. *Nat. Clim. Chang.* 5, 424–430. doi: 10.1038/nclimate2563

Peterson, T. C., and Vose, R. S. (1997). An overview of the global historical climatology network temperature database. *Bull. Am. Meteorol. Soc.* 78, 2837–2849. doi: 10.1175/1520-0477(1997)078<2837:aootgh>2.0.co;2

Price, D. T., McKenney, D. W., Papadopol, P., Logan, T., and Hutchinson, M. F. (2004). "High resolution future scenario climate data for North America," in *Proceedings of the 26th Conference on Agricultural and Forest Meteorology of American Meteorological Society*, Boston, MA.

Rohde, R., Muller, R., Jacobsen, R., Perlmutter, S., Rosenfeld, A., Wurtele, J., et al. (2013). Berkeley Earth Temperature averaging process. *Geoinform. Geostat. Overview* 1:2.

Sinha, S. K., Narkhedkar, S. G., and Mitra, A. K. (2006). Bares objective analysis scheme of daily rainfall over Maharashtra (India) on a mesoscale grid. *Atmosfera* 19, 109–126.

Van den Besselaar, E. J. M., Van der Schrier, G., Cornes, R. C., Iqbal, A. S., and Tank, A. M. G. K. (2017). SA-OBS: a daily gridded surface temperature and precipitation dataset for Southeast Asia. *J. Clim.* 30, 5151–5165. doi: 10.1175/jcli-d-16-0575.1

Wahba, G., and Wendelberger, J. (1980). Some new mathematical methods for variational objective analysis using splines and cross-validation. *Mon. Weather Rev.* 108, 1122–1145. doi: 10.1175/1520-0493(1980)108<1122:snmmfv>2.0.co;2

Wu, J., and Gao, X. (2013). A gridded daily observation dataset over China region and comparison with the other datasets. *Chin. J. Geophys.* 56, 1102–1111.

Xie, P., Yatagai, A., Chen, M., Hayasaka, T., Fukushima, Y., Liu, C., et al. (2007). A gauge-based analysis of daily precipitation over East Asia. *J. Hydrol.* 8, 607–626. doi: 10.1175/jhm583.1

Xu, C., Wang, J., and Li, Q. (2018). A new method for temperatures spatial interpolation based on sparse historical stations. *J. Clim.* 31, 1757–1770. doi: 10.1175/jcli-d-17-0150.1

Xu, W., Li, Q., Jones, P., Wang, X. L., Trewin, B., Yang, S., et al. (2018). A new integrated and homogenized global monthly land surface air temperature dataset for the period since 1900. *Clim. Dyn.* 50, 2513–2536. doi: 10.1007/s00382-017-3755-1

Xu, Y., Gao, X., Shen, Y., Xu, C., Shi, Y., and Giorgi, F. (2009). A daily temperature dataset over China and its application in validating a RCM simulation. *Adv. Atmos. Sci.* 26, 763–772. doi: 10.1007/s00376-009-9029-z

Xu, Y., Zhao, P., Si, D., Cao, L., Wu, X., Zhao, Y., et al. (2020). Development and preliminary application of a gridded surface air temperature homogenized dataset for China. *Theor. Appl. Climatol.* 139, 505–516. doi: 10.1007/s00704-019-02972-z

Yatagai, A., Arakawa, O., Kamiguchi, K., Kawamoto, H., Nodzu, M., and Hamada, A. (2009). A 44-year daily gridded precipitation dataset for Asia based on a dense network of rain gauges. *SOLA* 5, 137–140. doi: 10.2151/sola.2009-035

Yun, X., Huang, B., Cheng, J., Xu, W., Qiao, S., and Li, Q. (2019). A new merge of global surface temperature datasets since the start of the 20th Century. *Earth Syst. Sci. Data* 11, 1629–1643. doi: 10.5194/essd-11-1629-2019

Conflict of Interest: The authors declare that the research was conducted in the absence of any commercial or financial relationships that could be construed as a potential conflict of interest.

frontiers in Environmental Science

ORIGINAL RESEARCH
published: 16 February 2021
doi: 10.3389/fenvs.2021.628999

Evaluation of the Performance of CMIP5 Models to Simulate Land Surface Air Temperature Based on Long-Range Correlation

Shanshan Zhao[1,2], Wenping He[3], Tianyun Dong[3], Jie Zhou[4], Xiaoqiang Xie[3], Ying Mei[3], Shiquan Wan[5] and Yundi Jiang[1]*

[1]National Climate Center, China Meteorological Administration, Beijing, China, [2]Collaborative Innovation Center on Forecast and Evaluation of Meteorological Disasters, Nanjing University of Information Sciences and Technology, Nanjing, China, [3]School of Atmospheric Sciences, Key Laboratory of Tropical Atmosphere-Ocean System (Sun Yat-sen University), Ministry of Education, Southern Marine Science and Engineering Guangdong Laboratory (Zhuhai), Zhuhai, China, [4]Chongqing Climate Center, Chongqing Meteorological Bureau, Chongqing, China, [5]Yangzhou Meteorological Office, Yangzhou, China

The daily average land surface air temperature (SAT) simulated by 8 CMIP5 models historical experiments and that from NCEP data during 1960–2005, are used to evaluate the performance of the CMIP5 model based on detrended fluctuation analysis (DFA) method. The DFA results of NCEP data show that SAT in most regions of the world exhibit long-range correlation. The scaling exponents of NCEP SAT show the zonal distribution characteristics of larg in tropics while small in medium and high latitudes. The distribution characteristics of the zonal average scaling exponents of CMCC-CMS, GFDL-ESM2G, IPSL-CM5A-MR are similar to that of NCEP data. From the DFA errors of model-simulated SAT, the performance of IPSL-CM5A-MR is the best among the 8 models throughout the year, the performance of FGOALS-g2 is good in spring and summer, GFDL-ESM2G is the best in autumn, CNRM-CM5 and CMCC-CMS is good in winter. The scaling exponents of model-simulated SAT are closer to that of NCEP data in most areas of the mid-high latitude on the northern hemisphere. However, simulations of SAT in East Asia and Central North American are generally less effective. In spring, most models have better performance in Siberian (SIB), Central Asia (CAS) and Tibetan (TIB). SAT in Northern Europe area are well simulated by most models in summer. In autumn, areas with better performance of most models are Mediterranean, SIB and TIB regions. In winter, SAT in Greenland, SIB and TIB areas are well simulated by most models. Generally speaking, the performance of CMIP5 models for SAT on global continents varies in different seasons and different regions.

Keywords: detrended fluctuation analysis, long-range correlation, CMIP5, model intercomparision, surface air temperature

OPEN ACCESS

Edited by:
Boyin Huang,
National Oceanic and Atmospheric Administration, United States

Reviewed by:
Renguang Wu,
Zhejiang University, China
Liya Chao,
Sun Yat-sen University, China

****Correspondence:***
Wenping He
wenping_he@163.com

Specialty section:
This article was submitted to Interdisciplinary Climate Studies, a section of the journal Frontiers in Environmental Science

Received: *13 November 2020*
Accepted: *07 January 2021*
Published: *16 February 2021*

Citation:
Zhao S, He W, Dong T, Zhou J, Xie X, Mei Y, Wan S and Jiang Y (2021) Evaluation of the Performance of CMIP5 Models to Simulate Land Surface Air Temperature Based on Long-Range Correlation. Front. Environ. Sci. 9:628999. doi: 10.3389/fenvs.2021.628999

INTRODUCTION

Climate system models are important tools for simulating climate systems and projecting future climate change (Phillips and Gleckler, 2006; Zhou and Yu, 2006; Flato et al., 2013). Assessment of model simulation performance can help us understand the advantages and disadvantages of the models, so as to provide a basis for users to choose models suitable for different purposes, and

provide a scientific reference for model community to improve the performance of the models (Watterson et al., 2014). Coupled Model Intercomparison Project-Phase 5 (CMIP5) provides the dataset produced by multiple climate system models or earth system models (Taylor et al., 2012), which promotes the development of models themselves and the evaluation methods for model performance. The evaluation methods for model performance concentrate more on quantitative assessment than before, and emphasize the model evaluation criteria (Kharin et al., 2013; Elguindi et al., 2014; Sillmann et al., 2014). Most of these methods evaluate the outputs of multi-models on variant timescales, focusing on the climate states, climate change, or variations of indexes computed by meteorological elements (Sillmann et al., 2013; Yin et al., 2013; Jiang et al., 2016; Li et al., 2017), and provide the quantitative results of the differences between the model simulations and observations. However, the performance of models on simulating the intrinsic dynamical characteristics of climate system is rarely evaluated.

Climate systems are characterized by long-range correlation (LRC), which represents the self-similarity of climate evolution on different time scales (Bunde and Havlin., 2002; Bunde et al., 2005; Yuan et al., 2015; Fu et al., 2016a, 2016b; He et al., 2016). LRC has been found in meteorological observations, such precipitation (Kantelhardt et al., 2006) and as daily air temperature (Koscielny-Bunde, et al., 1996; Talkner and Weber, 2000; Gan et al., 2007; Jiang et al., 2015). LRC can be characterized by the power law of an autocorrelation coefficient (Beran, 1994). Some research pointed out that scaling exponents for daily air temperature were about universal over the continent (Koscielny-Bunde et al., 1998; Eichner et al., 2003). Weber and Talkner (2001) found LRC of daily air temperature depends on the altitude of the meteorological station. Király and Jánosi (2005) found that the scaling exponents of daily temperature over Australia were related with the geographic latitude, which exhibit a decrease tendency with increasing distance from the equator.

Detrended fluctuation analysis (DFA) is a well-known method to detect LRC in time series (Peng et al., 1994; Bunde and Havlin, 2002), and has been used to assess the capability of climate system models (Blender and Fraedrich, 2003; Kumar et al., 2013; Zhao and He, 2015; He and Zhao, 2018). Govindan et al. (2004) found that seven atmosphere-ocean general circulation models failed to reproduce the LRC of daily maximum temperature. Rybski et al. (2008) analyzed the LRC of daily temperature from historical simulation of global coupled general circulation model, and found that scaling exponents over most continent sites ranges from 0.6 to 0.8. By comparing the LRC with daily observational data over China, the performance of Beijing Climate Center Climate System Model 1.1(m) is systematically evaluated by using DFA methods (Zhao and He, 2014; Zhao and He, 2015). Therefore, it is a very well way to quantitatively evaluate the performance of climate model based on LRC of climate systems.

Because the spatial coverage of meteorological observation data is limited and varies with time, it is crucial to carry out homogenization and quality control of observational data. Reanalysis data can provide a set of meteorological data that is homogeneous in time and space (Marques et al., 2010). The National Centers for Environmental Prediction (NCEP) reanalysis data (Kalnay, 1996; Kanamitsu et al., 2002) is commonly used in climate research (Ma et al., 2008; Mooney et al., 2011). The quality of NCEP reanalysis datasets has been assessed on global and regional scales (Poccard et al., 2000; Josey, 2001; Mooney et al., 2011). He et al. (2018) showed that the daily average temperature from NCEP-2 and CFSR data exhibit LRC characteristics in China, which are similar to the results of observations, especially in central and eastern Northwest China, most of central and eastern China. Furthermore, the credibility of NCEP-2 and CFSR seasonal temperature were evaluated by DFA in China (Zhao et al., 2017). Based on this, we quantitatively evaluate the performance of CMIP5 models in simulating LRC of global daily land surface air temperature (SAT) by means of comparing the difference with LRC of NCEP-2 data in this study.

In this paper, DFA was used to evaluate the performance of CMIP5 models in simulating the global daily land SAT on a seasonal scale. The remainder of the present paper is organized as follows. *Methods and Data* briefly introduces the NCEP-2 data and the CMIP5 models used in this study, and then, the algorithm of the DFA is provided. In LRC *of Daily Average* SAT *Simulated by Multi-Models*, the LRC of the output datasets for all four seasons from CMIP5 models is analyzed by using DFA. Comparisons of the spatial differences of LRC between simulations and reanalysis data are also presented in this section. *Conclusion* summarizes the main results and conclusions of the present study with a brief discussion.

METHODS AND DATA

Data

The global daily average land SAT from 1960 to 2005 is available from NCEP reanalysis dataset. The simulated global daily average land SAT is from the present-day historical simulations performed by the 8 CMIP5 climate models. The basic information about the 8 global climate models (GCM) is provided in **Table 1**. The term "historical" (HIST) refers to coupled climate model simulations forced by observed concentrations of greenhouse gases, solar forcing, aerosols, ozone, and land-use change over the 1850–2005 period (Taylor et al., 2012). The qualities of the past 46 years (1960–2005) data from the selected CMIP5 models were evaluated. To facilitate the intercomparison of the selected models and evaluation of the performance of 8 models against the NCEP data, the daily fields of GCM temperature were remapped onto T62 Gaussian grid from their original spatial resolution based on Ordinary Kriging (Mueller et al., 2004), which is the same as the spatial resolution of the reanalysis data, 2.5° × 2.5 ° resolution horizontal grid.

To disclose the geographical heterogeneity of DFA for the daily air temperature in the continents, we divided the continents into 22 sub-continental land regions (**Table 2** and **Figure 1**), which are defined based on the literatures (Giorgi, 2002; Sillmann et al., 2013; Chan and Wu, 2015). The regions vary from a few thousand to several thousand km in each direction and cover global land areas with simple

TABLE 1 | Information about the eight CMIP5 climate models.

Modeling Center	Nation	Institution	Model information	
			Model name	Atmosphere resolution
CMCC	Italy	Centro euro-mediterraneo per I cambiamenti climatici	CMCC-CMS	T63 (~1.875° × 1.865°) L95
CNRM-CERFACS		Center national de recherches meteorologiques/Center europeen de recherche et formation avancees en calcul scientifique	CNRM-CM5	TL127 (~1.4° × 1.4°) L31
LASG	China	Institue of atmospheric physics Chinese academy of sciences	FGOALS-g2	(~2.81° × 1.66°) L26
GFDL	USA	NOAA geophysical fluid dynamics laboratory	GFDL-ESM2G	M45 (~2° × 2.5°) L24
INM	Russia	Institute for numerical mathematics	INM-CM4	(~1.5° × 2.0°) L21
IPSL	France	Institute pierre-simon laplace	IPSL-CM5A-MR	LMDZ4 (~1.2587° × 2.5°)
MOHC	United Kingdom	Met office hadley center	HadGEM2-AO	T63 (~1.875° × 1.865°) L38
MPI-M	Germany	Max planck institute for meteorology	MPI-ESM-MR	T63 (~1.875° × 1.865°) L47

shape. The selection of specific regions was intended to represent climatic regimes and physiograhic settings (Giorgi, 2002). We calculated the area-averaged scaling exponents in each region for the daily SAT of NCEP and CMIP5 models, respectively. And then the differences of the area-averaged scaling exponents between the NCEP and model outputs were compared.

Method

The DFA method can quantify LRC as an index, namely, scaling exponent (Peng et al., 1994). Consider a record of daily average temperature $\{T_i, i = 1, 2, \ldots, N\}$, the multi-year mean daily average temperature $\overline{T_i}$ is calculated by averaging T_i over all years on the same calendar date i. The variations ΔT_i is departure of T_i from $\overline{T_i}$. The profile $y(k)$ of cumulative of the time series ΔT_i is calculated.

$$y(k) = \sum_{i=1}^{k} \Delta T_i, \quad k = 1, 2, \ldots, N. \tag{1}$$

Then $y(k)$ is divided into n = Int (N/s) non-overlapping segments of equal length s. Usually, s is assumed not to be larger than $N/4$. In each segment, a pth-order polynomial function, $y_s(k)$, is used to fit the profile. The fluctuation function $F_p(s)$ is obtained by calculating the root mean square of the fluctuations in all segments.

$$F_p(s) = \sqrt{\frac{1}{ns} \sum_{k=1}^{ns} \left[y(k) - y_s(k) \right]^2}. \tag{2}$$

Typically, $F_p(s)$ will increase with the segment length s and can be characterized by a scaling exponent α.

$$F_p(s) \sim s^{\alpha}. \tag{3}$$

If $1 > \alpha > 0.5$, the time series $\{T_i, i = 1, 2, \ldots, N\}$ is LRC. If $\alpha = 0.5$, the time series is uncorrelated. If $0 < \alpha < 0.5$, the series $\{T_i\}$ has anti-persistent correlation. When $p = 2$, a 2nd-order polynomial function is used to fit the profile $y(k)$. DFA2 has been widely used in many researches. In this study, the DFA2 method is used to estimate the scaling exponent in a time series.

TABLE 2 | Names and coordinates for the 22 regions in the continents.

Region name	Abbreviation	Coordinates	
		Longitude	Latitude
Northern South America	NSA	80°–35°W	20°S–10°N
Southern South America	SSA	75°–40°W	60°–20°S
Southern Africa	SAF	10°–40°E	35°–10°S
Eastern Africa	EAF	20°–50°E	10°S–20°N
North Africa	NAF	20°W–65°E	20°–30°N
Western Africa	WAF	20°W–20°E	10°S–20°N
Australia	AUS	110°–155°E	40°–10°S
Mexio	MEX	115°–80°W	10°–30°N
Central North America	CNA	105°–85°W	30°–50°N
Eastern North America	ENA	85°–60°W	20°–50°N
Western North America	WNA	130°–105°W	30°–60°N
Alaska	ALA	170°–105°W	60°–70°N
Greenland	GRL	105°–10°W	50°–80°N
Mediterranean	MED	10°W–40°E	30°–50°N
Central asia	CAS	40°–75°E	30°–50°N
Tibetan	TIB	75°–100°E	30°–50°N
East asia	EAS	100°–145°E	20°–50°N
South asia	SAS	65°–100°E	5°–30°N
Southeast asia	SEA	90°–155°E	10°S–20°N
Siberian	SIB	40°E–180°E	50°–70°N
Northern europe	NEU	10°W–40°E	50°–75°N
Antarctic	ANT	0°E–180°W	90°–60°S

To estimate the uncertainties of the DFA2 method, we conducted six sets of independent tests for five given scaling exponents according to the reference (Zhao and He, 2015). In each test, 20,000 artificial time series were produced by Fourier-filtering method (Peng et al., 1991) with given scaling exponents varying from 0.6 to 1.0. **Table 3** demonstrates the 2.5th and 97.5th percentiles for the DFA2's estimated errors for each scaling exponent. Therefore, if the difference of LRC between the reanalysis data and the models is bigger than the estimated error of DFA2, the difference is statistically significant at a significance level of $alpha = 0.05$.

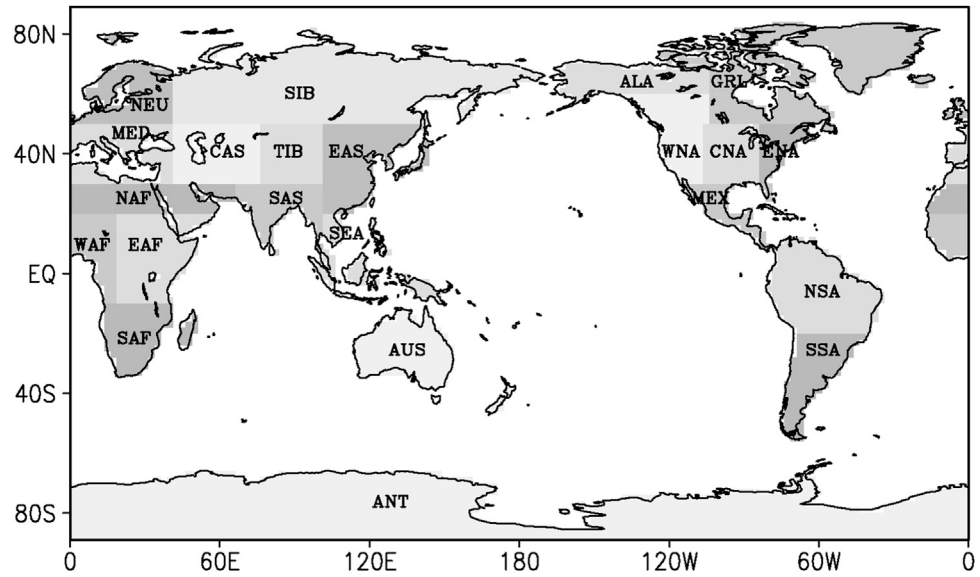

FIGURE 1 | Divisions of the continents on earth.

TABLE 3 | The values in the 2.5th and 97.5th percentiles for DFA2's estimated errors.

Scaling exponents	0.6	0.7	0.8	0.9	1
Estimated errors (year)	–0.06	–0.06	–0.07	–0.07	–0.07
	0.05	0.05	0.06	0.06	0.06
Estimated errors (season)	–0.06	–0.07	–0.08	–0.08	–0.09
	0.06	0.06	0.06	0.07	0.07

LRC OF DAILY AVERAGE SAT SIMULATED BY MULTI-MODELS

Characteristics of Daily Average SAT

As an example, one grid point (110°E, 23°N) located in the eastern part of Eurasia was randomly selected to show the LRC of SAT. The scaling exponent of NCEP SAT at this point is 0.6, which indicates a LRC. The scaling exponents of SAT at this point simulated by 8 CMIP5 models range from 0.52 to 0.74, which are quite different from the long-term correlation of the NCEP SAT (**Figure 2A**). Except for INM-CM4, the scaling exponents of SAT simulated by the models are bigger than those of NCEP SAT (**Figure 3**). As far as scaling exponents of SAT at the selected point are concerned, the differences between the most of CMIP5 simulations and NCEP data are greater than the uncertainties of the DFA2 calculation at a significance level of *alpha* = 0.05, except for IPSL-CM5A-MR. This means that only IPSL-CM5A-MR can relatively reliably reproduce the LRC of SAT of the selected point. In spring, scaling exponent of NCEP SAT at the grid point is 0.61, which is smaller than the scaling exponents of the model-simulated SAT, varying from 0.64 to 0.74 (**Figure 2B**). Except FGOALS-g2 and INM-CM4, the biases of scaling exponent of model-simulated SAT in spring are statistically significant at a significance level of *alpha* = 0.05 (**Figure 3**). In summer, LRC of NCEP SAT at this point becomes stronger with the scaling exponent of 0.65. There is a systematic overestimation of LRCs by CMIP5 models which are all significantly greater than that of NCEP SAT at a significance level of *alpha* = 0.05 (**Figure 3**). The logarithms of the fluctuation functions of the model-simulated SAT in summer are all bigger than that of NCEP SAT, which indicates that the variances of the model-simulated SAT are also bigger than those of NCEP SAT (**Figure 2C**). Scaling exponent of NCEP SAT at the point in autumn is the same as that in summer. The biases of scaling exponents of the model-simulated SAT are significant except IPSL-CM5A-MR (**Figures 2D**, **3**). In winter, scaling exponent of NCEP SAT at the point is 0.64, which is also systematic overestimated by the CMIP5 models. The biases of FGOALS-g2, INM-CM4 and IPSL-CM5A-MR are insignificant at a significance level of *alpha* = 0.05, which means these three models perform well at this point in winter (**Figures 2E**, **3**).

Scaling exponent of NCEP SAT throughout the year is less than those of all four seasons at the point, which is also true for most of the model-simulated SAT, except for GFDL-ESM2G (**Figure 3**). Scaling exponent of NCEP SAT at the point in spring is the smallest among four seasons, while those in summer and autumn are much bigger. The seasonal variations of scaling exponents of most model-simulated SAT are similar to that of NCEP SAT, except for HadGEM2-AO and CMCC-CMS. In general, the difference between the scaling exponent of model-simulated SAT and NCEP data is bigger in summer than that in other seasons.

Figure 4 shows box charts of scaling exponents of NCEP SAT and the biases of scaling exponents of model-simulated SAT on global continents for year and four seasons. The boxes indicate the interquartile distribution (range between the 25th and 75th quantiles). The hollow marked within the boxes show the median, and the short horizontal lines outside the boxes indicate the total

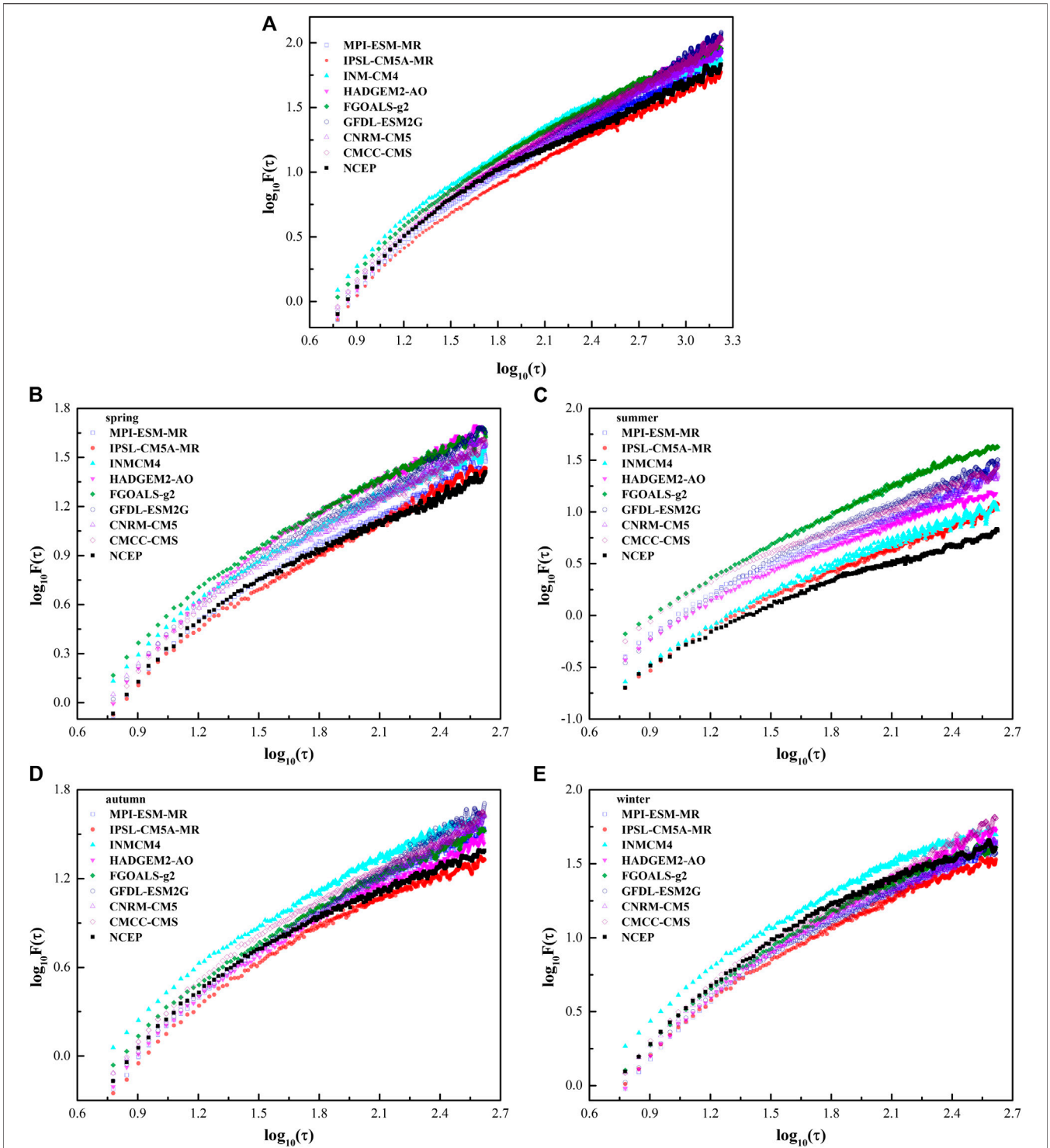

FIGURE 2 | The DFA2 results of SAT from NCEP and CMIP5 models at the point of (110°E, 23°N) for **(A)** year, **(B)** spring, **(C)** summer, **(D)** autumn, and **(E)** winter.

inter-model range. The whiskers show the 5% and 95% ranking values. The scaling exponents of SAT throughout the year range from 0.56 to 1.1, and the median value is 0.69 (**Figure 4A**). Scaling exponents in four seasons vary from 0.52 to 1.14. The median value of the scaling exponents in winter is 0.77, which is bigger than those in other seasons. The median values of the scaling exponent's biases of SAT throughout the year for CNRM-CM5, GFDL-ESM2G, HadGEM2-AO are close to zero

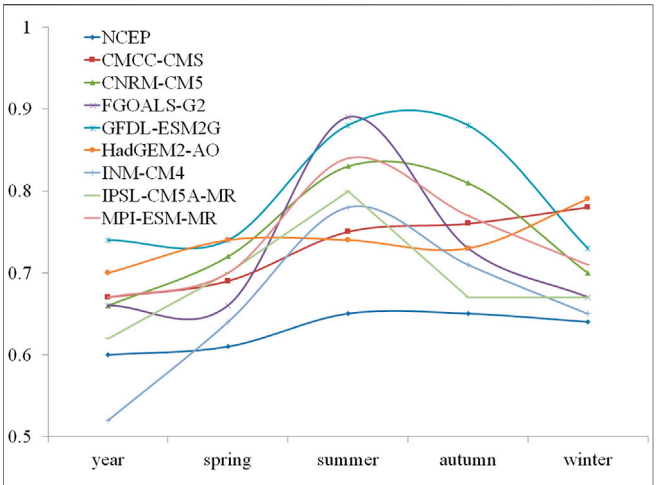

FIGURE 3 | The scaling exponents of SAT from NCEP and CMIP5 models at the point of (110°E, 23°N) for year and all four seasons.

(**Figure 4B**). The scaling exponents of SAT simulated by FGOALS-g2 and INM-CM4 in most part of world are less than those of NCEP SAT, which means SAT simulated by these two models have weaker LRCs. The scaling exponents of SAT from CMCC-CMS, IPSL-CM5A-MR and MPI-ESM-MR are much bigger than those of NCEP SAT, which shows stronger LRCs in the most part of global continents.

In boreal spring, the median value of simulation's errors of GFDL-ESM2G is close to zero, while that of MPI-ESM-MR is 0.06 (**Figure 4C**). Scaling exponents of SAT simulated by CMCC-CMS, CNRM-CM5, HadGEM2-AO, IPSL-CM5A-MR and MPI-ESM-MR are bigger than those of NCEP SAT in most part of global continents, while those of FGOALS-g2 and INM-CM4 are smaller in most areas of global continents. The median values of the simulation's error of FGOALS-g2 and HadGEM2-AO are close to zero, while those of CMCC-CMS and IPSL-CM5A-MR are up to 0.06 in boreal summer (**Figure 4D**). The scaling exponents of SAT simulated by INM-CM4 are smaller than those of NCEP SAT in most part of global continents. In boreal autumn, the median value of the simulation's errors of LRC in FGOALS-g2 is close to zero, however, the mean value of simulation's error in IPSL-CM5A-MR is up to 0.07 which is the biggest in all the models (**Figure 4E**). The scaling exponents of SAT simulated by INM-CM4 are less than those of NCEP SAT in most part of global continent, while the scaling exponents of other models are bigger. The median value of the simulation's error of LRC of FGOALS-g2 is the smallest, while those of HadGEM2-AO and IPSL-CM5A-MR are bigger than 0.04 in boreal winter (**Figure 4F**). The scaling exponents of SAT simulated by INM-CM4 are smaller than those of NCEP SAT in most part of global continents, while those of other six models except FGOALS-g2 are much bigger, especially for CMCC-CMS, IPSL-CM5A-MR and MPI-ESM-MR.

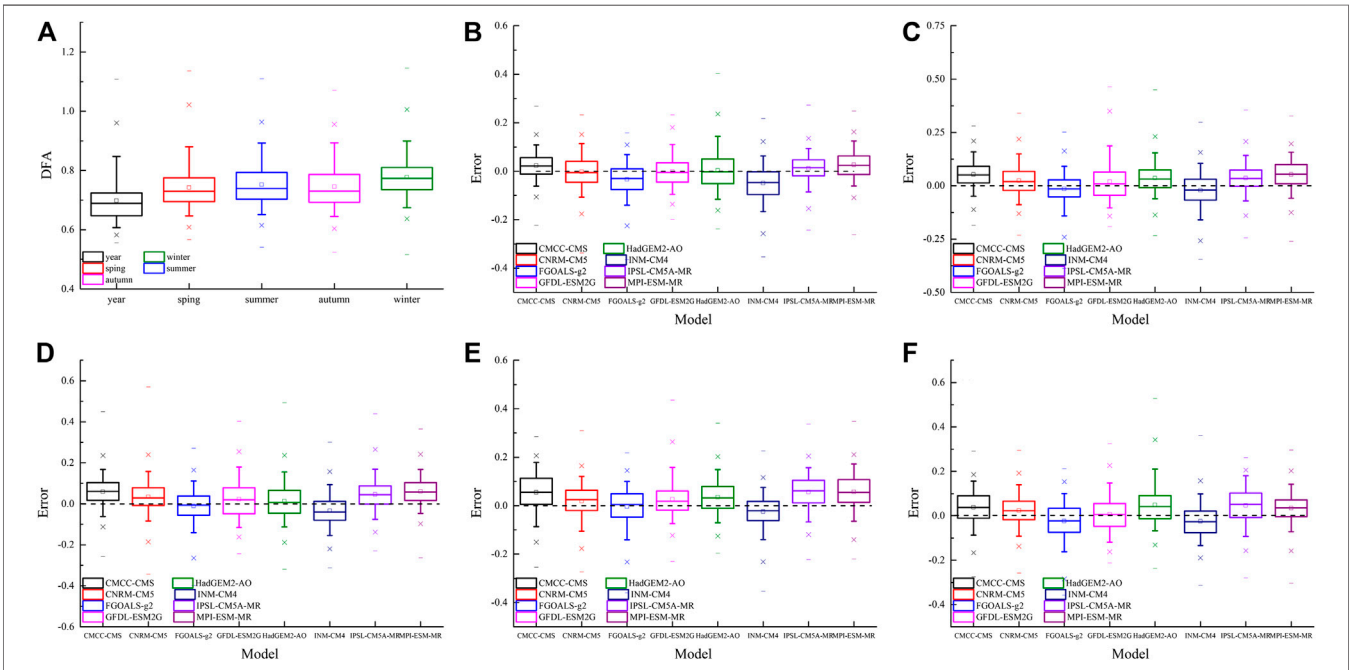

FIGURE 4 | Box charts of scaling exponents of NCEP SAT on global continents **(A)** and the simulation's errors of LRC of model-simulated SAT for **(B)** year, **(C)** spring, **(D)** summer, **(E)** autumn, **(F)** winter.

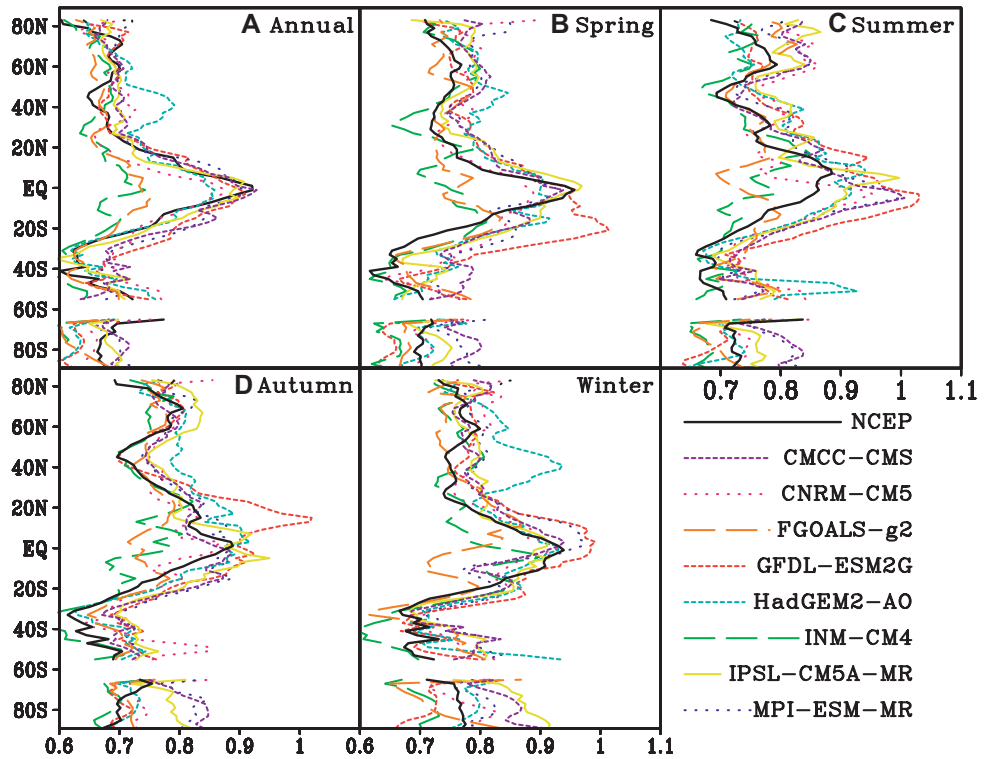

FIGURE 5 | Zonal distribution of scaling exponents of NCEP and the 8 model-simulated SAT throughout **(A)** whole year; **(B)** spring; **(C)** summer; **(D)**autumn; **(E)** winter.

The Zonal Distribution Characteristics of Global LRC of SAT

Scaling exponents of NCEP SAT are larger in the tropics than those in middle and high latitude, which shows pronounced latitude dependence (**Figure 5A**). The zonal mean scaling exponents decrease from equator to middle latitude rapidly. The zonal mean scaling exponents range from 0.7 to 1.0 in tropical areas. From middle latitude to high latitude, the decrement of zonal mean LRC is relatively small. Although the zonal mean of scaling exponents of SAT simulated by 8 CMIP5 models show similar distribution characteristics, there is a great difference among the models. The zonal mean scaling exponents of the model-simulated SAT are close to those of NCEP SAT in the tropics except INM-CM4 and FGOALS-g2. In middle and high latitudes, most of the zonal mean model-simulated scaling exponents are close to those of NCEP SAT except that of HadGEM2-AO. The correlations of zonal mean scaling exponents of model-simulated SAT and those of NCEP SAT all exceed 0.65, which are significant at a significance level of 0.05. The maximum correlation coefficient is 0.89 for CMCC-CMS, while the minimum is 0.66 for MPI-ESM-MR (**Table 4**).

In boreal spring, the zonal mean scaling exponent of NCEP SAT is close to 1 at the equator (**Figure 5B**). It means that NCEP SAT has strong LRC at the equator, and SAT in this area is unstable and very sensitive to small external disturbances. In other words, small disturbances in this area can propagate to other regions through the inner interaction of atmospheric system. From extratropical areas to high latitudes in the northern hemisphere, the zonal mean scaling exponents increase first and then decrease, and the maximum value is about 0.8 near 60°N. In the southern hemisphere, the zonal mean scaling exponents decrease to 0.6 at 40°S, and then increase to about 0.7 in the high latitude. The zonal mean scaling exponents of INM-CM4 and FGOAL-g2 in the tropics are much smaller than those of NCEP SAT, while those of GFDL-ESM2G in the southern tropics are much bigger than those of NCEP SAT. Most of the zonal mean scaling exponents of the model-simulated SAT are bigger than those of NCEP SAT in the high latitudes. The maximum correlation coefficient between

TABLE 4 | Correlation coefficients between zonal mean scaling exponents of NCEP and the model-simulated SAT.

	Year	Spring	Summer	Autumn	Winter
CMCC-CMS	0.89	0.88	0.77	0.7	0.7
CNRM-CM5	0.81	0.78	0.58	0.72	0.79
FGOALS-g2	0.78	0.52	0.3	0.52	0.58
GFDL-EMS2G	0.82	0.8	0.62	0.64	0.83
HadGEM2-AO	0.83	0.68	0.24	0.69	0.34
INM-CM4	0.71	0.66	0.59	0.61	0.73
IPSL-CM5A-MR	0.8	0.87	0.74	0.77	0.44
MPI-ESM-MR	0.66	0.55	0.56	0.59	0.5

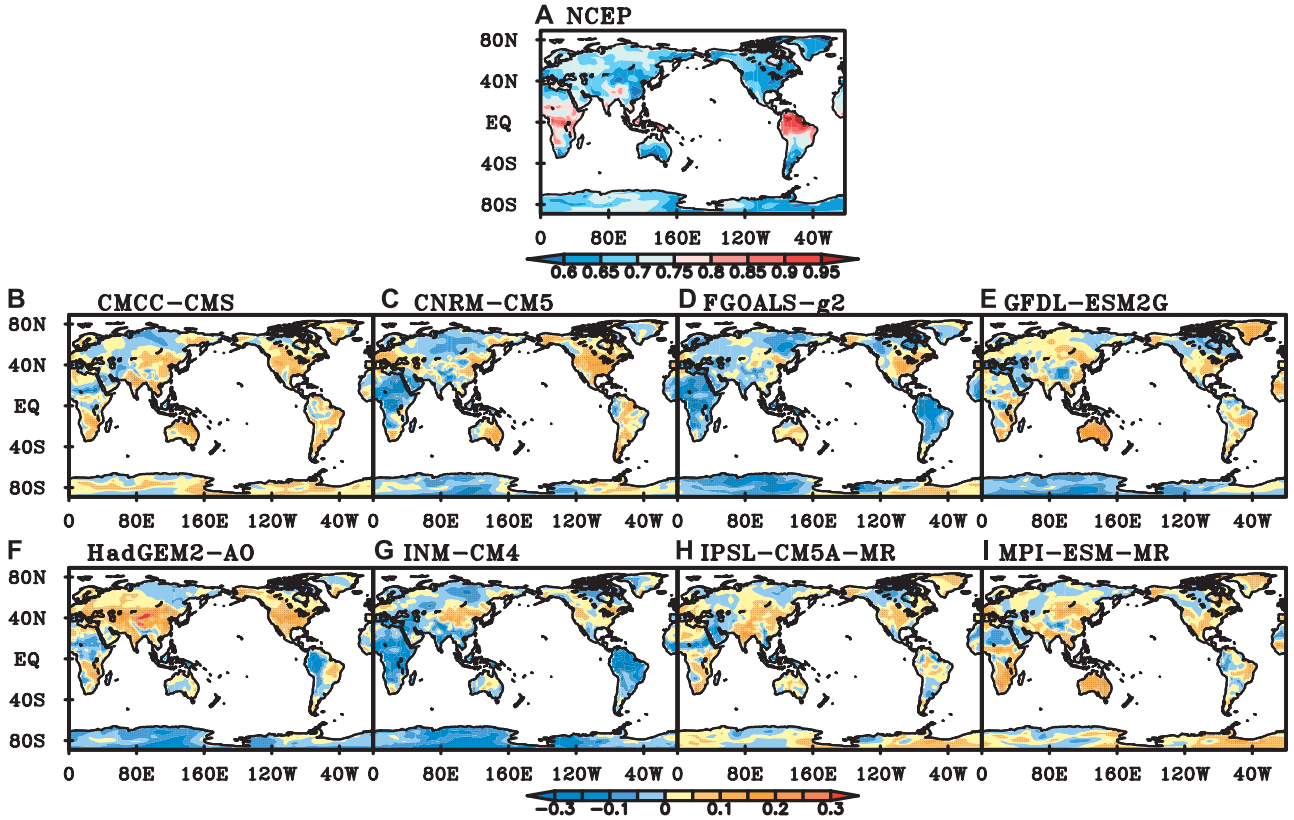

FIGURE 6 | Scaling exponents of NCEP SAT **(A)** and difference between NCEP and those of SAT simulated by **(B)** CMCC-CMS, **(C)** CNRM-CM5, **(D)** FGOALS-g2, **(E)** GFDL-ESM2G, **(F)** HadGEM-AO, **(G)** INM-CM4, **(H)** IPSL-CM5A-MR, **(I)** MPI-ESM-MR. (Black dot represents the difference is significant at a significance level of 0.05).

zonal mean scaling exponents of the model-simulated SAT and those of NCEP SAT is 0.88 for CMCC-CMS, while the minimum is 0.52 for FGOALS-g2.

In boreal summer, the zonal mean scaling exponents of NCEP SAT are bigger in the northern hemisphere than those in most of the southern hemisphere, and the maximum value is located at about 10°N (**Figure 5C**). In the northern hemisphere, there are two sub-peak values at 30°N and 60°N, respectively, while the minimum value is about 0.7 at 40°N. In the southern hemisphere, the zonal mean scaling exponents decrease from tropics to the middle-latitude and reach the minimum near 30°S, and then increase in the high latitudes. The differences between zonal mean scaling exponents of NCEP and the model-simulated SAT are bigger in the tropics than those in other areas. The correlation between the zonal mean scaling exponents of NCEP and the model-simulated SAT in summer is significantly reduced compared with that in spring. The maximum correlation coefficient is 0.77 for CMCC-CMS, while the minimum is only 0.24 for HadGEM2-AO.

In boreal autumn, the peak value of zonal mean scaling exponent is close to 0.9 near the equator, and then the zonal mean scaling exponent decreases to about 0.7 near the 40°N and 0.6 near 35°S (**Figure 5D**). Compared with the zonal mean scaling exponents of NCEP SAT, both INM-CM4 and FGOALS-g2 underestimated LRCs in the tropics, while GFDL-ESM2G significantly overestimates LRCs in northern tropics. The correlations between the zonal mean scaling exponents of the model-simulated SAT and the NCEP data all exceed 0.5. The maximum correlation coefficient is 0.77 for IPSL-CM5A-MR, while the minimum is 0.52 for FGOALS-g2.

In boreal winter, the maximum zonal mean scaling exponent of NCEP SAT is greater than 0.9 near the equator. The zonal mean scaling exponents in the middle and high latitudes of the northern hemisphere are between 0.7 and 0.8, which have smaller variations than those in the southern hemisphere. The zonal mean scaling exponents reach the minimum near 40°S, and then increase to 0.8 in the Antarctic region (**Figure 5E**). In the tropics, the zonal mean scaling exponents of SAT simulated by FGOALS-g2 are obviously smaller than those of NCEP SAT, while those of GFDL-ESM2G are larger. The zonal mean scaling exponents of HadGEM2-AO are larger than those of NCEP SAT in the middle and high latitudes in the northern hemisphere. The differences between the zonal mean scaling exponents of NCEP and most of the model-simulated SAT are relatively larger in the middle and high latitudes of the southern hemisphere than those in other areas. The correlation between zonal mean scaling exponents of the model-simulated SAT and those of NCEP SAT has large variations with the maximum coefficient of 0.84 for GFDL-ESM2G and the minimum of 0.34 for HadGEM2-AO.

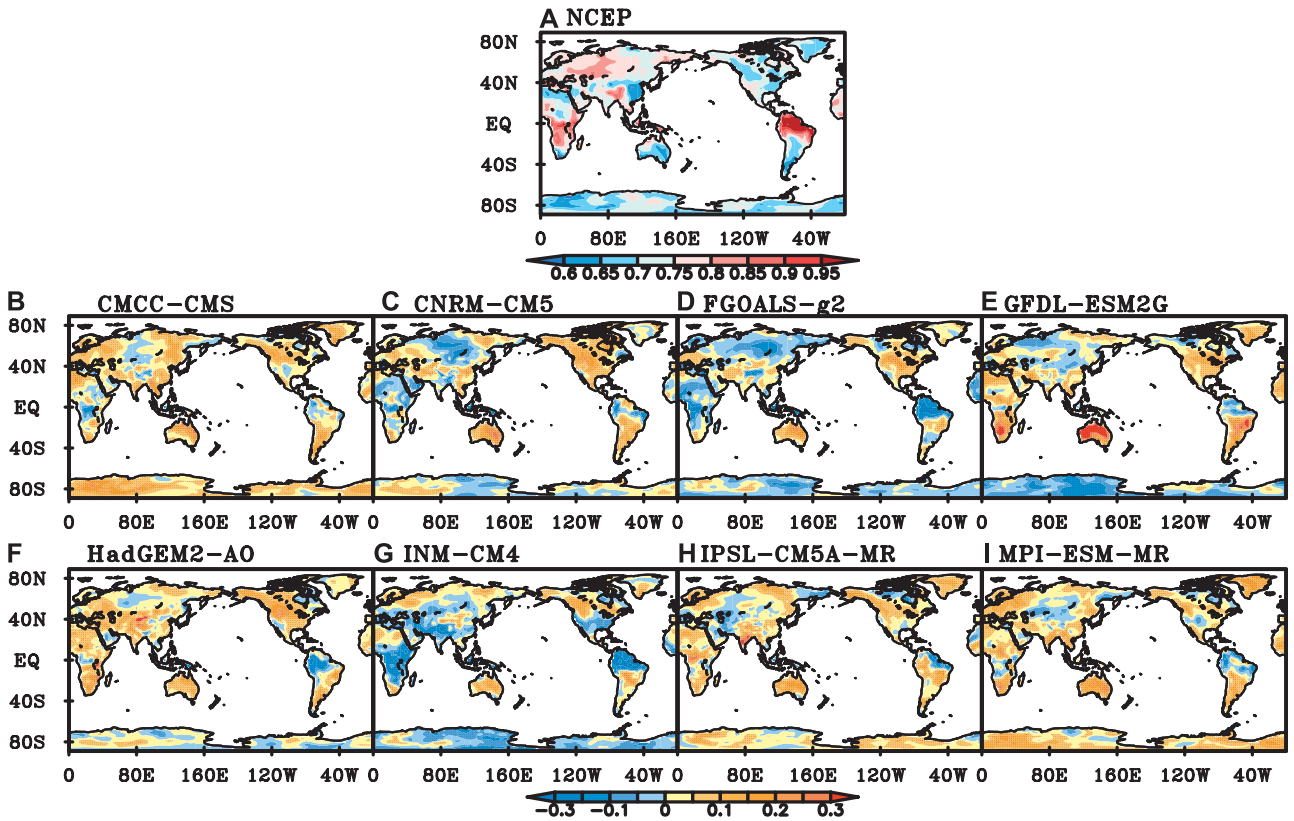

FIGURE 7 | Scaling exponents of NCEP SAT **(A)** and difference between NCEP and those of SAT simulated by **(B)** CMCC-CMS, **(C)** CNRM-CM5, **(D)** FGOALS-g2, **(E)** GFDL-ESM2G, **(F)** HadGEM-AO, **(G)** INM-CM4, **(H)** IPSL-CM5A-MR, **(I)** MPI-ESM-MR in spring. (Black dot represents the difference is significant at a significance level of 0.05).

In general, the zonal mean scaling exponents of NCEP SAT are big in the tropics and small in the middle and high latitudes, which also exhibit obvious seasonal variation. The zonal distributions of scaling exponents in boreal spring are similar with those in winter, with bigger scaling exponents in the northern hemisphere than the southern hemisphere. The zonal distributions of scaling exponents in summer and autumn are also similar, with two sub-peaks in the northern hemisphere and increasing trend from middle to high latitudes. In the tropics, the zonal mean scaling exponents of INM-CM4 and FGOALS-g2 are both smaller than those of NCEP SAT, while those of GFDL-ESM2G are bigger. In a word, the performance of CMIP5 models to LRC has seasonal variation.

Evaluation of Performance of the Model-Simulated SAT Based on the Spatial Distribution Characteristics of LRC

NCEP SAT has LRC characteristics in most parts of the global continents. The scaling exponents are bigger in the tropics than those in other regions. Scaling exponents range from 0.75 to 0.95 in Central Africa and South Asia, and exceed 0.95 in North South America (**Figure 6A**). Compared with the scaling exponents of NCEP SAT, more than 60% of the DFA differences of CMCC-CMS, CNRM-CM5, GFDL-ESM2G, IPSL-CM5A-MR and MPI-ESM-MR are not significant at a significance level of 0.05, which means the performance is good in most of global continents. The performance of IPSL-CM5A-MR is the best among all models with 69.1% of global continents where the simulation's errors are not significant, especially in the northern part of Eurasia, South America and Australia (**Figure 6H**). CMCC-CMS, CNRM-CM5, HadGEM2-AO and MPI-ESM-MR overestimate the LRC of SAT in most parts of the tropics (**Figures 6B,C,F,I**), while both FGOALS-g2 and INM-CM4 underestimate the LRC of SAT in most parts of the global continents (**Figures 6D,G**). The performance of INM-CM4, FGOALS-g2 and HadGEM2-AO is relatively poor.

To explore the performance of individual models in different regions, we calculated the percentage of grids with insignificant errors in each region. If the percentage of good performance grids in one region exceeds 50%, it's considered that the model performance is good in this region. Based on this, the performance of most CMIP5 models is good in SIB, NEU, CAS and GRL regions, while relatively poor in EAS, SAS, SEA and CNA. Both IPSL-CM5A-MR and FGOALS-g2 have five regions with the best performance among the 8 CMIP5 models. However, HadGEM2-AO has six regions of the poorest performance among the 8 models.

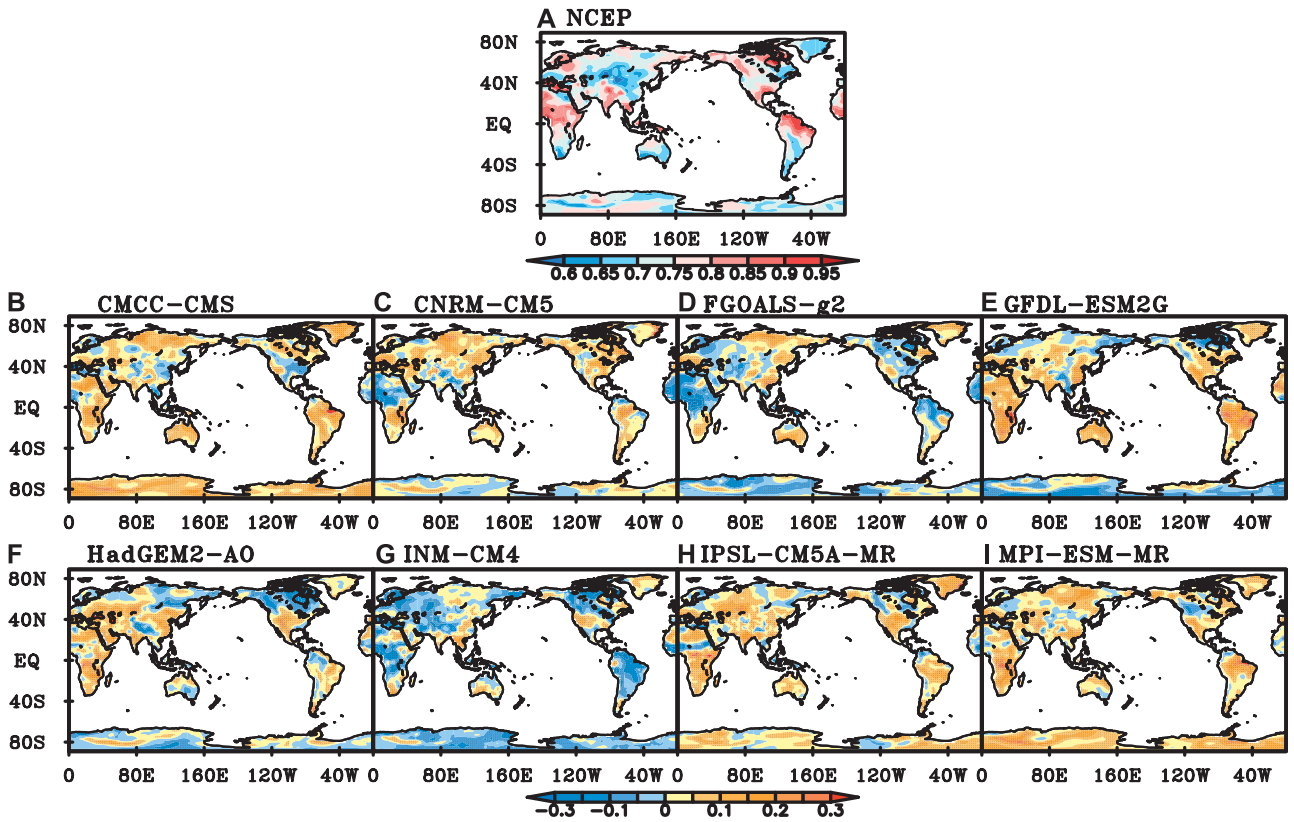

FIGURE 8 | Scaling exponents of NCEP SAT **(A)** and difference between NCEP and those of SAT simulated by **(B)** CMCC-CMS, **(C)** CNRM-CM5, **(D)** FGOALS-g2, **(E)** GFDL-ESM2G, **(F)** HadGEM-AO, **(G)** INM-CM4, **(H)** IPSL-CM5A-MR, **(I)** MPI-ESM-MR in summer. (Black dot represents the difference is significant at a significance level of 0.05).

In boreal spring, the scaling exponents of NCEP SAT in most parts of the global continents are greater than 0.6. The scaling exponents are between 0.6 and 0.7 in eastern China, northern Africa, northwestern North America, South America, eastern Australia and Antarctic, and exceed 0.9 in northern South America (**Figure 7A**). Compared with the scaling exponents of NCEP data, those of model-simulated SAT are smaller in northern South America, and those of SAT from CNRM-CM5, FGOALS-g2 and INM-CM4 are smaller in the tropics (**Figures 7B,D,G**). The percentage of insignificant simulation's errors of LRC is less than 60% for CMCC-CMS, GFDL-ESM2G and MPI-ESM-MR. SAT of GFDL-ESM2G has stronger LRC than NCEP SAT in Australia, southern Africa and southern South America (**Figure 7E**), while those of GFDL-ESM2G and INM-CM4 have weaker LRC in Antarctica (**Figures 7E,G**). The performance of FGOALS-g2 is the best with 71.9% of global continents where the simulation's errors of LRC are insignificant, while the performance of MPI-ESM-MR is the poorest among all eight models with 50.3% of global continents.

The performance of CMIP5 models is good in SIB, CAS and TIB, while poor in WAF, AUS and SEA. The percentage of good performance grids of 8 CMIP5 models exceeds 60% in SIB, while less than 50% in AUS. INM-CM4 has five regions of the best performance among 8 models. Followed by FGOALS-g2 and GFDL-ESM2G, both of them have four regions. However, CNRM-CM5 has six regions of the poorest performance, especially in CAN. Next, both GFDL-ESM2G and MPI-ESM-MR have four regions of the worst performance.

In boreal summer, the scaling exponents of NCEP SAT are bigger than those in spring in most of global continents except in the middle of Eurasia and northern South America. The scaling exponents in the tropical region are greater than 0.8 (**Figure 8A**). Compared with the scaling exponents of NCEP SAT, CNRM-CM5, FGOALS-g2 and INM-CM4 have relatively better capabilities in simulating SAT than the other five models, with more than 60% of global continents where the simulation's errors of LRC are insignificant. The LRCs of SAT from CMCC-CMS, IPSL-CM5A-MR and MPI-ESM-MR are weaker than those of NCEP SAT in local areas of North American (**Figures 8B,H,I**). Scaling exponents of FGOALS-g2 are bigger in eastern Eurasia, Australia and Greenland (**Figure 8D**). GFDL-ESM2G and HadGEM2-AO have smaller scaling exponents in the high latitudes (**Figures 8E,F**). INM-CM4 has smaller scaling exponents in most parts of the global continents (**Figure 8G**).

The percentage of good performance girds in NEU exceeds 62% for most models except INM-CM4. In EAF, GRL, SAF, MED and SEA, the performance of most models is poor. In EAF and GRL, the percentage of good performance grids for all models is less than

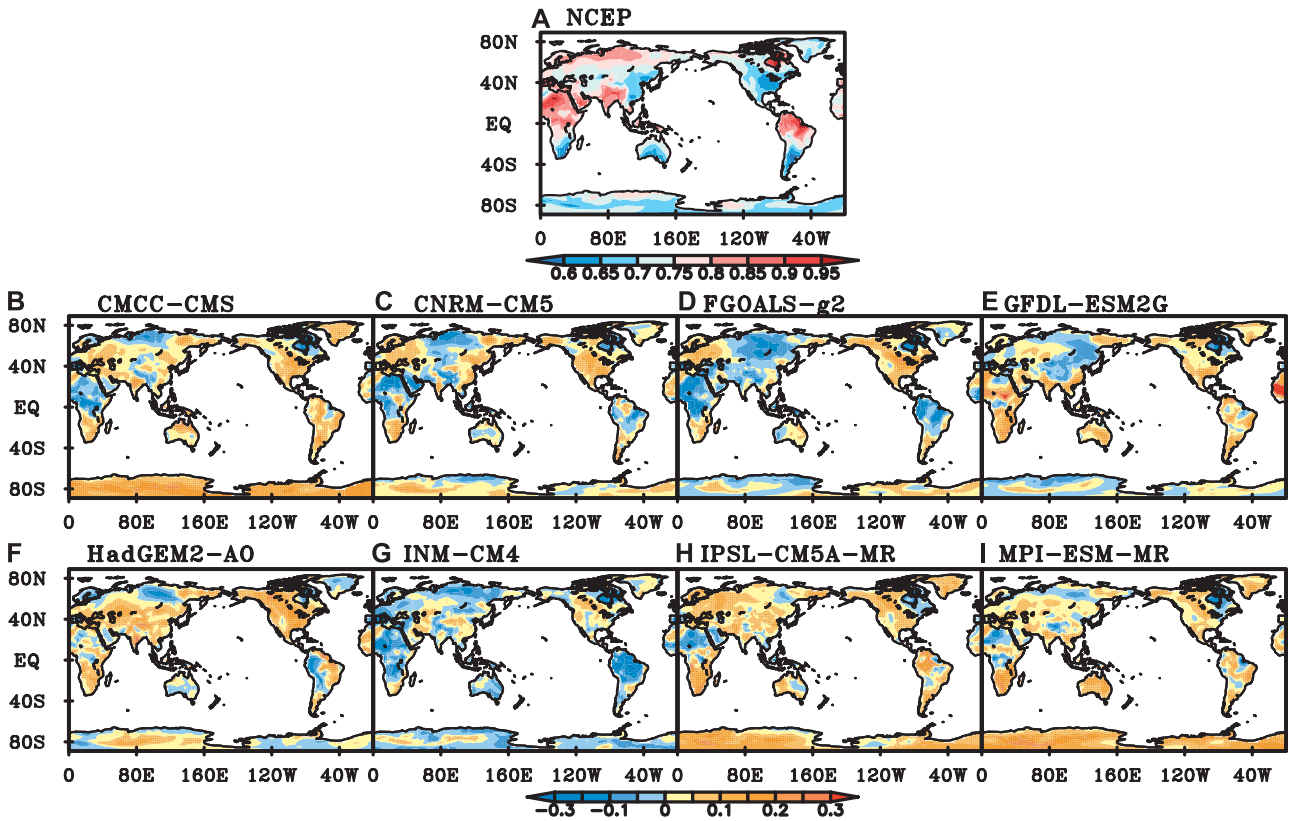

FIGURE 9 | Scaling exponents of NCEP SAT **(A)** and difference between NCEP and those of SAT simulated by **(B)** CMCC-CMS, **(C)** CNRM-CM5, **(D)** FGOALS-g2, **(E)** GFDL-ESM2G, **(F)** HadGEM-AO, **(G)** INM-CM4, **(H)** IPSL-CM5A-MR, **(I)** MPI-ESM-MR in autumn. (Black dot represents the difference is significant at a significance level of 0.05).

50%. FGOALS-g2 has seven best-performance regions, while GFDL-ESM2G has seven regions of the poorest performance.

In boreal autumn, the distributions of scaling exponents of NCEP SAT are similar to those in summer, with smaller values in most part of Eurasia than those in other regions. The scaling exponents of NCEP SAT are generally between 0.6 and 0.7 in the middle and high latitudes of the southern hemisphere, central and southern North America, and eastern Asia, while greater than 0.85 in northern South America, central and northern Africa, South Asia and North America (**Figure 9A**). Compared with the scaling exponents of NCEP SAT, those of CMCC-CMS, IPSL-CM5A-MR and MPI-ESM-MR are bigger in the southern hemisphere and North America, while smaller in northern Africa and northeastern North America (**Figures 9B,H,I**). The scaling exponents of CNRM-CM5 are close to those of NCEP in most parts of the global continents, except in the northern and southern parts of Eurasia, northern Africa, northeastern North America, and northern South America (**Figure 9C**). Scaling exponents of FGOALS-g2 are smaller in northern Eurasia, central and North Africa, North America, northeastern North America, and most parts of South America (**Figure 9D**). LRCs of DTA simulated by GFDL-ESM2G are stronger in parts of Africa, South Asia, eastern Australia, South America and North America, while weaker in the middle of Eurasia, the northeastern part of North America (**Figure 9E**). Scaling exponents of HadGEM2-AO are close to those of NCEP SAT in most regions of the southern hemisphere, while greater in most part of the northern hemisphere (**Figure 9F**). INM-CM4 has weaker LRC in parts of Africa, northern South America, eastern Australia, northern Eurasia, northeastern North America, and Antarctica (**Figure 9G**).

All the 8 CMIP5 models perform well in SIB. In MED and TIB, most of the models except HadGEM2-AO have good performance. The performance of most models is poor in NSA, MEX, CNA and SAF. In CNA, the percentage of good performance grids for CMCC-CMS, CNRM-CM5, FGOALS-g2 and HadGEM2-AO is less than 10%. INM-CM4 has six regions of the best performance among the 8 models. CMCC-CMS has four regions of the best performance. However, HadGEM2-AO has five regions of the poorest performance, and CMCC-CMS has four regions.

In boreal winter, the distributions of scaling exponents of NCEP SAT are similar to those in spring, with bigger values in Eurasia, northern South American and middle and southern South African than those in other areas. The scaling exponents are between 0.6 and 0.7 only in eastern China,

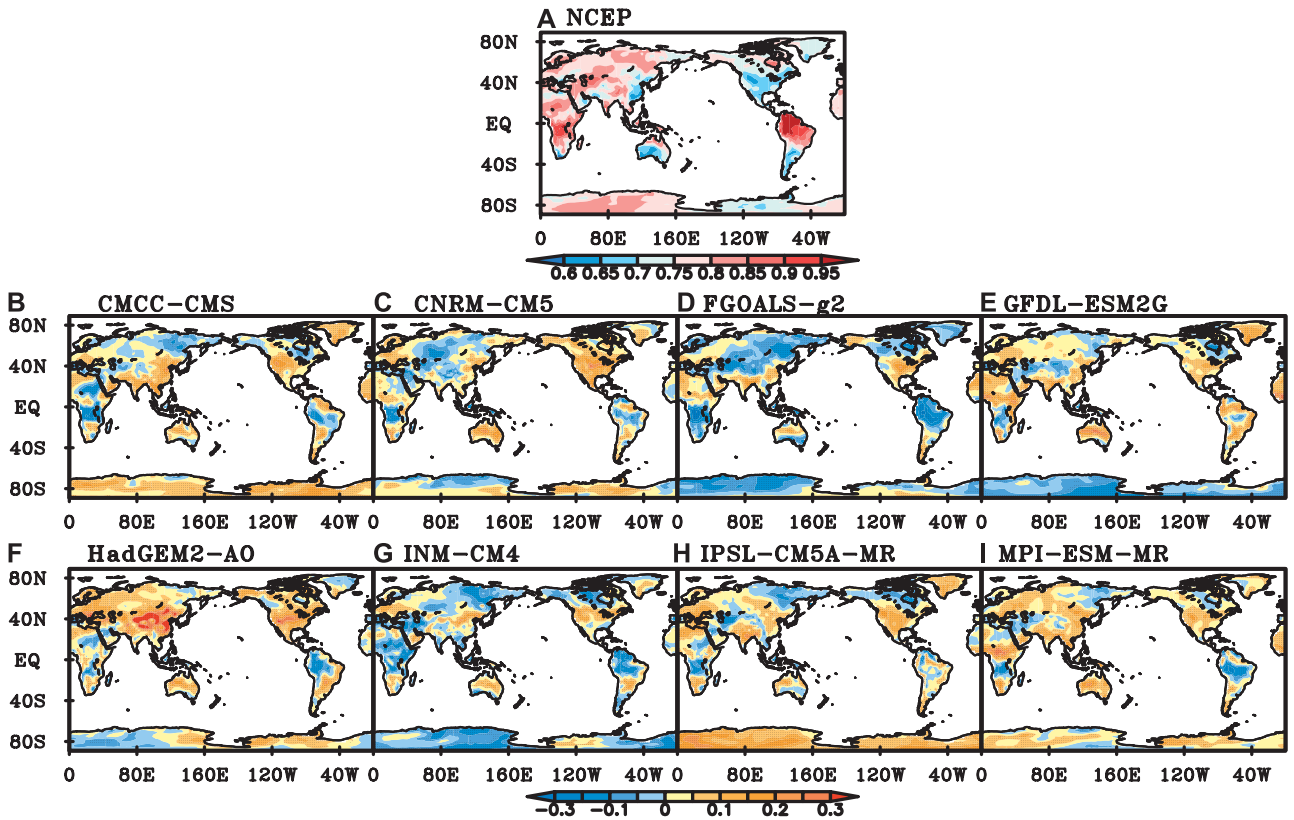

FIGURE 10 | Scaling exponents of NCEP SAT **(A)** and difference between NCEP and those of SAT simulated by **(B)** CMCC-CMS, **(C)** CNRM-CM5, **(D)** FGOALS-g2, **(E)** GFDL-ESM2G, **(F)** HadGEM-AO, **(G)** INM-CM4, **(H)** IPSL-CM5A-MR, **(I)** MPI-ESM-MR in winter. (Black dot represents the difference is significant at a significance level of 0.05).

southwestern Australia, south South America and south central North America. In the rest of the global continents, the scaling exponents are generally above 0.75, and exceed 0.9 in North America and Central Africa (**Figure 10A**).

Compared with scaling exponents of NCEP SAT, those of CMCC-CMS, IPSL-CM5A-MR and MPI-ESM-MR are greater in South Eurasia, northern South America, Antarctic, and parts of Australia, while smaller in middle and southern Africa, Greenland, northern South America (**Figures 10B,H,I**). Those of CNRM-CM5 are smaller in equator, Central Europe, northern South America, while greater in central Australia as well as middle and northern North America (**Figure 10C**). The scaling exponents of FGOALS-g2 and INM-CM4 are smaller in Greenland, northern South America, southeastern North America, central and southern African and Antarctic, while greater in southern North America, northern Australia (**Figures 10D,G**). LRCs of SAT simulated by GFDL-ESM2G are stronger in the tropics while weaker in Antarctic, northeastern North America and central Eurasia (**Figure 10E**). LRCs of SAT simulated by HadGEM2-AO are weaker in the tropics, while stronger in other areas (**Figure 10F**). Scaling exponents of INM-CM4 are smaller in most part of the global continents except in the mid-latitude regions (**Figure 10G**).

All the 8 models perform well in SIB and GRL region. In TIB, most of the models except HadGEM2-AO have good performance. The performance of most models is poor in CNA and SEA. In CAN, all the 8 models have poor performance. CMCC-CMS has the best performance in six regions, and CNRM-CM5 has five best-performance regions. However, HadGEM2-AO has seven regions in which the performance is the poorest. Both CMCC-CMS and CNRM-CM5 have five regions of the poorest performance.

CONCLUSION

Based on the LRCs of daily average SAT, the performance of 8 CMIP5 models in global continents is quantitatively evaluated using DFA method. The DFA results of NCEP SAT show that the SAT has a long-range correlation in most regions of the global continents. The scaling exponents of NCEP SAT show zonal distribution characteristics, which are bigger in tropics than that in middle and high latitudes. The zonal distribution of SAT from CMCC-CMS is the most similar to that of NCEP data in spring, summer and throughout the year. The zonal distributions of scaling exponents of IPSL-CM5A-MR and GFDL-ESM2G are the

most similar to those of NCEP data in autumn and winter,respectively. Compared with the zonal distribution of NCEP SAT, that of FGOALS-g2 has the greatest bias in spring and autumn. HadGEM2-AO has the greatest bias in summer, and HadGEM2-AO has the greatest bias in winter.

Although the performance of models varies in different seasons, there is still something in common. Scaling exponents of SAT simulated by CMCC-CMS, IPSL-CM5A-MR as well as MPI-ESM-MR are smaller in North American while greater in other regions than those of NCEP SAT in all four seasons. This means LRCs of the simulated SAT are stronger than those of NCEP in most areas except North American. Scaling exponents of SAT simulated by FGOALS-g2 and INM-CM4 are less than those of NCEP SAT in most areas, especially in northern South American, most part of African and parts of Eurasia. Scaling exponents of SAT from GFDL-ESM2G are greater in most part of middle latitude of southern hemisphere. Scaling exponents of SAT from CNRM-CM5 and HadGEM2-AO are greater in North American in all four seasons.

The performance of the 8 models also varies in different regions. The scaling exponents of most model-simulated SAT are close to those of NCEP data at middle and high latitudes of the Northern Hemisphere, such as SIB, NEU, GRL and CAS regions, which means the dynamical characteristics of climate systems in these areas are well simulated by the models. However, the DFA errors are big in East Asia and CAN regions. In spring, the performance of most models is good in SIB, CAS and TIB, especially in SIB, but poor in WAF, AUS and SEA. In summer, the performance of most models is good in NEU area, but poor in EAF, SAF, GRL, MED and SEA area. Kumar et al. (2014) showed that some CMIP5 models had warm bias in boreal summer and the performance of the models was poor over EAF, SAF and SEA. In autumn, most models have good performance in SIB, MED and TIB areas, but poor performance in NSA, MEX, CAN and SAF areas. In winter, most models have good performance in SIB, GRL and TIB areas, but poor performance in CAN and SEA areas.

The performance of IPSL-CM5A-MR is the best among the 8 models while that of HadGEM2-AO is the poorest throughout the year. Liu et al. (2014) also pointed out that HadGEM2-AO had poor performance on SAT over China, while INM-CM4 had good performance. The performance of models varies greatly with seasons. FGOALS-g2 has good performance in spring and summer. GFDL-ESM2G has good performance in autumn. CNRM-CM5 and CMCC-CMS has good performance in winter. However, MPI-ESM-MR has the poorest performance in spring. The performance of CMCC-CMS and GFDL-EMS2G is poor in summer. HadGEM2-AO has poor performance in autumn and winter.

Generally speaking, the comparison of individual models for certain regions and seasons reveals that the most of models can reasonably simulate the dynamical characteristics of climate systems in most regions, while there are inter-model differences in various regions and seasons. These differences maybe induced by the processes of climate models, which needs a further examination in the future. Therefore, appropriate models should be selected according to the research regions and seasons.

DATA AVAILABILITY STATEMENT

The original contributions presented in the study are included in the article/**Supplementary Material**, further inquiries can be directed to the corresponding author.

AUTHOR CONTRIBUTIONS

SZ analyzed the data and wrote the manuscript. WH revised the manuscript. TD, JZ, XX, YM, SW, and YJ offered the suggestion.

FUNDING

This research was jointly supported by National Natural Science Foundation of China (Grant Nos. 41875120, 41775092, 41975086, 42075051 and 41605069), and the Fundamental Research Funds for the Central Universities (Grant Nos. 20lgzd06).

SUPPLEMENTARY MATERIAL

The Supplementary Material for this article can be found online at: https://www.frontiersin.org/articles/10.3389/fenvs.2021.628999/full#supplementary-material.

REFERENCES

Beran, J. (1994). *Statistics for long-memory processes*. New York, NY: Chapman & Hall.

Blender, R., and Fraedrich, K. (2003). Long time memory in global warming simulations. *Geophys. Res. Lett.* 30, 1769–1722. doi:10.1029/2003GL017666

Bunde, A., Eichner, J. F., Kantelhardt, J. W., and Havlin, S. (2005). Long-term memory: a natural mechanism for the clustering of extreme events and anomalous residual times in climate records. *Phys. Rev. Lett.* 94, 048701. doi:10.1103/PhysRevLett.94.048701

Bunde, A., and Havlin, S. (2002). Power-law persistence in the atmosphere and in the oceans. *Phys. Stat. Mech. Appl.* 314, 15–24. doi:10.1016/s0378-4371(02)01050-6

Chan, D., and Wu, Q. (2015). Attributing observed SST trends and subcontinental land warming to anthropogenic forcing during 1979-2005. *J. Clim.* 28, 3152–3170. doi:10.1175/JCLI-D-14-00253.1

Eichner, J. F., Koscielny-Bunde, E., Bunde, A., Havlin, S., and Schellnhuber, H. J. (2003). Power-law persistence and trends in the atmosphere: a detailed study of long temperature records. *Phys. Rev. E - Stat. Nonlinear Soft Matter Phys.* 68, 046133. doi:10.1103/PhysRevE.68.046133

Elguindi, N., Grundstein, A., Bernardes, S., Turuncoglu, U., and Feddema, J. (2014). Assessment of CMIP5 global model simulations and climate change

projections for the 21 st century using a modified Thornthwaite climate classification. *Climatic Change* 122, 523–538. doi:10.1007/s10584-013-1020-0

Flato, G., Marotzke, J., Abiodun, B., and Braconnot, P. (2013). *Evaluation of climate models. Climate change 2013: the physical science basis. Contribution of working group I to the fifth assessment report of the intergovernmental panel on climate change*. Cambridge, United Kingdom: Cambridge University Press, 746–866.

Fu, Z., Shi, L., Xie, F., and Piao, L. (2016b). Nonlinear features of northern annular mode variability. *Phys. Stat. Mech. Appl.* 449, 390–394. doi:10.1016/j.physa.2016.01.014

Fu, Z., Xie, F., Yuan, N., and Piao, L. (2016a). Impact of previous one-step variation in positively long-range correlated processes. *Theor. Appl. Climatol.* 124, 339–347. doi:10.1007/s00704-015-1419-9

Gan, Z., Yan, Y., and Qi, Y. (2007). Scaling analysis of the sea surface temperature anomaly in the south China sea. *J. Atmos. Ocean. Technol.* 24, 681–687. doi:10.1175/JTECH1981.1

Giorgi, F. (2002). Variability and trends of sub-continental scale surface climate in the twentieth century. Part I: observations. *Clim. Dynam.* 18, 675–691. doi:10.1007/s00382-001-0204-x

Govindan, R. B., Vyushin, D., Bunde, A., Brenner, S., Havlin, S., and Schellnhuber, H. J. (2004). Global climate models violate scaling of the observed atmospheric variabilit. *Phys. Rev. Lett.* 92, 028501. doi:10.1103/PhysRevLett.92.159803

He, W.-P., and Zhao, S.-S. (2018). Assessment of the quality of NCEP-2 and CFSR reanalysis daily temperature in China based on long-range correlation. *Clim. Dynam.* 50, 493–505. doi:10.1007/s00382-017-3622-0

He, W., Zhao, S., Liu, Q., Jiang, Y., and Deng, B. (2016). Long-range correlation in the drought and flood index from 1470 to 2000 in eastern China. *Int. J. Climatol.* 36, 1676–1685. doi:10.1002/joc.4450

Jiang, D., Tian, Z., and Lang, X. (2016). Reliability of climate models for China through the IPCC third to fifth assessment reports. *Int. J. Climatol.* 36, 1114–1133. doi:10.1002/joc.4406

Jiang, L., Li, N., Fu, Z., and Zhang, J. (2015). Long-range correlation behaviors for the 0-cm averages ground surface temperature and average air temperature over China. *Theor. Appl. Climatol.* 119, 25–31. doi:10.1007/s00704-013-1080-0

Josey, S. A. (2001). A comparison of ECMWF, NCEP/NCAR, and SOC surface heat fluxes with moored buoy measurements in the subduction region of the Northeast Atlantic. *J. Clim.* 14, 1780–1789. doi:10.1175/1520-0442(2001)014<1780:acoenn>2.0.co;2

Kalnay, E., Kanamitsu, M., Kistler, R., Collins, W., Deaven, D., Gandin, L., et al. (1996). The NCEP/NCAR 40-year reanalysis project, *Bull. Am. Meteorol. Soc.* 77, 437–471. doi:10.1175/1520-0477(1996)077<0437:TNYRP>2.0.CO;2

Kanamitsu, M., Ebisuzaki, W., WoollenYang, J. S. K., Yang, S.-K., Hnilo, J. J., Fiorino, M., et al. (2002). NCEP-DOE AMIP-II reanalysis (R-2). *Bull. Am. Meteorol. Soc.* 83, 1631–1644. doi:10.1175/Bams-83-11-1631

Kantelhardt, J. W., Koscielny-Bunde, E., Rybski, D., Braun, P., Bunde, A., and Havlin, S. (2006). Long-term persistence and multifractality of precipitation and river runoff records. *J. Geophys. Res.* 111, D01106. doi:10.1029/2005JD005881

Kharin, V. V., Zwiers, F. W., Zhang, X., and Wehner, M. (2013). Changes in temperature and precipitation extremes in the CMIP5 ensemble. *Climatic Change.* 119, 345–357. doi:10.1007/s10584-013-0705-8

Király, A., and Jánosi, I. M. (2005). Detrended fluctuation analysis of daily temperature records: geographic dependence over Australia. *Meteorol. Atmos. Phys.* 88, 119–128. doi:10.1007/s00703-004-0078-7

Koscielny-Bunde, E., Bunde, A., Havlin, S., and Goldreich, Y. (1996). Analysis of daily temperature fluctuations. *Phys. Stat. Mech. Appl.* 231, 393–396. doi:10.1016/0378-4371(96)00187-210.1016/0378-4371(96)00187-2

Koscielny-Bunde, E., Roman, H. E., Bunde, A., Havlin, S., and Schellnhuber, H. J. (1998). Long-range power-law correlations in local daily temperature fluctuation. *Phil. Mag. B* 77, 1331–1340. doi:10.1080/13642819808205026

Kumar, D., Kodar, E., and Ganguly, A. R. (2014). Regional and seasonal intercomparison of CMIP3 and CMIP5 climate model ensembles for temperature and precipitation. *Clim. Dynam.* 43, 2491–2518. doi:10.1007/s00382-014-2070-3

Kumar, S., Merwade, V., Kinter, J. L., and Niyogi, D. (2013). Evaluation of temperature and precipitation trends and long-term persistence in CMIP5 twentieth-century climate simulations. *J. Clim.* 26, 4168–4185. doi:10.1175/JCLI-D-12-00259.1

Li, Q., Zhang, L., Xu, W., Zhou, T., Wang, J., Zhai, P., et al. (2017). Comparisons of time series of annual mean surface air temperature for China since the 1900s: observations, model simulations, and extended reanalysis. *Bull. Am. Meteorol. Soc.* 98, 699–711. doi:10.1175/BAMS-D-16-0092.1

Liu, Y., Feng, J., and Ma, Z. (2014). An analysis of historical and future temperature fluctuations over China based on CMIP5 simulations. *Adv. Atmos. Sci.* 31, 457–467. doi:10.1007/s00376-013-3093-0

Ma, L., Zhang, T., Li, Q., Frauenfeld, O. W., and Qin, D. (2008). Evaluation of ERA-40, NCEP-1, and NCEP-2 reanalysis air temperature with ground-based measurements in China. *J. Geophys. Res.* 113, D15115. doi:10.1029/2008jd010981

Marques, C. A. F., Rocha, A., and Corte-Real, J. (2010). Comparative energetics of ERA-40, JRA-25 and NCEP-R2 reanalysis, in the wave number domain. *Dynam. Atmos. Oceans* 50, 375–399. doi:10.1016/j.dynatmoce.2010.03.003

Mooney, P. A., Mulligan, F. J., and Fealy, R. (2011). Comparison of ERA-40, ERA-interim and NCEP/NCAR reanalysis data with observed surface air temperature over Ireland. *Int. J. Climatol.* 31, 545–557. doi:10.1002/joc.2098

Mueller, T. G., Pusuluri, N. B., Mathias, K. K., Cornelius, P. L., Barnhisel, R. I., and Shearer, S. A. (2004). Map quality for ordinary kriging and inverse distance weighted interpolation. *Soil Sci. Soc. Am. J.* 68, 2042–2047. doi:10.2136/sssaj2004.2042

Peng, C. K., Havlin, S., Schwartz, M., and Stanley, H. E. (1991). Directed-polymer and ballistic-deposition growth with correlated noise. *Phys. Rev. A.* 44, R2239–R2242. doi:10.1103/PhysRevA.44.R2239

Peng, C. K., Buldyrev, S. V., Havlin, S., Simons, M., Stanley, H. E., and Goldberger, A. L. (1994). Mosaic organization of DNA nucleotides. *Phys. Rev. E.* 49, 1685–1689. doi:10.1103/PhysRevE.49.1685

Phillips, T. J., and Gleckler, P. J. (2006). Evaluation of continental precipitation in 20th century climate simulations: the utility of multimodel statistics. *Water Resour. Res.* 42, W03202. doi:10.1029/2005WR004313

Poccard, I., Janicot, S., and Camberlin, P. (2000). Comparison of rainfall structure between NCEP/NCAR reanalysis and observed data over tropical Africa. *Clim. Dynam.* 16, 897–915. doi:10.1007/s003820000087

Rybski, D., Bunde, A., and von Storch, H. (2008). Long-term persistence in 1000-year simulated temperature records. *J. Geophys. Res.* 113, D02106. doi:10.1029/2007JD008568

Sillmann, J., Kharin, V. V., Zhang, X., Zwiers, F. W., and Bronaugh, D. (2013). Climate extremes indices in the CMIP5 multimodel ensemble: Part 1. Model evaluation in the present climate. *J. Geophys. Res. Atmos.* 118, 1716–1733. doi:10.1002/jgrd.50203

Sillmann, J., Kharin, V. V., Zwiers, F. W., Zhang, X., Bronaugh, D., and Donat, M. G. (2014). Evaluating model-simulated variability in temperature extremes using modified percentile indices. *Int. J. Climatol.* 34, 3304–3311. doi:10.1002/joc.3899

Talkner, P., and Weber, R. O. (2000). Power spectrum and detrended fluctuation analysis: application to daily temperatures. *Phys. Rev. E.* 62, 150–160. doi:10.1103/PhysRevE.62.150

Taylor, K. E., Stouffer, R. J., and Meehl, G. A. (2012). An overview of CMIP5 and the experiment design. *Bull. Am. Meteorol. Soc.* 93, 485–498. doi:10.1175/BAMS-D-11-00094.1

Watterson, I. G., Bathols, J., and Heady, C. (2014). What influences the skill of climate models over the continents?. *Bull. Am. Meteorol. Soc.* 95, 689–700. doi:10.1175/BAMS-D-12-00136.1

Weber, R. O., and Talkner, P. (2001). Spectra and correlations of climate data from days to decades. *J. Geophys. Res.* 106, 20131–20144. doi:10.1029/2001JD000548

Yin, L., Fu, R., Shevliakova, E., and Dickinson, R. E. (2013). How well can CMIP5 simulate precipitation and its controlling processes over tropical south America?. *Clim. Dynam.* 41, 3127–3143. doi:10.1007/s00382-012-1582-y

Yuan, N., Ding, M., Huang, Y., Fu, Z., Xoplaki, E., and Luterbacher, J. (2015). On the long-term climate memory in the surface air temperature records over Antarctica: a nonnegligible factor for trend evaluation. *J. Clim.* 28, 5922–5934. doi:10.1175/JCLI-D-14-00733.1

Zhao, S., He, W., and Jiang, Y. (2017). Evaluation of NCEP-2 and CFSR reanalysis seasonal temperature data in China using detrended fluctuation analysis. *Int. J. Climatol.* 38, 252–263. doi:10.1002/joc.5173

Zhao, S. S., and He, W. P. (2014). Performance evaluation of Chinese air temperature simulated by Beijing Climate Center Climate System Model on the basis of the long-range correlation [in Chinese]. *Acta Phys. Sin.* 63, 209201. doi:10.7498/aps.63.209201

Zhao, S. S., and He, W. P. (2015). Performance evaluation of the simulated daily average temperature series in four seasons in China by Beijing Climate system model. *Acta Phys. Sin.* 64, 049201, 2015 [In Chinese, with English summary]. doi:10.7498/aps.64.049201

Zhou, T., and Yu, R. (2006). Twentieth-century surface air temperature over Chinaand the globe simulated by coupled climate models. *J. Clim.* 19, 5843–5858. doi:10.1175/JCLI3952.1

Conflict of Interest: The authors declare that the research was conducted in the absence of any commercial or financial relationships that could be construed as a potential conflict of interest.

frontiers in Environmental Science

ORIGINAL RESEARCH
published: 19 March 2021
doi: 10.3389/fenvs.2021.641122

Resilience of Grain Yield in China Under Climate Change Scenarios

Jieming Chou[1], Mingyang Sun[2], Yuan Xu[1], Fan Yang[1], Jiangnan Li[1] and Weixing Zhao[1]*

[1]State Key Laboratory of Earth Surface Processes and Resource Ecology, Beijing Normal University, Beijing, China, [2]State Key Laboratory of Earth Surface Processes and Resource Ecology, Faculty of Geographical Science, Beijing Normal University, Beijing, China

As global warming issues become increasingly serious, grain yield and socioeconomic development have been seriously threatened. The key to ensuring grain yield is to recognize the risks caused by climate change. In this paper, the trends of temperature and precipitation over the next thirty years in China are analysed using CMIP6 under the SSP1–2.6, SSP2–4.5 and SSP 5–8.5 climate scenarios. The resilience indicators of grain yield are proposed for the first time. We find that the higher the emission concentration is, the greater the temperature increase will be and further northward the precipitation belt will move. Meanwhile, the resilience varies across different climate zones. The temperate monsoon climate zone has a stronger resilience to adapt to climate change compared to that of other areas. The resilience of the temperate continental and plateau alpine climate zones are moderate. However, the resilience of the subtropical and tropical monsoon climates zones are poor.

Keywords: global warming, grain yield, resilience index, risk, adoption

OPEN ACCESS

Edited by:
Qingxiang Li,
Sun Yat-Sen University, China

Reviewed by:
Zhixin Hao,
Institute of Geographic Sciences and Natural Resources Research, China
Yanling Song,
Chinese Academy of Meteorological Sciences, China

****Correspondence:***
Mingyang Sun
201821051163@mail.bnu.edu.cn

Specialty section:
This article was submitted to Interdisciplinary Climate Studies, a section of the journal Frontiers in Environmental Science

Received: *13 December 2020*
Accepted: *02 February 2021*
Published: *19 March 2021*

Citation:
Chou J, Sun M, Xu Y, Yang F, Li J and Zhao W (2021) Resilience of Grain Yield in China Under Climate Change Scenarios. Front. Environ. Sci. 9:641122. doi: 10.3389/fenvs.2021.641122

INTRODUCTION

Grain security is the foundation for the overall sustainable development of the economy. Climate change poses significant risks and uncertainties for the sustainable development of grain production in all countries. The Intergovernmental Panel on Climate Change (IPCC) notes that significant impacts from climate change have become widespread and widely sensed across different regions and areas of the world (IPCC et al., 2014; CMACCC, 2018). Among them, agriculture is the industry that is most directly affected by and sensitive to climate change, mainly because climate change can cause high-temperature heat waves, droughts and floods as well as increasingly severe and frequent extreme weather and climate events, resulting in fluctuations in grain yield. Climate change is the most important natural factor affecting grain yield (Holst et al., 2013; Tao et al., 2014; Belyaeva and Bokusheva, 2018; Osman et al., 2020). Climate change presents significant risks and uncertainties to the global grain yield.

Identifying the resilience of grain yield under climate change and determining the temporal and spatial scales of their impacts are key factors in coping with climate change and promoting the sustainable development of grain production. Many theoretical and numerical models have attempted to reveal the connection between changes in grain yield and global warming. There are two primary research methods in this field. First, statistical modelling methods use multiple regressions, first-order differences, deep neural networks and other methods to establish statistical models for grain to forecast the influence of climate change on grain output (Crane-Droesch, 2018; Lu et al., 2019; Wang et al., 2019). The reliability of this method can be assessed through statistical testing, but it is difficult to detect a clear intensity change trend in the observation results. The second is the crop model simulation method. By inputting parameters describing soil, sunlight, temperature,

precipitation and other conditions required for crop growth, crop growth conditions under future climate change conditions can be simulated (Abraha and Savage, 2006; Devkota et al., 2013; Mishra et al., 2013; Masud et al., 2019). However, the crop model simulation does not include socioeconomic factors such as policy, management, economy, technology, etc., so the results may have more uncertainty than the actual situation.

Grain yield is the result of the interaction between climatic factors and socioeconomic factors; therefore, comprehensive multidisciplinary and multidomain cross-analysis is required (Chou et al., 2004). With continuous changes in the global climate, the risks of climate change are increasing, which seriously affects the safety and sustainable development of China's grain yield. The importance of improving the resilience of China's grain yield has become a consensus in response to climate change. There are different types of resilience in the context of climate. Holling, an ecologist, first proposed resilience. He defined resilience as the ability of a system to absorb disturbances and continue to exist (Holling, 1973). Later, scholars in various fields, such as engineering, society, and economics, continued to enrich the connotation of resilience. In the field of climate change, the IPCC defines resilience as the ability of a system to adapt to the adverse effects of climate change and recover and resist. The National Research Council (NRC) of the United States defines resilience as the ability to prepare, plan, absorb, recover and more successfully adapt to adverse events. In this definition, resilience is composed to capability, process, and goal (Cutter et al., 2013). Based on the theory of resilience, this article innovatively constructs an evaluation index for the resilience of grain yield under the background of climate change. This article defines "resilience" as the ability to achieve sustainable and stable production through policy, economy, and technology in the face of increasingly severe climate conditions. The lower the resilience of an area is, the higher the risk of climate change; the higher the resilience is, the lower the risk of climate change. This article takes China as an example to carry out an analysis of a grain yield and resilience assessment under different climate scenarios.

In addition, this article considers that the influence of precipitation and temperature on grain yield is a significant nonlinear relationship. To solve this problem, a comprehensive climate factor was constructed to reflect the influence of grain yield under global climate change. This article chiefly applies the economy-climate model as a bridge to connect the analysis of natural science and humanities with socioeconomic analyses. Duzheng Ye and Jieming Chou and Du, 2006 proposed an economic-climate model based on the traditional production function model (C-D) (Chou and Ye, 2006). This model was used to build an input-output model of grain yield that systematically reveals the changing trends in the future pattern of grain yield under different emissions situations; it also identifies areas of higher resilience to determine key production areas and generate breakthroughs in future grain security work. This study provides a scientific basis and policy recommendations for promoting the realization of sustainable development goals (SDGs).

MATERIALS AND METHODS

Previous studies on China's grain yield have mostly examined changes in grain output on the basis of subregions such as the north and south regions (Chou et al., 2019), the three major zones, and the eight major grain-producing regions (Xu and Zhu, 2015). The North and South regions are divided with the Qinling Huai River acting as the boundary. The three major zones include the eastern coastal zone (Liaoning, Hebei, Tianjin, Beijing, Shandong, Jiangsu, Shanghai, Zhejiang, Fujian, Guangdong, Guangxi and Hainan), the central zone (Heilongjiang, Jilin, Inner Mongolia, Shanxi, Anhui, Jiangxi, Henan, Hubei and Hunan) and the western zone (Shaanxi, Gansu, Ningxia, Qinghai, Xinjiang, Sichuan, Yunnan, Guizhou and Tibet). The eight major grain-producing regions in China are the Sanjiang Plain, Songnen Plain, Jianghuai Area, Taihu Plain, Jianghan Plain, Poyang Lake Plain, Dongting Lake Plain and Chengdu Plain.

It is difficult to fully reflect the natural geographical future of all of China. As shown in **Figure 1**, China's north-south latitude is wide, and it is located within five major climate regions. The amount of heat received from the sun varies from place to place. Within the same climate zone, the basic characteristics of the climate are similar. This article divides the grain production areas in China into five regions by climate zone (see **Table 1**) and discusses the changes in temperature and precipitation in the different climate regions under SSP1–2.6, SSP2–4.5, and SSP5–8.5. It also analyses the influence of climate change on grain yield in the different climate regions and proposes a resilience evaluation for grain yield under global climate change.

DATA AND METHODS

Data

Data Sources

The historical data used in this article are climate and economic data from twenty nine provinces and autonomous regions in China from 1981 to 2018. The climate data include the monthly precipitation and average temperature of each province during the growing period (April to September), which were obtained from the National Meteorological Information Center (http://data.cma.cn). The economic data include the annual data on rural labour, grain sown area, agricultural fertilizer, grain yield and population. The data were obtained from the China National Statistical Center (http://www.bjstats.gov.cn) and the China Statistical Yearbook.

Future climate data include the monthly average of the 2020–2050 growth period (April-September) output by the BCC-CSM2-MR, which is newly developed by the National Climate Center. It is a mode resolution model participating in the sixth phase of the Coupled Model Intercomparison Project (CMIP6). The ability of the BCC-CSM2-MR climate model to simulate the climate mean state and global warming trend, quasi-biennial oscillation (QBO), tropical intraseasonal oscillation (MJO) and diurnal variation in precipitation in the 20th century has significantly improved. (Wu et al., 2019). CMIP6

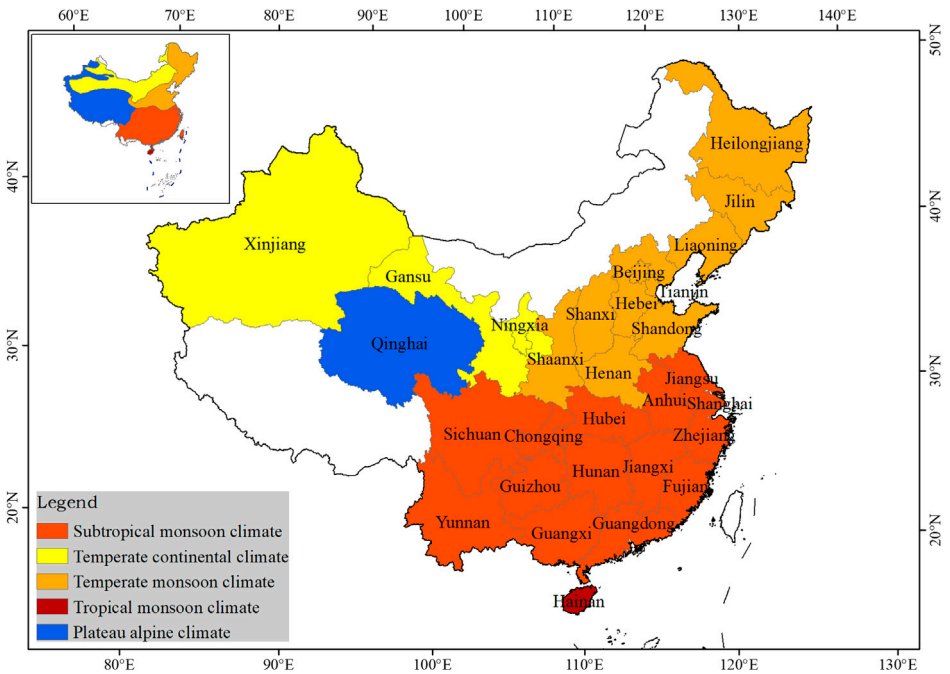

FIGURE 1 | Distribution of five climatic regions for grain yield in China

TABLE 1 | The division of five climatic regions for grain yield in China.

Climate type	Province	Location
Temperate monsoon climate	Heilongjiang, Jilin, Liaoning, Hebei, Beijing, Tianjin, Henan, Shandong, Shanxi, Shaanxi	Approximately 35°~55°N, 108°~138°E,
Subtropical monsoon climate	Chongqing, Hubei, Hunan, Anhui, Jiangsu, Shanghai, Guizhou, Yunnan, Zhejiang, Jiangxi, Fujian, Guangdong, Guangxi, Sichuan	Approximately 25°~35°N 98°~120°E
Temperate continental climate	Gansu, Ningxia, Xinjiang	Approximately 35°~50°N 90°~105°N,
Plateau alpine climate	Qinghai	Approximately 26°~40°N 74°~104°E
Tropical monsoon climate	Hainan	Approximately 15°~25°N 108°~112°N,

TABLE 2 | CMIP scenario experimental design.

Scenario prediction test	Test description
SSP1–2.6	In the low forcing scenario, resulting in the radiation forcing level of 2.6 W/m^2 in 2100.
SSP2–4.5	In the moderate forcing scenario, resulting in the radiation forcing level of 4.5 W/m^2 in 2100.
SSP5–8.5	In the high forcing scenario, resulting in the radiation forcing level of 8.5 W/m^2 in 2100.

designed a series of new scenario prediction experiments based on the possible anthropogenic emissions and land use changes caused by the energy structure in different shared socioeconomic paths. This paper mainly focuses on the three radiative forcing scenarios shown in **Table 2** (Pu et al., 2020). These three different radiative forcing scenarios represent three future emissions levels, e.g., low, moderate and high, and provide a theoretical basis for studying the impacts of different climate changes on grain yield.

Method

Economy-Climate and Grey System Model

Grain yield is affected not only by the input of socioeconomic elements such as rural labour, grain cultivation area, and agricultural fertilizer but also by meteorological elements, including climatic elements. This article is based on the Cobb-Douglas, which can map the relationship between input and output under certain technical conditions. Chou et al. presented a

novel approach by introducing the comprehensive climatic factor into the Cobb-Douglas model. It is called the economy-climate model (C-D-C model) (Chou and Ye, 2006). Then, we use grey system model GM(1,1) to predict the future socioeconomic data. GM(1,1) establishes a grey differential prediction model through a small amount of incomplete information to make long-term fuzzy information. It is of higher adaptability and accuracy (Yin, 2013). We use economy-climate and grey system models to construct a comprehensive model to predict the future grain yield using the following equations:

$$Y_{it} = \mu * x_1^{\beta 1} x_2^{\beta 2} x_3^{\beta 3} C^{\gamma} \quad (1)$$

Its logarithmic function is as follows:

$$\ln Y = \beta_1 \ln x_1 + \beta_2 \ln x_2 + \beta_3 \ln x_3 + \gamma \ln C + \ln \mu \quad (2)$$

where Y_{it} represents grain yield; X_1, X_2, and X_3 represent the rural labour, the grain cultivation area, and the agricultural fertilizer in each province, respectively; β_1, β_2, β_3, and γ are the coefficients of each element; and μ represents the other elements.

Construct Comprehensive Climate Factor C by Principal Component Analysis

Principal component analysis (PCA) is probably the most commonly used dimensionality reduction method. To ensure that the original information is not missing or is missing as little data as possible, this method uses a few unrelated comprehensive indexes to express the majority of interrelated indexes (Brunetti et al., 2006). Let the original index temperature and precipitation be X_1 and X_2 and the main components be F_1 and F_2.

$$\begin{cases} F_1 = a_{11}X_1 + a_{12}X_2 \\ F_2 = a_{21}X_1 + a_{22}X_2 \end{cases} \quad (3)$$

First, a sample matrix was constructed. Suppose a provincial administrative region in China has a sample size of monthly mean temperature precipitation from 1981 to 2018, and the observed climate indicator is temperature and precipitation.

$$X = (X_1, X_2)^{\mathrm{T}} \begin{pmatrix} x_{11} & x_{12} & \\ x_{21} & x_{22} & \\ \vdots & \vdots & \vdots \\ x_{n1} & x_{n2} & \end{pmatrix} \quad (4)$$

Second, the principal component was determined. MATLAB was used to normalize the original climate data and calculate the relevant coefficient matrix r, principal component correlation coefficient e_{ij} and eigenvalues of the matrix λ_j

$$\theta_j = \frac{\lambda_j}{\sum \lambda} \quad (5)$$

According to **Eq. 5**, the variance contribution rate θ_j was obtained. Then, the correlation coefficient a_{ij} of the i–th index in the j–th principal component was calculated according to **Eq. 6**.

$$a_{ij} = e_{ij} \Big/ \sqrt{\lambda_j} \quad (6)$$

Finally, the index weight was calculated, and the coefficient of each index was calculated according to **Eq. 7**.

$$F_j = \sum_{j=1}^{p} a_{ij} X_i \quad (7)$$

The weight vector was constructed, and **Eq. 8** was used to calculate the weight of each index of the original data matrix.

$$q = \frac{\lambda_1 F_1 + \lambda_2 F_2 + \cdots + \lambda_j F_j}{\sum_{i=1}^{p} \lambda_i} \quad (8)$$

PCA was used to determine the weight of the comprehensive climatic factor C (Chou et al., 2019). It can represent the relative importance of a certain indicator. If the weight is greater, it means that it has a greater influence overall.

$$C = q_1 X_1 + q_2 X_2 \quad (9)$$

where X_1 and X_2 are the temperature and precipitation, respectively, q_1 and q_2 are the weights obtained by PCA calculation. Although the comprehensive climate factors of the different provinces were calculated in the same way, their weights in the principal component analysis were differed due to various factors, such as terrain and climate, that lead to differences in the comprehensive climate factors of each province.

Resilience Indicators

Resilience in physics refers to the ability of an object to resist the deformation of external forces and spring back into shape. Ecologically, resilience is defined as the stability of an ecosystem. In the field of disaster science, Patton defined resilience as the ability of the system to maintain its regular function, as well as its ability to cope with alterations and adjustments under extraneous conflict (Paton and Johnston, 2001). Bruneau believes that resilience focuses on the ability to quickly recover from disasters (Bruneau et al., 2003). Cai believes that resilience is the unique capability of an ecosystem to preserve the operation of its main functions when the system resolves a crisis (Cai et al., 2012). The United Nations defines resilience as the ability of a city to confront risks to withstand, maintain and cope with the influence of risk in a prompt and effective way. Climate change poses significant risks and uncertainties for the sustainable development of grain yield in all countries. As one of the important means of identifying grain yield status in grain yield areas, the assessment of grain yield has attracted the attention of many scholars, and there has been a lot of theoretical, methodological and applied research on this topic (Xu et al., 2013; Ji et al., 2014; Davenport et al., 2015). To quantitatively assess the resilience of future grain yield in China, this paper innovatively proposes climate change resilience indicators for grain yield. "Resilience" is used to indicate the ability of grain-producing areas to recover from the disturbance of climate change and realize stable grain production. Due to the obvious spatial heterogeneity of grain yield affected by climate change, the resilience of grain yield varies across different climate regions. Considering the negative

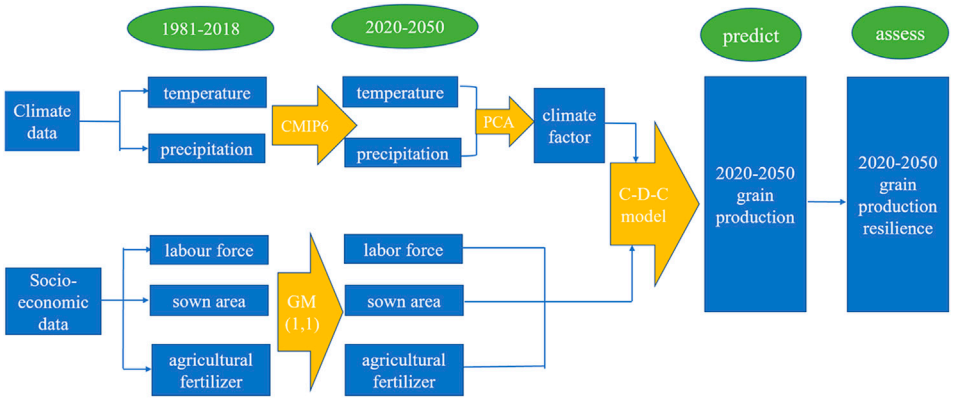

FIGURE 2 | Flow chart of China's grain yield resilience under global climate change.

correlation between grain yield resilience and climate change risk, previous research has developed grain yield risk indicators under global climate change (Wu et al., 2017; Sun et al., 2020). The article quantitatively assesses the sustainability of grain yield using two factors: grain output per person and grain unit yield.

We define the resilience index of grain output per person as the ratio of the 2000–2018 average annual grain output per person to the 2020–2050 grain output per person under global climate change. The index is calculated as follows:

$$H_m = \frac{1}{n}\sum_j F_{jm}, F_{jm} = G_{jm}/P_{jm}, j = 2000-2018, n = 19 \quad (10)$$

$$F'_{wm} = G_{wm}/P_{wm}, w = 2020-2050 \quad (11)$$

$$S_{wm} = H_m/F'_{wm} \quad (12)$$

where G_{jm} is the grain yield of province m in year j, P_{jm} is the population of province m in year j, F_{jm} is the grain output per person of p mrovince in year j, and H_m is the average annual grain output of province m. F'_{wm} is the grain output per person of province m in year w, G_{wm} is the grain yield of province m in year w, P_{wm} is the population of province m in year w, and S_{wm} is the grain output per person resilience index of province m in year w.

We define the resilience index of grain unit yield as the ratio of the 2000–2018 average grain unit yield to the 2020–2050 grain unit yield under global climate change. The index is calculated as follows:

$$N_m = \frac{1}{n}\sum_j M_{jm}, M_{jm} = G_{jm}/A_{jm}, j = 2000-2018, n = 19 \quad (13)$$

$$M'_{wm} = G_{wm}/A_{wm}, w = 2020-2050 \quad (14)$$

$$R_{wm} = N_m/M'_{wm} \quad (15)$$

where G_{jm} is the grain yield of province m in year j, A_{jm} is the grain sown area of province m in year j, M_{jm} is the grain unit yield of province m in year j, and N_m is the average annual grain unit yield of province m. M'_{wm} is the grain unit yield of province m in year w, G_{yi} is the grain yield of province m in year w, A_{wm} is the planting area of province m in year w, and R_{wm} is the grain unit yield resilience index of province m in year w.

Based on socioeconomic and climatic data, this paper forecasts the grain yield for SSP1–2.6, SSP2–4.5, and SSP5–8.5. **Figure 2** is the flow chart of China's grain yield resilience under global climate change.

RESULTS AND DISCUSSION

Temperature and precipitation differences under different scenarios in China.

Due to the complexity and variability of climate systems, climate models have become a powerful tool for studying future climate systems and climate change. CMIP6 simulation results are an important basis for climate predictions and climate change risk assessments. However, due to the differences in their mechanisms, structural principles, climate forcing parameters, resolutions and emissions scenario designs, different climate models predict different impacts from climate change. The simulation performance of climate change models is also quite variable. The prediction of temperature change trends in China in the 21st century show good consistency among models, but there are large differences in predictions between precipitation simulations. We selected the BCC-CSM2-MR model, which belongs to a medium resolution model. This model was developed by the National Climate Center of China. This model is closer to the actual distribution of precipitation in China and is more realistic. Therefore, the BCC-CSM2-MR model in CMIP6 was selected for this paper. The ability of the BCC-CSM2-MR climate system model to simulate quasi-biennial oscillation (QBO), tropical intraseasonal oscillation (MJO) and diurnal variation in precipitation in the 20th century has been significantly improved. (Wu et al., 2019).

Figure 3 shows the BCC-CSM2-MR model simulated the situations in temperature and precipitation differently between 2050 and 2015 under different scenarios. The temperature and precipitation in 2050 are the average values from 2046 to 2055. Compared with the historical climate data of 2015, the annual

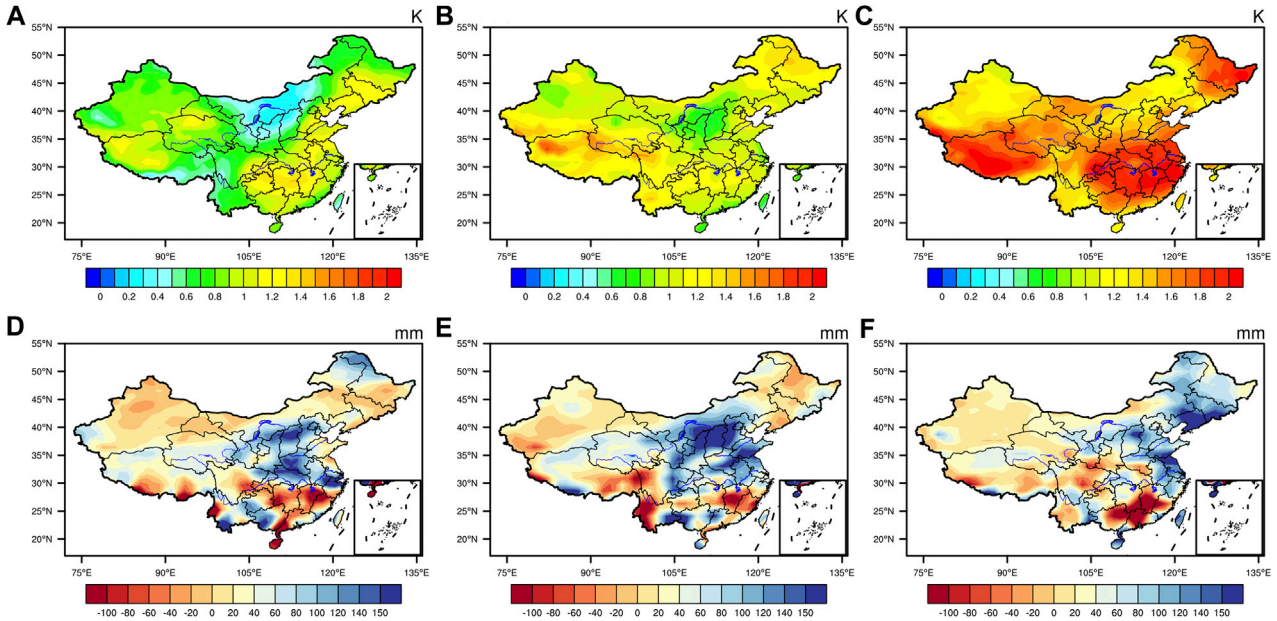

FIGURE 3 | Temperature and precipitation difference between 2050 and 2015 under different scenarios; **(A)** SSP1–2.6 temperature, **(B)** SSP2–4.5 temperature, **(C)** SSP5–8.5 temperature, **(D)** SSP1–2.6 precipitation, **(E)** SSP2–4.5 precipitation, and **(F)** SSP5–8.5 precipitation.

mean temperature for SSP5–8.5 is significantly higher than that for SSP2–4.5 and SSP1–2.6. In other words, the temperature changes are larger for higher emission scenarios. The areas with faster warming rates in the future are mainly concentrated in the central subtropical and northern temperate monsoon climate zones.

The precipitation values in each climate region in China presents a fluctuating trend from 2015 to 2050. In the low emission scenario SSP1–2.6, the precipitation centers are mainly concentrated in the south of the temperate monsoon region; in the medium emission scenario SSP2–4.5, the precipitation center area is further expanded; in the high emission scenario SSP5–8.5, the precipitation center moves further toward the north. The driving force of the northward movement of the rain belt in China is the summer monsoon. The strength of the summer wind power depends on the thermal difference between the terrace and ocean, which is located between the Eurasian continent and Pacific Ocean. Global warming will increase the thermal difference between the terrace and ocean, which is located between Eurasia and the Pacific Ocean, strengthening the summer monsoon and moving the rain belt northward faster and wider.

Discussion and Analysis of the Future Grain Yield in China

In the process of agricultural planting development, grain yield is tightly related to diverse aspects of the external environment, such as the sowing area and temperature. They are comprehensive actions of socioeconomic elements and climate elements. The report of the 19th National Congress of the Communist Party of China points out that from 2020 to 2035, China will be built into a powerful socialist country. Therefore, we will take 2035 as our boundary. **Figure 4** shows the future grain yield of provinces in China in the next fifteen years (2021–2035) and in 2036–2050 under the different emissions scenarios.

Generally, China's grain yield is mainly concentrated in the zone of the monsoon climate (temperate and subtropical monsoon climates). The monsoon climate is a comprehensive phenomenon under the combined influence of three factors, including the thermal effects of the land-sea distribution, seasonal variations in atmospheric circulations and specific topographies. During the period of rainfall and heat in the monsoon area, water is provided at times when crops grow vigorously, i.e., when they need it most, which is very beneficial to agricultural development. The provinces with the highest future grain yield are mainly concentrated in the temperate continental climate zone to the north of the Qinling Mountains, and Heilongjiang Province is the largest producer of grain in China. In addition, Heilongjiang's grain production is most affected by global warming; it has the highest grain yield under SSP1–2.6. This is because as emissions increase, the temperature will gradually increase; thus, the crop growth period will lengthen, and the cultivation system will also change accordingly. In addition, the cold damage that affects crops will also be significantly reduced or disappear. As the climate warms, more food will be harvested at high latitudes. For subtropical and tropical monsoon climate regions at middle-low latitudes, the difference in grain yield under the different emissions scenarios is relatively small. The grain yield in the high-emissions scenario, SSP5–8.5, is slightly lower than that in the moderate-emissions scenario, SSP2–4.5, and low-emissions

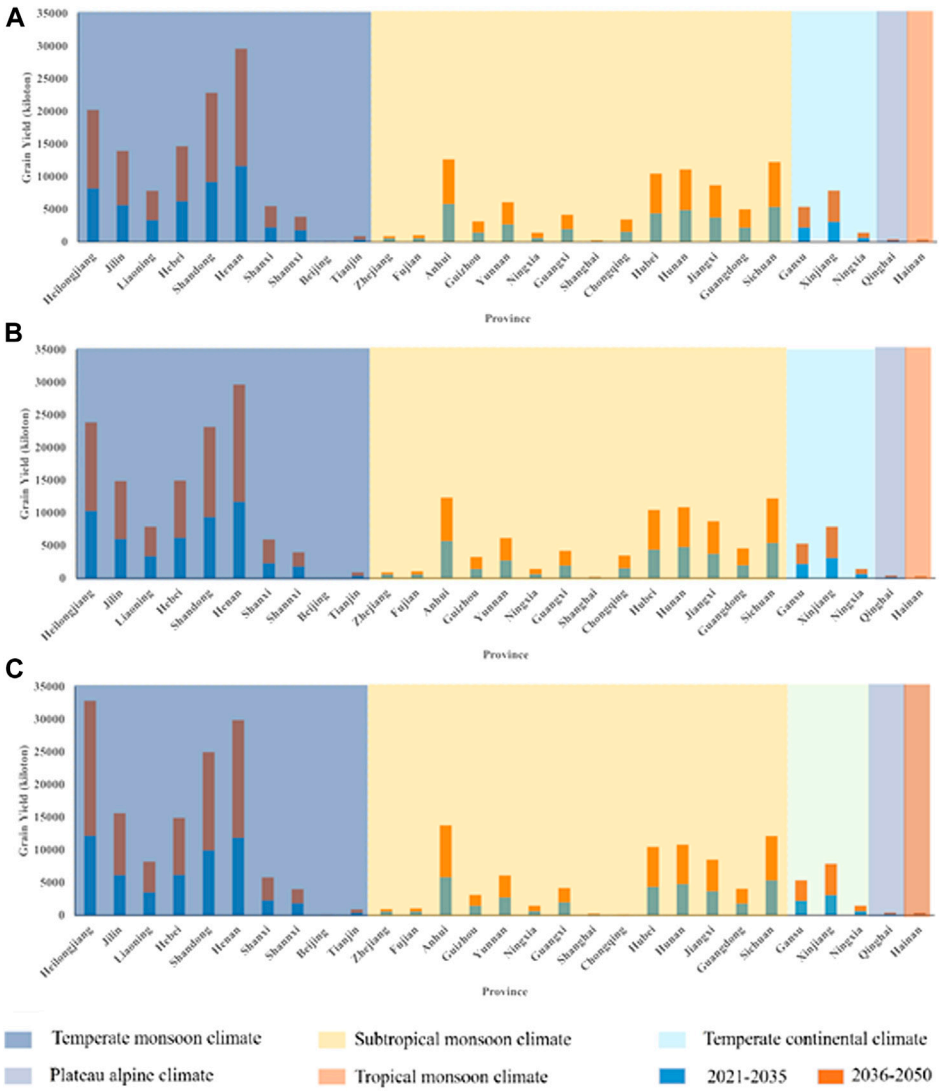

FIGURE 4 | China's total grain yield in 2020–2050 under different emissions scenarios **(A)** SSP1–2.6, **(B)** SSP2–4.5, **(C)** SSP5–8.5.

scenario, SSP1–2.6. Temperature warming has a negative effect on grain yield at middle and low latitudes. For the plateau alpine and the temperate continental climate regions, there is no significant difference under the different scenarios.

Resilience Assessment of Grain Yield in China From 2020 to 2050

Climate change presents great risks and uncertainties to the sustainable development of grain yield worldwide. In assessments of grain yield systems, the stability of grain production is an important focus. In this paper, "resilience" is used to indicate the ability of grain-producing areas to recover from the disturbance of climate change and realize stable grain production. This paper discusses the resilience from the aspects of grain output per person and grain unit yield to characterize the influence of climate change on China's grain yield.

Resilience Assessment for Grain Output per Person in China From 2020 to 2050

This article analyses the resilience of grain output per person from the perspective of the grain supply balance, i.e., grain yield and grain consumption. Considering the negative correlation between grain yield resilience and climate change risk, previous research has developed grain yield risk indexes (Wu et al., 2017; Sun et al., 2020). This paper defines the resilience index of grain output per person as the ratio of the 2000–2018 average grain output per person to the 2020–2050 grain output per person under different scenarios. According to the principle of dividing by the grain production risk index, the risk index for grain output per person is as follows: if the risk index value is greater than 1.20, there is no risk, and a value under 1.20 is risky. If the risk index value is higher than 1.00, there is a low risk to grain production; if the value is below 0.90, there is high risk; and values between the two indicate moderate risk (Sun et al., 2020).

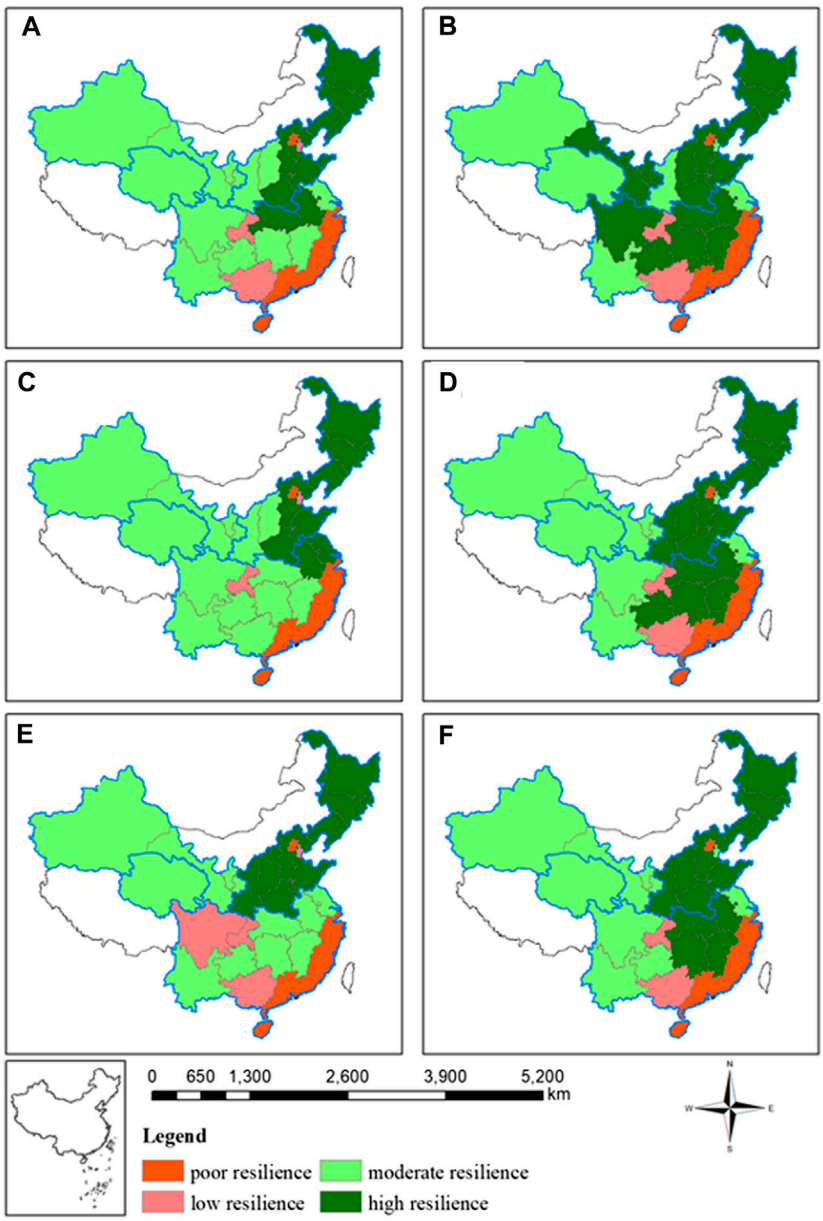

FIGURE 5 | Resilience assessment for grain output per person under different scenarios; **(A)** 2035 SSP1–2.6, **(B)** 2050 SSP1–2.6, **(C)** 2035 SSP2–4.5, **(D)** 2050 SSP2–4.5, **(E)** 2035 SSP5–8.5, **(F)** 2050 SSP5–8.5.

Therefore, "resilience" here is inversely proportional to the risk indicator, i.e., the reciprocal of the risk indicator. In this paper, we define a resilience index of grain yield per capita value of less than 0.83 as a high resilience; other values indicate fragile conditions. A value of less than one indicates moderate resilience; a value of higher than 1.11 indicates poor resilience; and values between them indicate low resilience.

In **Figure 5**, the regions with poor resilience for grain output per person in China are mainly concentrated in the regions of the subtropical monsoon climate and the tropical monsoon climate. At the same time, under SSP1–2.6, SSP2-4.5, and SSP5-8.5, with increased emissions, the resilience of grain output per person in the regions of the subtropical monsoon climate and the tropical monsoon climate worsens. The gradual increase in temperature exceeds the appropriate temperature required for grain yield, resulting in a reduction in grain yield. Therefore, in subtropical monsoon climate regions and tropical monsoon climate regions, energy-saving measures and emission reductions are important measures for maintaining and stabilizing local grain yield. The grain output per person depends on the grain demand and grain supply. The eastern coastal provinces are located in the tropical monsoon climate region. The cities include Jiangsu, Zhejiang, Fujian, and Guangdong. Due to reform and opening-up policies, the spatial pattern of China's grain-producing areas has changed significantly, the regional differences between grain

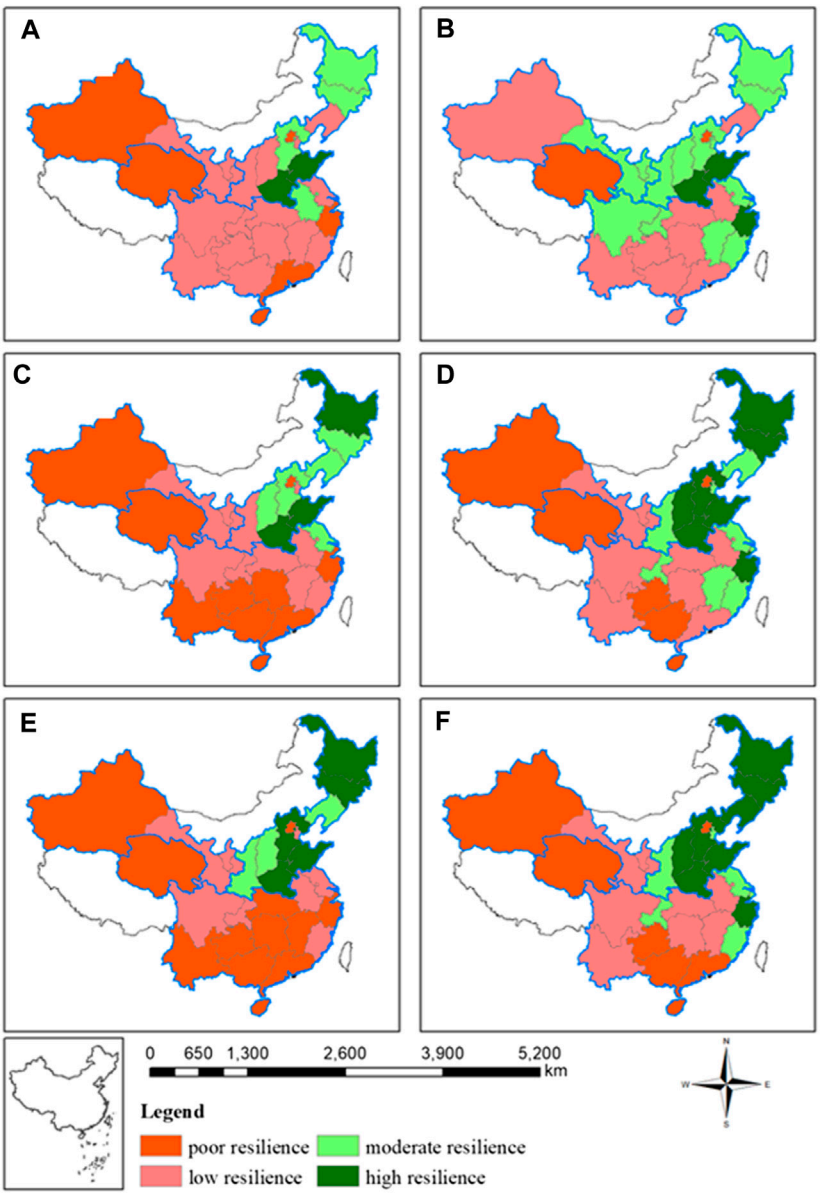

FIGURE 6 | Resilience assessment for grain unit yield under different scenarios; **(A)** 2035 SSP1–2.6, **(B)** 2050 SSP1–2.6, **(C)** 2035 SSP2–4.5, **(D)** 2050 SSP2–4.5, **(E)** 2035 SSP5–8.5, and **(F)** 2050 SSP5–8.5.

yield and population flow have gradually increased, and the population has gradually flowed to areas with higher urbanization levels. In the eastern coastal provinces, industrialization, urbanization and internationalization activities are much higher than those in other provinces and cities, which lead to a poor resilience. However, the resilience of grain output per person in the temperate monsoon climate region remained high under the different scenarios; at the same time, with the increase in the emissions intensity under SSP1–2.6, SSP2–4.5, and SSP5–8.5, the resilience of grain output per person improved. The resilience of grain output per person in temperate continental climate regions and plateau alpine climate regions did not change significantly under SSP1–2.6, SSP2–4.5, and SSP5–8.5, and the resilience of grain output per person was maintained in these regions.

Resilience Assessment for Grain Unit Yield in China From 2020 to 2050

Grain security is not only based on grain supply and demand but rather grain yield also reflects the land production capacity, and the agricultural production level is also an important factor in determining grain security. Considering the negative correlation between grain yield resilience and climate change risk, previous research has developed grain yield risk indexes (Wu et al., 2017; Sun et al., 2020). This paper defines the resilience index of the grain unit yield as the ratio of the 2000–2018 average grain unit yield to the 2020–2050 grain unit yield under SSP1–2.6, SSP2–4.5, and SSP5–8.5. According to the principle of dividing by the grain production risk index, the risk index for grain unit yield is as follows: if the risk index value is greater than 1.75, there

is no risk; however, a value under 1.75 is risky. If the risk index value is higher than 1.50, there is a low risk to grain production; if the value is below 1.25, there is high risk; and values between the two indicate moderate risk (Sun et al., 2020). Therefore, "resilience" here is inversely proportional to the risk indicator, i.e., the reciprocal of the risk indicator. In this paper, we define a resilience index of grain unit yield value of less than 0.57 as a high resilience; other values indicate fragile conditions. A value of less than 0.67 indicates a moderate resilience; a value of higher than 0.8 indicates a poor resilience; and values in between indicate a low resilience.

Figure 6 shows that, in general, the resilience of grain unit yield in China's temperate monsoon climate regions is higher than that in the other climate zones in China. This is mainly due to the rapid growth of grain yield in temperate monsoon regions; on one hand, it is due to the development and upgrading of the industry; on the other hand, it benefits from global warming, which has led to an increase in the multiple cropping index and an increase in land production capacity. The increase in grain unit yield in the high-latitude area (Heilongjiang) is obvious. Due to the quick industrialization of subtropical and tropical monsoon climate regions, the loss of cultivated land in these regions is severe. In the process of balancing occupied and available cultivated land, the difference in the quality of occupied and available field land causes a decline in terms of grain production, resulting in a lower grain yield sustainability. In addition, the average temperatures in the subtropical and tropical monsoon climate zones are higher during the grain growth period than that in other climate zones. In the high-emissions scenario, SSP5–8.5, the higher the emissions intensity is, the greater the temperature increase. This increase would exceed the appropriate temperature for crop growth, weakening the land production capacity, which is also a key factor causing the low resilience of grain unit yield. In the SSP5–8.5 scenario, the resilience of grain unit yield in the monsoon region will gradually decrease from north to south. In the future, the resilience of grain unit yield in temperate continental climate regions and plateau alpine climate regions will not change substantially. Because the temperate continental climate zone is located inland, rainwater is not sufficient for crop growth; the increase in water discharge leads to temperature increases that further aggravate water shortages (Liu and Lin, 2007). The results show that the increase in temperature in the plateau alpine climate region aggravates the melting of ice and sown, increases the area of ice lakes, and increases the risk of glacier debris flows and ice lake breaks (Cui et al., 2014). However, the change in grain yield in these areas mainly depends on improving production efficiency, increasing investments in science and technology, strengthening farmland infrastructure conditions, increasing the promotion of water-saving irrigation technology, and adjusting the regional layout and variety structure of grains to a achieve sustainable and stable grain unit yield.

CONCLUSION AND DISCUSSION

Based on the economy-climate and grey system models, we find that forecasts of the grain yield show obvious regional differences under different emissions scenarios (SSP1–2.6, SSP2–4.5, and SSP5–8.5). To quantify the impact of climate change on grain yield, we propose a resilience index of grain yield. Main contributions of this work are as follows:

(1) The higher the emission concentration is the greater the temperature increase will be, and the more northward the precipitation belt moves in the future.
(2) In the future (2020–2050), China's grain yield will be mainly concentrated in the temperate and subtropical monsoon climate zones. China's grain yield in the temperate monsoon climate zone will maintain rapid growth, while that in the subtropical monsoon climate zone will grow slowly. Grain transportation from north to south will be further intensified.
(3) The resilience of grain output per person and grain unit yield in temperate monsoon climate regions is relatively high and positively affected by climate change. The high latitudes of the temperate monsoon climate region will significantly reduce or eliminate cold damage to crops.
(4) The resilience of grain output per person and grain unit yield in the regions with subtropical and tropical monsoon climates is poor. These areas are located at middle and low latitudes. Climate change will have negative impacts in these zones.
(5) The resilience of grain output per person and grain unit yield in temperate continental and plateau alpine climate regions is fair.

Overall, this paper uses a multidisciplinary approach to assess the sustainability of China's grain yield under the impacts of climate change and creatively defines a resilience index for grain yield. Future research should consider the potential effects of climate change more carefully by viewing, for example, the impact of extreme weather on grain yield. Due to space limitations, this study only used the BCC-CSM2-MR model, and the aggregate average of multiple models still needs to be further studied.

DATA AVAILABILITY STATEMENT

The datasets presented in this article are not readily available because These are private and there are many relevant work which have not been published. Requests to access the datasets should be directed to 201821051163@mail.bnu.edu.cn.

AUTHOR CONTRIBUTIONS

Conceptualization, MS and JC; methodology, MS; software, MS; validation, MS, JL and WZ; formal analysis, FY; investigation, YX; resources, MS; data curation, JC; writing—original draft preparation, MS; writing—review and editing, MS; visualization, JC; supervision, MS; project administration, YX; funding acquisition, JC. All authors have read and agreed to the published version of the manuscript.

FUNDING

This work was supported by the National Key Research and Development Program of China (2018YFC1509003; 2016YFA0602703) the National Natural Science Foundation of China (42075167).

REFERENCES

Abraha, M. G., and Savage, M. J. (2006). Potential impacts of climate change on the grain yield of maize for the midlands of KwaZulu-Natal, South Africa[J]. *Agric. Ecosyst. Environ.* 115, 150–160. doi:10.1016/j.agee.2005.12.020

Belyaeva, M., and Bokusheva, R. (2018). Will climate change benefit or hurt Russian grain production? A statistical evidence from a panel approach[J]. *Clim. Change* 149, 205–217. doi:10.1007/s10584-018-2221-3

Bruneau, M., Stephanie, E. C., and Ronald, T. E. (2003). Eguchi, et al. A Framework to Quantitatively Assess and Enhance the Seismic Resilience of Communities [J]. *Earthq. spectra* 19 (4), 733–752. doi:10.1193/1.1623497

Brunetti, M., Maugeri, M., Monti, F., and Teresa, R. (2006). Temperature and precipitation variability in Italy in the last two centuries from homogenised instrumental time series[J]. *Int. J. Climatol. J. R. Meteorol. Soc.* 26, 345–381. doi:10.1002/joc.1251

Cai, J., Guo, H., and Wang, D. (2012). Review on the resilient city research overseas[J]. *Process Geogr.* 31 (10), 1245–1255. doi:10.11820/dlkxjz.2012.10.001

Chou, J., and Ye, D. (2006). Assessing the effect of climate changes on grains yields with a new economy-climate model. *Climatic Environ. Researc.* 11, 347–353.

Chou, J., Feng, G., Dong, W., Ye, D., and Chen, H. (2004). A new approach the economy evaluation of influence on China agriculture by climate change. *Climatic Environ. Res.* 9, 361–368.

Chou, J., Xu, Y., Dong, W., Xian, T., Xu, H., and Wang, Z. (2019). Comprehensive climate factor characteristics and quantitative analysis of their impacts on grain yields in China's grain-producing areas[J]. *Heliyon* 116, 102837. doi:10.1016/j.heliyon.2019.e02846

CMACCC (2018). China blue book on climate change. Beijing, China: Climate Change Center of China Meteorological Administration.

Crane-Droesch, A. (2018). Machine learning methods for crop yield prediction and climate change impact assessment in agriculture[J]. *Environ. Res. Lett.* 13, 114003. doi:10.1088/1748-9326/aae159

Cui, P., Chen, R., Xiang, L., and Fenghuan, S. (2014). Risk analysis of mountain hazards in Tibetan plateau under global warming[J]. *Progressus Inquisitiones De Mutatione Climatis* 2, 103–109. doi:10.3969/j.issn.1673-1719.2014.02.004

Cutter, S. L., Ahearn, J. A., Amadei, B., Crawford, P., Eide, E. A., Galloway, G. E., et al. (2013). Disaster resilience: a national imperative[J]. *Environ. Sci. Pol. Sust. Develop.* 55 (2), 25–29. doi:10.1080/00139157.2013.768076

Davenport, F., Husak, G., and Jayanthi, H. (2015). Simulating regional grain yield distributions to support agricultural drought risk assessment[J]. *Appl. Geogr.* 63, 136–145. doi:10.1016/j.apgeog.2015.06.010

Devkota, K. P., Manschadi, A. M., Devkota, M., Lamers, J. P. A., Ruzibaev, E., Egamberdiev, O., et al. (2013). Simulating the impact of climate change on rice phenology and grain yield in irrigated drylands of Central Asia[J]. *J. Appl. meteorol. clim.* 52, 2033–2050. doi:10.1175/jamc-d-12-0182.1

Holling, C. S. (1973). Resilience and stability of ecological systems[J]. *Annu. Rev. Ecol. Syst.* 4 (1), 1–23. doi:10.1146/annurev.es.04.110173.000245

Holst, R., Yu, X. H., and Gruen, C. (2013). Climate change, risk and grain yields in China[J]. *J. Integr. Agric.* 12, 1279–1291. doi:10.1016/s2095-3119(13)60435-9

Ji, X., Liu, L., and Qi, X. (2014). Risk assessment method of grain production guarantee capacity of regional cultivated land[J]. *Trans. Chin. Soc. Agric. Eng.* 30, 219–226. doi:10.3969/j.issn.1002-6819.2014.07.026

Liu, Y., and Lin, E. (2007). Effects of climate change on agriculture in different regions of China[J]. *Adv. Clim. Change Res.* 3, 229–233. doi:10.1016/0959-3780(96)00018-0

Lu, S., Bai, X., Li, W., and Wang, N. (2019). Impacts of climate change on water resources and grain production[J]. *Technol. Forecast. Soc. Change* 143, 76–84. doi:10.1016/j.techfore.2019.01.015

Masud, M. B., Wada, Y., Goss, G., and Faramarzi, M. (2019). Global implications of regional grain production through virtual water trade. *Sci. Total Environ.* 659, 807–820. doi:10.1016/j.scitotenv.2018.12.392

Mishra, A., Singh, R., Raghuwanshi, N. S., Chatterjee, C., and Froebrich, J. (2013). Spatial variability of climate change impacts on yield of rice and wheat in the Indian Ganga Basin. *Sci. Total Environ.* 468-469, S132–S138. doi:10.1016/j.scitotenv.2013.05.080

Osman, R., Zhu, Y., Ma, W., Zhang, D., Ding, Z., Liu, L., et al. (2020). Comparison of wheat simulation models for impacts of extreme temperature stress on grain quality[J]. *Agric. For. Meteorology* 288, 107995. doi:10.1016/j.agrformet.2020.107995

Paton, D., and Johnston, D. (2001). Disasters and communities: vulnerability, resilience and preparedness[J]. *Disaster Prev. Manag.* 10 (4), 270–277. doi:10.1108/eum0000000005930

Pu, Y., Liu, H., Yan, R., Yang, H., Xia, K., Li, Y., et al. (2020). CAS FGOALS-g3 model datasets for the CMIP6 scenario model Intercomparison project (ScenarioMIP)[J]. *Adv. Atmos. Sci.* 37 (10), 1081–1092. doi:10.1007/s00376-020-2032-0

IPCC (2014). "Climate change," in Synthesis report. Contribution of working groups I, II and III to the fifth assessment report of the intergovernmental Panel on climate change [core writing team. Editors R. K. Pachauri and L. A. Meyer (Geneva, Switzerland: IPCC), 151 .

Sun, M., Chou, J., Xu, Y., Yang, F., and Li, J. (2020). Study on the thresholds of grain production risk from climate change in China's main grain-producing areas[J]. *Phys. Chem. Earth* 116. doi:10.1016/j.pce.2020.102837

Tao, F. L., Zhang, Z., Xiao, D. P., and Zhang, S. (2014). Responses of wheat growth and yield to climate change in different climate zones of China, 1981-2009. *Agric. For. Meteorology* 189, 91–104. doi:10.1016/j.agrformet.2014.01.013

Wang, P., Deng, X., and Jiang, S. (2019). Global warming, grain production and its efficiency: case study of major grain production region[J]. *Ecol. Indicators* 105, 563–570. doi:10.1016/j.ecolind.2018.05.022

Wu, S. H., Pan, T., Liu, Y. H., Deng, H., Jiao, K., Lu, Q., et al. (2017). Comprehensive climate change risk regionalization of China[J]. *Acta. Geographica. Sinica.* 72, 3–17. doi:10.11821/dlxb201701001

Wu, T., Lu, Y., Fang, Y., Xin, X., Li, L., Li, W., et al. (2019). The Beijing Climate Center climate system model (BCC-CSM): the main progress from CMIP5 to CMIP6[J]. *Geoscientific Model Develop.* 12 (4), 1573–1600. doi:10.5194/gmd-12-15573-2019

Xu, H., and Zhu, H. (2015). Spatial change of China's grain production based on geographical division of natural factors during 1990–2010[J]. *Acta. Geographica. Sinica.* 70, 582–590. doi:10.11821/dlxb201504006

Xu, L., Zhang, Q., Zhou, A. L., and Ran, H. U. O. (2013). Assessment of flood catastrophe risk for grain production at the provincial scale in China based on the BMM method [J]. *J. Integr. Agric.* 12, 2310–2320. doi:10.1016/s2095-3119(13)60587-0

Yin, M. S. (2013). Fifteen years of grey system theory research: a historical review and bibliometric analysis[J]. *Expert Syst. Appl.* 40, 2767–2775. doi:10.1016/j.eswa.2012.11.002

Conflict of Interest: The authors declare that the research was conducted in the absence of any commercial or financial relationships that could be construed as a potential conflict of interest.

frontiers in Environmental Science

ORIGINAL RESEARCH
published: 22 March 2021
doi: 10.3389/fenvs.2021.639931

Study of Four Rainstorm Design Methods in Chongqing

Daiqiang Liao[1], *Qiang Zhang*[2]*, *Ying Wang*[1], *Haonan Zhu*[1] *and Jia Sun*[1]

[1]Chongqing Climate Center, Chongqing, China, [2]National Climate Center, Beijing, China

Based on minute-by-minute precipitation data from 1961 to 2016 obtained from the National Basic Weather Station of Shapingba, Chongqing, China, the Chicago rainstorm method, the Pilgrim & Cordery (P&C) method, the Common-frequency method and the natural rainstorm moving regularity (NRMR) method were used to design short-duration (1–3 h) and long-duration (24 h) rainstorm hyetographs. Then, a standardization method for test samples was designed to ensure that each test sample was standardized and underwent an actual precipitation process. The designed rainstorm hyetographs and test samples were compared and analyzed, and the results show that the hyetographs for the 1, 3, and 24-h durations obtained with the NRMR method best represented the actual corresponding precipitation processes. The hyetograph for the 2-h duration obtained with the Chicago rainstorm method was best for the actual 2-h precipitation process. The design results of the Common-frequency method were generally good, but not outstanding. Finally, the P&C method showed a relatively poor performance for each duration.

Keywords: standardization of test samples, Pilgrim & Cordery method, Chicago rainstorm method, common-frequency method, NRMR method

OPEN ACCESS

Edited by:
Qingxiang Li,
Sun Yat-Sen University, China

Reviewed by:
Xander Wang,
University of Prince Edward Island, Canada
Zhihong Jiang,
Nanjing University of Information Science and Technology, Nanjing, China

***Correspondence:**
Qiang Zhang
zhq62@cma.gov.cn

Specialty section:
This article was submitted to Interdisciplinary Climate Studies, a section of the journal Frontiers in Environmental Science

Received: *10 December 2020*
Accepted: *08 February 2021*
Published: *22 March 2021*

Citation:
Liao D, Zhang Q, Wang Y, Zhu H and Sun J (2021) Study of Four Rainstorm Design Methods in Chongqing. Front. Environ. Sci. 9:639931. doi: 10.3389/fenvs.2021.639931

INTRODUCTION

Chongqing, an important city in central China, is an economic center in the upper reaches of the Yangtze River, an important junction between "the Belt and Road" and an inland opening highland. In particular, since the area came under the jurisdiction of the People's Government in 1997 and due to its continuous urbanization, the impervious surface area in Chongqing has increased significantly. This increase has led to waterlogging disasters (especially on July 17, 2007 and July 16 and 17, 2020), which have caused considerable loss of life for urban residents and negative socioeconomic impacts. At present, the low design standard for urban underground water distribution networks in China is one of the important causes of urban flood and waterlogging disasters. Rainstorm hyetograph design is an important factor for drainage design standards and is the basis for scientifically and reasonably planning and designing urban drainage systems (Pochwat et al., 2017). Therefore, a reasonably designed rainstorm hyetograph is particularly important.

The intensity-duration-frequency (IDF) relationship of rainfall extremes is usually summarized in the evaluation process and widely used as a convenient tool for understanding the characteristics of extreme rainfall events at given locations (Ben-Zvi, 2009). Wang presented an effective approach for assessing the impacts of climate change on both the intensity and frequency of extreme rainfall events by integrating regional climate modeling and IDF curves into a general framework (Wang et al., 2014). The classic methods that are currently used are described as follows: Keifer and Chu (1957) proposed a method that is based on an intensity-duration-frequency (IDF) curve and a rainstorm intensity formula. This method is known as the Chicago rainstorm method. Pilgrim and Cordery

(1975) developed an order-average hyetograph based on the principle of statistics (referred to as the P&C method). Yen and Chow (1980) proposed a triangular-shaped hyetograph. In addition to the abovementioned classic methods, other methods for deriving hyetographs have been developed more recently; please refer to Lin and Wu (2007), Lee and Ho (2008), Powell et al. (2008), Yin et al. (2014), Kottegoda et al. (2014), NRMR (Liao et al., 2019b) for detailed descriptions (Wang et al., 2018). Furthermore, there are advantages and disadvantages among the different rainstorm hyetograph design methods. Cen (1993), Cen et al. (1998), Cen (1999) compared four methods for designing rainstorm hyetographs, including the methods of Keifer and Chu (1957), Huff (1967), Pilgrim and Cordery (1975), Yen and Chow (1980), and the results showed that the flood peak discharges obtained by the different rainstorm hyetograph design methods were significantly different, and the sensitivities of the different methods to the duration of precipitation events and to precipitation data varied.

The purpose of designing a rainstorm hyetograph is to allow the designed results to represent the natural precipitation process in an actual local rainstorm. However, scholars in China and abroad have rarely conducted comparative studies to determine if rainstorm hyetograph designs represent local conditions. To address this situation, minute-by-minute precipitation data from 1961 to 2016 were obtained from the National Basic Weather Station of Shapingba, Chongqing, China, and the Chicago rainstorm method, the P&C method, the Common-frequency method and the natural rainstorm moving regularity (NRMR) method were used to design short-duration (1–3 h) and long-duration (24 h) rainstorm hyetographs. Then, the rainstorm hyetograph designs were compared with samples from actual precipitation processes that led to waterlogging from 1961 to 2016 (these samples were not used for the rainstorm hyetograph designs). These methods were compared to determine the method that had the optimal design results.

DATA AND SAMPLING METHODS

The data used in this study are minute-by-minute precipitation data from 1961 to 2016 from the National Basic Weather Station of Shapingba in Chongqing, China, and these data were provided by the Chongqing Municipal Center of Weather Information and Technology Support. The precipitation data from 1961 to 2008 are the self-recording minute-by-minute paper records, and the data from 2009 to 2016 are the observation data of automatic stations. Using the color scanning digitizing processing system of the precipitation autographic record paper (Wang et al., 2004) provided by the China Meteorological Administration (CMA), the precipitation autographic record papers were subjected to scanning, inspection, and extraction of minute-by-minute precipitation data. However, the 6-year (1968, 1971, 1975, 2000, 2001, 2005) record papers cannot be digitized since they are not well preserved; thus, these data were excluded. The remaining 50 years of data were used. The sampling method used in this paper was the natural rainfall moving sampling method for heavy precipitation (Liao et al., 2019a). The two largest samples of each year were selected, in which the largest sample was used for the rainstorm hyetograph design, and the second largest sample was used as the test sample (a total of 47 samples were used in this paper). When the samples were selected by the natural rainfall moving sampling method for heavy precipitation, the 3-year (2008, 1980, 1987) samples with less than 50 mm of rainfall were excluded).

RESULTS OF DIFFERENT RAINSTORM HYETOGRAPH DESIGN METHODS

Four methods commonly used in China were used for the rainstorm hyetograph design, including the Chicago rainstorm method, P&C method, Common-frequency method and NRMR method.

Chicago Rainstorm Method

The Chicago rainstorm method is based on the storm intensity formula, and the rainstorm peak position is determined by rainstorm statistics (Dai et al., 2017). By introducing the position coefficient r of the rainstorm peak to describe the time when the rainstorm peak occurs, the time series of rainfall duration is divided into two parts of prepeak and postpeak.

The duration of a rainstorm process is t_0, the instantaneous rainfall intensity before the peak is I_a, the corresponding duration is t_a, the cumulative rainfall is H_a, the instantaneous rainfall intensity after the peak is I_b, the corresponding duration is t_b, the cumulative rainfall is H_b and the total rainfall is $H_T = H_a + H_b$. Let $t_0 = 1$ and the intensity peak position r be between 0 and 1, then $t_0 = t_a/r = t_b/(1-r)$. The rainstorm intensity formula is $i = A/(T+b)^n$, the rainstorm peak time is set as 0 and the average intensities before and after the peak are i_a and i_b, respectively:

When $0 \le t \le t_a$, $i_a = \frac{A}{(t/r+b)^n} = \frac{r^n A}{(t+rb)^n}$

When $0 \le t \le t_b$, $i_b = \frac{A}{(t/1-r+b)^n} = \frac{(1-r)^n A}{[t+b(1-r)]^n}$

Therefore, the instantaneous rainfall intensity before and after the peak (I_a and I_b) is obtained as follows:

When $0 \le t \le t_a$,

$$I_a = \frac{d}{dt}\left(\frac{r^n A}{(t+rb)^n}t\right) = \frac{(1-n)r^n A}{(t+rb)^n} + \frac{nbr^{n+1}A}{(t+rb)^{n+1}}$$

When $0 \le t \le t_b$,

$$I_b = \frac{d}{dt}\left(\frac{(1-r)^n A}{[t+(1-r)b]^n}t\right) = \frac{(1-n)(1-r)^n A}{[t+(1-r)b]^n} + \frac{nb(1-r)^{n+1}A}{[t+(1-r)b]^{n+1}}$$

Based on the two equations above, the cumulative rainfall hyetograph is calculated as follows:

When $0 \le t \le rT$,

$$H = \int_0^t I_a dt = H_T\left\{r - \left(r - \frac{t}{T}\right)\left[1 - \frac{t}{r(T+b)}\right]^{-n}\right\}$$

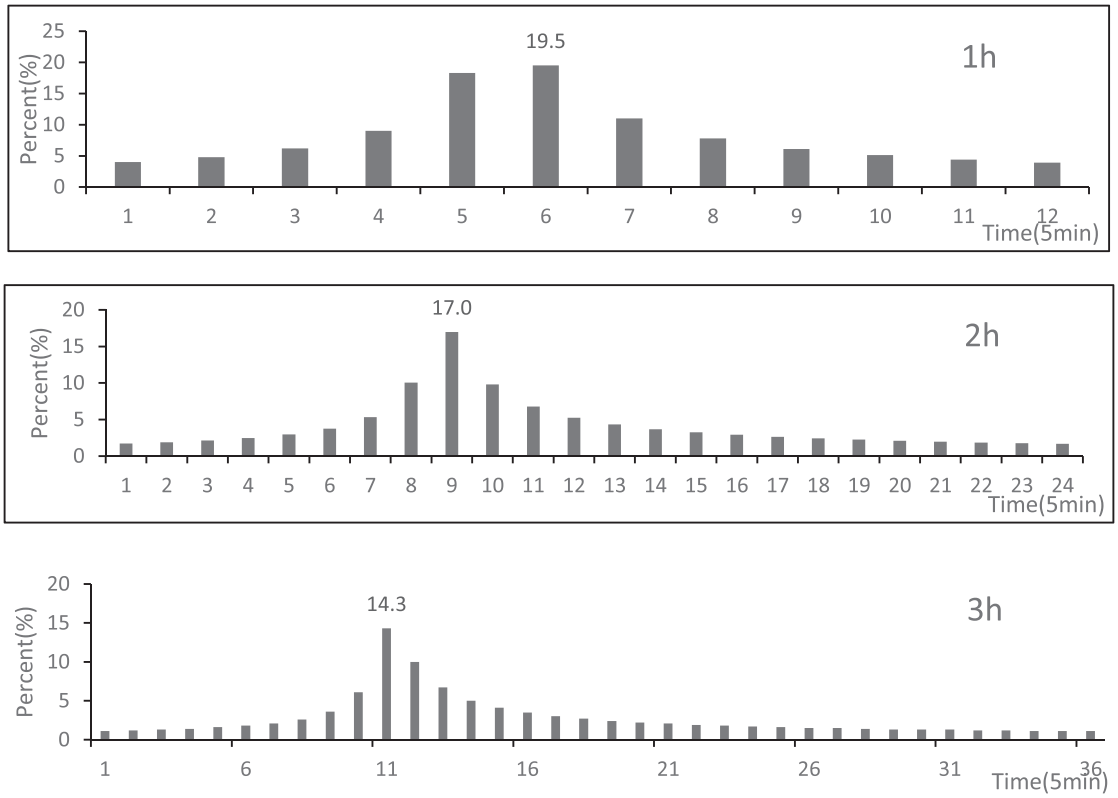

FIGURE 1 | The designed rainstorm hyetographs for 1, 2, and 3-h durations obtained with the Chicago rainstorm method.

When $rT \le t \le T$,

$$H = rH_T + \int_{rT}^{T} I_b dt = H_T \left\{ r + \left(\frac{t}{T} - r \right) \left[1 + \frac{t - T}{(1 - r)(T + b)} \right]^{-n} \right\}$$

Figure 1 shows the short-duration design rainstorm hyetographs according to the above steps. Since the maximum sampling time of this method is only 180 min, it was not used for the design rainstorm hyetograph for the 24-h duration.

P&C Method

The P&C method places the rainstorm peak period at the position with the highest possibility of occurrence, the percentage of precipitation in the peak period in each rainstorm is taken to calculate the average percentage of precipitation and the positions and percentages of other periods are calculated in the same way (Jiang, 2015). The specific steps are described as follows:

(1) The rainstorm samples with a certain duration are selected. Multiple rainfall events with the largest amounts of precipitation are selected, and the more rainfall events there are, the greater the statistical significance.
(2) The duration is divided into several periods. The length of the period is determined by the desired time unit for the time distribution, and generally, the smaller this value is, the better. For example, if a 5-min unit is used for a 180-min rainstorm hyetograph design, the 180-min duration selected in step 1 is divided into 36 periods.
(3) For every rainfall event selected, according to the rainfall of each period, the time series number of each period is determined from largest to smallest, and the period with large rainfall corresponds to the small time series number. The time series number of each corresponding period is averaged, and the average time series number from smallest to largest corresponds to rainfall intensities from largest to smallest.
(4) The percentage of rainfall in each period compared with the total rainfall is calculated, and the average percentage of each period is taken.
(5) A rainfall hyetograph is formed by arranging periods according to the time series with the maximum possibility determined in step 3 and the distribution percentage determined in step 4.

Figure 2 shows the designed rainstorm hyetographs of all durations according to the above steps.

Common-Frequency Method

The Common-frequency method, also known as the "long-duration including short-duration," provides a long-duration hyetograph that includes a short-duration hyetograph. This method determines the time series using the situation with the

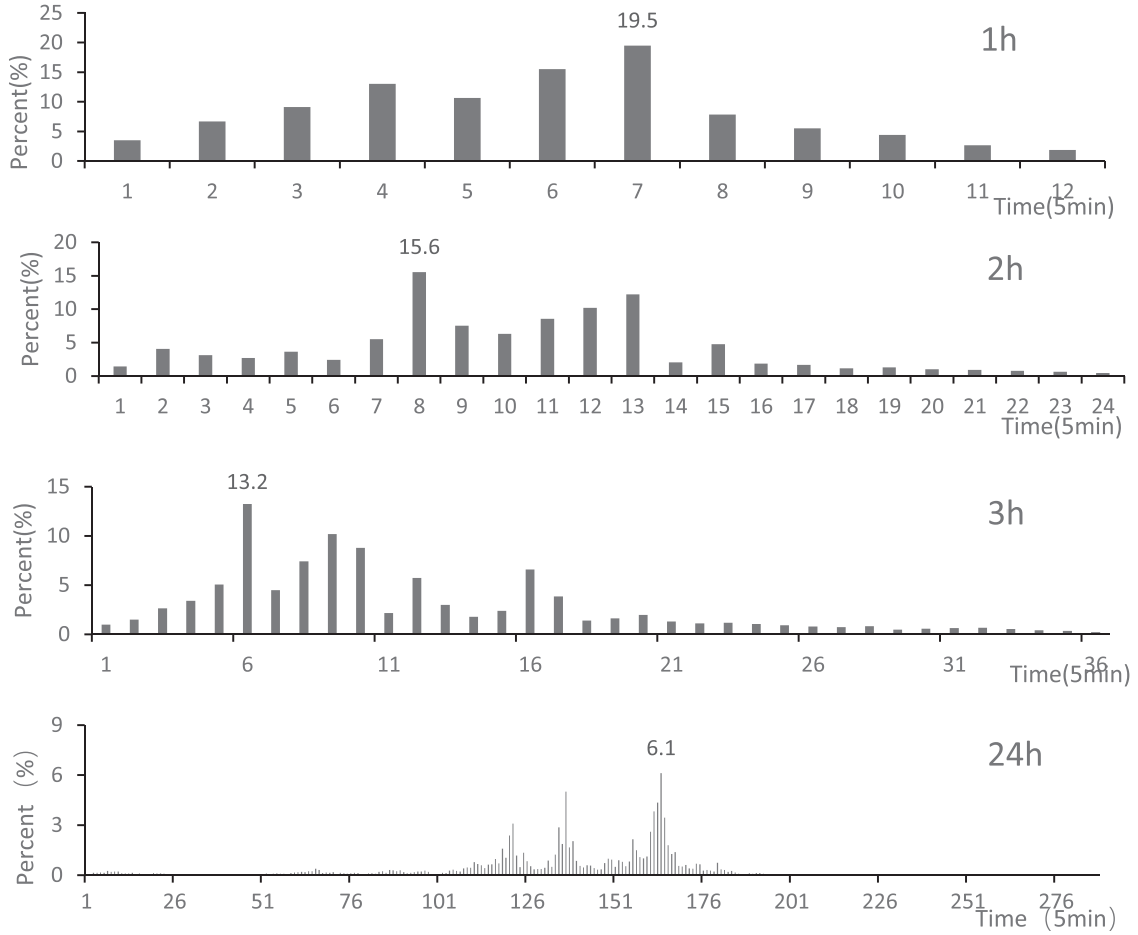

FIGURE 2 | The rainstorm hyetograph design of four durations obtained with the P&C method.

most occurrences (namely, the mode value) and uses the average situation (namely, the mean value) to define the rainfall in each period (Li et al., 2018). The 1,440-min rainstorm hyetograph design with a 5-min unit is used as an example. The specific steps are described as follows:

(1) Based on the rainfall standard, multiple rainstorms with a duration of 1,440 min are selected, the starting position of H_{720}, which is the maximum rainfall in a 720-min window in each rainstorm, is determined by using time-based sliding windows, and the starting time of H_{720} in the rainstorm hyetograph design is determined by the position of the mode value.

(2) The main peaks of the selected typical rainstorm samples with a duration of 1,440 min are superimposed, and the percentage of precipitation in each period (H_{720}–H_{1440}) compared with the total rainfall in each rainstorm sample is calculated. Then, the average precipitation percentage of each period (H_{720}–H_{1440}) in multiple rainstorm samples is calculated, i.e., the precipitation distribution percentage of each period (H_{720}–H_{1440}).

(3) In the same way, according to steps (1) and (2), multiple rainstorms with a duration of 720 min are selected based on the rainfall standard. Using the method in step 1 for H_{720}, the starting position of H_{360}, which is the maximum rainfall in a 360-min window in each rainstorm, is determined using time-based sliding windows, and the starting time of H_{360} in the rainstorm hyetograph design is determined by the position of the mode value. The main peaks are aligned and superimposed to calculate the percentage of precipitation in each period (H_{360}–H_{720}) compared with the total rainfall in each rainstorm sample, and the average precipitation percentage of each period (H_{360}–H_{720}) in multiple rainstorm samples is calculated, i.e., the precipitation distribution percentage of each period (H_{360}–H_{720}).

(4) The precipitation distribution percentages of H_{240}–H_{360}, H_{180}–H_{240}, H_{150}–H_{180}, H_{120}–H_{150}, H_{90}–H_{120}, H_{60}–H_{90}, H_{45}–H_{60}, H_{30}–H_{45}, H_{15}–H_{30}, and H_5–H_{15} corresponding to 360, 240, 180, 150, 120, 90, 60, 45, 30, and 15 min, respectively, are calculated. Finally, the percentage of the maximum 5-min precipitation is 100%.

(5) In summary, the distribution results of the rainstorm hyetograph design with a duration of 1,440 min and a 5-min unit are obtained.

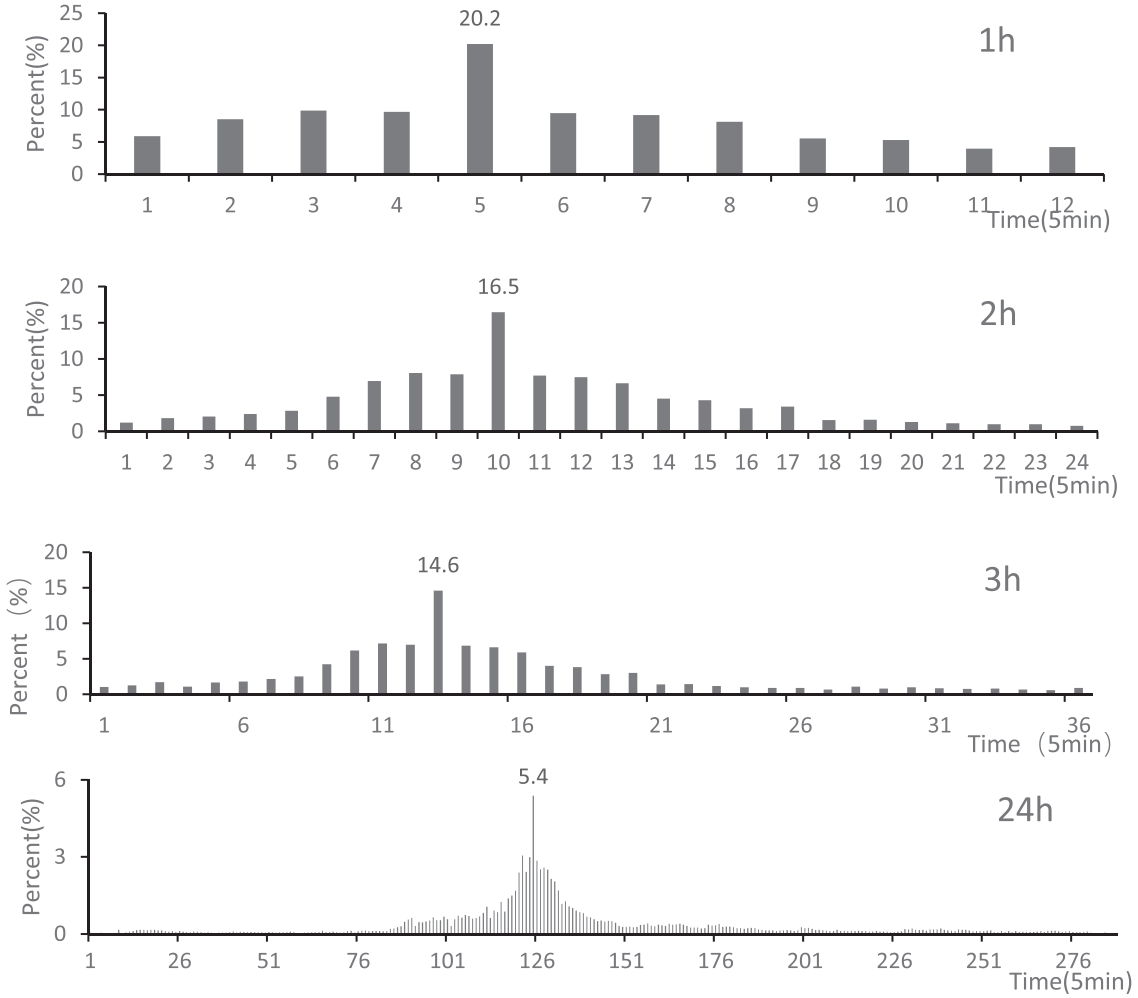

FIGURE 3 | The rainstorm hyetograph designs for four durations obtained with the Common-frequency method.

In this paper, according to the idea of the Common-frequency method, the peak position is determined using the average position, the peak intensity is the average maximum 5-min intensity, and the distribution percentages of remaining periods are determined based on the averages. **Figure 3** shows the designed rainstorm hyetographs of all durations according to the above steps.

NRMR Method

After sampling with the natural rainfall moving sampling method for heavy precipitation, the rain hyetograph is calculated using **Eq. 1**, which is the NRMR method (Liao et al., 2019a).

$$P_k = \frac{\sum_{j=(k-1)\times 5+1}^{k\times 5} X_j}{\sum_{i=1}^{n} X_i} \quad (1)$$

X represents a minute-based precipitation series for a given duration (there are multiple durations), n is the total number of minutes for a given duration, k represents the index of a 5-min period in the series, P represents the percentage of the precipitation during a 5-min period and P_k is the percentage of the precipitation during the kth 5-min period in the current precipitation series.

Figure 4 shows the rainstorm hyetograph designs with different durations according to the above steps.

DETERMINATION OF TEST SAMPLES

Standardization of Test Samples

The second largest sample of each year from 1961 to 2016 selected by the natural rainfall moving sampling method for heavy precipitation was taken, and all of them were used as the test samples. Because the peak positions of selected test samples were different, it was difficult to use them for verification. To this end, standardization was conducted for the selected test samples. First, the peak position of each sample

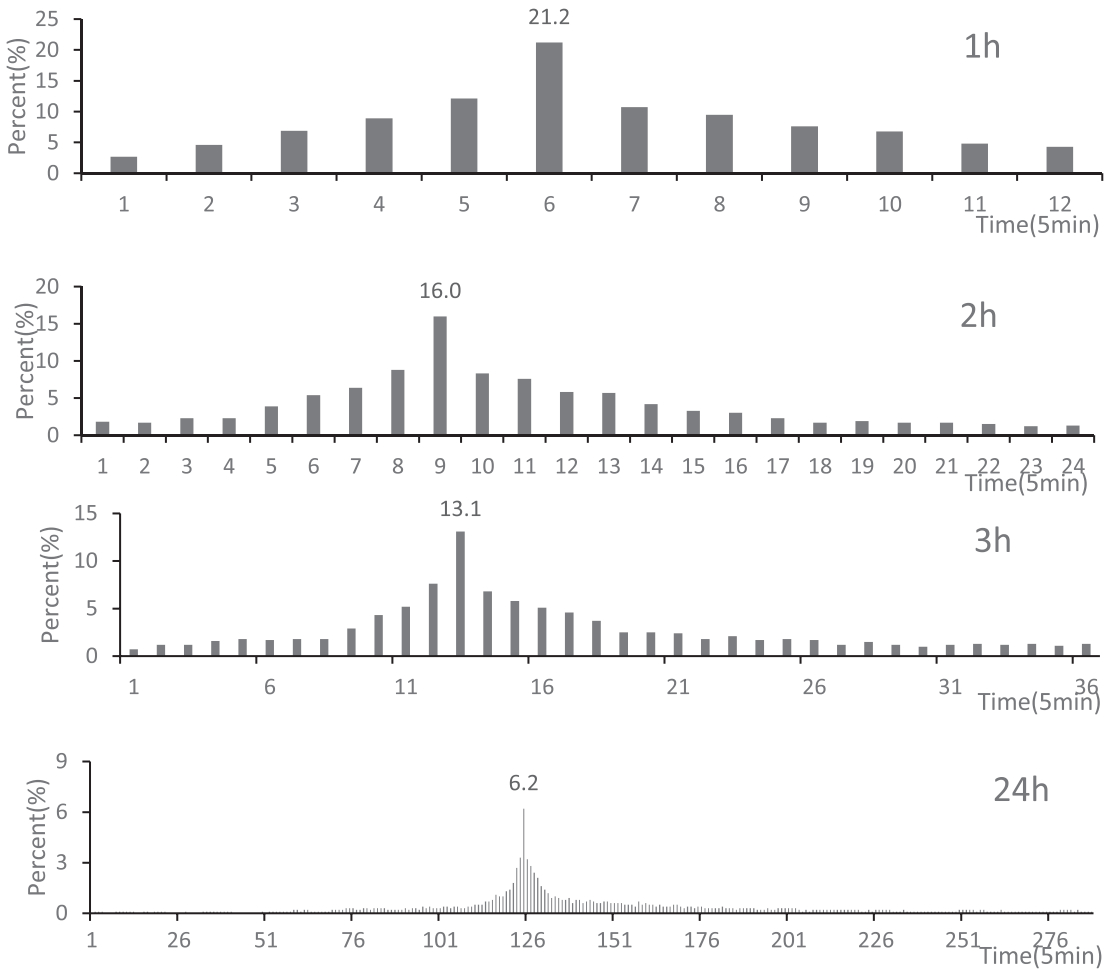

FIGURE 4 | Four durations of rainstorm hyetograph designs obtained with the NRMR method.

was determined. This position was determined using the designed rainstorm hyetograph method, and different methods provided different peak positions. The purpose of moving the peak position in the second time is for the convenience of inspection. Then, the peak position of each sample was moved to the determined peak position. To ensure that the test sample was still a true natural precipitation process, the vacant precipitations caused by the left-right movement in the test sample were supplemented with the original precipitations. The specific process is shown in **Figure 5**. **Figure 5A** shows the standardization process of a 3 h-duration test sample from 2003 by the NRMR method, in which the gray parts are the sample time intervals before moving, and the oblique line marks the peak position of the sample the moving, i.e., the 28th 5-min interval of the sample. The gray parts in **Figure 5B** are the sample time intervals after moving, i.e., the 28th 5-min interval is moved forward by 15 intervals and aligned with the 13th interval (the determined peak position of the test sample). The front 15 intervals are removed due to moving, therefore, 15 intervals from the original sample are used, which ensures that the sample is still a natural precipitation process. The test samples of the other durations and other rainstorm hyetograph design methods were standardized in the same way.

Determination of Peak Positions in Test Samples

The peak positions of the test samples were determined based on the results of the designed rainstorm hyetographs. The peak positions of the test samples varied with different methods. **Table 1** shows the peak positions for different durations by the four methods.

Table 1 shows that for the 1 and 2-h durations, the differences in the peak positions obtained by the different rainstorm hyetograph design methods are relatively small; however, the differences between the peak positions at the 3 and 24-h durations are considerable. Especially for the 3-h duration, the peak position by the P&C method was five to seven units (intervals) away from the results of other methods. For the peak position of 3-h duration, the P&C method moved the peak position in all test samples to the sixth interval, the Chicago rainstorm method

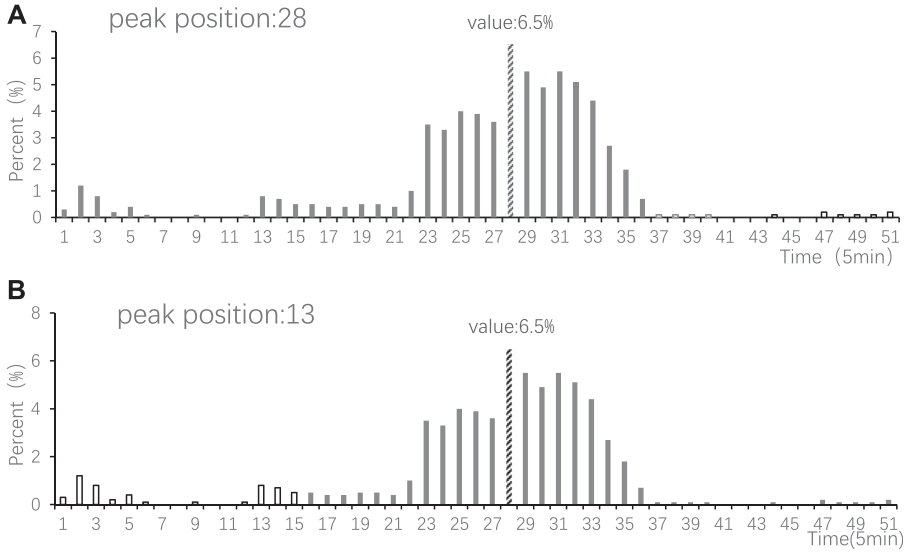

FIGURE 5 | The gray parts in **(A)** are the samples selected before moving, and the gray parts in **(B)** are the selected samples after moving. Abscissa: time (5 min), ordinate: precipitation (mm).

TABLE 1 | Peak positions for different durations determined by the four rainstorm hyetograph design methods.

Duration (h)	P&C method	Chicago rainstorm method	Common-frequency method	NRMR method
1	7	6	5	6
2	8	9	10	10
3	6	11	13	13
24	164	—	125	125

TABLE 2 | Comparison of total rainfall in test samples with different durations before and after the natural moving process.

Method	Total precipitation of samples	1 h	2 h	3 h	24 h
—	Before standardization (mm)	1,579.6	1946.5	2,205.2	3,343.0
P&C method	After standardization (mm)	1,424.6	1778.1	1925.9	3,063.6
	Before standardization/after standardization (%)	90.2	91.4	87.3	91.6
Chicago rainstorm method	After standardization (mm)	1,445.9	1788.1	2024.4	—
	Before standardization/after standardization (%)	91.5	91.9	91.8	—
Common-frequency method	After standardization (mm)	1,449.3	1787.9	2033.4	3,101.3
	Before standardization/after standardization (%)	91.8	91.9	92.2	92.8
NRMR method	After standardization (mm)	1,445.9	1787.9	2033.4	3,101.3
	Before standardization/after standardization (%)	91.5	91.9	92.2	92.8

moved it to the 11th interval, and the Common-frequency method and the NRMR method moved it to the 13th interval, as did the other durations.

Representativeness of Standardized Samples

The standardization of the test samples may result in changes in the precipitation of the test samples. Therefore, it is necessary to test and analyze the standardized test samples. **Table 2** shows the variations in precipitation in each test sample before and after standardization (the 1,579.6 mm in the table is the sum of the 47 1 h precipitation samples before standardization, which is the same for other methods). **Table 2** shows that the difference in the total rainfall between the periods before and after standardization is not large, and the variation is basically within 9% (only the variation in the total rainfall for the 3-h duration by the P&C method is 12.7%). Therefore, the standardized test samples can basically represent the original samples. Meanwhile, this finding indicates that the standardization is reasonable.

TABLE 3 | Correlations between the results of the different rainstorm hyetograph designs and the test samples.

Method	Correlation characteristics	1 h	2 h	3 h	24 h
P&C method	The average correlation coefficient	0.322	0.507	0.531	0.122
	Percentage of samples that are significant at the 5% level (%)	23.4	76.6	83.0	78.7
Chicago rainstorm method	The average correlation coefficient	0.576	0.569	0.526	—
	Percentage of samples that are significant at the 5% level (%)	55.3	80.9	80.9	—
Common-frequency method	The average correlation coefficient	0.509	0.518	0.463	0.449
	Percentage of samples that are significant at the 5% level (%)	42.6	68.1	80.9	91.5
NRMR method	The average correlation coefficient	0.620	0.483	0.520	0.471
	Percentage of samples that are significant at the 5% level (%)	63.8	63.8	83.0	93.6

VALIDATION AND ANALYSIS OF THE RESULTS OF THE RAINSTORM HYETOGRAPH DESIGNS

The results of the rainstorm hyetograph designs are represented by the distribution diagram of rainfall with time. The continuous percentage data can be obtained by dividing the precipitation of each period by the total precipitation (hereinafter referred to as fixed samples). The standardized test samples can be transformed into continuous multiple percentage data so that all test samples can be used for correlation analysis with fixed samples. The greater the correlation coefficient between the fixed samples (the rainstorm hyetographs designed by the different design methods) and the test samples (the second heaviest rainstorm of every year) is, the closer the fixed samples are to the real precipitation process, and vice versa. A correlation analysis (Spearman's Rank correlation, 5% significance level) was performed on the test samples for the different methods with different durations and the corresponding fixed samples, and a significance test was also conducted on the correlations. **Table 3** lists the detailed results.

Table 3 shows that the P&C method had the smallest average correlation coefficient for each duration, indicating that the rainstorm hyetograph designs obtained with the P&C method were the least representative of the actual precipitation processes. For the P&C method, the percentages of samples that were significant at the 1 and 3-h durations were the smallest. For the P&C method, although the correlation coefficient between the designed rainstorm hyetograph and the test sample for the 24-h duration was significant, the average correlation coefficient was significantly lower than that of both the Common-frequency method and the NRMR method. Therefore, using the P&C method to design rainstorm hyetographs in Chongqing was the least effective. For the rainstorm hyetograph design obtained with the Chicago rainstorm method, both the average correlation coefficient and the percentage of samples that were significant were the highest among all the methods for the 2-h duration, indicating that the rainstorm hyetograph design for the 2-h duration obtained with the Chicago rainstorm method can best represent the actual 2 h precipitation process, but for other durations, the performance of the Chicago rainstorm method was relatively poor. The performance of the design rainstorm hyetographs for the four durations obtained with the Common-frequency method was moderate and stable but not outstanding. For the rainstorm hyetograph designs obtained with the NRMR method, in addition to the one for the 2-h duration, the average correlation coefficient and the percentage of samples that were significant for the other durations were the highest among all the methods, indicating that the rainstorm hyetograph designs obtained with the NRMR method for these three durations can best represent the actual precipitation processes in Chongqing.

SUMMARY AND DISCUSSION

Based on minute-by-minute precipitation data from 1961 to 2016 obtained from the National Basic Weather Station of Shapingba, Chongqing, China, the Chicago rainstorm method, the P&C method, the Common-frequency method and the NRMR method were used to design short-duration (1–3 h) and long-duration (24 h) rainstorm hyetographs. The second largest sample in each year during 1961–2016 was taken as a test sample, and all them were used to verify the design results of different methods. The following conclusions were obtained:

(1) The results of the rainstorm hyetograph designs obtained with the Chicago rainstorm method, the P&C method, the Common-frequency method and the NRMR method show that the differences in the peak intensity (the percentage of the maximum 5 min precipitation compared with the total precipitation) were small, the differences between the peak positions at the 1 and 2-h durations were not large, and the peak positions at the 3 and 24-h durations were far apart.
(2) The test sample standardization method designed in this study can make the peak position of the test sample the same as the peak position determined by the rainstorm hyetograph design method; in addition, there were no significant changes in the precipitation before and after standardization for all the test samples, and the variations were all within 9%. This finding indicates that the standardization was reasonable, and it ensured that the test sample was still a true natural precipitation process.
(3) The analysis and verification of the results of the four methods showed that the designed rainstorm hyetographs for the 1, 3, and 24-h durations obtained with the NRMR method were the most representative of the actual precipitation processes; the rainstorm hyetograph for the 2-h duration obtained with the Chicago rainstorm method was the most prominent; and the results of the Common-frequency method were generally good but not

outstanding; additionally, the performance of the P&C method was relatively poor. Therefore, this paper recommends the NRMR method for rainstorm hyetographs with durations of 1, 3, and 24 h and the Chicago rainstorm method for rainstorm hyetographs with a duration of 2 h. The test method for rainstorm hyetograph design and the recommendations proposed in this paper need to be verified in more areas. We hope that this test method can be used to provide a better basis for urban drainage network design and to achieve the goal of reducing urban waterlogging disasters and flood disasters.

DATA AVAILABILITY STATEMENT

The original contributions presented in the study are included in the article/Supplementary Material, further inquiries can be directed to the corresponding author.

AUTHOR CONTRIBUTIONS

DL put forward the idea. QZ is the instructor of the manuscript. YW, HZ, and JS analyzed the data. All authors revised the manuscript.

FUNDING

Financial support for this research was provided by the National Key Research and Development Plan of China (No. 2017YFC1502701).

ACKNOWLEDGMENTS

We thank Xiaochun Liu for translating some of the documents. We are particularly grateful to the Chongqing Meteorological Information and Technology Support Center for providing the minute-by-minute precipitation data from the National Basic Weather Station of Shapingba from 1961 to 2016.

REFERENCES

Ben-Zvi, A. (2009). Rainfall intensity-duration-frequency relationships derived from large partial duration series. *J. Hydrol.* 367, 104–114. doi:10.1016/j.jhydrol.2009.01.007

Cen, G. P. (1993). A comparison of design storm patterns for calculating the volume of detention ponding. *Water Res. Water Eng.* 4 (2), 30–35.

Cen, G. P. (1999). Sample selection and statistical method of rainstorm data. *Water Wastewater Eng.* 25 (4), 1–4.

Cen, G. P., Jin, S., and Fan, R. S. (1998). Research on rainfall pattern of urban design storm. *Adv. Water Sci.* 9 (1), 42–46.

Huff, F. A. (1967). Time distribution of rainfall in heavy storms. *Water Resour. Res.* 3 (4), 1007–1019. doi:10.1029/wr003i004p01007

Dai, Y. X., Wang, Z. H., Dai, L. D., Wang, Q. L., and Cao, T. (2017). Application of Chicago hyetograph method in design duration rainstorm pattern. *J. Arid Meteorl.* 35 (6), 1061–1069. doi:10.11755/j.issn.1006-7639(2017)-06-1061

Jiang, M. (2015). Study of Shanghai design rainstorm profile under the new rainstorm situation. *J. Hunan Inst. Sci. Technol. Nat. Sci.* 28 (2), 69–80. doi:10.3969/j.issn.1672-5298.2015.02.015

Kottegoda, N. T., Natale, L., and Raiteri, E. (2014). Monte Carlo simulation of rainfall hyetographs for analysis and design. *J. Hydrol.* 519, 1–11. doi:10.1016/j.jhydrol.2014.06.041

Keifer, C. J., and Chu, H. H. (1957). Synthetic storm pattern for drainage design. *J. Hydraul. Div.* 83 (4), 1–25. doi:10.1061/jyceaj.0000104

Lee, K. T., and Ho, J.-Y. (2008). Design hyetograph for typhoon rainstorms in Taiwan. *J. Hydrol. Eng.* 13, 647–651. doi:10.1061/(asce)1084-0699(2008)13:7(647)

Liao, D. Q., Zhu, H. N., Zhou, J., Sun, J., and Wang, Y. (2019a). Research on storm intensity formula and design rain pattern sampling method. *Meteor. Mon.* 45 (10), 1375–1181.

Liao, D. Q., Zhu, H. N., Zhou, J., Wang, Y., and Sun, J. (2019b). Study of the natural rainstorm moving regularity method for hyetograph design. *Theor. Appl. Climatol.* 138 (4), 1311–1321. doi:10.1007/s00704-019-02890-0

Li, Z. Y., Huang, X. J., and He, Y. Y. (2018). Research on derivation method of design rainstorm pattern. *Water Supply Drain. Eng.* 36 (1), 141–144.

Lin, G.-F., and Wu, M.-C. (2007). A SOM-based approach to estimating design hyetographs of ungauged sites. *Journal of Hydrology* 339, 216–226. doi:10.1016/j.jhydrol.2007.03.016

Pilgrim, D. H., and Cordery, I. (1975). Rainfall temporal patterns for design floods. *J. Hydr. Div.* 101 (1), 81–95. doi:10.1061/jyceaj.0004197

Powell, D. N., Khan, A. A., and Aziz, N. M. (2008). Impact of new rainfall patterns on detention pond design. *J. Irrig. Drain Eng.* 134, 197–201. doi:10.1061/(asce)0733-9437(2008)134:2(197)

Pochwat, K., Słyś, D., and Kordana, S. (2017). The temporal variability of a rainfall synthetic hyetograph for the dimensioning of stormwater retention tanks in small urban catchments. *J. Hydrol.* 549, 501–511. doi:10.1016/j.jhydrol.2017.04.026

Wang, A., Qu, N., Chen, Y., Li, Q., and Gu, S. (2018). A 60-minute design rainstorm for the urban area of Yangpu district, Shanghai, China. *Water* 10, 312. doi:10.3390/w10030312

Wang, S.-s., Liu, D.-y., and Zhang, Q. (2004). Spatial query preprocessing in distributed GIS. *J. Appl. Meteorol. Sci.* 15 (6), 737–744. doi:10.1007/978-3-540-30208-7_98

Wang, X. Q., Huang, G. H., and Liu, J. L. (2014). Projected increases in intensity and frequency of rainfall extremes through a regional climate modeling approach. *J. Geophys. Res.: Atmos.* 119 (23), 13–271. doi:10.1002/2014jd022564

Yen, B. C., and Chow, V. T. (1980). Design hyetographs for small drainage structures. *J. Hydr. Div.* 106 (6), 1055–1076. doi:10.1061/jyceaj.0005442

Yin, S. Q., Wang, Y., Xie, Y., and Liu, A. L. (2014). Characteristics of intra-storm temporal pattern over China. *Adv. Water Sci.* 25 (5), 617–624.

Conflict of Interest: The authors declare that the research was conducted in the absence of any commercial or financial relationships that could be construed as a potential conflict of interest.

frontiers in Earth Science

ORIGINAL RESEARCH
published: 06 April 2021
doi: 10.3389/feart.2021.656594

Precipitation Variations in the Flood Seasons of 1910–2019 in Hunan and Its Association With the PDO, AMO, and ENSO

*Yuxing Zeng[1], Chao Huang[1], Yihao Tang[1] and Jiadong Peng[1,2]**

[1] Climate Center of Hunan Province, Changsha, China, [2] Key Laboratory of Hunan Province for Meteorological Disaster Prevention and Mitigation, Changsha, China

Floods in the middle reaches of the Yangtze River threaten thousands of million people, causing casualties and economic loss. Yet, the prediction of floods in this region is still challenging. To better understand the floods in this region, we investigate the interdecadal-interannual rainfall variation of the flood season (April–September) in Hunan province. The relationship between the rainfall and the Pacific decadal oscillation (PDO), Atlantic Multidecadal Oscillation (AMO), and El Niño-Southern Oscillation (ENSO) are also analyzed. The results show that the precipitation in the flood seasons shows an interdecadal oscillation with a period of about 20 years, which is caused by the joint effect of the PDO and AMO. When the PDO and AMO are in the same phase, the corresponding flood season is characterized by more precipitation, and conversely, it is less precipitation. Further analyses show that in the year after El Niño, when the PDO and AMO are both in the positive phase, it is favorable for the west Pacific subtropical high (WPSH) to be stronger and more southward than normal. Such circulation anomaly is conducive to the water vapor transport to the southern China, and as a result there is more precipitation in Hunan. When the PDO and AMO are both in the negative phase, the WPSH is weaker than normal, but the India-Burma trough is obviously stronger, which is also favorable for the southwesterly water vapor transport to the southern China. However, in the next year of the La Niña year, regardless of the phase combination of the PDO and AMO, the southern coast of China are controlled by a negative geopotential height anomaly and the WPSH retreats to the sea, which is not conducive to the northward transport of water vapor, and the precipitation in Hunan is less than normal. But if only the cold SST background in the previous stage is considered (without reaching the standard of a La Niña event),is more precipitation in most of the Hunan Province. Therefore, at the interannual scale, the PDO and AMO also have a modulating effect on the precipitation signal. However, the interannual-scale ENSO signal has a greater influence on the precipitation in Hunan flood seasons. Our results will give implications for the predications of floods in Hunan.

Keywords: Hunan province, precipitation in the flood seasons, Pacific decadal oscillation, Atlantic Multidecadal Oscillation, El Niño-Southern Oscillation

OPEN ACCESS

Edited by:
Qingxiang Li,
Sun Yat-sen University, China

Reviewed by:
Zhiqiang Gong,
Beijing Climate Center (BCC), China
Bosi Sheng,
Sun Yat-sen University, China

****Correspondence:***
Jiadong Peng
14865976@qq.com

Specialty section:
This article was submitted to Interdisciplinary Climate Studies, a section of the journal Frontiers in Earth Science

Received: *21 January 2021*
Accepted: *05 March 2021*
Published: *06 April 2021*

Citation:
Zeng Y, Huang C, Tang Y and Peng J (2021) Precipitation Variations in the Flood Seasons of 1910–2019 in Hunan and Its Association With the PDO, AMO, and ENSO. Front. Earth Sci. 9:656594. doi: 10.3389/feart.2021.656594

INTRODUCTION

Hunan Province is located in the central China, downstream of the Tibetan Plateau and south of the middle reaches of the Yangtze River. Hunan is surrounded by mountains on three sides, and belongs to the subtropical monsoon climate zone. The precipitation distribution is uneven and has large interannual variation. April to September is the flood season in Hunan Province, accounting for about 70% of the annual precipitation (Duan et al., 1999). The ENSO is the strongest interannual variability signal of the coupled tropical sea-air system, and is also the main modulator of the precipitation interannual variability in China during the flood season (e.g., Fu and Teng, 1988; Ye, 1990; Jin and Tao, 1999; Gao and Wang, 2007; Zong et al., 2010). Both the PDO and the AMO could significantly modulate the precipitation impact from the interannual variability of ENSO.

The PDO is a long-lived El Niño-like pattern of Pacific climate variability, and the characteristics and roles of the PDO are summarized by Mantua and Hare (2002). The PDO can affect the interdecadal variability of the summer precipitation in the eastern China by influencing the atmospheric circulations in East Asia.Moreover, the PDO can significantly influence the interdecadal north-south movement of the main summer rainfall belt in eastern China. When the PDO is in a positive phase, a wave train from the Sea of Japan to the East China Sea (Pacific-Japan teleconnection pattern, also called the P-J wave train) will be excited off the coast of East Asia, which will affect the precipitation in the southern China, making the summer precipitation less in northern China and more in the middle-lower reaches of the Yangtze River (Zhang et al., 2007). When the PDO is in a negative phase, the response of the circulation is generally opposite to that during the positive phase, making the East Asian subtropical westerly jet weaken, and thereby resulting in more summer precipitation in the Huanghuai area and less summer precipitation in the middle-lower reaches of the Yangtze River (Zhu et al., 2015). Besides, if the PDO is in a positive phase, East Asia is dominated by the anomalous western North Pacific anticyclone and the cyclonic circulation near Japan in El Niño decaying summers, and the average precipitation anomaly in China shows a tripolar distribution, i.e., more precipitation in the central region and less precipitation in the north and south. But, if the PDO is in a negative phase East Asia is mainly influenced by the anomalous western North Pacific anticyclone circulation in El Niño decaying summers, and the precipitation anomaly is in a dipolar distribution with significant intra-seasonal variability (Feng et al., 2015). Dong (2016) distinguished the similarities and differences between the PDO and ENSO effects on the East Asian summer monsoon. They also found that after excluding the effect of ENSO, the anomalous characteristics of the East Asian summer monsoon during different PDO phases are similar to those with the effect of the ENSO.

The AMO is the most significant interdecadal characteristic of the North Atlantic sea surface temperature (SST) (Sutton and Hodson, 2007), and its phase variations are closely related to the Atlantic meridional overturning circulation. The warming of most of Eurasia during the warm AMO phase enhances the sea-land thermal difference between Eurasia and the Pacific Ocean in summer, resulting in enhanced East Asian summer monsoon (Lu et al., 2006; Wang et al., 2009). Also, the warm AMO phase can excite the wave train of the Eurasian teleconnection pattern at middle and high latitudes and the teleconnection wave train propagating along the East Asian subtropical westerly jet at middle latitudes during the boreal summer, and the wave trains can lead to cyclonic anomalies over the Huanghuai area and anticyclonic anomalies over the Yangtze River, thereby causing more precipitation in the Huanghuai area and less precipitation in the middle-lower reaches of the Yangtze River (Si and Ding, 2016). The AMO can also affect the interdecadal variability of SST in the tropical western Pacific through atmospheric teleconnection, further influencing the interdecadal variability of the summer monsoon circulation in East Asia and summer precipitation in the eastern China (Sun et al., 2017). Zhang and Delworth (2010) also found that the changes in precipitation patterns in the east-central China in the early 1990s were closely associated with the AMO changes.

However, any single factor could not determine the precipitation variability, and the interannual and interdecadal variabilities of precipitation are the results of multiple factors (Li et al., 2018). The above previous studies have shown that the ENSO, PDO, and AMO all have relatively good correlations with summer precipitation in the eastern China. However, the interrelationships among them on interdecadal scales and the synergistic effects on the precipitation in the Hunan flood seasons need to be further investigated. The remainder of this article is organized as follows. Data and methods are given in section "Data and Methods." Section "Results" presents the main results of this study. The cause analysis is performed in section "Circulation Analysis." Finally, the conclusions and discussion are given in section "Conclusions and Discussion."

DATA AND METHODS

Data

The data used in this article includes the 1910–2019 monthly homogenized precipitation data in Hunan, the PDO, AMO, and SST data, the daily precipitation observation data and the reanalysis data.

Previous studies on the interdecadal variability of precipitation are mostly based on reanalysis data. However, Peng et al. (2017) got a 100-year long precipitation dataset of Hunan's flooding season based on station data. This dataset fills in the missing values of some Hunan stations before 1950 by univariate linear regression. The dataset is already examined and corrected by a two-phase regression model, metadata of station location history, and the standard normal homogeneity test. The homogenized precipitation data in Hunan would better explain the regional characteristics of long-term precipitation changes, particularly given that the precipitation data before 1950 are incomplete due to war and other reasons in this region and the inhomogeneity problems of the precipitation data in China,it fill in the missing data of each station with a regression model based on the adjacent stations' data.

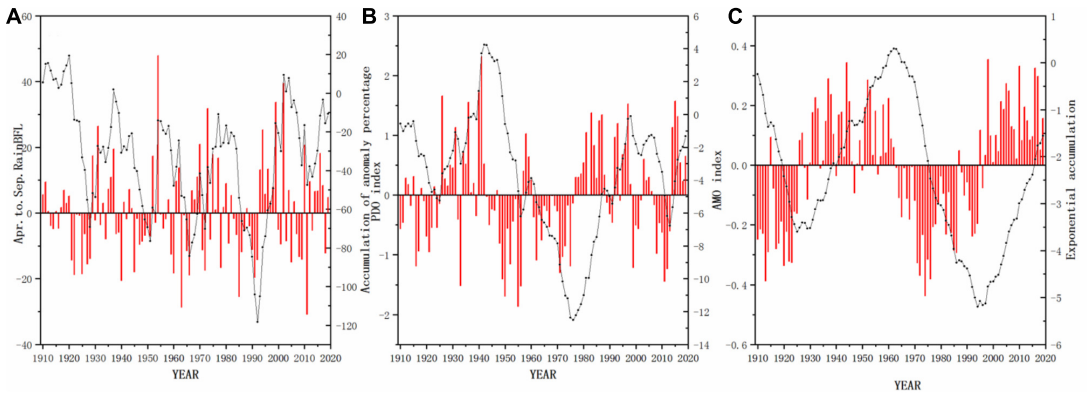

FIGURE 1 | Time series of **(A)** the precipitation anomaly percentage, **(B)** PDO index, and **(C)** AMO index in Hunan flood seasons during 1910–2019 (the red line is the exponential sequence and the black line is the anomaly accumulation value).

The SST data is from the Extended Reconstructed SST version 4 from the National Oceanic and Atmospheric Administration, with a spatial resolution of 2.0° × 2.0°, and this dataset starts from January 1854 (Smith et al., 2008). Moreover, the daily precipitation observation data is from 97 meteorological stations in Hunan, and the time length from January 1, 1961 to August 31, 2020. The data is strictly processed for quality control. The geopotential height data is provided by the National Centers for Environmental Prediction/National Center for Atmospheric Research, with a spatial resolution of 2.5° × 2.5°(Kalnay, 1996). In addition, the data has 17 vertical levels from 1000 hPa to 10 hPa, and the main level used is 500 hPa. The start time of the reanalysis data is January 1948. Note that the climatic averages of each meteorological element used in the article are averaged between 1981 and 2010.

The PDO index quantifies the strength of SST oscillations and is defined as the time coefficient from the first mode of the empirical orthogonal function analysis for monthly average SST anomalies in the north of 20°N in the North Pacific (Hare and Mantua, 2000). The AMO is a quasi-periodic warm-cool anomaly of the SST in the North Atlantic region, with a basin-wide scale and a multidecadal scale (Kerr, 2000). The AMO index is defined as the regional average SST value in the North Atlantic of 0°N–60°N, 0°W–80°W.

Methods

In this article, the Nino 3.4 zone (170°W–120°W, 5°S–5°N) is used as the monitoring zone for the El Niño (La Niña) events. The 3-month moving average of the NINO3.4 index is calculated (one decimal is retained, same below), if the value is greater than or equal to 0.5°C (less than or equal to −0.5°C) and maintains for at least 5 months, then an El Niño (La Niña) event is determined.

To obtain the interdecadal scale components of meteorological elements, we use the Lanczos filter method to perform an 11-year low-pass filter (Duchon, 1979). In the low-pass filter the low-frequency signals can pass, while high-frequency signals above a defined threshold are blocked or attenuated. However, the amplitude of blocking and attenuation varies according to the signals' frequency and the filter purpose.

Wavelet analysis can analyze the one-dimensional signal in terms of both time and frequency, and can finely characterize the local features of the climate system and the oscillations near arbitrary points. It also can distinguish local singularities. Moreover, it can analyze the perturbation characteristics at different scales according to the periodic evolution with different scales over time, and determine the significant cycles of the climate series (Hudgins and Huang, 1996).

RESULTS

Temporal Variations of the Precipitation, PDO, and AMO in Hunan Flood Seasons

From 1910 to 2019, there is no significant change of precipitation during Hunan flood seasons (April–September, same below), with overall more precipitation in the 1910s, 1930s, 1950s, 1970s, 1990s and 2010s and overall less precipitation in the 1920s, 1940s, 1960s, 1980s and 2000s (**Figure 1A**). The variations are almost the same as the precipitation trends in southern China (e.g., Ding et al., 2008; Huang et al., 2011; Zhu et al., 2011; Xu et al., 2015). The wavelet transform shows that the precipitation in Hunan flood seasons has an interdecadal fluctuation on an about 20-year scale, with a short period of 2–3 years in the 1930s, 1950s, 1970s and 21st century (**Figure 2**). The correlation coefficient of the precipitation in Hunan flood seasons with the PDO index is quite small, and the correlation coefficient with the AMO is only 0.12 without passing the significance test at 90% confidence level.

For the variations of the PDO and AMO, the PDO (**Figure 1B**) is mainly in a negative phase before the 1920s and then turns into a positive phase after the 1920s. In the 1940s, the PDO turns back to the negative phase and maintains until the mid-1970s, and after that the PDO is mainly in a positive phase except around 2010. The AMO (**Figure 1C**) is mostly in a negative phase until the mid-1920s, and then changes into a positive phase until the early 1960s. Then, the AMO is in a negative phase from the 1960s to the late 20th century. In the 21st century the AMO changes into a positive phase.

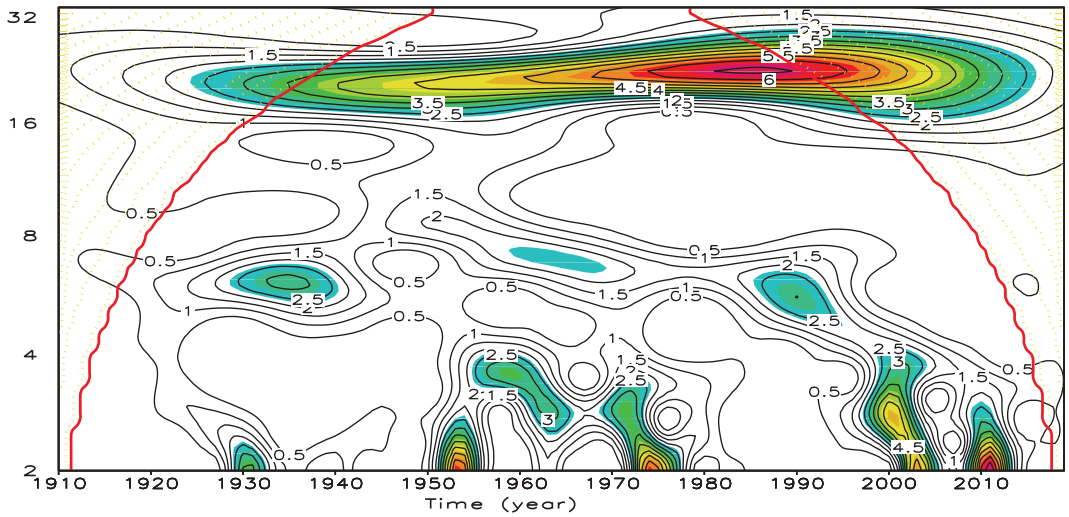

FIGURE 2 | Wavelet analyses for the precipitation anomaly percentage in Hunan flood seasons during 1910–2019. The shaded areas pass the significance test at 95% confidence level.

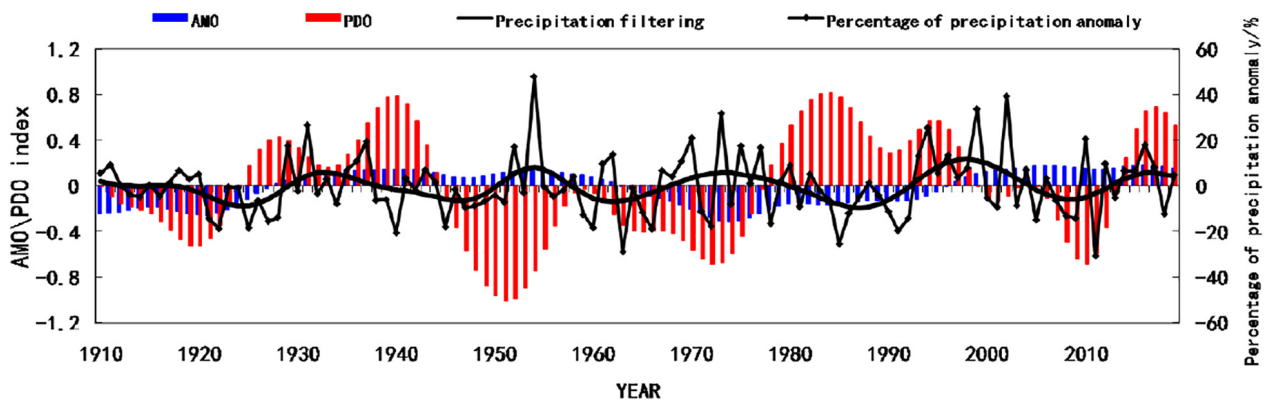

FIGURE 3 | Temporal variations of the AMO index, the PDO index, the precipitation and the precipitation anomaly percentage in Hunan flood seasons during 1910–2019.

Relationships Between the Precipitation Interdecadal Variations in Hunan Flood Seasons and the PDO and AMO

Temporal Variations of Precipitation, the Pacific Decadal Oscillation and the Atlantic Multidecadal Oscillation

Figure 3 shows the time series of the PDO, AMO and the precipitation after low-pass filtering, as well as the precipitation anomaly percentage during Hunan flood seasons. As can be seen, the PDO and AMO are in the same phase in 53 years, of which there are more precipitation in 32 years, accounting for 60.4% (32/53, **Table 1**). While the PDO and AMO are in the opposite phase in 57 years, of which there are less precipitation in 38 years, accounting for 66.7% (38/57, **Table 1**), i.e., Hunan flood seasons are dominated by less precipitation. This situation is especially obvious from the 1960s, i.e., when the PDO and AMO are in the same phase 81.8% (18/22) of the years are with more precipitation, and when the PDO and AMO are in the opposite phase 64.9% (24/37) of the years are with less precipitation. Therefore, the following analysis of precipitation anomalies began in 1961.

Spatial Variations of the Precipitation in Hunan Flood Seasons

As can be seen in **Figure 4** (The frequency of positive precipitation anomaly is the proportion of the years with positive precipitation anomaly. In the following, the analysis of precipitation is based on its positive anomaly frequency), when the PDO and AMO are in the same phase, the precipitation in Hunan flood seasons is more than normal in most of the regions. Moreover, the excess precipitation is more significant in the years with the same positive phase than in the years with the same negative phase except in southeast Hunan. In the years with both negative phase, the precipitation in east Hunan is locally less than normal. In the years with a positive PDO phase and a

TABLE 1 | The periods of different PDO and AMO phases, the corresponding average precipitation in the flood season, and the years with excess precipitation during 1910–2019.

Phases	Periods	Precipitation anomaly/mm	Years with excess precipitation/Total years
PDO + AMO +	1928–1944, 1997–1998, 2014–2019	29.7	16/25
PDO- AMO-	1910–1923 and 1964–1977	10	16/28
PDO + AMO-	1924–1927 and 1978–1996	−36.3	8/23
PDO- AMO +	1945–1963 and 1999–2013	−6.6	11/34

negative AMO phase, the precipitation during flood seasons is less than normal in most of the regions, except the northwest Hunan. In the years with a negative PDO phase and a positive AMO phase the precipitation is only slightly more than normal in the southeast Hunan. If the results processed by the low-pass filtering are similar, i.e., the precipitation is mainly more than normal in the years with the same PDO and AMO phase and less than normal in the years with the opposite phase,but the excess precipitation is more extensive and more frequent (figure omitted).

Impacts of ENSO Events on Interannual Precipitation Fluctuations

Impacts of El Niño Events

In the next years of the El Niño events after 1961, when the PDO and AMO are in the same phase, the precipitation in Hunan flood season is mainly more than normal, accounting for 80% (8/10, **Table 2**). When the PDO and AMO are in the opposite phase, the years with the precipitation less than normal account for 46.2% of the total (6/13, **Table 2**).

The precipitation series in the next years of El Niño events the results are shown in **Figure 5**. It can be found that when the PDO and AMO are in the same phase, the precipitation is more than normal in most of the regions in Hunan, except for local areas of southeast Hunan. Moreover, when the PDO and AMO are both in a positive phase, the positive precipitation anomaly is larger and distribute more wide. However, less precipitation

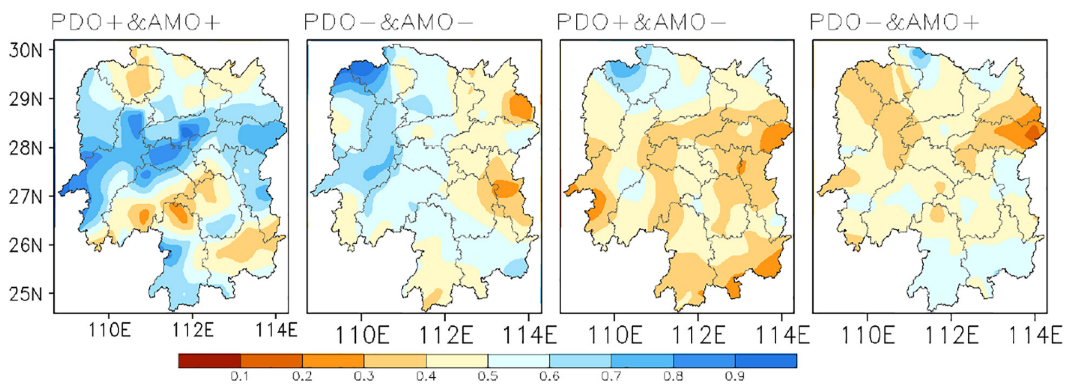

FIGURE 4 | Composition graph of the frequency of positive precipitation anomaly during Hunan flood seasons corresponding to different PDO and AMO phases from 1961 to 2019.

TABLE 2 | Statistics of the precipitation in Hunan flood seasons in the next years of the El Niño events during 1910–2019.

	Years with excess precipitation/ Total years	PDO and AMO same phase	Precipitation anomaly/mm	PDO and AMO opposite phase	Precipitation anomaly/mm
April to September	18/32	12/17	55.8	6/15	−10.2
April to June	21/32	12/17	78.2	9/15	−23.3
June to August	17/32	12/17	66.1	5/15	−56.8
July to September	13/32	8/17	22.3	5/15	−62.3

TABLE 3 | Statistics of the precipitation in Hunan flood seasons in the next years of the La Niña events during 1910–2019.

	Years with less precipitation/ Total years	PDO and AMO same phase	Precipitation anomaly/mm	PDO and AMO opposite phase	Precipitation anomaly/mm
April to September	23/32	7/13	−30.7	16/19	−57.7
April to June	21/32	8/13	−36.3	13/19	−46.5
June to August	23/32	8/13	−67	15/19	−81.9
July to September	20/32	7/13	−21.4	13/19	−76.3

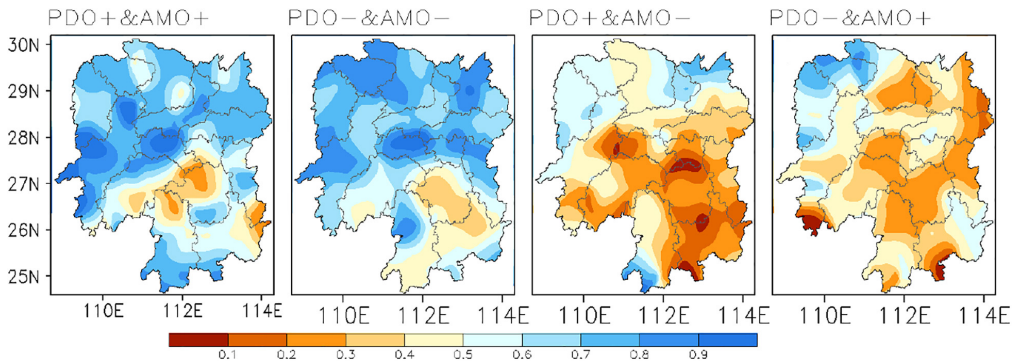

FIGURE 5 | The same as **Figure 4**, but for the next years of El Niño events.

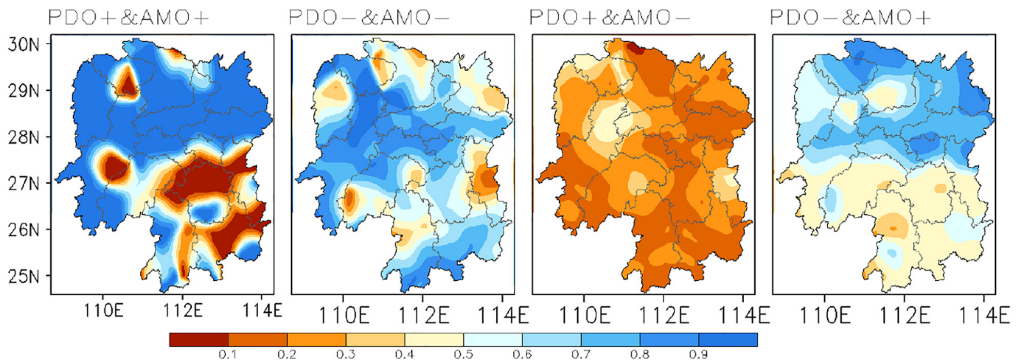

FIGURE 6 | The same as **Figure 4**, but for the next years of La Niña events and the precipitation series is processed by the low-pass filtering.

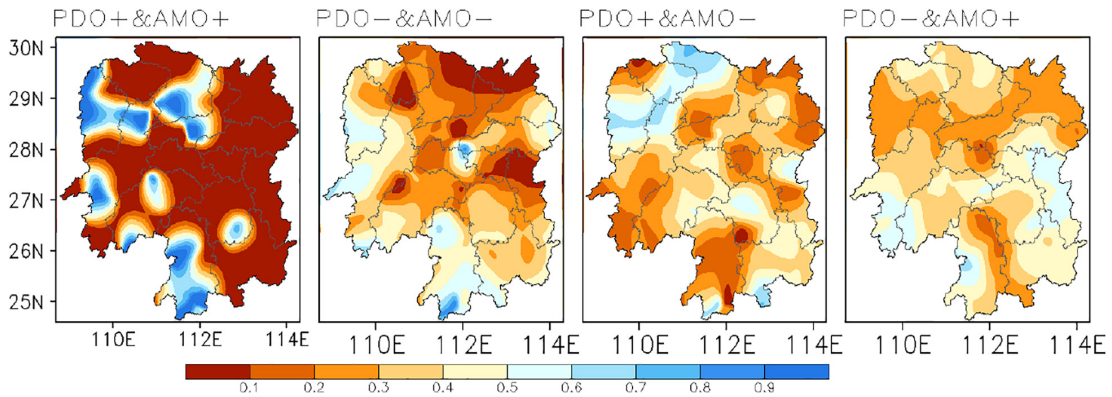

FIGURE 7 | The same as **Figure 4**, but for the next years of La Niña events.

occurs in most of Hunan in the years with the positive PDO phase and negative AMO phase, except for the northern Hunan. Under the negative PDO phase and positive AMO phase, the results are slightly different, with less precipitation in most areas except for the northwest and southeast Hunan. Compared with the results in **Figure 4**, it can be found that the frequency of positive or negative anomaly of precipitation is higher under the impacts of ENSO than without the impacts of ENSO. If the time series of precipitation is also processed by the low-pass filtering, the results are similar to **Figure 5**. When the AMO and PDO are in the positive phase, the precipitation is more than normal. However, the range of less precipitation is significantly enlarged when both PDO and AMO are in the negative phase (figure omitted).

Impacts of La Niña Events

In the next years of La Niña events, when the PDO and AMO are in the same phase, the precipitation in Hunan flood seasons is less than normal at a percentage of 66.7% (4/6). When the PDO

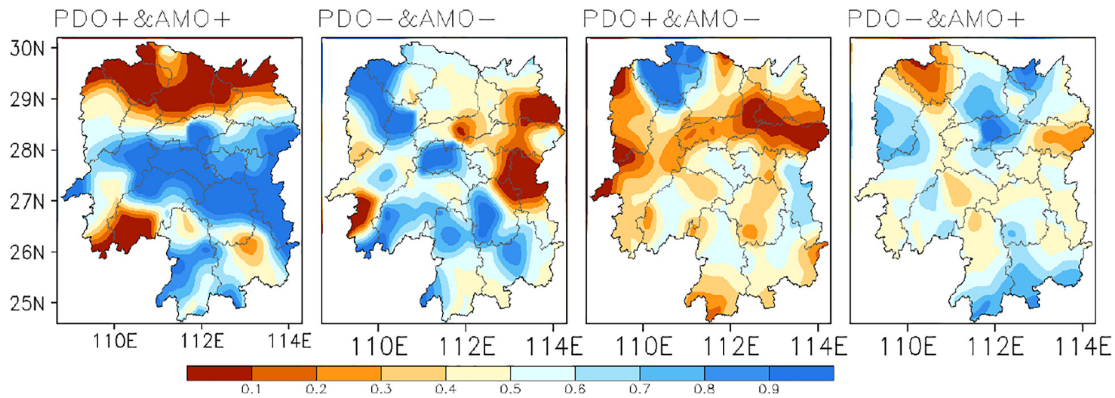

FIGURE 8 | Composition of precipitation anomaly percentage in flood season of Hunan Province for the cold SST background in the previous stage (without reaching the standard of a La Niña event).

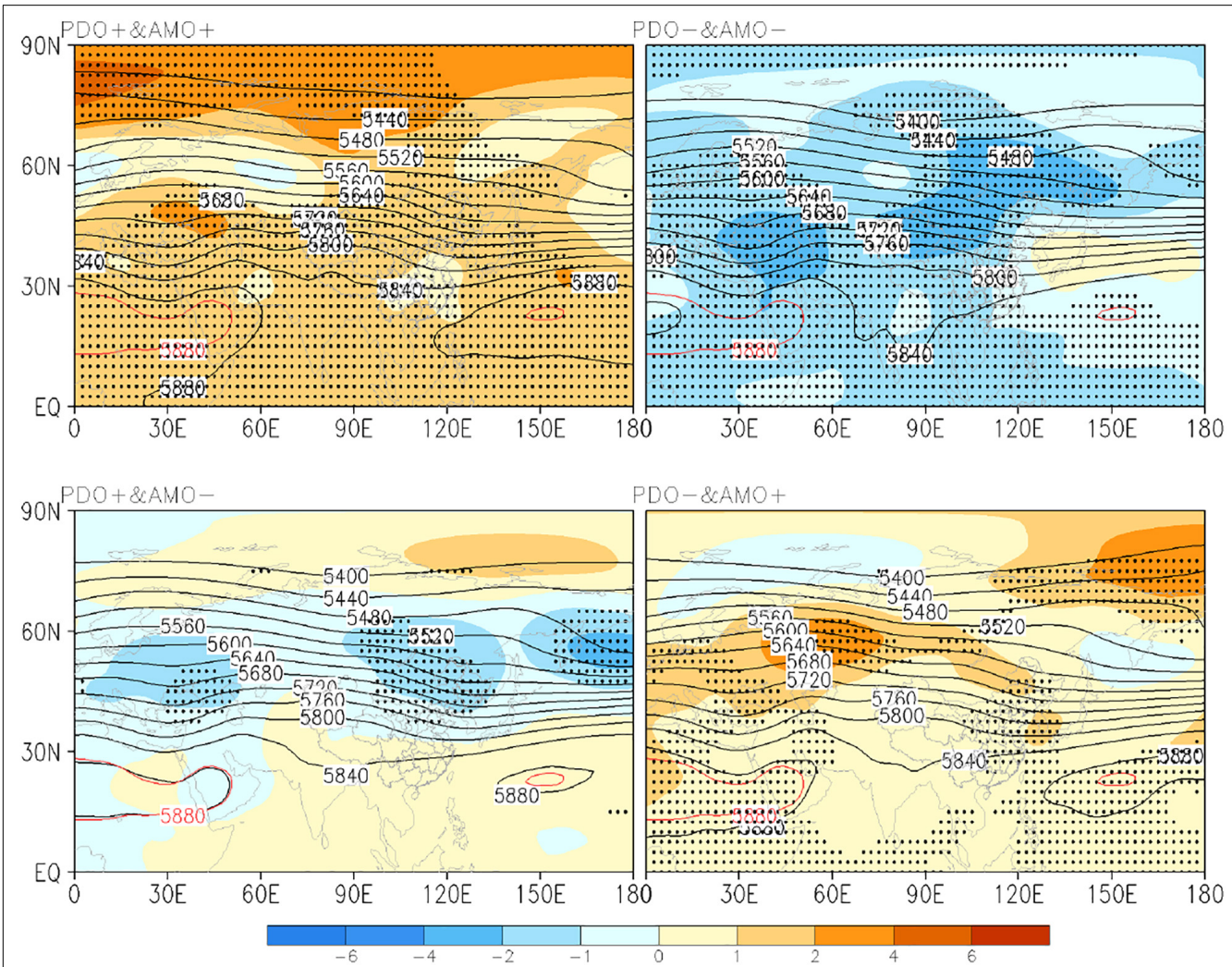

FIGURE 9 | The composite 500 hPa geopotential height in the next years of El Niño events during 1961–2019 under different PDO and AMO phases. The punctate areas pass the significance test at 90% confidence level.The red lines denote 588 dagpm of climatology and shaded area denotes 500 hPa anomalies (the same below).

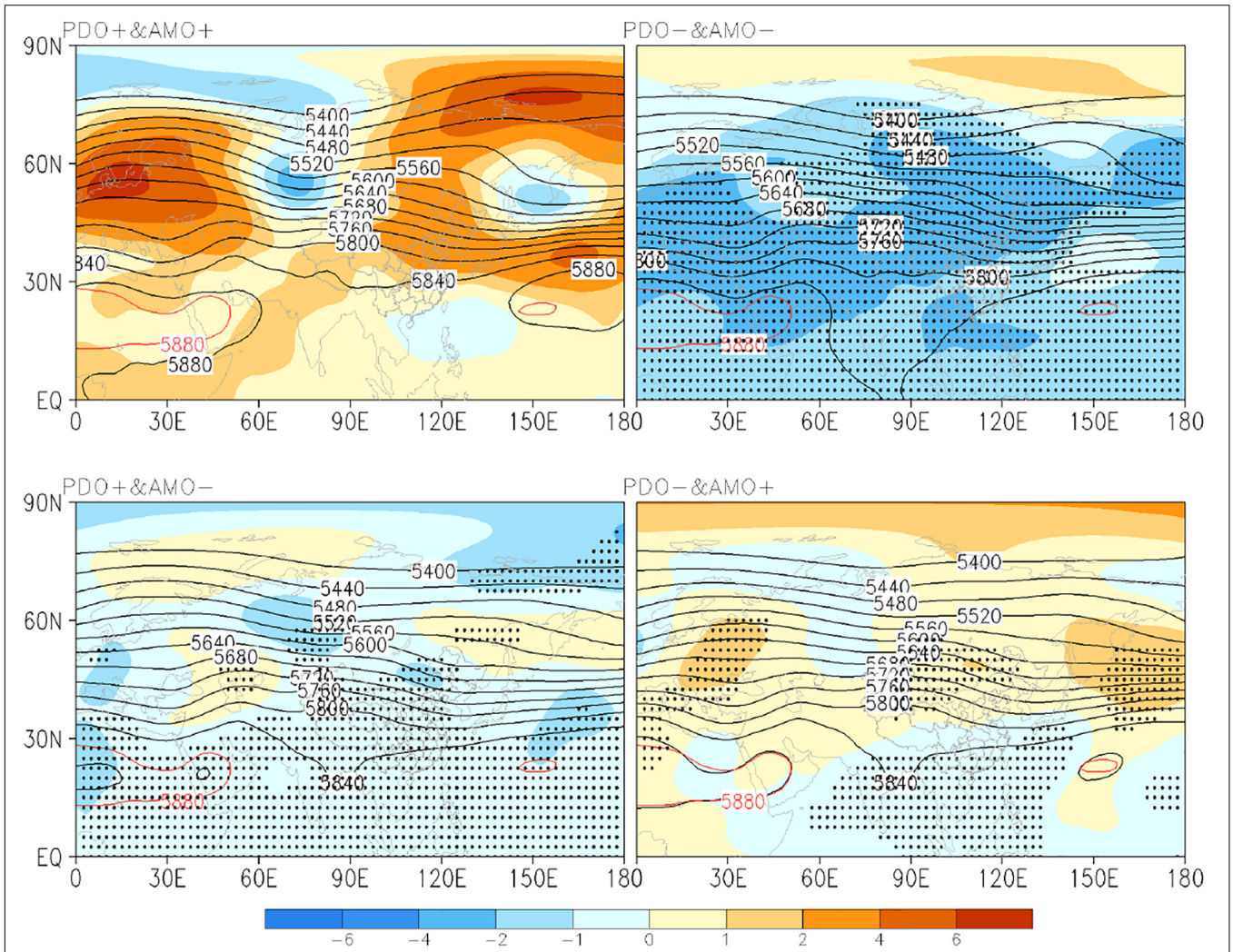

FIGURE 10 | The same as **Figure 8**, but for the next years of La Niña events.

and AMO are in the opposite phase, the Hunan flood season is also dominated by less precipitation, and the years with less precipitation accounts for 75% (9/12, **Table 3**). In a word, the overall precipitation in Hunan flood seasons is mainly less than normal in the next years of La Niña events, and the years with less precipitation account for 72.2% (13/18, **Table 3**) of the total.

The precipitation series in the next years of La Niña events is processed by the low-pass filtering, and the results are shown in **Figure 6**. The previous studies have shown that in the next years of La Niña events, the precipitation is mainly less than normal during the flood seasons in the middle and lower Yangtze River. However, for the precipitation in Hunan flood seasons (**Figure 6**), when the PDO and AMO are in the same phase, the precipitation in Hunan in the flood season is more than normal. Note that only in 2018 the PDO and AMO are both in the positive phase. In the years when the PDO and AMO are both in the negative phase, the precipitation in southeastern Hunan is mainly more than normal. Under the positive PDO phase and the negative AMO phase the precipitation in flood season is consistently less than normal in the whole province, and the degree of less precipitation is also more significant than that in the next years of El Niño events. In addition, the precipitation distribution in Hunan flood season is more in the north and less in the south under the negative PDO phase and the positive AMO phase. Note that without the low-pass filtering for the precipitation series, the precipitation is mainly less than normal regardless of the combination of PDO and AMO phases (**Figure 7**).

If only the cold SST background in the previous stage is considered (without reaching the standard of a La Niña event) and the precipitation series is not processed by the low pass filtering, the results are shown in **Figure 8**. When the PDO and AMO are in the same phase, the precipitation in flood seasons is mainly more in south-central Hunan and less in the northern Hunan. However, the precipitation is less than normal in most areas when the PDO and AMO are in the opposite phase. Therefore, on the interdecadal scale the precipitation in Hunan flood seasons is mainly affected by the joint effect of the PDO and AMO. Besides, the PDO and AMO also have a modulating

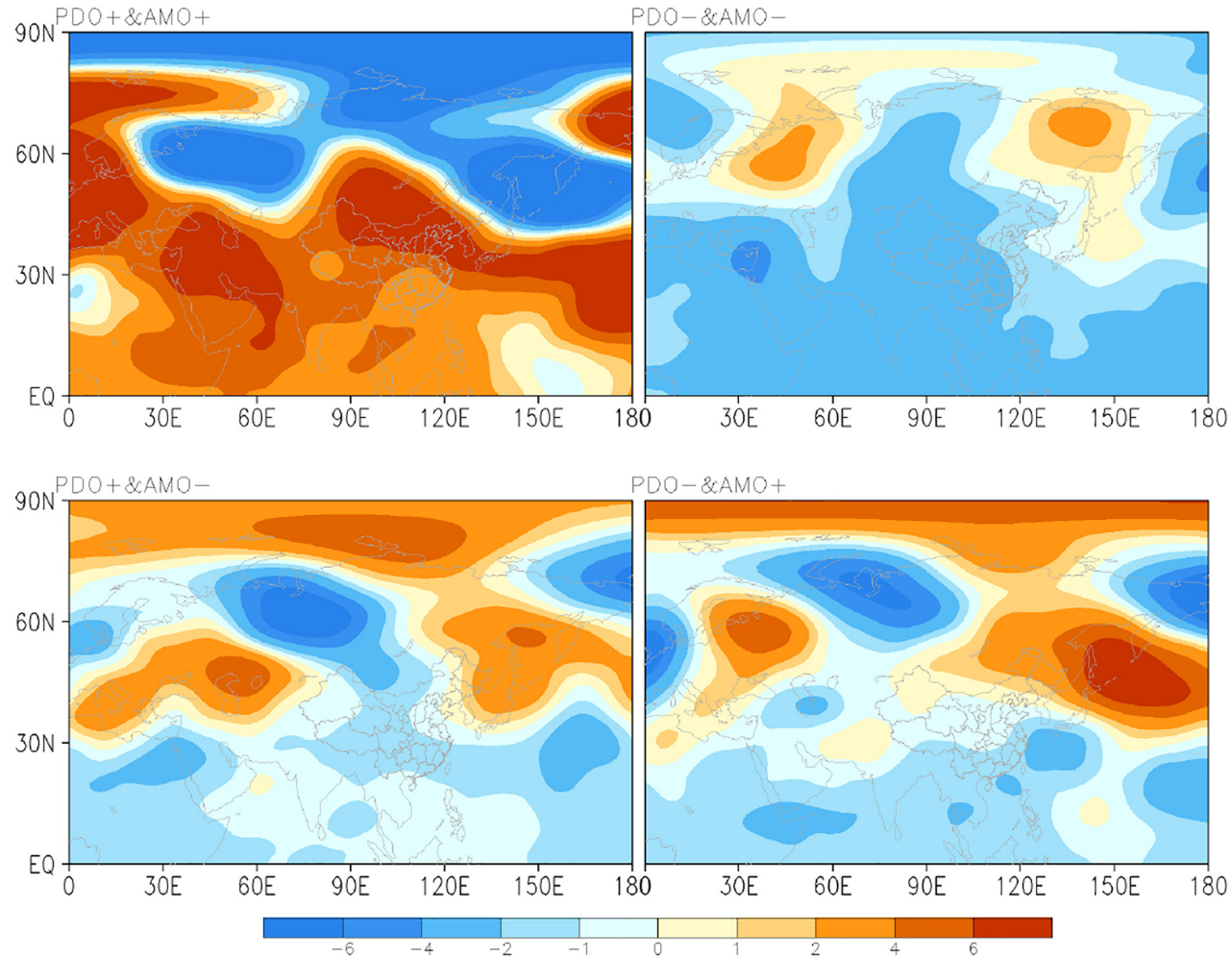

FIGURE 11 | The same as **Figure 9**, but for the results after the low-pass filtering.

effect on the precipitation on the interannual scale. However, the ENSO signal has more influence on the anomalous precipitation in Hunan flood seasons on the interannual scale.

CIRCULATION ANALYSIS

The above analyses have shown that regardless of the PDO and AMO phases, the precipitation anomaly in the next years of ENSO events is more significant than in normal years. Thus, the following cause analysis focuses on the precipitation and circulations in the next years of ENSO events.

As shown in **Figure 9**, in the next years of El Niño events, when the PDO and AMO are both in the positive phase the 500 hPa height field is the opposite to that when the PDO and AMO are both in the negative phase, but the influence on the precipitation in Hunan flood seasons is generally the same (**Figure 9**). Under the positive phase of the PDO and AMO, the area near Lake Baikal is in a low-pressure trough and is controlled by the negative geopotential height anomaly, so the circulation situation is favorable for the cold air to advance southward and affect southern China from the westward path. In addition, the middle and low latitudes are controlled by the positive geopotential height anomaly. However, the west Pacific subtropical high (WPSH, black lines of 5880) is obviously stronger and more southward than normal (red lines of 5880), favoring the water vapor transport to southern China. Therefore, precipitation in most Hunan is more than normal. Under the negative phase of the PDO and AMO, the significantly weaker East Asian trough is conducive to the southward movement of cold air. In addition, the WPSH is weaker than normal, but the India-Burma trough is significantly stronger, also contributing to the southwesterly water vapor transport to Hunan, and thereby resulting in more precipitation. However, the temperature is lower than that in the positive phase of the PDO and AMO (figure omitted). Under the positive PDO phase and the negative AMO phase, the middle latitudes are controlled by the negative geopotential height anomaly, and the southward cold air is strong. Meanwhile, the WPSH is on the sea and far from the mainland, and the India-Burma trough is weak, which is not conducive to the

water vapor transport, resulting in less precipitation in Hunan. Under the negative PDO phase and the positive AMO phase, the middle latitudes are controlled by the positive geopotential height anomaly. Moreover, the weak cold air in the north is favorable for water vapor transport to the farther north. This circulation situation results in less precipitation in Hunan.

As shown in **Figure 10**, in the next years of La Niña events, the eastern coast of China presents a positive-negative-positive anomalous distribution of the East Asia/Pacific teleconnection under the positive phase of the PDO and AMO (the samples are only for 2018). The WPSH retreats back to the sea and the positive geopotential height anomaly controls southern China, which is not conducive to water vapor transport, easily causing high temperature and less precipitation in Hunan. Under the negative phase of the PDO and AMO, the WPSH is anomalously weak and the negative geopotential height anomaly controls the whole low latitudes, leading to the weak water vapor transport and less precipitation in Hunan. The results under the opposite phase of the PDO and AMO are similar to those under the same negative phase.

As shown in section "Impacts of La Niña Events," after the low pass filtering the precipitation in Hunan flood seasons is mainly more than normal in the south-central parts under the same phase of the PDO and AMO in the next years of La Niña events. Therefore, we also perform the low pass filtering on the 500 hPa geopotential height in the next years of La Niña events. Note that when the PDO and AMO are in the same positive phase, only 2018 is the next year of the La Niña event, And the results in shown in **Figure 11**. As can be seen, under the same positive phase of the PDO and AMO the 500 hPa circulation situation in the middle and low latitudes in the next years of La Niña events is similar to that in the next years of El Niño events. At this time, the WPSH is obviously stronger and more southward than normal, favoring the water vapor transport to southern China, so the precipitation in most of Hunan is more than normal. Under the same negative phase of the PDO and AMO, the significantly weaker East Asian trough is conducive to the southward movement of cold air. Meanwhile, the WPSH is weaker than normal, but the India-Burma trough is significantly stronger, contributing to the southwesterly water vapor transport to southern China, and thereby resulting in more precipitation in Hunan. While under the two kinds of the opposite phase, the circulation situation is generally the same. The WPSH is anomalously weak and the negative geopotential height anomaly controls the whole low latitudes, leading to the weak water vapor transport and less precipitation in Hunan.

CONCLUSION AND DISCUSSION

Based on the above analyses, the following conclusions can be obtained.

Since 1910, the precipitation in Hunan flood seasons has an obvious 20-year variation cycle. The PDO index has an obvious period of 5–6 years from the early 1920s to the early 1960s and in 1990s. In the 21st century, the period is about eight years. The AMO index is a multidecadal climatic factor, and its interannual cycle is not significant. Since the 1960s, in 81.8% of the years the precipitation in Hunan flood seasons is mainly more than normal in the years when the PDO and AMO are in the same phase. Conversely, the precipitation in Hunan flood seasons is mainly less than normal, accounting for 64.9% of the total years.

Since 1961, the precipitation in flood seasons is mainly more than normal in most Hunan under the same positive phase of the PDO and AMO, except for the northwest Hunan and parts of southeast Hunan, especially in summer. Under the same negative phase of the PDO and AMO, the precipitation during the first rainy season is more than normal in northern Hunan, and the precipitation during the later flood season is more than normal in southern Hunan. Overall, the summer precipitation is more than normal in most areas. Under the positive PDO phase and negative AMO phase, the precipitation in flood seasons is less than normal in most regions of Hunan, especially in the first rainy season. The precipitation in summer and in the later flood season is more in the west and less in the east. Under the negative PDO phase and positive AMO phase, the precipitation is more than normal in most of the regions in the first rainy season, and in other time the precipitation is less than normal in Hunan, especially in northern Hunan.

In the next years of El Niño events since 1961, the precipitation in Hunan flood season is more than normal in most areas of Hunan under the same phase of the PDO and AMO, except for parts of southeastern Hunan. Under the positive PDO phase and the negative AMO phase, the precipitation is less than normal in most areas, except for northern Hunan. Under the negative PDO phase and the positive AMO phase, the precipitation is less than normal except in northwest Hunan and parts of southeast Hunan. The main reason is that under the same positive PDO and AMO phase, the WPSH is stronger and more southward than normal, favoring the water vapor transport to southern China, and thereby resulting in more precipitation in most Hunan. When the PDO and AMO are in the same negative phase, the significantly weaker East Asian trough is conducive to the southward movement of cold air. Meanwhile, the WPSH is weaker than normal, but the India-Burma trough is significantly stronger, contributing to the southwesterly water vapor transport to southern China, and thereby resulting in more precipitation in Hunan. Under the positive PDO phase and the negative AMO phase, the WPSH is on the sea and far from the mainland, and the India-Burma trough is weak, which is not conducive to the water vapor transport, resulting in less precipitation in Hunan. Under the negative PDO phase and the positive AMO phase, the middle latitudes are controlled by the positive geopotential height anomaly. Moreover, the weak cold air in the north is favorable for water vapor transport to the farther north, and this circulation situation results in less precipitation in Hunan.

In the next years of La Niña events since 1961, after the low pass filtering the precipitation in Hunan flood seasons is mainly more than normal under the same phase of the PDO and AMO on the interdecadal scale, and the precipitation in southeastern Hunan is mainly more than normal when the PDO and AMO are in the opposite phase. Under the positive PDO phase and

the negative AMO phase, the precipitation is consistently less than normal in the whole province, and the anomaly of less precipitation is more significant than that in the next years of El Niño events. Moreover, under the negative PDO phase and the positive AMO phase, the precipitation in Hunan flood seasons is more in the north and less in the south. Note that the circulation situation in the next years of La Niña events is similar to those in the next years of El Niño events, indicating that the critical climatic systems causing the more precipitation in Hunan are the same.

It is worth noting that this study only explains the differences of the precipitation in Hunan flood seasons under different phases of the PDO and AMO from the statistic method. So, the related physical mechanisms need to be further analyzed in future work. At the same time, this study only analyzes one province, Hunan. Further research is needed to study the decadal variability over the whole Yangtze River reaches. In addition, how PDO and AMO affect the subtropical high and surrounding circulation needs further investigations.

DATA AVAILABILITY STATEMENT

The original contributions presented in the study are included in the article/supplementary material, further inquiries can be directed to the corresponding author.

AUTHOR CONTRIBUTIONS

YZ analyzed the data. JP put forwarded the idea. YZ wrote the manuscript. All authors revised the manuscript.

FUNDING

This study was supported by the Innovation Development Project of China Meteorological Administration (Grant No. CXFZ2021Z033) and the Capacity Building Project of Hunan Meteorological Bureau in 2020 (Grant No. NLJS04).

REFERENCES

Ding, Y., Wang, Z., and Sun, Y. (2008). Inter-decadal variation of the summer precipitation in East China and its association with decreasing Asian summer monsoon. Part I: Observed evidences. *Int. J. Climatol.* 28, 1139–1161. doi: 10.1002/joc.1615

Dong, X. (2016). Influences of the Pacific Decadal Oscillation on the East Asian Summer Monsoon in non-ENSO years. *Atmos. Sci. Lett.* 17, 115–120. doi: 10.1002/asl.634

Duan, D. Y., Chen, Y. X., and Ju, J. L. (1999). Discussion on the division and variation of precipitation in flood season in Hunan Province (in Chinese). *Resources and environment in the Yangtze River Basin.* 8, 440–444.

Duchon, C. E. (1979). Lanczos Filtering in One and Two Dimensions. *J. Appl. Meteor* 18, 1016–1022. doi: 10.1175/1520-04501979018<1016:LFIOAT<2.0.CO;2

Feng, J., Wang, L., and Chen, W. (2015). How Does the East Asian Summer Monsoon Behave in the Decaying Phase of El Niño during Different PDO Phases? *J. Clim.* 27, 2682–2698. doi: 10.1175/JCLI-D-13-00015.1

Fu, C. B., and Teng, X. L. (1988). Climate anomalies in China associated with E1Nino/Southern Oscillation (in Chinese). *Chin. J. Atmos. Sci* 12, 133–141. doi: 10.3878/j.issn.1006-9895.1988.t1.11

Gao, H., and Wang, Y. G. (2007). ON the weakening relationship between summer precipitation in China and ENSO (in Chinese). *Acta Meteorol. Sin.* 65, 131–137. doi: 10.3321/j.issn:0577-6619.2007.01.013

Hare, S. R., and Mantua, N. J. (2000). Empirical evidence for North Pacific regime shifts in 1977 and 1989. *Prog. Oceanogr.* 47, 103–145. doi: 10.1016/S0079-6611(00)00033-1

Huang, R. H., Chen, J. L., and Liu, Y. (2011). Interdecadal Variation of the Leading Modes of Summertime Precipitation Anomalies over Eastern China and Its Association with Water Vapor Transport over East Asia (in Chinese). *Chin. J. Atmos. Sci.* 35, 589–606. doi: 10.3878/j.issn.1006-9895.2011.04.01

Hudgins, L., and Huang, J. P. (1996). Bivariate wavelet analysis of Asia monsoon and ENSO. *Adv. Atmos. Sci.* 13, 299–312. doi: 10.1007/BF02656848

Jin, Z. H., and Tao, S. Y. (1999). A Study on the Relationships between ENSO Cycle and Rainfalls during Summer and Winter in Eastern China (in Chinese). *Chin. J. Atmos. Sci.* 23, 663–672. doi: 10.3878/j.issn.1006-9895.1999.06.03

Kalnay, E. (1996). NCEP/NCAR 40-year reanalysis project. *Bull. amer. meteor.Soc* 77, 437–471. doi: 10.1175/1520-04771996077<0437:TNYRP<2.0.CO;2

Kerr, R. (2000). A North Atlantic climate pacemaker for the centuries. *Science.* 288, 1984–1985. doi: 10.1126/science.288.5473.1984

Li, W. J., Liu, J. P., and Ren, H. L. (2018). Characteristics and Corresponding Mechanisms of the Leading Modes of Interdecadal Variability of Summer Rainfall in Southern China (in Chinese). *Chin. J. Atmos. Sci.* 42, 859–876. doi: 10.3878/j.issn.1006-9895.1802.17283

Lu, R., Dong, B., and Ding, H. (2006). Impact of the Atlantic Multidecadal Oscillation on the Asian summer monsoon. *Geophys. Res. Lett.* 33, 194–199. doi: 10.1029/2006GL027655

Mantua, N. J., and Hare, S. R. (2002). The Pacific Decadal Oscillation. *J. Oceanogr.* 58, 35–44. doi: 10.1023/A:1015820616384

Peng, J. D., Liao, Y. F., Jiang, Y. H., Zhang, J., and Qi, X. (2017). Development of the homogenized monthly precipitation series during 1910–2014 and its changes in Hunan Province, China. *J. Water Clim. Change.* 8, 791–801. doi: 10.2166/wcc.2017.178

Si, D., and Ding, Y. H. (2016). Oceanic Forcings of the Interdecadal Variability in East Asian Summer Rainfall. *J. Clim.* 29, 7633–7649. doi: 10.1175/JCLI-D-15-0792.1

Smith, T. M., Reynolds, R. W., Peterson, T. C., and Lawrimore, J. (2008). Improvements to NOAA's Historical Merged Land–Ocean Surface Temperature Analysis (1880–2006). *J. Clim.* 21, 2283–2296. doi: 10.1175/2007JCLI2100.1

Sun, C., Kucharski, F., Li, J. P., Jin, F.-F., Kang, I.-S., and Ding, R. (2017). Western tropical Pacific multidecadal variability forced by the Atlantic multidecadal oscillation. *Nat. Commun.* 8, 15998. doi: 10.1038/ncomms15998

Sutton, R. T., and Hodson, D. L. R. (2007). Climate Response to Basin-Scale Warming and Cooling of the North Atlantic Ocean. *J. Clim.* 20, 891–907. doi: 10.1175/JCLI4038.1

Wang, Y. M., Shuang, L. L., and Luo, D. H. (2009). Seasonal response of Asian monsoonal climate to the Atlantic Multi-decadal Oscillation. *J. Geophys. Res* 114, D02112. doi: 10.1029/2008JD010929

Xu, Z. Q., Fan, K., and Wang, H. J. (2015). Decadal variation of summer precipitation over China and associated atmospheric circulation after the late 1990s. *J. Clim.* 28, 4086–4106. doi: 10.1175/JCLI-D-14-00464.1

Ye, D. Z. (1990). *Research progress of drought and flood climate (in Chinese)*. Bei Jing: Meteorological Press.

Zhang, Q. Y., Lu, J. M., and Yang, L. M. (2007). The Interdecadal Variation of Precipitation Pattern over China during Summer and Its Relationship with the Atmospheric Internal Dynamic Processes and Extra-Forcing Factors (in Chinese). *Chin. J. Atmos. Sci.* 31, 1290–1300. doi: 10.3878/j.issn.1006-9895.2007.06.23

Zhang, R., and Delworth, T. L. (2010). Simulated Tropical Response to a Substantial Weakening of the Atlantic Thermohaline Circulation. *J. Clim* 18, 1853–1860. doi: 10.1175/JCLI3460.1

Zhu, Y., Wang, H., Ma, J., Wang, T., and Sun, J. (2015). Contribution of the phase transition of Pacific Decadal Oscillation to the late 1990s' shift in East China summer rainfall. *J. Geophys. Res.: Atmos.* 120, 8817–8827. doi: 10.1002/2015JD023545

Zhu, Y., Wang, H., Zhou, W., and Ma, J. (2011). Recent changes in the summer precipitation pattern in East China and the background circulation. *Clim. Dyn.* 36, 1463–1473. doi: 10.1007/s00382-010-0852-9

Zong, H. F., Chen, L. T., and Zhang, Q. Y. (2010). The Instability of the Interannual Relationship between ENSO and the Summer Rainfall in China (in Chinese). *Chin. J. Atmos. Sci.* 34, 184–192. doi: 10.3878/j.issn.1006-9895.2010.01.17

Conflict of Interest: The authors declare that the research was conducted in the absence of any commercial or financial relationships that could be construed as a potential conflict of interest.

frontiers in Environmental Science

ORIGINAL RESEARCH
published: 09 April 2021
doi: 10.3389/fenvs.2021.655521

Discrepancies of Upper Troposphere Summer Thermal Contrast Between Tibetan Plateau and Tropical Indian Ocean in Multiple Data

Xiaoqing Luo[1,2], *Jianjun Xu*[1,2]* *and Kai Li*[3]

[1] South China Sea Institute of Marine Meteorology, Guangdong Ocean University, Zhanjiang, China, [2] College of Ocean and Meteorology, Guangdong Ocean University, Zhanjiang, China, [3] Maritime College, Guangdong Ocean University, Zhanjiang, China

Under the background of global warming, the summer land-sea thermal contrasts at the upper troposphere exists great discrepancies in radiosonde data (IUK, RICH, and RAOBCORE), reanalysis data (JRA-55, NCEP/DOE, and ERA5) and CMIP6 models results (MPI, FGOALS, and CESM2) for the period of 1979-2014. It can be found that the descriptive statistical indicators (i.e., maximum, minimum, and skewness) of the summer land-sea thermal contrasts index (TTI) between the Tibetan Plateau (TP) and the Tropical Indian Ocean (TIO) vary greatly. The ERA5 and JRA-55 data have the best correlation with radiosonde data. The linear trend and running linear trend (RTL) of the radiosonde data are significantly correlated with the reanalysis data, and both show that the land-sea thermal contrast rapidly increasing are in 1990s and the late 2000s, and the period of rapid weakening was early 2000s. This interannual variation may modulated by the decadal signals such as Pacific Decadal Oscillation (PDO). Except for the NCEP/DOE and IUK, other data show that the most significant warming in the TP-TIO region is at the upper troposphere, and the vertical profiles of the summer temperature trend are quite different in different data, and CMIP6 shows an obvious warm bias in the upper troposphere.

Keywords: summer thermal contrast, Tibetan Plateau, tropical Indian Ocean, upper troposphere, discrepancies

OPEN ACCESS

Edited by:
Qingxiang Li,
Sun Yat-sen University, China

Reviewed by:
Laurent Li,
UMR 8539 Laboratoire de Météorologie Dynamique (LMD), France
Minyan Wang,
China Meteorological Administration, China

***Correspondence:**
Jianjun Xu
gmuxujj@163.com

Specialty section:
This article was submitted to Interdisciplinary Climate Studies, a section of the journal Frontiers in Environmental Science

Received: *19 January 2021*
Accepted: *04 March 2021*
Published: *09 April 2021*

Citation:
Luo X, Xu J and Li K (2021) Discrepancies of Upper Troposphere Summer Thermal Contrast Between Tibetan Plateau and Tropical Indian Ocean in Multiple Data. Front. Environ. Sci. 9:655521. doi: 10.3389/fenvs.2021.655521

INTRODUCTION

The Asian monsoon onset that results from the land–sea thermal contrast between Eurasia and the tropical ocean (Webster et al., 1998) is characterized by changes in the prevailing wind direction and the appearance of severe precipitation (Wu et al., 2013). Several studies have been carried out on the relationship between the meridional land–sea thermal contrast (Li and Yanai, 1996; Sun et al., 2010; Zhang et al., 2017; Luo et al., 2021), or the zonal land–sea thermal contrast (Qian et al., 2004; Qi et al., 2007; Si et al., 2019), and the Asian monsoon. He et al. (2003) revealed that the reversal time of the meridional temperature gradient in upper troposphere is concurrent with (one pentad earlier than) the onset time of the summer monsoon. Dai et al. (2013) showed that the summer thermal structure and winds over Asia produce a larger land–sea thermal gradient in the upper than in the lower troposphere, and identified the greater role of the upper troposphere in driving the Asian summer monsoon circulation.

The South Asian summer monsoon (SASM) is the strongest among the three members of the Asian monsoon system (Wang et al., 2017), and its onset and intensity are regulated by the meridional thermal contrast in the upper troposphere (Dai et al., 2013; Luo et al., 2021). The obvious features during summer in the upper troposphere of the Asian monsoon region are the warm center and the South Asian high located on the southern side of the TP (Boos and Kuang, 2010). The thermal condition of the Tibetan Plateau (TP) and tropical Indian Ocean (TIO) are the two key impact factors and the interactive system to modulate SASM. In summer, the thermal contrast between the TP and TIO reaches the strongest, and the SASM region is accompanied by strong baroclinicity (Luo et al., 2021). A reduced (increased) meridional upper-tropospheric thermal contrast will lead to a weakened (strengthened) SASM circulation in climate models (Sun et al., 2010) and reanalysis data (Luo et al., 2021). The physical explanation is the thermal wind relationship (Holton, 2004).

Since the rapid warming period after the 1970s (IPCC, 2014), the degree of warming has varied greatly in the radiosonde and satellite data for the mid-troposphere (Thorne et al., 2011; Guo et al., 2020a), and there are also many uncertainties in the trend of the upper tropospheric temperature (Seidel et al., 2004). The upper troposphere above the TP and TIO is warming (Zhao et al., 2015; Ming et al., 2019; Shangguan et al., 2019), and there are uncertainties in the interannual variation of the meridional land–sea thermal contrast (Dai et al., 2013; Guo et al., 2017). Due to the strong positive relationship between the summer thermal contrast between TP-TIO with SASM, and the it is necessary to discussed the discrepancies of upper troposphere summer thermal contrast between TP and TIO in multiple data, especially the discrepancies of the trends. This work can provide a foundation for our further research on the relationship between the TP-TIO thermal contrasts and the SASM in interannual and interdecadal scale. The article is organized as follows. In section "Data and Methods," we describe the data and the procedure. We then introduce two SASM indices (SASMIs) and the definition of the meridional land–sea thermal contrast index (TTI). Section "Results" presents the results and section "Summary and Discussion" provides a summary and discussion.

DATA AND METHODS

Data

The data used in this article are listed in **Table 1**, and the details are as follows.

Radiosonde Data

The Iterative Universal Kriging (IUK) radiosonde dataset since 1959 from 527 radiosonde stations was developed by Sherwood et al. (2008) using a statistical model to simultaneously identify artificial shifts and natural atmospheric fluctuations. Haimberger (2007) and Haimberger et al. (2008, 2012) carried out homogeneity adjustments of the Radiosonde Observation Correction using reanalysis (RAOBCORE) and Radiosonde Innovation Composite Homogenization (RICH) for the upper air temperatures from the global radiosonde network. The resulting datasets include the RAOBCORE and RICH data. The former was calculated from the mean of the radiosonde minus the reference time series before and after breakpoints. The latter is based on the breakpoint detection method of RAOBCORE, but it also considers neighbor station time series as a reference (Pattantyús-Ábrahám and Steinbrecht, 2015). The RAOBCORE and RICH 10° × 5° gridded data were averaged over 108 latitude bands, while the IUK is the station data averaged by latitude band without gridding (Free, 2011). According to the area of the TP (75°E –103°E, 28°N–38°N) and TIO (60°E- 100°E, 15°S–5°N), we choose 3 stations (station number: 61967,48657,48698) represent the TIO, and 5 stations (42027,42101,42182,51828,51848) represent the TP, and then defined the thermal contrast for IUK data.

TABLE 1 | Data used in this study.

	Center and location	Data set
Radiosonde	Climate Change Research Centre, University of New South Wales Sydney (Australia)	IUK
	University of Vienna (Austria)	RICH
	University of Vienna (Austria)	RAOBCORE
Reanalyses	Japan Meteorological Agency (Japan)	JRA-55
	National Centers for Environmental Prediction Department of Energy (United States)	NCEP/DOE
	European Centre for Medium Range Weather Forecasts (Europe)	ERA5
CMIP6	Max Planck Institute for Meteorology (Germany)	MPI-ESM1.2 LR_historical
	Chinese Academy of Sciences (China)	FGOALS-f3 L_historical
	National Center for Atmospheric Research (United States)	CESM2_historical

Reanalysis Data

The JRA-55, which is the second Japanese global atmospheric reanalysis based on TL319, is the first comprehensive reanalysis to apply four-dimensional variational analysis up to the present (Kobayashi et al., 2015). The NCEP–Department of Energy (DOE) reanalysis is an updated version of the NCEP–NCAR reanalysis (Kanamitsu et al., 2002). It has good applicability in describing precipitation and temperature (Chen et al., 2014; Harada et al., 2016). ERA5 is the fifth-generation ECMWF (European Centre for Medium-Range Weather Forecasts) global atmospheric reanalysis from 1950 to the present, based on the Integrated Forecasting System (IFS) Cy41r2, which started operation in 2016. Compared with the 80 km horizontal resolution of the ERA Interim reanalysis data, ERA5 has a horizontal resolution of 31 km, which performs better in describing temperature, wind, precipitation, and weather systems (Hersbach et al., 2020). The present study used temperature at 1000–200hPa from 1979 to 2014 for ERA5 (1° ×1°), JRA-55 (1.25° ×1.25°) and NCEP/DOE (2.5° ×2.5°).

Model Data

The Max Planck Institute for Meteorology Earth System Model version 1.2 (MPI-ESM1.2, hereafter MPI) is the update of MPI-ESM1.1 and includes improvements in all its components (Mauritsen et al., 2019). The MPI-ESM1.2 LR is the low-resolution version. The low-resolution version of the Chinese Academy of Sciences (CAS) Flexible Global Ocean–Atmosphere–Land System model finite-volume version 3 (FGOALS-f3-L, hereafter FGOALS) climate system model was developed at the State Key Laboratory of Numerical Modeling for Atmospheric Sciences and Geophysical Fluid Dynamics (LASG) which has six tiles and is irregular in the horizonal direction (He et al., 2019). The Community Earth System Model Version 2 (CESM2) has improved historical simulations compared with CESM1 and available observations (Danabasoglu et al., 2020). In this study, we used the simulated historical temperatures of three models from Phase 6 of the Coupled Model Intercomparison Project (CMIP6). The CMIP6 includes the latest generation of comprehensive Earth Systems, driven by historical greenhouse gas concentrations, and followed by different future greenhouse gas and aerosol concentrations according to the Shared Socioeconomic Pathways (SSP) scenarios (Tokarska et al., 2020). The historical forcings of CMIP6 are based as far as possible on observations and cover the period from 1850 to 2014 (Eyring et al., 2016). The present study used temperatures at 1000–200hPa from the above three historical simulation results of CMIP6 for the period from 1979 to 2014.

Method

Thermal Contrast Index (TTI)

The thermal contrast between the TP and the TIO reaches the maximum in summer (Luo et al., 2021), while the vertical fall in TP-TIO is reached at about 5000 m. Dai et al. (2013) found that the land–sea thermal contrast in the mid-upper troposphere contributes about three times more than the thermal contrast in the mid-lower troposphere in determining the Asian summer monsoon circulation. Therefore, this study applies the thermal contrast index (TTI), which is the meridional gradient of the 400-200 hPa average summer temperature in the TP-TIO region [formula (1)] to represents the summer thermal contrast between land and sea. The larger (smaller) the positive TTI, the stronger (weaker) the meridional thermal contrast in the upper troposphere. In formula (1), T represents the area-averaged of monthly temperature anomaly in summer at 400–200hPa.

$$\mathrm{TTI} = T_{\mathrm{TP}(75^\circ\mathrm{E}-103^\circ\mathrm{E},\ 28^\circ\mathrm{N}-38^\circ\mathrm{N})} - T_{\mathrm{TIO}(60^\circ\mathrm{E}-100^\circ\mathrm{E},\ 15^\circ\mathrm{S}-5^\circ\mathrm{N})} \quad (1)$$

South Asian Summer Monsoon Indices (SASMIs)

There are several SASMIs to describe the different features of the monsoon (Webster and Yang, 1992; Wang and Fan, 1999; Li and Zeng, 2002, 2003). This study used two SASMIs, one of which is the Webster and Yang (1992) index, here named MI-2, and the other is MI-1. The atmospheric kinetic energy of the vertical mean flow and the shear flow can be referred to as the barotropic and baroclinic component, respectively. MI-1 is based on the atmospheric baroclinic component over the region (0°–20°N, 60°–100°E) due to the strong baroclinicity in the SASM region (Xu and Chan, 2002). For the specific definition of MI-1, please refer to our previous publication (Luo et al., 2021). MI-2 is defined by the zonal wind difference between 850 and 200 hPa over the region (0°–20°N, 40°–110°E), which can reflect the variability of the broad-scale SASM (Wang and Fan, 1999). MI-1 and MI-2 have a significant positive correlation (Luo et al., 2021).

Trend Calculation

The trend is computed using linear least squares fitting (Wei, 2007) and running linear least square fitting (Zhao et al., 2013). The running linear least square fitting is used to estimate the thermal contrast trends with a moving 10-year temporal window that can describe the variations of the trend with time. The t-statistic is used to test for a significant linear regression relationship and correlation coefficient relationship (Wei, 2007). The significance level is set to be 0.05.

In addition, because RAOBCORE and RICH are anomaly monthly data based on 1981-2010, in order to maintain consistency, the rest data in our study also used this basis to calculate anomalies.

RESULTS

There are great differences in the different data describing the basic characteristics of the thermal contrasts (**Figure 1** and **Table 2**). The maximum TTI varied from 0.94°C (JRA-55) to 1.59°C (FGOALS), and the minimum TTI changed from –2.87°C (IUK) to –1.08°C (CESM2). The IUK data were relatively scattered (range value = 4.3°C) and had the largest standard deviation (σ = 1.02), while the ERA5 was the most concentrated (range value = 2.28°C) with the smallest standard deviation (σ = 0.49). The reason for this is that the IUK data consist of 460 radiosonde stations (Sherwood et al., 2008), while the RAOBCORE and RICH are assimilated from more than 1000 daily radiosonde stations (Haimberger et al., 2008). The ERA5 provides a detailed record of the global atmosphere, land surface and ocean waves from 1950 onward with a horizontal resolution of up to 0.28° (Hersbach et al., 2020). It also assimilates the RAOBCORE and RICH. In addition, NCEP/DOE in the reanalysis data and the FGOALS in the models are also relatively scattered. According to the skewness coefficient, the results are left-biased, except for NCEP/DOE, CESM2, and MPI. The models and NCEP/DOE have insufficient kurtosis distribution, whereas the others have excessive kurtosis distribution.

The reanalysis data have significant correlation with the radiosonde data, and the results of JRA-55 and ERA5 are the most significant. This indicates that reanalysis data, especially ERA5 and JRA-55, can reproduce the summer land–sea thermal contrasts in the upper troposphere of the TP-TIO region. Because the model simulation were not designed to match the temporal evolution of observed climate, or the raw climate variables at interannual or decadal time scale, our research wasn't analyze

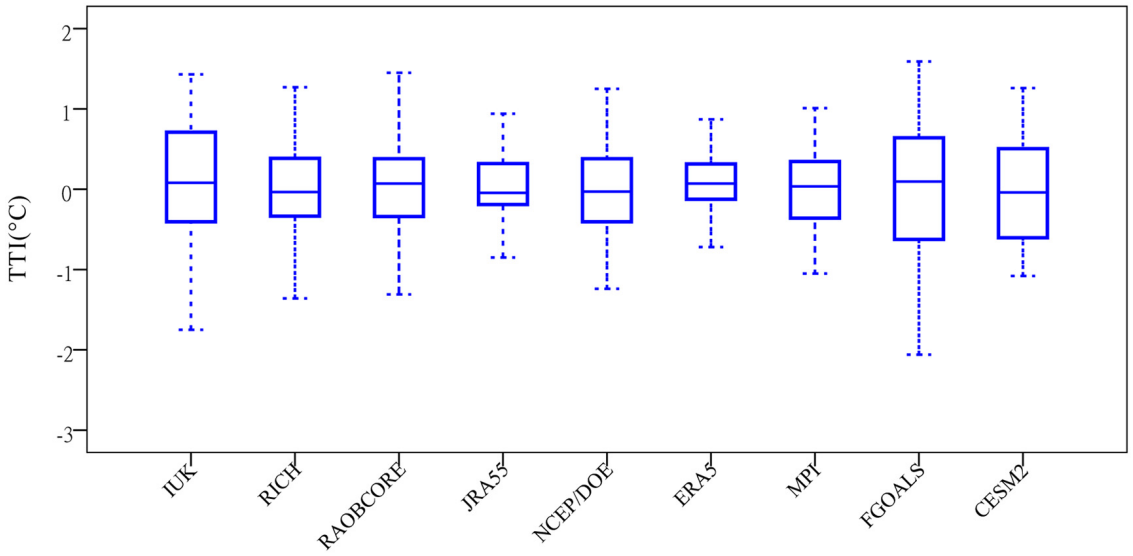

FIGURE 1 | Boxplot of the summer land–sea thermal contrasts (TTI) (°C).

the correlation between the simulation results and other data. The standard deviation of IUK is the largest, and the standard deviation of RICH and RAOBCORE is relatively small (**Table 3**), resulting in the ratios of the standard deviation in **Figure 2** are different from each other. In addition, the standard deviation of the reanalyses are smaller than the value of the radiosonde data.

The maximum and minimum values of the TTI are inconsistent with their corresponding years (**Figure 3**), but the interannual fluctuations of summer land–sea thermal contrast in the reanalysis and radiosonde data are more consistent (**Figures 3A,B**). The TTI is relatively strong in 1981, 2000, and 2013 and weak in 1983, 1987, 1992, and 2011. Radiosonde data show an obvious increasing trend of summer thermal contrast (0.4 °C/dec), the reanalysis data have a slight increasing trend (0.1°C/dec), and models show no clear trend. The increasing trends of IUK, RICH, and RAOBCORE are 0.62°C/dec, 0.15°C/dec and 0.28°C/dec, respectively (**Figure 4B**), and the trends of JRA-55 (0.13°C/dec) and ERA5 (0.08°C/dec) are positive, while the NCEP/DOE (−0.07°C/dec) is negative. There is also a decreasing trend in the 1980s and an increasing trend in the 2000s in the reanalysis data. ERA5 shows improved quality compared with ERA-Interim and performs the best agreement with the Global Positioning System radio occultation (GPS RO) data for the 2002-2017 trends of upper troposphere and lower stratosphere (0.2–0.3°C/dec) (Shangguan et al., 2019). In our research we found that the ERAI trends are all stronger than the ERA. The upper troposphere in TP and TIO have warming trends in ERA5 and ERA-I, and the trend of the land-sea thermal contrasts of TTI are 0.08°C/dec and 0.15°C/dec, respectively (Figure omitted). After 1999, the warming bias of ERAI was obvious until 2006 due to the variation of data assimilation (Simmons et al., 2014).

All data show a warming trend in the summer temperature of the upper troposphere in the TP (**Figure 4A**), and in the TIO, except for the IUK data (**Figures 4A,C**). The warming of the summer temperature over the TP and the TIO has been noted in many previous studies (Zhao et al., 2015; Ming et al., 2019). Comparing the trend of the TP and TIO for radiosonde data, the thermal contrast is dominated by the TP heating. Under the background of global warming, the tropospheric temperature of the TP in summer increases faster than the TIO, which leads to the increasing land–sea thermal contrast. However, the simulation results of CESM2 and FGOALS show that the increasing temperature trend of the TIO was stronger than that of the TP, which led to the weakening of the thermal contrast.

TABLE 2 | The statistics of the summer thermal contrasts (TTI) for the different data.

		Min (°C)	Max (°C)	Range value(°C)	Std	Skewness	Kurtosis
Radiosondes	IUK	−2.87	1.43	4.30	1.02	−0.87	1.02
	RICH	−1.69	1.27	2.96	0.64	−0.59	0.71
	RAOBCORE	−1.83	1.45	3.28	0.67	−0.60	1.10
Reanalyses	JRA-55	−1.37	0.94	2.31	0.51	−0.47	0.60
	NCEP/DOE	−1.24	1.25	2.49	0.60	0.09	−0.11
	ERA5	−1.30	0.98	2.28	0.49	−0.54	1.00
CMIP6	MPI	−1.05	1.01	2.06	0.53	0.012	−0.47
	FGOALS	−2.06	1.59	3.65	0.87	−0.49	−0.04
	CESM2	−1.08	1.26	2.34	0.67	0.17	−0.96

TABLE 3 | Correlation coefficients of TTI between radiosonde and the reanalysis data (bold indicates a correlation coefficient above 0.32, representing the significance test at the 95% confidence level).

		IUK	RICH	RAOBCORE
Reanalyses	JRA-55	**0.641**	**0.875**	**0.882**
	NCEP/DOE	**0.341**	**0.773**	**0.699**
	ERA5	**0.628**	**0.888**	**0.876**

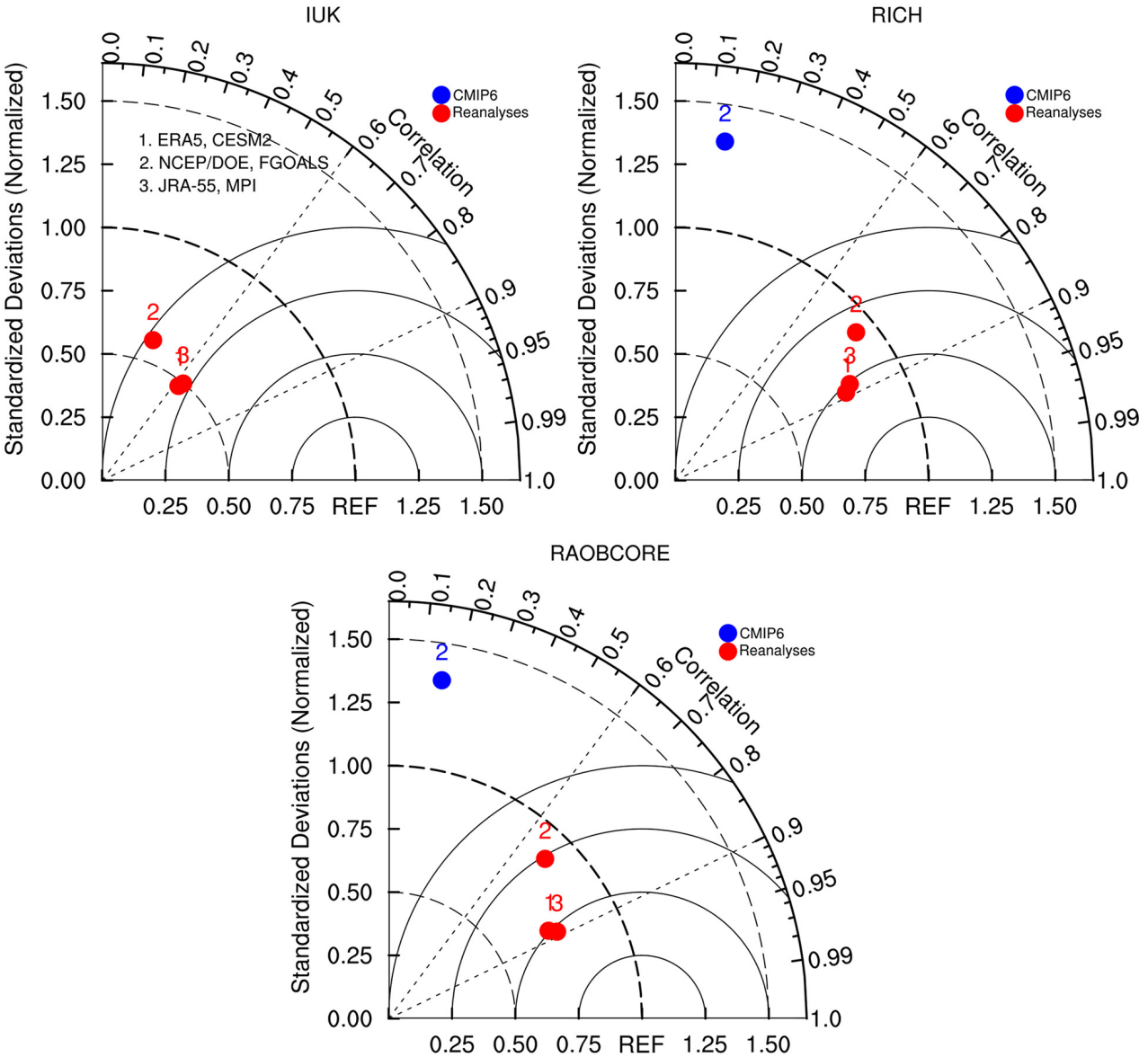

FIGURE 2 | Taylor plot of the reanalysis data and model results with radiosonde data.

The running linear trends (RLTs) of the thermal contrast of TTI show a similar fluctuation, especially after 1995, for reanalysis and radiosonde data (**Figures 5A,B**). Furthermore, the correlations of the RLTs all passed the significance test (**Table 4**), which further illustrates the similarity between the reanalysis and the radiosonde data in describing the land–sea thermal contrast. **Figure 5** shows that the RLTs are positive, negative, and positive from approximately 1995–1999, 2003–2005, and 2006–2010, respectively, indicating that the land–sea thermal contrasts between the TP and the TIO increased in the 1990s and the late 2000s, and weakened in the early 2000s. The most rapid period of land–sea thermal contrast strengthening occurred in the 1990s. This is because the maximum of the RLT was in 1997, which indicates that from 1992 to 2001, especially from 1997 to 2000, the summer TP-TIO thermal contrast increased rapidly. The model results are very different from the reanalysis and radiosonde data (**Figure 5**), including the RLT after the 2000s.

The land-sea thermal contrast is significantly positive correlation with SASM, and the interannual variations of the SASM indices (MI-1 and MI-2) and the land-sea thermal contrast index (TTI) are basically the same (Figure omitted). The RLTs of TTI is also consistent with the change of the SASMI (**Figure 6**). The RLTs calculated by the JRA-55, ERA5, IUK, and RAOBCORE have a strong positive correlation with MI-1 and MI-2, indicating that when the summer land–sea thermal contrast increased rapidly, the intensity of the SASM and the atmospheric baroclinic component also increased rapidly in the monsoon region, and vice versa. For example, from 1997 to 2000, the thermal contrasts

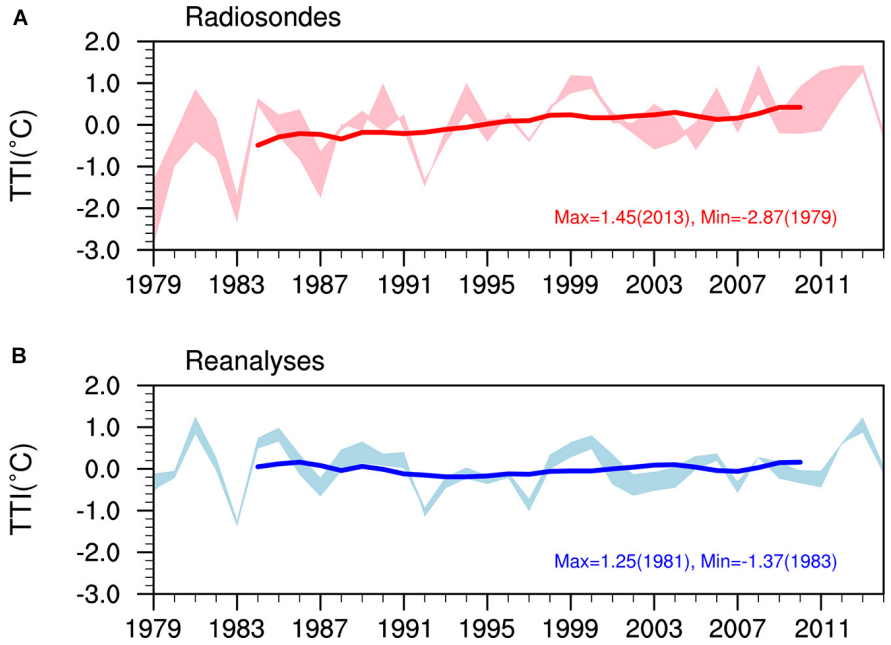

FIGURE 3 | The interannual variations of the thermal contrasts TTI in Radiosondes **(A)** and Reanalyses **(B)** (solid lines represent 10-year running averaged of three datasets in each panel, and the shading represents the ensemble of the three datasets).

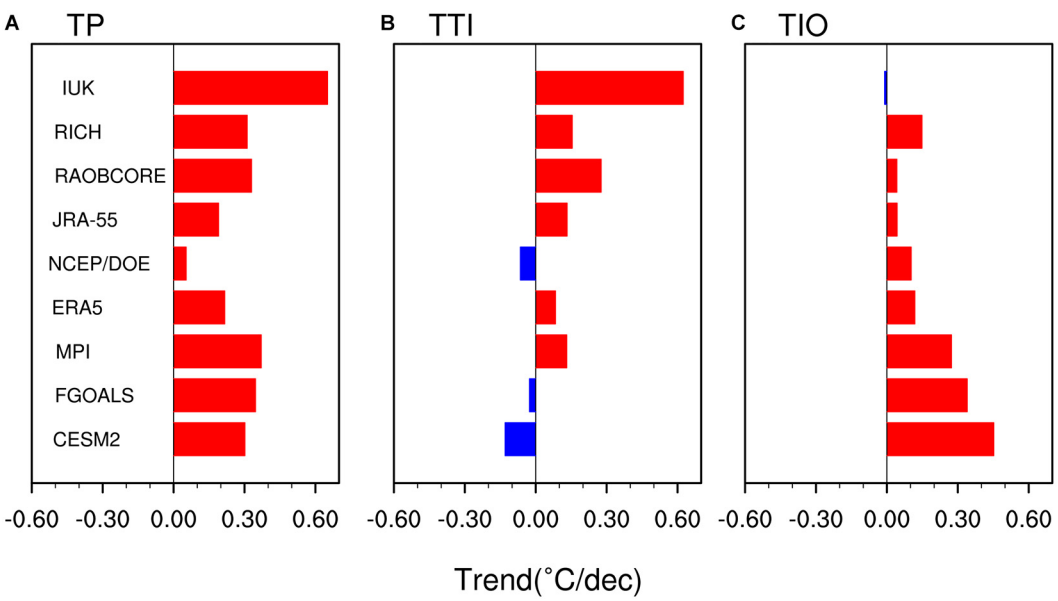

FIGURE 4 | The trends for the **(B)** TTI and **(A,C)** the summer temperature at 400–200 hPa in the troposphere for TP and TIO, respectively (°C/dec).

in the TP-TIO region increased rapidly, accompanied by a rapid increasing intensity of the SASM. This was the time period when the El Niño–Southern Oscillation (ENSO) event changed from the strong warm phase to the strong cold phase. **Figure 6** shows that the TTI weakened rapidly in the early 2000s (at about 2002–2006), and increased rapidly in the late 2000s (after 2007) with the rapid weakening and strengthening of the SASM. This is due to the fact that the RLTs of upper troposphere summer temperature in the TIO is greater than that in the TP in early 2000s, and smaller in the late 2000s (Figure omitted). We speculate that this interannual transition is likely to be related to the Pacific Decadal Oscillation (PDO). In the first period, the summer PDO index is a small positive value, while in the second period, the PDO index is a larger negative value. During positive PDO phases, the transport of moisture from the Bay of Bengal and the South China Sea to Eurasia is inhibited (Lyu, 2019), and Indian

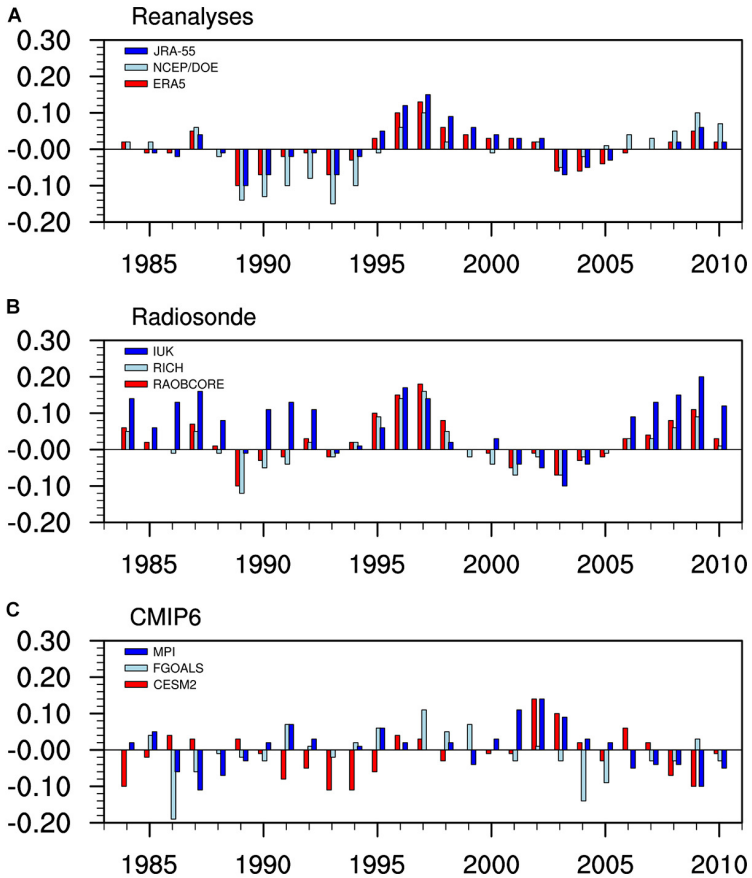

FIGURE 5 | The RLTs of TTI (°C/dec) in Reanalyses **(A)**, Radiosonde **(B)**, and CMIP6 **(C)**.

TABLE 4 | Correlation of the RLTs of TTI between reanalysis data and radiosonde data the SASMIs (bold indicate a correlation coefficient above 0.37, representing a significance test at the 95% confidence level).

		IUK	RICH	RAOBCORE	JRA-55	NCEP/DOE	ERA5	MI-1	MI-2
Radiosondes Reanalyses SASMI	IUK	1	**0.640**	**0.682**	**0.400**	**0.440**	**0.473**	**0.687**	**0.682**
	RICH		1	**0.986**	**0.776**	**0.668**	**0.776**	**0.376**	0.240
	RAOBCORE			1	**0.828**	**0.685**	**0.833**	**0.494**	0.367
	JRA-55				1	**0.748**	**0.984**	**0.532**	**0.454**
	NCEP/DOE					1	**0.783**	0.289	0.199
	ERA5						1	**0.578**	**0.512**
	MI-1							1	**0.958**
	MI-2								1

rainfall decrease with weaker SASM (Krishnan and Sugi, 2003), which accompanied by the weak thermal contrast in the TP-TIO (Luo et al., 2021). During positive PDO phases, the situation is almost opposite.

The vertical profiles of the summer temperature trend are quite different in the TP-TIO region (**Figure 7**). Radiosonde data, reanalysis data (except NCEP/DOE and IUK) and the model results all show that the temperature in the upper troposphere are increasing significantly in the TP-TIO region. In climate models, with increasing greenhouse gas concentrations, the surface and troposphere are consistently projected to warm, with an enhancement of that warming in the tropical upper troposphere (Thorne et al., 2011). Allen and Sherwood (2008) analyzed thermal winds and suggested a warming maximum in the tropical upper troposphere. The TP has a stronger warming trend in the upper troposphere than the TIO area for the radiosonde and reanalysis data (except for NCEP/DOE), while the model results generally display a significant warming, which is consistent with **Figure 4C**. The clear warm bias in CMIP6 in the troposphere has received a lot of attention (Li et al., 2020; McKitrick and Christy, 2020; Mitchell et al., 2020). **Figure 7** also shows a warm bias in the upper troposphere. In

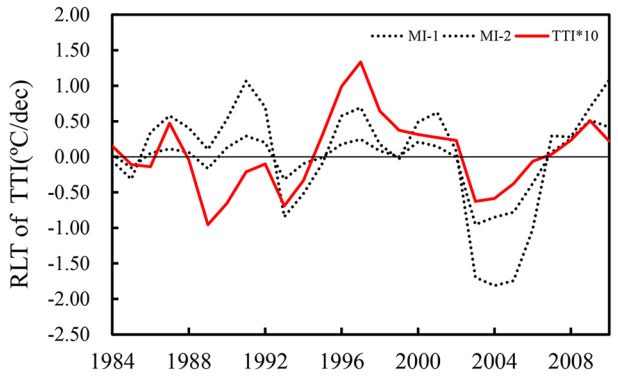

FIGURE 6 | The RLTs of the (TTI, °C/dec) and SAMIs (MI1-1, MI-2) based on ERA5.

the troposphere, the observed warming trends are located in the upper troposphere, which are correctly captured by FGOALS (Guo et al., 2020b). The CMIP6 historical simulations aim to evaluate the ability of models to reproduce the climate on various time scales (Guo et al., 2020b), and serve as important tools to determine consistency of climate model forcing and sensitivity with the observational record (Eyring et al., 2016; Srivastava et al., 2020). However, observational data are scarce in the upper troposphere, and the satellite data (Mears and Wentz, 2009) is inconsistent with the altitude selected in our research. In the absence of numerical simulation experiments, it is necessary to use the CMIP6 historical simulations for research. Of course, there are also some studies that have used models simulations to study interannual issues (Zhao et al., 2013, 2015). Therefore, we still use CMIP6 historical simulations for interannual scale analysis in this study.

SUMMARY AND DISCUSSION

With the accelerated global warming over the past 100 years (Xu et al., 2018), research of the land–sea thermal contrast has received much more attention (Li and Yanai, 1996; Sun et al., 2010; Dai et al., 2013). The present study used a summer meridional land–sea thermal contrast index (TTI) to study the discrepancies in nine datasets in the summer thermal contrasts of the TP-TIO region for the upper troposphere. We also analyzed the relationship between the interannual variations of TTI with the two SASMIs. The results are as follows.

(1) There are great differences in the reanalysis data (JRA-55, NCEP/DOE, ERA5), radiosonde data (IUK, RICH, and RAOBCORE) and CMIP6 model results (MPI, FGOALS, CESM2) describing the basic characteristics (e.g., maximum, minimum, and standard deviation) of the thermal contrasts in the TP-TIO region. The maximum and minimum of the TTI varied from one dataset to another. The IUK data were relatively scattered, while the ERA5 were the most concentrated. The IUK results were significantly different from RAOBCORE and RICH due to the different homogenization methods applied. The reanalysis data were significantly correlated with the radiosonde data, with JRA-55 and ERA5 data the most significant.

(2) The radiosonde data showed a clear increasing trend in the summer thermal contrast, and the reanalysis data had a slight increasing trend, whereas the models showed no obvious trend. The TP-TIO region showed a warming trend in the upper troposphere in most of the data. The intensity of the thermal contrast was dominated by the TP heating in the radiosonde data, while CESM2 and FGOALS showed that the increasing temperature trend of the TIO was stronger than that of the TP, which led to the weakening of the thermal contrast.

(3) The RLTs of TTI shows a similar fluctuation, especially after 1995 for reanalysis and radiosonde data. In the 1990s and the late 2000s, the land–sea thermal contrasts increased, while they weakened in the early 2000s. This interannual variation may modulated by the decadal signals such as Pacific Decadal Oscillation (PDO). The most rapid strengthening period in the land–sea thermal contrast occurred in the 1990s.

(4) For the reanalysis and radiosonde data, the TTI was significantly positively correlated with the intensity of the SASM, as well as the RLTs. This suggests that if the meridional thermal contrast between the TP and the TIO increases rapidly, the intensity of the SASM also increases abruptly. The vertical profiles of the summer temperature trend are quite different in the TP-TIO region, and CMIP6 shows a warm bias in the upper troposphere

There is a strong correlation between the intensity of the SASM and the meridional land–sea thermal contrasts in the TP-TIO region, while the value of the TTI varies greatly between different datasets. The reanalysis and radiosonde data are inconsistent in describing the interannual variations of the TTI. The radiosonde observations have been used to create long-term global upper-air temperature datasets, which figure prominently in studies of large-scale climate variability and change (Seidel et al., 2004). However, the radiosonde stations are sparse, especially over the oceans of the southern hemisphere (Thorne et al., 2011), resulting in the deviations in the TTI calculations. Many studies have therefore used a variety of tools to detect and adjust the non-climatic artifacts in the radiosonde data (Allen and Sherwood, 2008; Zhou et al., 2020). The possible reason for the large differences in the results of the CMIP model simulation and reanalysis is that the climate models have a strong warm bias in the upper troposphere (Zhao et al., 2016). The overestimation of both the climate feedbacks and the aerosol forcing can result in a historical warming to the present day that is similar to the observations, but has a poor temporal agreement with the observations. Another key point is that the relative contribution of the TP and TIO to the land–sea thermal contrasts is not clear and, like in the present study, the contribution of the TP or the TIO to the TTI changes with the data. In future work, we plan to collect multiple data (Guo et al., 2020a) to solve this problem.

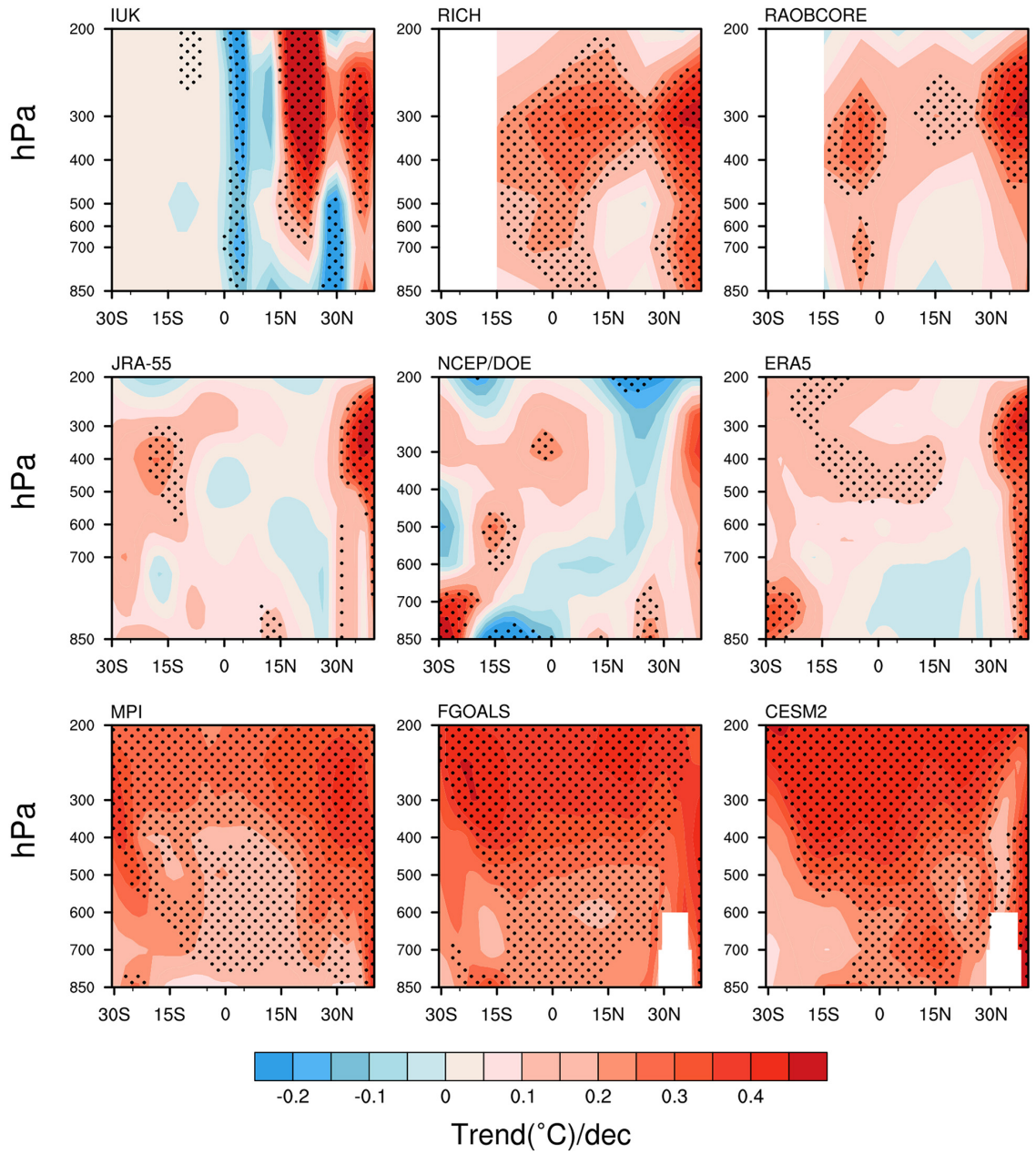

FIGURE 7 | The vertical profile of the summer temperature trend at 80°E–100°E (°C/dec).

DATA AVAILABILITY STATEMENT

The original contributions presented in the study are included in the article/supplementary material, further inquiries can be directed to the corresponding author.

AUTHOR CONTRIBUTIONS

JX proposed an idea and revised the article. XL was responsible for data processing and manuscript writing. KL was responsible for manuscript writing and format checking. All authors contributed to the article and approved the submitted version.

FUNDING

This research was supported by the Second Tibetan Plateau Scientific Expedition and Research (STEP) program (No. 2019QZKK0105), the Strategic Priority Research Program of Chinese Academy of Sciences (No. XDA20060501), and the 2019 Non-funded Science and Technology Research Project

of Zhanjiang (No. 20051817454-6338). The data providers are University of Vienna, Climate Change Research Centre, University of New South Wales Sydney, European Centre for Medium Range Weather Forecasts, Japan Meteorological Agency, National Centers for Environmental Prediction Department of Energy, National Center for Atmospheric Research, Chinese Academy of Sciences, and Max Planck Institute for Meteorology.

REFERENCES

Webster, P. J., Magana, V. O., Palmer, T. N., Shukla, J., Tomas, R. A., Yanai, M. U., et al. (1998). Monsoons: Processes, predictability, and the prospects for prediction. *Journal of Geophysical Research: Oceans* 1031, 14451–14510. doi: 10.1029/97jc02719

Wu, G. X., Duan, A. M., Liu, Y. M., Yan, J., Liu, B., Ren, S., et al. (2013). Recent advances in the study on the dynamics of the Asian summer monsoon onset. *Chinese Journal of Atmospheric Sciences* 37, 211–228. (in Chinese),

Li, C., and Yanai, M. (1996). The onset and interannual variability of the Asian summer monsoon in relation to land–sea thermal contrast[J]. *Journal of Climate* 9, 358–375. doi: 10.1175/1520-0442(1996)009<0358:toaivo>2.0.co;2

Sun, Y., Ding, Y., and Dai, A. (2010). Changing links between South Asian summer monsoon circulation and tropospheric land−sea thermal contrasts under a warming scenario[J]. *Geophy. Res. Lett.* 37, L02704.

Zhang, Y., Fan, G., Hua, W., Zhang, Y., Wang, B., and Lai, X. (2017). Differences in atmospheric heat source between the Tibetan Plateau–South Asia region and the southern Indian Ocean and their impacts on the Indian summer monsoon outbreak[J]. *Journal of Meteorological Research* 31, 540–554. doi: 10.1007/s13351-017-6042-5

Luo, X. Q., Xu, J. J., Zhang, Y., and Li, K. (2021). Relationship between the Tibetan Plateau–Tropical Indian Ocean Thermal Contrast and the South Asian Summer Monsoon[J]. *Frontiers of Earth Science* doi: 10.1007/s11707-020-0846-9 *Q,

Qian, Y. F., Jiang, J., Zhang, Y., Yao, Y. H., and Xu, Z. F. (2004). The earliest onset area of the tropical Asian summer monsoon and its mechanisms[J]. *Acta Meteorologica Sinica* 42, 129–139. (in Chinese),

Qi, L., He, J. H., Zhang, Z. Q., and Song, J. N. (2007). Seasonal transition of zonal land-sea thermal contrast and East Asian subtropical monsoon circulation [J]. *Chinese Science Bulletin* 52, 2895–2899. Chinese,

Si, D., Zhao, P., and Wang, M. (2019). Inter−decadal change of the middle−upper tropospheric land–sea thermal contrast in the late 1990s and the associated Northern Hemisphere hydroclimate[J]. *International Journal of Climatology* 39, 3271–3281. doi: 10.1002/joc.6017

He, H., Sui, C. H., Jian, M., Wen, Z., and Lan, G. (2003). The evolution of tropospheric temperature field and its relationship with the onset of Asian summer monsoon[J]. *Journal of the Meteorological Society of Japan. Ser. II* 81, 1201–1223. doi: 10.2151/jmsj.81.1201

Dai, A., Li, H., Sun, Y., Hong, L. C., Chou, C., and Zhou, T. (2013). The relative roles of upper and lower tropospheric thermal contrasts and tropical influences in driving Asian summer monsoons[J]. *Journal of Geophysical Research: Atmospheres* 118, 7024–7045. doi: 10.1002/jgrd.50565

Wang, P. X., Wang, B., Cheng, H., Fasullo, J., Guo, Z., Kiefer, T., et al. (2017). The global monsoon across time scales: Mechanisms and outstanding issues. *Earth-Science Reviews* 174, 84–121. doi: 10.1016/j.earscirev.2017.07.006

Boos, W. R., and Kuang, Z. (2010). Dominant control of the South Asian monsoon by orographic insulation versus plateau heating[J]. *Nature* 463, 218–222. doi: 10.1038/nature08707

Holton, J. R. (2004). in *An Introduction to Dynamic Meteorology: International Geophysics Series*, 4th Edn, Vol. 88, eds R. Dmowska, J. R. Holton, and H. T. Rossby (Cambridge, MA: Elsevier Academic press), 535.

IPCC (2014). "Climate Change 2014: Synthesis Report," in *Contribution of Working Groups I, II and III to the Fifth Assessment Report of the Intergovernmental Panel on Climate Change*, eds Core Writing Team, R. K. Pachauri, and L. A. Meyer (Geneva: IPCC), 151.

Thorne, P. W., Lanzante, J. R., Peterson, T. C., Seidel, D. J., and Shine, K. P. (2011). Tropospheric temperature trends: History of an ongoing controversy[J]. *Wiley Interdisciplinary Reviews: Climate Change* 2, 66–88. doi: 10.1002/wcc.80

Guo, Y., Weng, F., Wang, G., and Xu, W. (2020a). The Long-Term Trend of Upper-Air Temperature in China Derived from Microwave Sounding Data and Its Comparison with Radiosonde Observations[J]. *Journal of Climate* 33, 7875–7895. doi: 10.1175/jcli-d-19-0742.1

Seidel, D. J., Angell, J. K., Christy, J., Free, M., Klein, S. A., Lanzante, J. R., et al. (2004). Uncertainty in signals of large-scale climate variations in radiosonde and satellite upper-air temperature datasets[J]. *Journal of Climate* 17, 2225–2240. doi: 10.1175/1520-0442(2004)017<2225:uisolc>2.0.co;2

Ming, S. H., Qin, Z. K., and Huang, Y. (2019). Satellite data reveals the trend of the upper troposphere temperature over the Tibetan Plateau[J]. *Plateau Meteorology* 38, 264–277.

Zhao, L., Xu, J., Powell, A. M., and Jiang, Z. (2015). Uncertainties of the global-to-regional temperature and precipitation simulations in CMIP5 models for past and future 100 years[J]. *Theoretical and applied climatology* 122, 259–270. doi: 10.1007/s00704-014-1293-x

Shangguan, M., Wang, W., and Jin, S. (2019). Variability of temperature and ozone in the upper troposphere and lower stratosphere from multi-satellite observations and reanalysis data[J]. *Atmospheric Chemistry and Physics* 19, 6659–6679. doi: 10.5194/acp-19-6659-2019

Guo, P. W., Shen, C., Dong, L. N., Zhang, P. Q., and Yin, Y. W. (2017). The observation analysis and simulation valuations of land-sea thermal contrast over Asian monsoon region[J]. *Trans Atmos Sci* 40, 215–223. (in Chinese),

Sherwood, S. C., Meyer, C. L., Allen, R. J., and Titchner, H. A. (2008). Robust tropospheric warming revealed by iteratively homogenized radiosonde data[J]. *Journal of Climate* 21, 5336–5352. doi: 10.1175/2008jcli2320.1

Haimberger, L. (2007). Homogenization of radiosonde temperature time series using innovation statistics[J]. *Journal of Climate* 20, 1377–1403. doi: 10.1175/jcli4050.1

Haimberger, L., Tavolato, C., and Sperka, S. (2008). Toward elimination of the warm bias in historic radiosonde temperature records—Some new results from a comprehensive intercomparison of upper-air data[J]. *Journal of Climate* 21, 4587–4606. doi: 10.1175/2008jcli1929.1

Haimberger, L., Tavolato, C., and Sperka, S. (2012). Homogenization of the global radiosonde temperature dataset through combined comparison with reanalysis background series and neighboring stations[J]. *Journal of Climate* 25, 8108–8131. doi: 10.1175/jcli-d-11-00668.1

Pattantyús-Ábrahám, M., and Steinbrecht, W. (2015). Temperature trends over Germany from homogenized radiosonde data[J]. *Journal of Climate* 28, 5699–5715. doi: 10.1175/jcli-d-14-00814.1

Free, M. (2011). The seasonal structure of temperature trends in the tropical lower stratosphere[J]. *Journal of climate* 24, 859–866. doi: 10.1175/2010jcli3841.1

Kobayashi, S., Ota, Y., Harada, Y., Ebita, A., Moriya, M., Onoda, H., et al. (2015). The JRA-55 reanalysis: General specifications and basic characteristics[J]. *Journal of the Meteorological Society of Japan. Ser. II* 93, 5–48. doi: 10.2151/jmsj.2015-001

Kanamitsu, M., Ebisuzaki, W., Woollen, J., Yang, S. K., Hnilo, J. J., Fiorino, M., et al. (2002). Ncep–doe amip-ii reanalysis (r-2)[J]. *Bulletin of the American Meteorological Society* 83, 1631–1644. doi: 10.1175/bams-83-11-1631(2002)083<1631:nar>2.3.co;2

Chen, G., Iwasaki, T., Qin, H., and Sha, W. (2014). Evaluation of the warm-season diurnal variability over East Asia in recent reanalyses JRA-55, ERA-Interim, NCEP CFSR, and NASA MERRA[J]. *Journal of climate* 27, 5517–5537. doi: 10.1175/jcli-d-14-00005.1

Harada, Y., Kamahori, H., Kobayashi, C., Endo, H., Kobayashi, S., Ota, Y., et al. (2016). The JRA-55 Reanalysis: Representation of atmospheric circulation and climate variability[J]. *Journal of the Meteorological Society of Japan. Ser. II* 94, 269–302. doi: 10.2151/jmsj.2016-015

Hersbach, H., Bell, B., Berrisford, P., Hirahara, S., Horányi, A., Muñoz-Sabater, J., et al. (2020). The ERA5 global reanalysis[J]. *Quarterly Journal of the Royal Meteorological Society* 146, 1999–2049.

Mauritsen, T., Bader, J., Becker, T., Behrens, J., Bittner, M., Brokopf, R., et al. (2019). Developments in the MPI−M Earth System Model version 1.2 (MPI−ESM1. 2) and its response to increasing CO_2[J]. *Journal of Advances in Modeling Earth Systems* 11, 998–1038.

He, B., Bao, Q., Wang, X., Zhou, L., Wu, X., Liu, Y., et al. (2019). CAS FGOALS-f3-L model datasets for CMIP6 historical atmospheric model Intercomparison

project simulation[J]. *Advances in Atmospheric Sciences* 36, 771–778. doi: 10.1007/s00376-019-9027-8

Danabasoglu, G., Lamarque, J. F., Bacmeister, J., Bailey, D. A., DuVivier, A. K., Edwards, J., et al. (2020). The Community Earth System Model version 2 (CESM2)[J]. *Journal of Advances in Modeling Earth Systems* 12, e2019MS001916.

Tokarska, K. B., Stolpe, M. B., Sippel, S., Fischer, E. M., Smith, C. J., Lehner, F., et al. (2020). Past warming trend constrains future warming in CMIP6 models[J]. *Science advances* 6, eaaz9549. doi: 10.1126/sciadv.aaz9549

Eyring, V., Bony, S., Meehl, G. A., Senior, C. A., Stevens, B., Stouffer, R. J., et al. (2016). Overview of the Coupled Model Intercomparison Project Phase 6 (CMIP6) experimental design and organization[J]. *Geoscientific Model Development* 9, 1937–1958. doi: 10.5194/gmd-9-1937-2016

Wang, B., and Fan, Z. (1999). Choice of South Asian summer monsoon indices[J]. *Bulletin of the American Meteorological Society* 80, 629–638. doi: 10.1175/1520-0477(1999)080<0629:cosasm>2.0.co;2

Li, J., and Zeng, Q. (2002). A unified monsoon index[J]. *Geophysical Research Letters* 29, 1151–1154.

Webster, P. J., and Yang, S. (1992). Monsoon and Enso: Selectively Interactive Systems. *Quarterly Journal of the Royal Meteorological Society* 118, 877–926. doi: 10.1002/qj.49711850705

Li, J. P., and Zeng, Q. C. (2003). A new monsoon index and the geographical distribution of the global monsoons[J]. *Advances in Atmospheric Sciences* 20, 299–302. doi: 10.1007/s00376-003-0016-5

Xu, J. J., and Chan, J. C. L. (2002). Relationship between the planetary−scale circulation over East Asia and the intensity of the South Asian Summer Monsoon. *Geophysical Research Letters* 29, 1866.

Wei, F. Y. (2007). *Zhenduan Yu Yuce Jishu[M]*. Beijing: Meteorological Press. *.

Zhao, L., Xu, J., and Powell, A. M. Jr. (2013). Discrepancies of surface temperature trends in the CMIP5 simulations and observations on the global and regional scales[J]. *Climate of the Past Discussions* 9, 6161–6178.

Simmons, A. J., Poli, P., Dee, D. P., Berrisford, P., Hersbach, H., Kobayashi, S., et al. (2014). Estimating low-frequency variability and trends in atmospheric temperature using ERA-Interim[J]. *Quarterly Journal of the Royal Meteorological Society* 140, 2014.

Lyu, L. (2019). Tree rings reveal hydroclimatic fingerprints of the Pacific Decadal Oscillation on the Tibetan Plateau[J]. *Climate Dynamics* 53, 1023–1037. doi: 10.1007/s00382-019-04629-z

Krishnan, R., and Sugi, M. (2003). Pacific decadal oscillation and variability of the Indian summer monsoon rainfall[J]. *Climate Dynamics* 21, 233–242. doi: 10.1007/s00382-003-0330-8

Allen, R. J., and Sherwood, S. C. (2008). Warming maximum in the tropical upper troposphere deduced from thermal winds[J]. *Nature Geoscience* 1, 399–403. doi: 10.1038/ngeo208

McKitrick, R., and Christy, J. (2020). Pervasive Warming Bias in CMIP6 Tropospheric Layers[J]. *Earth and Space Science* 7, e2020EA001281.

Mitchell, D. M., Lo, Y. T. E., Seviour, W. J. M., Haimberger, L., and Polvani, L. M. (2020). The vertical profile of recent tropical temperature trends: Persistent model biases in the context of internal variability[J]. *Environmental Research Letters* 15, 1040b4. doi: 10.1088/1748-9326/ab9af7

Li, J. L. F., Xu, K. M., Jiang, J. H., Lee, W. L., Wang, L. C., Yu, J. Y., et al. (2020). An Overview of CMIP5 and CMIP6 Simulated Cloud Ice, Radiation Fields, Surface Wind Stress, Sea Surface Temperatures, and Precipitation Over Tropical and Subtropical Oceans[J]. *Journal of Geophysical Research: Atmospheres* 125, e2020JD032848.

Guo, Y., Yu, Y., Lin, P., Liu, H., He, B., Bao, Q., et al. (2020b). Overview of the CMIP6 Historical Experiment Datasets with the Climate System Model CAS FGOALS-f3-L[J]. *Advances in Atmospheric Sciences* 37, 1057–1066. doi: 10.1007/s00376-020-2004-4

Srivastava, A., Grotjahn, R., and Ullrich, P. A. (2020). Evaluation of historical CMIP6 model simulations of extreme precipitation over contiguous US regions[J]. *Weather and Climate Extremes* 29, 100268. doi: 10.1016/j.wace.2020.100268

Mears, C. A., and Wentz, F. J. (2009). Construction of the RSS V3. 2 lower-tropospheric temperature dataset from the MSU and AMSU microwave sounders[J]. *Journal of Atmospheric and Oceanic Technology* 26, 1493–1509. doi: 10.1175/2009jtecha1237.1

Xu, Y., Ramanathan, V., and Victor, D. G. (2018). Global warming will happen faster than we think[J]. *Nature* 564, 30–32. doi: 10.1038/d41586-018-07586-5

Zhou, C., Wang, J., Dai, A., and Thorne, P. W. (2020). A new approach to homogenize global sub-daily radiosonde temperature data from 1958 to 2018[J]. *Journal of Climate* 34, 1–64.

Zhao, L., Xu, J., Powell, A. M., Jiang, Z., and Wang, D. (2016). Use of SSU/MSU satellite observations to validate upper atmospheric temperature trends in CMIP5 simulations[J]. *Remote Sensing* 8, 13. doi: 10.3390/rs8010013

Conflict of Interest: The authors declare that the research was conducted in the absence of any commercial or financial relationships that could be construed as a potential conflict of interest.

frontiers in Earth Science

ORIGINAL RESEARCH
published: 22 April 2021
doi: 10.3389/feart.2021.655128

Changes in Extreme Climate Events in Rice-Growing Regions Under Different Warming Scenarios in China

Jieming Chou[1,2], Weixing Zhao[1], Jiangnan Li[1], Yuan Xu[1], Fan Yang[1], Mingyang Sun[1] and Yuanmeng Li[1]*

[1] State Key Laboratory of Earth Surface Processes and Resource Ecology, Faculty of Geographical Science, Beijing Normal University, Beijing, China, [2] Southern Marine Science and Engineering Guangdong Laboratory (Zhuhai), Zhuhai, China

Scientific prediction of critical time points of the global temperature increases and assessment of the associated changes in extreme climate events can provide essential guidance for agricultural production, regional governance, and disaster mitigation. Using daily temperature and precipitation model outputs from the Coupled Model Intercomparison Project Phase 6 (CMIP6), the time points of the temperature that will increase by 1.5 and 2.0°C were assessed under three different scenarios (SSP126, SSP245, and SSP585). To characterize the change of extreme climate events in the rice-growing regions in China, six indices were designed, and a time slice method was used. An analysis from an ensemble of CMIP6 models showed that under SSP245, the global mean temperature will rise by 1.5°C/2.0°C by approximately 2030/2049. A global warming of 2.0°C does not occur under SSP126. The time for a 1.5°C/2.0°C warming all becomes earlier under SSP585. Under 1.5°C of global warming, the number of warm days (TX90p), rice heat damage index (Ha), consecutive dry days (CDD), 5-day maximum precipitation (Rx5day), and number of annual total extreme precipitation events (R99pTOT) will clearly increase, while the number of cold damage (Cd) events will decrease. All the indices show a strong variability regionally. For example, the CDD increased significantly in the Central China and South China rice-growing regions. The monthly maximum consecutive 5-day precipitation increased by as much as 6.8 mm in the Southwest China rice-growing region.

Keywords: global warming, 15°C and 2°C warming target, extreme climate events, rice growing regions, risk

OPEN ACCESS

Edited by:
Boyin Huang, National Centers for Environmental Information, National Oceanic and Atmospheric Administration, United States

Reviewed by:
Wenping He, Sun Yat-sen University, China
Wenbin Sun, Sun Yat-sen University, China

***Correspondence:**
Weixing Zhao
201921051146@mail.bnu.edu.cn

Specialty section:
This article was submitted to Interdisciplinary Climate Studies, a section of the journal Frontiers in Earth Science

Received: *18 January 2021*
Accepted: *04 March 2021*
Published: *22 April 2021*

Citation:
Chou J, Zhao W, Li J, Xu Y, Yang F, Sun M and Li Y (2021) Changes in Extreme Climate Events in Rice-Growing Regions Under Different Warming Scenarios in China. Front. Earth Sci. 9:655128. doi: 10.3389/feart.2021.655128

INTRODUCTION

Affected by human activities, the global climate is undergoing changes characterized by warming. A 1.5°C special report of the Intergovernmental Panel on Climate Change (IPCC) Sixth Assessment Report estimated that human-induced warming has caused a temperature rise of approximately 1.0[0.8–1.2]°C above the preindustrial level. If the current rate of temperature rise continues, then the global temperature will increase by 1.5°C between 2030 and 2052 (IPCC, 2018). A range of studies has shown that warming temperatures will lead to an increase in the frequency and intensity of extreme climate events (Tian-Yun et al., 2018; Almazroui et al., 2020; Wu et al., 2020). In order to cope with the adverse effects of climate change on society, nearly 200 parties under the United Nations Framework Convention on Climate Change (UNFCCC) reached an agreement to adopt

the Paris Agreement in December 2015. The agreement clearly states that the global warming should be controlled within 2°C above the industrialized level, and efforts should be made to control the warming within 1.5°C. Many studies have shown that it is necessary to limit the global warming to a level below a 1.5°C increase (Li et al., 2018; Nangombe et al., 2018; Zhang et al., 2018). IPCC reports (IPCC, 2018) have pointed out that under the background of global warming, the frequency and intensity of extreme weather events have increased significantly in the past few decades. With increasing temperature, the frequency of extreme weather will continue to increase. Focusing on the change in and risk of extreme events controlled by 2 and 1.5°C of global warming, some research (Knutti et al., 2016) has found that changes in precipitation increased linearly with the increase in temperature, and the frequency of heavy precipitation also increased significantly. As the temperature continues to rise, the number of days of high-temperature heat waves over a certain threshold will increase nonlinearly with increasing temperature.

Many studies in China and in the world have used global and regional climate models to assess the change in extreme climate events and possible societal impacts as global warming continues (Xuejie et al., 2002; Haylock et al., 2006; Xu et al., 2006; Hu et al., 2007; Li et al., 2010; Ren et al., 2010; Dosio, 2016). Advances in climate models provide strong support for future climate change risk assessment. At present, a large amount of output from the Coupled Model Intercomparison Project Phase 6 (CMIP6) is available for analysis. Extensive dedicated studies have evaluated the performance of the CMIP6 models. The CMIP6 models have been shown to be significantly improved in comparison to the CMIP5 models. The simulation of extreme climate events has also improved (Dan et al., 2002; Feng et al., 2014; Yang et al., 2014; Chen et al., 2020; Ukkola et al., 2020; Zhou et al., 2020; Zhu et al., 2020).

Climate change due to global warming has a significant impact on the economy (Chou et al., 2016). Agriculture is vulnerable to climate change. Although warming temperatures could be conducive to crop growth in some particular regions, continuously warming temperatures, changing precipitation patterns, and increasing extreme climate events in terms of number and intensity have a dramatic negative impact on food security (Gaupp et al., 2019). Recent studies have assessed the direct impact of climate change on food production (Ju et al., 2013; Wheeler and von Braun, 2013; Xiong et al., 2016; Chou et al., 2019a). China is the most populous country in the world. Rice is the most important food source in China. The rice-growing region in China is approximately 3 $\times 10^7 hm^2$, which accounts for 27% of the farmland in the country. The total rice output accounts for 42% of the total grain production (Chen et al., 2017). Thus, assessing the change in extreme climate events on rice production in China is uniquely important.

Research is greatly needed on how global warming changes Chinese rice production. The existing research has been based on economic-climate models, production function models, and crop models (Wang et al., 2016; Chou et al., 2019b). No dedicated studies on the impact of changes in extreme climate events arising from global warming on rice production exist. There are studies on the impact of extreme climate events (Sun and Huang, 2011), but they are based on historical data. These studies also cover only a certain area. Quantitative and scientific assessments of changes in extreme climate events and their impact on rice production are necessary to provide a scientific basis for rice planting layout, transformation, adjustment, and adaptation to climate change.

This study uses outputs from an ensemble of CMIP6 models to assess when 1.5 and 2.0°C global warming will occur under different scenarios. Based on the time of the moderate emission scenario (SSP245), the change in extreme climate events in the rice-growing regions in China under different scenarios is characterized. This study will help to further understand the climate change trend and risk in Chinese rice-growing regions. This study will also help provide information for early warning and forecasting of extreme disaster events and preventing and mitigating disasters, as well as for rationally laying out rice production and responding to risks to rice production, which have important scientific significance and practical value.

TABLE 1 | Basic information and atmospheric resolution of eight CMIP6 global climate models.

Model name	Group	Resolution
AWI-CM-1-1-MR	AWI/Germany	0.93° × 0.9375°
BCC-CSM2-MR	BCC/China	1.112° × 1.125°
ACCESS-ESM1-5	ACCESS/Australia	1.25° × 1.875°
NESM3	NESM3/China	1.85° × 1.875°
INM-CM4-8	INM/Russia	1.5° × 2°
MPI-ESM1-2-HR	MPI/Germany	0.93° × 0.9375°
MRI-ESM2-0	MRI/Japan	1.1°× 1.1°
NorESM2-MM	NCC/Norway	0.94° × 1.25°

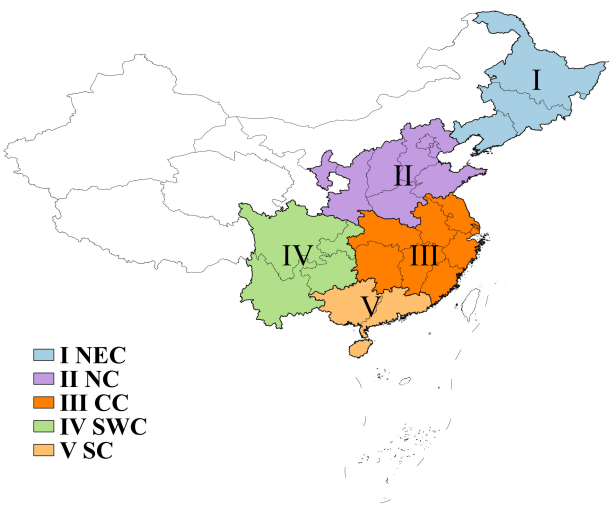

FIGURE 1 | China rice-growing regions. I, Northeast China rice-growing region (NEC); II, North China rice-growing region (NC); III, Central China rice-growing region (CC); IV, Southwest China rice-growing region (SWC); and V, South China rice-growing region (SC).

TABLE 2 | Definitions of six extreme climate indices.

Acronym	Indicator	Definitions	Units
TX90p	Warm days	Days when Tmax >90th percentile	days
CDD	Consecutive dry days	Maximum number of consecutive days with precipitation <1 mm	days
Rx5day	5-day maximum precipitation	Monthly maximum consecutive 5-day precipitation	mm
R99pTOT	Annual total extreme precipitation	Annual total precipitation when RR > 99p	mm
Ha	Rice heat damage index	High-temperature damage intensity of rice during the booting and flowering and filling stages	°C/day
Cd	Rice cold damage index	Low-temperature damage times of rice during the booting and flowering and filling stages	Times

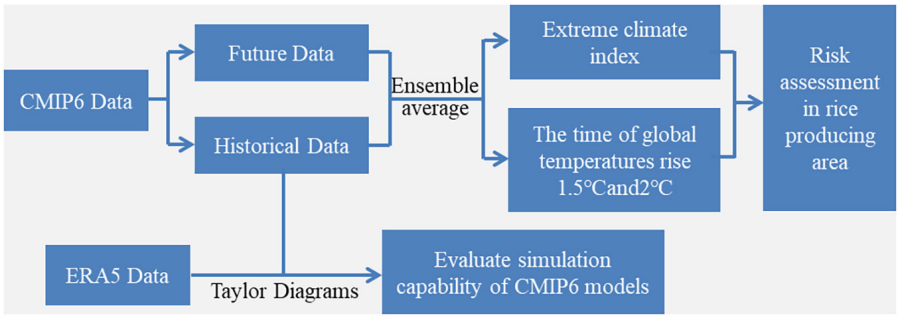

FIGURE 2 | Flow chart of changes in extreme climate events in rice-growing regions under different warming scenarios in China.

MATERIALS AND METHODS

Reanalysis Data and CMIP6 Data

The historical reanalysis data were from ERA5. ERA5 is the latest generation of reanalysis data created by the European Centre for Medium-Range Weather Forecasts (ECMWF). The data cover the historical period from 1950 to the present. In comparison with reanalysis data, ERA5 data incorporate more historical observational data, especially satellite data, into its data assimilation system to improve the accuracy of atmospheric condition estimations. In addition, in comparison with previous versions, ERA5 has a higher spatial and temporal resolution, with a temporal resolution of 1 h and a spatial resolution of 0.25° × 0.25°.

The future climate scenario data were obtained from the climate model data from CMIP6[1]. The data used in this study were daily near-surface air temperature, daily maximum near-surface air temperature, daily minimum near-surface air temperature, daily precipitation, monthly near-surface air temperature, and monthly precipitation. The selected scenarios were SSP126, SSP245, and SSP585. The data selection time period was 1950–2100. The fundamental information on the selected models is listed in **Table 1**.

Research Area and Index Selection

Combining the rice-cropping system and growing environment, the entire study area was divided into five rice-growing regions (Luo et al., 2020). The five rice-growing regions were as follows (**Figure 1**): (I) Northeast China rice-growing region (NEC), (II) North China rice-growing region (NC), (III) Central China rice-growing region (CC), (IV) Southwest China rice-growing region (SWC), and (V) South China rice-growing region (SC).

The selection of extreme climate event indicators was mainly based on 27 typical climate indexes defined by the Expert Team on Climate Change Detection and Indices (ETCCDI) jointly established by organizations such as the World Meteorological Organization (WMO). The ETCCDI

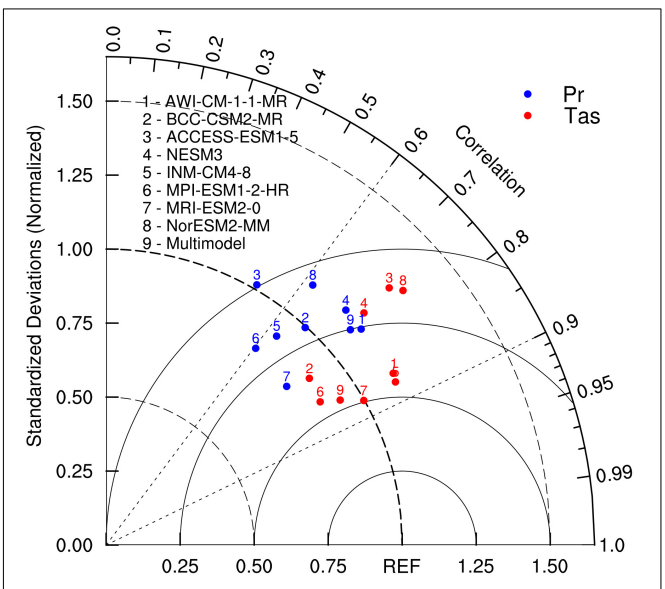

FIGURE 3 | Taylor diagram of annual mean Tas and Pr between the CMIP6 data and reanalysis data in China.

[1]https://esgf-node.llnl.gov/projects/cmip6/

include 16 temperature indices and 11 precipitation indices. In this study, we selected warm days (TX90p), consecutive dry days (CDD), 5-day maximum precipitation (Rx5day), and annual total extreme precipitation (R99pTOT). These four indices provided substantial information on the extreme climate events that will affect rice. The rice heat damage index (Ha) and rice cold damage index (Cd) are stipulated in "meteorological grade of hot damage to rice" and "grade of chilling damage for rice and maize," respectively. Information on the selected indexes is described in **Table 2**. And **Figure 2**

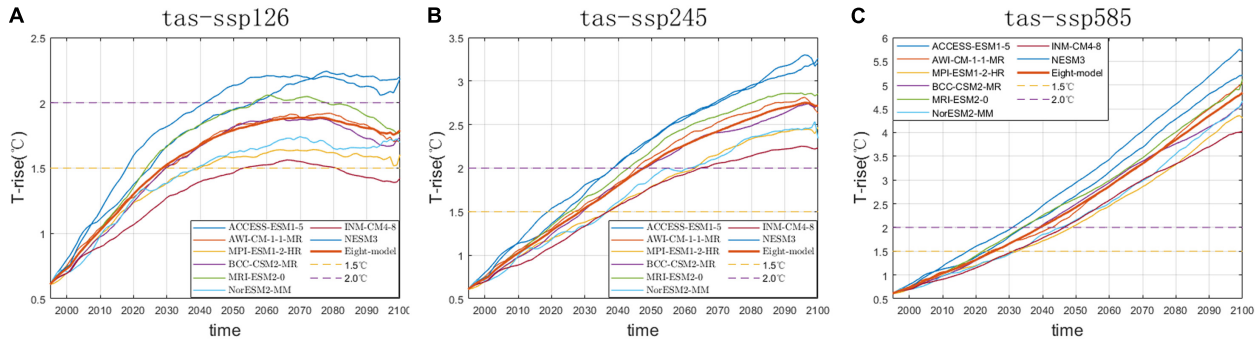

FIGURE 4 | Global warming under different scenarios [SSP126 **(A)**, SSP245 **(B)**, and SSP585 **(C)**].

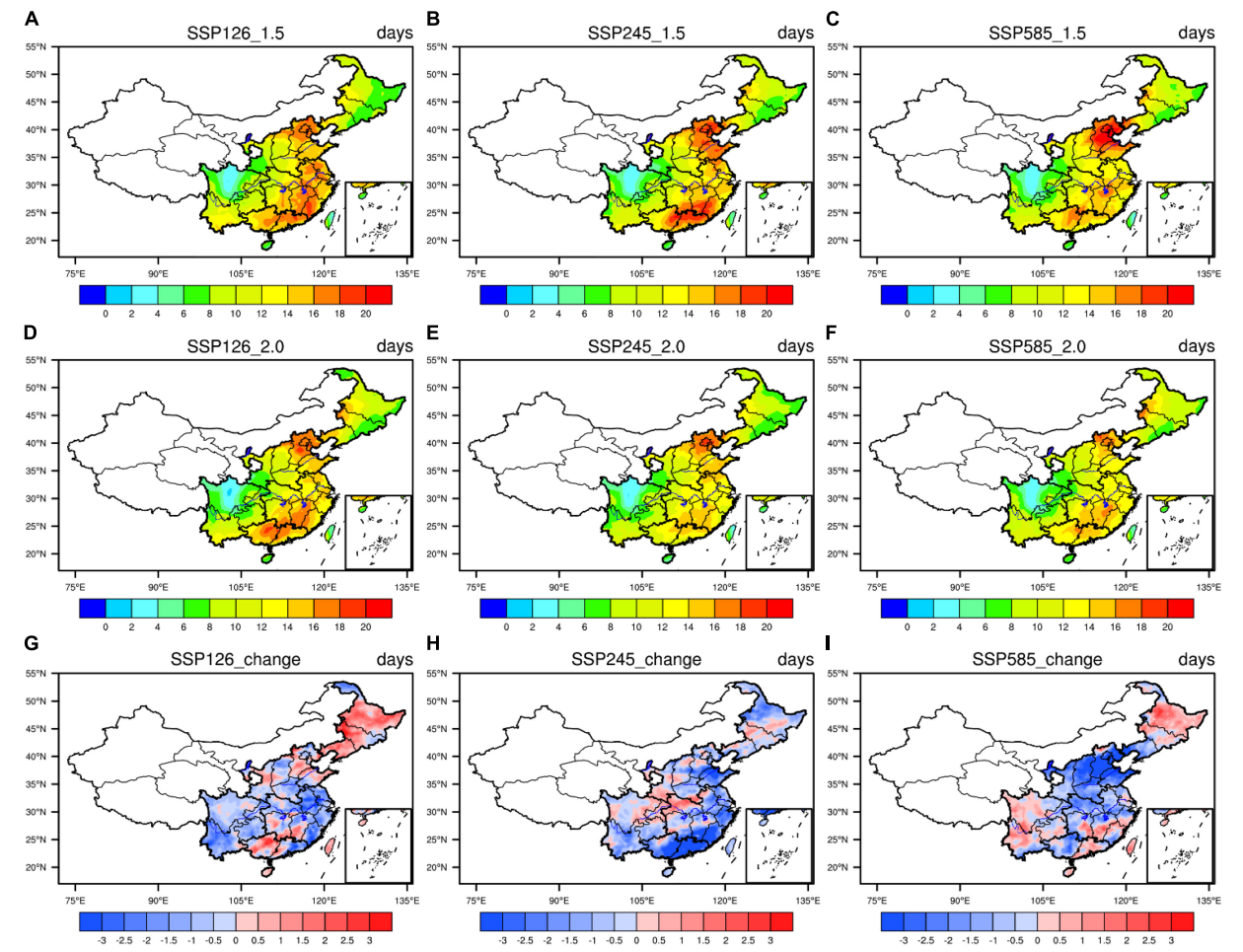

FIGURE 5 | Distribution of consecutive dry days (CDD) at 1.5 and 2°C. **(A–C)** Global warming at 1.5°C under SSP126, SSP245, and SSP585, respectively. **(D–F)** Global warming at 2°C under SSP126, SSP245, and SSP585, respectively. **(G–I)** The differences between global warming at 1.5 and 2°C.

is the flow chart of changes in extreme climate events in rice-growing regions under different warming scenarios in China.

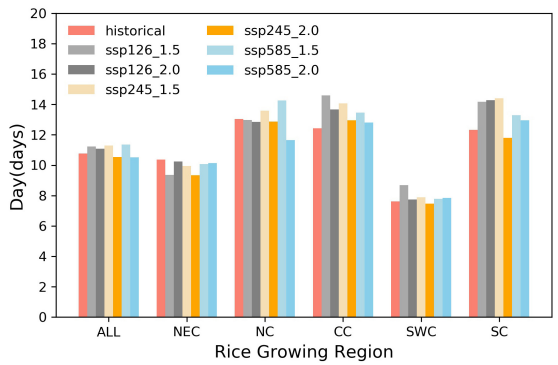

FIGURE 6 | Regional average of consecutive dry days (CDD) at the historical temperature and 1.5 and 2°C temperature increases. The rice-growing regions are the Chinese rice-growing region (ALL), Northeast China rice-growing region (NEC), North China rice-growing region (NC), Central China rice-growing region (CC), Southwest China rice-growing region (SWC), and South China rice-growing region (SC).

Methods

Evaluation Model Simulation Results

First, we used Taylor diagrams (Taylor et al., 2001) to briefly evaluate the reliability of the CMIP6 model data. The spatial correlation coefficient, standard deviation, and root mean square error between the historical period (1986–2005) data simulated by the CMIP6 model and the ERA5 reanalysis data were analyzed. The root mean square error is defined in formula (1).

$$RMSE = \sqrt{\frac{1}{n}\sum_{i=1}^{n}\left(X_{sim,i} - X_{obs,i}\right)^2} \quad (1)$$

According to formula (1), RMSE is the root mean square error of the grid, $X_{\mathrm{sim},i}$ is the simulated value of the grid in year i, and $X_{\mathrm{obs},i}$ is the corresponding reanalysis data.

Time of a 1.5°C/2°C Temperature Increase and Extreme Weather Indices

According to the IPCC AR5, the global temperature from 1986 to 2005 was 0.61°C warmer than that before industrialization (IPCC, 2013). Therefore, we defined 0.89°C higher than the temperature in 1986–2005 as 1.5°C warmer than the temperature before industrialization and 1.39°C higher than the temperature

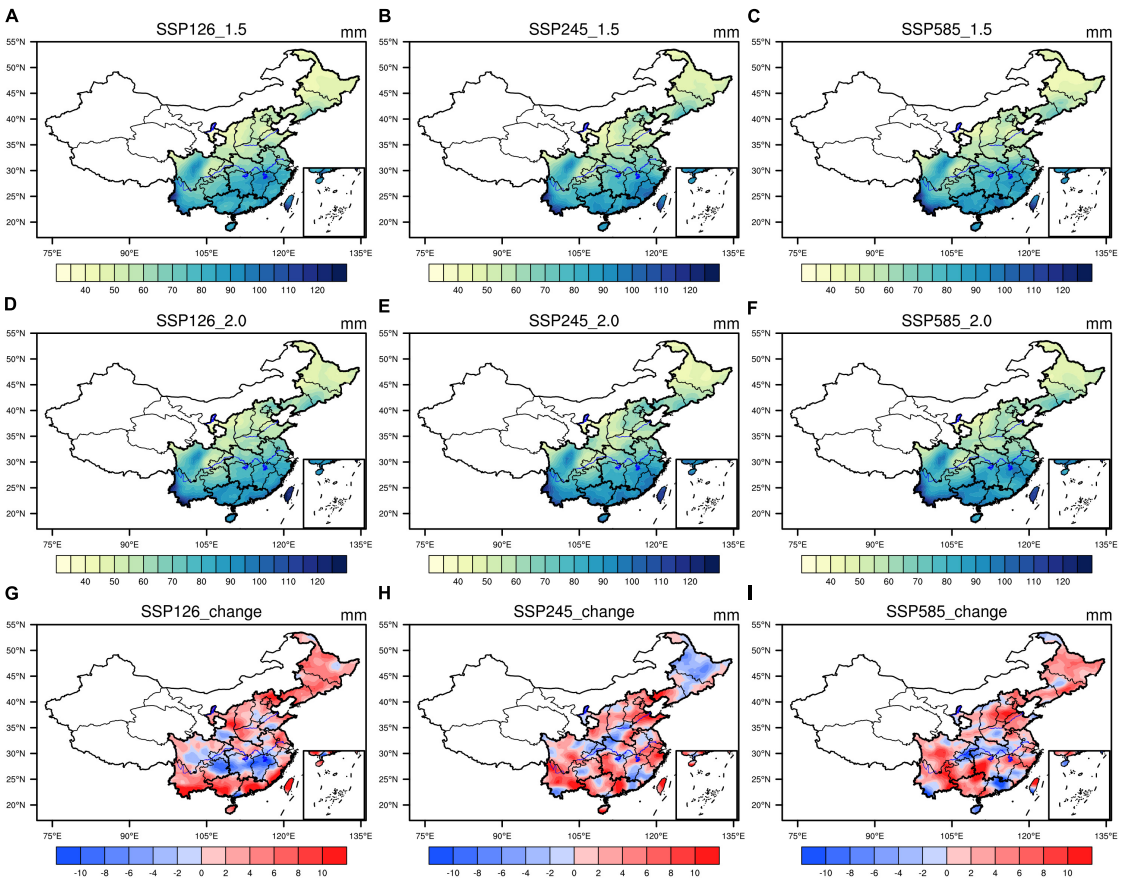

FIGURE 7 | Distribution of 5-day maximum precipitation (Rx5day) at 1.5 and 2°C. **(A–C)** Global warming at 1.5°C under SSP126, SSP245, and SSP585, respectively. **(D–F)** Global warming at 2°C under SSP126, SSP245, and SSP585, respectively. **(G–I)** The differences between global warming at 1.5 and 2°C.

in 1986–2005 as 2°C warmer than that before industrialization. The bilinear interpolation method was used to uniformly interpolate the data to a 0.5° × 0.5° Gaussian grid, and the multimode ensemble method was used to obtain a data set. The time points of when 1.5 and 2°C increases in temperature would occur under the three social scenarios (SSP) were calculated. Finally, the time slice method (Guo et al., 2017) was used to explore the changes in extreme climate events in the rice-producing areas under global temperature increases of 1.5 and 2°C. Taking the time points when 1.5 and 2°C temperature increases would occur under the SSP245 scenario as the benchmark, ten years before and after this time point (totally 20 years) were regarded as the research period. According to the calculation results, the time periods when the temperature would increase 1.5 and 2°C in this paper were 2019–2038 and 2039–2058, respectively. In addition, we selected 1986–2005 as the historical reference period. The method of calculating the rice heat damage index is shown in formulas (2) and (3).

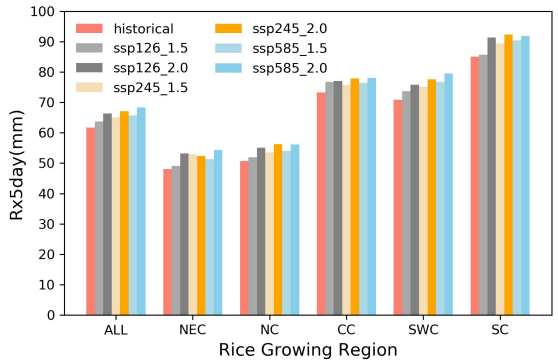

FIGURE 8 | The same as **Figure 6** but for the changes in 5-day maximum precipitation (Rx5day) (mm).

$$Ha = \sum_{j=1}^{m} \sum_{i=1}^{n_j} f(T_h^{ij}) \tag{2}$$

$$f\left(T_h^{ij}\right) = \begin{cases} T_h^{ij} - 35.0 & 35.0 \le T_h^{ij} < 40.0 \\ 3 \times \left(T_h^{ij} - 40\right) + 5 & T_h^{ij} \ge 40.0 \end{cases} \tag{3}$$

where ***Ha*** is the rice heat damage index. ***m*** is the total number of rice heat damage processes. ***j*** is the sequence number of the multiple heat damage processes of rice. ***i*** is the different grids. $f\left(T_h^{ij}\right)$ is the accumulated heat per day.

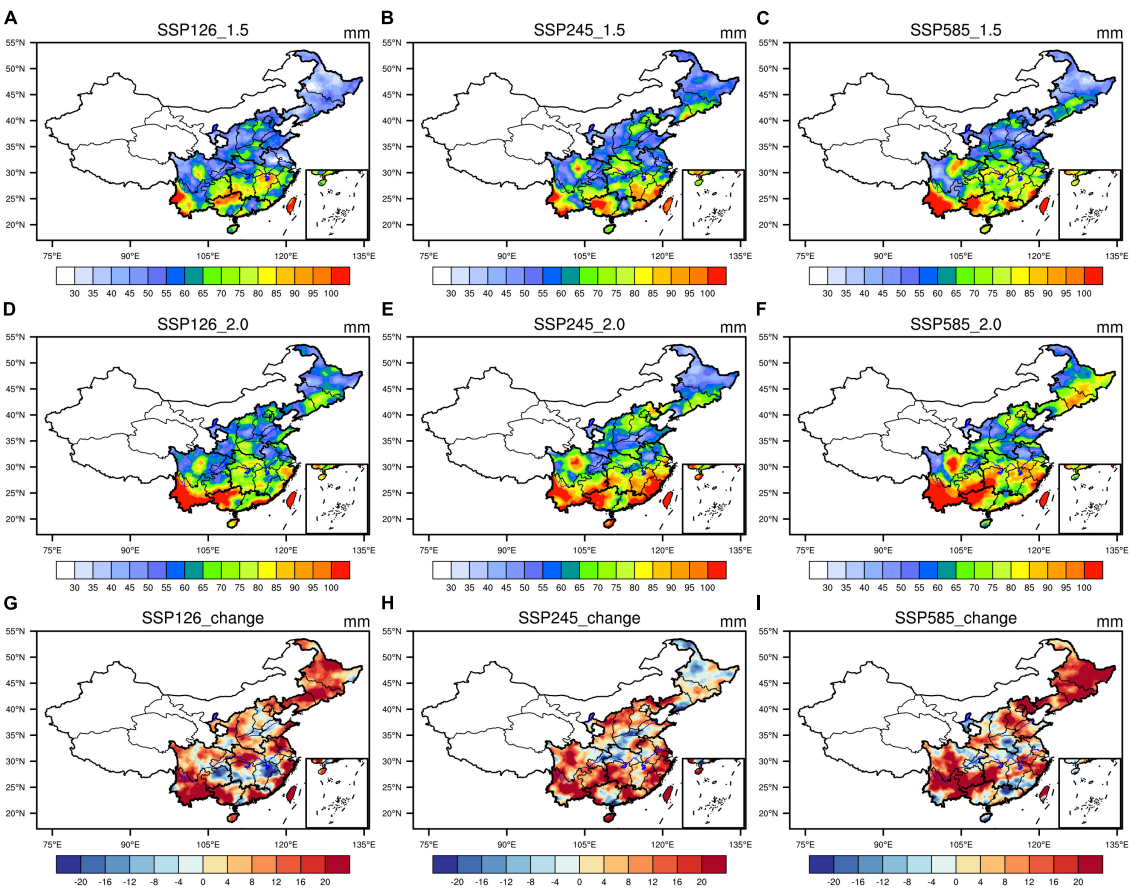

FIGURE 9 | Distribution of annual total extreme precipitation (R99pTOT) at 1.5 and 2°C. **(A–C)** Global warming at 1.5°C under SSP126, SSP245, and SSP585, respectively. **(D–F)** Global warming at 2°C under SSP126, SSP245, and SSP585, respectively. **(G–I)** The differences between global warming at 1.5 and 2°C.

RESULTS AND DISCUSSION

Comparison of CMIP6 Data and Reanalysis Data

Figure 3 is a Taylor diagram that shows the difference between the CMIP6 global model data and the ERA5 reanalysis data. The spatial correlation coefficient of surface temperature was 0.8–0.9, while the spatial correlation coefficient of precipitation was 0.6–0.7. The CMIP6 data reproduced the historical temperature and precipitation to a certain extent, but the simulation ability of the data for precipitation was obviously lower than that for temperature. At the same time, the results also showed that in comparison with the reanalysis data, multimode ensemble data can better reproduce history. Therefore, the multimode ensemble data were used to analyze the changes in extreme climate events in China.

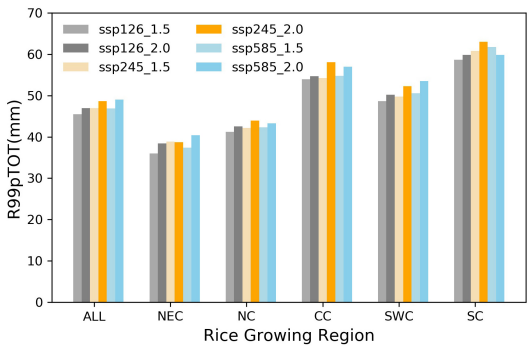

FIGURE 10 | The same as **Figure 6** but for the changes in annual total extreme precipitation (R99pTOT) (mm).

Time Point When Global Temperature Increases by 1.5°C/2°C

As shown in **Figure 4**, under different social scenarios, there were large differences in the increases in global temperature. Under the SSP126 scenario, most models showed a temperature peak in approximately 2,065, and global temperature showed a downward trend after reaching the peak. Under the SSP245 scenario, the global temperature showed a more dramatic increase than that under the SSP126 scenario, but the rate of increase gradually decreased, reaching its peak by 2,100. Under the SSP585 scenario, global warming was intense and the rate of temperature rise gradually increased. Although the

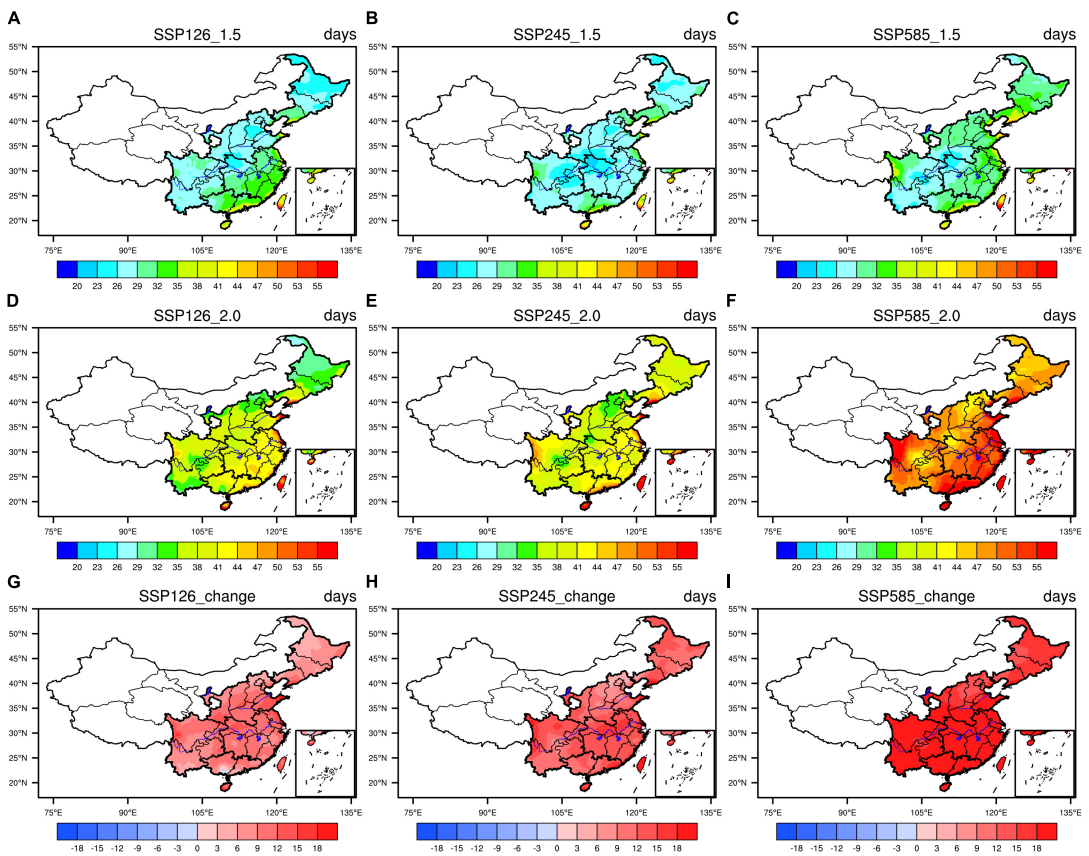

FIGURE 11 | Distribution of warm days (TX90p) at 1.5 and 2°C. **(A–C)** Global warming at 1.5°C under SSP126, SSP245, and SSP585, respectively. **(D–F)** Global warming at 2°C under SSP126, SSP245, and SSP585, respectively. **(G–I)** The differences between global warming at 1.5 and 2°C.

simulation results of each model showed a similar trend in general, the time it took for the temperature to increase by 1.5 and 2°C in the different models was quite different. This difference was related to the internal variability of the model and climate sensitivity.

Due to the large differences between the various modes, a multimode method was adopted to determine the time at which the temperature will increase. From the results of multimode ensemble averaging, the times when 1.5°C warming occurred under the SSP126, SSP245, and SSP585 scenarios were 2030, 2029, and 2026, respectively. The times when 2°C warming occurred under the SSP245 and SSP585 scenarios were 2,049 and 2,039, respectively. The SSP126 scenario did not result in 2°C warming.

Compared with the results of existing research (Li et al., 2018; Nangombe et al., 2018; Zhang et al., 2018), the results of this study showed that the times when the global temperature will reach 1.5 and 2.0°C warming were similar. The results showed that the time it would take to reach 1.5°C warming were 1–2 years earlier and that the time it would take to reach 2°C warming was 2–3 years later than the results in other studies. These differences are acceptable due to the different calculation methods of global temperature and the different results from different climate models.

Changes in the Extreme Climate Indices

Consecutive Dry Days

Under 1.5°C of global warming, the CDD in the rice-growing regions were generally consistent under the different scenarios (**Figure 5**). Taking the SSP245 scenario as an example, the number of CDD in the NC, CC, and SC was significantly higher than those in the other rice-growing regions, reaching 13.6, 14.1, and 14.4 days, respectively (**Figure 6**). Compared with the historical reference period, the number of CDD in the NEC decreased by approximately 1.0 days. In comparison with those in the historical period, the number of CDD in the NC, CC, and SC increased significantly with the number of CDD increasing by 0.6, 1.3, and 1.9 days, respectively.

Under 2°C of global warming, the distribution of CDD in the rice-growing regions was similar to that under 1.5°C of global

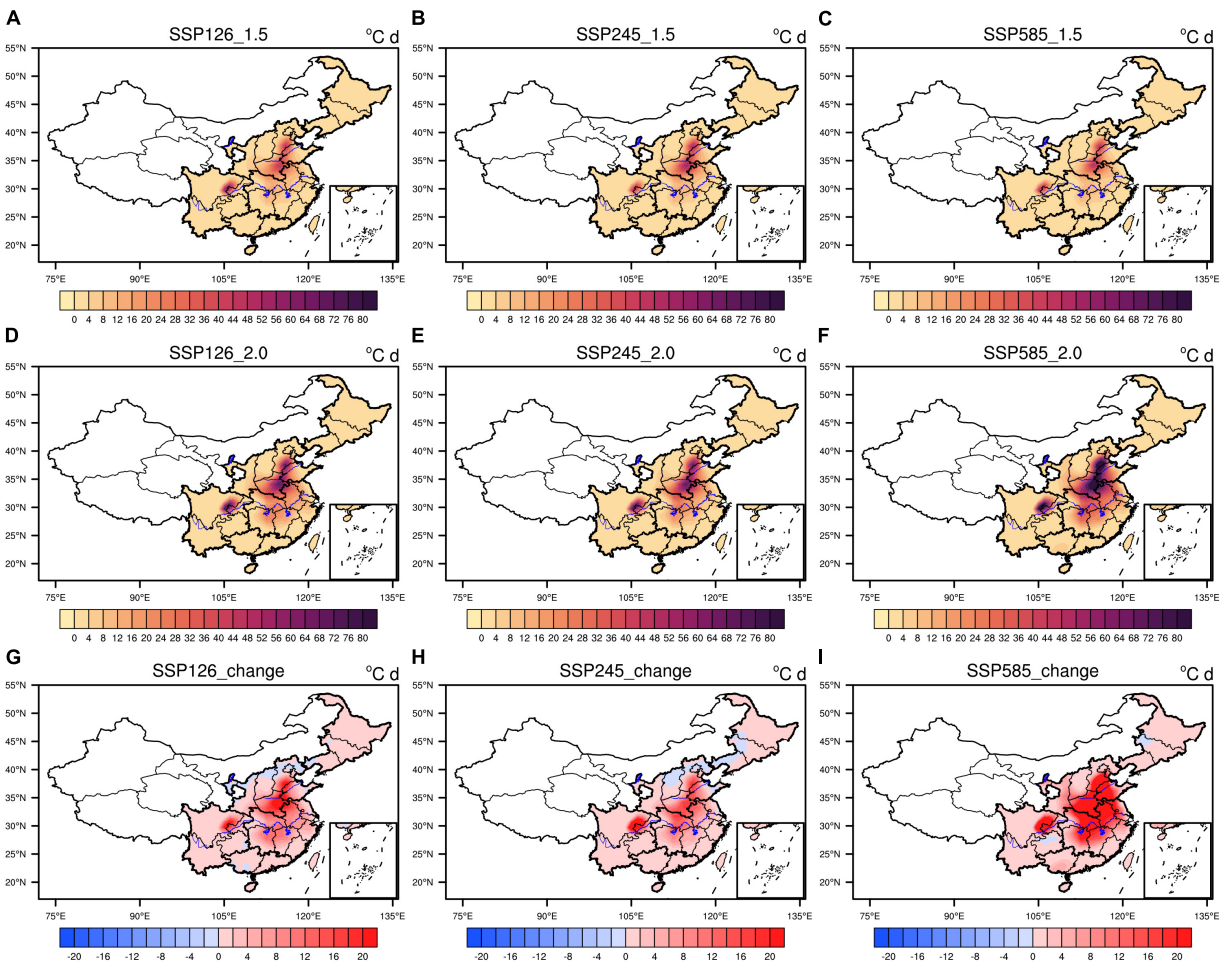

FIGURE 12 | Distribution of rice heat damage index (Ha) at 1.5 and 2°C. **(A–C)** Global warming at 1.5°C under SSP126, SSP245, and SSP585, respectively. **(D–F)** Global warming at 2°C under SSP126, SSP245, and SSP585, respectively. **(G–I)** The differences between global warming at 1.5 and 2°C.

warming. The high-value areas of CDD were still located in the NC, CC, and SC.

Under the scenario of an additional 0.5°C increase in global temperature from to 2°C, the number of CDD in the rice-growing regions showed a decreasing trend. However, in the NC, the SSP126 and SSP585 scenarios showed that the number of CDD will increase by 0.9 and 0.2 days, respectively, and those under the SSP585 scenario will decrease by 0.6 days.

Five-Day Maximum Precipitation

Under a 1.5°C increase in global warming, the Rx5day values in the rice-growing regions under different scenarios were generally consistent, showing a distribution pattern of more precipitation in the south and less precipitation in the north (**Figure 7**). Taking the SSP245 scenario as an example, the Rx5day in the NEC, NC, CC, SWC, and SC reached 53.0, 53.5, 75.8, 75.0, and 89.4 mm, respectively. Compared with the historical reference period, the increase was up to 4.9, 2.8, 2.5, 4.2, and 4.4 mm, respectively (**Figure 8**). However, at the junction of the CC and SC, this variable slightly decreased.

Under 2°C of global warming, the distribution of the Rx5day in the rice-growing regions was similar to that under 1.5°C of global warming. Taking the SSP245 scenario as an example, the Rx5day in the NEC, NC, CC, SWC, and SC reached 52.3, 56.2, 77.9, 77.6, and 92.3 mm, respectively.

Under the scenario of an additional 0.5°C increase in global temperature from 1.5 to 2°C, the Rx5day showed an increase of approximately 2.5 mm in almost every rice-growing region. However, there were large differences under different scenarios in the NC. Under the SSP126 scenario and SSP585 scenario, the Rx5day showed increases of 3.2 and 3.1 mm, respectively, but under the SSP585 scenario, it showed a decrease of 0.6 mm.

Annual Total Extreme Precipitation

Under a 1.5°C of global warming, the R99pTOT in the rice-growing regions under the different scenarios mainly showed a gradually decreasing distribution from south to north (**Figure 9**). Taking the SSP245 scenario as an example, the R99pTOT in the NEC, NC, CC, SWC, and SC reached 38.9, 42.2, 54.2, 49.8, and 60.8 mm, respectively (**Figure 10**).

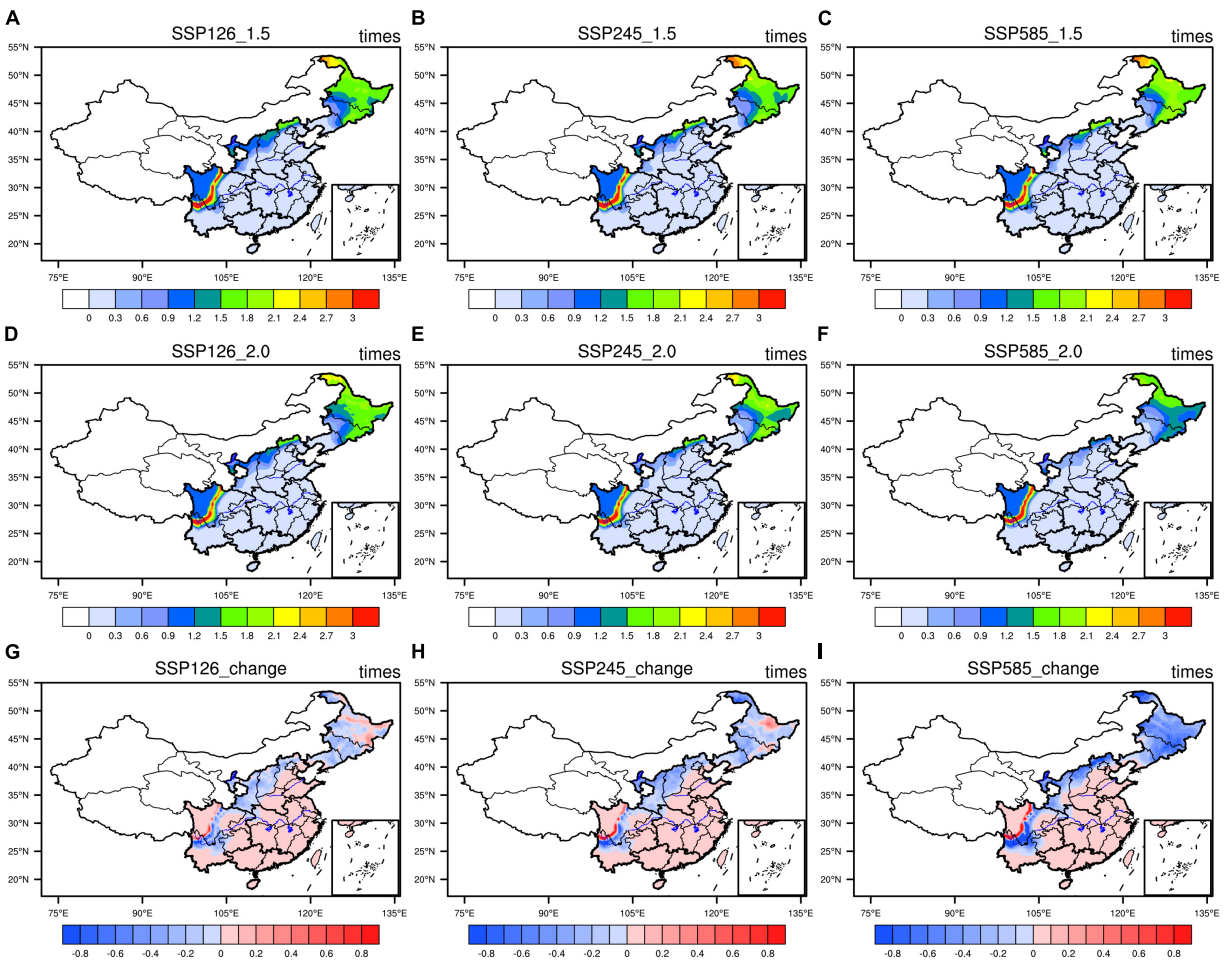

FIGURE 13 | Distribution of rice cold damage index (Cd) at 1.5 and 2°C. **(A–C)** Global warming at 1.5°C under SSP126, SSP245, and SSP585, respectively. **(D–F)** Global warming at 2°C under SSP126, SSP245, and SSP585, respectively. **(G–I)** The differences between global warming at 1.5 and 2°C.

Under 2°C of global warming, the distribution of R99pTOT in the rice-growing regions was similar to that under global warming of 1.5°C. Taking the SSP245 scenario as an example, the R99pTOT in the CC, SWC, and SC reached 58.0, 52.2, and 63.0 mm, respectively.

Under the scenario of an additional 0.5°C increase in global temperature from 1.5 to 2°C, the R99pTOT showed an increasing trend in rice-growing regions. The R99pTOT increased significantly, especially in the SWC. Under the SSP245 scenario, the R99pTOT increased by as much as 3.8 mm. However, under the different scenarios, there were large differences in the NC. Under the SSP126 scenario and SSP585 scenario, the R99pTOT increased by 2.5 and 2.9 mm, respectively, but under the SSP585 scenario, it decreased by 0.2 mm.

Warm Days

The TX90p were calculated based on the historical time period. Under 1.5°C of global warming, the TX90p in the CC and SC were significantly higher than those in the other rice-growing regions. There were large differences among the different scenarios. The number of Tx90p increased significantly under the high emission pathway, especially in the NEC and NC.

Under the scenario of an additional 0.5°C increase in global temperature from 1.5 to 2°C, the number of Tx90p showed an increasing trend in the rice-growing regions (**Figure 11**). Under the same amount of temperature rise, the increase in the number of Tx90p under the high-emission scenario was significantly greater than that under the low-emission scenario. Under the SSP245 scenario, the number of Tx90p in the NEC, NC, CC, SWC, and SC was increased by 12.1, 11.0, 14.4, 12.6, and 13.7 days, respectively, and the increase under the SSP585 scenario was as high as 16.2, 18.5, 22.2, 22.0, and 25.1 days, respectively.

Rice Heat Damage Index

Based on the rice booting-flowering period and rice filling period in the different regions, the Ha of each region was calculated. Future heat damage to rice mainly occurred in the NC and CC (**Figure 12**).

Under the scenario of an additional 0.5°C increase in global temperature from 1.5 to 2°C, the area and intensity of heat damage in the NC and CC increased significantly, and the increase was more significant under the high-emission scenario than under the low-emission scenario. Taking the SSP245 scenario as an example, the Ha in the NC and CC increased by 3.4 and 4.3°C/day under different temperature rise scenarios, respectively, and the amount of heat damage increased 0.4- and 0.6-fold, respectively.

Rice Cold Damage Index

times**Figure 13** shows that the Cd mainly occurred in the NEC and SWC.

Under the scenario of an additional 0.5°C increase in the global temperature from 1.5 to 2°C, the Cd in the NEC and SWC decreased. Moreover, different scenarios were consistent. Taking the SSP245 scenario as an example, the Cd in the NEC decreased by 0.33 compared with that in the historical period. Under a 2°C temperature increase, the Cd was 0.14 times less than that under a 1.5°C temperature increase.

CONCLUSION AND DISCUSSION

This article is mainly based on CMIP6 data, and it explores the time points when the global temperature is projected to increase by 1.5 and 2.0°C under different social scenarios. Based on the time period in the moderate emission scenario (SSP245) when the global temperature will increase by 1.5 and 2.0°C, the risk of extreme climate events in rice-growing regions was explored. Then, we analyzed the changes in extreme climate events in the rice-growing regions in the future under different temperature increase targets. The main conclusions obtained are as follows:

(1) The years when global temperature was projected to increase by 1.5 and 2.0°C were different under the different scenarios. The years when 1.5°C of warming occurred in the SSP126, SSP245, and SSP585 scenarios were 2,030, 2,029, and 2,026, respectively. The years when 2°C of global warming occurred in the SSP245 and SSP585 scenarios were 2049 and 2039, respectively. Under the high emission scenarios, the global temperature easily increased by 2°C. To control global warming and ensure an increase of 1.5°C, more stringent emission reduction measures need to be implemented.

(2) The risk of extreme climate events occurring in the rice-growing regions of China at a temperature increase of 2.0°C was significantly higher than the risk at a temperature increase of 1.5°C. The number of TX90p, Ha, Rx5day and R99pTOT in the rice-growing regions of China increased. In contrast, the CDD and Cd decreased. However, the changes in the different rice-growing regions were relatively different. The R99pTOT and the Rx5day increased significantly in the CC and the SWC. The CDD decreased significantly in the NC and SC. The Ha of the NC and the CC increased by 3.4 and 4.3, respectively. The rice cold damage index in the NEC decreased by 0.33.

(3) Under the different socio-scenarios of SSP126, SSP245 and SSP585, the CDD, the Rx5day, the R99pTOT, the number of Tx90p, and the Ha increased, and the Cd decreased. The increase in extreme climate events under the high emission scenario was more obvious. However, there were differences in the results under the different social scenarios for the CDD, the Rx5day, and the R99pTOT in the NEC.

(4) In general, the risk of extreme high-temperature events occurring in the rice-growing regions of China will increase in the future, and the risk of extreme low-temperature events occurring will decrease. In particular, the NC and CC will experience a significant increase in the risk of extreme heat disasters. The risk of low-temperature disasters in the NEC will be reduced. In addition, in the future, the risk of extreme precipitation events in the rice-producing areas will increase, especially in the SWC and the SC. The risk of extreme precipitation events in the NEC in the future is highly uncertain.

(5) This study helps to understand the climate change trend and risk situation in Chinese rice-production areas. The risk of extreme high-temperature events and extreme precipitation events occurring in the rice-producing areas will increase. In addition, this study also provides information that will help with early warning and forecasting of extreme disaster events, preventing disasters and mitigating disasters, as well as with rationally laying out rice production and responding to risk, which are important scientifically and practically. This study is mainly based on CMIP6 model data. Although in comparison to other models, the CMIP6 model can better simulate changes in historical periods, future climate changes will be affected by various natural and human factors and other uncertain factors. In addition, there are uncertainties within global climate models such as those related to the simulation of future temperature and precipitation. This article only studied the overall trend in the changes in future extreme climate events in the five main rice producing areas of China, but for specific small areas, there is a lack of more refined research. In future work, dynamic downscaling of the climate model could be used to improve the resolution of the model and to conduct a more refined study of changes in future extreme climate events in the rice-growing regions.

DATA AVAILABILITY STATEMENT

Publicly available datasets were analyzed in this study. This data can be found here: https://esgf-node.llnl.gov/projects/cmip6/.

AUTHOR CONTRIBUTIONS

WZ and JC: conceptualization. WZ: methodology, software, resources, writing-review and editing, writing-original draft preparation, and supervision. WZ, JL, and MS: validation. FY: formal analysis. YX and YL: investigation. JC: data curation, visualization, and funding acquisition. YX: project administration. All authors have read and agreed to the published version of the manuscript.

FUNDING

This work was supported by the National Key Research and Development Program of China (2016YFA0602703; 2018YFC1509003) and the National Natural Science Foundation of China (42075167).

REFERENCES

Almazroui, M., Saeed, S., and Saeed, F. (2020). Projections of precipitation and temperature over the South Asian Countries in CMIP6. *Earth Syst. Environ.* 4, 297–320. doi: 10.1007/s41748-020-00157-7

Chen, H., Sun, J., Lin, W., and Xu, H. (2020). Comparison of CMIP6 and CMIP5 models in simulating climate extremes. *Sci. Bull.* 65, 1415–1418. doi: 10.1016/j.scib.2020.05.015

Chen, W., Xu, Z., and Tang, L. (2017). 20 years; development of super rice in China—The 20th anniversary of the super rice in China. *J. Integr. Agric.* 16, 981–983. doi: 10.1016/S2095-3119(16)61612-X

Chou, J., Dong, W., and Yan, X. (2016). The impact of climate change on the socioeconomic system: a mechanistic analysis. *Chin. J. Atmos. Sci.* 40, 191–200. doi: 10.3878/j.issn.1006-9895.1507.15131

Chou, J., Xian, T., Dong, W., and Xu, Y. (2019a). Regional temporal and spatial trends in drought and flood disasters in china and assessment of economic losses in recent years. *Sustainability* 11:55. doi: 10.20944/preprints201811.0340.v1

Chou, J., Xu, Y., and Dong, W. (2019b). Research on the variation characteristics of climatic elements from April to September in China's main grain-producing areas. *Theor. Appl. Climatol.* 137, 3197–3207. doi: 10.1007/s00704-019-02795-y

Dan, L., Ji, J., and Li, Y. (2002). Climate simulations based on a different-grid nested and coupled model. *Adv.Atmos. Sci.* 19, 487–499. doi: 10.1007/s00376-002-0081-1

Dosio, A. (2016). Projections of climate change indices of temperature and precipitation from an ensemble of bias-adjusted high-resolution EURO-CORDEX regional climate models. *J. Geophys. Res. Atmos.* 121, 5488–5511. doi: 10.1002/2015JD024411

Feng, J., Yonghe, L., and Yan, Z. (2014). Analysis of surface air temperature warming rate of China in the last 50 years (1962–2011) using k-means clustering. *Theor. Appl. Climatol.* 120, 785–796. doi: 10.1007/s00704-014-1216-x

Gaupp, F., Hall, J., and Hochrainer-Stigler, S. (2019). Changing risks of simultaneous global breadbasket failure. *Nat. Clim. Chang.* 10, 54–57. doi: 10.1038/s41558-019-0600-z

Guo, X., Huang, J., and Luo, Y. (2017). Projection of heat waves over China for eight different global warming targets using 12 CMIP5 models. *Theor. Appl. Climatol.* 128, 507–522. doi: 10.1007/s00704-015-1718-1

Haylock, M., Cawley, G., Harpham, C., Wilby, R., and Goodess, C. (2006). Downscaling heavy precipitation over the United Kingdom: a comparison of dynamical and statistical methods and their future scenarios. *Int. J. Climatol.* 26, 1397–1415. doi: 10.1002/joc.1318

Hu, Y., Dong, W., and He, Y. (2007). Progress of the study of extreme weather and climate events at the beginning of the twenty first century. *Adv. Earth Sci.* 10, 1066–1075.

IPCC (2013). *Climate Change (2013): The Physical Science Basis*. Cambridge: Cambridge University Press, 1535.

IPCC (2018). *Global Warming of 1.5 C (2018). An IPCC Special Report on the Impacts of Global Warming of 1.5 C Above Pre-Industrial levels and Related Global Greenhouse gas Emission Pathways, in the Context of Strengthening the Global Response to the Threat of Climate Change, Sustainable Development, and Efforts to Eradicate Poverty*. Geneva: IPCC.

Ju, H., van der Velde, M., Lin, E., Xiong, W., and Li, Y. (2013). The impacts of climate change on agricultural production systems in China. *Clim. Change* 120, 313–324. doi: 10.1007/s10584-013-0803-7

Knutti, R., Rogelj, J., Sedláček, J., and Fischer, E. M. (2016). A scientific critique of the two-degree climate change target. *Nat. Geosci.* 9, 13–18. doi: 10.1038/ngeo2595

Li, D., Zhou, T., Zou, L., Zhang, W., and Zhang, L. (2018). Extreme high-temperature events over East Asia in 1.5°C and 2°C warmer futures: analysis of NCAR CESM low-warming experiments. *Geophys. Res. Lett.* 45, 1541–1550. doi: 10.1002/2017GL076753

Li, Q., Dong, W., and Li, W. (2010). Assessment of the uncertainties in temperature change in China during the last century. *Chin. Sci. Bull.* 55, 1974–1982. doi: 10.1007/s11434-010-3209-1

Luo, Y., Zhang, Z., Chen, Y., Li, Z., and Tao, F. (2020). ChinaCropPhen1km: a high-resolution crop phenological dataset for three staple crops in China during 2000–2015 based on leaf area index (LAI) products. *Earth Syst. Sci. Data* 12, 197–214. doi: 10.5194/essd-12-197-2020

Nangombe, S., Zhou, T., and Zhang, W. (2018). Record-breaking climate extremes in Africa under stabilized 1.5°C and 2°C global warming scenarios. *Nat. Clim. Change* 8, 375–380. doi: 10.1038/s41558-018-0145-6

Ren, G., Feng, G., and Yan, Z. (2010). Progresses in observation studies of climate extremes and changes in Mainland China (in Chinese). *Clim. Environ. Res.* 15, 337–353. doi: 10.3878/j.issn.1006-9585.2010.04.01

Sun, W., and Huang, Y. (2011). Global warming over the period 1961-2008 did not increase high-temperature stress but did reduce low temperature stress in irrigated rice across China. *Agric. For. Meteorol.* 151, 1193–1201. doi: 10.1016/j.agrformet.2011.04.009

Tian-Yun, D., Dong, W., Yan, G., and Chou, J. (2018). Future temperature changes over the critical Belt and Road region based on CMIP5 models. *Adv. Clim. Change Res.* 9, 57–65.

Ukkola, A. M., De Kauwe, M. G., Roderick, M. L., Abramowitz, G., and Pitman, A. J. (2020). Robust future changes in meteorological drought in CMIP6 projections despite uncertainty in precipitation. *Geophys. Res. Lett.* 46:e2020GL087820. doi: 10.1029/2020GL087820

Wang, P., Zhang, Z., and Chen, Y. (2016). How much yield loss has been caused by extreme temperature stress to the irrigated rice production in China? *Clim. Change* 134, 635–650. doi: 10.1007/s10584-015-1545-5

Wheeler, T., and von Braun, J. (2013). Climate change impacts on global food security. *Science* 341, 508–513. doi: 10.1126/science.1239402

Wu, J., Han, Z., Xu, Y., Zhou, B., and Gao, X. (2020). Changes in extreme climate events in China under 1.5 C–4 C global warming targets: projections using an ensemble of regional climate model simulations. *J. Geophys. Res. Atmos.* 125:e2019JD031057. doi: 10.1029/2019JD031057

Xiong, W., Skalský, R., Porter, C. H., Balkovič, J., Jones, J. W., and Yang, D. (2016). Calibration-induced uncertainty of the EPIC model to estimate climate change impact on global maize yield. *J. Adv. Model. Earth Syst.* 8, 1358–1375. doi: 10.1002/2016MS000625

Xu, Y., Zhang, Y., Lin, Y., Lin, E., Lin, W., and Dong, W. (2006). Analysis of regional climate change response in China under SRES B2 scenario using PRECIS (in Chinese). *Chin. Sci. Bull.* 17, 2068–2074. doi: 10.1360/csb2006-15-17-2068

Xuejie, G., Zongci, Z., and Giorgi, F. (2002). Changes of extreme events in regional climate simulations over East Asia. *Adv. Atmos. Sci.* 19, 927–942. doi: 10.1007/s00376-002-0056-2

Yang, S., Feng, J., Dong, W., and Chou, J. (2014). Analyses of extreme climate events over China based on CMIP5 historical and future simulations. *Adv. Atmos. Sci.* 31, 1209–1220. doi: 10.1007/s00376-014-3119-2

Zhang, W., Zhou, T., and Zou, L. (2018). Reduced exposure to extreme precipitation from 0.5°C less warming in global land monsoon regions. *Nat. Commun.* 9:3153. doi: 10.1038/s41467-018-05633-3

Zhou, T., Chen, Z., Zou, L., and Chen, X. (2020). Development of climate and earth system models in China: past achievements and new CMIP6 results. *J. Meteorol. Res.* 34, 1–19. doi: 10.1007/s13351-020-9164-0

Zhu, H., Jiang, Z., and Li, J. (2020). Does CMIP6 inspire more confidence in simulating climate extremes over China? *Adv. Atmos. Sci.* 37, 1119–1132. doi: 10.1007/s00376-020-9289-1

Conflict of Interest: The authors declare that the research was conducted in the absence of any commercial or financial relationships that could be construed as a potential conflict of interest.

frontiers in Environmental Science

ORIGINAL RESEARCH
published: 28 April 2021
doi: 10.3389/fenvs.2021.665394

The Characteristics of Northeast China Cold Vortex With Different Active Paths in June and Their Relationship With Precipitation and Pre-SST

Yi-He Fang[1,2,3], Meng-Meng Zhang[4], Chun-Yu Zhao[1,3], Zhi-Qiang Gong[5,6], Xiao-Yu Zhou[1] and Wei-Qi Zhang[7]*

[1] Regional Climate Center of Shenyang, Shenyang, China, [2] The Institute of Atmospheric Environment, China Meteorological Administration, Shenyang, China, [3] Key Opening Laboratory for Northeast China Cold Vortex Research, China Meteorological Administration, Shenyang, China, [4] Liaoning Provincial Meteorological Service Center, Shenyang, China, [5] College of Physics and Electronic Engineering, Changshu Institute of Technology, Jiangsu, China, [6] Laboratory for Climate Studies, National Climate Research Center, China Meteorological Administration, Beijing, China, [7] Sujiatun District Bureau of Meteorology, Shenyang, China

OPEN ACCESS

Edited by:
Boyin Huang, National Centers for Environmental Information, National Oceanic and Atmospheric Administration, United States

Reviewed by:
Hailong Liu, Shanghai Jiao Tong University, China
Shaobo Qiao, Sun Yat-sen University, China

***Correspondence:**
Zhi-Qiang Gong
gongzq@cma.gov.cn

Specialty section:
This article was submitted to Interdisciplinary Climate Studies, a section of the journal Frontiers in Environmental Science

Received: *08 February 2021*
Accepted: *29 March 2021*
Published: *28 April 2021*

Citation:
Fang Y-H, Zhang M-M, Zhao C-Y, Gong Z-Q, Zhou X-Y and Zhang W-Q (2021) The Characteristics of Northeast China Cold Vortex With Different Active Paths in June and Their Relationship With Precipitation and Pre-SST. Front. Environ. Sci. 9:665394. doi: 10.3389/fenvs.2021.665394

In this study, a K-means clustering (KMC) method was used to identify the paths of the Northeast China (NEC) Cold Vortex (NCCV). The NCCV was divided into four types according to the identified active paths: (1) Eastward movement type (EM); (2) Southeastward long-distance movement type (SLM); (3) Eastward short-distance movement type (ESM); and (4) Southward short-distance movement type (SSM). The characteristics of the four types of the NCCV, along with their impacts on the precipitation during early summer in NEC, were studied. The results showed that the KMC method can effectively divide the NCCV events into four different types. The maintaining days of these four types of the NCCV were found to have obvious interannual and interdecadal variation features. For example, the maintaining days of the EM and ESM types were mainly characterized by interannual variability, while the SLM and SSM types have the obvious 10–13a interdecadal variation along with interannual variability. In terms of the spatial distributions and impacts on precipitation, the EM type was found to appear in the majority of the areas located in NEC, the SLM type mainly occurred in the northwestern region of NEC and the highest rain center was located in the south-central portion, while the ESM type and SSM type were observed precipitation only appear in a small portion of the northeastern region. In addition, it is also observed the distribution of the sea-surface temperature (SST) anomalies had close relationship with the formation of these four types of the NCCV. The tripole distributions of the SST anomalies in the Atlantic Ocean corresponded to the EM type of the NCCV, the positive anomalies of SST in the eastern equatorial Pacific Ocean and negative anomalies in the western equatorial Pacific corresponded to the SLM type, the positive SSTs in the Northwest Pacific correspond to the ESM type, while negative anomalies SST in the western equatorial Pacific Ocean corresponded to the SSM type of the NCCV.

Keywords: Northeastern China, NCCV, early summer months, precipitation levels, interannual variations

INTRODUCTION

Northeast China (NEC) located in the middle and high latitude areas of Northeast Asia, which includes Heilongjiang Province, Jilin Province, Liaoning Province, and the eastern portion of the Inner Mongolia Autonomous Region. The total area of NEC accounts for 13% of the entire country. The region is characterized by mountains and water bodies, as well as vast expanses of fertile land. NEC is considered to be an important commodity grain base, animal husbandry base, forestry base, and heavy industry base in China. The Northeastern China Cold Vortex (NCCV) is a special and important weather system which impacts the region. As an important cutoff low-pressure system affecting NEC, its activities are also key factors involved in the flood, drought, and low-temperature damages which may occur (Sun and An, 2001; Sun et al., 2002; Wang et al., 2007). The NCCV not only has major impacts on the weather and climate conditions in NEC, but its peripheral activities are also of major significance for the weather and climate conditions in eastern China and even Eastern Asia (Sun, 1997; Liu et al., 2002; Lian et al., 2016).

The NCCV can potentially appear during any season, and the activities of the NCCV change significantly among the seasons. Generally speaking, the NCCV system is more active during the summer months, with the most frequent activities of the NCCV occurring in June. Its activities are characterized by mass occurrences and persistence (Zhang and Li, 2009; Shen et al., 2011). The statistical data collected by Liu et al. (2015) revealed that from May to August, the NCCV activities have obvious spatial distribution characteristics, and the main active areas tend to be concentrated in the region of 121 to 131°E, 48 to 53°N. In addition, the previous research results have indicated that under the control of the persistent NCCV in local regions of NEC, the localized precipitation tend to be high in the spring and summer seasons (Hu et al., 2011). In addition, Ding et al. (2019) pointed out that the weak NCCV is one of the reasons for the unusually high summer temperature in China in 2018. Lian et al. (2010) and Liu et al. (2017) proposed that NCCV precipitation has also has significant "cumulative effects," which are generally reflected in the distribution characteristics of the precipitation anomalies in NEC during the early summer months. In addition, there has been found to be a significant positive correlation between the intensity levels of the NCCV during the summer and the precipitation levels in the Huaihe River Basin during the same periods (Li et al., 2015). Combined with the close relationship between the NCCV and precipitation in China, meteorologists have also carried out extended research and development of summer climate prediction methods (Feng et al., 2001; Fan and Wang, 2010; Gong et al., 2014; Liu and Ren, 2015; Ren et al., 2019). Zhao et al. (2015) found that the dynamical-statistical combining principle can more accurately grasp the summer NCCV trend, providing a strong diagnosis basis for precipitation prediction.

Liang et al. (2009) found through statistical examinations that the spatial distributions of the NCCV are quite different during different seasons. For example, during the early spring (April), the NCCV concentration areas are generally in the north portion of the NEC, which is located at approximately 52°N. However, at the end of the spring season and the beginning of the summer season, the high-frequency areas of NCCV activities will potentially reach the southernmost point of the region, or at approximately 43°N. Fang et al. (2020) found that there is a significant relationship between the interannual anomalies of the south-north positions of the NCCV and the Sea Surface Temperatures (SSTs) During the Early Summer Periods. Liu et al. (2015) found through in-depth analysis of the NCCV activities that there were obvious spatial distribution characteristics for the NCCV from May to August. The concentration areas of longitude circle activity ranged between 121 and 131°E, and the concentration areas of parallel circle activity ranged between 48 and 53°N. Xie and Bueh (2015) got meaningful conclusions on the research of the classification of circulation patterns. From the perspective of research progress to date, there has few studies on the effective classification of the activity range of the NCCV, and the relevant research on its influencing effects and mechanism require further investigation.

The previous studies have generally focused on the climate impacts of all the NCCV processes (Yang et al., 2012; Xie and Buhe, 2016). However, due to the obvious differences in the causes and variation characteristics of the NCCV, as well as its different impacts on climatic conditions in different regions of NEC during early summer, this study considered that the current findings were not enough to meet the urgent need for refined climate predictions in NEC if the NCCV was studied only as a whole. Therefore, this study carried out a classified study based on the characteristics of the activity paths of the NCCV, and then analyzed the climatologic characteristics of the different paths of the NCCV and their impacts on the precipitation in NEC during early summer. The goal of this study was to further the understanding of the causes of the NCCV, as well as potentially providing important references for the cause diagnoses and refined predictions of the NCCV anomalies.

DATA AND METHOD

This study's investigations were mainly based on (1) The daily precipitation observation data of 245 stations in NEC from June of 1979 to June of 2018, which were provided by the National Meteorological Information Center. (2) NCEP/NCAR reanalysis dataset, variables are monthly mean wind field and geopotential height, the grid resolution is 2.5° × 2.5°. (3) Sea surface temperature (SST) data from Hadley Centre, the grid resolution is 1° × 1°, This study classified the NCCV activity paths during the early summer months in NEC by adopting a K-means clustering method (K-Means, KM) (Fang et al., 2020). We use wavelet analysis, correlation analysis and significance testing in this study. The timeframe of study selected in this investigation ranged from June of 1979 to June of 2018.

K-Means Clustering Method (K-Means, KM)

K-means clustering originated from the field of signal processing and belongs to the category of unsupervised clustering in

machine learning clustering analysis methods. The Euclidean distance is used to measure the similarity between samples, and data clustering is performed according to the degree of similarity. These methods are widely used in many fields due to their intuitive and fast characteristics (Fang et al., 2021).

The definition of the NCCV index: The absolute values of the field anomaly calculations of the lowest potential height fields in the inner circles of the NCCV occurrence days from June of 1979 to June of 2018. The adopted index calculation method was not only able to accurately reflect the number of cold vortex days, but also represented the intensities of cold vortex centers. At the same time, the cold vortex weather processes within the NEC region were transformed into a climate time scale.

Screening of the NCCV Parameters

The objective identification data of the NCCV processes during the early summer months in the study area were collected, including the duration times, longitudes, latitudes, geopotential heights of the NCCV centers, NCCV radii, and so on. The NCCV processes were screened by the factors of the occurrence times and durations of the NCCV. In the present study, the occurrence time condition of the NCCV was that the process contained at least one record in June, and the duration condition of the NCCV was that the total duration of the process was 72 h in length. The screened NCCV processes were then used as the research samples.

Calculations of the Path Description Parameters of the NCCV Samples

The longitudes and latitudes (source information), radial variances, zonal variances, meridional mean values, latitudinal mean values, diagonal variances (moving directions and distances of the NCCV), and the longitude and latitude of the NCCV process tracks within the geographical range of NEC (relationships between tracks and the geographical locations of NEC) were calculated, respectively. The aforementioned parameters were preliminarily used to describe the activity paths of the NCCV. In addition, other parameters which could be utilized to characterize the properties of the NCCV were also added according to the actual needs of the investigation. The formula was as follows:

$$\overline{X} = \frac{\sum_{i=1}^{n} x_i}{n} \tag{1}$$

$$\overline{Y} = \frac{\sum_{i=1}^{n} y_i}{n} \tag{2}$$

$$Var(x) = \frac{\sum_{i=1}^{n} (x_i - \overline{X})^2}{n} \tag{3}$$

$$Var(y) = \frac{\sum_{i=1}^{n} (y_i - \overline{Y})^2}{n} \tag{4}$$

$$Var(xy) = \frac{\sum_{i=1}^{n} (x_i - \overline{X})(y_i - \overline{Y})}{n} \tag{5}$$

Where x_i and y_i represent the longitude and latitude at time i on the NCCV paths, and n indicates the times of the positioning.

Objective Classifications of the NCCV Paths

Prior to using the KMC method to classify the NCCV activity paths, the values of the number of classifications K were first determined. Then, taking the path parameters obtained in Step 2 as the data set, combined with relevant research findings and expert opinions, the 2–7 initial classification numbers were preliminarily determined in this study in order to calculate the silhouette coefficients corresponding to 2–7 initial classification numbers, respectively. It was found that the closer the silhouette coefficient was to 1, the more reasonable the classification number. Therefore, the optimal classification numbers could be determined. This study's flow chart of KMC method was as **Figure 1**:

Since KMC clustering methods cannot determine the number of classifications independently, this study set the number of

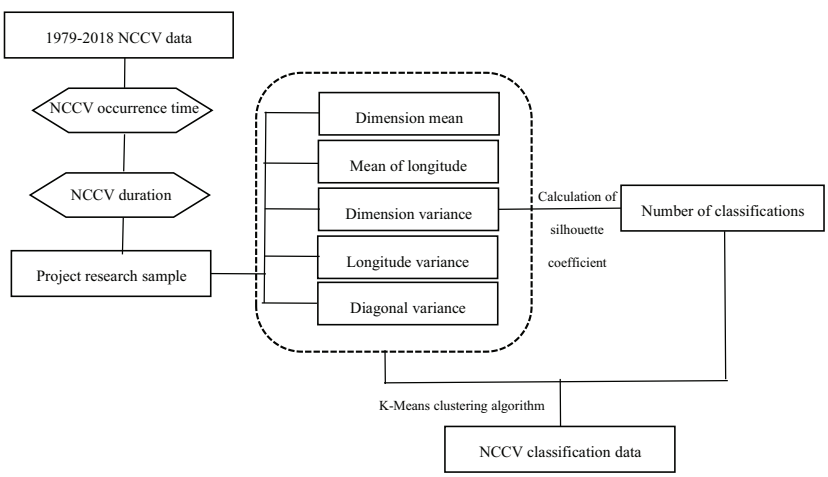

FIGURE 1 | Flow chart of the K-means clustering method for the NCCV path classifications.

clusters as integers between 2 and 9, and then compared the Silhouette Coefficients of the different clustering results. The Silhouette Coefficient is calculated by the dissimilarity degree between inside and outside of the cluster, and its value is between −1 and 1. The closer the value is to 1, the better the classification result is. Because it can show the cohesion and separation of clustering results, the Silhouette Coefficients are important parameters used to measure the clustering effects. The larger the Silhouette Coefficient, the better the classification effects (Wang et al., 2018).

Wavelet Analysis

Wavelet analysis is an important tool for periodic analysis processes (Lau and Weng, 1995; Torrence and Compo, 1998). The most commonly used methods in Morlet wavelet analysis processes are non-orthogonal wavelet methods. The general mathematical form of that method is as follows:

$$\varphi(t) = e^{-j\omega_0 t e^{\frac{1}{2}t^2}} \quad (6)$$

Where ω_0 represents the center frequency of a wavelet. Its Fourier Transform can be written as follows:

$$\phi(\omega) = \sqrt{2\pi e}^{-\frac{1}{2}(\omega-\omega_0)^2} \quad (7)$$

Morlet wavelets are a type of single frequency complex sinusoidal modulated Gaussian wave, and are also considered to be common complex valued wavelets. Their time-frequency domains have good locality.

STATISTICAL ANALYSIS OF THE CLIMATIC CHARACTERISTICS OF VARIOUS TYPES OF NCCV IN NEC

Activity Characteristics of Various NCCV Types in NEC

It was found that from the early summer months of 1979 to the early summer months of 2018, there were 97 NCCV processes which had effects in NEC. A total of 588 NCCV occurrence days were identified, with an average duration of 5.8 days. In the present study, based on a KMC method, the aforesaid 97 NCCV processes were divided into four categories according to the similarities and differences of their main evolution paths (Fang et al., 2021). **Figure 2** shows the spatial distributions of the activity path classifications of the NCCV in early summer. Among those, as can be seen in the figure, the Eastward movement type (EM) mainly occurred in the west, at the borders between eastern Inner Mongolia and Mongolia and Russia. The majority then disappeared near the Japanese Sea, with an activity scope covering the entire northeastern region. The southeastward long-distance movement type (SLM) mainly occurred in Baikal Lake area and its northwestern region, with the majority disappearing into the eastern part of Inner Mongolia and dying out. The

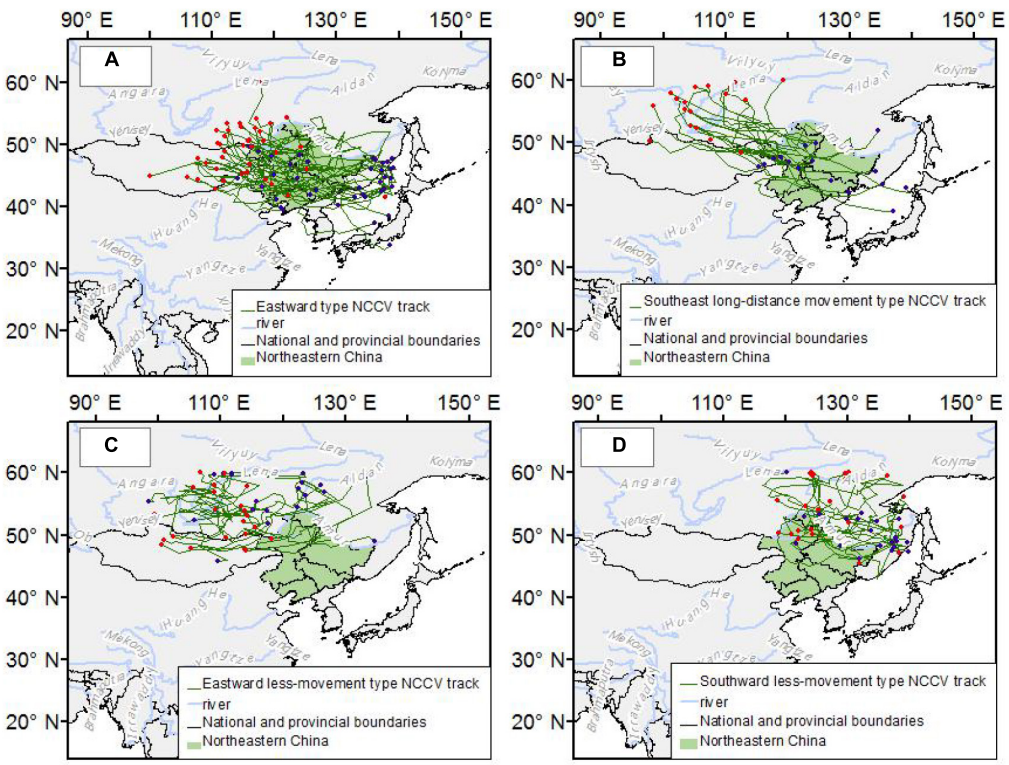

FIGURE 2 | Spatial distributions of the NCCV with four types of paths: **(A)** EM type; **(B)** SLM type; **(C)** ESM type; **(D)** SSM type.

activity range was found to be concentrated in the eastern section of Inner Mongolia and northeastern Mongolia. The eastward short-distance movement type (ESM) was found to be mainly generated in the northeastern section of Mongolia, and then disappeared into the northern region of the northwestern and northeastern Mongolia, with an activity scope covering the northwestern section of the study region. The southward short-distance movement type (SSM) mainly generated and disappeared in the northeastern section of the study area, with the activity range was found to be limited to the northeastern portion of the region. In the present study, from the perspective of the influencing effects of the NCCV, it was believed that the EM type may have affected the entirety of NEC. The SLM type had potentially mainly affected the central and northern areas of NEC, as well as the northwestern areas in particular. The ESM and SSM type were found to have little influence in NEC, with affects observed only in some parts of the northern areas of the NEC.

The activity characteristics of the four types of the NCCV are detailed in **Table 1**. The EM type NCCV was found to have the highest frequency of occurrence, as well as the longest duration times. It was identified for a total 23 occurrences, which accounted for 31.6% of the total frequency of occurrences during the early summer seasons. The average duration was 9.8 days. The SLM type NCCV had the lowest frequency of occurrence, accounting for 19.2% of the total frequency during the early summer months in the study area. In addition, the SSM type NCCV had the shortest duration, with an average duration of 5.8 days.

It was found that according to the wavelet analysis spectrum for the durations of the four types of NCCV from June of 1979 to June of 2018 (**Figure 3**), the number of days of the EM type NCCV mainly averaged 4 to 8a prior to 2010, and a significant power spectrum was concentrated in 3 to 5a frequency band after 2010. In addition to the significant 2 to 3a period before and after the 2010s, there was also a significant interdecadal variation period observed for the SLM type NCCV. The interdecadal variation characteristics were 8 to 12a before 2000 and 10 to 14a after 2000. Then, after 2010, the ESM type NCCV displayed the interannual variation characteristics of 2 to 3a periods. The SSM type NCCV had interannual variations of 4 to 6a periods prior to 2000 and 10 to 14a interdecadal variations after 2000, with 2 to 3a significant periods observed around 2010. Therefore, the number of process days of the EM and ESM type NCCV were also characterized by the interdecadal variations of 10 to 13a as well as interannual periods.

TABLE 1 | Statistical characteristics of the four types of NCCV activities for the period ranging from June of 1979 to June of 2018.

Type of NCCV	Frequency	Number of NCCV days	Average duration of NCCV/(days)	Proportion of frequency (%)
All types	73	558	7.6	100
EM type	23	225	9.8	31.5
SLM type	14	112	8.0	19.2
ESM type	17	110	6.1	23.3
SSM type	19	111	5.8	26.0

Spatial Distributions of Duration Days of NCCV

Figure 4 details the spatial distributions of the number of occurrence days of the northeastern NCCV during the period ranging from June of 1979 to June of 2018. The EM type NCCV was observed to appear in the majority of the areas in NEC, and the high value areas of the number of duration days were mainly distributed in the central and southern sections of the region. The number of duration days reached the highest value at the junction of Liaoning and Jilin. Fang et al. (2020) found that when the SLM type NCCV occurred, the consistent results were that the temperature levels in NEC were relatively low. The high value areas of the number of duration days of the SLM and ESM type NCCV were consistently located in the northwestern sections of the region. It was found that when compared with the SLM type NCCV, the ESM type NCCV had a smaller scope of activity. In addition, the latter type only appeared in a small scope in NEC. The high value areas of the number of duration days of the SSM type NCCV were generally more eastward and northward than those of the other types. Therefore, the distributions of the number of duration days of the NCCV with different paths further indicated the activity scopes of the four types of NCCV, as well as the differences and relationships among the activity intensities.

INFLUENCING EFFECTS OF THE NCCV ON THE PRECIPITATION IN THE STUDY AREA

Distribution Patterns of the Precipitation

The influencing factors of terrestrial precipitation are numerous (Li, 2020). The main influencing factors of the precipitation during the early summer months (May to June) in NEC have been determined to be the effects of the NCCV (Shen et al., 2011). Gao and Gao (2018) analyzed the influencing effects of the NCCV on the summer precipitation levels in NEC in 2013 and pointed out that the NCCV played a major role in the abnormally high precipitation levels during that period of time. It has been found that from the perspective of interdecadal differences, some studies have theorized that the interdecadal variations of the NCCV could be considered as being closely related to the interdecadal variations of the summer precipitation patterns in NEC (Han et al., 2015).

In the present study, by synthesizing the precipitation data during the maintenance period (June of 1979 to June of 2018) of the various types of NCCV, it could be concluded that the overall precipitation pattern of the NCCV displayed the distribution characteristics of "more in the east and less in the west." The characteristics of the precipitation during the process of the eastward moving NCCV were found to be similar to the distribution characteristics of the overall NCCV precipitation, in

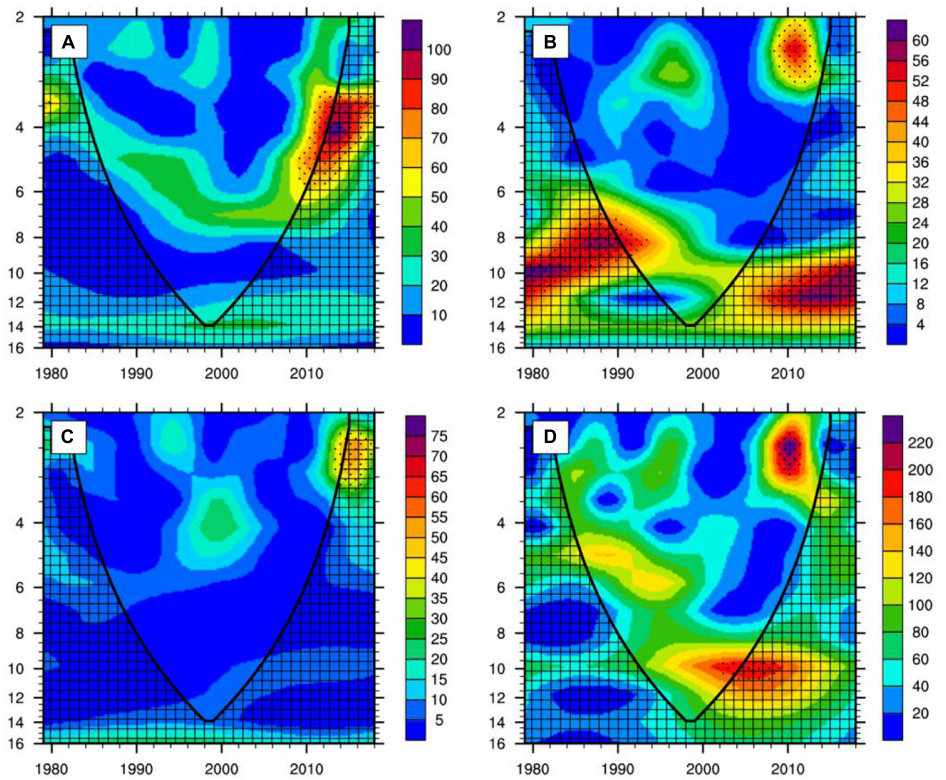

FIGURE 3 | The wavelet analysis spectrogram of the four types of NCCV during 1979–2018: **(A)** EM type; **(B)** SLM type; **(C)** ESM type; **(D)** SSM type.

that they also displayed the distribution characteristics of "more in the east and less in the west." However, the characteristics of the precipitation during the process of the SLM type NCCV revealed the meridional distribution characteristics of "more in the center and less in the east and west." In addition, it was found that the characteristics of the precipitation during the eastward short-range NCCV type process showed the meridional distribution characteristics of "more in the north and less in the south." These findings were observed to be consistent with the synthetic analysis results of Fang et al. (2020).

In the present research investigation, in order to further analyze the impacts of the NCCV with four types of paths on the precipitation patterns in NEC, the correlations between the four types of the NCCV indexes and the precipitation patterns during the maintenance period of various types of NCCV in early summer months from 1979 to 2018 were calculated. Due to the short length of data, the correlation results are mainly reflect interannual characteristics. The results are presented in **Figure 5**. It can be seen in the figure that there were significant differences in the influence ranges of the four types of the NCCV on the precipitation patterns in NEC. For example, when the EM type NCCV occurred, the range of the NCCV activity was mainly distributed in the central to southern areas of NEC. Overall, the central to the eastern sections of the NEC had more precipitation, as well as the rainy central areas located in the eastern portion of the region. It was observed that when the SLM type NCCV occurred, the high value areas of the number of the NCCV days were located in the northwestern section of NEC. Meanwhile, the central part of the region had more precipitation, and the rainy central area was located in the center of the southern section of the region. This was found to be consistent with the precipitation synthesis results of the four types of the NCCV. In addition, when the ESM type NCCV occurred, the activity scope of the NCCV was small in NEC, and there was a weak correlation observed between the NCCV indexes and the precipitation patterns of the region. However, when the SSM NCCV type occurred, the activity scope of the NCCV was found to be mainly in the northeastern section of the region, with more precipitation occurring in the south. From the above-mentioned data, it was concluded that the precipitation in NEC was obviously greater during the maintenance period of the four types of the NCCV, and there were consistent differences in the ranges of the precipitation. These distribution differences were found to have good corresponding relationships with the precipitation synthesis distributions and the activity ranges of the different types of NCCV.

Interannual Variation Characteristics of the Number of Precipitation Days

The days with daily precipitation of 0.1 mm and above were defined as the effective precipitation days. **Figure 6** shows the interannual variation sequences of the number of days in which rainstorms (daily precipitation greater than or equal to 50 mm);

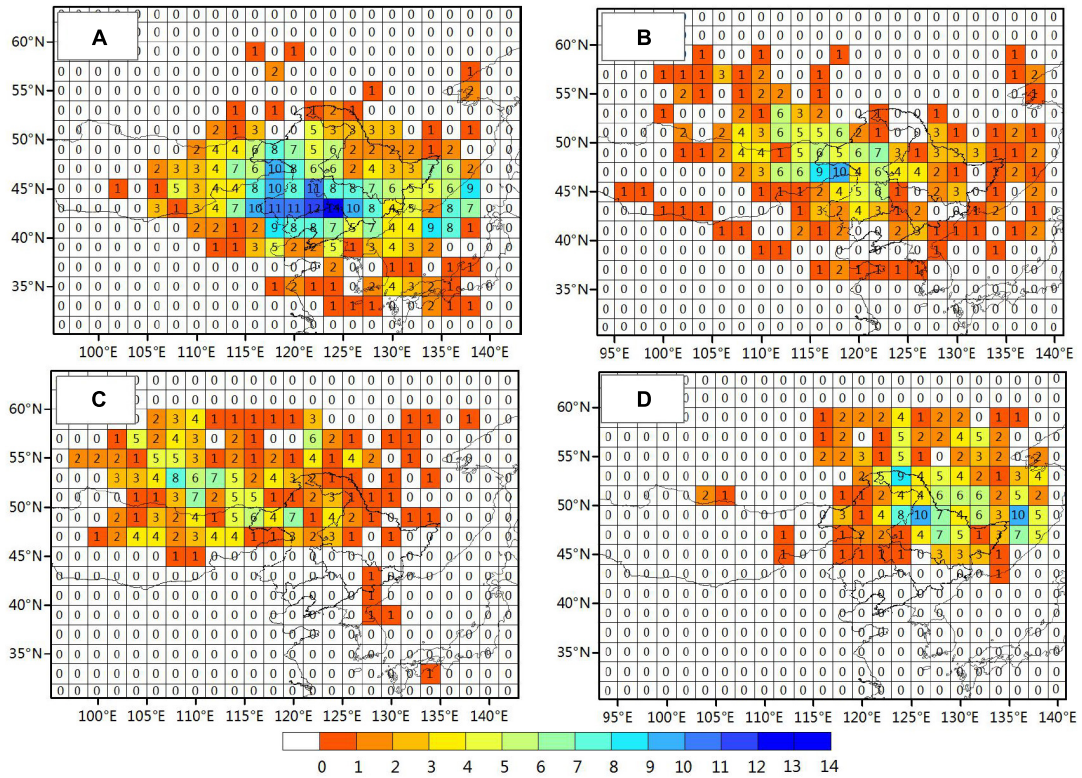

FIGURE 4 | Spatial distributions of duration days of the NCCV during 1979–2018 (unit: day): **(A)** EM type; **(B)** SLM type; **(C)** ESM type; **(D)** SSM type.

heavy rain (daily precipitation of 25 to 50 mm); moderate rain (daily precipitation of 10 to 25 mm); and light rain (daily precipitation of 0.1 to 10 mm) occurred during the maintenance period of the NCCV types (1 to 4) in the early summer months of the period ranging from 1979 to 2018. In order to filter out the interdecadal characteristics of more than 8 years, a 9-year moving average was determined for the sequences of the number of precipitation days at various orders of magnitude during the maintenance period of the four NCCV types. The filtered data were observed to exhibit many typical interannual variability characteristics. For example, it could be seen that there were significant interannual variation characteristics in the sequences of the number of precipitation days at various orders of magnitude during the maintenance period of the four NCCV types, and the interannual variation trends of the number of precipitation days at various orders of magnitude were found to be generally consistent. Among those, the number of precipitation days at various orders of magnitude was found to be the highest during the maintenance period of the EM type NCCV. This was followed by the number of precipitation days during the maintenance period of the SLM type NCCV. In addition, it was determined that the number of precipitation days at the various orders of magnitude was the least during the maintenance period of the EM type NCCV. Also, there were observed to be good correspondence relationships between the number of precipitation days corresponding to the four NCCV types and their corresponding activity ranges. That is to say, the EM type NCCV had the widest activity range in NEC and had caused the highest number of precipitation days at the various orders of magnitude. Meanwhile, only a small portion of the ESM type NCCV had passed through the northern part of the NEC, which resulted in the least number of precipitation days at the various orders of magnitude in NEC.

During the maintenance period of the EM and southeast long-distance movement NCCV types, the interannual growth trends of the number of precipitation days at the various orders of magnitude were not obvious. It was found that during the maintenance period of the ESM type NCCV, the precipitation at the various orders of magnitude had displayed a certain growth trend. In particular, a growth trend of light rain days was the most obvious, while the growth trend of heavy rain days had been the weakest. During the maintenance period of the SSM type NCCV, there was a certain decreasing trend observed in the precipitation at various orders of magnitude, with the exception of the occurrences of heavy rain events. A decreasing trend in the light rain days was the most obvious, and the decreasing trend of rainstorm days was observed to be the weakest.

Spatial Distributions of the Precipitation Occurrence Days

The distributions of the number of precipitation days at various orders of magnitude generated by the NCCV types with different paths were also found to differ. **Figures 7–9** show the

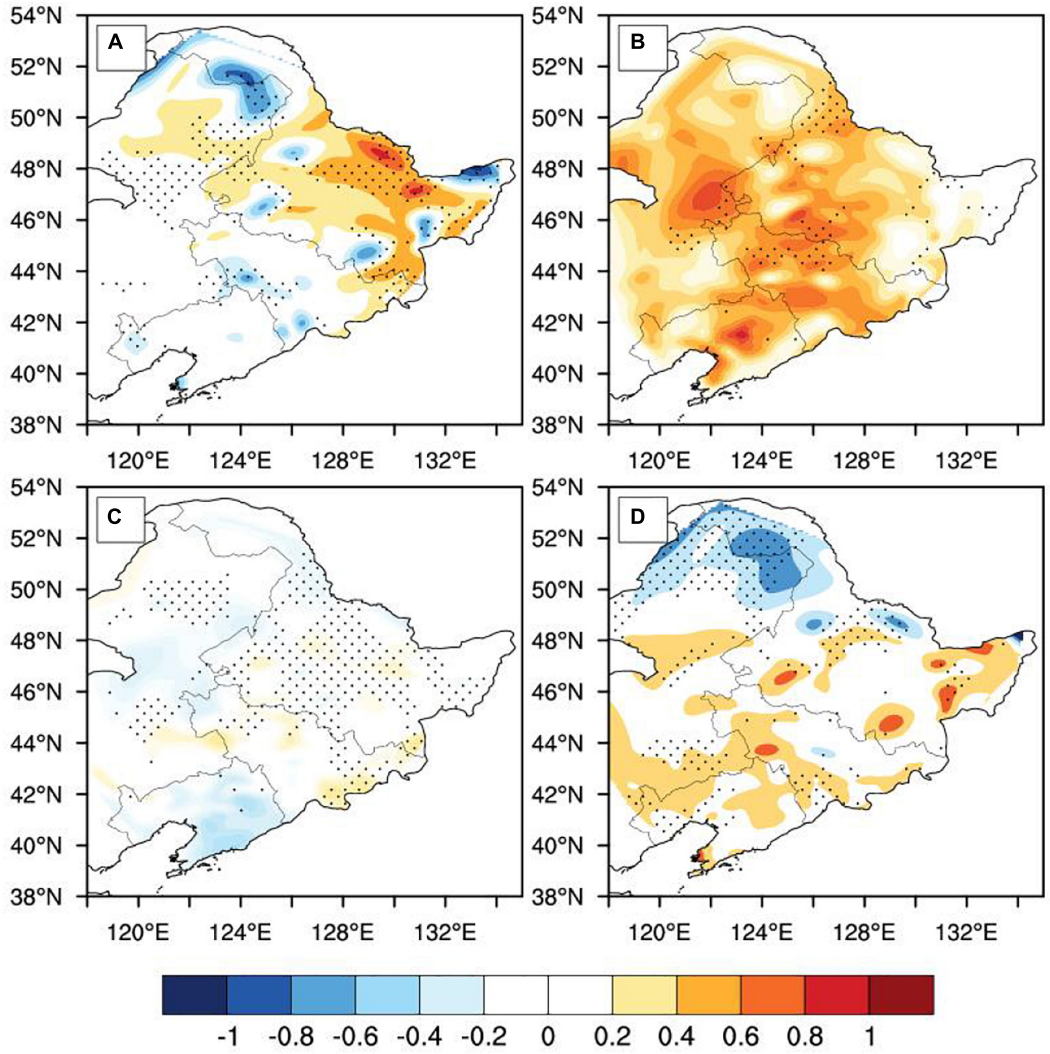

FIGURE 5 | Distribution of the correlation coefficients between the NCCV index and precipitation anomalies in NEC during all the NCCV maintaining days ranging from 1978 to 2018: **(A)** EM type; **(B)** SLM type; **(C)** ESM type; **(D)** SSM type. In the figure, the dotted areas indicate the areas passed the 95% significance test.

distributions of the number of precipitation days at various orders of magnitude during the maintenance period of the four NCCV types for the period ranging from June of 1979 to June of 2018. It can be seen in the figures that the main differences in the precipitation of four NCCV types were reflected in the number of light rain days and moderate rain days. It was determined that during the maintenance period of the EM type NCCV, the number of light rain and moderate rain days was higher in the southeast section of the NEC. In addition, during the maintenance period of the SLM type NCCV, the number of days in which light rain and moderate rain occurred was consistent in the majority of the areas of NEC, and especially in northwestern China. During the maintenance period of the ESM type NCCV, the days in which light rain and moderate rain had occurred were greater in the northwestern and eastern sections of the NEC. During the maintenance period of the SSM type NCCV, the number of days of light rain and moderate rain were greater in the northeastern area of the region. These findings were found to correspond well with the activity paths of the four types of the NCCV.

RELATIONSHIPS BETWEEN THE FOUR NCCV TYPES AND THE SST

Fang et al. (2021) completed a great deal of relevant research regarding the analysis of the circulation characteristics corresponding to the four types of the NCCV. It was found that there were obvious differences in the atmospheric circulation configurations of the NCCV with four types of paths when the origins of the generations were considered. For example, it was found that they were consistent with the activity paths of the NCCV. The circulation configurations of the total days, as well as the peak value

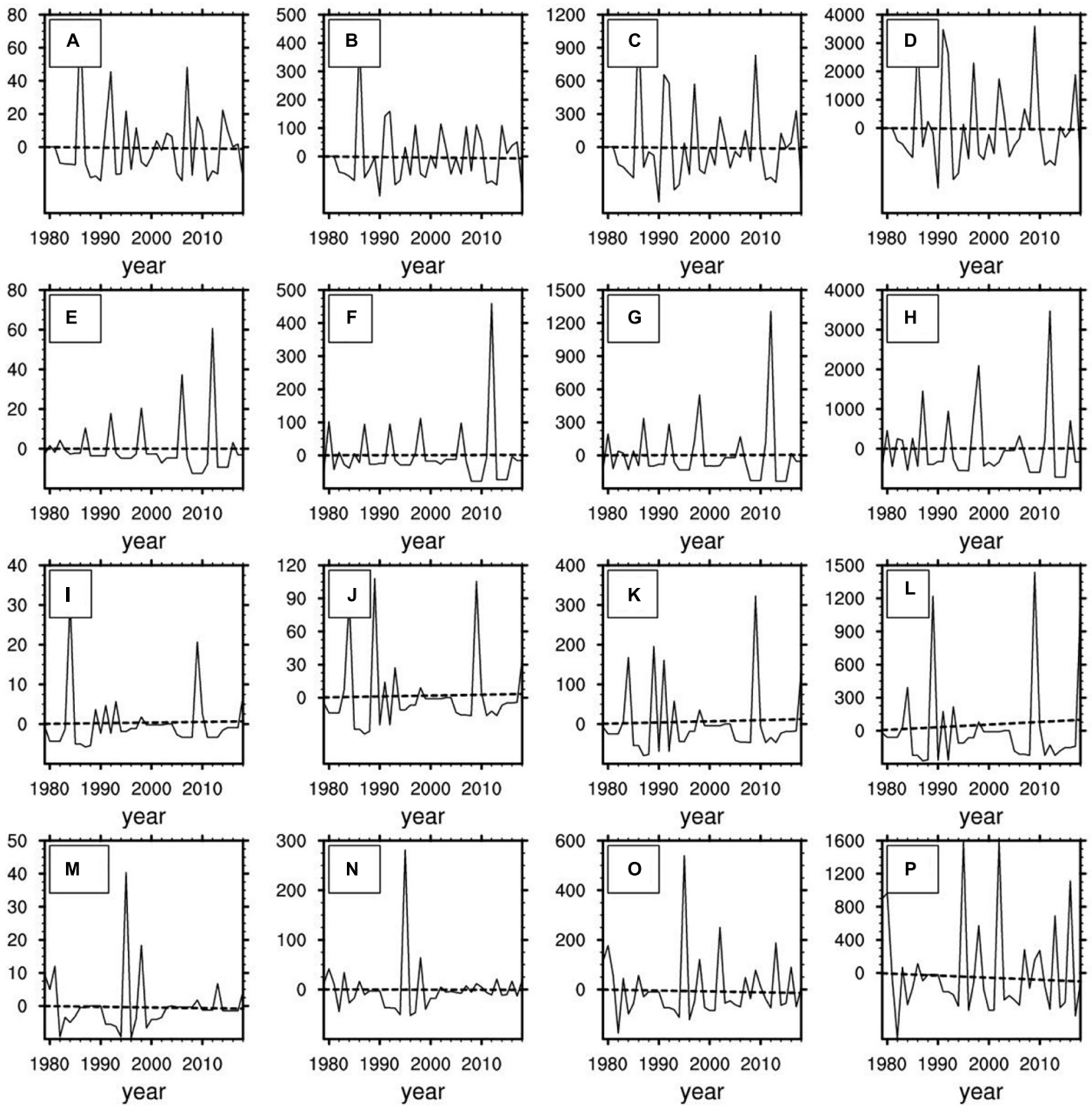

FIGURE 6 | Interannual variation sequences of the precipitation anomalies at various magnitude levels for these four types of NCCV events ranging from 1979 to 2018 (unit: mm): **(A,E,I,M)** Rainstorms; **(B,F,J,M)** Heavy rain; **(C,G,K,O)** Moderate rain; **(D,H,L,P)** Light rain.

days, of the NCCV processes with four types of paths were also observed to match well with the NCCV activity paths. This study focused on the analysis of the correlation relationships between the four types of NCCV processes and the previous SSTs.

Figure 8 shows the distributions of correlation coefficients between the NCCV indexes from 1979 to the early summer of 2018, along with the SST anomalies during the early period (March to May). It can be seen in the figure that there were major differences in the distribution patterns of SST anomalies during the early period which corresponded to the four types of NCCV. For example, when there were abnormally more EM and SSM type NCCV during the early summer months, the SSTs in the Equatorial Central Pacific Ocean had also been higher during the early spring months, which were reflected by the CP type ENSO SST distribution characteristics. However, when there were abnormally more SLM type NCCV during the early summer months, it was observed that the SSTs in the Equatorial Pacific Ocean during the early spring months had displayed the EP type ENSO sea surface distribution characteristics of "higher in the

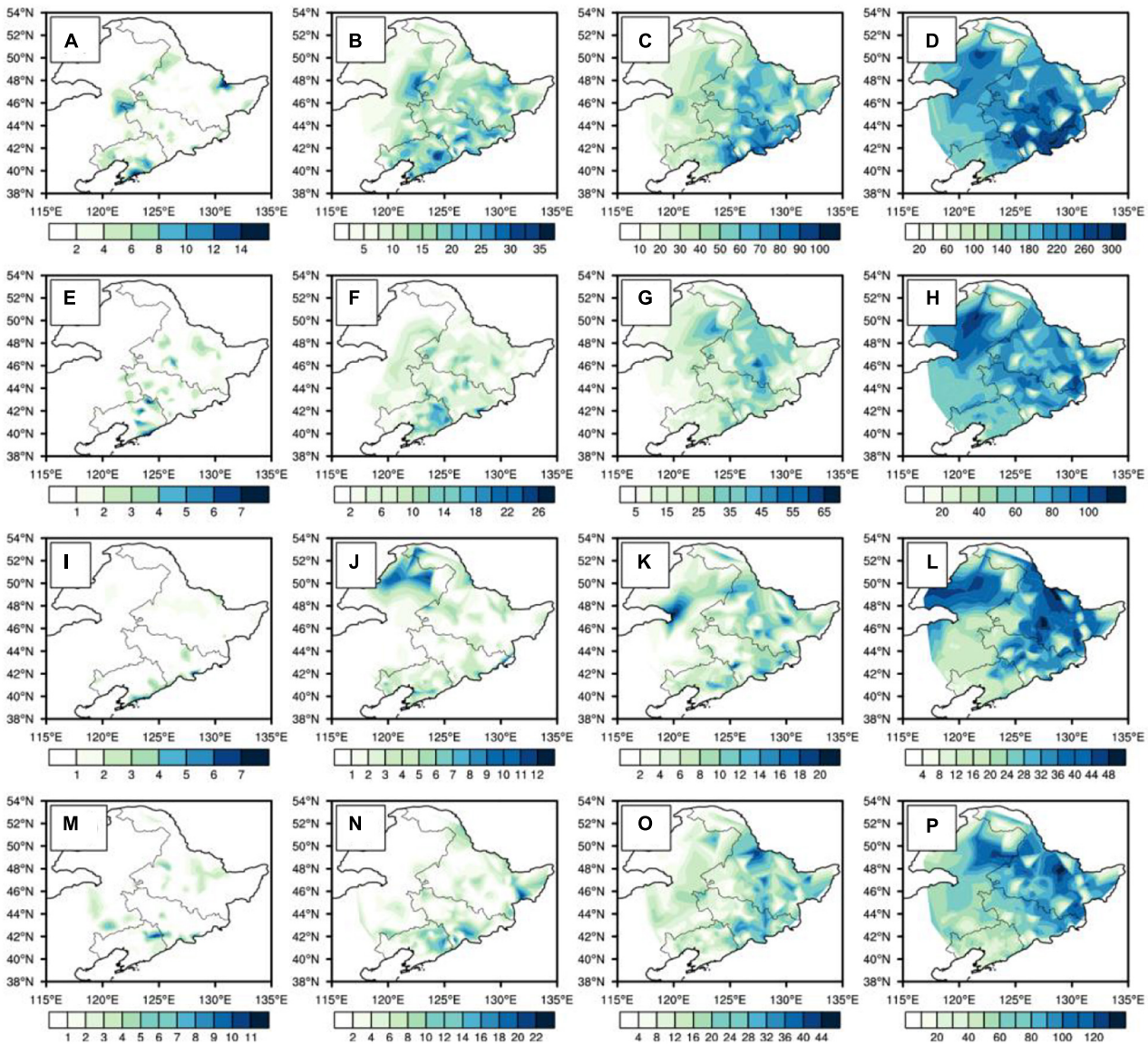

FIGURE 7 | Spatial distribution of the raining days corresponding to various precipitation levels during the NCCV maintaining days ranging from 1979 to 2018 (unit: day): **(A,E,I,M)** Rainstorms; **(B,F,J,M)** Heavy rain; **(C,G,K,O)** Moderate rain; **(D,H,L,P)** Light rain.

east and lower in the west," and the positive anomaly center was located in the Equatorial Eastern Pacific Ocean.

There were also significant differences observed in the SSTs over the Atlantic Ocean region. For example, when there were abnormally more EM, ESM, and SSM type NCCV observed, the North Atlantic Ocean had presented a negative-positive-negative distribution characteristics of a "tri-pole" during the early spring months. Meanwhile, the SST anomalies in the North Atlantic Ocean during the early spring months were not significant when there was more SSM type NCCV.

This study found that the SSTs of the Indian Ocean showed the distribution characteristics of "positive in the west and negative in the east" of the Indian Ocean positive dipole when the EM type NCCV occurred. However, when the SLM and SSM type NCCV occurred, it was found that the Indian Ocean had large-scaled positive SST anomalies. In particular, the anomalies were more obvious when the SLM type NCCV occurred. Also, when the ESM type NCCV occurred, the Indian Ocean was found to have large-scaled negative SST anomalies.

Fang et al. (2018) carried out diagnostic analysis and numerical simulation processes in order to determine the causes of the precipitation anomalies in NEC during early summer months. It was pointed out that the anomalies in the SST tri-pole of the North Atlantic Ocean, along with the SSTs of the Kuroshio area, had resulted in anomalies of the high pressure circulation system due to the blocking of the upstream and downstream NCCV. It was theorized that this blockage affected the NCCV precipitation during the early summer months in

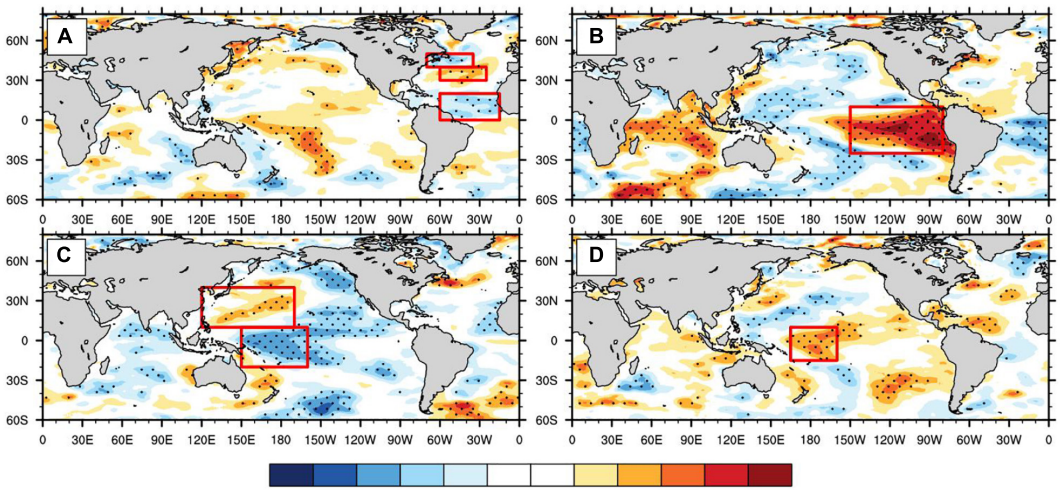

FIGURE 8 | Spatial distribution of the correlation coefficients between the summer NCCV indexes and the proceeding spring SST anomalies during 1979–2018. **(A)** EM type; **(B)** SLM type; **(C)** ESM type; **(D)** SSM type. Dotted areas indicate the 99% confidence level.

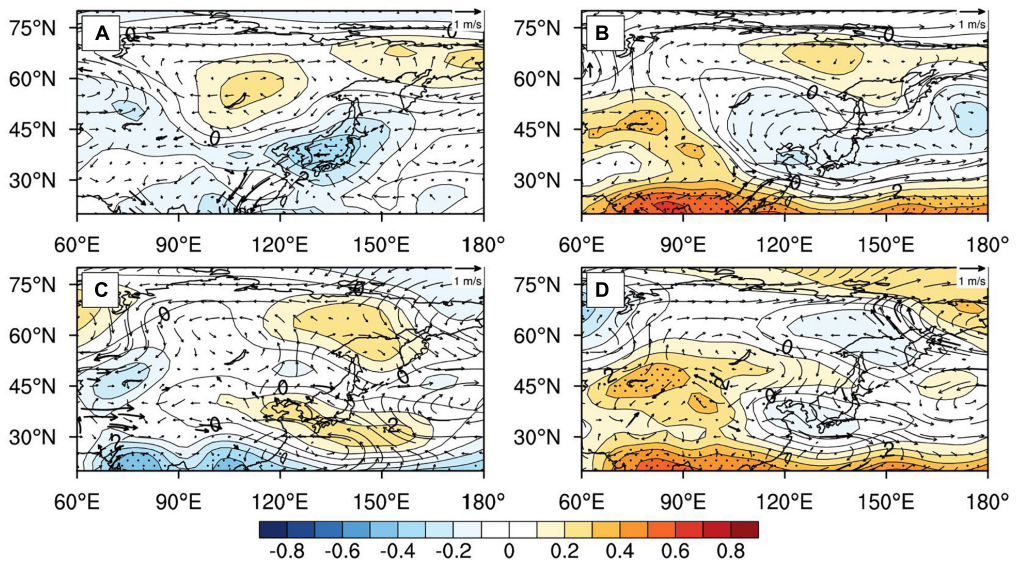

FIGURE 9 | Spatial distribution of regression coefficients of early winter 500 hPa height (contour) and 850 hPa wind (vectors) anomalies against the key area SST indices corresponding to the four types of the NCCV during 1979–2018. **(A)** EM type; **(B)** SLM type; **(C)** ESM type **(D)** SSM type. Dotted areas and bold arrows indicate the 99% significance level.

NEC. It was found that the sensitivity tests of numerical models could be used to verify the effects of the SSTs during the earlier periods on the atmospheric circulation processes of the early summer months. Buhe and Xie (2013) summarized the deep dynamic causes for the formation and maintenance of the various types of NCCV and found that the Western Pacific (WP) teleconnection patterns were the downstream background circulation patterns of the NCCV activities, and the negative phases were conducive to the generation and maintenance of the NCCV.

In the present study, in order to further clarify the differences in the influencing effects of different types of SST areas on four types of the NCCV, the characteristic indexes of the early SST anomalies corresponding to the four types of the NCCV were first calculated. These included the Pacific CP type ENSO SST index (the mean SST values of the region [165°E−160°W; 15°S−10°N]); the Pacific EP type ENSO SST index (the mean SST values of the region [80−150°W; 20°S−10°N]); Western Pacific SST positive anomaly index (the mean SST values of the region [150°W−160°E; 20°S−10°N]); Atlantic tri-pole index (the differences in the mean SST values between the region [25°−60°W; 30°−40°N] and the region [15°−60°W; 0°−20°N] and [35°−70°W; 40°−50°N]); and the Indian Ocean positive dipole

index (the differences in the mean SST values between the region [40°−80°E; 0°−30°S] and the region [80°−120°E; 0°−30°S]). The results of the regression analysis of the aforementioned indices with the circulation fields of June which corresponded to the four types of the NCCV revealed that the circulation fields of the SST regression in the following four key areas corresponded well to the NCCV circulation situations, which had certain physical significance. Therefore, this study selected the SST of the following four key areas. The tri-pole type SST of the Atlantic Ocean was taken as the characteristic SST region corresponding to the EM type NCCV. In other words, the differences in the mean SST values between the region [25°−60°W; 30°−40°N] and the region [15°−60°W; 0°−20°N] and [35°−70°W; 40°−50°N] (red box area in **Figure 8A**) from March to May were defined as the SST index N1. Similarly, the mean SST values of the eastern Equatorial Pacific Ocean region [80°−150°W; 20°S−10°N] (red box area in **Figure 8B**) from March to May were selected and defined as the characteristic SST index N2 of the SLM type NCCV. Subsequently, the differences in the mean SST values between the Equatorial Northwestern Pacific Ocean region [120°E−170°W; 10°−40°N] and the Equatorial Western Pacific Ocean region [150°E−160°W; 20°S−10°N] (red box region in **Figure 8C**; red box area in **Figure 8B**) from March to May were defined as the characteristic SST index N3 of the ESM type NCCV. Finally, the mean SST values of the Equatorial Pacific Ocean region [165°E−160°W; 15°S−10°N] (red box area in **Figure 8D**) from March to May were defined as the characteristic SST index N4 of the SLM type NCCV.

The atmospheric circulation configurations of the four types of NCCV are quite different (Fang et al., 2021). The four types NCCV corresponded to the following circulation configurations: The interaction type between the Okhotsk Sea blockage and the eastern low vortex of the Mongolian Plateau (EM); the interaction type between the Yenisei River blockage and the low vortex of the upper reaches of the Lena River (SLM); the interaction type between the Obi River blockage and Okhotsk Sea-Japan Sea blockage and the low vortex of Baikal Lake (ESM); and the interaction type between the Central Siberia-East Siberia blockage and southern low vortex in East Siberia (SSM). Then, the circulation fields of the four types of NCCV in the month of June from 1979 to 2018 were regressed to the four types of SST indexes, as detailed in **Figure 9**. It can be seen in the figure that the EM type NCCV corresponded to the abnormally high SSTs in the North Pacific Ocean during the early summer months, resulting in an anticyclonic circulation pattern near Lake Baikal in the early summer and a cyclonic circulation pattern in NEC and its southwestern portion. The generated wind fields were conducive to the NCCV moving from its source to the southwest. These findings were in good agreement with the moving path of the EM type NCCV. During the early stages of the SLM type NCCV, the SSTs in the Equatorial Eastern Pacific Ocean region were abnormally high, which caused the easterly airflow of the source location (upstream of the Lena River) in the northern section of the cyclonic circulation. Therefore, the conditions were not conducive to the movement of the NCCV to the southeast. Furthermore, during the early stages of the ESM type NCCV, it was observed that the SSTs in the Equatorial Western Pacific Ocean region were abnormally low, which caused the NCCV source location (near Lake Baikal) to be controlled by the cyclonic circulation. As a result, the southwestern airflow into the southeast of the circulation assisted the NCCV to move to the northeast, which was consistent with the moving path of the ESM type NCCV. In addition, during the early stages of the SSM type NCCV, the abnormally high SSTs in the Equatorial Western Pacific Ocean region caused the Mongolia area to be controlled by the anticyclone circulation processes. Therefore, since the source location of the NCCV (south of East Siberia) had been affected by the northwest airflow, the conditions were conducive to the NCCV moving to the southeast. These findings were consistent with the moving paths of the SSM type NCCV.

CONCLUSION AND DISCUSSION

In this study, we try to classify the NCCV into different types according to their active path by using the KMC method (Fang et al., 2020). The climatic characteristics of these types of NCCV and their impacts on the precipitation over NEC were analyzed. It is also revealed the distribution of the sea-surface temperature (SST) anomalies had close relationship with the formation of these four types of the NCCV. Main conclusion are listed as follows:

(1) The KMC method can effectively divide the NCCV events into four different types according to the identified active paths and durations: (i) Eastward movement type (EM); (ii) Southeastward long-distance movement type (SLM); (iii) Eastward short-distance movement type (ESM); and (iv) Southward short-distance movement type (SSM). The characteristics of the four types of the NCCV, along with their impacts on the precipitation during early summer in NEC, were studied. The maintaining days of these four types of the NCCV were found to have obvious interannual and interdecadal variation features. For example, the maintaining days of the EM and ESM types were mainly characterized by interannual variability, while the SLM and SSM types have the obvious 10–13a interdecadal variation along with interannual variability.

(2) Climatic features of four types of the NCCV events exist significant differences and their impacts on the precipitation anomalies in NEC also present obvious differences. The activity range of the EM type covered the entire NEC. This type was found to have the highest occurrence frequency and longest maintenance days with the high value area mainly distributed in the central-south area of NEC. The activity range of the SLM type was concentrated in the eastern Inner Mongolia and northeastern Mongolia. This type had the lowest occurrence frequency. The ESM type was found to only have a small activity range concentrated in the northwestern region of NEC with the high value area of maintenance days located near Arxan??? The activity range of the SSM type was found to be limited to the northeastern region of Heilongjiang Province. This type had the least

number of maintenance days with large value distributed in the northern Heilongjiang.

(3) Four types of NCCV events had different impacts on the precipitation patterns in NEC. For example, when the EM type occurred, the rainy center mainly located in the eastern part of NEC. The SLM type bring more precipitation in the central part of the NEC. When the ESM type NCCV occurred, it was observed that there was a weak correlation between the NCCV index and the precipitation in NEC. In addition, when the SSM type NCCV occurred, there was generally more precipitation in the northern area of the region. Therefore, this study revealed that the EM and SLM (especially the former type) should be mainly considered when analyzing the impacts of the NCCV events on precipitation patterns in NEC.

(4) Four types of NCCV events were found to have different impacts on precipitation days at various magnitude levels in NEC. The interannual growth trends of precipitation days were not found to be obvious during the maintenance duration of the EM and SLM types. During the maintenance period of the ESM type, the precipitation days displayed a certain growth trend at various magnitude levels, while the SSM type displayed a certain weakening trend. The main differences of precipitation feature among these four types of NCCV events mainly existed in the light rain and moderate rain levels.

(5) The distributions of the SST anomalies which had significant correlation with the four NCCV types were also observed to be quite different from each other. It was found close relationships existed between the circulation fields and the moving paths of the four NCCV types under different SST backgrounds. For example, the Atlantic Ocean tripole distribution of the SSTs corresponded well with the EM type NCCV. The rises of the SSTs in the Equatorial Eastern Pacific Ocean correspond well with the SLM type. Besides, the abnormally low SSTs in the Equatorial Western Pacific Ocean and high SSTs in the Northwestern Pacific Ocean had significant correlation with the ESM type NCCV. Similarly, the abnormally low SSTs in the Equatorial Western Pacific Ocean present the close relationship with the SSM type of NCCV events.

Based on previous similar studies, the Atlantic SST anomalies can induce atmospheric diabatic heating, which stimulates quasi-barotropic mid- to high-latitude Rossby wave trains to the downstream along a parallel circle through the sea-air interactions, which caused the formation of circulation configuration as high resistance on the northwest and southeast sides of Lake Baikal high with NCCV coordination circulation. It is beneficial to the occurrence and development of the NCCV. For The cold vortexes affected by the Pacific SST, by blocking the upstream circulation, atmospheric circulation anomalies such as the EU teleconnection are formed, which causes the anomaly of NCCV in early summer.

This paper only analyze the influence of SST, but in fact, both sea ice and land may affect atmospheric circulation and thus affect the NCCV.

DATA AVAILABILITY STATEMENT

The original contributions presented in the study are included in the article/supplementary material, further inquiries can be directed to the corresponding author/s.

AUTHOR CONTRIBUTIONS

Y-HF contributed to the data collection and classification of NCCV. M-MZ, C-YZ, Z-QG, X-YZ, and W-QZ contributed to the data processing and analysis. All authors contributed to the article and approved the submitted version.

FUNDING

This work was jointly supported by the National Key Research and Development Program of China (2018YFC1507702 and 2018YFC1505601); National Natural Science Foundation of China (Grant Nos. 42005037 and 42075057); Special Project of Innovative Development, CMA (CXFZ2021J022 and CXFZ2021Z034); Liaoning Provincial Natural Science Foundation Project (Ph.D. Start-up Research Fund 2019-BS-214); and Research Project of the Institute of Atmospheric Environment, CMA (2020SYIAE08).

REFERENCES

Buhe, C., and Xie, Z. W. (2013). Northeastern China cold vortex circulation and its dynamical features. *Adv. Meteorol. Sci. Technol.* 3, 34–39.

Ding, T., Yuan, Y., Zhang, J., and Gao, H. (2019). 2018 the hottest summer in China and possible causes. *J. Meteorol. Res.* 33, 577–592. doi: 10.1007/s13351-019-8178-y

Fan, K., and Wang, H. J. (2010). Seasonal prediction of summer temperature over Northeast China using a year-to-year incremental approach. *Acta Meteor. Sin.* 24, 269–275.

Fang, Y. H., Chen, H. S., Lin, Y., Zhao, C. Y., Lin, Y. T., and Zhou, F. (2021). Classification of the Northeast China cold vortex activity paths in early summer based on K-means clustering and their climate impact. *Adv. Atmos. Sci.* 38, 400–412. doi: 10.1007/s00376-020-0118-3

Fang, Y. H., Chen, K. Q., Chen, H., Xu, S.-Q., Geng, X., and Li, T.-Y. (2018). The remote responses of early summer cold vortex precipitation in northeastern china compared with the previous sea surface temperatures. *Atmos. Res.* 214, 399–409. doi: 10.1016/j.atmosres.2018.08.007

Fang, Y. H., Lin, Y. T., Ren, H. L., Zhao, C. Y., Zhou, F., Li, Q., et al. (2020). Possible relationships between the interannual anomalies of the south-north positions of the northeastern china cold vortexes and the sea surface temperatures (SSTs) during the early summer periods. *Front. Earth Sci.* 8:557014.

Feng, G. L., Hongxing, C., Xinquan, G., Wenjie, D., and Jifan, C. (2001). Prediction of precipitation during summer monsoon with self-memorial model. *Adv. Atmos. Sci.* 18, 701–709. doi: 10.1007/bf03403495

Gao, J., and Gao, H. (2018). Influence of the Northeast cold vortex on flooding in Northeast China in summer 2013. *J. Meteor. Res.* 32, 172–180. doi: 10.1007/s13351-018-7056-3

Gong, Z. Q., Zhao, J. H., Feng, G. L., and Fan, C. J. (2014). Dynamic-statistics combined forecast scheme based on the abrupt decadal change component of summer precipitation in East Asia. *Sci. China Earth Sci.* 58, 404–419. doi: 10.1007/s11430-014-4967-4

Han, T., Chen, H., and Wang, H. (2015). Recent changes in summer precipitation in Northeast China and the background circulation. *Int. J. Climatol.* 35, 4210–4219. doi: 10.1002/joc.4280

Hu, K. X., Lu, R. Y., and Wang, D. H. (2011). Cold Vortex over NEC and its climate effect. *Chin. J. Atmos. Sci.* 35, 179–191.

Lau, K. M., and Weng, H. Y. (1995). Climate signal detection using wavelet transform. How to make a time series sing. *Bull. Amer. Meteor. Soc.* 76, 2391–2402. doi: 10.1175/1520-0477(1995)076<2391:csduwt>2.0.co;2

Li, C., Han, G. R., and Sun, Y. (2015). Anomalous features of Northeast cold vortex in late 50a and its correlation with rainfall in Huaihe river valley. *J. Meteorol. Sci.* 35, 216–222.

Li, Q. X. (2020). Statistical modeling experiment of land precipitation variations since the start of the 20th century with external forcing factors. *Chin. Sci. Bull.* 65, 2266–2278. doi: 10.1360/tb-2020-0305

Lian, Y., Buhe, C., Xie, Z. W., Shen, B. Z., and Li, S. F. (2010). The anomalous cold vortex activity in Northeast China during the early summer and the low-frequency variability of the Northern hemispheric atmosphere circulation. *Chin. J. Atmos. Sci.* 34, 429–439.

Lian, Y., Shen, B., Li, S., Liu, G., and Yang, X. (2016). Mechanisms for the formation of Northeast China cold vortex and its activities and impacts. An overview. *J. Meteor. Res.* 30, 881–896. doi: 10.1007/s13351-016-6003-4

Liang, H., Wang, Y., and Guo, Z. Q. (2009). :The teleconnection relationship between the northeast cold vortex and the subtropical high, the Okhotsk high in summer. *J. Meteorol. Sci.* 29, 793–796.

Liu, G., Feng, G. L., Qin, Y. L., Zeng, Y. X., Yang, X., and Yao, S. (2017). "Cumulative Effect" of Cold Vortex precipitation in Northeast China in early summer. *Chin. J. Atmos. Sci.* 41, 202–212.

Liu, G., Lian, Y., Yan, P. C., Zeng, Y. X., Yang, X., and Cao, L. (2015). The objective recognition and classification of Northeast Cold Vortex and the Northern hemisphere atmospheric circulation characters in May to August. *Sci. Geogr. Sin.* 35, 1042–1050.

Liu, Y., and Ren, H. L. (2015). A hybrid statistical downscaling model for prediction of winter precipitation in China. *Int. J. Climatol.* 35, 1309–1321. doi: 10.1002/joc.4058

Liu, Z. X., Lian, Y., Gao, Z. T., Sun, L., and Shen, B. Z. (2002). Analyses of the Northern hemisphere circulation characters during Northeast Cold Vortex persistence. *Chinese J. Atoms Sci.* 26, 361–372.

Ren, H.-L., Yujie, W., Bao, Q., Ma, J., Liu, C., and Wan, J. (2019). China multi-model ensemble prediction system version 1.0 (CMMEv1.0) and its application to flood-season prediction in 2018. *J. Meteorol. Res.* 33, 542–554.

Shen, B. Z., Lin, Z. D., Lu, R. Y., and Lian, Y. (2011). Circulation anomalies associated with interannual variation of early and late summer precipitation in Northeast China. *Sci China Earth Sci.* 41, 402–412.

Sun, L. (1997). A study of the persistence activity of Northeast Cold Vortex in China. *Chinese J. Atoms Sci.* 21, 297–307.

Sun, L., and An, G. (2001). A diagnostic study of Northeast Cold Vortex heavy rain over the Songhuajiang-Nenjiang river basin in the summer of 1988. *Chin. J. Atmos. Sci.* 25, 342–354.

Sun, L., An, G., Gao, C. T., Tang, X. L., Ding, L., and Shen, B. Z. (2002). A composite diagnostic of heavy rain caused by the Northeast Cold Vortex over Songhuajiang-Nenjiang river basin in the summer of 1988. *J. Appl. Meteorol. Sci.* 13, 156–162.

Torrence, C., and Compo, G. P. (1998). A practical guide to wavelet analysis. *Bull. Amer. Meteor. Soc.* 79, 61–78.

Wang, D. H., Zhong, S. X., Liu, Y., Li, J., Hu, K. X., and Yang, S. (2007). Advances in the study of rainstorm in Northeast China. *Adv. Earth Sci.* 22, 549–560.

Wang, M., Abrams, Z. B., Kornblau, S. M., and Coombes, K. R. (2018). Thresher: determining the number of clusters while removing outliers. *BMC Bioinformatics* 19:9. doi: 10.1186/s12859-017-1998-9

Xie, Z. W., and Bueh, C. (2015). Different types of cold vortex circulations over Northeast China and their weather impacts. *Mon. Weather Rev.* 43, 845–863. doi: 10.1175/mwr-d-14-00192.1

Xie, Z. W., and Buhe, C. (2016). Cold vortex events over Northeast China associated with the Yakutsk-Okhotsk blocking. *Int. J. Climatol.* 37, 381–398. doi: 10.1002/joc.4711

Yang, H. Y., Feng, G. L., and Shen, B. Z. (2012). The quantitative research on cold vortex in summer over Northeast China. *Chin. J. Atmos. Sci.* 36, 487–494.

Zhang, L. X., and Li, Z. C. (2009). A summary of research on cold vortex over Northeast China. *Clim. Environ. Res.* 14, 218–228.

Zhao, J. H., Yang, L., Hou, W., Liu, G., and Zeng, Y. X. (2015). Extra-seasonal prediction at summer 500 hPa height field in the area of cold vortices over East Asia with a dynamical- statistical method. *Chin. Phys. B* 24:059202. doi: 10.1088/1674-1056/24/5/059202

Conflict of Interest: The authors declare that the research was conducted in the absence of any commercial or financial relationships that could be construed as a potential conflict of interest.

frontiers in Environmental Science

ORIGINAL RESEARCH
published: 29 April 2021
doi: 10.3389/fenvs.2021.656794

Development and Assessment of the Monthly Grid Precipitation Datasets in China

Jiadong Peng[1,2], Lijie Duan[1], Wenhui Xu[3] and Qingxiang Li[4]†*

[1]Climate Center of Hunan Province, Changsha, China, [2]Key Laboratory of Hunan Province for Meteorological Disaster Prevention and Mitigation, Changsha, China, [3]National Meteorological Information Center, Beijing, China, [4]School of Atmospheric Sciences, Sun Yat-sen University, and Key Laboratory of Tropical Atmosphere–Ocean System, Ministry of Education, Zhuhai, China

Based on the high-quality homogenized precipitation data from all 2,419 national weather stations in China, the climatology and anomaly percentage fields are derived, and then the digital elevation model (DEM) is employed to reduce the influence of elevation on the spatial interpolation accuracy of precipitation due to the unique topography in China. Then, the gradient plus inverse distance squared (GIDS) method and the inverse distance squared (IDS) method are used to grid the climatology field and the anomaly percentage field, respectively, and the 0.5 × 0.5° gridded datasets during 1961–2018 in China are obtained by combining them together. The evaluation shows that the mean absolute error (MAE) between the analysis value and the observation is 15.8 mm/month. The MAE in South China is generally higher than that in North China, and the MAE is obviously larger in summer than in other seasons. Specifically, 94.6, 54.4, 4.6, and 53.8% of the MAE are below 10 mm/month in winter (DJF), spring (MAM), summer (JJA), and autumn (SON), respectively, and 99.5, 79.9, 22.8, and 82.1% of them are less than 20 mm/month. The MAE over China in four seasons is 3.8, 13.2, 33.5, and 12.7 mm/month, respectively. This dataset has the potential of broad application prospects in the evaluations of weather and climate models and satellite products.

Keywords: China, precipitation, GIDS, IDS, gridded dataset, accuracy evaluation

OPEN ACCESS

Edited by:
Folco Giomi,
Independent researcher, Milan, Italy

Reviewed by:
Nathaniel K. Newlands,
Agriculture and Agri-Food Canada (AAFC), Canada
Shahzada Adnan,
Pakistan Meteorological Department, Pakistan

****Correspondence:***
Qingxiang Li
liqingx5@mail.sysu.edu.cn

†Present address:
Southern Laboratory of Ocean Science and Engineering (Guangdong Zhuhai), Zhuhai, China

Specialty section:
This article was submitted to Interdisciplinary Climate Studies, a section of the journal Frontiers in Environmental Science

Received: *21 January 2021*
Accepted: *09 April 2021*
Published: *29 April 2021*

Citation:
Peng J, Duan L, Xu W and Li Q (2021) Development and Assessment of the Monthly Grid Precipitation Datasets in China. Front. Environ. Sci. 9:656794. doi: 10.3389/fenvs.2021.656794

INTRODUCTION

In the study of global or regional large-scale climate change, it is necessary to grid the climate series to effectively reduce or avoid spatial sampling errors (Shen et al., 2010; Wu and Gao, 2013; Zhao et al., 2014; Zhao and Zhu, 2015; Cheng et al., 2020). Precipitation is one of the most important meteorological elements. High-resolution gridded precipitation data are important input parameters for atmospheric, climatic, hydrological, and ecological models, and they are necessary for the evaluations of numerical forecast products. However, due to the geographical conditions and the shortage of meteorological observations, it may be difficult to obtain the accurate regional area precipitation amount in certain areas. Despite the difficulties, several daily or monthly precipitation series have been developed on regional scales in China in the past 30–100 years (Xie et al., 2007; Shen et al., 2010; Li et al., 2012; Wu and Gao, 2013; Zhao et al., 2014). However, a series of problems, such as the low density of stations, the uneven distribution of stations, the quality of raw data, and the inadequacy of interpolation methods, lead to the systematic evaluation on the gridded precipitation datasets still being open to discussion, especially using higher quality observation and more state-of-the-art interpolation methods.

Generally speaking, the accuracy of spatial gridded precipitation data depends not only on the interpolation methods but also on the observation station density, the geographical location, the climatic characteristics, and the impact systems of precipitation, and varies with seasons (Dai et al., 1997; Xie et al., 2007; Yatagai et al., 2009; Peng et al., 2019). Most of the gridded precipitation datasets over China used only hundreds of stations in total due to the data access limits, which will make it difficult to further reduce the accuracy of precipitation gridding (Chen et al., 2002; Hong et al., 2005). The other high-resolution datasets emphasized the improvement of the spatial distribution of stations but did not consider the inhomogeneity due to inconsistent observational schedules in different years, relocations of stations, *etc*., which will cause problems in long-term climate change trend detection (Shen et al., 2010; Wu and Gao, 2013; Zhao et al., 2014). In addition, topography, geomorphology, and underlying surface characteristics are also important factors that affect the accuracy of gridded data (Daly et al., 1994; Xiong et al., 2011). Due to the large spatial variability of precipitation, the error of direct interpolation is relatively large. Therefore, a climatology field with spatial continuity and with the influences of topography and geomorphology taken into consideration is usually constructed. Furthermore, a new element, such as precipitation difference Chen et al. (2002) or ratio Daly et al. (1994), is defined based on the climatology field for the spatial interpolation. Thereby, the interpolation error caused by the spatial discontinuity of precipitation can be reduced. It has been revealed that higher interpolation accuracy can be obtained by defining a ratio (Xie et al., 2007).

Therefore, based on the precipitation observation network in the currently highest density in Mainland China, the interpolation method through defining the anomaly percentage of monthly precipitation based on the climatology field is adopted in this study to generate a new monthly gridded precipitation dataset, and the systematic and random data errors of the gridded data are assessed with the cross-validation method. The remainder of this article is arranged as follows: *Data and Methods* introduces the main data sources, interpolation methods, and validation methods used to develop high-resolution gridded precipitation datasets in this study. The interpolation errors and validation results of climatology and anomaly data are presented in *Gridding Error Analysis*. *Conclusion and Discussion* provides final discussion and conclusions.

DATA AND METHODS

Data

The monthly precipitation data from the period of January 1961 to December 2018 from the 2,419 national meteorological stations in China (excluding Hong Kong, Macao, and Taiwan) are used in this study. This dataset has been systematically homogenized and updated by Chinese scientists Li et al. (2012), Yang and Li (2014), and the 30-year (1981–2010) climatology dataset is derived. The digital elevation model (DEM) of GTOPO30 is used for the interpolation of precipitation.

Gridding Method for Precipitation Data

There are various gridding methods for the meteorological data, with advantages and disadvantages in each one (Gyalistras 2003; Qiang et al., 2016). In the gridding of the climatology precipitation dataset, the accuracy of the spatial distribution of precipitation on various timescales (monthly and annual) should be ensured. More importantly, the interannual trend and inter-decadal changes of precipitation in each region should be maintained. That is, the gridded series should have "climate quality" and be uniform. Therefore, the climatic mean (i.e., multiyear average value and climatic background field) and the anomalies (i.e., deviations from the climatic mean) should be gridded separately. The gridding of climatic mean is relatively more complicated, since multiple factors such as topography must be taken into account. However, the gridding of anomalies is usually simpler, in which only the relative changes of precipitation at different moments (years and months) should be accurately described. Thus, the technical methods adopted are relatively simple.

In this study, the gridding of monthly precipitation data includes the following three steps. First, the gridded climatic background field of monthly precipitation is created. Then, the monthly precipitation ratio at each station is calculated and interpolated into the gridded field. The ratio is a new element defined based on the climatic background field, namely, the monthly precipitation anomaly percentage. Finally, the gridded monthly precipitation is generated by multiplying the gridded monthly precipitation anomaly percentage with the corresponding climatic background field.

Establishment of the Climatic Background Field

Precipitation is discontinuously distributed, but its climatic mean demonstrates spatial continuity. The analysis errors caused by spatial discontinuity can be reduced or eliminated by constructing a gridded precipitation field based on the climatic background field; thus, the spatial interpolation accuracy can be significantly improved. In addition, the influence of topography on precipitation cannot be ignored. However, there is no effective method to amend the topographic effect on precipitation in the world. In this study, the gradient plus inverse distance squared (GIDS) method is adopted to grid the climatic mean field (Nalder and Wein, 1998; Price et al., 2000; Li et al., 2019). The advantage of this method over the IDS method is the consideration of gradients of meteorological elements with elevation, longitude, and latitude. **Eq. 1** is as follows:

$$v(x) = \frac{\left[\sum_{i=1}^{n} \frac{v_i + (X - X_i) \times C_x + (Y - Y_i) \times C_y + (Z - Z_i) \times C_z}{d_i^2}\right]}{\left(\sum_{i=1}^{n} \frac{1}{d_i^2}\right)}, \quad (1)$$

where N is the number of samples used in the calculation, with the maximum value of 9 in this study. The distances between all the stations and the prediction point S are calculated, and the

stations with distance from S beyond 4° are excluded. Then, the stations nearest to S (9 stations at most) are selected for calculation. X, Y, and Z are the coordinate values (longitude, latitude, and elevation) of the prediction point, and X_i, Y_i, and Z_i are the coordinate values of the meteorological station i. C_x, C_y, and C_z are the regression coefficients between the meteorological element values and X, Y, and elevation Z, respectively. The regression coefficients are calculated by using X, Y, or elevation Z at all the stations and the corresponding meteorological element values through the multiple regression equation. d_i is the distance from the interpolation point to the station i, and 2 is the power of the distance. The calculations of gradients with elevation, longitude, and latitude are added in this formula based on the IDS method.

Precipitation varies significantly with elevation, and the gridded data with higher resolution are more favorable for amending the topographic effect. Therefore, the 0.05 × 0.05° DEM data in China are generated by resampling GTOPO30 data (30″ × 30″ resolution). At the same time, for better terrain correction, the climatic background field is first interpolated to the grid point of 0.05 × 0.05° to obtain more accurate and high-resolution gridded values by fully using the elevation information, and then the area average method is used to obtain the final required 0.5 × 0.5° data, similar to Cheng et al. (2020).

Generation of Precipitation Anomaly Percentage Gridded Field

To reduce the interpolation error caused by the spatial discontinuity of precipitation, the monthly precipitation anomaly percentage defined based on the climatology value is gridded using the IDS method, instead of direct interpolation of the precipitation data. The IDS method is a deterministic interpolation method based on the principle of close similarity; that is, the closer two objects are, the more similar their values are, and *vice versa* (Dai et al., 1997). **Eq. 2** of IDS is as follows:

$$v(s) = \frac{\left(\sum_{i=1}^{n} \frac{v_i}{d_i^2}\right)}{\left(\sum_{i=1}^{n} \frac{1}{d_i^2}\right)} \quad (2)$$

,

where V (s) is the predicted value at the location s, N is the number of samples used in the interpolation (i.e., the number of stations), V_i is the value at the station i (i.e., the value of meteorological elements such as temperature and precipitation), d_i is the distance from the interpolation point to the station i, and 2 is the power of the distance.

The resolution of 0.5 × 0.5° is adopted for the precipitation anomaly gridding and for the final precipitation dataset.

Generation of Gridded Precipitation Data

The gridded precipitation data for a certain month are the product of the gridded precipitation anomaly percentage and the corresponding climatic background field, with a spatial resolution of 0.5 × 0.5°. Finally, a gridded dataset of monthly precipitation from 1961 to 2018 is constructed.

Validation Method for the Dataset

Since the value of gridded data is averaged over the grid, it is difficult to directly observe the true value. Therefore, there is no widely recognized estimation method for the gridded data error. The cross-validation method is being widely used at present, in which the error is estimated by analyzing various cross-validation statistics. It should be noted that the commonly used cross-validation method does not apply all the observed data to estimate the error, and as a result, the error is overestimated in some degree. On the other hand, a high correlation between the observation data and the gridded data may lead to underestimation of error. Even so, cross-validation is still the primary method used to analyze the gridded data error at present (Xiong et al., 2011).

Two cross-validation methods for the dataset are adopted in this study. In the first method, about 10% of the stations are removed randomly, similar to Jones et al. (2009). Then, the GIDS method is used to grid the climatology precipitation value, and the gridded value is interpolated to the removed 10% of the stations with the same method. The interpolated values are compared with the actual climatology values at these stations to obtain the errors. The same routine is repeated ten times with different stations removed each time, and the cross-validation errors at all the stations are obtained. Since only 90% of the data are used for grid interpolation, the accuracy of grid data is underestimated to a certain extent. However, the computation of interpolation with high spatial–temporal resolution, especially the cross-validation considering elevation, is very large. The method of keeping 10% of the station data for cross-validation is to limit the number of grid data calculations to 10 times in the process of the test, so as to keep the amount of calculation within a reasonable range. In the second method, a certain station is first removed, and then, the precipitation anomaly percentage is interpolated from the surrounding stations to this station with the IDS method. The interpolated value is compared with the actual value to obtain the errors and the correlation coefficients. The precipitation value at each station is derived by compositing the climatology value and the anomaly percentage obtained through the first method and the second method, and the cross-validation errors of precipitation are obtained by comparing the composited value with the actual value. The methods for assessment of cross-validation errors include mean absolute error (MAE) and root mean square error (RMSE).

The topography in China is complex, with obvious climatic contrast among different regions. To investigate the cross-validation errors of the gridding method described above in different climatic regions in China, the entire continent of China is divided into eight climatic regions. The distribution of meteorological stations and elevation in different regions is shown in **Figure 1**, and the climatological monthly precipitation of each region is shown in **Figure 2**. The precipitation in South China, East China, Southwest China, and Central China is the most, followed by Northeast and North China, and the precipitation in the Qinghai-Tibet Plateau and Northwest China is the least. The precipitation in JJA is the largest in a year for each region.

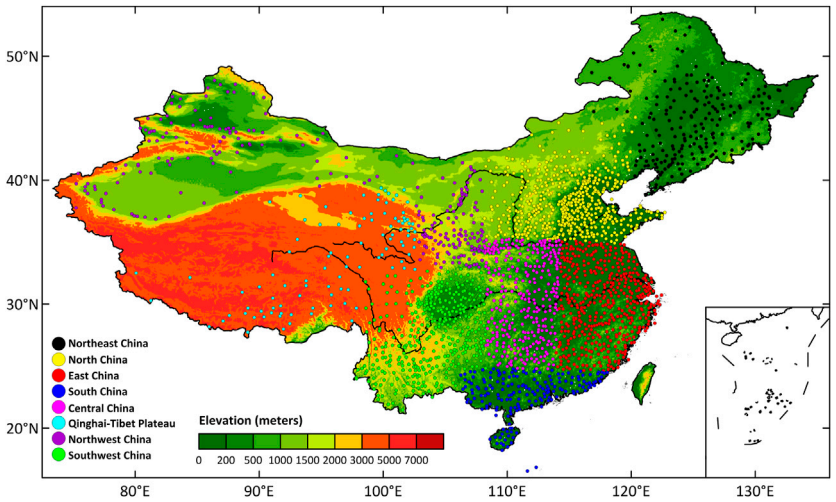

FIGURE 1 | Distribution of meteorological stations and elevation in different regions of China.

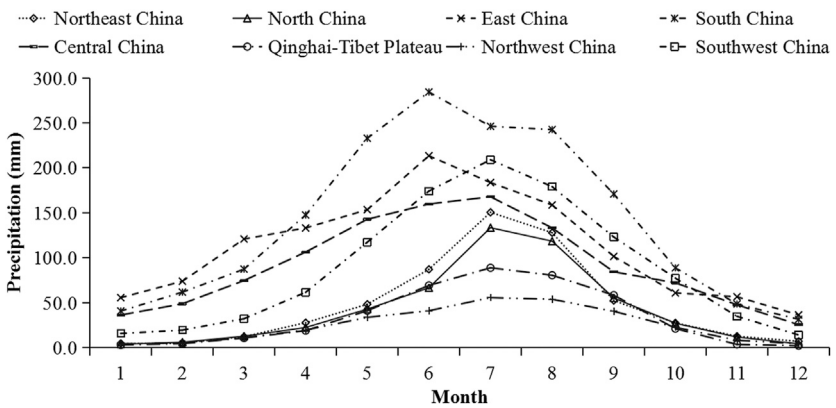

FIGURE 2 | Climatological monthly precipitation of each region in China.

GRIDDING ERROR ANALYSIS

Gridding Error Analysis of Climatology Precipitation Value

Tables 1,**2** show the MAE and RMSE of cross-validation for the climatology precipitation value, respectively. It is indicated that the large errors are mainly distributed in South China and Southwest China, while the errors in Northeast China, North China, and Northwest China are relatively small (black marks in **Tables 1**,**2**). This is closely related to the abundance degree of precipitation in different regions, especially in South China and Southwest China, and the large undulation of topography in Southwest China. However, the precipitation amount in the Qinghai–Tibet region is low, but the error is relatively large, which can be attributed to the sparse meteorological stations in this region. According to the temporal distribution, the errors in each region from June to August are significantly higher than those in other months (black marks in **Tables 1**,**2**), which is closely related to the concentrated rainfall in this period.

Figure 3 shows the spatial distributions of the MAE in each season. It can be seen that the MAE in southern regions is generally higher than that in northern regions in each season; 79.8, 55.7, 23.6, and 54.9% of the MAE are below 3 mm/month in DJF, MAM, JJA, and SON, respectively, and 96.6, 85.4, 59.8, and 86.3% of them are less than 10 mm/month. The MAE is 2.0, 5.6, 13.2, and 5.4 mm/month in DJF, MAM, JJA, and SON, respectively, with the error being largest in JJA. Throughout the whole year, the MAE for 53.5 and 82.0% of the samples is lower than 3 and 10 mm/month, respectively (**Figure 4**).

TABLE 1 | MAE of cross-validation for the climatology value (unit: mm).

Month / Region	1	2	3	4	5	6	7	8	9	10	11	12
Northeast China	0.8	1.2	1.9	2.7	3.4	**5.5**	**11.4**	**8.9**	4.8	2.8	1.7	1.2
North China	0.5	0.6	1.0	1.3	2.4	**4.4**	**8.8**	**8.1**	3.5	1.6	1.0	0.5
East China	3.5	3.8	5.0	5.0	7.5	**12.7**	**14.2**	**15.4**	10.5	4.5	3.6	2.5
South China	4.1	5.8	8.8	13.5	25.6	**31.2**	**27.6**	**21.4**	14.8	10.8	6.6	3.4
Central China	2.9	3.5	4.6	5.6	8.7	**11.4**	**14.1**	**12.2**	6.5	5.2	3.0	2.0
Qinghai–Tibet Plateau	1.8	2.9	5.9	6.6	9.4	**13.8**	**12.4**	**11.7**	10.8	5.9	1.6	1.2
Northwest China	1.2	1.3	2.5	3.8	5.4	**5.9**	**7.4**	**7.3**	4.7	3.5	2.2	1.4
Southwest China	2.9	3.3	4.8	6.2	11.9	**20.3**	**24.1**	**22.0**	14.5	9.7	4.4	2.6

Bold value shows : According to the temporal distribution, the errors in each region from June to August are significantly higher than those in other months, which is closely related to the concentrated rainfall in this period.

TABLE 2 | RMSE of cross-validation for the climatology value (unit: mm).

Month / Region	1	2	3	4	5	6	7	8	9	10	11	12
Northeast China	1.2	2.6	3.5	4.2	5.5	**7.5**	**16.6**	**13.0**	7.2	4.8	2.6	1.9
North China	0.7	0.9	1.4	1.9	3.3	**6.0**	**14.4**	**12.2**	4.8	2.3	1.9	0.8
East China	5.8	7.1	7.8	7.4	11.2	**19.0**	**19.7**	**26.1**	18.4	7.3	6.3	4.1
South China	6.8	8.8	14.8	19.3	36.3	**42.9**	**38.2**	**31.3**	20.8	21.1	12.1	6.0
Central China	4.4	5.5	7.3	9.4	14.5	**20.9**	**22.3**	**17.1**	9.9	8.8	4.5	3.3
Qinghai–Tibet Plateau	5.2	7.7	12.4	11.9	13.3	**20.3**	**18.3**	**18.7**	17.3	10.7	2.7	3.7
Northwest China	2.2	2.2	4.2	7.1	9.8	**10.3**	**13.4**	**12.5**	7.4	5.5	4.3	2.8
Southwest China	4.3	5.6	9.1	10.9	17.4	**29.6**	**35.3**	**31.9**	20.8	14.1	6.2	3.8

Bold value shows : According to the temporal distribution, the errors in each region from June to August are significantly higher than those in other months, which is closely related to the concentrated rainfall in this period.

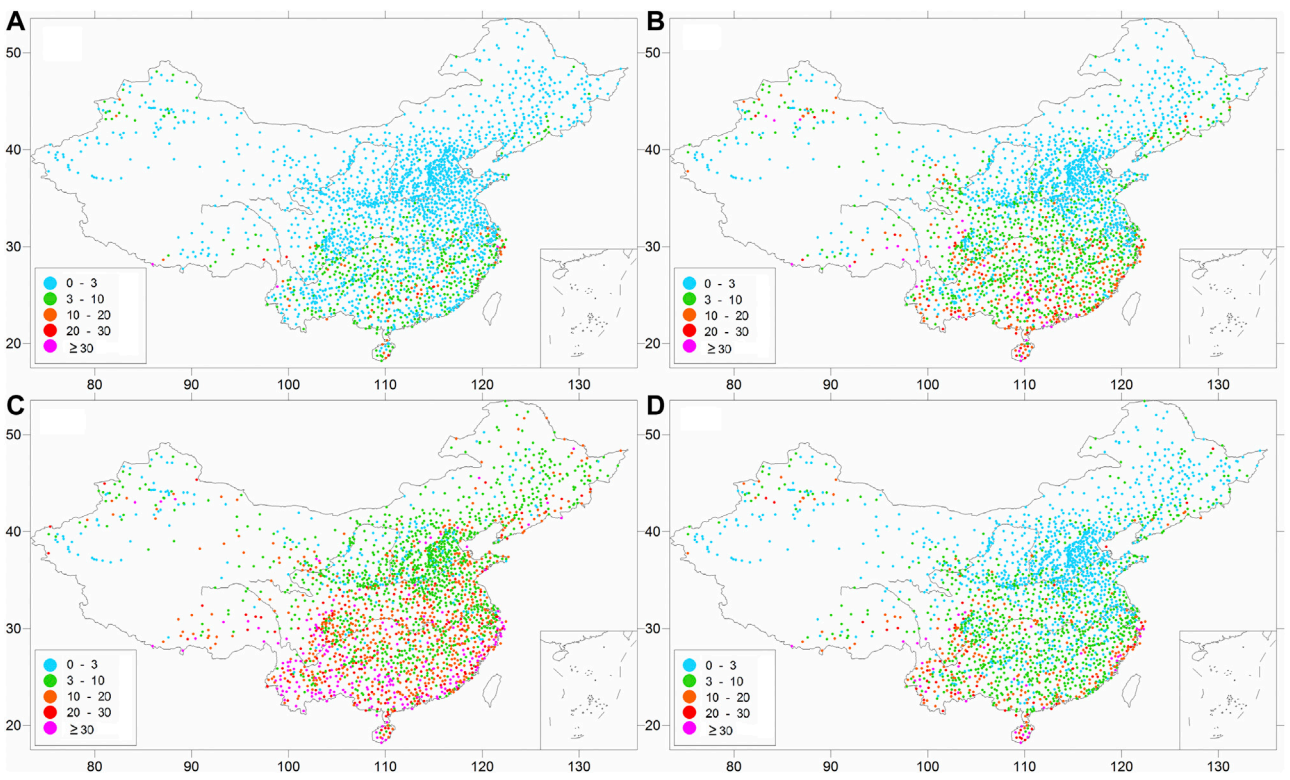

FIGURE 3 | Spatial distributions of the MAE for the climatology values (unit: mm/month) in **(A)** DJF, **(B)** MAM, **(C)** JJA, and **(D)** SON.

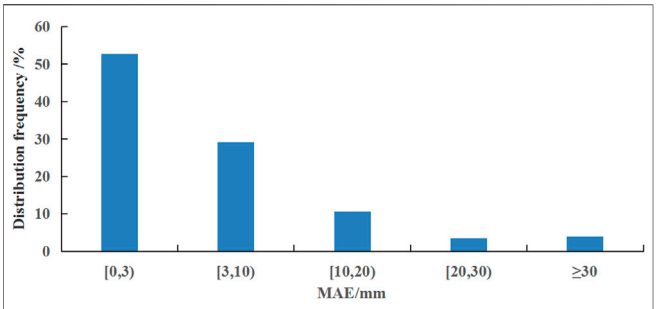

FIGURE 4 | Frequency distribution of the MAE for the climatology values.

Gridding Error Analysis of Precipitation Anomaly Percentage

Tables 3,4 show the MAE and the RMSE for the cross-validation of precipitation anomaly percentage, respectively. They show that the large errors are mainly distributed in Qinghai–Tibet and Northwest China, while the errors in other areas are relatively small. This distribution is associated with the sparse stations in the above two regions, which leads to the increased interpolation errors. In addition, the small climatology value of precipitation and the large spatial difference of precipitation anomaly percentage can also result in large errors in these regions. The temporal distribution indicates that the monthly errors in the rainy season are higher than those in the non-rainy season in North China, Central China, and East China, which is due to the relatively intense rainfall in this period. However, in the other regions, the errors in the non-rainy months are significantly higher than those in the rainy months, which is attributed to the small climatology value of precipitation in these regions, resulting in the large spatial difference of precipitation anomaly percentage. In general, the cross-interpolated precipitation anomaly percentage sequence is well correlated with the actual one, with the correlation coefficients generally being above 0.7 (**Table 5**) and the minimum value being in July and August, basically (black marks in **Table 5**).

Figure 5 shows the spatial distributions of correlation coefficients for the cross-validation of precipitation anomaly percentage in January, April, July, and October. It is shown that the correlation coefficient in the eastern regions is generally higher than that in the western regions. This is due to the small climatology value of precipitation and the large spatial difference of precipitation anomaly percentage, and also the sparse stations in the western regions. The correlation coefficients at 76.8, 64.1, 19.3, and 69.5% of the stations are above 0.9 in January, April, July, and October, respectively, and those at 94.9, 96.3, 90.2, and 96.8% of the stations are above 0.7 in these four months. The mean correlation coefficients are 0.915, 0.894, 0.823, and 0.913, with the smallest value being in July. This is closely related to the abundance degree of precipitation and high frequency of convectional precipitation in this particular month. Throughout the whole year, the correlation coefficients for 55.4 and 94.8% of the samples are above 0.9 and 0.7, respectively (**Figure 6**).

TABLE 3 | MAE for cross-validation of the precipitation anomaly percentage (unit: %).

Month / Region	1	2	3	4	5	6	7	8	9	10	11	12
Northeast China	28.9	35.5	24.1	20.7	20.9	23.7	22.0	22.7	27.5	22.7	26.6	26.6
North China	25.6	25.3	18.5	21.6	18.9	24.5	23.9	23.8	21.5	18.5	23.2	25.2
East China	9.7	9.8	9.6	13.7	15.6	16.7	21.3	24.4	25.1	19.1	13.9	12.3
South China	20.0	16.9	20.7	23.2	22.3	21.6	21.9	22.9	26.1	34.2	28.6	22.9
Central China	14.6	14.1	13.2	16.4	16.1	18.6	21.5	24.5	22.0	14.7	15.6	15.6
Qinghai–Tibet Plateau	62.1	62.9	49.0	38.8	26.5	23.8	20.9	23.1	22.3	35.7	63.5	60.9
Northwest China	38.1	40.0	34.5	35.7	29.5	31.5	32.8	33.4	29.2	31.0	45.5	39.6
Southwest China	27.8	24.6	22.5	22.0	19.4	19.4	19.9	21.7	22.3	20.2	22.6	30.5

TABLE 4 | RMSE for cross-validation of precipitation anomaly percentage (unit: %).

Month / Region	1	2	3	4	5	6	7	8	9	10	11	12
Northeast China	43.5	55.4	34.4	28.5	28.6	31.3	28.7	30.2	38.1	31.7	39.6	41.2
North China	42.9	40.0	27.8	32.0	26.8	33.4	31.7	31.9	30.7	27.5	38.0	41.8
East China	13.9	13.7	13.3	18.9	21.3	22.4	28.2	32.1	34.8	28.9	20.8	18.5
South China	31.0	25.7	30.7	31.8	29.3	28.5	29.0	29.7	34.6	51.4	45.5	35.7
Central China	21.3	19.8	18.0	22.8	21.7	25.0	28.6	32.7	30.6	20.7	22.6	23.1
Qinghai–Tibet Plateau	100.9	96.5	72.5	53.8	35.4	31.0	27.1	30.7	29.1	51.5	104.5	107.1
Northwest China	60.3	65.7	56.6	55.3	43.0	45.3	45.8	48.2	43.5	49.8	78.5	66.3
Southwest China	41.7	35.7	32	30.1	25.9	25.5	25.7	27.8	29.7	27.2	32.3	46.5

TABLE 5 | Correlation coefficients for the cross-validation of precipitation anomaly percentage.

Month / Region	1	2	3	4	5	6	7	8	9	10	11	12
Northeast China	0.899	0.901	0.904	0.916	0.897	0.803	**0.803**	0.839	0.853	0.905	0.915	0.901
North China	0.939	0.942	0.943	0.937	0.906	0.846	**0.834**	0.855	0.901	0.949	0.960	0.938
East China	0.981	0.975	0.967	0.938	0.913	0.913	0.877	**0.848**	0.881	0.951	0.972	0.982
South China	0.956	0.940	0.903	0.864	0.790	0.815	0.833	**0.831**	0.831	0.898	0.917	0.947
Central China	0.952	0.951	0.939	0.914	0.876	0.875	0.863	**0.849**	0.906	0.956	0.961	0.961
Qinghai–Tibet Plateau	0.635	**0.627**	0.635	0.723	0.773	0.727	0.729	0.749	0.770	0.802	0.724	0.699
Northwest China	0.845	0.815	0.835	0.828	0.834	0.778	**0.771**	0.792	0.837	0.837	0.847	0.841
Southwest China	0.863	0.885	0.889	0.846	0.836	0.799	**0.768**	0.786	0.795	0.864	0.899	0.877

Bold value shows : In general, the cross-interpolated precipitation anomaly percentage sequence is well correlated with the actual one, with the correlation coefficients generally being above 0.7 and the minimum value being in July and August, basically.

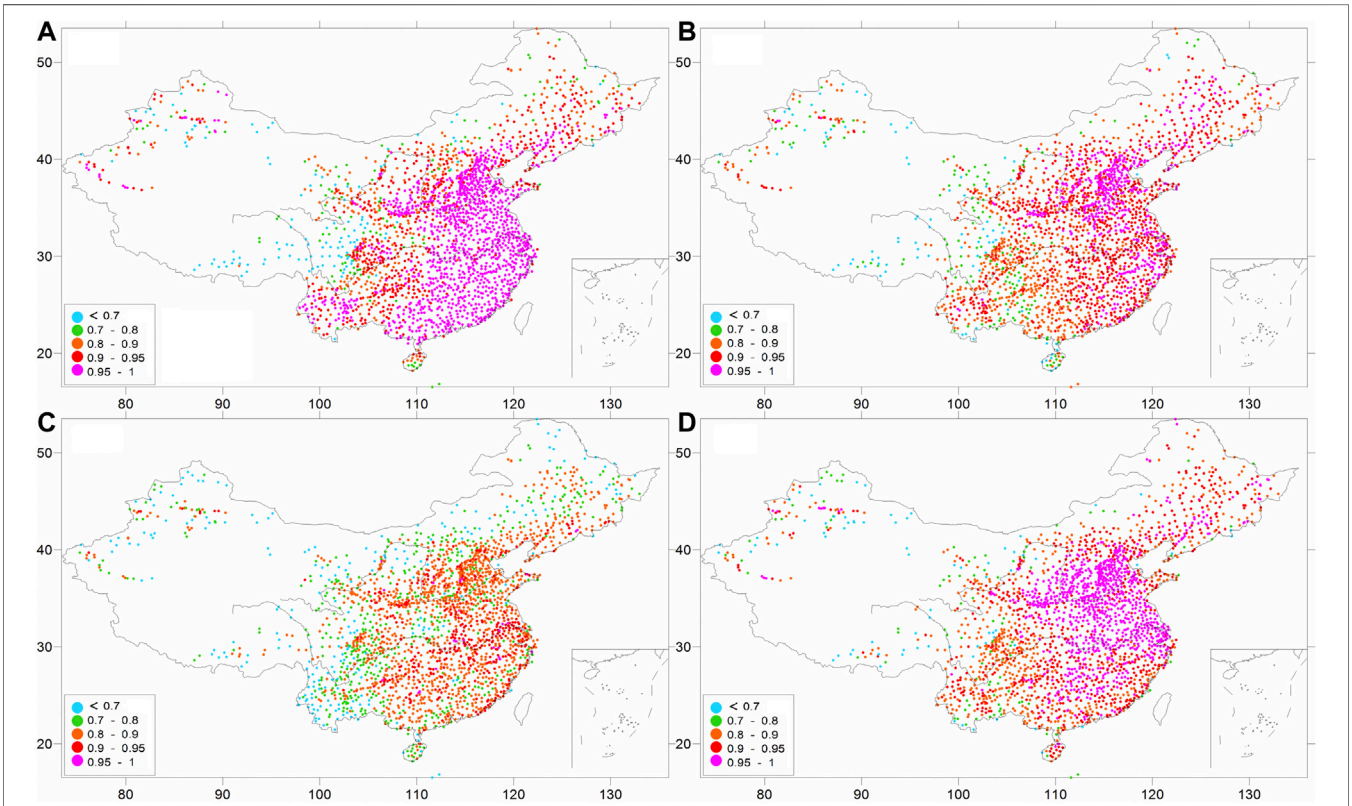

FIGURE 5 | Spatial distributions of correlation coefficients for the cross-validation of precipitation anomaly percentage in **(A)** January, **(B)** April, **(C)** July, and **(D)** October.

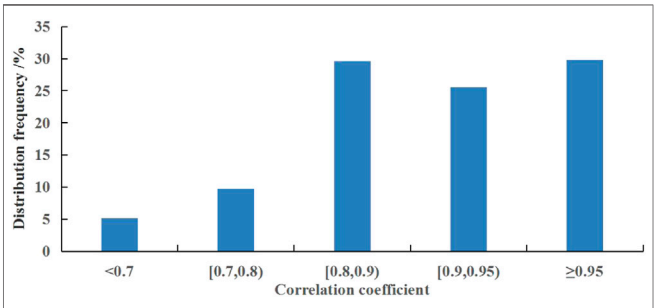

FIGURE 6 | Frequency distribution of correlation coefficients for the cross-validation of precipitation anomaly percentage.

Gridding Error Analysis of Precipitation

Tables 6,**7** show the MAE and the RMSE for the precipitation cross-validation, respectively. It is indicated that the temporal and spatial distribution of errors for the precipitation are similar to those of climatology value, which in areas or months with high precipitation are greater than those in areas or months with low precipitation, especially South China and Southwest China in space and JJA in time (black marks in **Tables 6**,**7**).

Figure 7 demonstrates the spatial distributions of the MAE for the precipitation in each season. The MAE in southern regions is generally higher than that in northern regions in each season, which is closely related to the abundance degree of precipitation

TABLE 6 | MAE for the cross-validation of precipitation (unit: mm).

Region / Month	1	2	3	4	5	6	7	8	9	10	11	12
Northeast China	1.3	1.8	3.0	5.8	9.5	**19.8**	**33.6**	**28.2**	13.2	6.5	3.1	1.9
North China	0.9	1.4	2.3	4.6	8.1	**16.1**	**31.8**	**28.8**	11.7	4.9	2.4	1.0
East China	5.4	7.2	11.0	16.1	23.0	**34.4**	**39.5**	**39.9**	26.4	11.4	7.4	4.6
South China	7.7	10.0	16.6	33.9	56.5	**66.9**	**57.5**	**58.3**	43.5	28.2	14.1	7.4
Central China	4.8	6.5	9.7	16.7	23.8	**30.6**	**37.9**	**34.2**	18.5	11.4	7.3	4.2
Qinghai–Tibet Plateau	1.8	2.9	6.7	9.3	13.9	**19.5**	**22.7**	**21.2**	16.4	8.8	2.5	1.4
Northwest China	1.7	2.0	3.8	6.4	9.3	**11.4**	**16.4**	**15.5**	9.6	5.8	3.3	1.8
Southwest China	4.2	5.1	7.8	14.1	25.1	**38.3**	**48.3**	**44.6**	30.8	18.2	8.4	4.2

Bold value shows : It is indicated that the temporal and spatial distribution of errors for the precipitation are similar to those of climatology value, which in areas or months with high precipitation are greater than those in areas or months with low precipitation, especially South China and Southwest China in space and JJA in time.

TABLE 7 | RMSE for the cross-validation of precipitation (unit: mm).

Month / Region	1	2	3	4	5	6	7	8	9	10	11	12
Northeast China	2.0	2.6	4.1	7.8	12.7	**26.2**	**43.5**	**37.4**	18.0	8.9	4.4	2.7
North China	1.5	2.1	3.5	6.8	11.6	**22.1**	**42.0**	**38.6**	16.7	7.2	3.8	1.6
East China	7.4	9.6	14.7	21.5	30.5	**45.2**	**52.3**	**52.0**	36.4	17.1	10.8	6.8
South China	11.3	14.8	23.2	46.2	74.0	**87.2**	**75.2**	**74.7**	57.9	41.7	22.3	11.4
Central China	6.5	8.8	12.7	22.2	31.5	**40.4**	**50.1**	**45.5**	25.6	16.0	10.5	5.9
Qinghai–Tibet Plateau	3.0	4.4	9.2	11.9	17.7	**24.6**	**28.6**	**26.9**	20.8	12.0	3.9	2.4
Northwest China	2.4	2.9	5.4	9.0	12.6	**15.5**	**21.7**	**21.0**	13.0	8.0	4.7	2.5
Southwest China	5.7	6.9	10.4	18.7	32.7	**49.0**	**60.8**	**56.2**	40.2	23.9	11.5	5.9

Bold value shows : It is indicated that the temporal and spatial distribution of errors for the precipitation are similar to those of climatology value, which in areas or months with high precipitation are greater than those in areas or months with low precipitation, especially South China and Southwest China in space and JJA in time.

in southern regions compared to that in northern regions. The MAE for 94.6, 54.4, 4.6, and 53.8% of the samples in China is below 10 mm/month in DJF, MAM, JJA, and SON, respectively, and 99.5, 79.9, 22.8, and 82.1% of the samples show the MAE below 20 mm/month. The MAE is 3.8, 13.2, 33.5, and 12.7 mm/month, with the largest value being in JJA, which is also closely related to the concentrated rainfall in this period. Over the whole year, the MAE for 51.8 and 71.1% of the samples is less than 10 and 20 mm/month, respectively (**Figure 8**).

CONCLUSION AND DISCUSSION

Based on the high-quality precipitation data from 2,419 meteorological stations in China, the climatic mean field and the anomaly percentage field are derived and gridded with the GIDS and IDS methods, respectively. The DEM data are employed to reduce the influence of elevation on the spatial interpolation accuracy of precipitation due to the unique topography in China. The $0.5 \times 0.5^{\circ}$ surface gridded dataset during 1961–2018 in China is obtained, and the accuracy evaluation is carried out. The main conclusions are as follows.

The cross-validation for the climatic precipitation shows that 79.8, 55.7, 23.6, and 54.9% of the MAE are below 3 mm/month in DJF, MAM, JJA, and SON, respectively, and 96.6, 85.4, 59.8, and 86.3% of them are below 10 mm/month. The MAE in the four seasons is 2.0, 5.6, 13.2, and 5.4 mm/month, respectively. The spatial distribution shows that the MAE in southern regions is generally higher than that in northern regions in each season, which is closely related to the abundance degree of precipitation in southern regions compared to that in northern regions. Among the four seasons, the MAE in JJA is the largest, which is closely related to the concentrated rainfall in this period.

The cross-validation for the precipitation anomaly percentage indicates that the correlation coefficients at 76.8, 64.1, 19.3, and 69.5% of the stations are above 0.9 in January, April, July, and October, respectively, and the correlation coefficients at 94.9, 96.3, 90.2, and 96.8% of the stations are above 0.7. The national mean correlation coefficients in the four months are 0.915, 0.894, 0.823, and 0.913, respectively. In the spatial distribution, the correlation coefficient in the eastern regions is generally higher than that in the western regions, which is associated with the small climatology value of precipitation and the large spatial difference of precipitation anomaly percentage, and also the sparse stations in the western regions. In terms of temporal distribution, the correlation coefficient in July is the smallest, which is closely related to the abundance degree of precipitation and high frequency of convectional precipitation in this particular month.

Regarding the cross-validation for the precipitation, the MAE for 94.6, 54.4, 4.6, and 53.8% of the samples is less than 10 mm/month in DJF, MAM, JJA, and SON, respectively, and 99.5, 79.9, 22.8, and 82.1% of the samples show the MAE below 20 mm/month. The MAE in the four seasons is 3.8, 13.2, 33.5, and

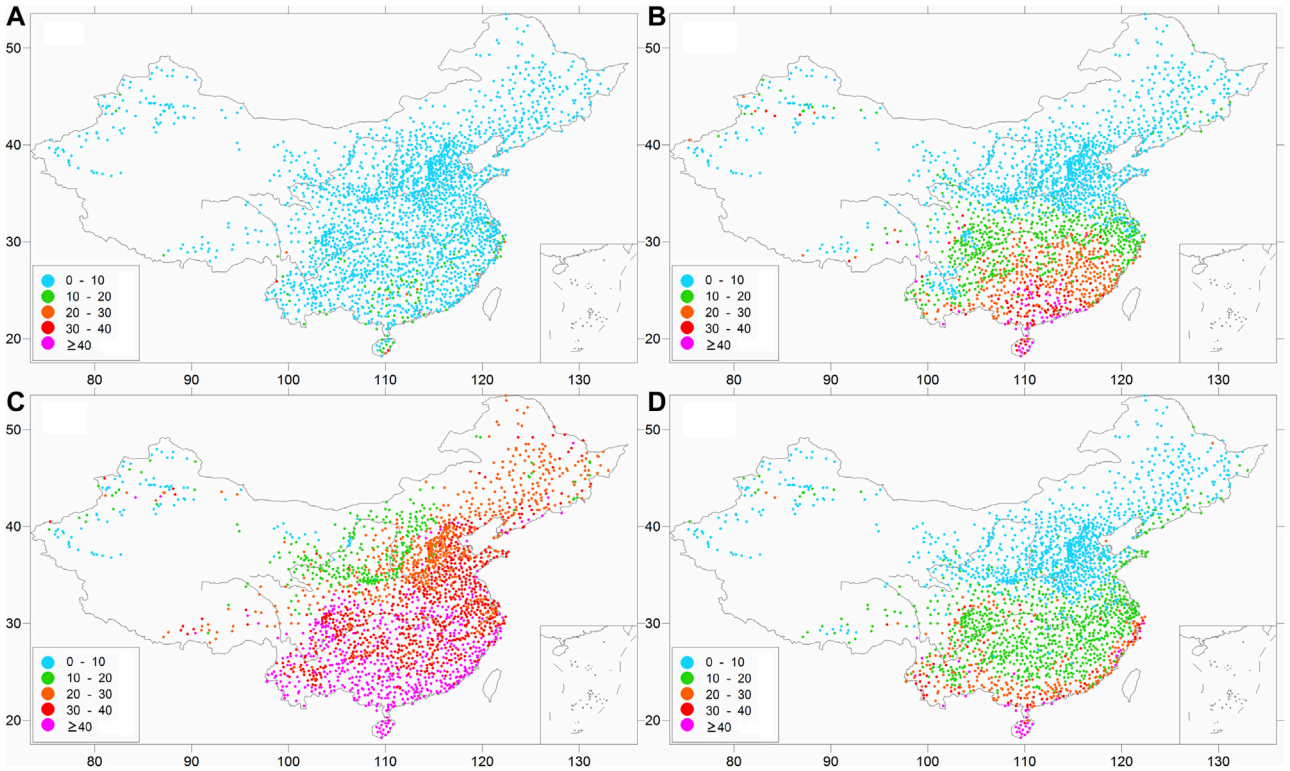

FIGURE 7 | Spatial distributions of the MAE for the precipitation (unit: mm/month) in **(A)** DJF, **(B)** MAM, **(C)** JJA, and **(D)** SON.

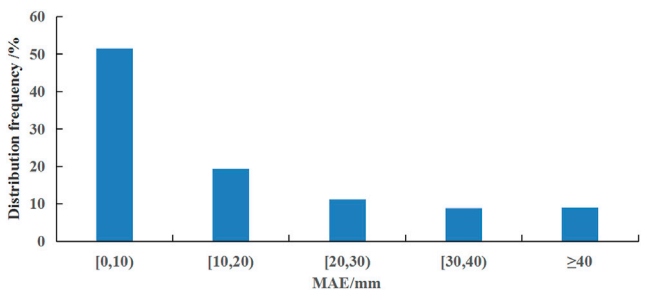

FIGURE 8 | Frequency distribution of the MAE for the cross-validation of precipitation.

12.7 mm/month, respectively. Spatially, the MAE in southern regions is generally higher than that in northern regions in each season, which is closely related to the abundance degree of precipitation in southern regions compared to that in northern regions. The temporal distribution presents the largest MAE in JJA, which is also closely related to the concentrated rainfall in this period.

Compared with the other research in China, our precipitation grid product has a similar accuracy. For example, Zhao et al. (2014) established the monthly grid precipitation datasets in China by using the TPS (thin plate spline) method, and the MAE for 51.5 and 75.2% of the samples was less than 5 mm/month and 15 mm/month for the whole year, respectively. However, their calculation of the MAE did not involve a cross-validation method, and that may lead to underestimation of error. Xiong et al. (2011) constructed the daily grid precipitation datasets in China by using the Barnes method, and the MAE was 1.3 mm/day for the whole year, and 0.25, 1.03, 3.06, and 0.85 mm/day in DJF, MAM, JJA, and SON, respectively.

The primary purpose of this study is to meet the urgent need in agriculture, hydrological modeling, and other fields. However, it should be pointed out that the gridding of station observation data is a very complex work. Taking this study as an example, there is still a lot to be improved. These include the following:

(1) More observation data should be collected. In addition to the stations used in this study, there are a large number of rainfall stations with a relatively poor observation quality in China. In the future, we can consider using these observations in interpolation after quality control by appropriate methods and fusion of satellite and radar data, which will greatly improve the accuracy of the final grid data, especially in the regions with scarcity in observations, such as the Qinghai–Tibet Plateau.

(2) More methods or parameterization schemes should be applied to the development and assessment of grid

products, similar to Cheng et al. (2020), Newlands et al. (2011). In this way, we can choose the best method or scheme to improve the accuracy of the grid.

Due to the scarcity of stations in western China, especially on the Tibetan Plateau, with few observations in present, it is difficult to evaluate the gridded precipitation dataset qualitatively and quantitatively. The users are suggested to be cautious when using the data from these regions in scientific research.

DATA AVAILABILITY STATEMENT

The original contributions presented in the study are included in the article/Supplementary Material, further inquiries can be directed to the corresponding author.

AUTHOR CONTRIBUTIONS

JP, LD, and WX analyzed the data. QL put forward the idea. JP wrote the manuscript. All authors revised the manuscript.

FUNDING

This study was supported by National Natural Science Foundation of China (Grant 42005058) and Natural Science Foundation of Hunan Provence (Grant 2020JJ5298)

ACKNOWLEDGMENTS

The authors thank the editor and the reviewers for their constructive suggestions/comments in the initial reviews.

REFERENCES

Chen, M., Xie, P., Janowiak, J. E., and Arkin, P. A (2002). Global Land Precipitation: A 50-year Monthly Analysis Based on Gauge Observations. *J. Hydrometeorol.* 3 (3), 249–266. doi:10.1175/1525-7541(2002)003<0249:glpaym>2.0.co;2

Cheng, J., Li, Q., Chao, L., Maity, S., Huang, B., and Jones, P. (2020). Development of High Resolution and Homogenized Gridded Land Surface Air Temperature Data: A Case Study over Pan-East Asia. *Front. Environ. Sci.* 8, 1–14. doi:10.3389/fenvs.2020.588570

Dai, A., Fung, I. Y., and Del Genio, A. D. (1997). Surface Observed Global Land Precipitation Variations during 1900–88. *J. Clim.* 10, 2943–2962. doi:10.1175/1520-0442(1997)0102.0.CO;2

Daly, C., Neilson, R. P., and Phillips, D. L. (1994). A Statistical-Topographic Model for Mapping Climatological Precipitation over Mountain Terrain. *J. Appl. Meteorol.* 33 (2), 140–158. doi:10.1175/1520-0450(1994)0332.0.CO;2

Gyalistras, D. (2003). Development and Validation of a High-Resolution Monthly Gridded Temperature and Precipitation Data Set for switzerland (1951-2000). *Clim. Res.* 25, 55–83. doi:10.3354/cr025055

Hong, Y., Nix, H. A., Hutchinson, M. F., and Booth, T. H. (2005). Spatial Interpolation of Monthly Mean Climate Data for china. *Int. J. Climatol.* 25, 1369–1379. doi:10.1002/joc.1187

Jones, D., Wang, W., and Fawcett, R. (2009). High-quality Spatial Climate Data-Sets for Australia. *Amoj* 58, 233–248. doi:10.22499/2.5804.003

Li, Q., Peng, J., and Shen, Y. (2012). Development of China Homogenized Monthly Precipitation Dataset during 1900-2009. *J. Geogr. Sci.* 22, 579–593. doi:10.1007/s11442-012-0948-8

Li, K. Y., Zhou, M., Chen, J. Y., Pan, M. M., Li, C. R., and Tang, L. L. (2019). An Approach of Improved Gradient Plus Inverse Distance Squared for Spatial Interpolation of Temperature (In Chinese). *J. Univ. Chin. Acad. Sci.* 36, 491–497.

Nalder, I. A., and Wein, R. W. (1998). Spatial Interpolation of Climatic Normals: Test of a New Method in the Canadian Boreal Forest. *Agric. For. Meteorology* 92, 211–225. doi:10.1016/S0168-1923(98)00102-6

Newlands, N. K., Davidson, A., Howard, A., and Hill, H. (2011). Validation and Inter-comparison of Three Methodologies for Interpolating Daily Precipitation and Temperature across Canada. *Environmetrics* 22, 205–223. doi:10.1002/env.1044

Peng, S., Ding, Y., Liu, W., and Li, Z. (2019). 1 Km Monthly Temperature and Precipitation Dataset for China from 1901 to 2017. *Earth Syst. Sci. Data* 11, 1931–1946. doi:10.5194/essd-11-1931-2019

Price, D. T., McKenney, D. W., Nalder, I. A., Hutchinson, M. F., and Kesteven, J. L. (2000). A Comparison of Two Statistical Methods for Spatial Interpolation of Canadian Monthly Mean Climate Data. *Agric. For. Meteorology* 101, 81–94. doi:10.1016/S0168-1923(99)00169-0

Qiang, F., Zhang, M., Wang, S., Liu, Y., Ren, Z., and Zhu, X. (2016). Estimation of Areal Precipitation in the Qilian Mountains Based on a Gridded Dataset since 1961. *J. Geogr. Sci.* 26, 59–69. doi:10.1007/s11442-016-1254-7

Shen, Y., Feng, M. N., Zhang, H. Z., and Gao, F. (2010). Interpolation Methods of China Daily Precipitation Data(in Chinese). *J. Appl. Meteorol. Sci.* 21, 279–286. doi:10.3969/j.issn.1001-7313.2010.03.003

Wu, J., and Gao, X. (2013). A Gridded Daily Observation Dataset over China Region and Comparison with the Other Datasets (In Chinese). *Chin. J. Geophy* 56, 1102–1111. doi:10.6038/cjg2013040610.1007/s11431-013-5390-3

Xie, P., Chen, M., Yang, S., Yatagai, A., Hayasaka, T., Fukushima, Y., et al. (2007). A Gauge-Based Analysis of Daily Precipitation over East Asia. *J. Hydrometeorol.* 8, 607–626. doi:10.1175/JHM583.1

Xiong, Q. F., Huang, M., Xiong, M. Q., and Hu, J. L. (2011). Cross-Validation Error Analysis of Daily Gridded Precipitation Based on China Meteorological Observations (In Chinese). *Plateau Meteorology* 30, 1615–1625. doi:10.1016/B978-0-444-53599-3.10005-8

Yang, S., and Li, Q. X. (2014). Improvement in Homogeneity Analysis Method and Update of China Precipitation Data (In Chinese). *Clim. Change Res.* 10, 276–281. doi:10.3969/j.issn.1673-1719.2014.04.008

Yatagai, A., Arakawa, O., Kamiguchi, K., Kawamoto, H., Nodzu, M. I., and Hamada, A. (2009). A 44-year Daily Gridded Precipitation Dataset for Asia Based on a Dense Network of Rain Gauges. *SOLA* 5, 137–140. doi:10.2151/sola.2009-035

Zhao, Y. F., and Zhu, J. (2015). Assessing Quality of Grid Daily Precipitation Datasets in China in Recent 50 years(in Chinese). *Plateau Meteorology* 34, 50–58.

Zhao, Y. F., Zhu, J., and Xu, Y. (2014). Establishment and Assessment of the Grid Precipitation Datasets in China for the Past 50 Years (In Chinese). *J. Meteorol. Sci.* 34, 414–420. doi:10.3969/2013jms.0008

Conflict of Interest: The authors declare that the research was conducted in the absence of any commercial or financial relationships that could be construed as a potential conflict of interest.

frontiers in Environmental Science

METHODS
published: 30 April 2021
doi: 10.3389/fenvs.2021.625418

A New Method for Correcting Urbanization-Induced Bias in Surface Air Temperature Observations: Insights From Comparative Site-Relocation Data

Tao Shi[1,2], *Yong Huang*[3], *Dabing Sun*[1], *Gaopeng Lu*[2] *and Yuanjian Yang*[4]*

[1]Wuhu Meteorological Bureau, Wuhu, China, [2]School of Earth and Space Sciences, University of Science and Technology of China, Hefei, China, [3]Key Laboratory of Atmospheric Sciences and Satellite Remote Sensing of Anhui Province, Anhui Institute of Meteorological Sciences, Hefei, China, [4]Collaborative Innovation Centre on Forecast and Evaluation of Meteorological Disasters, School of Atmospheric Physics, Nanjing University of Information Science and Technology, Nanjing, China

The effect of urbanization on surface air temperature (SAT) is one of the most important systematic biases in SAT series of urban stations. Correcting this so-called urbanization bias has the potential to provide accurate basic data for long-term climate change monitoring and research. In the western region of the Yangtze River Delta, 42 meteorological stations with site-relocation history from 2009 to 2018 were selected to analyze the statistical characteristics of the differences in comparative site-relocation daily average SAT. The annual average differences in comparative site-relocation SAT series between the old and the new stations (SAT_{DON}) were used to characterize the impact of urbanization bias on the air temperature observation series. Using remote sensing technology, spatial datasets of land-use, landscape, and geometric parameters of the underlying surface in the 5-km buffer zone around the station were established as the observed environmental factors of the site, and the differences in these observed environmental factors (DOEFs) between the old and the new stations were calculated to indicate the change induced by urbanization. Next, multiple linear regression models of SAT_{DON} and DOEFs were constructed, showing that the error range of the model for simulated SAT_{DON} was 3.66–18.21%, and the average error was 10.09%. Finally, this new correction method (NCM) and conventional correction method (CCM) were applied to the correction of the urbanization bias of SAT series at Hefei station. After comparison, it is found that the NCM could reveal clear contributions of the rapid and slow stages of the urbanization process and resultant environmental changes around the stations to the observed SAT. In summary, the NCM based on remote sensing technology can more reasonably and effectively correct the urbanization bias caused by local human activities,

OPEN ACCESS

Edited by:
Qingxiang Li,
Sun Yat-Sen University, China

Reviewed by:
Xuchao Yang,
Zhejiang University, China
Chunlüe Zhou,
University at Albany, United States

***Correspondence:**
Yuanjian Yang
yyj1985@mail.ustc.edu.cn

Specialty section:
This article was submitted to Interdisciplinary Climate Studies, a section of the journal Frontiers in Environmental Science

Received: *03 November 2020*
Accepted: *09 February 2021*
Published: *30 April 2021*

Citation:
Shi T, Huang Y, Sun D, Lu G and Yang Y (2021) A New Method for Correcting Urbanization-Induced Bias in Surface Air Temperature Observations: Insights From Comparative Site-Relocation Data. Front. Environ. Sci. 9:625418. doi: 10.3389/fenvs.2021.625418

Abbreviations: AR, area ratio; CCM, conventional correction method of urbanization bias correction; DIS, distance between the station and the gravity center of various lands; DOEFs, differences in these observed environmental factors; FRAC_MN, mean fractal dimension; LPI, largest patch index; LUCC, land use/cover change; NCM, new correction method of urbanization bias correction; NDVI, normalized difference vegetation index; SAT, surface air temperature; SAT_{DON}, differences in comparative site-relocation SAT series between the old and the new stations; YRD, Yangtze River Delta.

as well as reduce the error caused by the selection of reference stations *via* the conventional correction method.

Keywords: surface air temperature series, urbanization bias, remote sensing technology, relocation, correction method

INTRODUCTION

Urbanization directly affects the types of land use/cover and anthropogenic heat emissions around meteorological stations, leading to major changes in the observation environment (Gallo et al., 1996; Peterson, 2006; Trusilova et al., 2008; Chen et al., 2020), which in turn has an important impact on the accuracy, representativeness, and homogeneity of meteorological observation data (Davey and Sr, 2005; Vose, 2005). The contribution of the so-called urbanization bias (the effect of urbanization on surface air temperature (SAT), the list of abbreviations used in this article and their expanded names can be found in Appendix A) to meteorological observation data usually stems from changes in the observation environment against the background of urbanized areas (Ren et al., 2017). The urbanization bias is the largest systematic bias in SAT observation records in China and correcting this bias has the potential to provide accurate basic data for large-scale climate change monitoring and research (Wen et al., 2019b).

Urbanization bias has received a great deal of attention in the literature (Hansen et al., 2001; Fujibe, 2009; Zhang, 2009; Zhang, 2014; Wen et al., 2019a). Zhang (2009) used the method of subtracting the warming trend of rural stations from the warming trend of urban stations to correct the regional average SAT series of urban stations and obtained the regional average SAT series after removing the urbanization bias. Fujibe (2009) divided the meteorological stations in Japan into six categories in terms of the population density within a certain radius around the city station and corrected the urbanization bias in the third–sixth-category sites using the first and second types of stations as reference stations. Hansen et al. (2001) corrected the urbanization bias of one typical station by utilizing the two-stage linear trend based on the assumption that the SAT increased linearly in two periods. Zhou et al. (2019) pointed occurrence probability of the heatwave events in summer over the Yangtze River Delta is closely related to the contribution of urbanization effect. These imply that the correction method of urbanization bias is very crucial to explore accurately the regional climate change.

However, the conventional correction method (CCM) of urbanization bias still has some shortcomings as follows: 1) many studies have utilized the population density or city size as the criteria for classifying meteorological stations. For example, Bai and Ren (2006) chose meteorological stations with a population of more than 100,000 as urban stations, but Liu (2006) divided the stations with a population of more than 40,000 and the stations that were not described as "rural" into urban stations. However, there have also been some studies that have utilized satellite remote sensing data to select reference stations, such as Zhang. (2014), who visually selected the stations outside the closed contour as reference stations in the temperature field retrieved from remote sensing data. Thus, it can be seen that there is no unified standard for the selection of reference stations, and it is difficult to find a pure reference station near the urban station as reference stations are inevitably affected by urbanization, so the urbanization bias in the SAT series is the minimum estimate (Zhang, 2014). 2) Previous studies corrected the SAT series based on the assumption that the urbanization bias presents a linear increase trend (Hansen et al., 2001; Zhang, 2009). However, in reality, the urbanization processes at different times and in different regions are variable, so it is impossible to subdivide the specific degree of contribution of the urbanization bias to the SAT series on temporal and spatial scales. In addition, there are considerable differences in the mechanisms and magnitudes of the impact of urbanization on different temperature elements (Li et al., 2014), despite the possibly limited contribution to regional warming (Chao et al., 2020), while its impact on extreme temperatures are huge (Li and Huang, 2013; Li et al., 2014; Zhou et al., 2019).

In order to improve the representativeness of the observation environment of meteorological stations, many stations with severely damaged observation environments have been relocated. Taking 2015 as an example, 92 meteorological observation stations across the country were relocated in this year alone (Meteorological Observation Centre of CMA, 2013; Comprehensive Observation Department of China Meteorological Administration, 2015). According to the requirements of "the criterion of surface meteorological observation," "protection methods for meteorological exploration environment and facilities," and other documents formulated and issued by China Meteorological Administration, site selection has a series of strict restrictions on factors such as altitude, distance, and obstacles. The area around the relocated station should be dominated by open vegetation, and the representativeness of the meteorological observation environment must have been greatly improved. Meteorological observation series can represent the climate background of the region (Yang et al., 2013; Yang et al., 2017), so relocated stations can be used as relatively pure reference stations. In addition, "the criterion of surface meteorological observation" stipulates that the relocation of meteorological stations must involve the carrying out of at least one year of comparative observations between the new site and the old site, and the difference in comparative site-relocation annual average SAT between the old and the new stations (SAT_{DON}) provides high-quality data for us to study the impact of urbanization bias on the SAT series. Therefore, SAT_{DON} can reduce the error caused by the selection of reference stations *via* the traditional urban–rural comparison method.

The meteorological observation environment refers to the environmental space constituted by the minimum distance necessary to avoid various interferences and ensures that the

facilities of the meteorological observation station accurately obtain the meteorological observation information. With the rapid development of remote sensing technology, the use of satellite data to study changes in the meteorological environment has become an emerging method (Yang et al., 2013; Li et al., 2015; Shi et al., 2015). Yang et al. (2013) evaluated the observation environment by using land use/cover and normalized difference vegetation index (NDVI) in the buffer zone around the meteorological station. Li et al. (2015) quantitatively studied the relationship between land use/cover change (LUCC) and the thermal environment in the buffer zone and subdivided the stations into three types by the contribution index of the thermal environment. The above researches show that it is feasible to utilize satellite data to investigate and study the observation environment, and it has the advantages of visualization and remodeling. However, existing remote sensing research on the observation environment only uses indicators such as LUCC and NDVI and does not fully consider the impact of the spatial pattern and configuration of different land-use types on the observation environment. Consequently, this study uses remote sensing technology to establish land-use parameters, landscape parameters, geometric parameters, and other spatial datasets around meteorological stations to characterize the differences in observation environment factors (DOEFs) between the old and the new stations and analyzes and discusses the physical mechanisms by which urbanization bias influences the SAT series.

The Yangtze River Delta (YRD) urban agglomeration is one of the most highly urbanized areas in China for the past 30 years (National Bureau of Statistics, 2019). However, the development of Anhui in the western region of the YRD has been relatively slow, having not developed rapidly until the past 10 years. Therefore, the observation environments of national meteorological stations in Anhui Province have been seriously damaged in the past 10 years, and a large number of stations have been forced to relocate on a frequent basis (Meteorological Observation Centre of CMA, 2013; Comprehensive Observation Department of China Meteorological Administration, 2015), and this provides us with an opportunity to study the process of urbanization and station relocation. In summary, taking Anhui Province as the research area, meteorological stations with site-relocation history were selected in this study, and the SAT_{DON} results between the old and the new stations were used to characterize the impact of urbanization bias on the SAT series. Landscape parameters, geometric parameters, and other spatial datasets in the 5 km buffer zone around the stations were established to characterize the DOEFs between the old and the new stations, and statistical models of the SAT_{DON} and DOEFs were constructed. This paper corrected the urbanization bias of the SAT series at a typical station by the new method and the conventional method, respectively, and the advantages of the new method were discussed finally.

DATA AND METHODS

Data

1) Ground observation data. The SAT data mainly include national reference climatological stations, which observe 8 times a day (once every 3 h); national basic meteorological station, which observes four times a day [02:00, 08:00, 14:00, and 20:00 BT (Beijing time)]; national general meteorological stations, which observe three times a day (08:00, 14:00, and 20:00 BT) and obtain the daily-averaged SAT by calculating the arithmetic mean of the temperature values observed for each time per day.
2) Satellite remote sensing data. The remote sensing data used in this study were Landsat data from the United States' EOS (Earth Observation System) for the detection of earth resources and the environment. Specifically, this study uses the remote sensing images of the Landsat-7/ETM+ (Yao et al., 2010) and Landsat-8/OLI (Saputra et al., 2017) sensors to study the changes in the observation environment of the stations relocated before 2013 and after 2013, respectively. A comparison of the band information of the above two remote sensing images is given in **Table 1**.

Methods

Selecting Samples for Relocated Stations

For this study, we selected meteorological stations with site-relocation history as the research samples from 2009 to 2018, according to the historical evolution data and comparative observation data of the relocated stations, surveys and evaluation reports of the observation environment of the national ground meteorological stations, and high-resolution satellite remote sensing images. The selection criteria were as follows: 1) the main reason for the relocation was that the observation environment of the station had been seriously damaged; 2) in order to minimize the influence of the difference of regional and local climate background, the difference in altitude between the sites (before and after relocation) was less than 50 m, and a horizontal distance between the sites of 20 km was selected according to previous studies (Wen et al., 2019; Shi et al., 2011); 3) there was no significant difference in topography; and 4) the type of observation instrument, the frequency of daily observations, and daily mean methods of temperature series did not change before and after station relocation. Based on the above criteria, 42 samples of relocated stations were selected, as shown in **Figure 1**. The relocated station samples include 25 urban stations and 17 reference stations, according to the meteorological station classification method of Ren et al. (Ren et al., 2010), and the samples were evenly distributed throughout northern Anhui, the Yangtze–Huaihe region, Yangtze River area, southern Anhui, and other regions. Therefore, the samples in this study can represent the impact of the urbanization development level of different regions in Anhui Province on different types of stations.

Determining the Research Range of the Station Buffer Zone

Studies (Cai, 2008; Yang et al., 2013; Shi et al., 2015; Yang et al., 2020a) have shown that since the observation height of the thermometer shelter in the observation field is 1.5 m, the maximum impact of urbanization on the observation data usually does not exceed 5 km under advection and turbulence

TABLE 1 | Comparison of band information between the Landsat-7/ETM+ and Landsat-8/OLI sensors.

Band no	Landsat-7/ETM + sensor		Landsat-8/OLI sensor	
	Wavelength (μm)	Spatial resolution (m)	Wavelength (μm)	Spatial resolution (m)
1	0.45–0.515	30	0.433–0.453	30
2	0.525–0.605	30	0.450–0.515	30
3	0.63–0.690	30	0.525–0.600	30
4	0.75–0.90	30	0.630–0.680	30
5	1.55–1.75	30	0.845–0.885	30
6	10.40–12.50	60	1.560–1.660	30
7	2.09–2.35	30	2.100–2.300	30
8	0.52–0.90	15	0.500–0.680	15
9			1.360–1.390	30
10			10.60–11.19	100
11			11.50–12.51	100

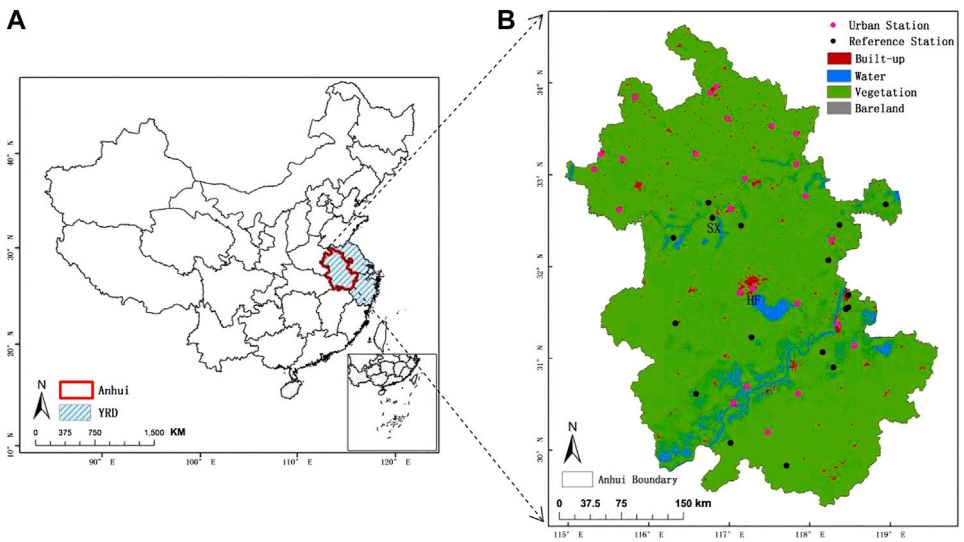

FIGURE 1 | (A) Location of Anhui in the western region of the YRD in China. **(B)** Land use/cover maps and the spatial distribution of the relocated station samples in Anhui Province from 2009 to 2018.

transport conditions. Therefore, for this study, we selected a station buffer zone with a center radius of 5 km to quantitatively study the impact of environmental changes on the SAT series.

Establishing a Dataset of Characterization Parameters of the Observation Environment in the Buffer Zone

Land-use parameters (Carolina et al., 2013) reflect the results of various land resource utilization activities produced by human beings, which are an important part of urban environmental change research. This study uses the supervised classification method to classify land use in ENVI software and establishes four parameter indicators: built-up area ratio (AR_{BT}), water area ratio (AR_W), vegetation area ratio (AR_V), and bare land area ratio (AR_B).

The landscape parameters mainly include the largest patch index (LPI) (Wu, 2000) and the mean fractal dimension (FRAC_MN) (Wu, 2000) of the land type. The LPI represents the dominant land type in the study area. The larger the LPI value, the more obvious the advantage of this type of patch in the overall landscape. The FRAC_MN represents the index of the patch shape. The larger the FRAC_MN, the more complex the shape of the patch and the more discrete the patch distribution. For this study, eight parameter indicators were calculated in the landscape index software Fragstats, including the built-up largest patch index (LPI_{BT}), water largest patch index (LPI_W), vegetation largest patch index (LPI_V), bare land largest patch index (LPI_B), built-up mean fractal dimension ($FRAC\_MN_{BT}$), water mean fractal dimension ($FRAC\_MN_W$), vegetation mean fractal dimension ($FRAC\_MN_V$), and bare land mean fractal dimension ($FRAC\_MN_B$).

The geometric parameters mainly include the distance between the stations and the gravity centers of different land types in the buffer zone, and the distance between the station and the city center (Liu et al., 2014). For this study, we used ArcGIS software to extract the land types of "built-up,"

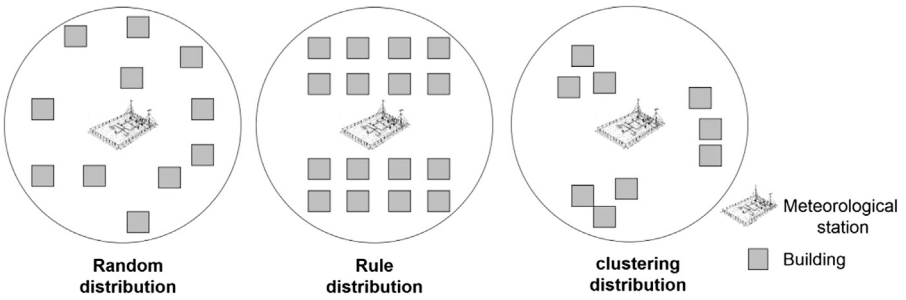

FIGURE 2 | Schematic diagram of the landscape pattern around the station.

"water," "vegetation," and "bare land" in the station buffer zone, then used the "Calculate Geometry" function to obtain the gravity centers of the different land types, and finally, the "Point Distance" function could then be used to calculate four parameter indicators, including the distance between the station and the gravity center of built-up land (DIS_{BT}), water (DIS_W), vegetation (DIS_V), and bare land (DIS_B). In the same way, the parameter indicator of the distance between the station and the city center (DIS_C) could be obtained in the ArcGIS software.

The current urbanization bias correction scheme still has deficiencies, mainly due to the limited assessment indicators for local observation environment around meteorological stations. Landscape ecological morphology (**Figure 2**) can be used to explore the relationship between the spatial pattern of urban land use and urban local microclimate (Zhou et al., 2011; Estoque et al., 2017). Landscape composition can distinguish land-use types, and landscape configuration can fully consider the respective geographic characteristics of different land-use types. In addition to the conventional land-use assessment indicators, therefore, our present work employs landscape ecological indicators and geometric indicators to assess observation environment around station. Finally, based on correlation analysis, six indicators, that is, AR_{BT}, AR_W, LPI_{BT}, LPI_W, DIS_{BT}, and DIS_W, were finally selected.

Simulation and Correction Method for the Urbanization Bias in the SAT Series

This article starts with the physical causes of the impact of urbanization bias on the observation environment and simulates the degree of impact of the urbanization bias on the SAT series by constructing statistical models of SAT_{DON} and DOEFs. Multiple linear regression is a statistical analysis method to determine the quantitative relationship between a dependent variable and multiple independent variables (Lynn, 2007; Li, 2020). Assuming there is a linear correlation between the dependent variable Y and the k independent variables X_1, X_2,..., X_k, then the functional relationship between Y and X can be expressed as:

$$Y = \beta + \beta_1 X_1 + \beta_2 X_2 + \cdots + \beta_k X_k + \varepsilon, \quad (1)$$

where β is the regression constant; $\beta 1$, $\beta 2$, ..., β_k are the regression coefficients; and ε is the regression residual.

After substituting the land-use, landscape, and geometric parameters in the buffer zone around the station into **Eq. 1**, the simulated values of the changes in the SAT series could be obtained, and then the urbanization bias could be corrected by the simulated values:

$$T'_i = T_i - \Delta T_i. \quad (2)$$

Here, i is the year number from the earliest year of recording to the latest year of correcting, T'_i is the annual average SAT after correction in the ith year (°C), and ΔT_i is the change in the annual average SAT series caused by urbanization bias in the ith year compared with the earliest observation year (°C).

RESULTS

Case Analysis of a Typical Station

Hefei National Meteorological Observation Station had been completely surrounded by built-up land before relocation because of the process of urbanization in recent years (**Figure 3**); the observational environment score of Hefei station was only 63.2. After relocation, Hefei station moved 30.2 km to the northwest of the old site, with an altitude difference of 6.0 m, and the observation environment of the station greatly improved, with the score increased to 99.3.

Table 2 shows the DOEFs between the old and the new stations in the 5-km buffer zone. AR_{BT} decreased from 42.17 to 4.23% after relocation, indicating that the area of built-up land around the station was greatly reduced; the $FRAC\_MN_{BT}$ declined to a certain extent, indicating that the distribution of built-up patches around the station was more concentrated than before relocation; and DIS_{BT} increased from 0.53 to 3.13km, indicating that the built-up land type had weakened the urbanization impact of the station after relocation. The parameters of water, vegetation, and bare land also improved to varying degrees. In addition, the SAT_{DON} in 2018 showed that the annual average SAT of the new station (**Figure 3B**) was 0.83°C lower than the old station (**Figure 3C**) and the decline reached 4.8%. In summary, the representativeness of the observation environment at Hefei station improved after relocation, and the SAT_{DON} could represent the degree of the impact of the urbanization bias on the SAT series.

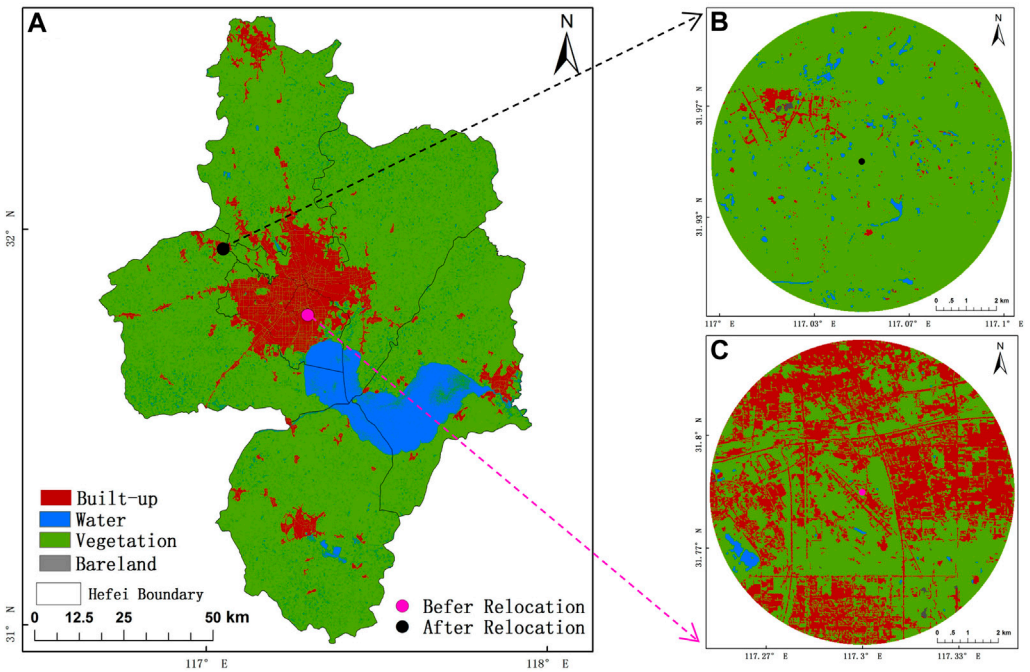

FIGURE 3 | (A) Location of Hefei station relative to Hefei city before and after relocation. **(B)** LUCC in the 5-km buffer zone of Hefei station after relocation. **(C)** LUCC in the 5-km buffer zone of Hefei station before relocation.

TABLE 2 | DOEFs in the 5-km buffer zone of Hefei station after and before relocation.

	Parameter	After relocation	Before relocation
Land-use parameters	AR_{BT} (%)	4.23	42.17
	AR_{W} (%)	3.11	1.01
	AR_{V} (%)	91.09	56.04
	AR_{V} (%)	0.57	0.78
Landscape parameters	LPI_{BT}	5.97	24.73
	LPI_{W}	1.13	0.30
	LPI_{V}	60.18	38.88
	LPI_{B}	0.73	0.91
	$FRAC\_MN_{BT}$	1.04	1.14
	$FRAC\_MN_{W}$	1.18	1.09
	$FRAC\_MN_{V}$	1.11	1.17
	$FRAC\_MN_{B}$	1.09	1.14
Geometric parameters	DIS_{BT} (km)	3.13	0.53
	DIS_{W}(km)	1.73	3.69
	DIS_{V}(km)	0.02	0.87
	DIS_{B}(km)	1.28	1.01
	DIS_{C}(km)	2.1	8.3

Analyzing the Statistical Characteristics of the Samples' Daily Average Differences

For this section, daily-averaged SAT_{DON} series were close to a normal distribution and fluctuated in the range of −2.3–4.4°C (**Figure 4**). The sample size, mean, and standard deviation were 15,347, 0.572, and 0.568°C (**Table 3**), respectively. The above statistics showed that the sample had a large variation range, but the data distribution was mainly concentrated near the mean value, and the overall sample volatility was relatively small. The kurtosis value of the sample was 2.057, the number of samples with a daily-averaged SAT_{DON} of 0.4°C was the largest, reaching 1,515, and the number of samples with a daily-averaged SAT_{DON} at 0.2–0.8°C reached 9,193, accounting for 59.6% of the total number of samples, indicating that the daily-averaged SAT_{DON} series was steeper than the normal distribution. The sample skewness value was 0.673, and the number of daily-averaged SAT_{DON} values greater than the mean was 8,226, accounting for 53.6% of the total sample and indicating that there were more points on the right-hand side of the data distribution, close to the mean.

In addition, there were 828 negative values in the sample, accounting for 5.39% of the total number of samples, which means that the SAT series of the old stations were lower than the new sites (**Figure 4**). The influence of the meteorological station observation environment on the SAT series was more complicated. Buildings cause the wind speed to decay downwind and reduce air circulation in the observatory, thereby enhancing the locality of temperature observation. However, under unstable stratification conditions during the daytime, the shadowing effect of solar radiation caused by buildings and aerosol cooling effects might make the SAT observed by the stations surrounded by buildings lower than the stations with open terrain (Li et al., 2011; Zheng et al., 2018; Zheng et al., 2020; Yang et al., 2020b).

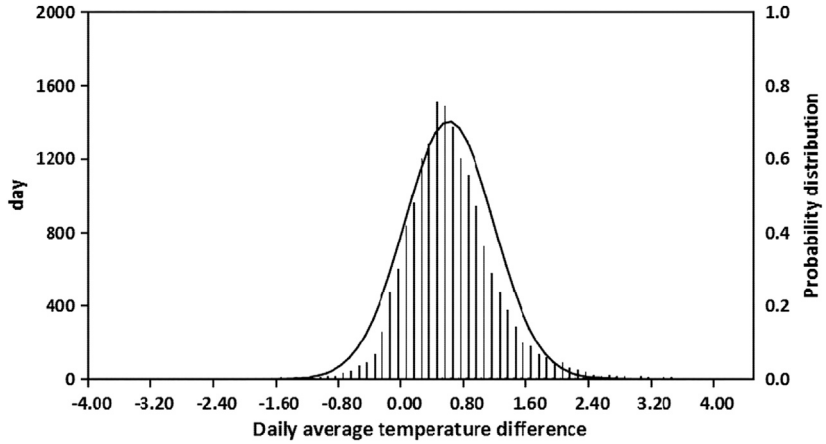

FIGURE 4 | Probability density distribution of the DCSSATda of samples.

TABLE 3 | Statistics of the DCSSATda of samples.

Data series	Sample size	Median (°C)	Mean (°C)	Standard deviation (°C)	Kurtosis	Skewness
ΔT_{avg}	15,347	0.500	0.572	0.568	2.057	0.673

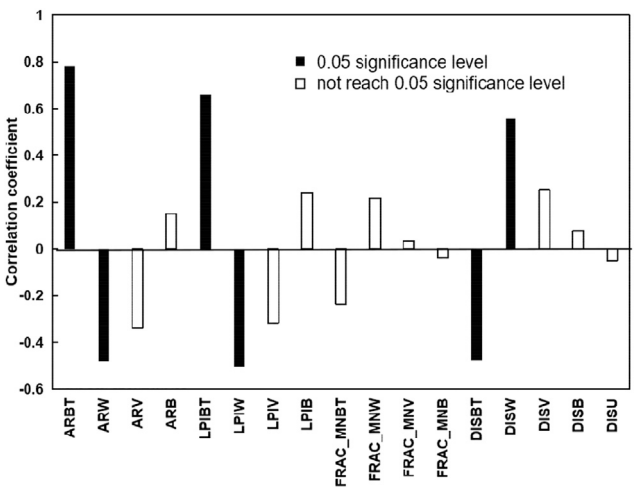

FIGURE 5 | Statistical significance test results and correlation coefficient histogram between SAT_{DON} and DOEFs.

Correlation Analysis of SAT_{DON} and DOEFs

A total of 37 samples were selected from the relocation samples to analyze the correlation between SAT_{DON} and DOEFs, and existing buffer parameters were filtered in order to establish a revised model of urbanization deviation in the next step. **Figure 5** presents the statistical significance test results and correlation coefficient histogram between the SAT_{DON} and DOEFs, in which the solid bars represent the significance level of the correlation reaching 0.05, while the hollow bars represent the opposite.

SAT_{DON} had a significant positive correlation with AR_{BT} after relocation, and the correlation coefficient reached 0.7843, which passed the significance level of 0.05. SAT_{DON} and AR_W showed a significant negative correlation, with a correlation coefficient of −0.4819, which also passed the significance level of 0.05. This showed that with the continuous increase in built-up land around the meteorological station, the decrease in heat capacity of the underlying surface and the increase in anthropogenic heat in the buffer zone led to warming in the SAT series. The heat capacity of water bodies is relatively large, meaning heat in the buffer zone of a station could be taken away as water evaporates, which would lead to a drop in the SAT series (Zeng et al., 2010). In addition, the SAT_{DON} also had a high correlation with LPI_{BT}, LPI_W, DIS_{BT}, and DIS_W after relocation, which showed that the more obvious the advantages in the buffer landscape and the closer the distance of the station to the built-up center of gravity, the greater the SAT_{DON}, while for water this was opposite. Accordingly, this article uses six indicators (AR_{BT}, AR_W, LPI_{BT}, LPI_W, DIS_{BT}, and DIS_W) to study the response SAT_{DON} to the change in the DOEF in the buffer zone.

Simulation and Accuracy Evaluation of Urbanization Bias in the Annual Average SAT Series

The parameter indicators in the buffer zone have undergone great changes after relocation. As shown in **Figure 6**, the change values in the proportion of built-up area (ΔAR_{BT}) of all the relocation samples were positive, which shows that the area of built-up land around the relocated stations was reduced and 92.18% of the ΔAR_{BT} values were concentrated in the range of 0–50%. The

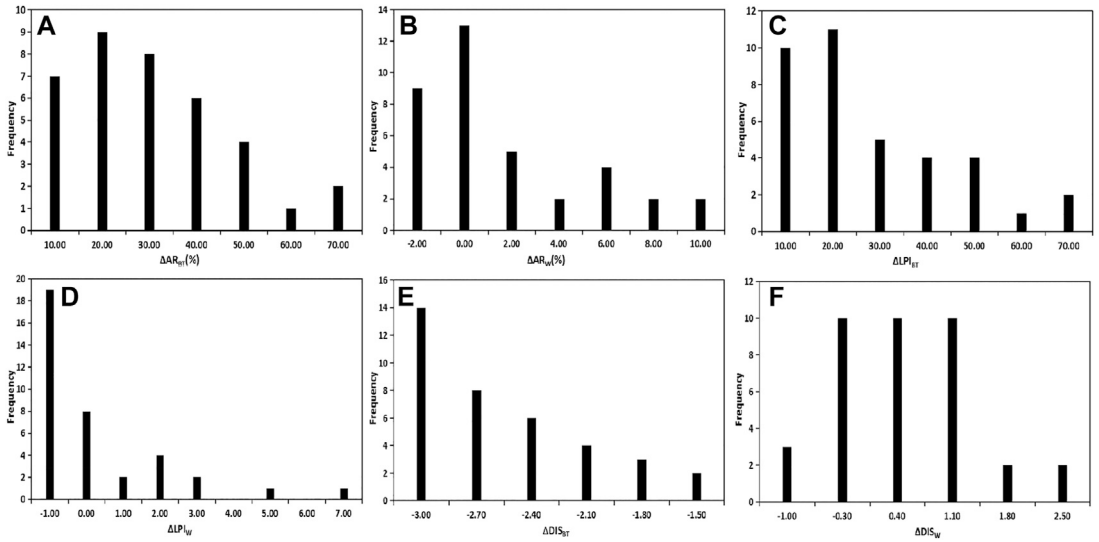

FIGURE 6 | DOEFs between the old and the new stations in the 5-km buffer zone: **(A)** ΔAR_{BT}; **(B)** ΔAR_W; **(C)** ΔLPI_{BT}; **(D)** ΔLPI_W; **(E)** ΔDIS_{BT}; and **(F)** ΔDIS_W.

TABLE 4 | Coefficient of determination (R^2) for stepwise regression of the fitting model.

Model	R^2	Standard deviation of the estimation
1	0.927	0.265
2	0.931	0.237
3	0.939	0.222
4	0.943	0.214
5	0.953	0.209

TABLE 5 | Accuracy evaluation of urbanization bias in the average SAT series.

Station no	ΔT_{avg}	Simulation value	Simulation error (%)
58,122	0.941	0.993	5.52
58,214	0.593	0.701	18.21
58,338	0.602	0.692	14.95
58,109	0.852	0.921	8.10
58,220	0.383	0.397	3.66

number of stations with a negative change value in water area ratio (ΔAR_w) reached 22, which showed that the water area of most stations increased after relocation. The change values of the built-up LPI (ΔLPI_{BT}) of all the relocation samples were positive, and 92.18% of the ΔLPI_{BT} values were concentrated in the range of 0–20. The number of stations with a negative change value of water LPI (ΔLPI_W) also reached 22, which showed that the water advantage of most stations increased after relocation. All the change values of the distance between the station and the built-up center of gravity (ΔDIS_{BT}) were negative, which showed that all samples of relocated stations were far away from the center of gravity of built-up patches. The change value of the distance between the station and the built-up center of gravity (ΔDIS_{BT}) was negative, revealing that all samples of relocated stations were far away from the center of gravity of built-up patches. The number of stations with a positive change value of the distance between the station and the water center of gravity (ΔDIS_w) reached 24, which showed that most samples of relocated stations were close to the center of gravity of built-up patches.

For this part of the study, we used statistics to analyze the response relationship between the SAT_{DON} and DOEFs and simulate the impact of the urbanization bias on the SAT series. The sample was subjected to colinearity diagnosis in SPSS; the statistical models of SAT_{DON} and DOEFs were constructed finally:

$$\Delta T_{avg} = 2.085 \times \Delta AR_{BT} - 1.515 \times \Delta AR_w - 0.017 \times \Delta LPI_w - 0.039 \times \Delta DIS_{BT} + 0.133 \times \Delta DIS_w. \quad (3)$$

Here, ΔT_{avg} is the annual averaged SAT_{DON} of meteorological stations. **Table 4** shows coefficient of determination (R^2) for stepwise regression of the fitted model. With the increase of independent variable, the R^2 of the model increases. The R^2 of the fitting model finally reached 0.953, which passed the 0.05 significance test, indicating that the above five influencing factors have a crucial impact on SAT_{DON}.

According to **Eq. 3**, the change values of the annual average SAT of the remaining five relocated stations in the sample were simulated to compare with the real change value of the sample. As shown in **Table 5**, the difference between the simulated and real value fluctuates in the range of 0.014–0.108°C. The simulation error range is 3.66–18.21%, and the average error is 10.09%.

DISCUSSION

The conventional correction method (Zhang, 2009; Zhang, 2014; Wen et al., 2019a) involves gradually decreasing the annual average urbanization impact from the earliest year of the target station series. The corrected series represents the

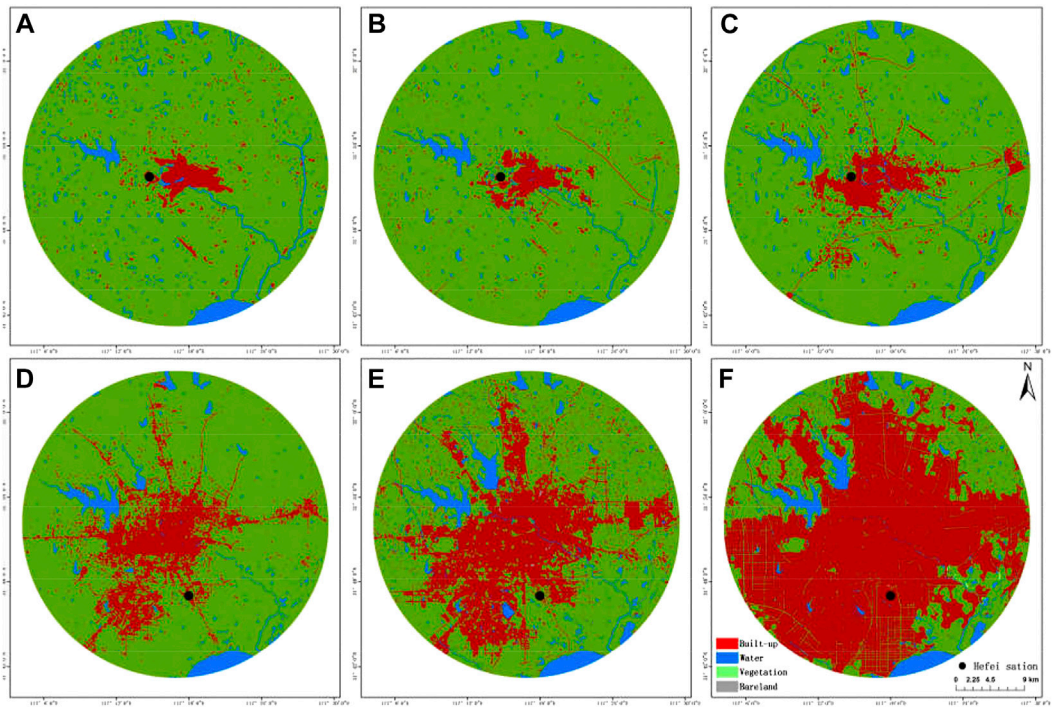

FIGURE 7 | Land use of Hefei city in the 20-km buffer zone and the location of Hefei station: **(A)** 1979; **(B)** 1987; **(C)** 1998; **(D)** 2004; **(E)** 2009; and **(F)** 2018.

regional annual average SAT series in which the urbanization bias has been removed:

$$T'_i = T_i - (\Delta T_{u-r}/10) \times (i-1). \quad (4)$$

Here, i is serial number from the earliest year of recording to the latest year of correcting, T'_i is the annual average SAT after correction in the ith year (°C), T_i is the annual average SAT before correction in the ith year (°C), and $\Delta T_{\text{u-r}}$ is the difference in the SAT warming rate between the urban and reference station (°Cdecade^{-1}). It should be noted that **Eq. 4** has an assumption that the urbanization bias shows a linear growth trend.

For this part of the study, we take the annual average SAT series of Hefei station from 1953 to 2018 (homogenization correction was carried out to remove discontinuities or jumping points caused by the relocation) as an example to discuss the correction of the urbanization bias. The $\Delta T_{\text{u-r}}$ of Hefei station was 0.065°Cdecade^{-1} with Shouxian station selected as the reference station (see **Figure 1**).

Because remote sensing images before the 1950s are not easy to obtain, and the observation environments of meteorological stations were basically unaffected by urbanization, we set the initial value of the various parameters in the station buffer zone in the earliest record year to be 0.

We used the new correction method based on remote sensing to correct the urbanization bias of Hefei station. According to the development process of Hefei's urbanization, the remote sensing image of six times (1979, 1987, 1998, 2004, 2009, and 2018) covering the Hefei area was selected (**Figure 7**). The five parameters of AR_{BT}, AR_W, LPI_W, DIS_{BT}, and DIS_W were interpreted and substituted into **Eq. 3** to obtain the change values of the annual average SAT series, and then the urbanization bias was corrected using **Eq. 2**. In addition, we also used the CCM to correct the urbanization bias of Hefei station in the above the remote sensing image of six times, and the results obtained by the CCM and NCM methods were compared and analyzed.

The correction results obtained by the CCM were higher than those of the NCM (**Table 6**). The CCM did not take into account the impact of the urbanization bias on the reference station, and therefore, the urbanization bias obtained from the reference station was the minimum estimate.

The rate of urban development in Hefei was relatively slow before 2004. From 2004 to 2018, the total GDP of Hefei increased by ¥723.321 billion, with an annual average growth rate of 81.77%, and its economic growth rate ranked first in the YRD region (National Bureau of Statistics, 2019). The warming rate in the SAT series caused by the urbanization bias should change with economic development, but the warming rate at Hefei station obtained by the CCM was a fixed value (0.065°Cdecade^{-1}), and this assumption that the impact of urbanization increases linearly year by year over time is questionable (Zhang, 2009). The results of the NCM show that the urbanization bias of Hefei station increased gradually from 0.233 to 0.457°C from 1979 to 1998. Due to the relocation of Hefei station in 2004, the observation environment improved significantly, and the NCM-based urbanization bias between 2004 and 2009 did not increase much, but the CCM-based

TABLE 6 | Comparison of results between the CCM and NCW at Hefei station.

Year	Observation (°C)	Urban bias (°C) (CCM)	After correction (°C) (CCM)	Urban bias (°C) (NCM)	After correction (°C) (NCM)	GDP
1979	16.124	0.169	15.954	0.233	15.891	-
1987	15.796	0.221	15.575	0.314	15.482	-
1998	17.129	0.293	16.836	0.457	16.672	270.47
2004	16.633	0.332	16.301	0.248	16.385	589.70
2009	16.720	0.364	16.356	0.436	16.284	2,102.12
2018	17.062	0.423	16.639	0.851	16.211	7,822.91

urbanization bias was increasing over time because station relocation was not taken into account. The urbanization bias of Hefei station increased quickly from 0.436 to 0.851°C as the city experienced rapid development from 2009 to 2018. The NCM constructed in this study produces results that are dynamically consistent with the observation environment of the station and the development of the city. In summary, the present work study mainly focused on the sample application exploration of our new urbanization bias correction method, which can make up for the shortcomings of the conventional linear method. We will find more relocation stations in the whole Yangtze River Delta region to extend our new method application in the future.

Based on the R^2 of the fitted results (**Table 4**), it is clear that all the selected parameters can explain more than 90% of the urbanization bias. In addition, urbanization is not only reflected by the two-dimensional horizontal urban expansion but also by the vertical morphology of the three-dimensional urban spatial structure. Previous studies suggested that the vertical geometry of urban canopy building also had an impact on local microclimate (Oke, 2004; Bonacquisti et al., 2006; Chen et al., 2020). In the future, we will expand three-dimensional indicators to supply the indicators of urbanization bias correction.

CONCLUSION

In this study, we selected 42 meteorological stations with site-relocation history in the western region of the YRD from 2009 to 2018 as research example samples and then utilized annual SAT_{DON} series between the old and the new stations to characterize the impact of the urbanization bias on SAT series. We proposed a new method for correcting urbanization-induced bias in surface air temperature observations based on comparative site-relocation data. The main conclusions are as follows.

Spatial land-use, landscape, and geometric parameters of the underlying surface in the 5-km buffer zone around the station were good to be as the DOEFs of the site. The comparative analysis revealed that parameters such as AR_{BT}, AR_W, LPI_{BT}, LPI_W, DIS_{BT}, and DIS_W in DOEFs had the highest correlation with SAT_{DON}, with absolute values of correlation coefficients exceeding 0.4, passing the 0.05 significance test. After colinearity diagnosis, a new linear regression model between five parameters (AR_{BT}, AR_W, LPI_W, DIS_{BT}, and DIS_W) and SAT_{DON} was finally constructed to correct urbanization bias, which clearly reflected the effects of rapid and slow phases of urbanization and environmental changes around the site on the observed SAT. The CCM did not take into account that the reference station was affected by the urbanization, which may underestimate urbanization bias. In addition, CCM cannot consider the station relocation situation, which may overestimate urban bias when the station relocated. In contrast, the NCM constructed in this study can make up these shortcomings to correct the urbanization bias caused by local human activities more reasonably and effectively and can also reduce the error caused by the selection of reference stations in the traditional urban–rural comparison method.

DATA AVAILABILITY STATEMENT

The original contributions presented in the study are included in the article/Supplementary Material, and further inquiries can be directed to the corresponding author.

AUTHOR CONTRIBUTIONS

TS: methodology, formal analysis, results and discussion, and writing—original draft preparation; DS, discussion, and writing reviewing and editing; YH, discussion, and writing reviewing and editing; GL, discussion, and writing reviewing and editing; YY: conceptualization, data curation, methodology, results and discussion, and writing—reviewing and editing.

ACKNOWLEDGMENTS

This study was supported by the National Key R and D Program of China (Fund No: 2018YFC1506502), NSFC-DFG (42061134009) and the Beijing Natural Science Foundation (8202022 and 8171002). The data that support the findings of this study are openly available. The Meteorological Information Center of the China Meteorological Administration provided the meteorological data (http://data.cma.cn/site/index.html); and the remote sensing data used in this study were Landsat data from the United States' EOS (Earth Observation System) refined by Department of Earth System Science/Institute for Global Change Studies Tsinghua University (http://data.ess.tsinghua.edu.cn/).

REFERENCES

Bai, Z. H., and Ren, G. Y. (2006). The effect urban heat island on change of regional mean temperature in Gansu Province, China. *Plateau Meteorol.* 25 (1), 91–94. doi:10.1016/S1003-6326(06)60040-X

Bonacquisti, V., Casale, G. R., Palmieri, S., and Siani, A. M. (2006). A canopy layer model and its application to Rome. *Sci. Total Environ.* 364 (4), 1–13. doi:10.1016/j.scitotenv.2005.09.097

Cai, X. H. (2008). Footprint analysis in micrometeorology and its extended applications. *Chin. J. Atmos. Sci.* 32, 123–132. doi:10.3878/j.issn.1006-9895.2008.01.11

Carolina, A., Tatiana, P., and Ferreira, R. (2013). The conservation success over time: evaluating the land use and cover change in a protected area under a long re-categorization process. *Land Use Policy* 30 (1), 177–185. doi:10.1016/j.landusepol.2012.03.004

Chao, L., Huang, B., Yuanjian, Y., Jones, P., Cheng, J., Yang, Y., et al. (2020). A new evaluation of the role of urbanization to warming at various spatial scales: evidence from the Guangdong-Hong Kong-Macau region, China. *Geophys. Res. Lett.* 47 (20), e2020GL089152. doi:10.1029/2020GL089152

Chen, G., Wang, D., Wang, Q., Li, Y., Wang, X., Hang, J., et al. (2020). Scaled outdoor experimental studies of urban thermal environment in street canyon models with various aspect ratios and thermal storage. *Sci. Total Environ.* 726, 138147. doi:10.1016/j.scitotenv.2020.138147

Comprehensive Observation Department of China Meteorological Administration (2015). *Basic information change table of national surface meteorological observation station*. Beijing, China: China Meterological Administration.

Davey, C. A., and Sr, A. P. (2005). Microclimate exposures of surface-based weather stations: implication for the assessment of long-term temperature trends. *Bull Amer. Meteorol. Soc.* 86 (4), 497–504. doi:10.1175/BAMS-86-4-497

Estoque, R. C., Murayama, Y., and Myint, S. W. (2017). Effects of landscape composition and pattern on land surface temperature: an urban heat island study in the megacities of Southeast Asia. *Sci. Total Environ.* 577, 349–359. doi:10.1016/j.scitotenv.2016.10.195

Fujibe, F. (2009). Detection of urban warming in recent temperature trends in Japan. *Int. J. Climatol.* 29 (12), 1811–1822. doi:10.1002/joc.1822

Gallo, K. P., Easterling, D. R., and Peterson, T. C. (1996). The influence of land use/land cover on climatological values of the diurnal temperature range. *J. Clim.* 9 (11), 2941–2944. doi:10.1175/1520-0442(1996)009<2941:tioluc>2.0.co;2

Hansen, J., Ruedy, R., Sato, M., Imhoff, M., Lawrence, W., Easterling, D., et al. (2001). A closer look at United States and global surface temperature change. *J. Geophys. Res.* 106 (D20), 23947–23963. doi:10.1029/2001JD000354

Li, Q., and Huang, J. (2013). Effects of urbanization on extreme warmest night temperatures during summer near Bohai. *Acta Meteorol. Sin* 27 (6), 808–818. doi:10.1007/s13351-013-0602-0

Li, Q., Huang, J., Jiang, Z., Zhou, L., Chu, P., and Hu, K. (2014). Detection of urbanization signals in extreme winter minimum temperature changes over northern China. *Clim. Change* 122, 595–608. doi:10.1007/s10584-013-1013-z

Li, Q. (2020). Statistical modeling experiment of land precipitation variations since the start of the 20th century with external forcing factors. *Chin. Sci. Bull.* 65 (21), 2266–2278. doi:10.1360/TB-2020-0305

Li, X., Guo, J. X., and Jin, L. J. (2011). The effect of meso-scale environment on temperature in Huang-Huai-Hai plain area. *J. Appl. Meteorol. Sci.* 22 (6), 740–746. doi:10.1016/B978-0-444-53599-3.10005-8

Li, Y.-B., Shi, T., Yang, Y.-J., Wu, B.-W., Wang, L.-B., Shi, C.-E., et al. (2015). Satellite-based investigation and evaluation of the observational environment of meteorological stations in Anhui Province, China. *Pure Appl. Geophys.* 172 (6), 1735–1749. doi:10.1007/s00024-014-1011-8

Liu, J., Kuang, W., Zhang, Z., Xu, X., Qin, Y., Ning, J., et al. (2014). Spatiotemporal characteristics, patterns, and causes of land-use changes in China since the late 1980s. *J. Geogr. Sci.* 24 (1), 195–210. doi:10.1007/s11442-014-1082-6

Liu, Y. L. (2006). *A preliminary analysis of the influence of urbanization on precipitation change trend in north China*. Lanzhou, China: Lanzhou University.

Liu, Y. L., Ren, G. Y., Zhang, G. Y., and Yu, H. (2018). Response of surface air temperature to micro-environmental change: results from mohe parallel observation experiment. *Meteorol. Sci. Tech.* 46 (2), 215–223. doi:10.19517/j.1671-6345.20170200

Lynn, E. E. (2007). Multiple linear regression. *Methods Mol. Biol.* 404, 165–187. doi:10.1007/978-1-59745-530-5_9

Meteorological Observation Centre of CMA (2013). *Investigation and evaluation report on detection environment of national surface meteorological observation station and aerological station*. Beijing, China: China Meterological Administration.

National Bureau of Statistic (2019). *China statistical yearbook*. Beijing, China: China Statistics Press, 107–153.

Oke, T. R. (2004). *Initial guidance to 0btain representative meteorological observations at urban sites*. Geneva, Switzerland: World Meteorological Organization..

Peterson, T. C. (2006). Examination of potential biases in air temperature caused by poor station locations. *Bull. Amer. Meteorol. Soc.* 87, 1073–1080. doi:10.1175/BAMS-87-8-1073

Ren, G., Ding, Y., and Tang, G. (2017). An overview of mainland China temperature change research. *J. Meteorol. Res.* 31 (1), 3–16. doi:10.1007/s13351-017-6195-2

Ren, G., Li, J., Ren, Y., Chu, Z., Zhang, A., Zhou, Y., et al. (2015). An integrated procedure to determine a reference station network for evaluating and adjusting urban bias in surface air temperature data. *J. Appl. Meteorol. Climatol.* 54 (6), 1248–1266. doi:10.1175/JAMC-D-14-0295.1

Ren, G. Y., Zhang, A. Y., Chu, Z. Y., et al. (2010). Principles and procedures for selecting reference surface air temperature stations in China. *Meteorol. Sci. Tech.* 38 (1), 78–85. doi:10.3969/j.issn.1671-6345.2010.01.015

Saputra, A. N., Danoedoro, P., and Kamal, M. (2017). Application of Landsat 8 OLI image and empirical model for water trophic status identification of riam kanan reservoir, banjar, south kalimantan. *IOP Conf. Ser. Earth Environ. Sci.* 98 (1), 012020. doi:10.1088/1755-1315/98/1/012020

Shi, T., Huang, Y., Wang, H., Shi, C.-E., and Yang, Y.-J. (2015). Influence of urbanization on the thermal environment of meteorological station: satellite-observed evidence. *Adv. Clim. Change Res.* 6, 7–15. doi:10.1016/j.accre.2015.07.001

Shi, T., Yang, Y. J., and Jiang, Y. L. (2011). Impact of the variation of urban heat island intensity on temperature series in Anhui Province. *Climatic Environ. Res.* 16 (6), 779–788. doi:10.3878/j.issn.1006-9585.2011.06.13

Trusilova, K., Jung, M., Churkina, G., Karstens, U., Heimann, M., and Claussen, M. (2008). Urbanization impacts on the climate in europe: numerical experiments by the PSU-NCAR mesoscale model (MM5). *J. Appl. Meteorol. Climatol.* 47 (5), 1442–1455. doi:10.1175/2007JAMC1624.1

Vose, R. S. (2005). Reference station networks for monitoring climatic change in the conterminous United States. *J. Clim.* 18 (24), 5390–5395. doi:10.1175/JCLI3600.1

Wen, K. M., Ren, G.-Y., Li, J.., and Ren, Y. (2019a). Adjustment of urbanization bias in surface air temperature over the mainland of China. *Prog. Geogr.* 38 (4), 600–611. doi:10.18306/dlkxjz.2019.04.012

Wen, K., Ren, G., Li, J., Zhang, A., Ren, Y., Sun, X., et al. (2019b). Recent surface air temperature change over mainland China based on an urbanization-bias adjusted dataset. *J. Clim.* 32 (10), 2691–2705. doi:10.1175/JCLI-D-18-0395.1

Wu, J. G. (2000). *Landscape ecology, pattern, process, scale and grade*. Beijing, China: Higher Education Press, 107–115.

Yang, Y., Zhang, M., Li, Q., Chen, B., Gao, Z., Ning, G., et al. (2020a). Modulations of surface thermal environment and agricultural activity on intraseasonal variations of summer diurnal temperature range in the Yangtze River Delta of China. *Sci. Total Environ.* 736, 139445. doi:10.1016/j.scitotenv.2020.139445

Yang, Y., Zheng, Z., Yim, S. H. L., Roth, M., Ren, G., Gao, Z., et al. (2020b). PM2.5 Pollution Modulates Wintertime Urban-Heat-Island Intensity in the Beijing-Tianjin-Hebei Megalopolis, China. *Geophys. Res. Lett.* 47 (1). doi:10.1029/2019gl084288

Yang, Y.-J., Wu, B.-W., Shi, C.-E., Zhang, J.-H., Li, Y.-B., Tang, W.-A., et al. (2013). Impacts of urbanization and station-relocation on surface air temperature series in Anhui Province, China. *Pure Appl. Geophys.* 170 (11), 1969–1983. doi:10.1007/s00024-012-0619-9

Yang, Y. j., Wang, L. B., and Huang, Y. (2017). Impact of urbanization on meteorological observation and its environment representativeness: a case study of shouxian national climate station. *Meteorol. Sci. Tech.* 45 (1), 7–13. doi:10.19517/j.1671-6345.20160062

Yao, W., Han, M., and Xu, S. (2010). Estimating the regional evapotranspiration in zhalong wetland with the two-source energy balance (TSEB) model and Landsat7/ETM+ images. *Ecol. Inform.* 5 (5), 348–358. doi:10.1016/j.ecoinf.2010.06.002

Zeng, Y. N., Zhang, S. J., and Zhang, H. H. (2010). Study on urban heat island effects and its associated surface indicators. *Remote Sensing Tech. Appl.* 25 (1), 1–7. doi:10.3724/SP.J.1087.2010.02819

Zhang, A. Y. (2009). *Identifying and correcting urban bias for surface air temperature series*. Beijing, China: China Academy of Meteorological Sciences.

Zhang, Y. (2014). *Assessment and correction of urban bias in surface air temperature series of eastern China over time period 1913-2012*. Beijing, China: China Academy of Meteorological Sciences.

Zheng, Z. F., Ren, G. Y., Wang, H., Dou, J. X., Gao, Z. Q., Duan, C. F., et al. (2018). Relationship between Fine Particle Pollution and the Urban Heat Island in Beijing, China: Observational Evidence. *Bound. Layer Meteorol.* 169 (1), 93–113. doi:10.1007/s10546-018-0362-6

Zheng, Z., Zhao, C., Lolli, S., Wang, X., Wang, Y., Ma, X., et al. (2020). Diurnal Variation of Summer Precipitation Modulated by Air Pollution: Observational Evidences in the Beijing Metropolitan Area. *Environ. Res. Lett.* 15 (9). doi:10.1088/1748-9326/ab99fc

Zhou, C., Wang, K., Qi, D., and Tan, J. (2019). Attribution of a record-breaking heatwave event in summer 2017 over the Yangtze River Delta. *Bull. Am. Meteorol. Soc.* 100, S97–S103. doi:10.1175/bams-d-18-0134.1

Zhou, W., Huang, G., and Cadenasso, M. L. (2011). Does spatial configuration matter? Understanding the effects of land cover pattern on land surface temperature in urban landscapes. *Landscape Urban Plann.* 102, 54–63. doi:10.1016/j.landurbplan.2011.03.009

Conflict of Interest: The authors declare that the research was conducted in the absence of any commercial or financial relationships that could be construed as a potential conflict of interest.

frontiers in Earth Science

ORIGINAL RESEARCH
published: 20 May 2021
doi: 10.3389/feart.2021.654848

Temporal and Spatial Variations of Soil Moisture Over Xinjiang Based on Multiple GLDAS Datasets

Zengyun Hu[1,2,3], *Xi Chen*[1,2,3]*, *Yaoming Li*[1,2,3], *Qiming Zhou*[4] *and Gang Yin*[5]

[1]State Key Laboratory of Desert and Oasis Ecology, Xinjiang Institute of Ecology and Geography, Chinese Academy of Sciences, Beijing, China, [2]Research Center for Ecology and Environment of Central Asia, Chinese Academy of Sciences, Ürümqi, Xinjiang, China, [3]College of Resources and Environment, University of Chinese Academy of Sciences, Beijing, China, [4]Department of Geography, Hong Kong Baptist University, Kowloon, China, [5]College of Resource and Envrionment Sciences, Xinjiang University, Urumqi, Xinjiang, China

Under the global warming, as the typical arid region of Central Asia, the Xinjiang Uygur Autonomous Region (Xinjiang) has been experienced the remarkable warming and increased precipitation based on large previous studies. The arid and semiarid ecosystem of Xinjiang is very sensitive and vulnerable to climate change and water resource variations. However, the sparse and highly unevenly distributed *in-situ* stations in this region provide limited data for understanding of the soil moisture variations. In this study, the spatial and temporal changes and variations of soil moisture were explored at annual and seasonal time scales during the period of 2000–2017. The soil moisture data are from the Global Land Data Assimilation System (GLDAS) models, including four GLDAS 1 models: CLM, Mosaic, VIC and Noah 2.7 and one GLDAS 2.1 model: Noah 3.3. Major results show that 1) Noah 3.3 and VIC have the significant positive trends of annual soil moisture with the values of 2.64°mm/a and 0.98°mm/a. The trend of CLM is significant negative. The other two models Mosaic and Noah 2.7 have the weak positive trends. The temporal variations of seasonal soil moisutre are similar the annual soil moisture for each of the model. 2) For the spatial characteristics of the soil mositure variations, CLM displays the negative trends over large part of Xinjiang. Mosaic and VIC have the similar spatial characteristics of the linear trends. Noah 3.3 has the significant positive trends over almost Xinjiang which is different with Noah 2.7. All the five models have the positive trends over KLM. Our results have a better understanding of the soil moisture variations across Xinjiang, and they also enhance the reconginzing of the complex hydrological circulation in the arid regions.

Keywords: linear trend, soil moisture, spatial and temporal variation, GLDAS product, Xinjiang

OPEN ACCESS

Edited by:
Qingxiang Li,
Sun Yat-Sen University, China

Reviewed by:
Xihui Gu,
China University of Geosciences, China
Minyan Wang,
China Meteorological Administration, China

***Correspondence:**
Xi Chen
chenxi@ms.xjb.ac.cn

Specialty section:
This article was submitted to Interdisciplinary Climate Studies, a section of the journal Frontiers in Earth Science

Received: *17 January 2021*
Accepted: *05 May 2021*
Published: *20 May 2021*

Citation:
Hu Z, Chen X, Li Y, Zhou Q and Yin G (2021) Temporal and Spatial Variations of Soil Moisture Over Xinjiang Based on Multiple GLDAS Datasets. Front. Earth Sci. 9:654848. doi: 10.3389/feart.2021.654848

INTRODUCTION

As one of the key hydrological variables, soil moisture plays a fundamental role in the complex physical processes, such as infiltration, rainfall-evapotranspiration-runoff circulation, photosynthesis, and groundwater recharge (Ford et al., 2015; Amani et al., 2017; Orth and Seneviratne, 2017; Dari et al., 2019; Gu et al., 2019a). It is known that soil moisture has remarkable impacts on the exchanges of water, energy and carbon fluxes between land surface, vegetation, and atmosphere (Western et al., 2004; Fischer et al., 2007; Trenberth et al., 2007; Qiu et al.,

2016; Gu et al., 2019a; Hu et al., 2021). Moreover, it is used to quantify the irrigation water consumption (Jalilvand et al., 2019) and to monitor the drounght variation (Dai et al., 2004; Li et al., 2017; Hu et al., 2019a; Xu et al., 2020). Therefore, the accurate representation and estimation of soil moisture in hydrological models will control the performances of simulations and predications of the hydrological cycle, such as the estimation of groundwater (Scanlon et al., 2018). It is very important to understand the soil moisture changes and variations which is essential to improve the scientific recognizing of regional and global hydrological processes, especially over the arid and semiarid regions.

Because of the importance of soil moisture on the mass and energy balance between the land surface and the atmosphere, lots of techniques have been developed to measure and to monitor its changes and variations. The *in-situ* measurement stations can describe the true changes of soil moisture in the successive years with high temporal resolution (e.g. in second or minute time scale), although some system errors and measurement errors are resulted from the instruments and the surrounding environments (Holgate et al., 2016). But it is difficult to install the instruments in high-density observation net-works for the poor regions over the world, such as Africa and northwest of China, because of the expensive measurements (Gu et al., 2019a). Satellite soil moisture products and model-based soil moisture products are sourced as the soil moisture data which are widely used to detect the temporal variaitons and spatial patterns of the soil moisture (Fan and Dool, 2004; Yao et al., 2004; Zhou et al., 2010; Beck et al., 2020). Compared with the *in-situ* measurements, model output of soil moisture has the advantages with the high spatial and temporal resolutions which have been widely employed in regional and global researches to explore different climate and hydrological processes, such as analyzing the historical and future variations of moisture (Cheng et al., 2015; Chen et al., 2016), monitoring the dry and wet changes (Robinson et al., 2016; Hu et al., 2019a), improving the hydrological model simulations (He et al., 2017), and explaining the dynamics of land-atmosphere interactions (Gerken et al., 2015; May et al., 2015).

Several types of soil moisture datasets as the model output are used in previous studies (Qin et al., 2009; Chen et al., 2016), such as Global Land Data Assimilation System (GLDAS; Rodell et al., 2004), Coupled Model Intercomparison Project phase 5 (CMIP5; Berg et al., 2017; Feng et al., 2017), and various reanalysis data sets (e.g. ERA-Interim and MERRA V2) (Modanesi et al., 2020; Spennemann et al., 2020; Zhou et al., 2020). In GLDAS, Land Surface Models (LSMs) and hydrological models were driven by meteorological forcing to simulate soil moisture of multilayers with different depths (Bi et al., 2016; Yuan and Quiring, 2017). Recent study (Gu et al., 2019b) pointed that the soil moisture data of GLDAS 2.1 is better than CMIP 5 when are compared with the satellite datasets.

Xinjiang is the typical arid and semiarid regions over Central Asia. The soil mositure plays a key role for the complex hydrological process, especially in the desert regions. However, there are only few *in-situ* measurements and they are very difficult employed. Therefore, four GLDAS 1 models: CLM, Mosaic, VIC and Noah 2.7 and one GLDAS 2.1: Noah 3.3 are employed to explore the soil moisture variations. In this study, we aim to 1) detect the temporal changes of soil moisture at different time scales since the 21st century: during the period of 2000–2017; 2) to analyze the spatial patterns of the soil moisture varaitions. The paper is organized as follows. In *Study Area, Dataset and Methodology, the study area*, dataset and methodology are introduced. In *Result and Discussion*, the major results and discussion are displayed. In the last section, a conclusion is provided.

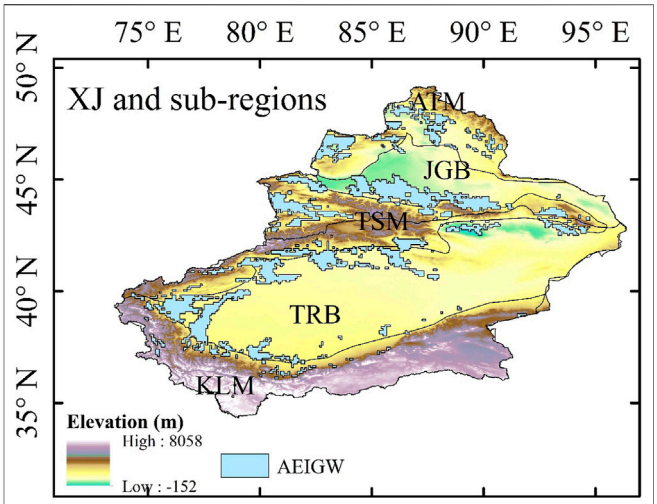

FIGURE 1 | Study area: Xinjiang (XJ) and the locations of the five sub-regions, i.e. Altain Mountainous (ATM), Junggar Basin (JGB), Tianshan Mountainous (TSM), Tarim Basin (TRB) and Kunlun Mountainous (KLM). The black line denotes the boundary of the sub-regions. The blue represents the area of irrigation from groundwater which are extracted from the Global Map of Irrigation Areas (GMIA) V5.0 of the Food and Agriculture Organization of the United Nations, AEIGW: area equipped for irrigation with groundwater.

STUDY AREA, DATASET AND METHODOLOGY

Study Area

The study area is located in Northwest China covering more than 1.6 million km^2 of 73°40′~96°23′E and 34°25′~49°10′N (**Figure 1**). Its complex topography characterizes with mountainous, plain and basin areas. There are three mountain ranges in Xinjiang, namely, the Altai Mountains (ATM) in the north, Tianshan Mountains (TSM; the "Water Tower" of Central Asia) in the middle, and the Kunlun Mountains (KLM) in the south. The Junggar Basin (JGB) and Tarim Basin (TRB) are situated between the three mountain ranges from north to south. Most of the irrigated areas are distributed in the piedmont plains and the edges of basins (**Figure 1**).

Xinjiang is dominated by an arid and semi-arid climate with very low precipitation and strong evaporation. The average of annual precipitation is 157 mm which only accounts for 24.2% of averaged precipitation (i.e. 650 mm) across China (Chen et al., 2012). In addition, precipitation in this region varies with high spatial difference and large inner-annual variation (e.g. more

precipitation in mountainous areas than in plain areas; more precipitation in spring and summer than in autumn and winter) (Hu et al., 2016a; Chen et al., 2018). In the past three decades, Xinjiang experienced a significant warm-wet trend (Hu et al., 2014; Hu et al., 2017; Hu et al., 2018). Although the Xinjiang's climate transited from warm-dry to a warm-wet in the 1980s (Shi, et al., 2007; Hu et al., 2016b), water resources are still limited and hardly meet the increasing water demand for economy development and population growth in Xinjiang. As an important and irreplaceable water source for Xinjiang, groundwater plays a key role for domestic water supplies and agricultural irrigation in oasis (Hu et al., 2019b).

Dataset and Methodology

Global Land Data Assimilation System (GLDAS) aims to consolidate satellite- and ground based observational data products to generate optimal fields of land surface states and fluxes by using advanced land surface modeling and data assimilation techniques (Rodell et al., 2004). At present, GLDAS consists of simulations of four Land Surface Models (LSMs): Noah, Catchment, the Community Land Model (CLM), and the Variable Infiltration Capacity (VIC). At present, GLDAS drives six land surface models (LSMs): Noah, Catchment, Mosaic, the Common Land Model (CLM), the Community Land Surface Model (CLSM), and the Variable Infiltration Capacity (VIC). The GLDAS datasets [GLDAS Version 1 (GLDAA-1), GLDAS Version 2.0 (GLDAS-2.0) and GLDAS Version 2.1 (GLDAA-2.1)] have the five temporal resolutions from 1 h to 1 month and the eight spatial resolutions from 0.1 ×0.1 –1.25 ×1.25 (https://disc.sci.gsfc.nasa.gov/datasets?keywords=GLDAS). GLDAS-1 forcing datasets include: bias-corrected European Center for Medium-Range Weather Forecasts (ECMWF) Reanalysis data for 1979–1993, bias-corrected National Center for Atmospheric Research (NCAR) Reanalysis data for 1994–1999 (Berg et al., 2003); National Oceanic and Atmospheric Administration (NOAA)/ Global Data Assimilation System (GDAS) atmospheric analysis fields for 2000 (Derber et al., 1991), and a combination of NOAA/GDAS atmospheric analysis fields, spatially and temporally disaggregated NOAA Climate Prediction Center Merged Analysis of Precipitation (CMAP) (Xie and Arkin, 1996) fields, and observation-based downward shortwave and longwave radiation fields from the Air Force Weather Agency (AFWA) for 2001-present. GLDAS-2.1 forcing datasets (2001-present) include a combination of NOAA/GDAS atmospheric analysis fields (Derber et al., 1991), temporally disaggregated Global Precipitation Climatology Project (GPCP) precipitation fields (Adler et al., 2003), and the Air Force Weather Agency's Agricultural Meteorological modeling system (AGRMET) radiation fields (March 2001 onwards) (https://disc.gsfc.nasa.gov/information/documents/5a70903bca6d24bac24118eb/gldas-lsm-description).

Because GLDAS datasets provide high spatiotemporal resolutions variables which makes it is an effective resource to study the water cycle based on these datasets, they have been widely used in many previous studies (Scanlon, et al., 2012; Mukheriee and Ramachandran, 2018; Kong et al., 2019; Chen and Yuan, 2020; Hoffmann et al., 2020; Niu, et al., 2020; Solander et al., 2020; Hu et al., 2021). To match the temporal (monthly) and spatial resolution (1.0 × 1.0) of the GRACE datasets, the GLDAS LSMs datasets examined in this study are those included in GLDAS V1 VIC and Mosaic with the period of 1979-present, and GLDAS V2.1 Noah V3.3 with the period of 2000-present.

The soil moisture from the GLDAS V1 (i.e. CLM, Mosaic, VIC and Noah 2.7) with the period of 1979-present and the spatial resolution of 1.0 × 1.0 and the GLDAS V2.1 (Noah 3.3) with the period of 2000-present and the spatial resolution of 1.0 × 1.0 are used in this study to estimate the changes in soil moisture. The soil moisture in this study is the summation of all the layers for each model, such as three layers for VIC, and four layers for Noah and Mosaic.

VIC was originally developed by Liang et al. (1994), Liang et al. (1996) at the University of Washington in early 90's. The model focuses on runoff processes that are represented by the variable infiltration curve, a parameterization of sub-grid variability in soil moisture holding capacity, and nonlinear baseflow. VIC is a stand-alone, 1-D column model that is run uncoupled. Various simulation models are available including water balance, energy balance, frozen soil, and other special cases. As a macroscale hydrological model, VIC models sub-grid variability in the soil moisture storage capacity and bas flow as a nonlinear recession. In GLDAS-1, VIC model includes three soil layers (0–10, 10–160, and 160–190 cm) and was simulated in water balance mode with computing energy fluxes (Cherkauer and Lettenmaier, 2003). Therefore, the VIC data includes water budget components and forcing fields but without energy budget components.

Noah is a National Centers for Environmental Prediction/ Oregon State University/Air Force/Hydrologic Research Lab (Noah) Model. The community Noah LSM was developed in 1993 through a collaboration of investigators from public and private institutions, spearheaded by the National Centers for Environmental Prediction. Current development efforts are consistent with the land surface scheme in Weather Research Forecast (WRF) system, under the Unified Noah LSM (Chen et al., 1996; Chen et al., 1997; Koren et al., 1999; Chen and Dudhia, 2001; Ek et al., 2003). Noah is a stand-alone, 1-D column model which can be executed in either coupled or uncoupled mode. The model applies finite-difference spatial discretization methods and a Crank-Nicholson time-integration scheme to numerically integrate the governing equations of the physical processes of the soil-vegetation-snowpack medium. It includes four soil layers (0–10, 10–40, 40–100, and 100–200 cm), single layer snowpack, and frozen soil physics. Canopy, snow, and soil moisture storage are included in Noah.

Mosaic (Koster and Suarez, 1996) is a well-established and theoretically sound LSM, as demonstrated by its performance in the Project for Intercomparison of Land-surface Parameterization Schemes (PILPS) and Global Soil Wetness Project (GSWP) experiments. Mosaic's physics and surface flux calculations are similar to the SiB (simple biosphere model) LSM (Sellers et al., 1986). It is a stand-alone, 1-D column model that can be run both uncoupled and coupled to the atmospheric column. Mosaic divides each model grid cell into a Mosaic of tiles based on the distribution of vegetation types within the cell. It has four soil layers: 0–2, 2–150, and 150–350 cm.

TABLE 1 | Linear trends (mm/a) of the soil moisture of the five models at annual and seasonal scales during the period of 2000–2017.

model	Annual	MAM	JJA	SON	DJF
CLM	−0.42**	−0.37**	−0.46**	−0.47**	−0.46**
Mosaic	0.67	0.98	0.76	0.26	0.10
VIC	0.98**	1.21**	0.93**	0.78**	0.6*
Noah 2.7	0.05	0.10	0.07	-0.01	−0.13
Noah 3.3	2.64**	2.51**	2.85**	2.78**	2.22**

*** denotes the trend is significant at the 95% or 99% significance level.*

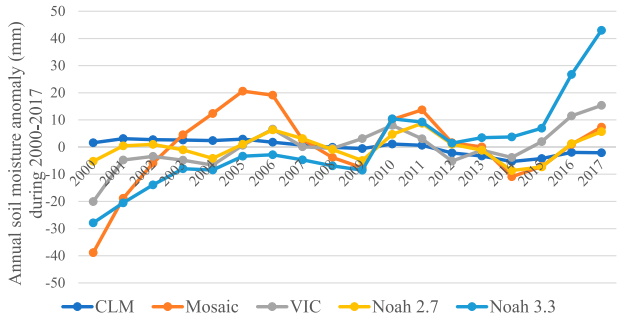

FIGURE 2 | Anomaly of annual soil moisture of the five different models: CLM, Mosaic, VIC, Noah 2.7 and Noah 3.3 over Xinjiang during the period of 2000–2017.

Because GLDAS datasets provide hydrological variables in high spatial and temporal resolutions, they have been widely used in many previous studies in the field of hydrology (Kong et al., 2019; Chen and Yuan, 2020; Hoffmann et al., 2020; Niu, et al., 2020; Solander et al., 2020). The soil moisture from the GLDAS V1 (i.e. CLM, Mosaic, VIC and Noah 2.7) and the latest GLDAS dataset (Noah 3.3) with the spatial resolution of 1.0 × 1.0 are used in this study to estimate the changes in soil moisture. The soil moisture in this study is the summation of the different layers for each model.

The soil moisture analysis is carried out at multiple time scales from monthly, seasonal to annual. The four seasons are spring [March-May (MAM)], summer [June-August (JJA)], autumn [September–November (SON)] and winter [December-February (DJF)]. The changes of the soil moisture is quantified by the linear trend which is computed by the linear least square method, and the significant of the linear trend is detected by the Student's test at the 95% or 99% confidence level ($p < 0.05$ or $p < 0.01$).

RESULT AND DISCUSSION

Temporal Variations of Soil Moisture During 2000–2017

The temporal variations and changes of soil moisture of the five GLDAS models: CLM, Mosaic, VIC, Noah 2.7 and Noah 3.3 over

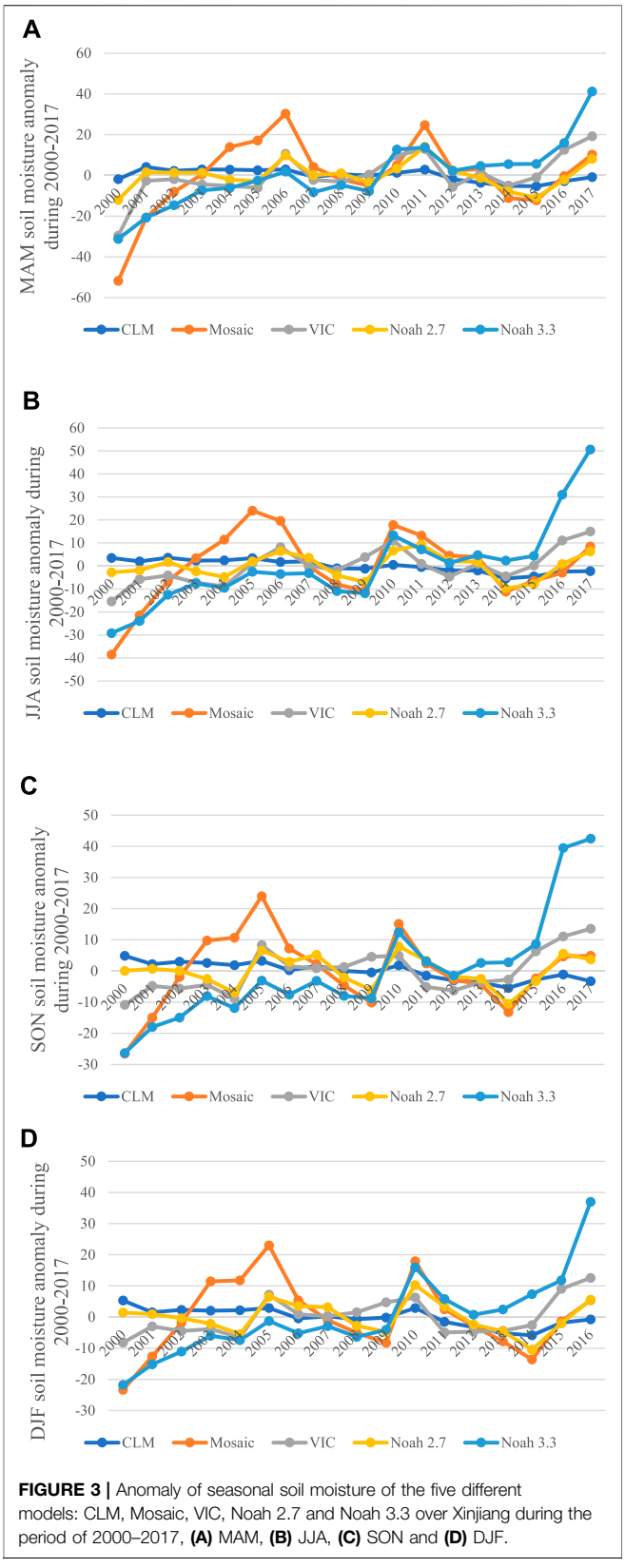

FIGURE 3 | Anomaly of seasonal soil moisture of the five different models: CLM, Mosaic, VIC, Noah 2.7 and Noah 3.3 over Xinjiang during the period of 2000–2017, **(A)** MAM, **(B)** JJA, **(C)** SON and **(D)** DJF.

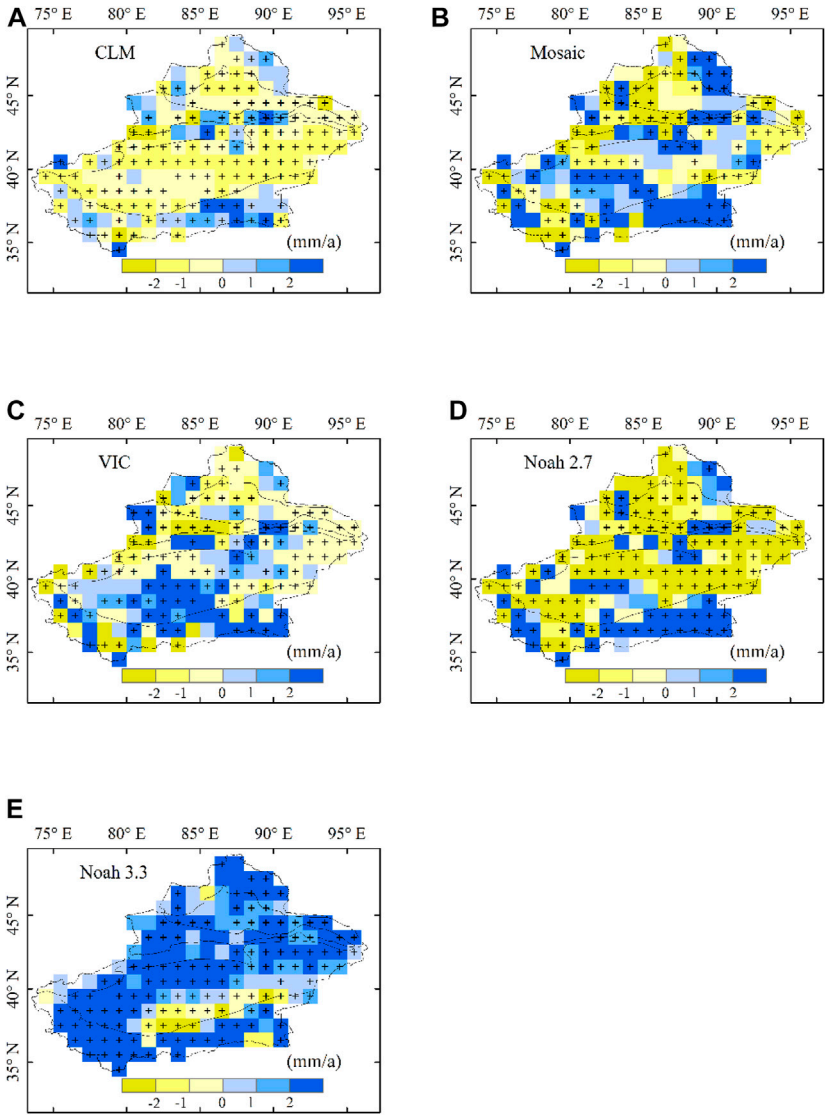

FIGURE 4 | Spatial distributions of the linear trends (mm/month) of the annual soil moisture for five models during 2000–2017, **(A)** CLM, **(B)** Mosaic, **(C)** VIC, **(D)** Noah 2.7 and **(E)** Noah 3.3. The cross signs denote the trends are significant at the 95% significance level.

Xinjiang are explored using the linear trends at annual and seasonal time scales (**Table 1**; **Figures 2**, **3**). For annual soil moisture, CLM displays the significant negative linear trend with the rate of −0.42 mm/a at a 99% confidence level ($p < 0.01$) which indicates the decreasing soil moisture in Xinjiang (**Table 1** and **Figure 2**). For the other four models, Noah 3.3 has the largest positive trend (2.64 mm/a), and followed by VIC with the rate of 0.98 mm/a. Moreover, the trends of Noah 3.3 and VIC are significant at 99% confidence level ($p < 0.01$). The positive trends of Mosaic and Noah 2.7 are not significant at 95% confidence level. Furthermore, all the five models show an obvious increasing during the period of 2000–2011 except CLM from **Figure 2**.

For the seasonal soil moisture, these models display the different variations. For the changes of the MAM soil moisture, CLM also has the negative trend with the value of −0.37 mm/a which is significant at the 99% confidence level ($p < 0.01$) (**Table 1**, **Figure 3A**). Noah 3.3 has the largest positive trend of MAM soil moisture among the five models with the value of 2.51 mm/a ($p < 0.01$) (**Table 1**) which displays the obvious variations in **Figure 3A**. VIC has the second largest positive trend (1.21 mm/a) which is also significant at the 99% confidence level ($p < 0.01$) (**Table 1** and **Figure 3A**). The trends of MAM soil moisture of Mosaic and Noah 2.7 are 0.98 mm/a and 0.1 mm/a, respectively (**Table 1**).

For JJA, Noah 3.3, VIC, Mosaic and Noah 2.7 have the positive trends with the values of 2.85, 0.93, 0.76, and 0.07 mm/a, respectively (**Table 1**). The trends of Noah 3.3 and VIC are also significant at the 99% confidence level. The significant negative trend of soil moisture is still obtained in CLM with the value of −0.46 mm/a ($p < 0.01$) (**Table 1**, **Figure 3B**).

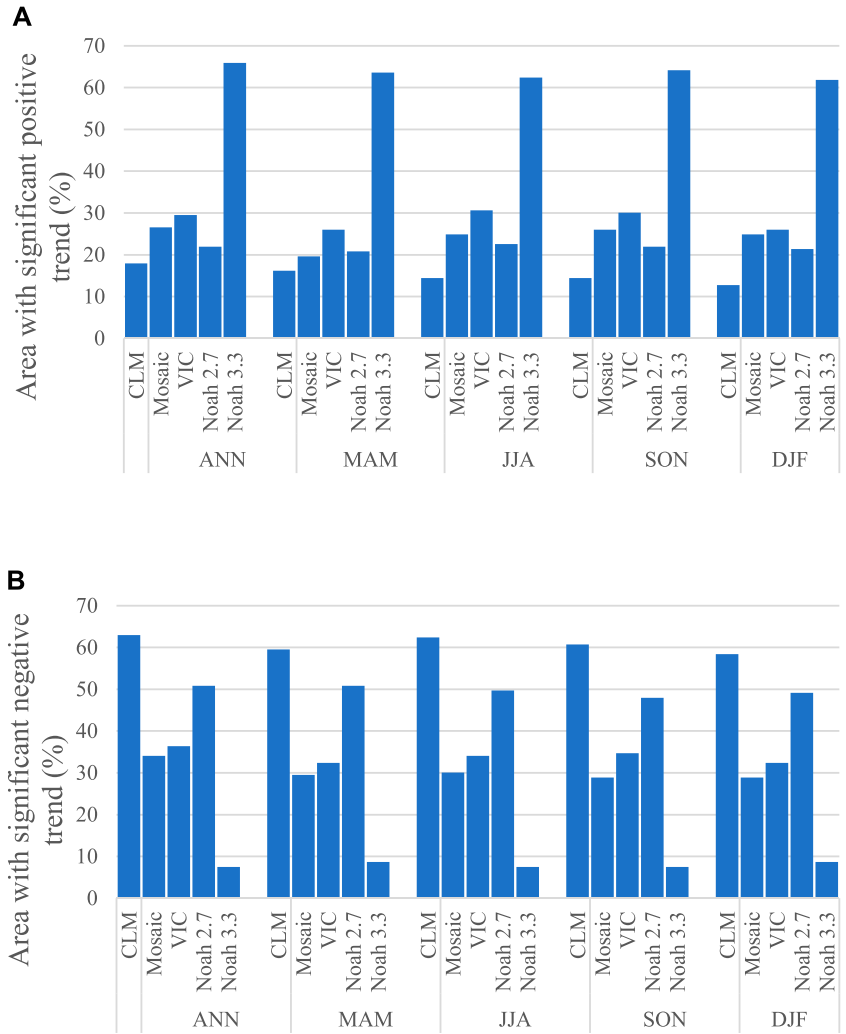

FIGURE 5 | Percentage of areas with significant positive **(A)** and negative **(B)** trends of the five different models at annual and seasonal scales.

As the other seasons, CLM still has the significant negative trends in both SON and DJF with the values −0.47 and −0.46 mm/a ($p < 0.01$) (**Table 1**). The weak negative trends are obtained for SON and DJF soil moisture in Noah 2.7 which are different from annual, MAM and JJA. Significant positive trends of VIC and Noah 3.3 are observed for SON and DJF soil moisture with the values of 0.78 and 0.6 mm/a for VIC, and 2.78 and 2.22 mm/a for Noah 3.3 ($p < 0.01$) (**Table 1**, **Figures 3C,D**). The positive trends of Mosaic are 0.26 and 0.1 mm/a for SON and DJF over Xinjiang during the period of 2000–2017.

On the whole, CLM has the significant negative trends of soil moisture at annual and seasonal scales. Mosaic, VIC and Noah 3.3 have the positive trends for annual and seasonal soil moisture. The annual and seasonal soil moisture trends of Noah 2.7 are weak which indicate the weak variations of soil moisture. Moreover, Noah 3.3 has the largest positive trends among the five models.

Spatial Distributions of Linear Trends of Annual Soil Moisture

For the spatial distributions of linear trends of annual soil moisture, the five models display the different spatial patterns (**Figure 4**). Specifically, for CLM, 18% areas have the significant positive trends with the distribution over mountainous areas, such as TSM and KLM (**Figures 4A**, **5A**). More than half areas have the significant negative trends mainly over JGB and TRB (63%, **Figures 4A**, **5B**). For Mosaic, 27% areas have the significant positive trends over part of ATM, TSM, TRB and KLM (**Figures 4B**, **5A**). For the areas with negative trends, they account for 34% over Xinjiang (**Figures 4B**, **5B**). VIC has the similar spatial patterns as Mosaic with the 29% significant positive areas and 36% significant negative areas (**Figures 4C**, **5**). The significant positive trends are distributed over 22% areas (e.g. eastern of KLM) and 51% areas have the significant negative trends for Noah 2.7 (**Figures 4D**, **5**). For Noah 3.3, largely areas show the positive trends with the significant positive trends over more than

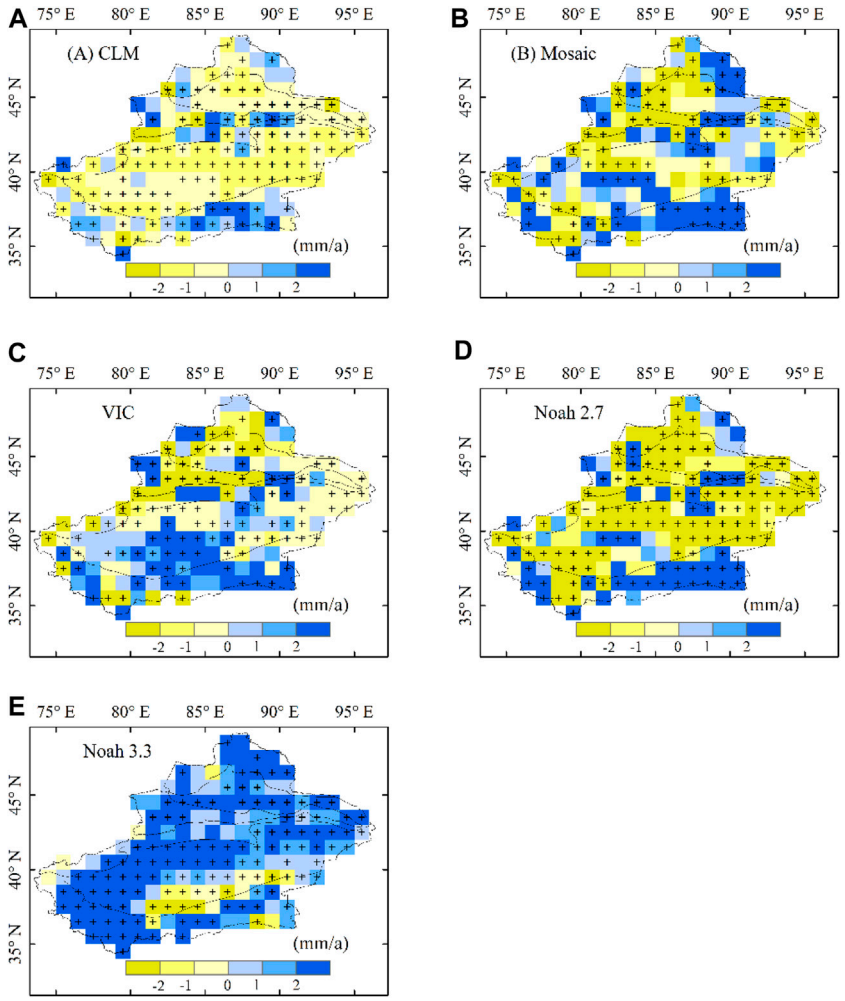

FIGURE 6 | Same as **Figure 4**, but for MAM soil moisture.

60% areas, and the significant negative trends only account for less than 8% areas (**Figure 4E**).

Overall, all the models show the positive trends over KLM. Mosaic and VIC has the similar distributions. Noah 2.7 and Noah 3.3 have the opposite linear trends. These differences among the five models may be caused by their different input datasets and different model structures.

Spatial Distributions of Linear Trends of MAM and JJA Soil Moisture

For the spring soil moisture (i.e. MAM soil moisture), the five models have the similar spatial distributions of the linear trends as the ANN soil moisture (**Figure 6**). In small areas (16%), CLM has the significant positive trends, and less than 60% areas have the significant negative trends (**Figures 5**, **6A**). For Mosaic, the significant positive areas account for 20% and the 29% areas have the significant negative linear trends (**Figure 5**). Moreover, the center of the positive trend areas is mainly in KLM (**Figure 6B**). In terms of VIC model, the areas with significant positive trends and significant negative trends are 26% and 32%, respectively (**Figure 5**). The large positive trends are distributed over south of TRB and KLM (**Figure 6C**). For Noah 2.7 and Noah 3.3, the spatial patterns are similar as the annual soil mositure (**Figures 6D,E**). the areas with the significant negative trends of Noah 2.7 are 51% and the significant positive areas of Noah 3.3 are 63% (**Figure 5**).

For JJA soil moisture, each of the five models have the similar distributions as annual and MAM (**Figure 7**). The significant positive areas of CLM, Mosaic, VIC, Noah 2.7 and Noah 3.3 are 14, 25, 31, 23, and 62%, respectively (**Figure 5A**). For the significant positive trends, CLM still has the largest areas (62%) among the five models, and followed by Noah 2.7 and VIC (**Figure 5B**).

Spatial Distributions of Linear Trends of SON and DJF Soil Moisture

For SON, CLM has the large significant negative trends over 61% areas, and 14% areas have the significant positive trends

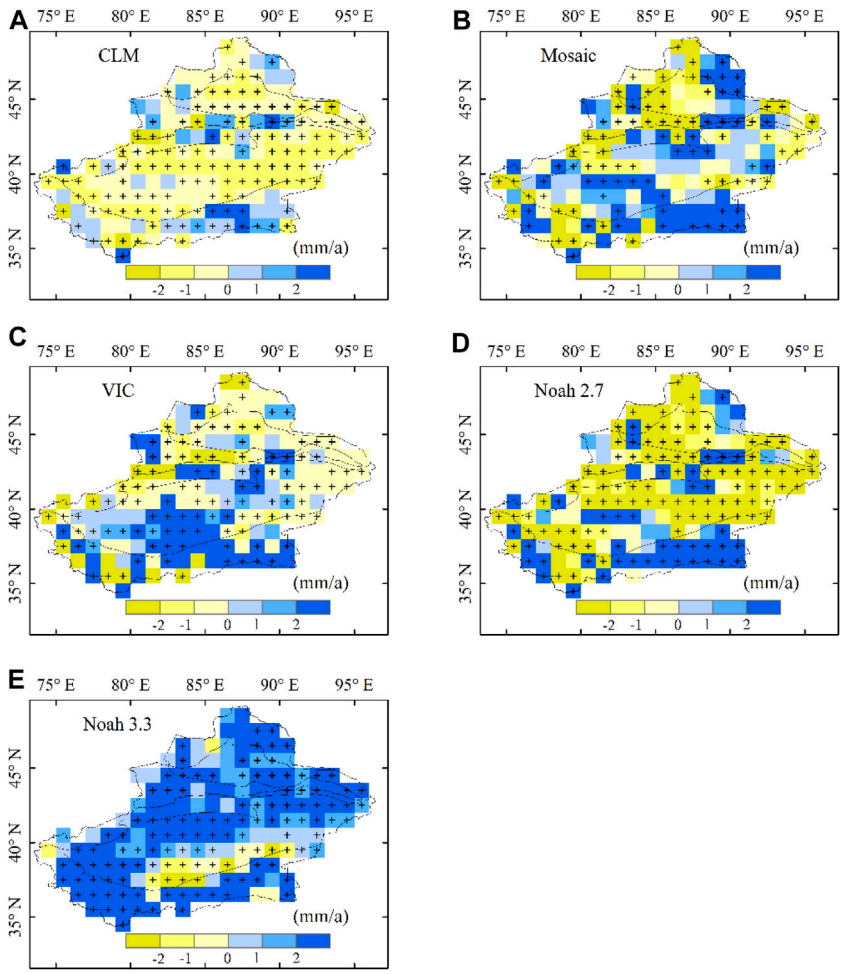

FIGURE 7 | Same as **Figure 4**, but for JJA soil moisture.

distributed over eastern KLM (**Figures 5**, **8A**). For Mosaic, large parts of areas have the positive trends of annual with 26% areas significant at 95% confidence level, and these areas are distributed over part of ATM, most of TRB and KLM (**Figures 5**, **8B**). The significant negative trends of soil moisture are fragmentally distributed over Xinjiang with the percentage of 29%. For VIC model, the significant negative trends account for 35% areas over Xinjiang, and are mainly distributed over ATM, JGB and part of TRB (**Figures 5**, **8C**). The areas with significant positive trends of soil moisture account for 30% which are also distributed over most of TRB and KLM. For the model of Noah 2.7, most of the negative trends have the values smaller than −2 mm/a, and the areas with the significant negative trends account for 49% (**Figures 5B**, **8D**). Almost all the positive trends have the values larger than 2 mm/a with the 21% significant areas. In terms of Noah 3.3, except the negative trends over the small parts of TRB, the other regions have the significant positive trends accounting for 62% areas over Xinjiang (**Figure 8E**).

Figure 9 displays the spatial distributions of DJF soil moisture linear trends based on the five models. The distributions of the five models are similar as the annual soil moisture and the other three seasons. For CLM, the significant increase trends and significant decrease trends account for 13% and 58% areas, respectively (**Figure 5**). Mosaic and VIC also have the same spatial patterns of the DJF soil moisture linear trends, and the significant positive trends account for 25 and 26% areas, respectively (**Figures 5A**, **9B,C**). For Noah 2.7 and Noah 3.3, the percentages of the positive areas are 21% and 62% (**Figures 5**, **9**).

DISCUSSION

Due to the lake of the *in-situ* observations, the accuracy of soil moisture from the five GLDAS models is not evaluated in this study. We only explored the temporal and spatial variations of the soil moisture over Xinjiang using multiple GLDAS datasets. In recent study (Supplementary Figure S3 in Hu et al., 2019b), it was proved that Noah, VIC, Mosaic had the positive linear trends of soil moisture in Xinjiang except the CLM model which are similar with the result of this study. Moreover, Gu et al. (2019a) concluded that GLDAS Noah soil moisture is in agreement

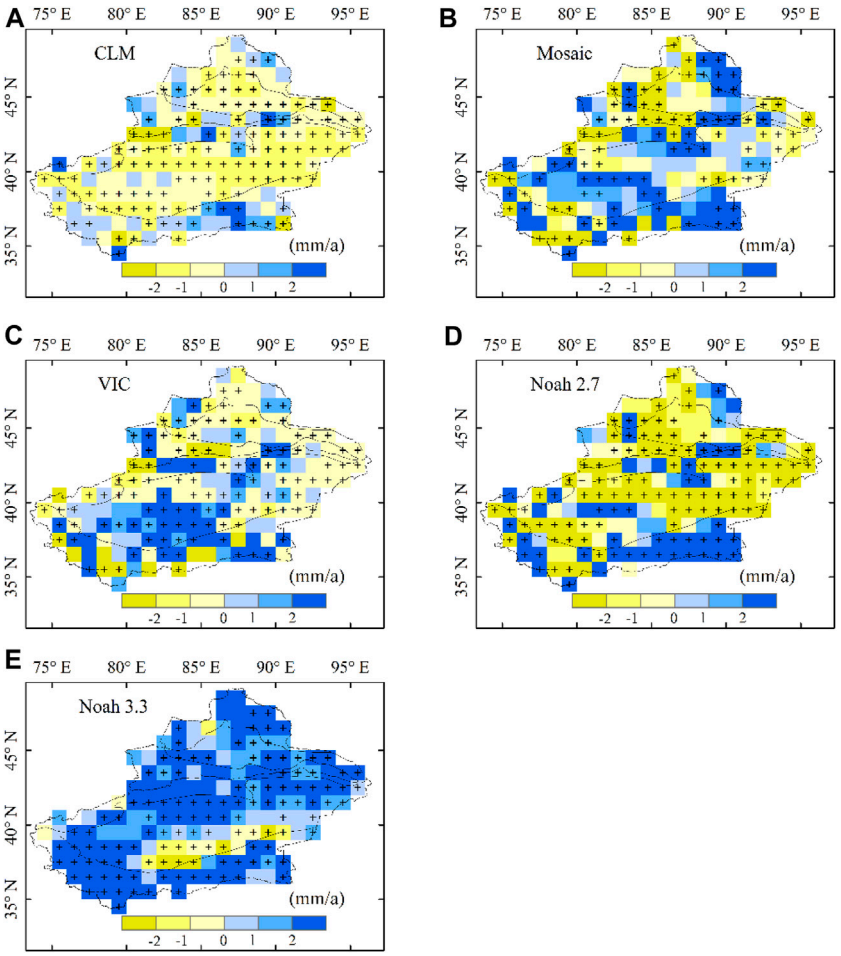

FIGURE 8 | Same as **Figure 4**, but for SON soil moisture.

with the observation in China. Therefore, the positive linear trend results from Noah 3.3 and VIC are more credible than CLM in Xinjiang.

For the spatial distrubutions of the annual soil moisture, the five different datasets have the spatial heterogeneity. In particularly, Mosaic, VIC, and Noah 3.3 have the positive linear trends over the same regions (**Figures 4B,C,E**), except the most negative trends of CLM (**Figure 4A**), which are agreement with the Supplementary Figure S3 in Hu et al. (2019b). These spatial differences of the annual soil moisture trends are mainly caused by the spatial distributions of the precipitation linear trends (Hu et al., 2019b). The accuracy and difference between the different GLDAS models are mainly caused by their different input data and different model sturctures which are comprehensively discussed in the Supplementary Text S2 of Hu et al. (2019b). For the long-term period of 1950–2015, the positive linear trends of the soil moisture are observed over nearly the whole Xinjiang which is similar with the spatial patterns of the positive precipitation in **Figures 6B,D** in Hu et al. (2019a). Other climate factors, such as temperature and evapotranspiration also impact on the soil moisture variations. We will discuss it in our future study.

The soil moisture also can moinitor the drought variations (Wang et al., 2011; Li et al., 2017; Hu et al., 2019a). The 1997–2003 drought was also pervasive in terms of both severity and spatial extent. It was also found that soil moisture in north central and northeastern China had significant downward trends, whereas most of Xinjiang (Wang et al., 2011). For the spatial distributions, most of the mountainous areas are wet regions and the plain areas are drought region based on the MODIS soil moisture information in Xinjiang (Li et al., 2017). For Central Asia, the spatial distributions of the soil moisture linear trends are same as the distributions of the PDSI linear trends in 1950–2015 (Hu et al., 2019a). The climate transformation (from a warm-dry to a warm-wet) in Bayanbuluk grassland of Xinjiang appears in the 1980s (Hu et al., 2016b) which agreed with the warm-dry to warm-wet shift over the northwest of China (Shi et al., 2007). While a recent work (Yao et al., 2021) proposed that a wet-to-dry shift over Xinjiang was detected in 1997 based on the temperature and precipitation. Therefore, the warming and wetting signal in soil moisture

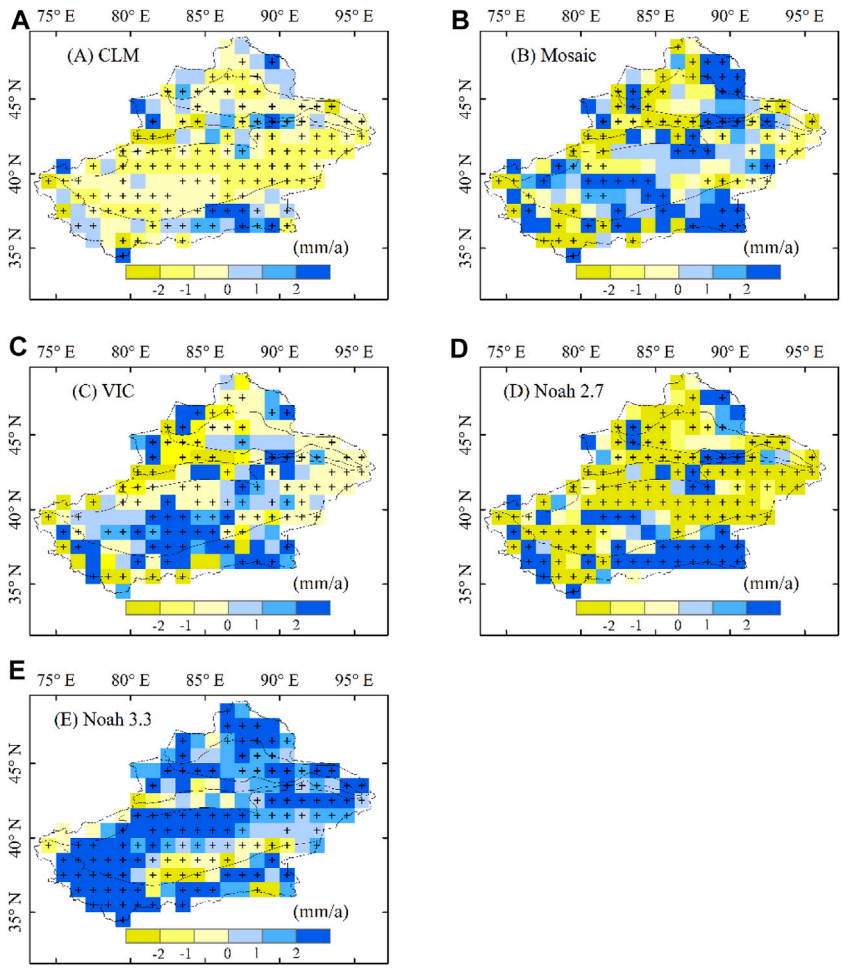

FIGURE 9 | Same as **Figure 4**, but for DJF soil moisture.

changes should be explored in different time period by different climate factors.

CONCLUSION

In this study, the distrubutions and dynamics of the soil moisture over Xinjiang have been explored using four GLDAS 1 models: CLM, Mosaic, VIC and Noah 2.7 and one GLDAS 2.1 model: Noah 3.3 during the period of 2000–2017. The annual soil moisture and seasonal soil moisture (i.e. MAM, JJA, SON, and DJF) are analyzed from the linear trend perspective. The conclusions are obtained as follows:

1) Noah 3.3 and VIC have the significant positive trends of annual soil moisture with the values of 2.64 mm/a and 0.98 mm/a. The trend of CLM is significant negative. The other two models Mosaic and Noah 2.7 have the weak positive trends.
2) For the seasonal soil moisture changes, Noah 3.3 and VIC also have the significant positive trends which indicates that the seasonal soil moisture is increased over Xinjiang during the period of 2000–2017. The significant negative trends are observed based on the CLM dataset.
3) Annual and seasonal soil moisture have the similar spatial distributions of the linear trends for each of the five models. CLM displays the negative trends over large part of Xinjiang. Mosaic and VIC have the similar spatial characteristics of the linear trends. Noah 3.3 has the significant positive trends over almost Xinjiang which is different with Noah 2.7. All the five models have the positive trends over KLM.

More *in situ* measurements, satellite remote-sensing missions, and reanalysis datasets will be essential for the continued assessment of the variations of soil moisture. Relationships between climate factors (e.g. temperature, precipitation and potential evapotranspiration) and soil moisture can help us to have a better understanding of the complex hydrological process in the arid regions. The impacts of soil moisture on the ecological system, such as vegetation and argriculture will provide important information for reaching a balance between the SDG (sustainable development goal) water resource and environment and human society over Xinjiang.

DATA AVAILABILITY STATEMENT

The original contributions presented in the study are included in the article/Supplementary Material, further inquiries can be directed to the corresponding author.

AUTHOR CONTRIBUTIONS

Study design: ZH and XC Writing: ZH Review and editing: ZH, XC, YL, QZ, and GY.

FUNDING

This study was supported by the Strategic Priority Research Program of Chinese Academy of Sciences, Pan-Third Pole Environment Study for a Green Silk Road (Pan-TPEXDA20060303), the Western Scholars of the Chinese Academy of Sciences (2020-XBQNXZ-010), General Research Fund (HKBU 12301820), and the National Natural Science Foundation of China (Grant Nos. 41971386). CAS International partnership Project (902020E01010) and Regional Collaborative Innovation Project of Xinjiang Uygur Autonomous Regions (2020E01010).

ACKNOWLEDGMENTS

A special acknowledgment should be expressed to K.C.Wong Education Foundation and China-Pakistan Joint Research Center on Earth Sciences that supported the implementation of this study. Soil moisture data from the five Global Land Data Assimilation System (GLDAS) models is from the National Eronautics and Space Administration (NASA) (https://disc.sci.gsfc.nasa.gov/datasets?keywords=GLDAS).

REFERENCES

Adler, R. F., Huffman, G. J., Chang, A., Ferraro, R., Xie, P.-P., Janowiak, J., et al. (2003). The Version-2 Global Precipitation Climatology Project (GPCP) Monthly Precipitation Analysis (1979-Present). *J. Hydrometeor.* 4, 1147–1167. doi:10.1175/1525-7541(2003)004<1147:tvgpcp>2.0.co;2

Amani, M., Salehi, B., Mahdavi, S., Masjedi, A., and Dehnavi, S. (2017). Temperature-Vegetation-soil Moisture Dryness Index (TVMDI). *Remote Sensing Environ.* 197, 1–14. doi:10.1016/j.rse.2017.05.026

Beck, H. E., Pan, M., Miralles, D. G., Reichle, R. H., Dorigo, W. A., Hahn, S., et al. (2020). Evaluation of 18 Satellite- and Model-Based Soil Moisture Products Using In Situ Measurements from 826 Sensors. *Hydrol. Earth Syst. Sci.* 25, 17–40. doi:10.5194/hess-2020-184

Berg, A. A., Famiglietti, J. S., Walker, J. P., and Houser, P. (2003). Impact of Bias Correction to Reanalysis Products on Simulations of North American Soil Moisture and Hydrological Fluxes. *J. Geophys. Res.* 108 (D16), 4490. doi:10.1029/2002jd003334

Berg, A., Sheffield, J., and Milly, P. C. D. (2017). Divergent Surface and Total Soil Moisture Projections under Global Warming. *Geophys. Res. Lett.* 44, 236–244. doi:10.1002/2016gl071921

Bi, H., Ma, J., Zheng, W., and Zeng, J. (2016). Comparison of Soil Moisture in GLDAS Model Simulations and In Situ Observations over the Tibetan Plateau. *J. Geophys. Res. Atmos.* 121, 2658–2678. doi:10.1002/2015jd024131

Chen, F., and Dudhia, J. (2001). Coupling an Advanced Land Surface-Hydrology Model with the Penn State-NCAR MM5 Modeling System. Part I: Model Implementation and Sensitivity. *Mon. Wea. Rev.* 129, 569–585. doi:10.1175/1520-0493(2001)129<0569:caalsh>2.0.co;2

Chen, F., Janjić, Z., and Mitchell, K. (1997). Impact of Atmospheric Surface-Layer Parameterizations in the New Land-Surface Scheme of the NCEP Mesoscale Eta Model. *Boundary-Layer Meteorology* 85, 391–421. doi:10.1023/a:1000531001463

Chen, F., Mitchell, K., Schaake, J., Xue, Y., Pan, H.-L., Koren, V., et al. (1996). Modeling of Land Surface Evaporation by Four Schemes and Comparison with FIFE Observations. *J. Geophys. Res.* 101 (D3), 7251–7268. doi:10.1029/95jd02165

Chen, X., Li, B., Li, Q., Li, J., and Abdulla, S. (2012). Spatio-temporal Pattern and Changes of Evapotranspiration in Arid Central Asia and Xinjiang of China. *J. Arid Land* 4, 105–113. doi:10.3724/sp.j.1227.2012.00105

Chen, X., Su, Y., Liao, J., Shang, J., Dong, T., Wang, C., et al. (2016). Detecting Significant Decreasing Trends of Land Surface Soil Moisture in Eastern China during the Past Three Decades (1979-2010). *J. Geophys. Res. Atmos.* 121, 5177–5192. doi:10.1002/2015jd024676

Chen, X., Wang, S., Hu, Z., Zhou, Q., and Hu, Q. (2018). Spatiotemporal Characteristics of Seasonal Precipitation and Their Relationships with ENSO in Central Asia during 1901-2013. *J. Geogr. Sci.* 28, 1341–1368. doi:10.1007/s11442-018-1529-2

Chen, Y., and Yuan, H. (2020). Evaluation of Nine Sub-daily Soil Moisture Model Products over China Using High-Resolution In Situ Observations. *J. Hydrol.* 588, 125054. doi:10.1016/j.jhydrol.2020.125054

Cheng, S., Guan, X., Huang, J., Ji, F., and Guo, R. (2015). Long-term Trend and Variability of Soil Moisture over East Asia. *J. Geophys. Res. Atmos.* 120, 8658–8670. doi:10.1002/2015jd023206

Cherkauer, K., and Lettenmaier, D. (2003). Simulation of spatial variability in snow and frozen soil. *J. Geophy. Res.-Atmos.* 108, 8858. doi:10.1029/2003JD003575

Dai, A., Trenberth, K. E., and Qian, T. (2004). A Global Dataset of Palmer Drought Severity Index for 1870-2002: Relationship with Soil Moisture and Effects of Surface Warming. *J. Hydrometeorol.* 5, 1117–1130. doi:10.1175/jhm-386.1

Dari, J., Morbidelli, R., Saltalippi, C., Massari, C., and Brocca, L. (2019). Spatial-temporal Variability of Soil Moisture: Addressing the Monitoring at the Catchment Scale. *J. Hydrol.* 570, 436–444. doi:10.1016/j.jhydrol.2019.01.014

Derber, J. C., Parrish, D. F., and Lord, S. J. (1991). The New Global Operational Analysis System at the National Meteorological Center. *Wea. Forecast.* 6, 538–547. doi:10.1175/1520-0434(1991)006<0538:tngoas>2.0.co;2

Ek, M. B., Mitchell, K. E., Lin, Y., Rogers, E., Grunmann, P., Koren, V., et al. (2003). Implementation of Noah Land Surface Model Advances in the National Centers for Environmental Prediction Operational Mesoscale Eta Model. *J. Geophys. Res.* 108 (D22), 8851. doi:10.1029/2002jd003296

Fan, Y., and Dool, H. (2004). Climate Prediction Center Global Monthly Soil Moisture Data Set at 0.5° Resolution for 1948 to Present. *J. Geophys. Res.* 109, D10102. doi:10.1029/2003jd004345

Feng, S., Trnka, M., Hayes, M., and Zhang, Y. (2017). Why Do Different Drought Indices Show Distinct Future Drought Risk Outcomes in the U.S. Great Plains?. *J. Clim.* 30, 265–278. doi:10.1175/jcli-d-15-0590.1

Fischer, E. M., Seneviratne, S. I., Vidale, P. L., Lüthi, D., and Schär, C. (2007). Soil Moisture-Atmosphere Interactions during the 2003 European Summer Heat Wave. *J. Clim.* 20, 5081–5099. doi:10.1175/jcli4288.1

Ford, T. W., Rapp, A. D., Quiring, S. M., and Blake, J. (2015). Soil Moisture-Precipitation Coupling: Observations from the Oklahoma Mesonet and Underlying Physical Mechanisms. *Hydrol. Earth Syst. Sci.* 19, 3617–3631. doi:10.5194/hess-19-3617-2015

Gerken, T., Babel, W., Herzog, M., Fuchs, K., Sun, F., Ma, Y., et al. (2015). High-resolution Modelling of Interactions between Soil Moisture and Convective Development in a Mountain Enclosed Tibetan Basin. *Hydrol. Earth Syst. Sci.* 19, 4023–4040. doi:10.5194/hess-19-4023-2015

Gu, X., Li, J., Chen, Y. D., Kong, D., and Liu, J. (2019a). Consistency and Discrepancy of Global Surface Soil Moisture Changes from Multiple Model-Based Data Sets against Satellite Observations. *J. Geophys. Res. Atmos.* 124, 1474–1495. doi:10.1029/2018jd029304

Gu, X., Zhang, Q., Li, J., Singh, V. P., Liu, J., Sun, P., et al. (2019b). Attribution of Global Soil Moisture Drying to Human Activities: A Quantitative Viewpoint. *Geophys. Res. Lett.* 46, 2573–2582. doi:10.1029/2018gl080768

He, B., Wang, H., Guo, L., and Liu, J. (2017). Global analysis of ecosystem evapotranspiration response to precipitation deficits. *J.f Geophy. Res.-Atmos.* 122, 13308–13318. doi:10.1002/2017JD027817

Hoffmann, D., Gallant, A., and Arblaster, J. (2020). Uncertainties in Drought from Index and Data Selection. *J. Geophys. Res. Atmospheres* 128, e2019JD031946. doi:10.1029/2019JD031946

Holgate, C. M., de Jeu, R. A. M., van Dijk, A. I. J. M., Liu, Y. Y., Renzullo, L. J., Vinod, K., et al. (2016). Comparison of Remotely Sensed and Modelled Soil Moisture Data Sets across Australia. *Remote Sensing Environ.* 186, 479–500. doi:10.1016/j.rse.2016.09.015

Hu, Z., Chen, X., Chen, D., Li, J., Wang, S., Zhou, Q., et al. (2019a). "Dry Gets Drier, Wet Gets Wetter": A Case Study over the Arid Regions of Central Asia. *Int. J. Climatol* 39, 1072–1091. doi:10.1002/joc.5863

Hu, Z., Hu, Q., Zhang, C., Chen, X., and Li, Q. (2016a). Evaluation of Reanalysis, Spatially Interpolated and Satellite Remotely Sensed Precipitation Data Sets in Central Asia. *J. Geophys. Res. Atmos.* 121, 5648–5663. doi:10.1002/2016jd024781

Hu, Z., Li, Q., Chen, X., Teng, Z., Chen, C., Yin, G., et al. (2016b). Climate Changes in Temperature and Precipitation Extremes in an Alpine Grassland of Central Asia. *Theor. Appl. Climatol.* 126, 519–531. doi:10.1007/s00704-015-1568-x

Hu, Z., Zhang, C., Hu, Q., and Tian, H. (2014). Temperature Changes in Central Asia from 1979 to 2011 Based on Multiple Datasets. *J. Clim.* 27, 1143–1167. doi:10.1175/jcli-d-13-00064.1

Hu, Z., Zhang, Z., Sang, Y.-F., Qian, J., Feng, W., Chen, X., et al. (2021). Temporal and Spatial Variations in the Terrestrial Water Storage across Central Asia Based on Multiple Satellite Datasets and Global Hydrological Models. *J. Hydrol.* 596, 126013. doi:10.1016/j.jhydrol.2021.126013

Hu, Z., Zhou, Q., Chen, X., Chen, D., Li, J., Guo, M., et al. (2019b). Groundwater Depletion Estimated from GRACE: A Challenge of Sustainable Development in an Arid Region of Central Asia. *Remote Sensing*. 11, 1908. doi:10.3390/rs11161908

Hu, Z., Zhou, Q., Chen, X., Li, J., Li, Q., Chen, D., et al. (2018). Evaluation of Three Global Gridded Precipitation Data Sets in Central Asia Based on Rain Gauge Observations. *Int. J. Climatol.* 38, 3475–3493. doi:10.1002/joc.5510

Hu, Z., Zhou, Q., Chen, X., Qian, C., Wang, S., and Li, J. (2017). Variations and Changes of Annual Precipitation in Central Asia over the Last Century. *Int. J. Climatol.* 37, 157–170. doi:10.1002/joc.4988

Jalilvand, E., Tajrishy, M., Ghazi Zadeh Hashemi, S. A., and Brocca, L. (2019). Quantification of Irrigation Water Using Remote Sensing of Soil Moisture in a Semi-arid Region. *Remote Sensing Environ.* 231, 111226. doi:10.1016/j.rse.2019.111226

Kong, X., Guan, X., Cao, C., Zhang, T., Shen, L., Gan, Z., et al. (2019). Decadal Change in Soil Moisture over East Asia in Response to a Decade-long Warming Hiatus. *J. Geophys. Res. Atmospheres* 124, 8619–8630. doi:10.1029/2019jd030294

Koren, V., Schaake, J., Mitchell, K., Duan, Q.-Y., Chen, F., and Baker, J. M. (1999). A Parameterization of Snowpack and Frozen Ground Intended for NCEP Weather and Climate Models. *J. Geophys. Res.* 104, 19569–19585. doi:10.1029/1999jd900232

Koster, R. D., and Suarez, M. (1996). Energy and Water Balance Calculations in the Mosaic LSM. *Natl. Aeronautics Space Adm. Tech. Memorandum* 9, 76. doi:10.1175/1520-0442(1996)009<2551:tiolsm>2.0.co;2

Li, H., Yang, J., Chen, Y., and Hao, X. (2017). Retrieval of Soil Moisture Information in Xinjiang Using MODIS (In Chinese). *Acta Prataculturae Sinica* 26, 16–27. doi:10.111686/cyxb2016331

Liang, X., Lettenmaier, D. P., Wood, E. F., and Burges, S. (1994). A Simple Hydrologically Based Model of Land Surface Water and Energy Fluxes for GSMs. *J. Geophys. Res.* 99 (14), 14415–14428. doi:10.1029/94jd00483

Liang, X., Lettenmaier, D. P., and Wood, E. (1996). One-dimensional Statistical Dynamic Representation of Subgrid Spatial Variability of Precipitation in the Two-Layer Variable Infiltration Capacity Model. *J. Geophys. Res.* 101 (D16), 403–421. doi:10.1029/96jd01448

May, W., Meier, A., Rummukainen, M., Berg, A., Chéruy, F., and Hagemann, S. (2015). Contributions of Soil Moisture Interactions to Climate Change in the Tropics in the GLACE-CMIP5 Experiment. *Clim. Dyn.* 45, 3275–3297. doi:10.1007/s00382-015-2538-9

Modanesi, S., Massari, C., Camici, S., Brocca, L., and Amarnath, G. (2020). Do Satellite Surface Soil Moisture Observations Better Retain Information about Crop-Yield Variability in Drought Conditions? *Water Resour. Res.* 56, e2019WR025855. doi:10.1029/2019WR025855

Mukherjee, A., and Ramachandran, P. (2018). Prediction of GWL with the Help of GRACE TWS for Unevenly Spaced Time Series Data in India : Analysis of Comparative Performances of SVR, ANN and LRM. *J. Hydrol.* 558, 647–658. doi:10.1016/j.jhydrol.2018.02.005

Niu, Q., Liu, L., and Heng, J. (2020). A Multi-Index Evaluation of Drought Characteristics in the Yarlung Zangbo River Basin of Tibetan Plateau, Southwest China. *Front. Earth Sci.* 8, 213. doi:10.3389/feart.2020.00213

Orth, R., and Seneviratne, S. I. (2017). Variability of Soil Moisture and Sea Surface Temperatures Similarly Important for Warm-Season Land Climate in the Community Earth System Model. *J. Clim.* 30, 2141–2162. doi:10.1175/jcli-d-15-0567.1

Qin, J., Liang, S., Yang, K., Kaihotsu, I., Liu, R., and Koike, T. (2009). Simultaneous Estimation of Both Soil Moisture and Model Parameters Using Particle Filtering Method through the Assimilation of Microwave Signal. *J. Geophys. Res.* 114, D15103. doi:10.1029/2008jd011358

Qiu, J., Gao, Q., Wang, S., and Su, Z. (2016). Comparison of Temporal Trends from Multiple Soil Moisture Data Sets and Precipitation: The Implication of Irrigation on Regional Soil Moisture Trend. *Int. J. Appl. Earth Observation Geoinformation* 48, 17–27. doi:10.1016/j.jag.2015.11.012

Robinson, D. A., Jones, S. B., Lebron, I., Reinsch, S., Domínguez, M. T., Smith, A. R., et al. (2016). Experimental Evidence for Drought Induced Alternative Stable States of Soil Moisture. *Scientific Rep.* 6 (1), 20018. doi:10.1038/srep20018

Rodell, M., Houser, P. R., Jambor, U., Gottschalck, J., Mitchell, K., Meng, C.-J., et al. (2004). The Global Land Data Assimilation System. *Bull. Amer. Meteorol. Soc.* 85, 381–394. doi:10.1175/bams-85-3-381

Scanlon, B. R., Longuevergne, L., and Long, D. (2012). Ground Referencing GRACE Satellite Estimates of Groundwater Storage Changes in the California Central Valley, USA. *Water Resour. Res.* 48, W04520. doi:10.1029/2011wr011312

Scanlon, B., Zhang, Z., Save, H., Sun, A., Muller, S., van Beek, L., et al. (2018). "Global Models Underestimate Large Decadal Declining and Rising Water Storage Trends Relative to GRACE Satellite Data," in Proceedings of the National Academy of the Sciences of the United States of America 115, E1080–E1089.

Sellers, P. J., Mintz, Y., Sud, Y. C., and Dalcher, A. (1986). A Simple Biosphere Model (SiB) for Use within General Circulation Models. *J. Atmos. Sci.* 43, 505–531. doi:10.1175/1520-0469(1986)043<0505:asbmfu>2.0.co;2

Shi, Y., Shen, Y., Kang, E., Li, D., Ding, Y., Zhang, G., et al. (2007). Recent and Future Climate Change in Northwest China. *Climatic Change* 80, 379–393. doi:10.1007/s10584-006-9121-7

Solander, K. C., Newman, B. D., Carioca de Araujo, A., Barnard, H. R., Berry, Z. C., Bonal, D., et al. (2020). The Pantropical Response of Soil Moisture to El Niño. *Hydrol. Earth Syst. Sci.* 24, 2303–2322. doi:10.5194/hess-24-2303-2020

Spennemann, P. C., Fernández-Long, M. E., Gattinoni, N. N., Cammalleri, C., and Naumann, G. (2020). Soil Moisture Evaluation over the Argentine Pampas Using Models, Satellite Estimations and In-Situ Measurements. *J. Hydrol. Reg. Stud.* 31, 100723. doi:10.1016/j.ejrh.2020.100723

Trenberth, K. E., Smith, L., Qian, T., Dai, A., and Fasullo, J. (2007). Estimates of the Global Water Budget and its Annual Cycle Using Observational and Model Data. *J. Hydrometeorol.* 8, 758–769. doi:10.1175/jhm600.1

Wang, A., Lettenmaier, D. P., and Sheffield, J. (2011). Soil Moisture Drought in China, 1950–2006. *J. Clim.* 24, 3257–3271. doi:10.1175/2011jcli3733.1

Western, A. W., Zhou, S.-L., Grayson, R. B., McMahon, T. A., Blöschl, G., and Wilson, D. J. (2004). Spatial Correlation of Soil Moisture in Small Catchments and its Relationship to Dominant Spatial Hydrological Processes. *J. Hydrol.* 286, 113–134. doi:10.1016/j.jhydrol.2003.09.014

Xie, P., and Arkin, P. A. (1996). Global Precipitation: a 17-year Monthly Analysis Based on Gauge Observations, Satellite Estimates, and Numerical Model Outputs. *Bull. Am. Meteorol. Soc.* 78, 2539–2558. doi:10.1175/1520-0477(1997)078<2539:GPAYMA>2.0.CO;2

Xu, L., Abbaszadeh, P., Moradkhani, H., Chen, N., and Zhang, X. (2020). Continental Drought Monitoring Using Satellite Soil Moisture, Data Assimilation and an Integrated Drought Index. *Remote Sensing Environ.* 250, 112028. doi:10.1016/j.rse.2020.112028

Yao, C., Zhang, Z., and Wang, X. (2004). Evaluating Soil Moisture Status in XinJiang Using the Temperature Vegetation Dryness Index (TVDI) (In Chinese). *Remote sensing Technology Appl.* 19, 473–478. doi:10.1016/j.csr.2003.12.006

Yao, J., Mao, W., Chen, J., and Dilinuer, T. (2021). Signal and Impact of Wet-To-Dry Shift over Xinjiang, China (In Chinese). *Acta Geographica Sinica* 76, 57–72. doi:10.11821/dlxb202101005

Yuan, S., and Quiring, S. M. (2017). Evaluation of Soil Moisture in CMIP5 Simulations over the Contiguous United States Using In Situ and Satellite Observations. *Hydrol. Earth Syst. Sci.* 21, 2203–2218. doi:10.5194/hess-21-2203-2017

Zhou, P., Ding, J., Wang, F., Guljmal, U., and Zhang, G. (2010). Retrieval Methods of Soil Water Content in Vegetation Covering Areas Based on Multi-Source Remote Sensing Data (In Chinese). *J. Remote Sensing* 14, 959–973.

Zhou, Y., Dong, X., Chen, H., Cao, L., Shao, Q., Sun, S., et al. (2020). Sub-seasonal Variability of Surface Soil Moisture over Eastern China. *Clim. Dyn.* 55, 3527–3541. doi:10.1007/s00382-020-05464-3

Conflict of Interest: The authors declare that the research was conducted in the absence of any commercial or financial relationships that could be construed as a potential conflict of interest.

frontiers in Environmental Science

ORIGINAL RESEARCH
published: 21 May 2021
doi: 10.3389/fenvs.2021.656779

A Comparison of Global Surface Air Temperature Over the Oceans Between CMIP5 Models and NCEP Reanalysis

Xian Zhu[1,2,3], *Tianyun Dong*[1,2], *Shanshan Zhao*[4]* and *Wenping He*[1,2,3]

[1]School of Atmospheric Sciences, Sun Yat-Sen University, Zhuhai, China, [2]Key Laboratory of Tropical Atmosphere-Ocean System, Ministry of Education, Zhuhai, China, [3]Southern Marine Science and Engineering Guangdong Laboratory, Zhuhai, China, [4]National Climate Center, China Meteorological Administration, Beijing, China

By utilizing eight CMIP5 model outputs in historical experiment that simulated daily mean sea surface temperature (SST) and NCEP reanalysis data over 12 ocean basins around the world from 1960 to 2005, this paper evaluates the performance of CMIP5 models based on the detrended fluctuation analysis (DFA) method. The results of National Centers for Environmental Prediction (NCEP) data showed that the SST in most ocean basins of the world had long-range correlation (LRC) characteristics. The DFA values of the SST over ocean basins are large in the tropics and small in high latitudes. In spring and autumn, the zonal average DFA of SST are basically distributed symmetrically in the Northern and Southern Hemispheres. In summer, the zonal average values of DFA in the Northern Hemisphere are larger than those in the southern hemisphere, and vice versa in winter. The performance of HadGEM2-AO, CNRM-CM5, and IPSL-CM5A-MR are all relative well among the eight models in simulating SST over most regions of the global ocean.

Keywords: detrended fluctuation analysis, long-range correlation, CMIP5, NCEP, SST

OPEN ACCESS

Edited by:
Boyin Huang,
National Oceanic and Atmospheric Administration, United States

Reviewed by:
Fei Xie,
Beijing Normal University, China
Ruiqiang Ding,
Beijing Normal University, China

***Correspondence:**
Shanshan Zhao
zhaoss@cma.gov.cn

Specialty section:
This article was submitted to Interdisciplinary Climate Studies, a section of the journal Frontiers in Environmental Science

Received: *21 January 2021*
Accepted: *06 May 2021*
Published: *21 May 2021*

Citation:
Zhu X, Dong T, Zhao S and He W (2021) A Comparison of Global Surface Air Temperature Over the Oceans Between CMIP5 Models and NCEP Reanalysis. Front. Environ. Sci. 9:656779. doi: 10.3389/fenvs.2021.656779

INTRODUCTION

Climate models and Earth system models that consider complex geo-bio-chemical processes are important tools for projecting future climate change (Zeng et al., 2008; IPCC, 2013; Prinn, 2012). Currently, the climate models commonly used worldwide are the Earth system models from the phase 5 of the Coupled Model Intercomparison Project (CMIP5), and the results of which have also been adopted by the IPCC fifth assessment report (Taylor et al., 2012). Based on these, large number of global and regional climate change simulations and projections under different historical and future greenhouse gas emission scenarios have been carried out using the results of the CMIP5 models (Tebaldi et al., 2005; Jiang and Tian, 2013; Wei and Qiao, 2016; Wang et al., 2017). However, before the Earth system models are applied to project future climate change, its performance needs to be evaluated (Grose et al., 2020).

To quantitatively evaluate model performance, a lot of research has been carried out, and some new progresses have been made in model evaluation methods. At present, the evaluation objects of model performance have changed from the evaluation of climate state to the climate extremes, climate trends, climate phenomena, etc. Model evaluation methods have developed from qualitative evaluation to quantitative evaluation, such as quantitative calculation of the reliability and uncertainty of the model simulation (Zhao et al., 2013). Many studies on the evaluation of CMIP5 model simulation capabilities (Alexander et al., 2006; Alexander and Arblaster,2009;

TABLE 1 | Information about the CMIP5 climate models.

Modeling center	Nation	Institution	Model name	Atmosphere resolution	Model information	
					Atmosphere component	Ocean component
CMCC	Italy	Centro euro-mediterraneo per I CambiamentiClimatici	CMCC-CMS	T63(~1.875° × 1.865°)L95	ECHAM5	OPA
CNRM-CERFACS	France	Centre national de RecherchesMeteorologiques /Centre europeen de recherche et formation avancees en CalculScientifique	CNRM-CM5	TL127 (~1.4° × 1.4°)L31	ARPEGE-climat	NEMO
LASG	China	Institue of atmospheric physics Chinese academy of sciences	FGOALS-g2	(~2.81° × 1.66°) L26	GAMIL2	LICOM2
GFDL	United States	NOAA geophysical fluid dynamics laboratory	GFDL-ESM2G	M45 (~2° × 2.5°)L24	AM2	GOLD
INM	Russia	Institute for numerical mathematics	INM-CM4	(~1.5° × 2.0°)L21	INM-CM4 atmospheric component	INM-CM4 ocean component
IPSL	France	Institute pierre-simon laplace	IPSL-CM5A-MR	LMDZ4 (~1.2587° × 2.5°)	LMDZ4	NEMO
MOHC	United Kingdom	Met office hadley centre	HadGEM2-AO	T63 (~1.875° × 1.865°)L38	Global atmosphere	Global land
MPI-M	Germany	Max planck institute for meteorology	MPI-ESM-MR	T63 (~1.875° × 1.865°)L47	ECHAM6	MPIOM

Rusticucci, 2012; Kharin et al., 2013; Kruger and Sekele, 2013; Zhou et al., 2016; Zhu et al., 2017; Gusain et al., 2019) and the application of these models to project future climate change (Tebaldi et al., 2006; Kharin et al., 2007; Sillmann et al., 2013; Zhou et al., 2014; Ji and Kang, 2015) have been carried out internationally. A great number of studies have confirmed that the current CMIP5 models have good ability to simulate global climate, and the results of these models can be used to project the characteristics of future global climate change. However, these evaluation methods mainly consider the statistical differences between the model simulations and the observation, but lack the comparison of the observation data and the simulation data in the sense of dynamic characteristics. Therefore, the method to quantitatively evaluate the dynamic characteristics of climate systems has been developed (Zhao, 2014).

Long-range correlation (LRC) is an important dynamic characteristic of climate system (Bunde and Havlin., 2002). Detrended fluctuation analysis (DFA) can effectively distinguish LRCs of time series from trend under the influence of non-stationarities. DFA and wavelet techniques have been used to analyze temporal correlations in the atmospheric variability (Koscielny-Bunde et al., 1996, Koscielny-Bunde et al., 1998). Some studies have analyzed the simulation results of the HadCM3 and ECHAM4/OPYC global models using the DFA method, and showed that the models can reproduce the scale features of the global surface temperature comparing with the reanalysis data of the National Centers for Environment Prediction (Blender and Fraedric, 2003). Some researchers also evaluated the result of Beijing Climate Center Climate System Model (BCC_CSM) in simulating daily temperature over China based the DFA method, and found that the model can simulate the LRCs of temperature in most part of China well (Zhao, 2014).

At present, the studies on evaluation of global climate models using DFA method mainly focus on the climate elements over land, while researches on the climate elements over ocean have seldom been carried out. Based on the DFA method, this paper evaluates the performance of eight CMIP5 coupled models on the daily mean sea surface temperature (SST) over ocean, indicating the shortcomings of the models on SST, and the similarities and differences among the models. The results can provide basis for model improvements and application for future predictions. Chapter 2 introduces the data and methods; Chapter 3 introduces the evaluation results of CMIP5 models on SST over ocean based on DFA method; Chapter 4 is the main conclusions and discussions.

DATA AND METHOD

Data

The observed DAT during 1960–2005 is from The National Centers for Environmental Prediction (NCEP) reanalysis data (Kalnay et al., 1996; Kanamitsu et al., 2002). The simulated SST of eight CMIP5 climate models is available from the IPCC Data Distribution Center (https://esgf-node.llnl.gov/search/cmip5/). **Table 1** provides basic information about the eight global climate models (GCM). The selected models include physical climate models as well as ESMs. The present-day historical simulations performed by the eight models in the CMIP5 are used in this study. The term "historical" (HIST) refers to coupled climate model simulations forced by observed concentrations of greenhouse gases, solar forcing, erosols, ozone, and land-use change over the 1850–2005 period (Taylor et al. 2012). CMIP5 provided the results of Earth System models (ESMs), which include carbon cycle models, and in some cases interactive prognostic erosol, chemistry, and dynamical vegetation components. The last 46 years (1960–2005) was analyzed to compare CMIP5 models with the observations. The GCM output used here are the daily sea surface temperature. To facilitate GCM intercomparison and validation against the gauge observations, both the daily fields of GCM temperature and the

TABLE 2 | Names and coordinates for 12 ocean basins.

Region name	Abbreviation	Coordinates	
		Longitude	Latitude
Tropical west pacific	TWP	110°–170°E	20°S–20°N
Tropical central pacific	TCP	170°E–125°W	20°S–20°N
Tropical eastern pacific	TEP	125°W–75°W	20°S–20°N
North pacific ocean	NPO	120°E–120°W	20°–70°N
South pacific ocean	SPO	140°E–70°W	60°–20°S
Tropical indian ocean	TIO	40°–120°E	20°S–20°N
South indian ocean	SIO	15°–140°E	60°–20°S
South atlantic ocean	SAO	65°W–15°E	60°–20°S
Tropical atlantic ocean	TAO	70°W–10°E	20°S–20°N
North atlantic ocean	NAO	90°W–0°	20°–60°N
Southern ocean	SO	0°E–180°W	80°–60°S
Arctic ocean	AO	0°E–180°W	60°–90°N

gauged data were interpolated to 1.0° × 1.0°grids using the inverse distance weighting approach. For all models and experiments, the results of the first ensemble member (r1i1p1) were used in this study.

To uncover the geographical heterogeneity of DFA for SST in the oceans, we divided the oceans into 12 ocean basins (**Table 2** and **Figure 1**). The 12 ocean basins are modified based on Chan et al (2015). We calculated the area-averaged DFA indexes in each ocean basin for NCEP and model output daily temperatures, then the area-averaged DFA indexes were compared to show the differences between the NCEP and model outputs.

METHOD

The DFA method can quantify LRC as index of power law exponent, namely, scaling exponent (Peng et al, 1994; Bunde et al., 2002, Bunde et al., 2005). DFA has been widely applied to study LRC in climate variabilities (Talkner and Weber, 2000; Kantelhardt et al., 2006; Gan et al., 2007; Jiang et al., 2013). For a giving time series, $\{X_i, i = 1, 2, \ldots, N\}$, the departures x_i of X_i is calculated and cumulated to get the profile $y(k)$.

$$y(k) = \sum_{i=1}^{k} x_i,\ k = 1,\ 2,\ \ldots,\ \mathrm{N} \tag{1}$$

Then profile $y(k)$ is divided into n = Int (N/τ) non-overlapping segments of equal length τ. In each segment, a polynomial function is used to fit the local trend. If l-order polynomial function is used for the fitting, the order of DFA is l (DFA1 if $l = 1$, DFA2 if $l = 2$, etc.). Next, the local trend $y_\tau(k)$ is subtracted from profile $y(k)$ in each segment, and the fluctuation function ($F(\tau)$) of each segment is calculated by

$$F(\tau) = \sqrt{\frac{1}{n\tau}\Sigma_{k=1}^{n\tau}\left[y(k) - y_\tau(k)\right]^2} \tag{2}$$

A linear relationship on a log-log plot indicates the presence of the power law. In this case, fluctuations functions can be characterized by a scaling exponent α.

$$F(\tau) \sim \tau^{\alpha} \tag{3}$$

If $\alpha > 0.5$, the time series $\{X_i, i = 1, 2, \ldots, N\}$ is positive long range correlation. If $\alpha = 0.5$, the time series is uncorrelated. If $\alpha < 0.5$, the time series has anti-persistent correlation. In this study, the DFA2 method is used to estimate the scaling exponent in a time series.

LONG-RANGE CORRELATIONS OF DAILY MEAN SST OVER OCEAN SIMULATED BY CMIP5 MODELS

Characteristics of Daily mean SST Over Ocean

The equatorial Pacific Ocean (185°E, 0°) was selected as an example to study the long-range correlation characteristics of

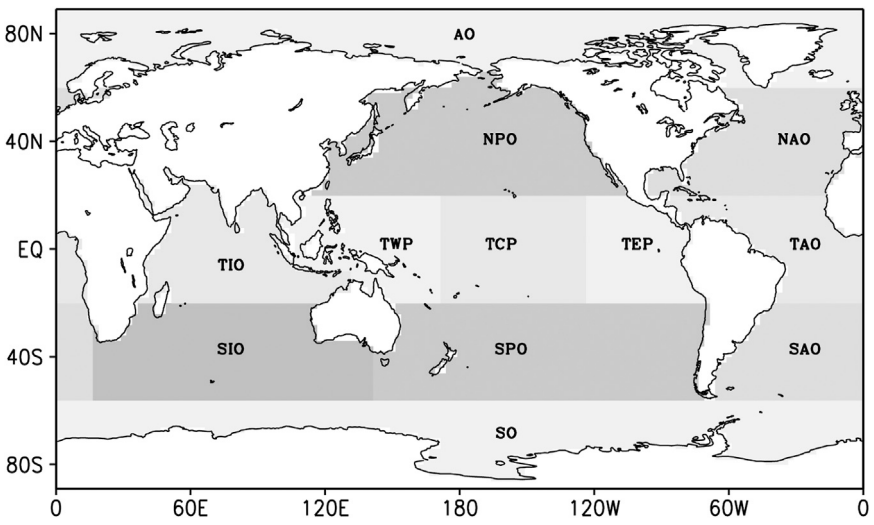

FIGURE 1 | Divisions of the oceans.

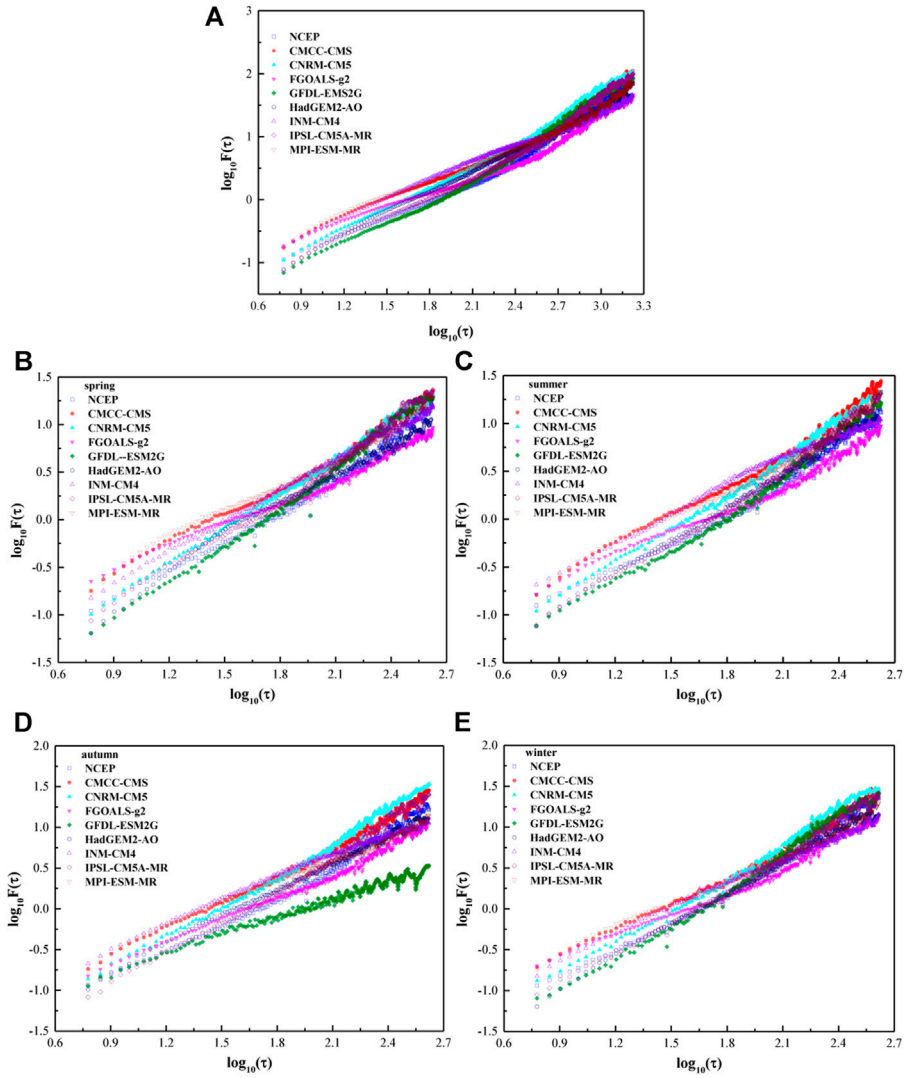

FIGURE 2 | The DFA2 results of daily mean SST from NCEP and CMIP5 models at the point of (185°E, 0°) for **(A)** year, **(B)** spring, **(C)** summer, **(D)** autumn, and **(E)** winter.

temperature over ocean. In the equatorial Pacific Ocean, the DFA value of NCEP daily temperature is 1.36, and the DFA values of the daily temperature simulated by the eight models vary between 0.91 and 1.41 (**Figure 2A**). In spring, the DFA value of NCEP's daily temperature is 1.25. Except for FGOALS-G2, DFA values of the daily temperature simulated by the other seven models are all greater than 1.0, and that of GFDL-ESM2G is the largest, reaching 1.44 (**Figure 2B**). In summer, the DFA value of NCEP's daily temperature is 1.23, slightly lower than that in spring. Except for FGOALS-G2 and INM-CM4, the DFA values of the other six models are all between one and 1.36 (**Figure 2C**). In autumn, the DFA value of NCEP's daily temperature is larger than these in spring and summer, reaching 1.31. Among the results of each model, the DFA value of daily temperature of GFDL-ESM2 is the smallest, reaching 0.72, and the largest is IPSL-CM5A-MR, reaching 1.41 (**Figure 2D**). In winter, the DFA value of NCEP's daily temperature is 1.35. Except for INM-CM4, the DFA values of the remaining seven models are all greater than 1, in which the maximum is1.47 of GFDL-ESM2G (**Figure 2E**).

Figure 3 shows that the DFA value of the daily temperature in this area over the years is larger than that of the four seasons, and the seasonal variation of the DFA value is not large, but the DFA value is smaller in spring and summer than that in autumn and winter. Except for GFDL-ESM2G, INM-CM4, and HadGEM2-AO, the seasonal changes of DFA values of the other models are close to NCEP data.

On the annual time scale, the median performance errors between the DFA values of the global daily mean SST simulated by CMCC-CMS, CNRM-CM5, HadGEM2-AO, and MPI-ESM-MR and those of the NCEP do not exceed ±0.01, while the median performance errors of INM-CM4 and FGOALS-g2 exceed −0.05 (**Figure 4A**). From the 5–95% error range of each model, the

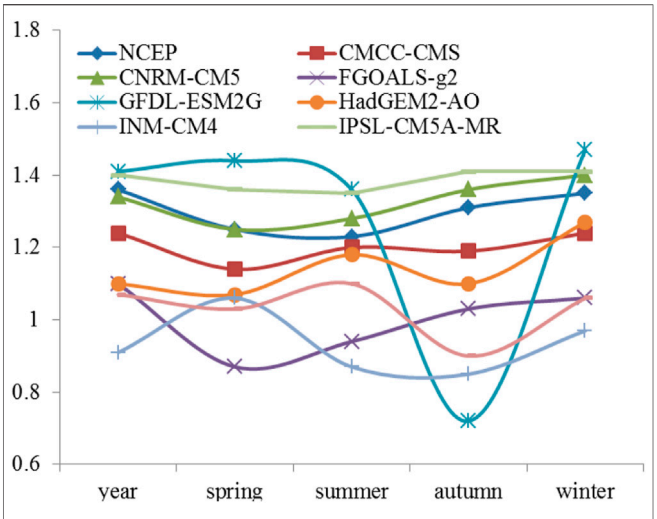

FIGURE 3 | The DFA2 indexes of daily mean SST from NCEP and CMIP5 models at the point of (185°E, 0°) for year and all four seasons.

error margins of CMCC-CMS, GFDL-ESM2G, HadGEM2-AO and IPSL-CM5A-MR are less than 0.3, while those of the remaining four models are above 0.3, in which the maximum is 0.47 of INM-CM4. In spring, the median performance errors of CMCC-CMS, GFDL-ESM2G, IPSL-CM5A-MR and MPI-ESM-MR do not exceed ±0.01, and that of INM-CM4 exceeds −0.08 (**Figure 4B**). From the 5–95% error range of each model, the error margins of GFDL-ESM2G and HadGEM2-AO are the minimum, reaching 0.28, while the maximum is 0.37 of MPI-ESM-MR, and those of the other models are between 0.31 and 0.36. In summer, the median performance errors of CMCC-CMS, GFDL-ESM2G and MPI-ESM-MR are no more than ±0.01, that of INM-CM4 is -0.07, and those of the rest models are between ±0.01 and 0.06 (**Figure 4C**). From the 5–95% error range, the error margins of CNRM-CM5, GFDL-ESM2G, HadGEM2-AO and IPSL-CM5A-MR are the minimum, reaching 0.31, while the maximum is 0.45 of FGOALS-g2, and those of the rest are between 0.32 and 0.38. In autumn, the median performance errors of IPSL-CM5A-MR and MPI-ESM-MR are less than ±0.01, while that of INM-CM4 exceeds −0.07, and those of other models are between ±0.01 and 0.03 (**Figure 4D**). From the 5–95% error range, the minimum error margin is 0.25 of IPSL-CM5A-MR, while the maximum is 0.46 of INM-CM4, and those of the rest are between 0.26 and 0.4. In winter, the median performance errors of CMCC-CMS and GFDL-ESM2G are less than ±0.01, while that of FGOALS-g2 is −0.05, and those of the rest models are between ±0.01 and 0.04 (**Figure 4E**). From the 5–95% error range, the minimum error margin is 0.3 of IPSL-CM5A-MR, while the maximum is 0.46 of MPI-ESM-MR, and those of the rest are between 0.33 and 0.45.

Long-Range Correlation Characteristics of Daily Mean SST in Various Regions of the Ocean

The zonal average value of the NCEP daily mean SST DFA index over the years shows that the DFA value is small in mid-high latitudes and large in tropical areas (**Figure 5A**), which decreases rapidly from the equator to the north and south direction. The zonal average DFA index exceeds 1.1 near the equator and decreases to 0.6 near the high latitudes of the southern and northern hemispheres. The DFA index of daily mean SST simulated by the eight models also shows similar characteristics of variation with the latitude, but the DFA values of the models in tropical regions are all smaller than the NCEP values, with large differences between the models. The zonal changes of DFA index in INM-CM4, MPI-ESM-MR and FGOALS-g2 models are smaller than NCEP. The minimum correlation coefficient between the INM-CM4 zonal average DFA value and the NCEP value is 0.78, and those of the other models are all above 0.9, in which the maximum correlation coefficient is 0.98 of IPSL-CM5A-MR.

In spring of the northern hemisphere, the zonal average value of the DFA index for NCEP daily mean SST is symmetrically distributed in the northern and southern hemispheres. DFA index of the tropical area is above 0.9, of which the equatorial area exceeds 1.1, and the mid-high latitude of the northern hemisphere is generally between 0.8 and 0.9, while that of the mid-high latitudes of the southern hemisphere is between 0.7 and 0.8 (**Figure 5B**). In the extratropical areas of the northern hemisphere, the zonal average DFA index changes slightly with latitudes, while that of the extratropical areas of the southern hemisphere increases slightly around 60°S, and then continues to decrease. The meridional changes of DFA index of INM-CM4, MPI-ESM-MR and FGOALS-g2 models are small. The zonal average DFA value of HadGEM2-AO has two peaks in the area outside the equator. The DFA values of GFDL-ESM2G and IPSL-CM5A-MR near the equator are larger than the NCEP values. The minimum correlation coefficient between the zonal average DFA index of INM-CM4 and MPI-ESM-MR and NCEP is 0.76, while those of the rest models are above 0.8, in which the maximum correlation coefficient is 0.97 of GFDL-ESM2G.

In summer of the northern hemisphere, the zonal average value of the NCEP daily temperature DFA index is still the largest near the equator, but the DFA value in the northern hemisphere is obviously larger than that in the southern hemisphere (**Figure 5C**). The zonal average DFA value displays a peak around 60°N in the northern hemisphere, reaching about 1.1, and then decreases toward higher latitudes rapidly. In the southern hemisphere, the zonal average DFA index rapidly decreases from the equator to around 40°S to a minimum of 0.7, and then goes up with the increase of latitudes. The zonal average DFA values of the eight models can all reflect the characteristic that the DFA value of the northern hemisphere is larger than that of the southern hemisphere. The zonal average DFA values of INM-CM4 and FGOALS-g2 do not reach a peak near the equator. The minimum correlation coefficient is 0.78 between the zonal average DFA index of FGOALS-g2 and NCEP, while those of the rest models are above 0.88, in which the maximum correlation coefficient is 0.96 of HadGEM2-AO.

In autumn of the northern hemisphere, the zonal average value of the DFA index for NCEP daily mean SST is symmetrically distributed in the northern and southern hemispheres, reaching a peak close to 1.2 near the equator,

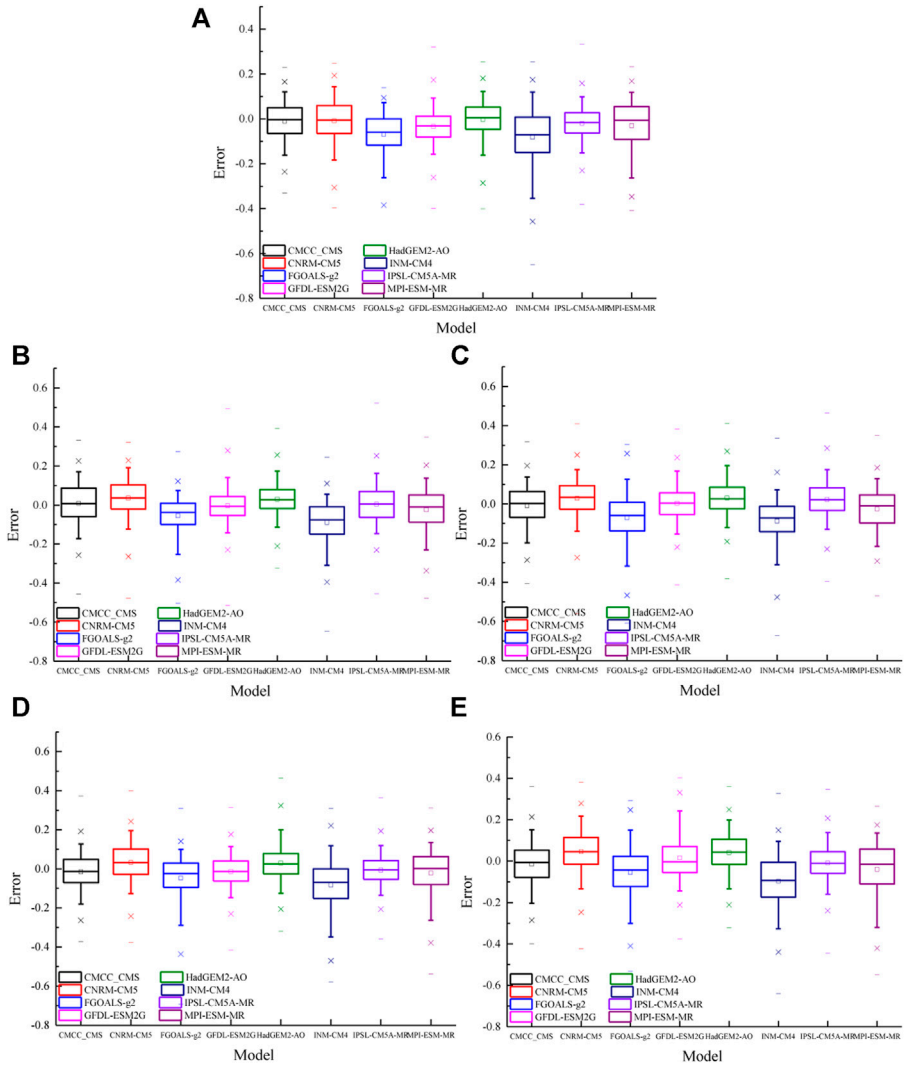

FIGURE 4 | Box charts of the errors of DFA values from CMIP5 models for **(A)** year, **(B)** spring, **(C)** summer, **(D)** autumn, and **(E)** winter.

two small peaks near 50°N and 70°N in the northern hemisphere, and a smaller peak in 60°S in the southern hemisphere and then decreases towards higher latitudes (**Figure 5D**). The eight models can all reflect the characteristics that the zonal average DFA value is the largest near the equator, and the distribution in the northern and southern hemispheres is relatively symmetric. The zonal average DFA indices of INM-CM4, FGOALS-g2, and CMCC-CMS models vary little with latitudes and are significantly smaller than the NCEP value in tropical regions. The DFA value of HadGEM2-AO has a large peak near 20°N in the northern hemisphere. The minimum correlation coefficient between the zonal average DFA value of INM-CM4 and the NCEP value is 0.64, while those of the other models are all above 0.81, among which the correlation coefficients of GFDL-ESM2G and IPSL-CM5A-MR are up to 0.97.

In winter of the northern hemisphere, the zonal average value of the DFA index for NCEP daily mean SST is greater in the southern hemisphere than that in the northern hemisphere, and the peak still appears near the equator, reaching about 1.2. The DFA index of the northern hemisphere drops sharply to 0.8 from the equator to 30°N, then slowly decreases towards mid-high latitudes, and to about 0.7 near the north pole. The DFA index of the southern hemisphere decreases rapidly to about 0.7 from the equator to high latitudes (**Figure 5E**). The zonal average DFA index of the INM-CM4 and FGOALS-g2 models varies slightly with latitudes and is smaller than the NCEP value in tropical regions. Except that the correlation coefficient of zonal average DFA value and the NCEP value of HadGEM2-aO and IPSL-CM5A-MR exceeds 0.9, the correlation coefficients of the rest models are all less than 0.9, in which the minimum value is 0.72 of INM-CM4.

In general, the zonal average value of the DFA index for NCEP daily mean SST is the largest near the equator and smaller at mid-high latitudes, with obvious seasonal changing pattern. The

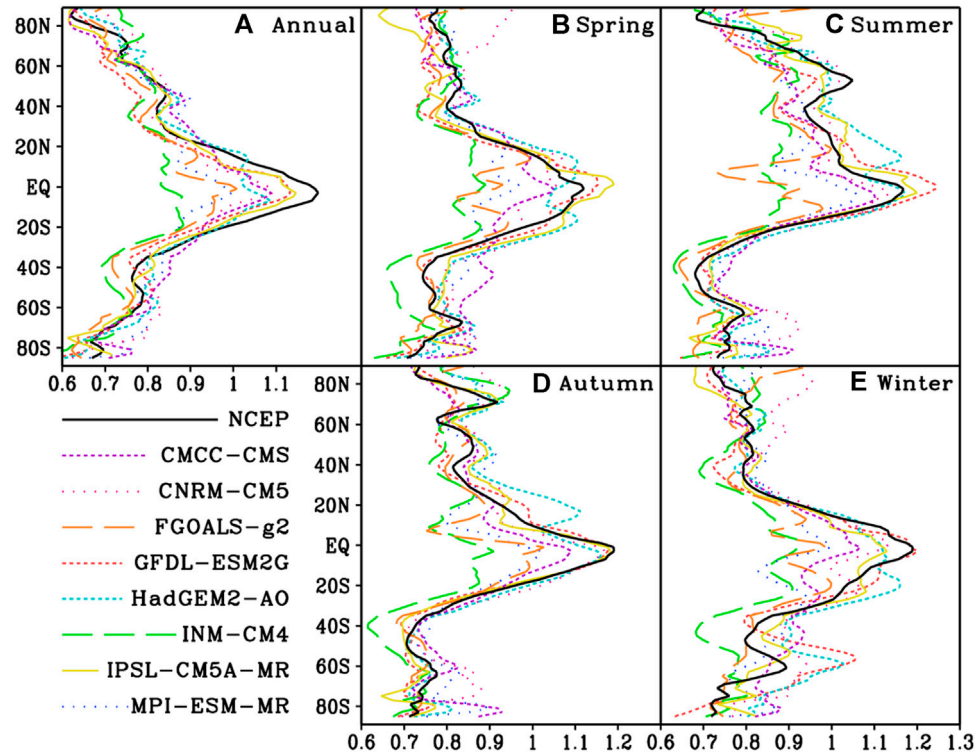

FIGURE 5 | The zonal average distribution of the DFA index of NCEP and eight models of daily mean SST **(A)** year, **(B)** spring, **(C)** summer, **(D)** autumn, **(E)** winter.

variation range of the zonal average DFA value of INM-CM4 and FGOALS-g2 is smaller than the NCEP value, and the correlation coefficient with NCEP is relatively lower, while that of IPSL-CM5A-MR and HadGEM2-AO is closer to the NCEP value, with similar variation characteristics with latitudes.

Judging from the DFA value for daily mean SST of each region, the difference between the models and the DFA value of the NCEP is large in tropical regions. Among them, the tropical Central and Eastern Pacific has the largest difference, while that in middle and high latitudes is relatively small, generally less than ±0.1 (**Figure 6A**). In the North Atlantic (NAO), the simulated DFA values of the eight models have an error of less than ±0.05; in the Southern Ocean and the South Atlantic (SO and SAO), one model has an error of more than ±0.05. The errors of INM-CM4 and FGOALS-g2 are larger than those of other models.

In spring, the difference between the simulated daily mean SST DFA value and NCEP is still large in tropical regions, but the error in the mid-high latitudes of the northern hemisphere is significantly smaller than that in other parts of the world (**Figure 6B**). In the North Pacific (NPO) and North Atlantic (NAO), there is one model whose error is greater than ±0.05. In the Arctic Ocean (AO) and Southern Ocean (SO), there are two models whose errors exceed ±0.05. For Tropical Eastern Pacific (TEP), only HadGEM2-AO and IPSL-CM5A-MR have errors of less than ±0.05. The errors of INM-CM4, FGOALS-g2, and MPI-ESM-MR are larger than those of other models.

In summer, the difference between the DFA and NCEP values of most models is still larger in the tropics and smaller in the southern hemisphere (**Figure 6C**). The errors of all models in the South Indian Ocean (SIO) are all within ±0.05, and only one model has an error exceeding ±0.05 in the South Pacific (SPO). For the Arctic Ocean (AO), South Atlantic (SAO) and Southern Ocean (SO), only two models have an error exceeding ±0.05. In the tropical western Pacific (TWP), only HadGEM2-AO and IPSL-CM5A-MR have an error less than ±0.05.

In autumn, the error between the models' DFA values and the NCEP values is larger in tropical regions, but smaller in mid-high latitudes in the northern and southern hemispheres (**Figure 6D**). In the North Atlantic (NAO), South Atlantic (SAO) and Southern Ocean (SO), the simulation error of only one model does not exceed ±0.05. In the North Pacific (NPO), Tropical Indian Ocean (TIO), South Indian Ocean (SIO) and South Pacific (SPO), there are two models with an error of more than ±0.05. In the tropical Atlantic, only GFDL-ESM2G and IPSL-CM5A-MRhave an error less than ±0.05.

In winter, the difference between the models' DFA values and NCEP values is larger in the tropics, but smaller in the mid-high latitudes of the northern hemisphere (**Figure 6E**). In the North Atlantic Ocean (NAO), the simulation errors of all models are less than ±0.05. In the North Pacific (NPO), only INM-CM4 has a simulation error greater than ±0.05. In the South Indian Ocean (SIO), only HadGEM2-AO and INM-CM4 have an error greater than ±0.05. In the Tropical Atlantic (TAO) and South Pacific (SPO), only two models have simulation errors less than ±0.05.

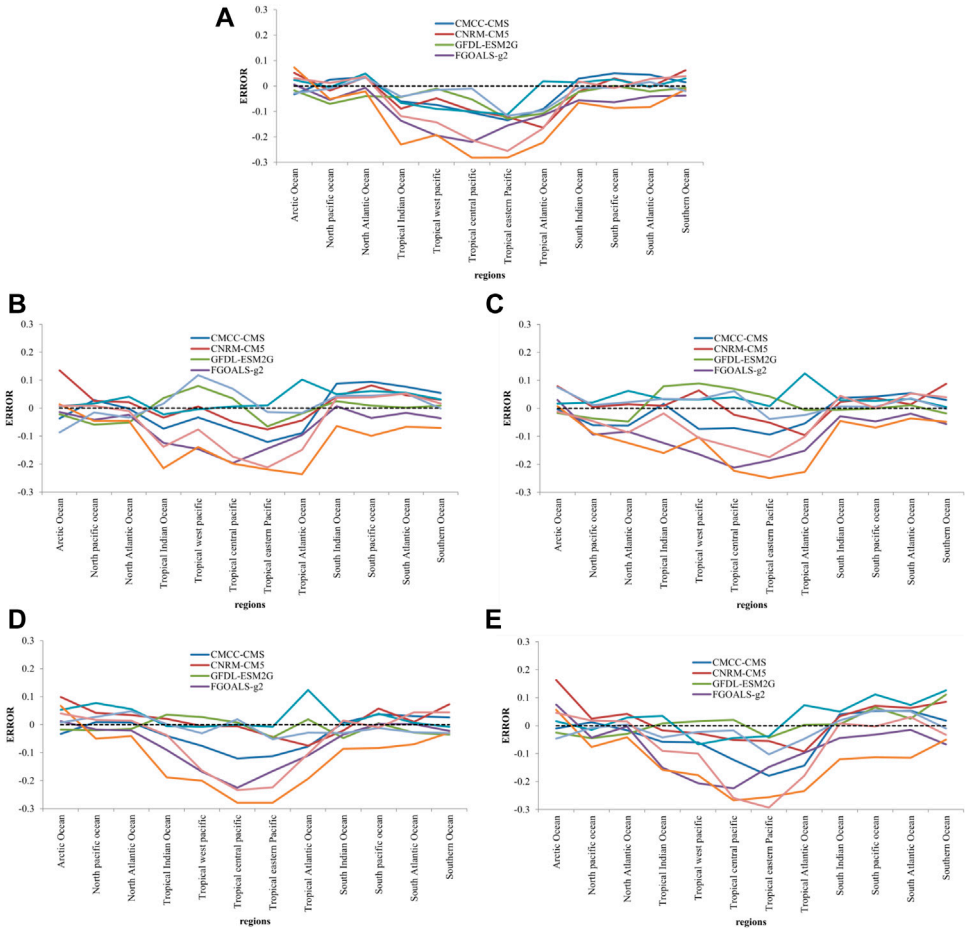

FIGURE 6 | Differences between the DFA index of daily mean SST and the NCEP value in each region simulated by eight models, **(A)** throughout the year, **(B)** spring, **(C)** summer, **(D)** autumn, **(E)** winter.

Long-Range Correlation Assessment of Daily Mean SST Over Ocean in Multiple Models

The NCEP global daily mean SST has long-range correlation characteristics in most parts of the world. The DFA value over the tropical ocean is generally between 0.9 and 1.3. The DTA value of daily mean SST over the tropical Central and Eastern Pacific is above 1.3, and that of the mid-high latitudes is relatively small, in which that in the high latitudes of the northern hemisphere is below 0.7 (**Figure 7A**). Compared with the NCEP values, the DFA values of CMCC-CMS, CNRM-CM5, HadGEM2-AO and MPI-ESM-MR are smaller in the tropics, while the NCEP values are close to or larger than those in the tropics (**Figure 7B,C,F,I**). The DFA values of FGOALS-g2 and INM-CM4 are relatively small in most regions of the world except in the Arctic Ocean (**Figure 7D,G**). The DFA values of GFDL-ESM2G and IPSL-CM5A-MR are larger in some parts of the tropical western Pacific and mid-high latitudes in the southern hemisphere, while those in the rest of the world are close to or smaller than NCEP values (**Figure 7H**).

In spring, the DFA index for NCEP daily mean SST over the global ocean is generally above 0.7, and the DFA value in tropical area is generally between 0.9 and 1.2, while that over the equatorial Central and Eastern Pacific is above 1.2 (**Figure 8A**). Compared with the NCEP data, the DFA values for daily mean SST of CMCC-CMS and MPI-ESM-MR are mainly smaller near the equator, larger outside the tropics, and close to the NCEP value in the high latitudes of the northern hemisphere (**Figure 8B,I**). The DFA value of CNRM-CM5 is only small near the equator, large in the Arctic Ocean, and close to the NCEP value in the rest of the world (**Figure 8C**). The DFA value of FGOALS-g2 is close to or smaller than the NCEP value in most parts of the world, especially near the equator (**Figure 8D**). The DFA value of GFDL-ESM2G is larger in most parts of the tropical Pacific, tropical Indian Ocean and South Atlantic, and is close to or smaller than the NCEP value in the rest of the world (**Figure 8E**). For HadGEM2-AO, except that the DFA value is relatively small in the equatorial Central and Eastern Pacific, the value is close to or relatively larger than the NCEP value in most of the rest of the world (**Figure 8F**). The DFA value of INM-CM4 is smaller in most of the areas except the Arctic Ocean (**Figure 8G**). The DFA value of IPSL-CM5A-MR is smaller in the Arctic Ocean and the North Pacific, and is close to or larger than the NCEP value in the rest of the world (**Figure 8H**).

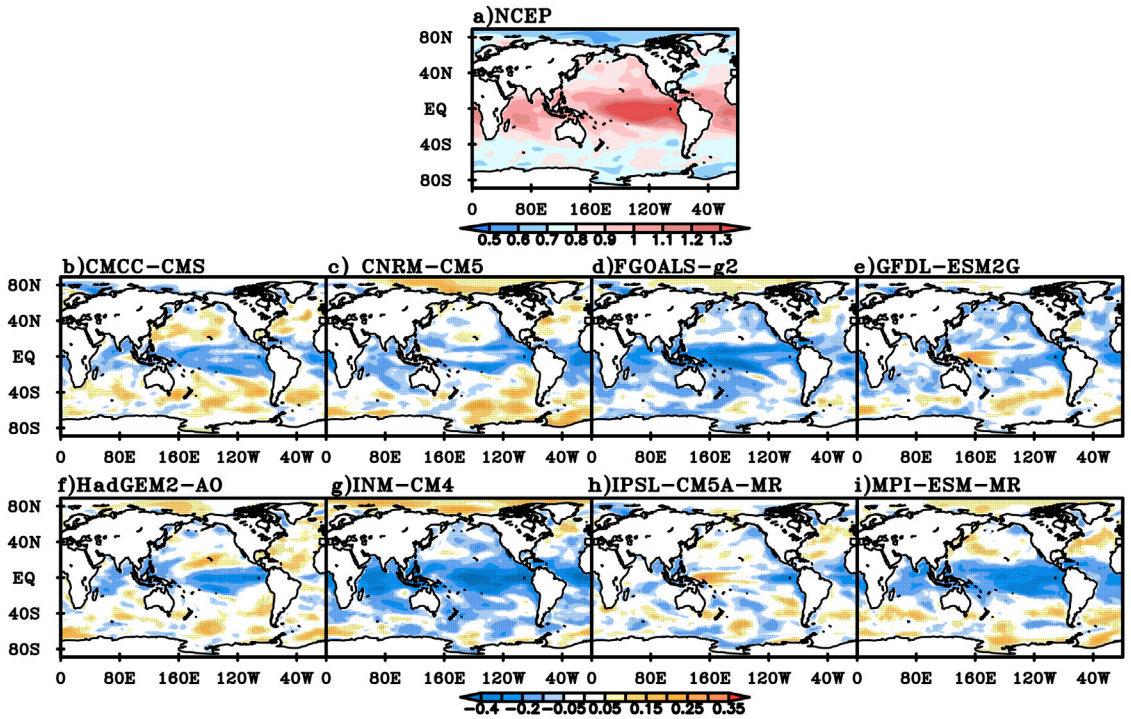

FIGURE 7 | The DFA index for NCEP daily mean SST over the years **(A)** and the difference between the DFA index for daily mean SST simulated in the eight models and NCEP value **(B)** CMCC-CMS, **(C)** CNRM-CM5, **(D)** FGOALS-g2, **(E)** GFDL-ESM2G, **(F)** HadGEM-AO, **(G)** INM-CM4, **(H)** IPSL-CM5A-MR, **(I)** MPI-ESM-MR.

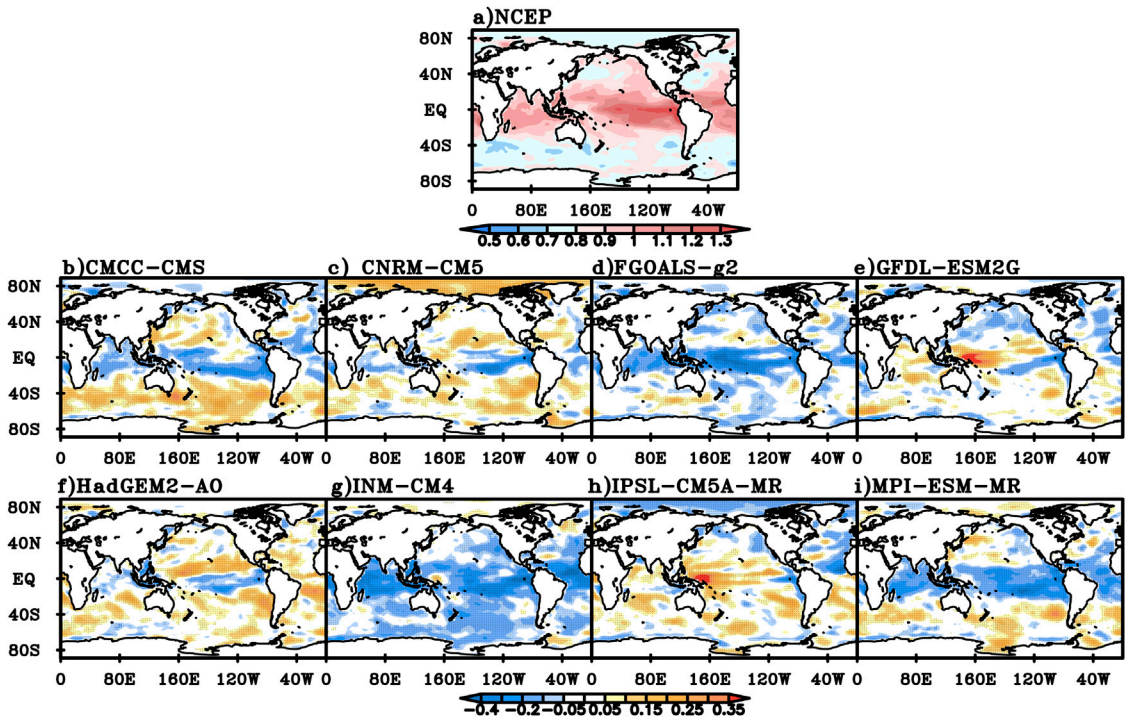

FIGURE 8 | The DFA index for NCEP spring daily mean SST **(A)** and the difference between the DFA index for daily mean SST simulated in the eight models and NCEP value **(B)** CMCC-CMS, **(C)** CNRM-CM5, **(D)** FGOALS-g2, **(E)** GFDL-ESM2G, **(F)** HadGEM-AO, **(G)** INM-CM4, **(H)** IPSL-CM5A-MR, **(I)** MPI-ESM-MR.

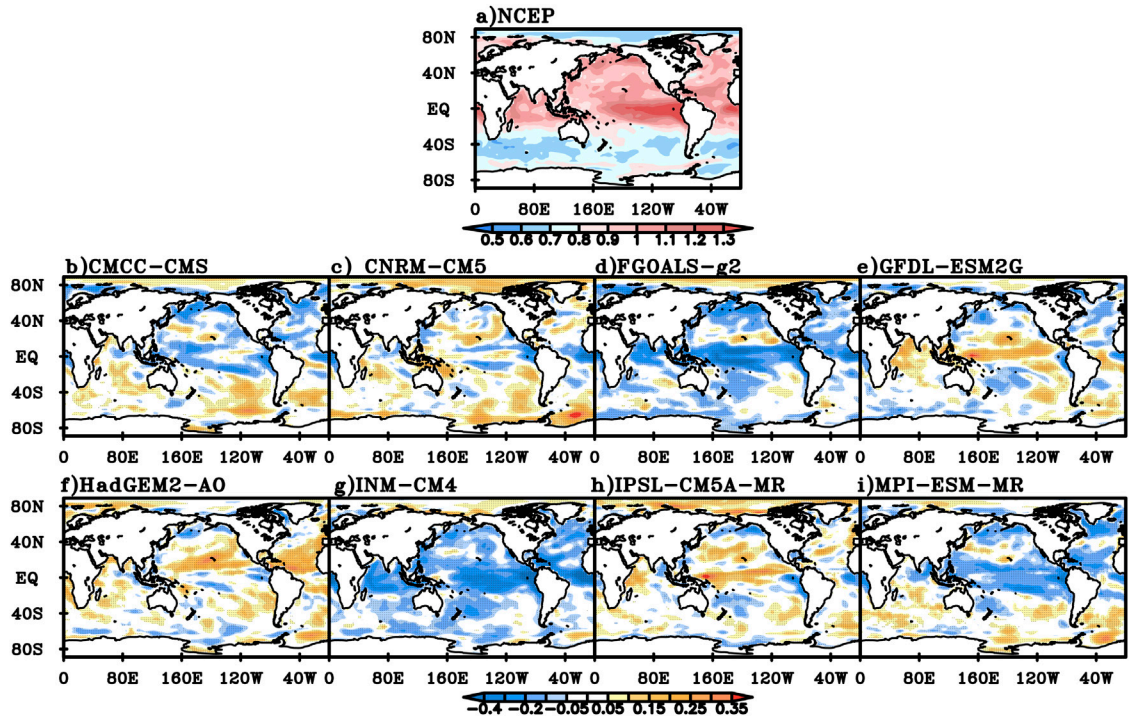

FIGURE 9 | The DFA index for NCEP summer daily mean SST **(A)** and the difference between the DFA index for daily mean SST simulated in the eight models and NCEP value **(B)** CMCC-CMS, **(C)** CNRM-CM5, **(D)** FGOALS-g2, **(E)** GFDL-ESM2G, **(F)** HADGEM-AO, **(G)** INM-CM4, **(H)** IPSL-CM5A-MR, **(I)** MPI-ESM-MR.

In summer, the DFA value of NCEP daily mean SST is generally below 0.9 at mid-high latitudes in the southern hemisphere and the Arctic Ocean, generally between 0.9 and 1.3 in tropical oceans and mid-high latitudes in the northern hemisphere, and above 1.3 in the equatorial Central and Eastern Pacific (**Figure 9A**). Compared with NCEP data, the DFA values for daily mean SST of the CMCC-CMS and MPI-ESM-MR models are smaller in the tropical Pacific, North Pacific, tropical Atlantic and North Atlantic, but close to or larger than the NCEP value in the rest of the world (**Figure 9B,I**). The DFA value of CNRM-CM5 is larger in parts of the Arctic Ocean and Southern Ocean, smaller in the equatorial ocean and close to the NCEP value in the rest of the world (**Figure 9C**). For FGOALS-g2 and INM-CM4, except that the DFA values are larger in the Arctic Ocean, the values are close to or smaller than the NCEP value in the rest areas, especially notably smaller in tropical regions (**Figure 9D,G**). For GFDL-ESM2G and HadGEM2-AO, the DFA values are larger over the tropical ocean, and close to or smaller than the NCEP value in the rest of the world (**Figure 9E,F**). The DFA value of IPSL-CM5A-MR is larger in the tropical Pacific and Arctic Ocean, and is close to or smaller than the NCEP value in the rest of the world (**Figure 9H**).

In autumn, the DFA index for NCEP daily mean SST greater than 0.9 is mainly concentrated in tropical areas, while that in the Arctic Ocean and the southern hemisphere mid-high latitudes areas is generally below 0.7 (**Figure 10A**). Compared with the NCEP data, the DFA values of CMCC-CMS, FGOALS-g2 and MPI-ESM-MR models are larger over tropical oceans, but close to or smaller than the NCEP value in most other regions of the world (**Figure 10B,D,I**). The DFA values of CNRM-CM5 and GFDL-ESM2G are smaller in the equatorial Pacific, equatorial Atlantic, and parts of the South Indian Ocean, larger in parts of the Arctic Ocean and Southern Ocean, and close to the NCEP value in most parts of the world (**Figure 10C,E**). The DFA value of HadGEM2-AO is larger in the equatorial Pacific, the western and northern parts of the tropical Indian Ocean, and some parts of the Southern Ocean, and close to or larger than the NCEP value in the rest of the world, and is especially notably larger in the tropical North Pacific, the tropical North Atlantic and the Arctic Ocean (**Figure 10F**). The DFA value of INM-CM4 is only larger in the Arctic Ocean, but smaller in most parts of the world (**Figure 10G**). The DFA value of IPSL-CM5A-MR is smaller in parts of the South Indian Ocean, the tropical eastern Pacific, the South Atlantic, and the Southern Ocean, and is close to or larger than the NCEP value in most of the rest of the world (**Figure 10I**).

In winter, the DFA index for NCEP daily mean SST is generally between 0.9 and 1.3 in tropical regions and the Southern Ocean, and that in the tropical Central and Eastern Pacific is generally above 1.3 (**Figure 11A**). Compared with the NCEP data, the DFA values of CMCC-CMS, FGOALS-g2, IPSL-CM5A-MR and MPI-ESM-MR models are smaller in tropical regions and parts of the Southern Ocean, but close to or larger than the NCEP value in the rest of the world (**Figure 11B,D,H,I**). The DFA value of CNRM-CM5 is smaller in the equatorial region, but larger in parts of the Arctic Ocean and Southern Ocean, and close to the NCEP value in most other parts of the

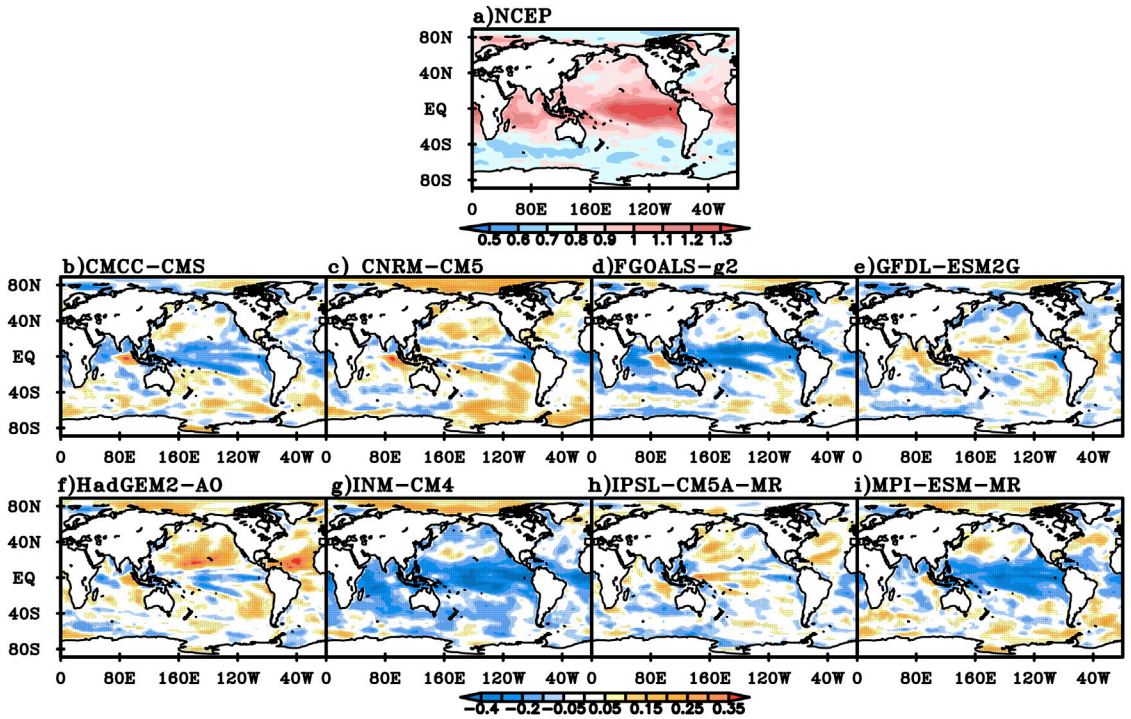

FIGURE 10 | The DFA index for NCEP daily mean SST in autumn **(A)** and the difference between the DFA index for daily mean SST simulated in the eight models and NCEP value **(B)** CMCC-CMS, **(C)** CNRM-CM5, **(D)** FGOALS-g2, **(E)** GFDL-ESM2G, **(F)** HadGEM-AO, **(G)** INM-CM4, **(H)** IPSL-CM5A-MR, **(I)** MPI-ESM-MR.

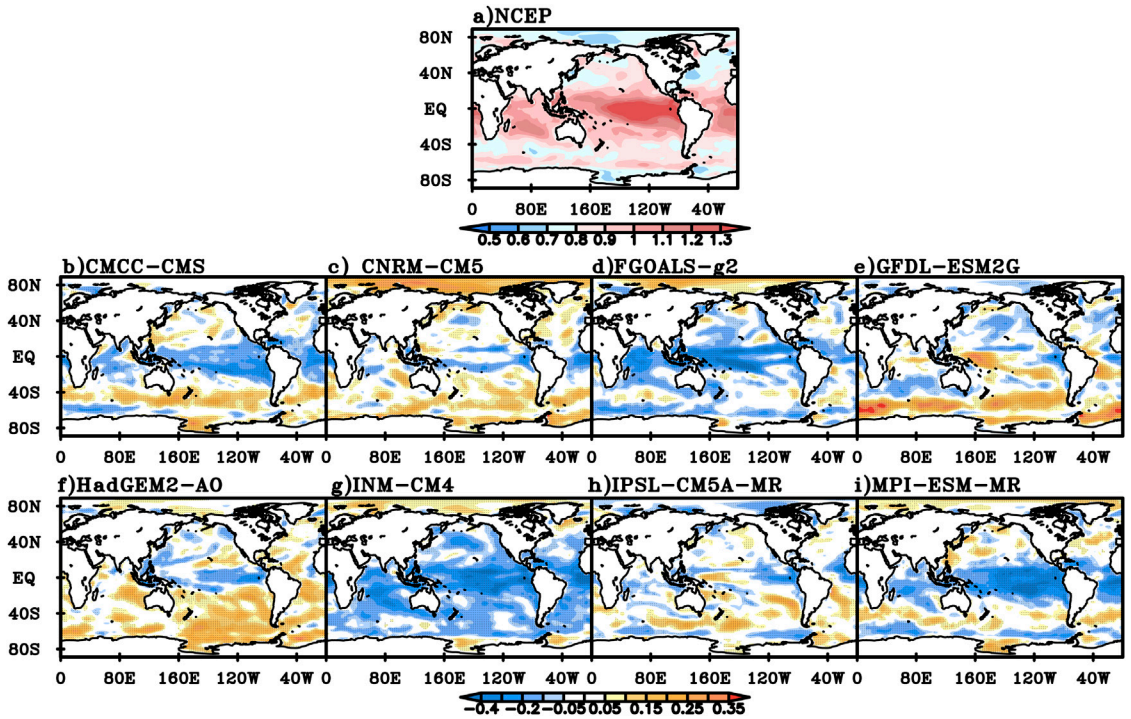

FIGURE 11 | The DFA index for NCEP winter daily mean SST **(A)** and the difference between the DFA index for daily mean SST simulated in the eight models and NCEP value **(B)** CMCC-CMS, **(C)** CNRM-CM5, **(D)** FGOALS-g2, **(E)** GFDL-ESM2G, **(F)** HadGEM-AO, **(G)** INM-CM4, **(H)** IPSL-CM5A-MR, **(I)** MPI-ESM-MR.

world (**Figure 11C**). The DFA value of GFDL-ESM2G is close to or smaller than the NCEP value in the northern hemisphere, while close to or larger than the NCEP value in most parts of the southern hemisphere except the south Indian Ocean (**Figure 11E**). The DFA value of HadGEM2-AO is only smaller in parts of the tropical Pacific and North Pacific, and close to or larger than the NCEP value in most other parts of the world, of which the value in South Pacific and Southern Ocean is significantly larger (**Figure 11F**). The DFA value of INM-CM4 value is larger in the Arctic Ocean and smaller in most other parts of the world (**Figure 11G**).

DISCUSSION AND CONCLUSION

Based on NCEP data, the simulations of daily mean SST by eight CMIP5 models during 1960–2005 are evaluated using DFA method. The results of NCEP data showed that the daily mean SST in most regions of the ocean has long-range correlation characteristics. The DFA values of daily mean SST over ocean basins are large in the tropics while small in mid-high latitudes. The zonal average DFA values of IPSL-CM5A-MR and HadGEM2-AO had a meridional variation characteristic, which was close to NCEP. The regional average of the DFA values of eight models are all close to those of the NCEP data in North Atlantic, Southern Ocean, and North Pacific.

The DFA value of daily mean SST over the years showed that the DFA values of DAT is relatively large in tropical regions, especially in the equatorial Central and Eastern Pacific. In the view of the DFA bias of different models, there were fewer areas where the DFA bias exceeds ±0.05 for CNRM-CM5, HadGEM2-AO and ISPL-CM5A-MR. In spring, the DFA value of the NCEP DAT was generally above 0.7 over the global ocean, between 0.9 and 1.2 in tropical areas, and above 1.2 over the equatorial Central and Eastern Pacific. In the view of DFA bias, the performance of CNRM-CM5, GFDL-ESM2G, HadGEM2-AO and IPSL-CM5A-MR was better than other models. In summer, the DFA values of NCEP DAT was larger in the northern hemisphere than those in the southern hemisphere. The DFA values of CNRM-CM5, GFDL-ESM2G, HadGEM2-AO and ISPL-CM5A-MR are close to those of NCEP in most parts of the global ocean, indicating good performance. In autumn, the DFA values of NCEP DAT were generally above 0.9 in tropical regions and above 1.3 in the equatorial Central and Eastern Pacific. The DFA bias of CNRM-CM5, GFDL-ESM2G, and IPSL-CM5A-MR were relatively small in most regions of the global ocean. In winter, the DFA values of NCEP DAT were generally above 1.0 in tropical regions, while below 0.8 only in the Arctic Ocean and the North Atlantic. The performance of CNRM-CM5, FGAOLS-g2, and IPSL-CM5A-MR were good in most parts of the global ocean.

The LRC method has been widely used to verify the performance of climate models for the climate simulation (Zhao et al., 2017; He and Zhao, 2018). However, most of previous studies focus on the land surface air temperature, little research on sea surface temperature has been conducted. Therefore, some significant conclusions in this paper have been shown for the revelation of sea surface temperature simulation by climate models using LRC method. Although, it is important to make sure that the different sources of uncertainty are identified when using CMIP models to conduct climate projection. Future emissions, internal variability of the climate system and model response uncertainty are the three main sources of uncertainty in CMIP MME. Different responses to the same forcing can emerge due to different processes and feedbacks as well as due to the parametrization used in the different models (Zelinka et al., 2020). There are uncertainties exiting in the interpolation for outputs from CMIP models and the gauged data to $1.0^{\circ} \times 1.0^{\circ}$grids using the inverse distance weighting approach. Hence, the model weighting scheme for MME and dynamic downscaling method with more complete physical and dynamic processes will be adopted to conduct the region climate simulation and projection based on CMIP5/6 model output in the future, and it will significantly improve the reliability of simulations and projections. These will be the topic of our research in future.

DATA AVAILABILITY STATEMENT

The original contributions presented in the study are included in the article/Supplementary Material, further inquiries can be directed to the corresponding author.

AUTHOR CONTRIBUTIONS

SZ and WH conceived of the presented idea. XZ and TD carried out the implementation. XZ performed the calculations. All authors discussed the results and contributed to the final manuscript.

FUNDING

This work was funded by National Key R&D Program of China (2016YFA0602703), the National Natural Science Foundation of China (Grant No. 41775092, 41875120, and 41605069), the China Postdoctoral Science Foundation (Grant No. 2020M672942), the Fundamental Research Funds for the Central Universities from Sun Yat-Sen University (Grant No. 20lgzd06 and 19lgpy31).

REFERENCES

Alexander, L. V., and Arblaster, J. M. (2009). Assessing Trends in Observed and Modelled Climate Extremes over Australia in Relation to Future Projections. *Int. J. Climatol.* 29, 417–435. doi:10.1002/joc.1730

Alexander, L. V., Zhang, X., Peterson, T. C., Caesar, J., Gleason, B., Klein Tank, A. M. G., et al. (2006). Global Observed Changes in Daily Climate Extremes of Temperature and Precipitation. *J. Geophys. Res.* 111, D05109. doi:10.1029/2005JD006290

Blender, R., and Fraedrich, K. (2003). Long Time Memory in Global Warming Simulations. *Geophys. Res. Lett.* 30 (14), 1769. doi:10.1029/2003gl017666

Bunde, A., Eichner, J. F., Kantelhardt, J. F., and Havlin, S. (2005). Long-Term Memory: A Natural Mechanism for the Clustering of Extreme Events and Anomalous Residual Times in Climate Records. *Phys. Rev. Lett.* 94, 048701. doi:10.1103/physrevlett.94.048701

Bunde, A., and Havlin, S. (2002). Power-law Persistence in the Atmosphere and in the Oceans. *Physica A: Stat. Mech. its Appl.* 314, 15–24. doi:10.1016/s0378-4371(02)01050-6

Chan, D., and Wu, Q. (2015). Attributing Observed SST Trends and Subcontinental Land Warming to Anthropogenic Forcing during 1979-2005. *J. Clim.* 28, 3152–3170. doi:10.1175/jcli-d-14-00253.1

Gan, Z., Yan, Y., and Qi, Y. (2007). Scaling Analysis of the Sea Surface Temperature Anomaly in the South China Sea. *J. Atmos. Ocean. Tech.* 24, 681–687. doi:10.1175/jtech1981.1

Grose, M. R., Narseym, S., Delage, F., Dowdy, A. J., Bador, M., Boschat, G., et al. (2020). Insights from CMIP6 for Australia's Future Climate. *Earth's Future* 8 (5), e2019EF001469. doi:10.1029/2019EF001469

Gusain, A., Ghosh, S., and Karmakar, S. (2020). Added Value of CMIP6 over CMIP5 Models in Simulating Indian Summer Monsoon Rainfall. *Atmos. Res.* 232, 104680. doi:10.1016/j.atmosres.2019.104680

He, W. P., and Zhao, S. S. (2018). Assessment of the Quality of NCEP-2 and CFSR Reanalysis Daily Temperature in China Based on Long-Range Correlation. *Clim. Dyn.* 50, 493–505. doi:10.1007/s00382-017-3622-0

IPCC (2013). *Climate Change 2013: The Physical Science Basis. Contribution of Working Group I to the Fifth Assessment Report of the Intergovernmental Panel on Climate Change*. Cambridge, UK, and New York, NY: Cambridge University Press.

Ji, Z., and Kang, S. (2015). Evaluation of Extreme Climate Events Using a Regional Climate Model for China. *Int. J. Climatol.* 35, 888–902. doi:10.1002/joc.4024

Jiang, D., and Tian, Z. (2013). East Asian Monsoon Change for the 21st century: Results of CMIP3 and CMIP5 Models. *Chin. Sci. Bull.* 58, 1427–1435. doi:10.1007/s11434-012-5533-0

Jiang, L., Zhao, X., Li, N., Li, F., and Guo, Z. (2013). Different Multifractal Scaling of the 0 Cm Average Ground Surface Temperature of Four Representative Weather Stations over China. *Adv. Meteorology* 2013, 1–8. doi:10.1155/2013/341934

Kalnay, E., Kanamitsu, M., Kistler, R., Collins, W., Deaven, D., Gandin, L., et al. (1996). The NCEP/NCAR 40-year Reanalysis Project. *Bull. Amer. Meteorol. Soc.* 77, 437–471. doi:10.1175/1520-0477(1996)077<0437:tnyrp>2.0.co;2

Kanamitsu, M., Ebisuzaki, W., Woollen, J., Yang, S.-K., Hnilo, J. J., Fiorino, M., et al. (2002). NCEP-DOE AMIP-II Reanalysis (R-2). *Bull Amer. Meteorol. Soc.* 83, 1631–1643. doi:10.1175/bams-83-11-1631(2002)083<1631:nar>2.3.co;2

Kantelhardt, J. W., Koscielny-Bunde, E., Rybski, D., Braun, P., Bunde, A., and Havlin, S. (2006). Long-term Persistence and Multifractality of Precipitation and River Runoff Records. *J. Geophys. Res.* 111. doi:10.1029/2005JD005881

Kharin, V. V., Zwiers, F. W., Zhang, X., and Hegerl, G. C. (2007). Changes in Temperature and Precipitation Extremes in the IPCC Ensemble of Global Coupled Model Simulations. *J. Clim.* 20, 1419–1444. doi:10.1175/jcli4066.1

Kharin, V. V., Zwiers, F. W., Zhang, X., and Wehner, M. (2013). Changes in Temperature and Precipitation Extremes in the CMIP5 Ensemble. *Climatic Change* 119 (2), 345–357. doi:10.1007/s10584-013-0705-8

Koscielny-Bunde, E., Roman, H. E., Bunde, A., Havlin, S., and Schellnhuber, H. J. (1998). Long-range Power-Law Correlations in Local Daily Temperature Fluctuation. *Philosophical Mag. B* 77 (5), 1331–1340.

Koscielny-Bunde, E., Bunde, A., Havlin, S., and Goldreich, Y. (1996). Analysis of Daily Temperature Fluctuations. *Physica A: Stat. Mech. its Appl.* 231 (4), 393–396. doi:10.1016/0378-4371(96)00187-2

Kruger, A. C., and Sekele, S. S. (2013). Trends in Extreme Temperature Indices in South Africa: 1962-2009. *Int. J. Climatol.* 33, 661–676. doi:10.1002/joc.3455

Peng, C.-K., Buldyrev, S. V., Havlin, S., Simons, M., Stanley, H. E., and Goldberger, A. L. (1994). Mosaic Organization of DNA Nucleotides. *Phys. Rev. E* 49, 1685–1689. doi:10.1103/physreve.49.1685

Prinn, R. G. (2012). Development and Application of Earth System Models,*Proc. Natl. Acad. Sci.* 110. (Supplement_1): 3673–3680. doi:10.1073/pnas.1107470109pnas.1107470109

Rusticucci, M. (2012). Observed and Simulated Variability of Extreme Temperature Events over South America. *Atmos. Res.* 106, 1–17. doi:10.1016/j.atmosres.2011.11.001

Sillmann, J., Kharin, V. V., Zwiers, F. W., Zhang, X., and Bronaugh, D. (2013). Climate Extremes Indices in the CMIP5 Multimodel Ensemble: Part 2. Future Climate Projections. *J. Geophys. Res. Atmos.* 118, 2473–2493. doi:10.1002/jgrd.50188

Talkner, P., and Weber, R. O. (2000). Power Spectrum and Detrended Fluctuation Analysis: Application to Daily Temperatures. *Phys. Rev. E* 62 (1), 150–160. doi:10.1103/physreve.62.150

Taylor, K. E., Stouffer, R. J., and Meehl, G. A. (2012). An Overview of CMIP5 and the experiment Design. *Bull. Amer. Meteorol. Soc.* 93, 485–498. doi:10.1175/bams-d-11-00094.1

Tebaldi, C., Smith, R. L., Nychka, D., and Mearns, L. O. (2005). Quantifying Uncertainty in Projections of Regional Climate Change: a Bayesian Approach to the Analysis of Multimodel Ensembles. *J. Clim.* 18, 1524–1540. doi:10.1175/jcli3363.1

Wang, Y., Zhou, B., Qin, D., Wu, J., Gao, R., and Song, L. (2017). Changes in Mean and Extreme Temperature and Precipitation over the Arid Region of Northwestern China: Observation and Projection. *Adv. Atmos. Sci.* 34 (3), 287–305. doi:10.1007/s00376-016-6160-5

Wei, M., and Qiao, F. (2016). Attribution Analysis for the Failure of CMIP5 Climate Models to Simulate the Recent Global Warming Hiatus. *Sci. China Earth Sci.* 60 (2), 397–408. doi:10.1007/s11430-015-5465-y

Zelinka, M. D., Myers, T. A., McCoy, D. T., Po-Chedley, S., Caldwell, P. M., Ceppi, P., et al. (2020). Causes of Higher Climate Sensitivity in CMIP6 Models. *Geophys. Res. Lett.* 47, 1–12.Z. doi:10.1029/2019gl085782

Zeng, Q. C., Zhou, G. Q., Pu, Y. F., Chen, W., Li, R. F., Liao, H., et al. (2008). Research on the Earth System Dynamic Model and Some Related Numerical Simulations. *Chin. J. Atmos. Sci.* 32 (4), 653–690. doi:10.3724/SP.J.1148.2008.00288

Zhao, S. S., and He, W. P. (2014). Performance Evaluation of Chinese Air Temperature Simulated by Beijing Climate Center Climate System Model on the Basis of the Long-Range Correlation. *Acta Physica Sinica* 63 (20), 209201

Zhao, S. S., He, W. P., and Jiang, Y. (2017). Evaluation of NCEP-2 and CFSR Reanalysis Seasonal Temperature Data in China Using Detrended Fluctuation Analysis. *Int. J. Climatol* 38, 252–263. doi:10.1002/joc.5173

Zhao, Z. C., Luo, Y., and Huang, J. B. (2013). A Review on Evaluation Methods of Climate Modeling[J]. *Progressus Inquisitiones de Mutatione Climatis* 9 (1), 1–8.

Zhou, B., Wen, Q. H., Xu, Y., Song, L., and Zhang, X. (2014). Projected Changes in Temperature and Precipitation Extremes in china by the Cmip5 Multimodel Ensembles. *J. Clim.* 27, 6591–6611. doi:10.1175/jcli-d-13-00761.1

Zhu, X., Dong, W., Wei, Z., Guo, Y., Gao, X., Wen, X., et al. (2017). Multi-decadal Evolution Characteristics of Global Surface Temperature Anomaly Data Shown by Observation and CMIP5 Models. *Int. J. Climatol* 38, 1533–1542. doi:10.1002/joc.5264

Conflict of Interest: The authors declare that the research was conducted in the absence of any commercial or financial relationships that could be construed as a potential conflict of interest.

frontiers in Environmental Science

ORIGINAL RESEARCH
published: 25 May 2021
doi: 10.3389/fenvs.2021.678450

Article Title Variations in Growing Season NDVI and Its Sensitivity to Climate Change Responses to Green Development in Mountainous Areas

Ming Zhu[1], *Jingjing Zhang*[1,2] *and Lianqi Zhu*[1]*

[1]College of Environment and Planning, Henan University, Kaifeng, China, [2]College of Geography and Tourism, Zhengzhou Normal University, Zhengzhou, China

The Normalized Difference Vegetation Index (NDVI) is sensitive to changes in surface vegetation cover. Research into how climate change impacts surface vegetation cover is essential to manage ecological systems and promote green development. The Western Henan Mountains, located in the transitional zone between the northern subtropical and warm temperate zones of China, is an ideal location to study the impacts of climate change on surface vegetation cover. Combining a digital elevation model (DEM) with temperature and precipitation data; and MODIS-NDVI imagery (2000~2017) for the Western Henan Mountains, this study explores variations in the growing season NDVI and its response to climate change. Results show that there are significant changes with fluctuations in NDVI values from 2000 to 2017. NDVI increased at a growth rate of 0.027 per decade ($p < 0.05$) overall, indicating vegetation conditions have gradually improved. Although the NDVI value showed an overall increasing trend, 19.12% of the areas showed a decreasing trend, interspersing and intersecting spatially, showing significant spatial differences. NDVI increased initially, but then decreased as a function of elevation, which was shown to be proportional to slope and independent of aspect. Variables including elevation and slope gradient are shown to provide high explanation of NDVI variability, whilst temperature is shown to have a more significant impact on NDVI than precipitation. However, vegetation responses to temperature and precipitation covaried with both slope and aspect. Positive NDVI trends were strongest at low elevations (i.e., <1,100 masl), which we attribute to vegetation restoration activities. Lower NDVI values characterized gentle slopes (<5°), whilst higher values were, in contrast, associated with steeper slopes (5~10°). This study highlights the complex mechanisms and their relations governing vegetation response to climate change and should form an instructive basis for both future modeling studies investigating the response of vegetation to future global warming.

Keywords: growing season NDVI, climate change, green development, correlation analysis, western henan mountains

OPEN ACCESS

Edited by:
Qingxiang Li,
Sun Yat-Sen University, China

Reviewed by:
Binhui Liu,
Northeast Forestry University, China
T. P. Sabin,
Indian Institute of Tropical Meteorology (IITM), India

***Correspondence:**
Lianqi Zhu
lqzhu@henu.edu.cn

Specialty section:
This article was submitted to Atmosphere and Climate, a section of the journal Frontiers in Environmental Science

Received: *09 March 2021*
Accepted: *11 May 2021*
Published: *25 May 2021*

Citation:
Zhu M, Zhang J and Zhu L (2021) Article Title Variations in Growing Season NDVI and Its Sensitivity to Climate Change Responses to Green Development in Mountainous Areas. Front. Environ. Sci. 9:678450. doi: 10.3389/fenvs.2021.678450

INTRODUCTION

Vegetation comprises a critical component of ecosystems connecting the atmospheric, hydrological and pedological systems (Yang et al., 2010; Piao et al., 2011). The sensitivity of vegetation cover to climate change has become a major research focus considering the unprecedented rates and impacts of anthropogenic global warming on the biosphere.

The Normalized Difference Vegetation Index (NDVI) is commonly used to indicate changes to vegetation cover in response to climate variability (Nemani et al., 2003). Several studies have investigated the relationships between NDVI and climate factors (e.g., temperature and precipitation at global (Ichii et al., 2002; Liu et al., 2016) and regional (Herrmann et al., 2005; Du et al., 2016; Yin et al., 2016) scales *via* correlation analysis (Tong, 2014), factor analysis and regression analysis(Zhang et al., 2017).

Notably, 67% of China's total land area is mountainous, of concern, given the high sensitivity of mountain ecosystems to climate change. Therefore, understanding the elevation-dependent composition of vegetation within different mountain environments is crucial for understanding the varied impacts of climate on these environments (Zhu and Li, 2017; Zhang et al., 2018). Mountain vegetation provides vital ecosystem services, but is highly sensitive to environmental change and is influenced by numerous factors (Pepin et al., 2015). Understanding the driving mechanisms controlling mountain vegetation is essential to project future spatial patterns of vegetation change in response to global warming in these regions, and as such constitutes a pressing issue for climate change research. Extensive research has been conducted on mountain ecosystems in the European Alps, Kilimanjaro in Africa, Cordillera in North America, and the Andes in South America (Habeck, 1987; Hemp, 2006; Gehrig-Fasel et al., 2007; Erschbamer et al., 2009; Asam et al., 2018). Some progress has also been made in the study of mountain vegetation changes in China, specifically the Sanjiangyuan area of Tibet Plateau, Hengduan Mountains, Tianshan Mountains, Changbai Mountains, Qilian Mountains and Qinling Mountains (Kessler, 2000; Long, 2003; Zhang et al., 2004; Yao et al., 2010). The Western Henan Mountains are in the transition zone between the northern subtropical and warm temperate zones of China. The region also represents a topographical transition zone between the second and third steps, displaying diverse topographic characteristics (Zhang et al., 2019).

Research on mountain vegetation growth relies heavily on the NDVI, which is an important indicator for assessing the status of mountain vegetation growth, particularly during the growing season (Geng et al., 2019). In particular NDVI has been used to investigate dynamic changes in the horizontal structure of mountain vegetation. In China, nine vertical vegetation zones in the West Kunlun Mountains were identified using SPOT-VGT NDVI and digital elevation model (DEM) data. Several studies have investigated the drivers of vegetation changes in mountain regions. For example, studies of dynamic vegetation cover changes in the European Alps found that climate change was less significant compared to anthropogenic activities (Erschbamer et al., 2009). Furthermore, trends in NDVI variations and regional responses along different elevation gradients were analyzed in the Qinling Mountains. The results indicated that the vegetation in high-elevation areas was mainly controlled by temperature changes (Geng et al., 2019). Disentangling the relative impacts of climate changes and geographic factors such as slope, altitude and aspect is needed to more fully assess the controls on vegetation within different mountain regions (Song, 1994; Lunetta et al., 2006; Eastman et al., 2013). The Western Henan mountains represent a key gap in the field of mountain vegetation research and therefore is investigated in the present study.

In this study, the Savitsky-Golay (S-G) filtering algorithm was applied to the 2000~2017 MODIS-NDVI time series data. Combined with DEM, temperature, and precipitation data, and using trend- and correlation analyses, this study discusses the multi-dimensional change of vegetation and its climate response accounting for terrain factors such as altitude, slope, and aspect. The characteristics of NDVI change and the response of vegetation on both the northern and southern slopes of the Western Henan mountains were investigated to characterize the vegetation dynamics and their responses to climate change. The value of this study lies in the fact it can provide a crucial basis for decision-making in terms of vegetation protection measures and green development for different ecological units within mountain ecosystems under different global warming scenarios.

MATERIALS AND METHODS

Study Area

The western mountainous area of Henan Province belongs to the Qinling Mountains (110°20′~113°40′ E, 32°40′~35°10′ N). The region includes the Xiaoqinling and Songshan Mountains from east to west; the Xiaoshan, Xiong'er, and Waifang Mountains from east to north; and Funiu Mountain from east to south in total covering an area of ~4,300 km^2 (**Figure 1**). The research area is located in a transitional zone between the northern subtropical and warm temperate zones of China. The annual average temperature in this area is 13~15°C, the annual average precipitation is 600~1,200 mm and the average annual sunshine hours are generally 2,000–2,600 h. The elevation of the region ranges from 75 to 2,384 m above sea level (masl herein), decreasing gradually from west to east.

Data Resources and Pre-Processing

This NDVI data used in this study was obtained from a NASA 250 m resolution MOD13Q1 (https://ladsweb.modaps.eosdis.nasa.gov/) product which was synthesized every 16 days from the years 2000~2017. The DEM data was derived from the ASTER Global Digital Elevation Model (ASTGTM2; http://www.gscloud.cn/) at a spatial resolution of 30 m and was interpolated to a 250 m resolution by mosaic processing, cropping and re-sampling in ArcGIS. Temperature and precipitation data were obtained from monthly data records of 27 meteorological stations (2000~2017) of the Henan Meteorological Service (**Figure 1**).

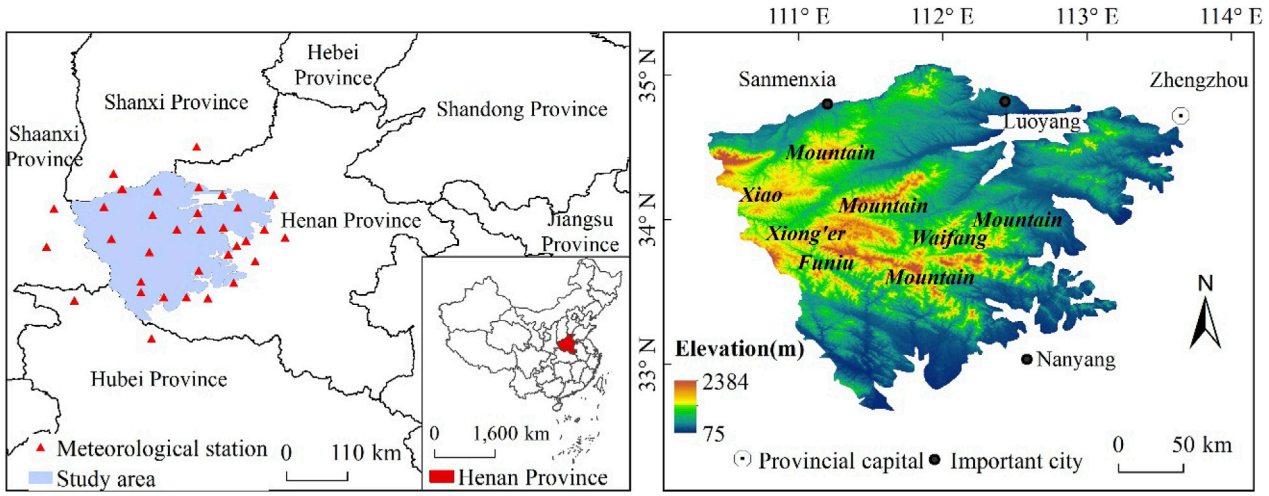

FIGURE 1 | The location and elevation of the study area. Note the positions of the meteorological stations used in this study are shown on the left.

NDVI Reconstruction and Extraction

MODIS Reprojection Tools (MRT) was used to splice, project, and cut the MODIS-NDVI data. The Savitsky-Golay (SG) filter algorithm of the TIMESAT tool was adopted to reconstruct NDVI data to eliminate mutation points and decrease systematic errors from clouds, aerosols, angle of view and solar height (Tucker et al., 2005).

Vegetation in the Western Henan Mountains is dormant during winter and sometimes covered by snow. We therefore only analyzed NDVI in the growing season. Using TIMESAT to extract phenological information from pixels coupled with data on the spatiotemporal distribution of long leaves and withered vegetation, the growing season for the region was determined to be from May to September. Thus, the ninth and eighteenth phases of the annual image represent the beginning and end of the growing season, respectively. Then, the mean value of NDVI under annual and multi-year growth seasons can be calculated (Jarlan et al., 2008; Peng et al., 2012).

Meteorological Data Processing

Meteorological station data were interpolated onto a 250 m resolution grid. The DEM was used as a covariant whilst thin plate spline smoothing algorithms (ANUSPLIN) and Kriging were used to interpolate annual temperature and precipitation respectively (Jarlan et al., 2008; Zhang et al., 2016). Annual average air temperature and precipitation were also estimated using ArcGIS 10.4 software.

Permission to Reuse and Copyright

Elevation, slope and aspect were extracted from the DEM using ArcGIS 10.4. With reference to the distribution characteristics of the vertical vegetation types (as reported in the Scientific survey of the Funiu Nature Reserve) (Song, 1994), the study area was divided into five vertical zones: <800, 800~1,100, 1,100~1,700, 1,700~2,000, and >2,000 masl, accounting for 70.3, 16.6, 12.3, 5.3, and 0.5% of the total area, respectively.

The slope was divided into <5°, 5~10°, 10~20°, 20~30°, 30~40°, and > 40°, accounting for 17.6, 22.0, 29.2, 19.2, 9.4, and 2.6% of the total area, respectively. Slopes between 5 and 20° were the most common (51.2%). Furthermore, slope direction was divided into the slope-free direction (−1), north (0~22.5°, 337.5~360°), northeast (22.5~67.5°), east (67.5~112.5°) southeast (112.5~157.5°), south (157.5~202.5°), southwest (202.5~247.5°), west (247.5~292.5°) and northwest (292.5~337.5°); accounting for 0.5, 11.3, 13.5, 12.9, 12.4, 13.3, 11.8, and 11.6% of the total area, respectively. This classification was necessary because complex terrain features meant that the distribution of the slope directions was highly fragmented.

The classified layers of elevation, slope, and aspect were extracted by the Attribute Extraction Tool in ArcGIS 10.4. Then, the spatial distribution of mean NDVI, annual air temperature, and annual precipitation in the growing season were superimposed using mask extraction. Finally the spatiotemporal distribution of NDVI, temperature and precipitation for different elevations, slopes, and aspects was analyzed.

Methods

Trend Analysis

To analyze the spatiotemporal changes of NDVI at each grid unit, a simple linear slope analysis model was employed in MATLAB 4.1 (Tucker et al., 2005; Lunetta et al., 2006; Jarlan et al., 2008; Peng et al., 2012; Eastman et al., 2013; Tong et al., 2016; Zhang et al., 2016).

The software SPSS 21.0 was used for correlation analysis and significance testing between NDVI at different elevations, slopes, and aspects and annual temperature and precipitation. Then, the response of vegetation to temperature and precipitation over complex mountain topography was obtained.

Correlation Analysis

Changes in the NDVI are affected by multiple factors. In order to better analyze the relationship between NDVI and a given variable,

the influence of other variables needs to be eliminated. Therefore, a partial correlation analysis method based on pixels is used to determine the relationship between annual NDVI, precipitation and temperature. This yields a coefficient with which to explore the relationship between annual NDVI and climate factors.

In addition, the significance of partial correlation coefficients between NDVI, precipitation, and temperature was determined using a *t*-test.

To assess the degree of autocorrelation between climate and terrain factors and the resultant impacts on NDVI, correlation analysis and statistical tests for significance were carried out in SPSS 21.0 on: (i) NDVI, (ii) annual average temperature; and (iii) annual precipitation for different altitudes and slopes in the western Henan Mountains. From these data, we demonstrate the response of vegetation dynamics to both temperature and precipitation in the study area.

RESULTS

NDVI Changes

Trends in NDVI Variability

An analysis of growing season NDVI values from 2000 to 2017 reveals significant changes in NDVI values with large fluctuations (**Figure 2**). Overall, NDVI increased at a growth rate of 0.027 per decade ($p < 0.05$), indicating a gradual increase in vegetation. Minimum (0.598) and maximum (0.696) NDVI values occurred in 2001 and 2015, respectively (**Figure 2**).

Spatial NDVI Changes

Figure 3 indicates the spatial distribution of the mean annual NDVI and the annual trends of change within each grid for the years 2000–2017. Mean annual NDVI values between 0.364 and 0.999 occupied most of the area across the whole region. Low NDVI values (i.e., 0~0.537) were always distributed along the northern and southern margins. Grids with high NDVI values (i.e., 0.752~0.999) were mainly distributed in the central areas and parts of the northwest (**Figure 3A**). It can be seen from

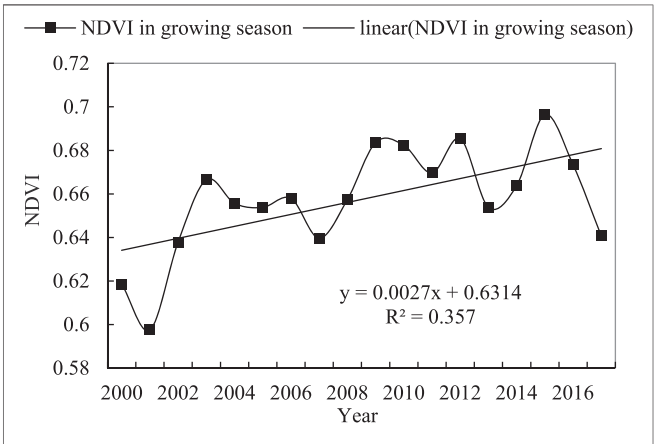

FIGURE 2 | Normalized difference vegetation index (NDVI) trends during the growing season.

Figure 2 that the NDVI value generally showed an increasing trend from 2000 to 2017. Grids under an increasing trend overall and were widely distributed across the whole region, indicating that the vegetation in the study area has gradually improved. Although the NDVI value showed an overall increasing trend, 19.12% of the areas showed a decreasing trend, which were mainly distributed in the central areas, part of the northeastern and southeastern areas, interspersing and intersecting spatially, showing significant spatial differences (**Figure 3B**).

Influence of Terrain Factors on NDVI

We selected the variables of elevation, slope, and aspect to explore the effect of terrain on NDVI. **Figure 4A** shows that after an initial increase, NDVI values decreased with elevation. The minimum NDVI value (0.606) occurred below 800 masl. The maximum NDVI value (0.822) occurred at 1,700~2,000 masl in areas undisturbed by human activities, thus promoting vegetation growth. In areas above 2,000 masl the NDVI exhibited a downward trend. **Figure 4B** shows a positive correlation between NDVI and slope gradient. Maximum NDVI values (0.797) occurred on slopes ranging from 30 to 40°, above which NDVI declined. Minimum NDVI were attained (0.569) for slope gradients of <5°. **Figure 4C** shows that the aspect had no significant impact on NDVI values. The NDVI of the southern slope was low (0.636) relative to the northwestern slope (0.685). This difference can be explained by the fact that the southern slopes are dominated by cultivated lands, while forests dominate the northwestern slopes.

Comparison of NDVI Trends for Different Terrain Factors

Figure 5 shows the variations in NDVI trends as a function of elevation, slope and aspect. The variation in NDVI trends at elevation zones from 800 to 2,000 masl was 0.029 ($p < 0.05$), 0.028 ($p < 0.05$), 0.020, 0.009, and 0.004 per decade. Trends in NDVI variability were significant on slopes at elevations less than 1,700 masl (**Figure 5A**). In general, NDVI growth rates decreased as elevation increased. The NDVI growth trend in areas with the slope between 0 and 5°and above 40°was increased at first and then decreased, then increased slightly. NDVI growth was the highest (0.038 per decade, $p < 0.05$) in areas with the slope of 5~10° and the lowest in areas with the slope of 30~40°, indicating that vegetation improvement was less apparent as the slope increased (**Figure 5B**). The effect of aspect on NDVI growth trends was relatively consistent (approximately 0.028 per decade). NDVI growth rates on shady slopes (0.029 per decade) were slightly higher compared to sunny slopes (0.026 per decade) (**Figure 5C**).

The spatial distribution of NDVI trends in different vegetation change areas is shown in **Figure 6A**. 40% of the area exhibited improved vegetation cover, 56.68% remained stable, whilst 3.35% exhibited a decline. Vegetation recovery decreased with increasing elevation, whilst the largest improvements (i.e., 42%) to vegetation recovery were observed on slopes at elevations ranging from 800 to 1,100 masl (**Figure 6B**). The

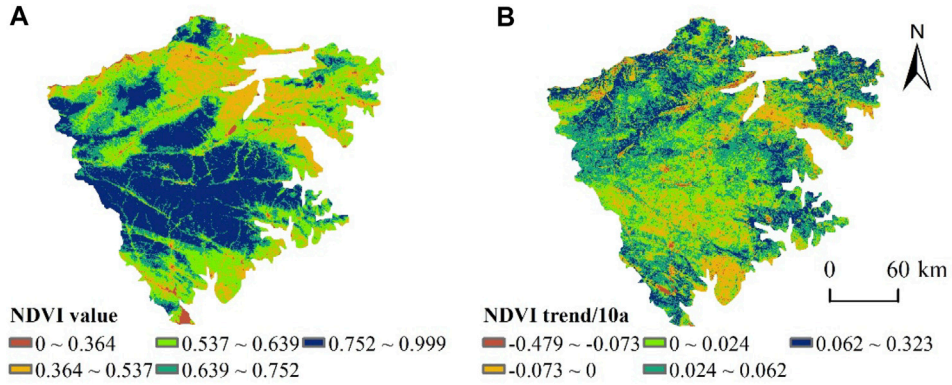

FIGURE 3 | Spatial distribution of the annual mean NDVI **(A)** and trends of changing NDVI values **(B)**.

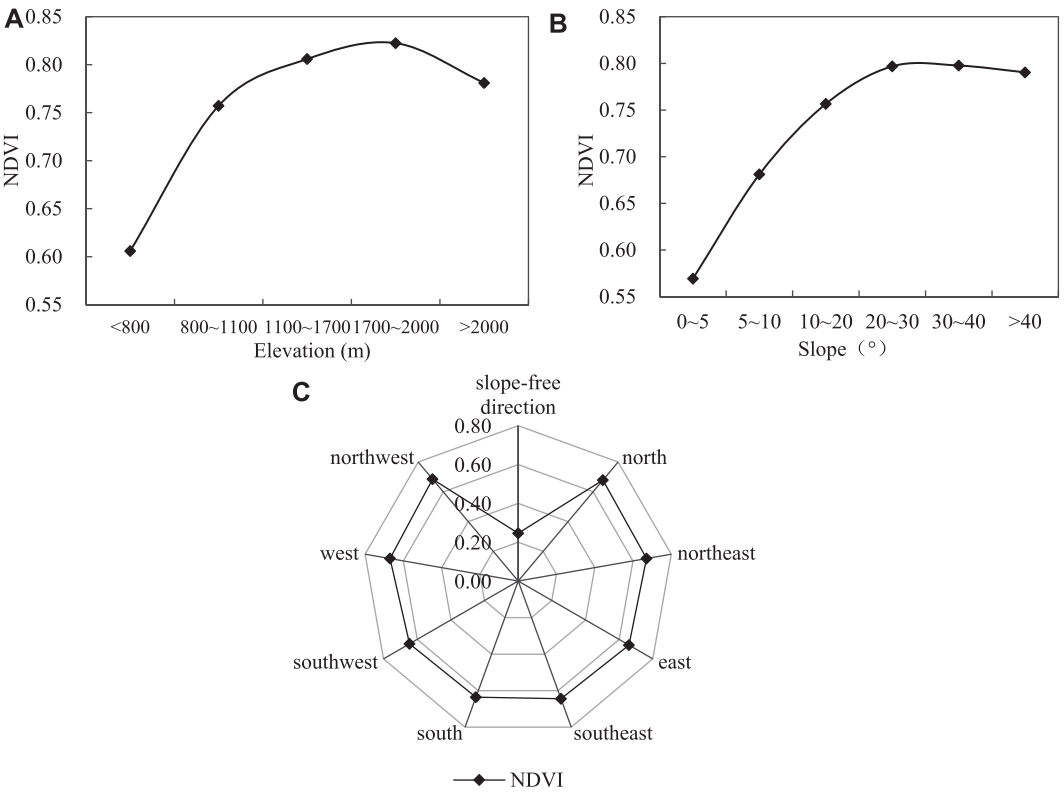

FIGURE 4 | NDVI variations with elevation **(A)**, slope **(B)**, and aspect **(C)**.

maximum ratio of stable vegetation (approximately 93%) occurred on slopes at elevations ranging from 1,100 to 2,000 masl. Areas of degraded vegetation were most common under 800 masl (4.38%), followed by areas over 2,000 masl (1.8%).

Figure 6C indicates an initial increase in the ratio of improved vegetation which then decreased as a function of slope gradient. Improved vegetation was most common (52.77%) on slopes of 5~10°. Farmland at this slope gradient was the focus of the Grain for Green Project; hence, the forested area was increased, resulting in vegetation recovery. Degraded vegetation mostly occurred (6.07%) on slopes of 0~5° partly resulting from the impact of urbanization in recent years. Slope aspect did not markedly influence vegetation state (**Figure 6D**). Areas of improved, stable, and degraded vegetation accounted for 38~42, 55~58, and 2.5~4% of the land surface under different aspects, respectively.

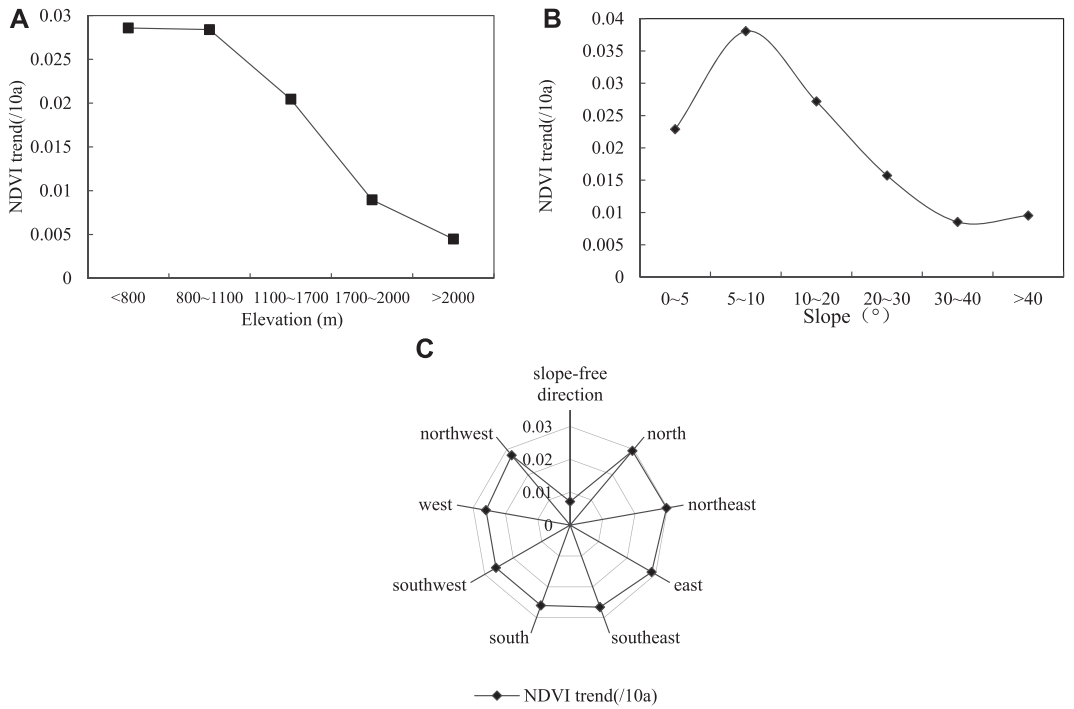

FIGURE 5 | Variations in NDVI trends with **(A)** elevation, **(B)** slope, and **(C)** aspect.

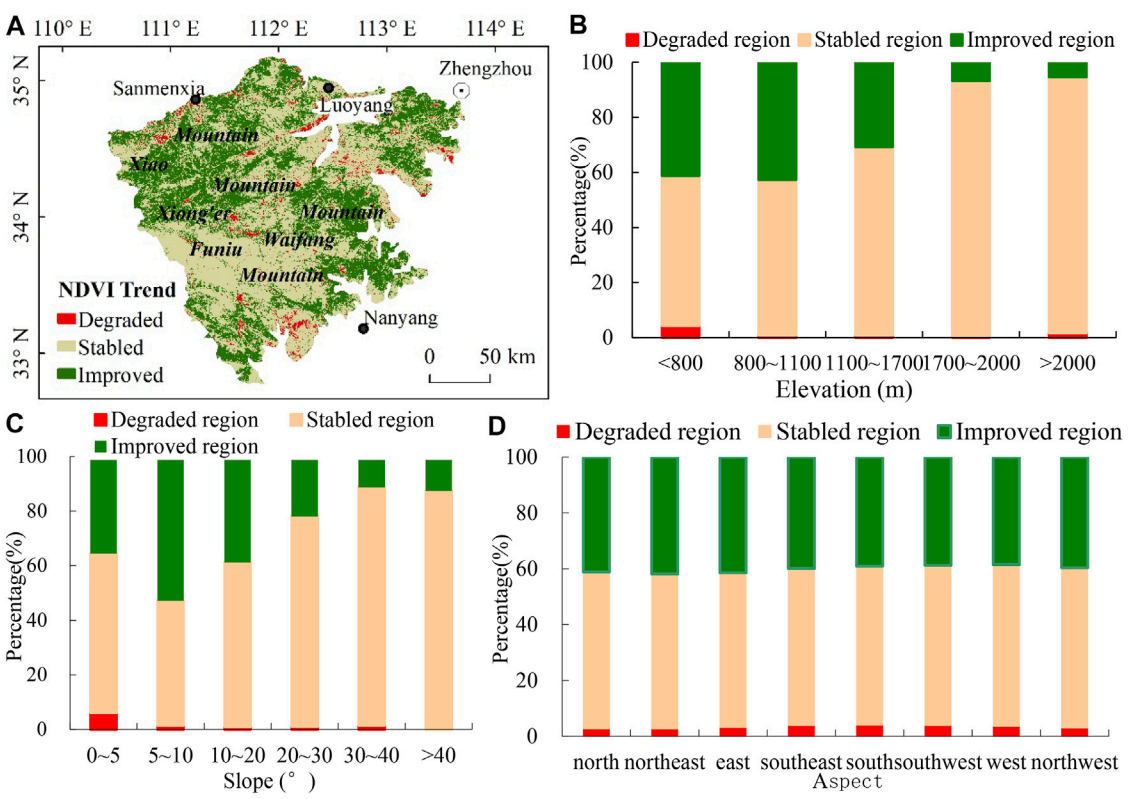

FIGURE 6 | The spatial distribution of vegetation classifications **(A)** and their occurrence at different elevations **(B)**, slopes **(C)**, and aspects **(D)**.

NDVI Responses to Temperature and Precipitation

The spatial distribution of annual average temperature and precipitation for each grid is shown in **Figure 7**. Mean annual temperature values from 2000 to 2017 ranged from 6.35 to 16.91°C. Most grids in the northwest fell under a low range of values (6.35~12.05°C). Grids with temperature values ranging from 13.42 to 16.91°C were mainly concentrated in the southern and northeastern parts of the region (**Figure 7A**). Mean annual precipitation values from 2000 to 2017 ranged from 341.92 to 1125.17 mm across the entire study area, whilst grids with precipitation values ranging from 517.69 to 900.07 mm occupied most of the region. Grids with high precipitation values ranging from 900.07 to 1125.17 mm were mainly distributed on the southern slope of Funiu Mountain. Low precipitation values were always located in the northern and southern most areas (**Figure 7B**).

Figure 8 indicates temperature and precipitation anomalies during the study period. Temperature anomalies showed an upward trend of 0.236°C per decade ($p < 0.05$). The highest (lowest) annual average temperature was 14.02°C (13.27°C) in 2006 (2001) (**Figure 8A**). Conversely, precipitation anomalies showed a downward trend of −61.255 mm per decade ($p > 0.05$). The highest (lowest) annual average precipitation was 983.3 mm (486.9 mm) in 2003 (2013) (**Figure 8B**).

The spatial distribution pattern of the partial correlation coefficient between NDVI, annual temperature and precipitation is shown in **Figure 9**. The partial correlation coefficient between NDVI and temperature is -0.52~0.47 and the regional mean is -0.03. NDVI is shown to be negatively correlated with temperature primarily in the northwestern, northeastern, and southern regions. The most significant negative correlation ($p < 0.1$) was found in the southwestern and northeastern parts of the study area. The area which exhibited a positive correlation between NDVI and temperature was relatively small (0.9%, $p < 0.1$), and was restricted to the northwest. The partial correlation coefficient between NDVI and precipitation is -0.53~0.51 (mean: 0.05). The northeastern, southwestern and eastern parts of the study area are shown to exhibit a negative correlation. Conversely, a positive correlation between NDVI and precipitation is evident around the northwestern, southeastern and northeastern parts of the study area.

NDVI Response to Terrain Factors

Table 1 indicates the relationship between NDVI, temperature and precipitation for different elevations, slopes and aspects. As

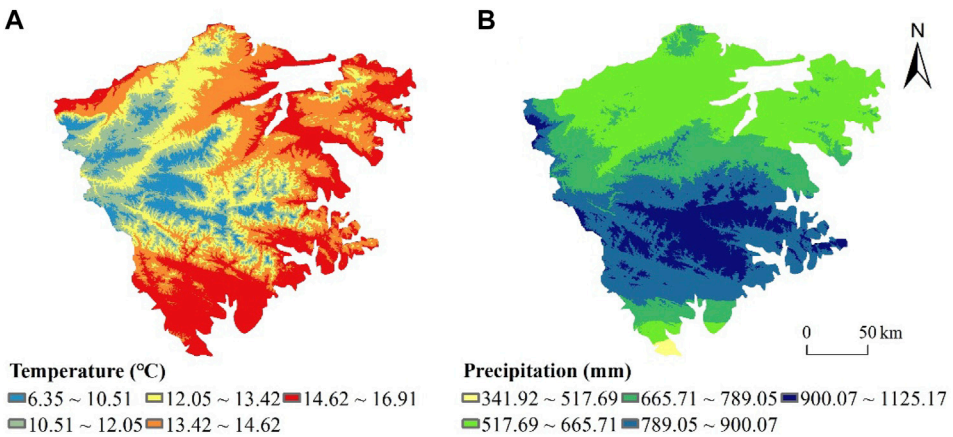

FIGURE 7 | Spatial patterns of annual average temperature **(A)**, annual average precipitation **(B)** from 2000 to 2017.

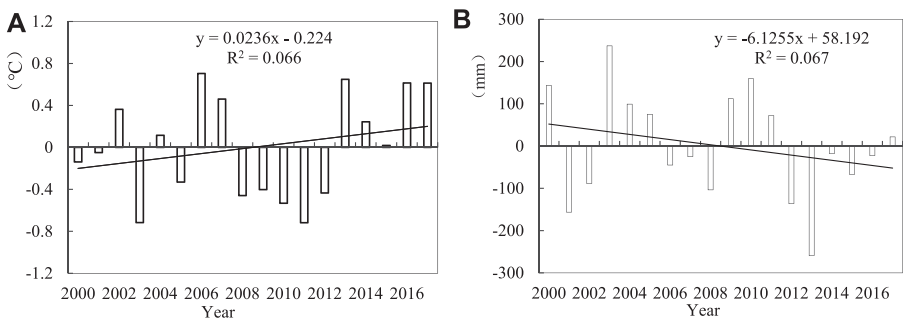

FIGURE 8 | Temperature **(A)** and precipitation **(B)** anomalies with trends over time.

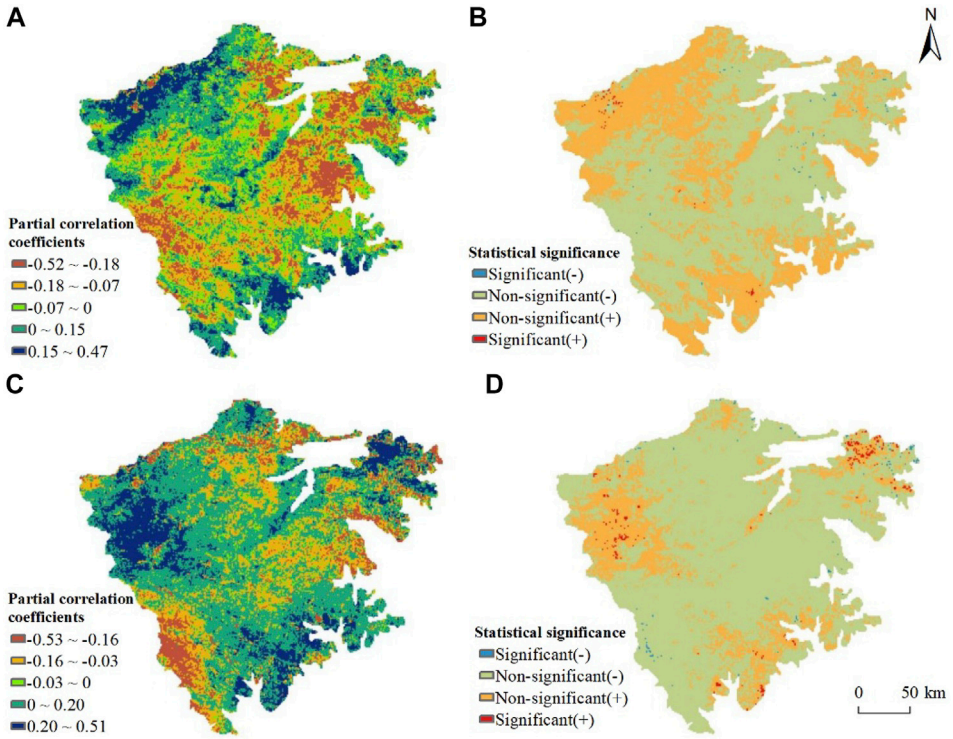

FIGURE 9 | Partial correlation coefficients between NDVI and temperature **(A)**, precipitation **(C)**; and statistical significance of the correlations between NDVI and temperature **(B)**, precipitation **(D)**.

TABLE 1 | Correlation coefficients for NDVI with temperature and precipitation at different elevations, slopes, and aspects.

Index	Grade	NDVI and temperature	NDVI and precipitation
Elevation (masl)	<800	−0.341	0.185
	800–1,100	−0.101	0.120
	1,100–1,700	−0.023	0.093
	1,700–2,000	0.254	0.058
	>2,000	0.147	0.095
Slope (°)	0–5°	−0.416*	0.288
	5–10°	−0.170	0.115
	10–20°	−0.111	0.003
	20–30°	−0.111	0.059
	30–40°	−0.112	0.007
	>40°	−0.177	0.275
Aspect	N	−0.246	0.173
	NE	−0.256	0.155
	E	−0.273	0.150
	SE	−0.293	0.163
	S	−0.309	0.191
	SW	−0.308	0.181
	W	−0.278	0.181
	NW	−0.245	0.175

Note: *Values marked with an * are significant (p < 1).*

elevation increased, the correlation between NDVI and temperature gradually adjusted from negative to positive. The correlation between NDVI and precipitation was generally positive, but notably the correlation was stronger at lower elevations where vegetation has been enhanced by cultivation. For all measured slope gradients, there was a negative correlation between NDVI and temperature. The correlation decreased as slope gradient increased at first and then strengthened slightly. Overall, there was a positive correlation between NDVI and precipitation with slope. The relationship was found to be

weakest for slope gradients of 10~40° where precipitation peaked. This then strengthened when the slope exceeded 40°. In terms of aspect, the correlations between NDVI, temperature and precipitation were negative and positive, respectively. No variations in the response of NDVI to slope aspects were observed.

DISCUSSION

This study has presented a detailed investigation of the response of vegetation cover to temperature and precipitation changes in the western Henan region from 2000 to 2017. As such, our results are instructive for informing governmental policy concerning green development planning.

Existing literature on the dynamic changes of mountain vegetation in western Henan primarily use the Maximum Value Composite (MVC) method to process MODIS-NDVI data. However, this fails to completely remove the noise points in the time series data, which can distort otherwise noise-free pixel values. In this study, the S-G filtering algorithm in TIMESAT 3.2 was used to: (i) perform time-series reconstruction on MODIS-NDVI data; (ii) remove noise points; and (iii) extract the phenological information from the pixels to ensure the reliability of the growing season NDVI and justify its application to characterize extent of surface vegetation cover. NDVI is thus an important indicator of the status of a landscape (i.e., degraded, or stable) in mountainous areas. This study demonstrated that the NDVI trends between 2000 and 2017 exhibited large fluctuations. Vegetation growth is closely related to prevailing hydroclimatic conditions which are then reflected in changes in NDVI. The eco-environment in the region has improved significantly since the implementation of the Returning Farmland to Forest Program from 2000, yielding a greening trend comparable with that observed in Eurasia and Northern China (Sun et al., 2015; Zhu et al., 2019). In addition, human activities sometimes have negative effects on vegetation change, such as periodic logging of economic forest and timber forest, which may also be an important reason for the large interannual fluctuation of NDVI.

Vegetation growth is highly dependent on terrain via its effects on temperature, precipitation, soil and nutrient availability etc. (Pei et al., 2019). The minimum NDVI value (0.606) which occurred below 800 m can be attributed to human activities such as urban construction, mining, road and water infrastructure development. In areas above 2,000 m NDVI showed a downward trend due to declining temperature. NDVI exhibited an increasing trend with slope up to 20°, above which poor soil conditions unfavorable to vegetation growth resulted in lower NDVI values. The different trends in NDVI between the southern and northwestern slopes can be attributed to the fact that the southern slopes are mainly dominated by cultivated lands, while forests are mainly located on the northwestern slopes. The changing NDVI trends were significant for slopes at elevations less than 1,700 masl due to the influence of human activities. Policies including the Returning Farmland to Forest Program and grassland and afforestation subsidies improved vegetation coverage below 1,700 masl. Conversely, the small changes in NDVI trends observed at higher elevations (>1,700 masl) can thus be mainly attributed to climate change.

A large number of studies have shown that climatic factors are important mechanisms responsible for driving vegetation growth and change (Hou et al., 2015; Wang et al., 2015). Temperature and precipitation are the most important factors affecting vegetation changes. Precipitation mainly affects the source of water for plant growth (Buitenwerf et al., 2015; Xu et al., 2019). The NDVI for the entire western Henan area was related to extreme climate and human activities. Correlation analysis shows that the response of NDVI to changes in temperature is more significant than for precipitation in general, though NDVI is still positively correlated with precipitation. Moderate precipitation is optimal to promote vegetation growth, but excessive precipitation would create an anaerobic environment in the root zone (Yang et al., 2015; Fu et al., 2016) causing a reduction in available soil nutrients (Schuur et al., 2001) inimical to vegetation growth.

Changes in vegetation cover are affected by both climate and human activities. Implementation of national ecological protection construction projects (e.g., the Three North Shelterbelt and Returning Farmland to Forests) has led to increased regional vegetation coverage which has yielded a range of ecosystem services (Gao and Yang, 2015; Zhao et al., 2017). However, some studies have suggested that there may be disadvantages associated with afforestation. This negative impact may be one of the important reasons for the sharp decline in vegetation coverage in the Loess Plateau at the beginning of the 21st century. Excessive dependence on afforestation and large-scale ecological planning in arid and semi-arid areas also entails certain risks. Therefore, future research on vegetation growth and climate change must also consider the impacts of human activities on vegetation growth, and quantitatively distinguish these from the impacts of climate change driving changes to vegetation cover.

Some uncertainties remain in this study. First, the temperature and precipitation data were interpolated from meteorological stations. Due to the scarcity of stations in high altitude areas (though the effect of altitude is taken into consideration) the accuracy of interpolation is still not as high as that of NDVI obtained directly via remote sensing. Second, the quantitative grading of the NDVI change trend in this study is based on the characteristics of the mountain vegetation in western Henan. There is also no unified classification standard in the existing literature against which to assess the grading of the NDVI change. Future research should explore the impact of the terrane, microclimate, and human activities on mountain NDVI, in order to guide ecological engineering and mountain vegetation restoration efforts.

CONCLUSION

In this study, we explored the response of vegetation changes to climate change and the effect of terrain factors (elevation, slope and aspect) on NDVI in the Western Henan Mountain region of

China. The results of this study provide an instructive basis for guiding policymaking and legislation pertaining to the protection and restoration of mountain vegetation. In summary:

1) From 2000 to 2017 NDVI changed significantly, exhibiting large fluctuations. NDVI increased at a growth rate of 0.027 per decade ($p < 0.05$) overall, indicating vegetation conditions have gradually improved. NDVI increased initially, but then decreased as a function of elevation, which was shown to be proportional to slope and independent of aspect. Although the NDVI value showed an overall increasing trend, 19.12% of the areas showed a decreasing trend, interspersing and intersecting spatially, showing significant spatial differences.
2) The positive trend in NDVI gradually decreased as elevation increased and NDVI in the high elevation areas remained stable, which was attributed to vegetation restoration activities below 1,100 m. NDVI positive trends exhibited an initial increase but then decreased as a function of increasing slope. The most significant improvements to vegetation occurred on slopes of 5~10°, while vegetation degradation peaked on slopes less than 5°. The impact of slope aspect on NDVI trends was not apparent.
3) Temperature and precipitation both have significant effects on NDVI, but the response of NDVI to temperature is more significant. The response of vegetation to climate change at different elevations, slopes, and aspects differed. Increased precipitation at lower elevations was beneficial to vegetation, while higher temperatures promoted vegetation growth at higher elevations. When the slope gradient was low (0~5°), the negative correlation between NDVI and temperature and the positive correlation between NDVI and precipitation peaked. The response of NDVI to temperature and precipitation for different slope aspects was not apparent.

DATA AVAILABILITY STATEMENT

The raw data supporting the conclusions of this article will be made available by the authors, without undue reservation.

AUTHOR CONTRIBUTIONS

MZ proposed the method, performed analysis and wrote the paper; JZ analyzed the data; LZ conceived the study. All authors read and approved the final manuscript.

FUNDING

This research was funded by the Natural Science Foundation of China (41671090).

ACKNOWLEDGMENTS

This is a short text to acknowledge the contributions of specific colleagues, institutions, or agencies that aided the efforts of the authors.

REFERENCES

Asam, S., Callegari, M., Matiu, M., and Fiore, G. (2018). Relationship between Spatiotemporal Variations of Climate, Snow Cover and Plant Phenology over the Alps-An Earth Observation-Based Analysis. *Remote Sensing* 10 (11), 1757. doi:10.3390/rs10111757

Buitenwerf, R., Rose, L., and Higgins, S. I. (2015). Three Decades of Multi-Dimensional Change in Global Leaf Phenology. *Nat. Clim Change* 5 (4), 364–368. doi:10.1038/nclimate2533

Du, J. Q., Ahati, J., ChenXi, Z., ShiFeng, F., WeiLing, L., JunQi, Y., et al. (2016). Analysis of Vegetation Dynamics Using GIMMS NDVI3g in the Three-Rivers Headwater Region from 1982 to 2012. *Acta Prataculturae Sinica* 25 (1), 1–12. doi:10.11686/cyxb2015111

Eastman, J., Sangermano, F., Machado, E., Rogan, J., and Anyamba, A. (2013). Global Trends in Seasonality of Normalized Difference Vegetation Index (NDVI), 1982-2011. *Remote Sensing* 5 (10), 4799–4818. doi:10.3390/rs5104799

Erschbamer, B., Kiebacher, T., Mallaun, M., and Unterluggauer, P. (2009). Short-term Signals of Climate Change along an Altitudinal Gradient in the South Alps. *Plant Ecol.* 202 (1), 79–89. doi:10.1007/s11258-008-9556-1

Fu, G., Li, S.-W., Sun, W., and Shen, Z.-X. (2016). Relationships between Vegetation Carbon Use Efficiency and Climatic Factors on the Tibetan Plateau. *Can. J. Remote Sensing* 42 (1), 16–26. doi:10.1080/07038992.2016.1131115

Gao, J. X., and Yang, Z. P. (2015). Restoration of Ecological Functions: Goal and Orientation of Ecological Restoration in China. *J. Ecol. Rural Environ.* 33 (1), 1–6. doi:10.11934/j.issn.1673-4831.2015.01.001

Gehrig-Fasel, J., Guisan, A., and Zimmermann, N. E. (2007). Tree Line Shifts in the Swiss Alps: Climate Change or Land Abandonment? *J. Vegetation Sci.* 18 (4), 571–582. doi:10.1111/j.1654-1103.2007.tb02571.x

Geng, L., Wang, X., and Wang, H. (2019). Detecting Spatiotemporal Changes in Vegetation with the BFAST Model in the Qilian Mountain Region during 2000-2017. *Remote Sensing* 11 (2), 103. doi:10.3390/rs11020103

Habeck, J. R. (1987). Present-day Vegetation in the Northern Rocky Mountains. *Ann. Mo. Bot. Garden* 74, 804–840. doi:10.2307/2399451

Hemp, A. (2006). Continuum or Zonation? Altitudinal Gradients in the forest Vegetation of Mt. Kilimanjaro. *Plant Ecol.* 184 (1), 27–42. doi:10.1007/s11258-005-9049-4

Herrmann, S. M., Anyamba, A., and Tucker, C. J. (2005). Recent Trends in Vegetation Dynamics in the African Sahel and Their Relationship to Climate. *Glob. Environ. Change* 15 (4), 394–404. doi:10.1016/j.gloenvcha.2005.08.004

Hou, W., Gao, J., Wu, S., and Dai, E. (2015). Interannual Variations in Growing-Season NDVI and its Correlation with Climate Variables in the Southwestern Karst Region of China. *Remote Sensing* 7 (9), 11105–11124. doi:10.3390/rs70911105

Ichii, K., Kawabata, A., and Yamaguchi, Y. (2002). Global Correlation Analysis for NDVI and Climatic Variables and NDVI Trends: 1982-1990. *Int. J. Remote Sensing* 23 (18), 3873–3878. doi:10.1080/01431160110119416

Jarlan, L., Mangiarotti, S., Mougin, E., Mazzega, P., Hiernaux, P., and Ledantec, V. (2008). Assimilation of SPOT/VEGETATION NDVI Data into a Sahelian Vegetation Dynamics Model. *Remote Sensing Environ.* 112 (4), 1381–1394. doi:10.1016/j.rse.2007.02.041

Kessler, M. (2000). Altitudinal Zonation of Andean Cryptogam Communities. *J. Biogeogr.* 27 (2), 275–282. doi:10.1046/j.1365-2699.2000.00399.x

Liu, Y., Wang, Y., Du, Y., Zhao, M., and Peng, J. (2016). The Application of Polynomial Analyses to Detect Global Vegetation Dynamics during 1982-2012. *Int. J. Remote Sensing* 37 (7), 1568–1584. doi:10.1080/01431161.2016.1142688

Long, J. N. (2003). Diversity, Complexity and Interactions: An Overview of Rocky Mountain forest Ecosystems. *Tree Physiol.* 23 (16), 1091–1099. doi:10.1093/treephys/23.16.1091

Lunetta, R. S., Knight, J. F., Ediriwickrema, J., Lyon, J. G., and Worthy, L. D. (2006). Land-cover Change Detection Using Multi-Temporal MODIS NDVI Data. *Remote sensing Environ.* 105 (2), 142–154. doi:10.1016/j.rse.2006.06.018

Nemani, R. R., Keeling, C. D., Hashimoto, H., Jolly, W. M., Piper, S. C., Tucker, C. J., et al. (2003). Climate-driven Increases in Global Terrestrial Net Primary Production from 1982 to 1999. *Science* 300 (5625), 1560–1563. doi:10.1126/science.1082750

Pei, Z., Fang, S., Yang, W., Wang, L., Wu, M., Zhang, Q., et al. (2019). The Relationship between NDVI and Climate Factors at Different Monthly Time Scales: A Case Study of Grasslands in Inner Mongolia, China (1982-2015). *Sustainability* 11 (24), 7243. doi:10.3390/su11247243

Peng, D., Zhang, B., Liu, L., Fang, H., Chen, D., Hu, Y., et al. (2012). Characteristics and Drivers of Global NDVI-Based FPAR from 1982 to 2006. *Glob. Biogeochem. Cycles* 26 (3), 1–15. doi:10.1029/2011gb004060

Pepin, N., Bradley, R. S., Diaz, H. F., Baraer, M., Caceres, E. B., Forsythe, N., et al. (2015). Elevation-dependent Warming in Mountain Regions of the World. *Nat. Clim. Change* 5 (5), 424–430. doi:10.1038/nclimate2563

Piao, S., Wang, X., Ciais, P., Zhu, B., Wang, T., and Liu, J. (2011). Changes in Satellite-Derived Vegetation Growth Trend in Temperate and Boreal Eurasia from 1982 to 2006. *Glob. Change Biol.* 17 (10), 3228–3239. doi:10.1111/j.1365-2486.2011.02419.x

Schuur, E. A. G., Chadwick, O. A., and Matson, P. A. (2001). Carbon Cycling and Soil Carbon Storage in Mesic to Wet Hawaiian Montane Forests. *Ecology* 82 (11), 3182–3196. doi:10.1890/0012-9658(2001)082[3182:ccascs]2.0.co;2

Song, C. (1994). *Scientific Survey of the Funiu-Mountain Nature reserve*. Beijing: China Forestry Publishing House, 10–11.

Sun, W., Song, X., Mu, X., Gao, P., Wang, F., and Zhao, G. (2015). Spatiotemporal Vegetation Cover Variations Associated with Climate Change and Ecological Restoration in the Loess Plateau. *Agric. For. Meteorology* 209-210, 87–99. doi:10.1016/j.agrformet.2015.05.002

Tong, X., Wang, K., Brandt, M., Yue, Y., Liao, C., Fensholt, R., et al. (2016). Assessing Future Vegetation Trends and Restoration Prospects in the Karst Regions of Southwest China. *Remote Sensing* 8 (5), 357. doi:10.3390/rs8050357

Tong, X. (2014). Trends in Vegetation and Their Responses to Climate and Topography in Northwest Guangxi. *Shengtai Xuebao/Acta Ecologica Sinica* 34 (12), 3425–3434. doi:10.5846/stxb201310162503

Tucker, C. J., Pinzon, J. E., Brown, M. E., Slayback, D. A., Pak, E. W., Mahoney, R., et al. (2005). An Extended AVHRR 8-km NDVI Dataset Compatible with MODIS and SPOT Vegetation NDVI Data. *Int. J. Remote Sensing* 26 (20), 4485–4498. doi:10.1080/01431160500168686

Wang, J., Wang, K., Zhang, M., and Zhang, C. (2015). Impacts of Climate Change and Human Activities on Vegetation Cover in Hilly Southern China. *Ecol. Eng.* 81, 451–461. doi:10.1016/j.ecoleng.2015.04.022

Xu, X., Du, H., Fan, W., Hu, J., Mao, F., and Dong, H. (2019). Long-term Trend in Vegetation Gross Primary Production, Phenology and Their Relationships Inferred from the FLUXNET Data. *J. Environ. Manage.* 246, 605–616. doi:10.1016/j.jenvman.2019.06.023

Yang, Y., Guan, H., Shen, M., Liang, W., and Jiang, L. (2015). Changes in Autumn Vegetation Dormancy Onset Date and the Climate Controls across Temperate Ecosystems in China from 1982 to 2010. *Glob. Change Biol.* 21 (2), 652–665. doi:10.1111/gcb.12778

Yang, Z.-p., Ou, Y. H., Xu, X.-l., Zhao, L., Song, M.-h., and Zhou, C.-p. (2010). Effects of Permafrost Degradation on Ecosystems. *Acta Ecologica Sinica* 30 (1), 33–39. doi:10.1016/j.chnaes.2009.12.006

Yao, Y., Zhang, B., Han, F., and Pang, Y. (2010). Diversity and Geographical Pattern of Altitudinal Belts in the Hengduan Mountains in China. *J. Mt. Sci.* 7 (2), 123–132. doi:10.1007/s11629-010-1011-9

Yin, G., Hu, Z., Chen, X., and Tiyip, T. (2016). Vegetation Dynamics and its Response to Climate Change in Central Asia. *J. Arid Land* 8 (3), 375–388. doi:10.1007/s40333-016-0043-6

Zhang, B. P., Tan, Y., and Mo, S. G. (2004). Digital Spectrum and Analysis of Altitudinal Belts in the Tianshan Mountains. *J. Mountain Res.* 2, 184–192. doi:10.3969/j.issn.1008-2786.2004.02.009

Zhang, J., Zhu, W., Zhao, F., Zhu, L., Li, M., Zhu, M., et al. (2018). Spatial Variations of Terrain and Their Impacts on Landscape Patterns in the Transition Zone from Mountains to plains-A Case Study of Qihe River Basin in the Taihang Mountains. *Sci. China Earth Sci.* 61 (4), 450–461. doi:10.1007/s11430-016-9158-2

Zhang, J., Zhu, W., Zhu, L., Cui, Y., He, S., and Ren, H. (2019). Topographical Relief Characteristics and its Impact on Population and Economy: A Case Study of the Mountainous Area in Western Henan, China. *J. Geogr. Sci.* 29 (4), 598–612. doi:10.1007/s11442-019-1617-y

Zhang, R., Ouyang, Z. T., Xie, X., Guo, H. Q., Tan, D. Y., Xiao, X. M., et al. (2016). Impact of Climate Change on Vegetation Growth in Arid Northwest of China from 1982 to 2011. *Remote Sensing* 8 (5), 364. doi:10.3390/rs8050364

Zhang, X. M., Kelin, W., Yuemin, Y., and Xiaowei, T. (2017). Factors Impacting on Vegetation Dynamics and Spatial Non-stationary Relationships in Karst Regions of Southwest China. *Shengtai Xuebao/Acta Ecologica Sinica* 37 (12), 4008–4018. doi:10.1016/j.chnaes.2016.12.008

Zhao, A., Zhang, A., Lu, C., Wang, D., Wang, H., and Liu, H. (2017). Spatiotemporal Variation of Vegetation Coverage before and after Implementation of Grain for Green Program in Loess Plateau, China. *Ecol. Eng.* 104, 13–22. doi:10.1016/j.ecoleng.2017.03.013

Zhu, W., and Li, S. (2017). The Dynamic Response of forest Vegetation to Hydrothermal Conditions in the Funiu Mountains of Western Henan Province. *J. Geogr. Sci.* 27 (5), 565–578. doi:10.1007/s11442-017-1393-5

Zhu, Y., Zhang, J., Zhang, Y., Qin, S., Shao, Y., and Gao, Y. (2019). Responses of Vegetation to Climatic Variations in the Desert Region of Northern China. *Catena* 175, 27–36. doi:10.1016/j.catena.2018.12.007

Conflict of Interest: The authors declare that the research was conducted in the absence of any commercial or financial relationships that could be construed as a potential conflict of interest.

frontiers in Earth Science

ORIGINAL RESEARCH
published: 02 June 2021
doi: 10.3389/feart.2021.650882

Changes in Flood Regime of the Upper Yangtze River

Yu Zhang[1], Guohua Fang[1], Zhengyang Tang[2,3], Xin Wen[1], Hairong Zhang[2,3], Ziyu Ding[1], Xin Li[1], Xinsheng Bian[4] and Zengyun Hu[5]*

[1]College of Water Conservancy and Hydropower Engineering, Hohai University, Nanjing, China, [2]Department of Water Resources Management, China Yangtze Power Co., Ltd., Yichang, China, [3]Hubei Key Laboratory of Intelligent Yangtze and Hydroelectric Science, Yichang, China, [4]The Eastern Route of South-to-North Water Diversion Project Jiangsu Water Source Co., Ltd., Nanjing, China, [5]State Key Laboratory of Desert and Oasis Ecology, Xinjiang Institute of Ecology and Geography, Chinese Academy of Sciences, Urumqi, China

River flooding affects more people worldwide than other natural hazards. Thus, analysis of the changes in flood regime caused by global warming and increasing anthropogenic activities will help us make adaptive plans for future flood management. The nonstationary flood behavior in the upper Yangtze River was examined comprehensively in terms of trend, change point, and periodicity with co-usage of different methods. Results show that there are decreasing tendencies in the corresponding series of annual maximum flood peak flow and flood volume in four out of six control stations, except Pingshan and Wulong stations in the Jinsha River and the Wu River, respectively, and the flood peak occurrence time appears earlier mostly. The uniformity of flood process increases in four main tributaries, while it decreases in mainstream of the Yangtze River (Yichang and Pingshan stations). The rates of both rising limb and recession limb of all the typical flood process flowing through the six stations were analyzed. 77.8% of the rates of rising limb decrease, while 61.1% of the rates of recession limb increase, which is almost consistent with the variation reflected by the uniformity. The change points of most evaluation indicators happened in 1970s–1990s. The first main periodicity of evaluation indicators in Yichang is about 45 years, while that of other stations is about 20 years. Invalidity of stationarity in the flood series can be attributed to the intensified construction on major water conservancy projects, changes of underlying surface, and influences of climatic variables. The contributions of both climatic control and the Three Gorges Dam (TGD) to the variation of the annual flood peak in Yichang station were further quantitatively evaluated, which has verified that the construction of the TGD has played a positive role in peak-flood clipping.

Keywords: flood regime, evaluation indicators, temporal trend, change point, periodicity, the upper Yangtze River

OPEN ACCESS

Edited by:
Xiaolan L. Wang, Environment and Climate Change, Canada

Reviewed by:
Panfeng Zhang, Jilin Normal University, China
Kangmin Wen, Fujian Meteorological Bureau, China
Huaming Yao, Georgia Institute of Technology, United States

****Correspondence:***
Guohua Fang
hhufgh@163.com

Specialty section:
This article was submitted to Interdisciplinary Climate Studies, a section of the journal Frontiers in Earth Science

Received: *08 January 2021*
Accepted: *10 May 2021*
Published: *02 June 2021*

Citation:
Zhang Y, Fang G, Tang Z, Wen X, Zhang H, Ding Z, Li X, Bian X and Hu Z (2021) Changes in Flood Regime of the Upper Yangtze River. Front. Earth Sci. 9:650882. doi: 10.3389/feart.2021.650882

INTRODUCTION

With the influence of changing climate, land cover, channel morphology, and other human activities, the spatial–temporal distribution of water resources and the characteristics of runoff generation and flow concentration in the basin have changed, resulting in the shifts in the mechanisms that generate inundations (Fang et al., 2012; Guo et al., 2018; Akbari and Reddy, 2020). River flood risks are expected to rise as climate change intensifies the global hydrological cycle and more people live in floodplains (Field et al., 2012), which may be revealed by changes in the flood regime, including

annual maximum flood peak flow, volume, flood peak occurrence time, rates of rising and recession limbs, and uniformity (Li et al., 2012; Bloschl et al., 2017; Slater and Wilby, 2017). Therefore, understanding the characteristics of changes in flood regime and further analyzing the reasons of these changes are important for flood management.

The Yangtze River Basin is home to 33% of China's population and plays an important role in China's economic development. The occurrence of flood in this basin is closely related to precipitation, while the spatial and temporal variability of precipitation in the basin is associated with monsoon activities that transport a huge amount of atmospheric moisture from the East and the South China Sea to the basin (Gao et al., 2012). In addition, the temporal distributions of precipitation are highly uneven, and over 60% of the annual precipitation occurs in summer, resulting in frequent floods. Historically, the Yangtze River catchment has been known for its frequent huge floods that halted the social advancement of the basin to a large degree.

The upstream of the Yichang hydrometric station is called the upper Yangtze River and has a drainage area of approximately 1.0 million km^2. The upper Yangtze River is abundant in hydropower potential, with a suite of large reservoirs having been constructed in the past five decades. With the large-scale development of hydropower, the hydrological regimes in the basin, especially the spatial–temporal distribution of runoff at the outlet control hydrometric station, have presented a new situation, which also changes the flood regimes, therefore negatively affecting the efficiency of the planning and design of water conservancy projects and flood prevention management (Yao et al., 2006). There have been a lot of research results on the change characteristics of runoff and their attribution analysis in the Yangtze River (Jiang et al., 2007; Chen et al., 2014; Wei et al., 2014; Yang et al., 2015). However, research about the all-round change characteristics of flood regime is relatively few, and how to quantitatively evaluate the Three Gorges Dam's (TGD) effect on peak-flood clipping is worthy of discussion. Specifically, it has been proven that the river engineering has amplified the flood hazard in the Mississippi River (Munoz et al., 2018).

Here, 12 evaluation indicators, including annual flood peak discharge, flood volume, flood timing, and uniformity, are used to comprehensively detect the flood regime change characteristics of the six control hydrometric stations in the upper Yangtze River from three perspectives of trend, change point, and periodicity, and the contributions of both climatic control and the TGD to the variation of the annual flood peak in Yichang station were further quantitatively evaluated. The main objectives of this study have been to: 1) detect the flood regime change, including the flood peak discharge, flood volume, time of flood peak occurrence, and uniformity of the upper Yangtze River; and 2) discuss how the annual maximum flood peak discharge is related to the TGD and the climatic control factors. This study will provide a better understanding on the all-round changes in flood regime of the upper Yangtze River, and how the dam-building activities and climate change affect the annual flood peak discharge in a long-term perspective.

Study Area

The upper Yangtze River (UYR) is located in southwest China, spanning 21°8′–34°20′N and 97°22′–110°11′E. The UYR has a drainage area of 1.054 million km^2, accounting for 59% of the total drainage area of the Yangtze River. It is composed of five river systems, that is, the Jinsha River, the Mintuo River, the Jialing River, the Wu River, and the trunk stream. The Jinsha River system is the main source of sediment in the Yangtze River, the Min River is the tributary with the largest water in UYR, the Jialing River is the tributary with the biggest drainage area in the UYR and the Wu River is the largest tributary on the right bank of the UYR. The flood in the Qing River always meets the flood in the trunk stream of the Yangtze River, which increases the threat to the Jingjiang embankment. The sketch map of the river systems and the digital elevation model (DEM) in the UYR are shown in **Figure 1**. The six key hydrometric stations and the TGD have been marked with asterisks and triangle symbol, respectively.

Data

The controlling hydrometric stations located at the outlets of the trunk stream, the Qing River, the Jialing River, the Wu River, the Min River, and the Jinsha River are Yichang, Changyang, Beibei, Wulong, Gaochang, and Pingshan, respectively. According to the multiyear daily runoff data of the six key hydrometric stations provided by the Hydrological Office, Yangtze Water Resources Committee, the typical flood events including the annual maximum peak discharge are selected to analyze the flood regime changes in the UYR. Due to the limitation of data availability, the length of data used in the six hydrometric stations is 139, 59, 61, 50, 55, and 71 years, respectively (see **Table 1**.

The climatic control factor data including the sunspot numbers (SSNs) and the North Atlantic Oscillation (NAO) are available at the websites https://psl.noaa.gov/gcos_wgsp/Timeseries/SUNSPOT/ and https://psl.noaa.gov/gcos_wgsp/Timeseries/NAO/, respectively.

Methods and Evaluation Indicators

On the basis of the measured daily runoff at six controlling hydrometric stations, namely, YC, CY, BB, WL, GC, PS, and the trend, abrupt change and periodicity analyses of 12 evaluation indicator time series extracted from the annual typical flood event are performed in each station. Therefore, the corresponding annual series derived from the daily data were actually analyzed in this study.

Methods

Recent evidences of the impact of regional climate variability, coupled with the intensification of human activities, have led hydrologists to study flood regime and test the hypothesis of stationarity (Bormann et al., 2011). In view of the magnitude and ubiquity of the human disturbances and hydro-climatic change, the stationarity of flood no long holds true because substantial anthropogenic and natural changes of climate are altering the means and extremes of precipitation, evapotranspiration, and

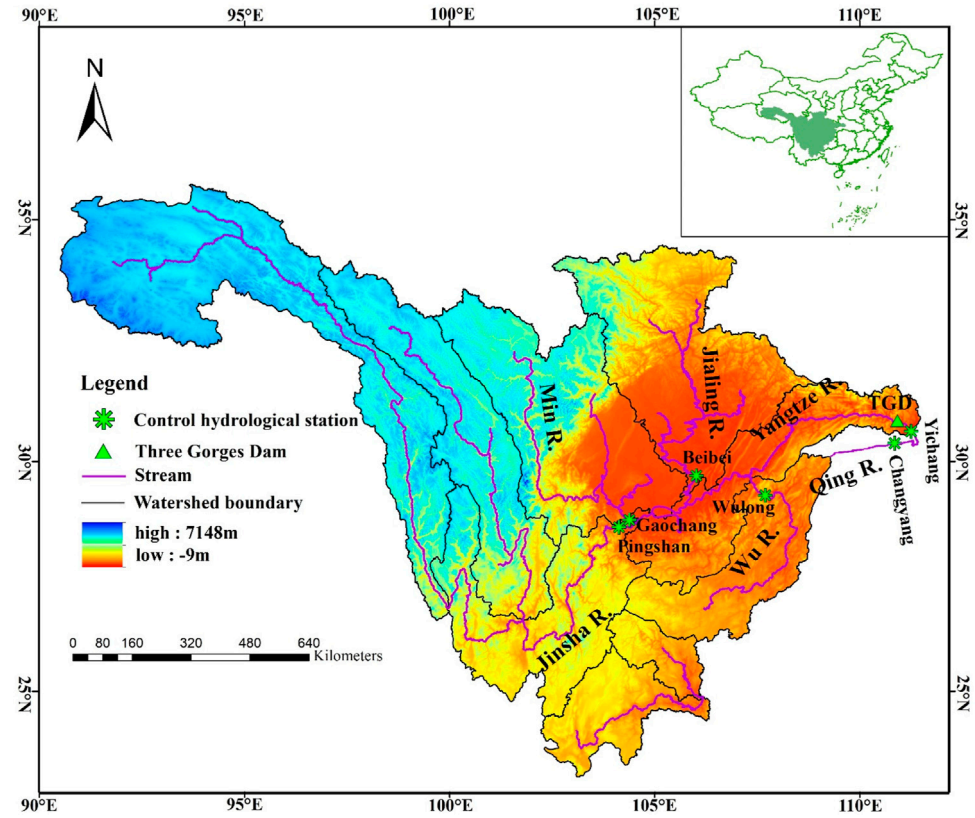

FIGURE 1 | River systems and DEM of the upper Yangtze River.

TABLE 1 | Detailed information about the data used.

The controlling hydrometric station at the basin outlet	Abbreviation	River	Length of data used (period)
Yichang	YC	Trunk stream	139 (1882–2020)
Changyang	CY	Qing river	59 (1951–2009)
Beibei	BB	Jialing river	61 (1950–2010)
Wulong	WL	Wu river	50 (1952–2001)
Gaochang	GC	Min river	55 (1956–2010)
Pingshan	PS	Jinsha river	71 (1940–2010)

rivers' discharge rates (Milly et al., 2008). Salas once pointed out that there were no trends, shifts, or periodicity (cyclicity) in a consistent hydrological time series (Salas et al., 1980), so the non-stationarity was mainly manifested as the trend, abrupt change, and periodicity.

Most standard statistical techniques, including the Mann–Kendall test (Mann, 1945; Kendall, 1975), require the assumption that the analyzed series are the realizations of the independent random variables. However, most of the hydrological or climatological series are somehow correlated in time, which will make it easier for the trend test to obtain a conclusion that the trend is significant at a presetting level, even if the original series have no trend (Storch, 1995). An iterative pre-whitening process which was originally proposed by Zhang et al. (2000) and later refined by Wang and Swail (2001) can effectively diminish the impact of the series correlation on trend estimate and the trend test. This algorithm has been widely used (Alexander et al., 2006) and can be easily performed through an open R package zyp (Bronaugh and Werner, 2019). Periodic fluctuation is a common form of hydrologic process evolution and an important manifestation of hydrologic variation. The wavelet analysis (Kumar and Foufoula-Georgiou, 1993; Venugopal and Foufoula-Georgiou, 1996) is the commonly used periodicity identification analysis methods. The Morlet and Mexican Hat wavelet transforms are two kinds of the

TABLE 2 | Meanings of evaluation indicators extracted from the annual typical flood event.

Evaluation indicator	Meaning	Unit
Flood peak discharge	Annual maximum peak discharge	m^3/s
Flood peak occurrence time	The time when the annual maximum discharge occurs	day
3-day flood volume	Annual maximum flood volume for three consecutive days	m^3
5-day flood volume	Annual maximum flood volume for five consecutive days	m^3
7-day flood volume	Annual maximum flood volume for seven consecutive days	m^3
Rate of rising limb (I)	$k_1 = \frac{0.5F_m - 0.25F_m}{\Delta T_1}$	–
Rate of rising limb (II)	$k_2 = \frac{0.75F_m - 0.5F_m}{\Delta T_2}$	–
Rate of rising limb (III)	$k_3 = \frac{F_m - 0.75F_m}{\Delta T_3}$	–
Rate of recession limb (I)	$k_4 = \frac{0.75F_m - F_m}{\Delta T_4}$	–
Rate of recession limb (II)	$k_5 = \frac{0.5F_m - 0.75F_m}{\Delta T_5}$	–
Rate of recession limb (III)	$k_6 = \frac{0.25F_m - 0.5F_m}{\Delta T_6}$	–
Uniformity	$J = -\sum_{i=1}^{N}(P_i \ln P_i)/\ln N$	–

most popularly used continuous wavelet transforms (CWT) in revealing period properties of meteorological and hydrological signals (Mallat, 1989; Daubechies and Bates, 1993; Torrence and Compo, 1998).

In this study, a Theil–Sen slope estimator (Sen, 1968), and the pre-whitening approaches of Zhang et al. (2000), Wang and Swail (2001), and Yue et al. (2002) were used for trend analysis; the penalized maximal *F* test was used to detect the abrupt change point since there are no reference series (Wang, 2003; Wang, 2008a; Wang, 2008b); the Morlet wavelet transform was used to recognize the main period (Zhang et al., 2006; Zhang et al., 2010; Yu et al., 2012).

Evaluation Indicators

Each typical flood process is defined by the flows at n moments. The typical flood process of a given year (i) can be described as **Eq. 1**.

$$X_i = (x_{i1}, x_{i2}, \cdots, x_{in}), i = (1, 2, \cdots, s). \quad (1)$$

The initial time of the selected typical flood process is defined as the occurrence time of the first trough before the annual maximum peak discharge. According to the book "the Heavy Flood in China—a Brief Description of Disastrous Floods" (Luo and Le, 1996), the duration of the flood process is intercepted to make it as long as 30 days, namely, $n = 30$, which can also determine the end time. Therefore, the annual typical flood processes of the six hydrological stations were selected.

The 12 evaluation indicators are concluded in **Table 2**, most of which have a clear meaning, except the rates of rising and recession limbs and the uniformity. F_m represents the annual maximum peak discharge when calculating $k_1, k_2, \cdots, k_6$. More descriptions about the uniformity are given below. The uniformity model of flood process is established by using information entropy due to its advantage in the characterization of uniformity (Chen et al., 2015). The calculation procedure of the uniformity is shown as follows:

(1) The flood duration is divided, and the corresponding flood volume is calculated as $Q_j\,(j = 1, 2, \cdots, n)$.

(2) The percentage of the flood volume in the total flood volume is calculated as **Eq. 2**.

$$P_j = Q_j \Big/ W\,(j = 1, 2, \cdots, n),\ W = \sum_{j=1}^{n} Q_j. \quad (2)$$

(3) The information entropy of the typical flood process is calculated as **Eq. 3**.

$$H = -\sum_{j=1}^{n}\left(P_j \ln P_j\right). \quad (3)$$

(4) The uniformity of the typical flood process is defined as the ratio of the actual entropy value to the maximum entropy value, as is shown in **Eq. 4**.

$$J = -\sum_{j=1}^{n}\left(P_j \ln P_j\right)\Big/ \ln n. \quad (4)$$

The uniformity of the flood process can be represented by entropy. The higher the entropy value, the more dispersed the distribution of flood volume, which further indicates that the difference of flood volume in different time periods is smaller and that the flood process is more uniform. The absolute uniform state of the flood process means that the flood volume in each period is the same, when $P_1 = P_2 = \cdots = P_n = 1/n$, and the entropy value reaches the maximum valueln n. As the same with entropy, the larger the uniformity, the smaller the variation of the distribution of flood volume in each period.

RESULTS

The Yichang hydrometric station located at the outlet of the upper Yangtze basin was selected to visualize the results for

TABLE 3 | The trend analysis results by the pre-whitening approaches.

Parameter method	Lbound	Trend	Trendp	Ubound	Tau	Sig	Nruns	Autocor	Valid-frac	Linear	Intercept
Zhang	−109.83	−60.86	−8460.22	−12.90	−0.14*	0.01	3.00	0.17	1.00	−55.84	55,601.87
Yuepilon	−100.00	−57.02	−7925.44	−16.67	−0.14*	0.01	1.00	0.17	1.00	−55.84	54,432.46

Note: Asterisk indicates the significant trend at the 0.05 level.

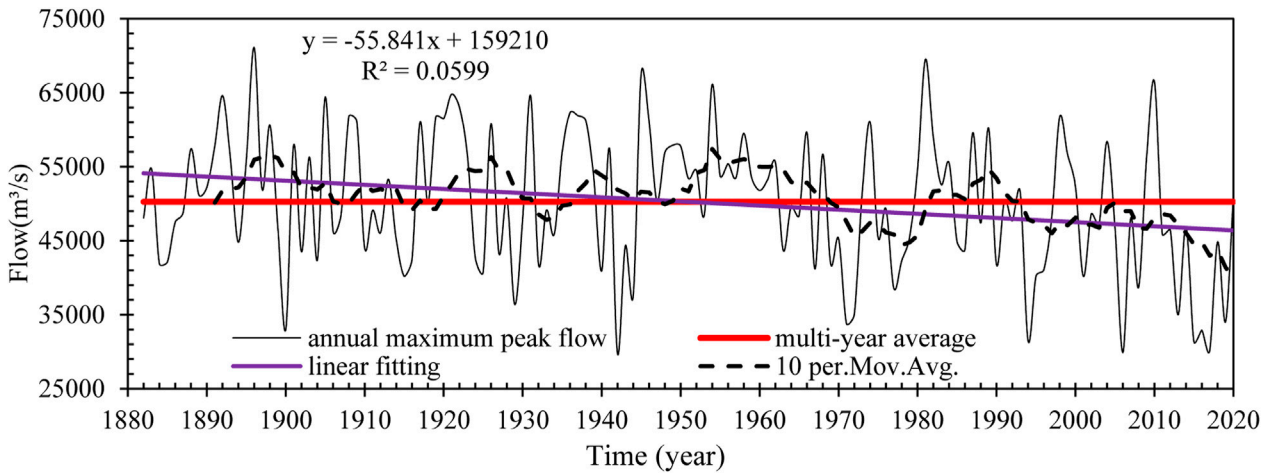

FIGURE 2 | Curve of annual maximum flood peak discharge in YC.

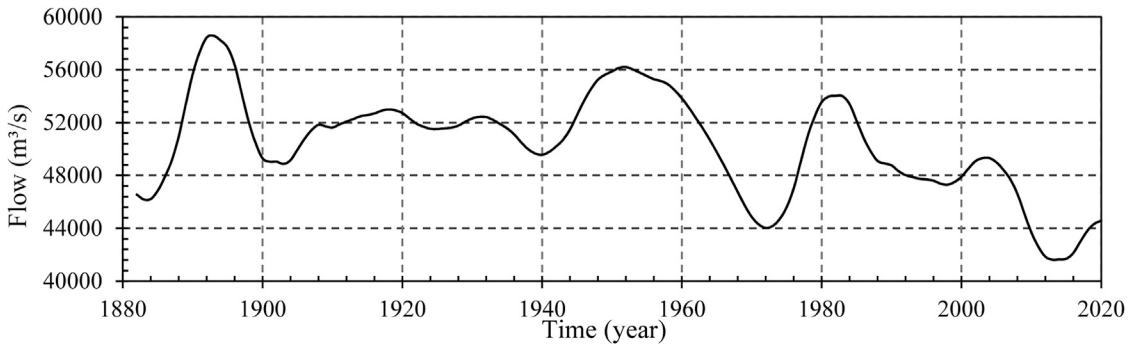

FIGURE 3 | Curve of Morlet wavelet decomposition (A3) of the annual maximum flood peak discharge in YC.

analyzing the flood regime changes because of the availability of long-term daily discharge data from 1882 to 2020, which can provide sufficient information as far back from present to obtain the range of flood regime variation. The YC hydrometric station is merely 44 km downstream of the TGD, and the flood regime changes at this station provide a direct measurement of the impacts of the TGD. The analysis of the annual maximum flood peak discharge in YC is taken as an example. The non-stationarity analysis is carried out from three perspectives, that is, the trend, abrupt change, and periodicity.

Trend Analysis

The Theil–Sen slope estimator, wavelet decomposition, and the pre-whitening approaches of Zhang et al. (2000), Wang and Swail (2001), and Yue et al. (2002) were used to determine trends of the corresponding time series of the evaluation indicators. The Theil–Sen slope estimator is −57.02 with the intercept of 161,682.46. The trend results obtained by the pre-whitening approaches are listed in **Table 3** (refer to the package "zyp" written by Bronaugh and Werner, (2019)) for the meanings of the parameters. And the trend calculated by the pre-whitening approach of Yue et al. (2002) is consistent with the Theil–Sen

TABLE 4 | The Theil–Sen slope estimator of evaluation indicators at the six stations in the UYR.

Indicators stations	Flood peak flow	Flood volume			Time of flood peak occurrence	Uniformity	Rate of rising limb			Rate of recession limb		
		3-day	5-day	7-day			I	II	III	I	II	III
Yichang (YC)	−57.0200	−153.4000	−230.4000	−294.4000	−0.0333	0.0000	−9.0740	−1.3280	−0.4939	10.9600	1.1710	−0.1780
Changyang (CY)	−19.2500	−45.0800	−67.2600	−79.1900	−0.1915	0.0033	−4.6790	−1.4710	−1.0120	2.0000	3.3650	1.4610
Beibei (BB)	−59.4900	−147.5000	−201.1000	−389.6000	−0.0698	0.0006	−15.7300	−12.0000	−5.5120	6.8760	7.7780	8.5370
Wulong (WL)	31.5800	67.7800	82.4100	114.5000	0.0000	0.0000	−1.6670	12.1500	0.8763	−16.3800	−6.0940	−2.8120
Gaochang (GC)	−57.6900	−213.8000	−291.0000	−332.9000	0.0938	0.0006	5.3570	−3.3330	−5.2500	3.3520	5.2880	2.8920
Pingshan (PS)	12.5000	35.9000	44.4400	76.4700	−0.1000	0.0000	−0.6211	3.2860	0.3272	−0.4922	−0.8631	0.2081

TABLE 5 | Kendall' tau statistic of evaluation indicators at the six stations in the UYR by zyp.zhang.

Indicators stations	Flood peak flow	Flood volume			Time of flood peak occurrence	Unifor-mity	Rate of rising limb			Rate of recession limb		
		3-day	5-day	7-day			I	II	III	I	II	III
Yichang (YC)	−0.1408*	−0.1292*	−0.1270*	−0.1232*	−0.0398	−0.0091	−0.1000	−0.0298	−0.0585	0.1679*	0.0348	−0.0361
Changyang (CY)	−0.0575	−0.0865	−0.0913	−0.0938	−0.0734	0.2005*	−0.0248	−0.0321	−0.0146	0.0175	0.0660	0.0427
Beibei (BB)	−0.1040	−0.0881	−0.0915	−0.1435	−0.0285	0.0579	−0.0893	−0.0749	−0.0576	0.0629	0.0618	0.0798
Wulong (WL)	0.0680	0.0612	0.0510	0.0476	0.0025	0.0008	−0.0139	0.1156	−0.0340	−0.1650	−0.1497	−0.0539
Gaochang (GC)	−0.1321	−0.2746*	−0.2495*	−0.2676*	0.0105	0.1879*	0.0273	−0.0182	−0.0524	0.0277	−0.0161	0.1388
Pingshan (PS)	0.0448	0.0407	0.0346	0.0330	−0.0435	−0.0128	−0.0185	0.1348	0.0994	−0.0097	−0.0612	0.0277

Note: Asterisk indicates the significant trend at the 0.05 level.

slope estimator. It is concluded that the annual maximum peak discharge in the Yichang station presents a significant decreasing trend at the 0.05 level from the **Table 3** and the Theil–Sen slope estimator value.

The linear fitting line and curve of Morlet wavelet decomposition are shown in **Figures 2**, **3**, respectively. The trend analyses of all the evaluation indicators time series at the six control hydrometric stations in the UYR are presented in **Tables 4**, **5**.

Figure 2 shows the linear fitting line, the line of the multiyear mean, and the 10-year moving average curve of the annual maximum peak discharge in YC. The decreasing trend and fluctuation are detected from the linear fitting line and the 10-year moving average curve, respectively. The multiyear mean of annual flood peak discharge is 50,264.91 m^3/s. The maximum flood peak flow during the period from 1882 to 2011 occurred in 1896, with the value of 71,100 m^3/s, while the minimum flood peak flow occurred in 1942, with the value of 29,800 m^3/s. The linear fitting curve and the line of the multiyear mean intersected in the year of 1951, which means the multiyear average before 1951 was higher than 50,264.91 m^3/s, while the multiyear average after 1951 was lower than 50,264.91 m^3/s.

Figure 3 shows the wavelet decomposition (A3) graph of the time series of the annual maximum flood peak flow. There was a steep rise in 1889, and a steep fall in 1897, then a relatively flat change during 1900–1940, and a drastic change during 1940–1980. After 1980, there were two clear phases with a decreasing trend, namely, 1980–2000 and 2000–2020.

From **Tables 4**, **5**, it can be seen that the annual maximum flood peak flow and flood volume in YC, CY, BB, and GC showed a decreasing trend, with a significant decrease in flood volume of YC and GC, while those in WL and PS showed an increasing trend. The flood peak occurrence time showed an insignificant forward (decreasing) trend, except for that in GC and WL. The uniformity of typical flood processes in YC and PS had an insignificant decreasing trend, while that of other stations in the four tributaries had an increasing trend, and a significant increasing trend in CY and GC at the significance level of 5%. There are 18 evaluation indicators of the rate of rising limb for typical flood processes in the six stations: 77.8% of which showed a decreasing trend, while 61.1% of evaluation indicators of rates of recession limb showed an increasing trend. It reflects that the flood events in the UYR are getting gradually uniform from the perspective of local fluctuation of the typical flood processes.

Change Point Analysis

The penalized maximal *F* test allows the time series being tested to have a linear trend throughout the whole period of data record, with the annual cycle, linear trend, and lag-1 autocorrelation of the base series being estimated in tandem through iterative procedures, while accounting for all the identified mean shifts. No reference series will be used in functions including the *FindU* and *Stepsize* of PMF, according to Wang and Feng (2013). As for

TABLE 6 | List of abrupt change points of evaluation indicators at the six stations in the UYR by PMF.

Indicators stations	Flood peak flow	Flood volume			Time of flood peak occurrence	Uniformity	Rate of rising limb			Rate of recession limb		
		A	5-day	7-day			I	II	III	I	II	III
Yichang (YC)	**1994**	**1978**	1970	**1971**	—	**1983**	—	**1991**	1962	—	**1994**	—
Changyang (CY)	—	—	—	—	—	—	—	1966; **1995**	—	—	—	1968;**1993**
Beibei (BB)	1989	1989	1989	1989	—	—	1991	1989	—	—	1992	1959; 1972; 1999
Wulong (WL)	—	**1990**	**1990**	—	1961	**1983**	—	—	1968	1968; **1984**	—	—
Gaochang (GC)	—	—	—	—	—	1970	1996	1997	—	1988	1993	—
Pingshan (PS)	1974	1974	1974	1974	—	1952	—	1974	1969	—	—	—

Note: Bold values indicate the change points confirmed by the causes of dam-building activities.

TABLE 7 | The commencement and completion time of key water conservancy projects in the upper Yangtze River.

River	Control hydrometric station	Key water conservancy project	Commencement time	Completion time
Mainstream of the Yangtze river	Yichang (YC)	Gezhouba	**1971**	1988
		Three Gorges dam	**1994**	2009
	Pingshan (PS)	Xiangjiaba	2006	2014
		Xiluodu	2007	2014
		Baihetan	2013	2022 (expected)
		Wudongde	2015	2021
Min river	Gaochang (GC)	Zipingpu	2001	2005
Jialing river	Beibei (BB)	Tingzikou	2009	2014
Wu river	Wulong (WL)	Wujiangdu	1970	**1983**
		Goupitan	2003	2009
Qing river	Changyang (CY)	Geheyan	1987	**1995**
		Gaobazhou	**1995**	2000
Yalong river	Xiaodeshi	Jinping I	2005	2014
		Jinping II	2007	2014
		Guandi	2010	2013
		Ertan	1991	2000

Note: Bold values indicate the change points consistent with the commencement or completion time of dam-building activities.

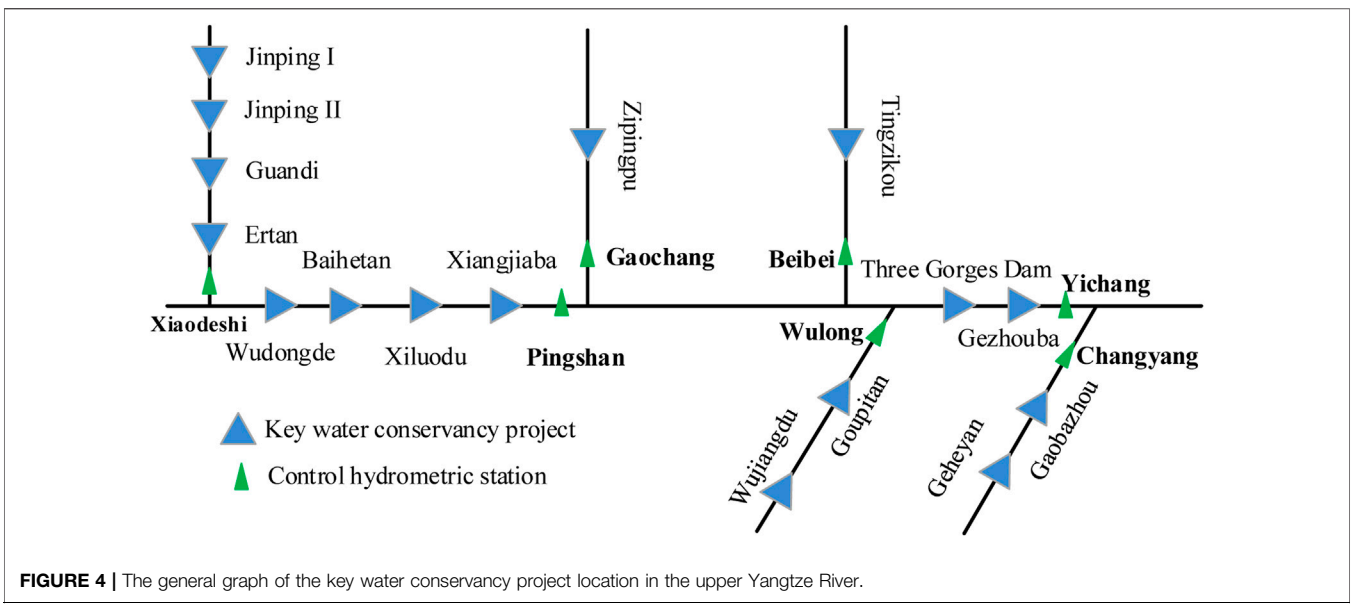

FIGURE 4 | The general graph of the key water conservancy project location in the upper Yangtze River.

the annual maximum peak discharge time series of Yichang station, there are no Type-1 change points when the *FindU* function was called. From **Table 6**, we can know that the change points of the annual flood peak flow time series in BB and PS happened in 1989 and 1974, respectively, while no change points exist in other four stations; all the change points of flood volume (3-day; 5-day; and 7-day) time series in the six stations happened in 1970s–1990s; the change points of uniformity happened in 1980s–1990s, except for that in GC and PS; and the most change points of rates of rising and recession limb happened in 1960s–1990s.

The upper reaches of the Yangtze River are the most highly developed water system in China. Numerous large- and medium-sized reservoirs have been constructed along the upper reaches of the Yangtze River since 1970, forming the world's largest reservoir group with the Three Gorges reservoir at its core. Here, we list the commencement and completion time of 16 key water conservancy projects closely related to the six control hydrometric stations in the mainstream of the Yangtze River and other five tributaries, as described in **Table 7**, and we draw the general graph of the location of these projects, as shown in **Figure 4**. All the documented changes in **Table 7** that could cause a mean shift to be added in the file named Example_mCs.txt if they are not already here according to procedure 5) and procedure 7) of *Trend Analysis* and F5 of *Periodicity Analysis* in the RHtestsV4_UserManual. We found that 1994 (commencement time of the TGD) for flood peak flow in the Yichang station, and 1983 (completion time of Wujiangdu) for uniformity in Wulong station are the potential Type-0 change points which are statistically significant, and these two change points have been added in **Table 6**.

These reservoirs realize comprehensive utilization benefits by changing the spatial and temporal distribution characteristics of the natural streamflow, and transform flood regimes directly. For example, the construction of the TGD and the Gezhouba hydropower station in mainstream of the Yangtze River caused the abrupt change of the 5-day and 7-day flood volume, and the rate of recession limb (II) of Yichang station; the construction of Gaobazhou hydropower station in the Qing River caused the abrupt change of the rate of rising limb (II) of Changyang station, and the construction of Wujiangdu hydropower station corresponding to the change of rate of recession (I) in the Wulong station. In conclusion, the change points of flood peak discharge, 3-day flood volume, 7-day flood volume, uniformity, the rate of rising limb (II) and the rate of recession limb (II) in YC, the rate of rising limb (II) and the rate of recession limb (III) in CY, and 3-day flood volume, 5-day flood volume, uniformity, and the rate of recession limb (I) in WL are confirmed by the causes of dam-building activities listed in **Table 7**, which happened during or after the construction of corresponding water conservancy project; and the change points of the flood peak discharge, 7-day flood volume, the rate of recession limb (II) in YC, the rate of rising limb (II) in CY, and the uniformity in WL are completely consistent with the commencement time of the TGD and Gezhouba, the commencement time of Gaobazhou, and the completion time of Wujiangdu, respectively.

Although the intensified dam-building activities directly affected the flood regime change, the influence of the precipitation structure change is also non-negligible, since the Min River, the Jialing River, and the Yalong River are located in the rainstorm area in western Sichuan. From **Table 6**, we can find that the abrupt change points of Pingshan, Gaochang, and Beibei are not consistent with the commencement or completion time of corresponding major water conservancy projects. The change of precipitation structure is the most obvious indicator of the variation of water cycle (Moberg et al., 2006; Brommer et al., 2007; Zolina et al., 2010), and precipitation in July and August over the upper reaches of the Yangtze River is highly correlated with annual peak discharge (Li et al., 2020). Two abrupt climate change points of summer precipitation in China that occurred in 1978 and 1992 were identified by Ding et al. (2008), and the shift of the summer rainfall over the Yangtze River valley in the late 1970s was also identified (Gong and Ho, 2002; Gao and Xie, 2016). In addition, Ye et al. (2014) analyzed the spatiotemporal variability characteristics of precipitation structure across the upper reaches of the Yangtze River and found that the year of 1976 was marked by an abrupt change for the contribution rate of short-duration (1 and 2 days) precipitation events, while the timing of abrupt changes for the occurrence rate and the contribution rate of long duration (6 and 10 days) was in 1984 and 1999, respectively, all of which happened during 1970s–1990s and were consistent with the abrupt change points of Pingshan, Gaochang, and Beibei. Therefore, it can be concluded that the abrupt change points of Yichang, Changyang, and Wulong during 1970s–1990s are mainly caused by the dam-building activities, while those in Pingshan, Gaochang, and Beibei are mainly caused by the precipitation change in the late 1970s across the Yangtze River Basin, especially in the rainstorm area in western Sichuan.

Periodicity Analysis

The periodicity of all evaluation indicators was analyzed according to the Morlet wavelet transformation. The real part of the wavelet transform coefficient contains the information of the signal distribution and phase along the time axis under certain time scale. In the contour map of the real part of the wavelet coefficient, the positive value indicates that the annual maximum flood peak presents an increasing trend, while the negative value indicates that the annual maximum flood peak presents a decreasing trend. The modulus of the wavelet coefficient is equivalent to the wavelet energy spectrum, from which the oscillation energy of different scales (period) can be analyzed. When the modulus is larger, the periodicity of the corresponding time and scale is more obvious.

In regard to the annual peak-flood series in YC, the contour plot of the real part and modulus of the wavelet transformation coefficients and the global power spectrum are shown in **Figures 5A–C**, respectively. The periodicity analysis results of all evaluation indicators are concluded in **Table 8**.

For **Figures 5A–C**, the Y-coordinate represents period, while the X-coordinate represents time in (A) and (B) and power in (C), respectively. The positive value and the negative value in

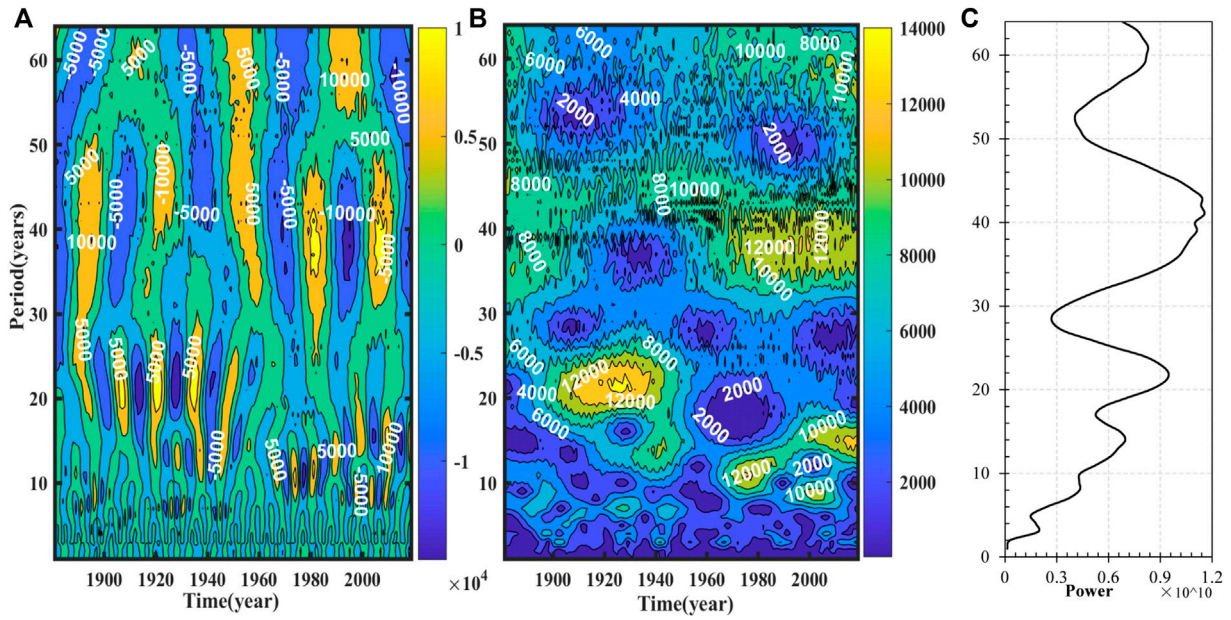

FIGURE 5 | Contour plots of the real part **(A)**, the modulus **(B)**, and the global power spectrum **(C)** of Morlet wavelet transform coefficients.

TABLE 8 | Periodicity analysis of evaluation indicators at the six stations in the UYR.

Indicators stations	Flood peak flow	Flood volume			Time of flood peak occurrence	Uniformity	Rate of rising limb			Rate of recession limb		
		3-days	5-days	7-days			I	II	III	I	II	III
Yichang (YC)	41; 22; 61	44; 22; 59	22; 44; 59	22; 44; 59	56; 6; 36	—	22; 40; 7	—	—	46; 20; 11	46; 20; 11	46; 20; 11
Changyang (CY)	21; 11; 5	20; 11; —	21; 11; —	20; 11; —	23; 4; —	6; 14; 25	16; 22; 10	6; 14; 25	6; 14; 25	16; 22; 10	16; 22; 10	16; 22; 20
Beibei (BB)	14; 8; 5	8; 14; 5	13; 8; 5	14; 8; —	7; —; —	27; 9; 15	15; 8; 4	9; 6; 13	27; 14; 8	8——	5; 26; 14	8; 6; 4
Wulong (WL)	22; 30; 6	30; 6; 22	7; 22; 31	7; 21; 11	13; 5; 30	7; 4; —	30; 7; 13	26; 18; 12	22; 15; 7	30; 22; 12	30; 6—	30; 7; 14
Gaochang (GC)	11; 3; —	11; 3—	11; 21; 3	11; 21; 3	13; 9—	—	15; 11; 5	15; 11; 5	15; 11; 5	15; 11; 5	15; 11; 5	15; 11; 5
Pingshan (PS)	26; 13; 6	26; 13; 6	26; 13; 6	26; 13; 6	23; 17; 7	—	20; 8; 12	6; 11; 27	—	22; 8; 4	20; 8; 12	17; 25; 9

Figure 5A indicate that the annual maximum flood peak presents an increasing trend and a decreasing trend, respectively. And the modulus in **Figure 5B** represents the intensity of the periodicity: the larger the modulus, the stronger the periodicity.

It can be seen from **Figure 5A** that there were four clear periodicities of annual maximum flood peak flow time series in YC during the period from 1892 to 2020, which were 14a, 22a, 41a, and 61a, respectively. The periodicity of 41a existed throughout the whole study period with relatively stable performance, while 22a mainly existed from 1880s to 1960s, and 14a mainly existed from 1960s to 2020s. It can be seen from **Figure 5B** that the wavelet coefficient modulus corresponding to the periodicity of 41a is the largest, so the periodicity is the strongest, followed by 22a, as shown in **Figure 5C**.

From **Table 8**, we can know that the first main periodicity of most evaluation indicators in Y was about 45a. The first main periodicity of annual maximum flood peak time and flood volume series in CY was about 21a; the first main periodicity of the flood peak occurrence time and uniformity, and most rates of rising and recession limb were 23a, 6a, and 16a, respectively. The first main period of all evaluation indicators in BB and WL varied obviously, while that in GC are mainly 11a and 15a, and that in PS are mainly 26a and 20a.

SUMMARY AND DISCUSSION

The "stationarity" of flood-generating mechanism is lost under the changing environment. Climate and human forcings

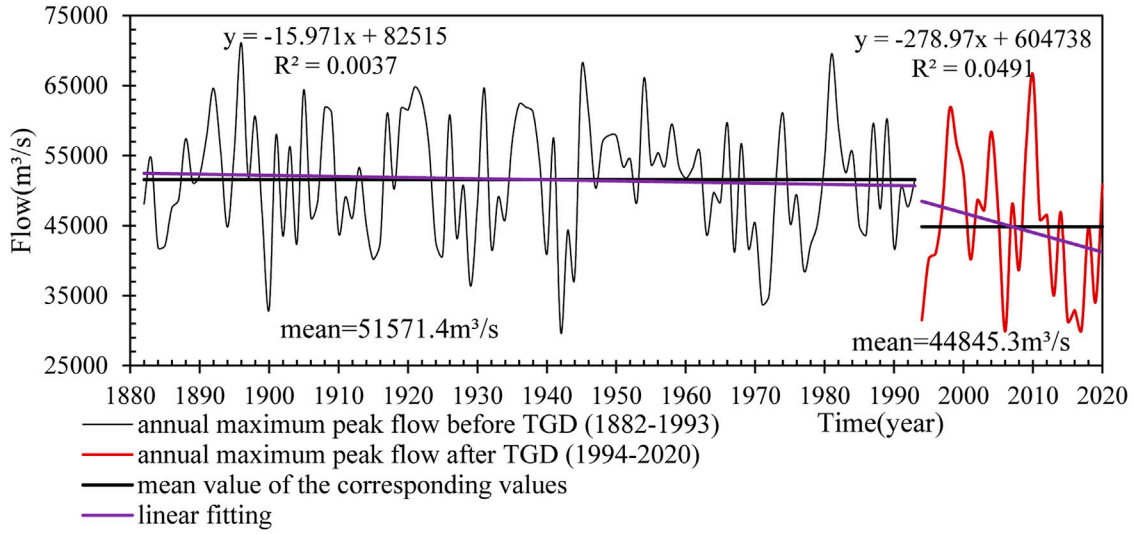

FIGURE 6 | Variation of annual peak discharge before and after the Three Gorges Dam (TDG) construction.

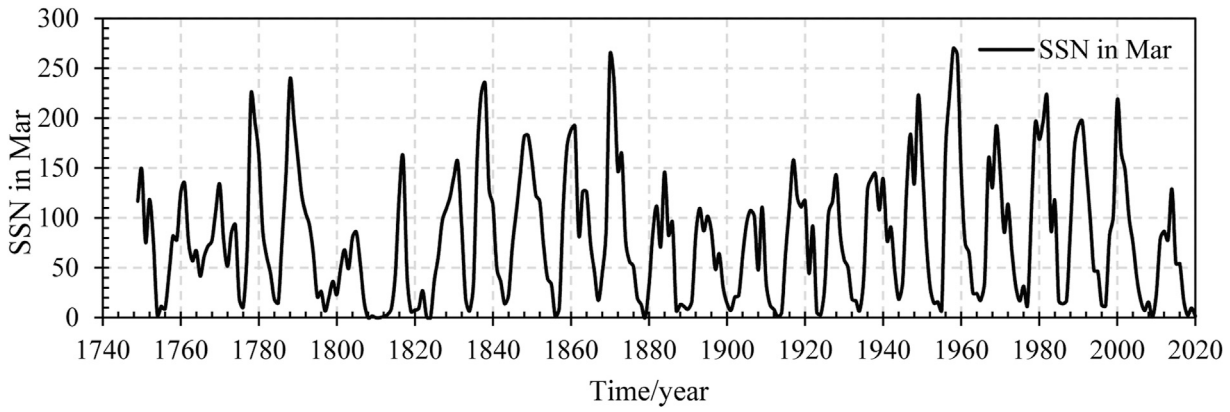

FIGURE 7 | Sunspot numbers (SSNs) in March during 1749–2020.

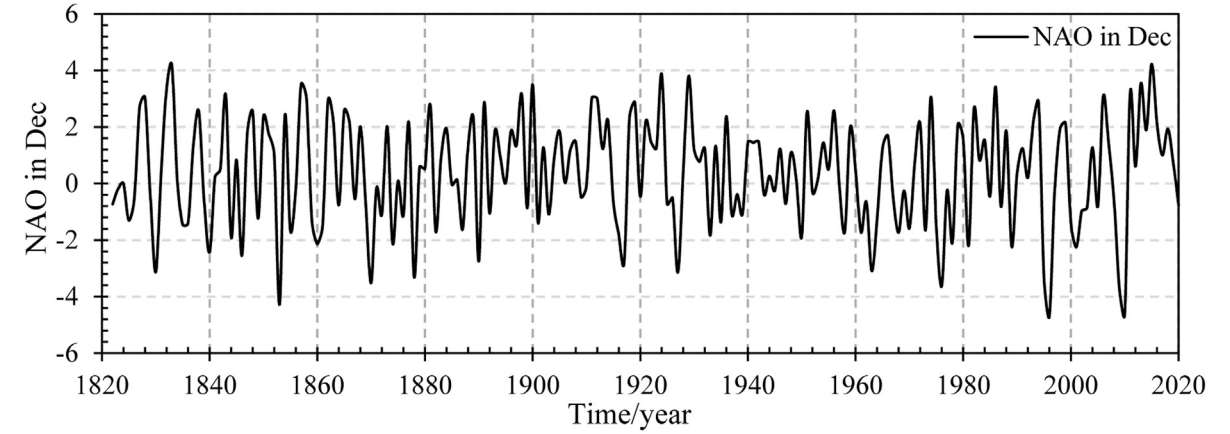

FIGURE 8 | North Atlantic Oscillation (NAO) in December (1822–2020).

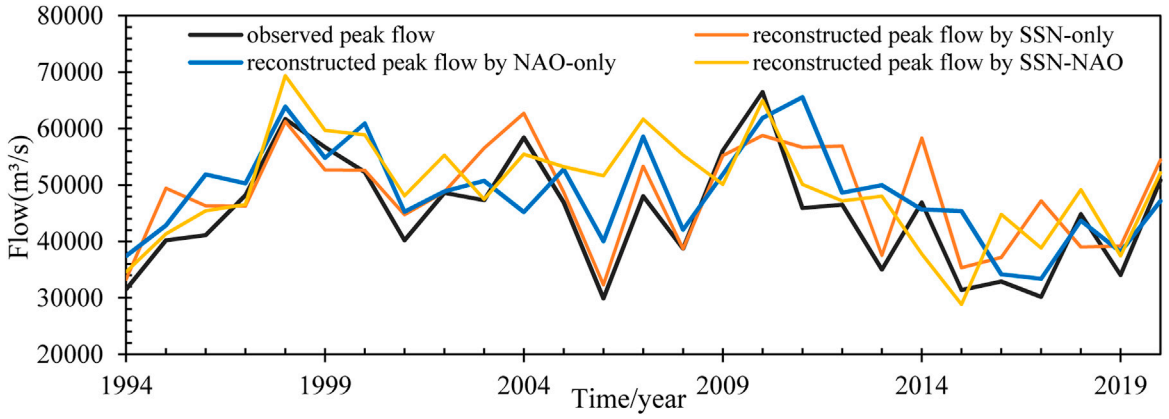

FIGURE 9 | Reconstructed discharge through the BP neural network and observed discharge in the modern period.

TABLE 9 | Observed and reconstructed flood magnitudes with different recurrence intervals by the BP model after the construction of the TGD (1994–2020).

Climate control	Q_{10} (m^3/s)	Q_{100} (m^3/s)	Q_{1000} (m^3/s)	Q_{10000} (m^3/s)
Reconstruction by SSN-only	61,283.24	74,061.72	86,288.66	93,281.61
Reconstruction by NAO-only	60,732.33	75,315.46	86,544.45	89,634.87
Reconstruction by SSN-NAO	62,467.30	78,042.56	91,686.82	94,405.70
Observed flow at baseline period	65,173.17	78,765.88	89,832.51	91,678.12
Observed flow at modern period	59,024.21	73,070.49	84,458.67	94,561.79

TABLE 10 | Contributions of climatic control and human activities to floods with different recurrence intervals.

Climate control	Factors	Q_{10} (%)	Q_{100} (%)	Q_{1000} (%)	Q_{10000} (%)
SSN-only	Natural	0.63	0.83	0.66	0.56
	Human	0.37	0.17	0.34	0.44
NAO-only	Natural	0.72	0.61	0.61	0.40
	Human	0.28	0.39	0.39	0.60
SSN-NAO	Natural	0.44	0.13	−0.35	−0.53
	Human	0.56	0.87	1.35	1.53

combined have been imposed on the flood regimes in the upper Yangtze River. Ye et al. (2015) applied univariate and the multivariate Mann–Kendall method to test the stationarity of the annual peak discharge and annual maximum 15-day volume of four control hydrological stations in the UYR. Xiong and Guo (2004) carried out the trend test and change-point analysis of the annual maximum, annual minimum, and annual mean discharge series in Yichang station during the period of 1882–2001. Zhang et al. (2006) detected the trend and periodicity of the annual maximum water level and streamflow of Yichang, Hankou, and the Datong station across the Yangtze River Basin. Most of the research aforementioned found the decreasing trend of flood peak discharge and flood volume due to the intensified dam-building, yet the other characteristics of flood regime, such as the timing of flood peak occurrence (Bloschl et al., 2017; Rokaya et al., 2018) and uniformity (Chen et al., 2015), were ignored. To improve the understanding of the all-round flood regime change in the UYR, the non-stationarity analysis of hydrological series, including 12 evaluation indicators time series extracted from the annual typical flood event, was performed.

For trend analysis, the annual flood peak discharge and flood volume present a decreasing trend except Pingshan and Wulong, since the length of the two stations are 71 (1940–2010) and 50 (1952–2001), respectively. The Xiangjiaba and Xiluodu dams were not fully built, and the construction of the Baihetan and Wudongde dams were not started yet before 2010. The four reservoirs are located in the lower reaches of the Jinsha River, which have direct influence on the flood regime in Pingshan station. The reason for the increasing trend of annual peak discharge and flood volume is similar for Wulong station, since the key reservoirs in the lower reaches of the Wu River have not been constructed yet. And therefore, the uniformity of the two stations exhibited no obvious change during the corresponding study period.

For abrupt change analysis, the abrupt change of flood regimes in YC, CY, and WL is mainly caused by the dam-building activities, while that in PS, GC, and BB is mainly caused by the precipitation change in the late 1970s across the Yangtze River Basin, especially in the rainstorm area in western Sichuan. For periodicity analysis, the major period of the Yichang station is longer than that of other stations. As the controlling station of the upper Yangtze River, it has stronger regulatory capacity, while other stations are more prone to be influenced by the human activities and climate change.

To better understand the role of peak-flood clipping the TGD plays, we quantitatively evaluate the contribution of the climatic

control factors and the TDG to the variation of the annual flood peak in Yichang station. According to the time at which the TDG-building activities commenced, the whole study period (1882–2020) was divided into two phases: the period before 1994 (defined as the "baseline period") and the period after 1994 (defined as the "modern period"). Accordingly, the observed discharge was also divided into two types: the observed discharged during the baseline period and that during the modern period as shown in **Figure 6**. It is clear that the mean value of the annual peak discharge before and after the TGD construction is 51,571.4 m^3/s and 44,845.3 m^3/s, respectively, which shows the important role of peak-flood clipping the TGD plays.

To assess the effects of climatic control on flood peak discharge, the climate control factors need to be identified. The SSNs in March and the NAO in December were found to be highly correlated with annual peak discharges (Li et al., 2020). The SSNs in March during 1749–2020 and the North Atlantic Oscillation in December (1882–2020) are shown in **Figures 7**, **8**, respectively. Over the nearly past 300 years, SSNs have exhibited an average 11-year cycle (Clette et al., 2014), while the NAO presents irregular oscillation without any obvious cycle (Gu et al., 2009).

To separate the impacts of natural and human activities on the variation of the flood peak discharge, the reconstructed annual peak discharge during 1994–2020 was derived based on the back propagation neural network (BPNN) model, which was trained by the corresponding discharge, SSNs in March, NAO in December, and SSN–NAO, respectively (R^2 = 0.69; 0.62; 0.57), as shown in **Figure 9**. In the absence of human activities, the SSN-only model predicts that Q_{10}, Q_{100}, Q_{1000}, and Q_{10000} obtained by P-III fitting were 61,283.24; 74,061.72; 84,288.66; and 93,281.61 m^3/s (in **Table 9**), respectively, accounting for approximately 56–83% of the observed decrease in discharge. This implies the remainder (approximately 17–44%) of the decline in flood magnitude is the result of the TGD construction. However, the results predicted by SSN–NAO (in **Table 10**) indicate that climatic controls and the TGD construction contribute – 53–44% and 56–153%, respectively. Therefore, the TGD construction has played a positive role in reducing flood magnitude with different recurrence intervals, especially for the flood with a 0.01% chance of exceedance in any year.

DATA AVAILABILITY STATEMENT

The original contributions presented in the study are included in the article, further inquiries can be directed to the corresponding author.

AUTHOR CONTRIBUTIONS

Conceptualization, review, and editing: GF, XW, and ZH; methodology, formal analysis, original draft preparation, and visualization: YZ; validation: ZD and XL; data curation and resources: XB, ZT, and HZ; supervision, funding acquisition, and project administration: GF and XW. All authors have read and agreed to the version of the manuscript.

FUNDING

The research was supported by the National Key Research and Development Program of China (2019YFE0105200 and 2018YFC0407902) and the National Natural Science Foundation of China (U1765201, 51909010, and 52079040).

ACKNOWLEDGMENTS

Thanks are due to the Hydrological Office, Yangtze Water Resources Committee for providing the hydrologic data, and to Liu, S. Q. for her linguistic assistance during the preparation of this manuscript.

REFERENCES

Akbari, S., and Reddy, M. J. (2020). Non-stationarity Analysis of Flood Flows Using Copula Based Change-point Detection Method: Application to Case Study of Godavari River basin. *Sci. Total Environ.* 718, 134894. doi:10.1016/j.scitotenv.2019.134894

Alexander, L. V., Zhang, X., Peterson, T. C., Caesar, J., Gleason, B., Klein Tank, A. M. G., et al. (2006). Global Observed Changes in Daily Climate Extremes of Temperature and Precipitation. *J. Geophys. Res.* 111, 111. doi:10.1029/2005JD006290

Bloschl, G., Hall, J., Parajka, J., Perdigão, R. A. P., Merz, B., Arheimer, B., et al. (2017). Changing Climate Shifts Timing of European Floods. *Science* 357, 588–590. doi:10.1126/science.aan2506

Bormann, H., Pinter, N., and Elfert, S. (2011). Hydrological Signatures of Flood Trends on German Rivers: Flood Frequencies, Flood Heights and Specific Stages. *J. Hydrol.* 404, 50–66. doi:10.1016/j.jhydrol.2011.04.019

Brommer, D. M., Cerveny, R. S., and Balling, R. C. (2007). Characteristics of Long-Duration Precipitation Events across the United States. *Geophys. Res. Lett.* 34, 34. doi:10.1029/2007gl031808

Bronaugh, D., and Werner, A. (2019). Zyp: Zhang + Yue Pilon Trends Package. Available at: https://cran.r-project.org/web/packages/zyp/index.html.

Chen, H. J., Xie, P., Xie, J. H., et al. (2015). Variation Analysis Method for Flood Process Homogeneity Based on the Information entropy:Taking the Flood Series of Longchuan Station in Dongjiang River Basin as an Example (In Chinese). *J. Hydraulic Eng. [J]* 46 (10), 1233–1239.

Chen, J., Wu, X., Finlayson, B. L., Webber, M., Wei, T., Li, M., et al. (2014). Variability and Trend in the Hydrology of the Yangtze River, China: Annual Precipitation and Runoff. *J. Hydrol.* 513, 403–412. doi:10.1016/j.jhydrol.2014.03.044

Clette, F., Svalgaard, L., Vaquero, J. M., and Cliver, E. W. (2014). Revisiting the Sunspot Number. *Space Sci. Rev.* 186, 35–103. doi:10.1007/s11214-014-0074-2

Daubechies, I., and Bates, B. J. (1993). Ten Lectures on Wavelets. *The J. Acoust. Soc. America* 93, 1671. doi:10.1121/1.406784

Ding, Y., Wang, Z., and Sun, Y. (2008). Inter-decadal Variation of the Summer Precipitation in East China and its Association with Decreasing Asian Summer monsoon.Part I: Observed Evidences. *Int. J. Climatol.* 28, 1139–1161. doi:10.1002/joc.1615

Fang, H., Han, D., He, G., and Chen, M. (2012). Flood Management Selections for the Yangtze River Midstream after the Three Gorges Project Operation. *J. Hydrol.* 432-433, 1–11. doi:10.1016/j.jhydrol.2012.01.042

Field, C. B., Barros, V., Stocker, T. F., et al. (2012). Managing the Risks of Extreme Events and Disasters to Advance Climate Change Adaptation. IPCC Special Report [M]. in *IEEE Transactions on Automatic Control*. Cambridge: Cambridge University Press, 582.

Gao, B., Yang, D., Zhao, T., and Yang, H. (2012). Changes in the Eco-Flow Metrics of the Upper Yangtze River from 1961 to 2008. *J. Hydrol.* 448-449, 30–38. doi:10.1016/j.jhydrol.2012.03.045

Gao, T., and Xie, L. (2016). Spatiotemporal Changes in Precipitation Extremes over Yangtze River basin, China, Considering the Rainfall Shift in the Late 1970s. *Glob. Planet. Change* 147, 106–124. doi:10.1016/j.gloplacha.2016.10.016

Gong, D.-Y., and Ho, C.-H. (2002). Shift in the Summer Rainfall over the Yangtze River valley in the Late 1970s. *Geophys. Res. Lett.* 29, 78–81. doi:10.1029/2001gl014523

Gu, W., Li, C., Li, W., Zhou, W., and Chan, J. C. L. (2009). Interdecadal Unstationary Relationship between NAO and east China's Summer Precipitation Patterns. *Geophys. Res. Lett.* 36, 36. doi:10.1029/2009GL038843

Guo, L., Su, N., Zhu, C., and He, Q. (2018). How Have the River Discharges and Sediment Loads Changed in the Changjiang River basin Downstream of the Three Gorges Dam? *J. Hydrol.* 560, 259–274. doi:10.1016/j.jhydrol.2018.03.035

Jiang, T., Su, B., and Hartmann, H. (2007). Temporal and Spatial Trends of Precipitation and River Flow in the Yangtze River Basin, 1961-2000. *Geomorphology* 85, 143–154. doi:10.1016/j.geomorph.2006.03.015

Kendall, M. G. (1975). *Rank Correlation Methods*. 4th Edition. London: Charles Griffin.

Kumar, P., and Foufoula-Georgiou, E. (1993). A Multicomponent Decomposition of Spatial Rainfall fields: 1. Segregation of Large- and Small-Scale Features Using Wavelet Transforms. *Water Resour. Res.* 29, 2515–2532. doi:10.1029/93WR00548

Li, H., Liu, P., Guo, S., Cheng, L., and Yin, J. (2020). Climatic Control of Upper Yangtze River Flood hazard Diminished by Reservoir Groups. *Environ. Res. Lett.* 15, 124013. doi:10.1088/1748-9326/abc4fe

Li, S. F., Yu, P., and Sun, S. H. (2012). Flood Flow Processes Variation and Influencing Factors in Zijingguan Watershed (In Chinese). *Eng. J. Wuhan Univ. [J]* 45 (2), 166–170.

Luo, C. Z., and Le, J. X. (1996). The Heavy Flood in China - a Brief Description of Disastrous Floods [M]. *Cathay Bookshop*. doi:10.1142/9789814447195_0001

Mallat, S. G. (1989). A Theory for Multiresolution Signal Decomposition: the Wavelet Representation. *IEEE Trans. Pattern Anal. Machine Intell.* 11, 674–693. doi:10.1109/34.192463

Mann, H. B. (1945). Nonparametric Tests against Trend. *Econometrica* 13, 245–259. doi:10.2307/1907187

Milly, P. C. D., Betancourt, J., Falkenmark, M., Hirsch, R. M., Kundzewicz, Z. W., Lettenmaier, D. P., et al. (2008). Stationarity Is Dead: Whither Water Management? *Science* 319, 573–574. doi:10.1126/science.1151915

Moberg, A., Jones, P. D., Lister, D., Walther, A., Brunet, M., Jacobeit, J., et al. (2006). Indices for Daily Temperature and Precipitation Extremes in Europe Analyzed for the Period 1901-2000. *J. Geophys. Res.* 111, 111. doi:10.1029/2006JD007103

Munoz, S. E., Giosan, L., Therrell, M. D., Remo, J. W. F., Shen, Z., Sullivan, R. M., et al. (2018). Climatic Control of Mississippi River Flood hazard Amplified by River Engineering. *Nature* 556, 95–98. doi:10.1038/nature26145

Rokaya, P., Budhathoki, S., and Lindenschmidt, K.-E. (2018). Trends in the Timing and Magnitude of Ice-Jam Floods in Canada. *Sci. Rep.* 8, 5834. doi:10.1038/s41598-018-24057-z

Salas, J. D., Delleur, J. W., and Yevjevich, V. (1980). *Applied Modeling of Hydrologic Time Series[M]*. Littleton: Colorado and Water Resources Publications.

Sen, P. K. (1968). Estimates of the Regression Coefficient Based on Kendall's Tau. *J. Am. Stat. Assoc.* 63 (324), 1379–1389. doi:10.1080/01621459.1968.10480934

Slater, L. J., and Wilby, R. L. (2017). Measuring the Changing Pulse of Rivers. *Science* 357, 552. doi:10.1126/science.aao2441

Storch, H. V. (1995). "Misuses of Statistical Analysis in Climate [M]." in *Analysis of Climate Variability*, Berlin Heidelberg: Springer.

Torrence, C., and Compo, G. P. (1998). A Practical Guide to Wavelet Analysis. *Bull. Amer. Meteorol. Soc.* 79, 61–78. doi:10.1175/1520-0477(1998)079<0061:apgtwa>2.0.co;2

Venugopal, V., and Foufoula-Georgiou, E. (1996). Energy Decomposition of Rainfall in the Time-Frequency-Scale Domain Using Wavelet Packets. *J. Hydrol.* 187, 3–27. doi:10.1016/s0022-1694(96)03084-3

Wang, X. L. (2008a). Accounting for Autocorrelation in Detecting Mean Shifts in Climate Data Series Using the Penalized Maximal T or F Test. *J. Appl. Meteorology Climatology [J]* 47, 2423–2444. doi:10.1175/2008jamc1741.1

Wang, X. L. (2003). Comments on "Detection of Undocumented Changepoints: A Revision of the Two-phase Regression Model". *J. Clim.* 16, 3383–3385. doi:10.1175/1520-0442(2003)016<3383:codouc>2.0.co;2

Wang, X. L., and Feng, Y. (2013). RHtestsV4 User Manual. Available at: https://github.com/ECCC-CDAS/RHtests.

Wang, X. L. (2008b). Penalized Maximal F Test for Detecting Undocumented Mean Shift without Trend Change. *J. Atmos. Oceanic Technology [J]* 25, 368–384. doi:10.1175/2007jtecha982.1

Wang, X. L., and Swail, V. R. (2001). Changes of Extreme Wave Heights in Northern Hemisphere Oceans and Related Atmospheric Circulation Regimes. *J. Clim.* 14, 2204–2221. doi:10.1175/1520-0442(2001)014<2204:coewhi>2.0.co;2

Wei, W., Chang, Y., and Dai, Z. (2014). Streamflow Changes of the Changjiang (Yangtze) River in the Recent 60 years: Impacts of the East Asian Summer Monsoon, ENSO, and Human Activities. *Quat. Int.* 336, 98–107. doi:10.1016/j.quaint.2013.10.064

Xiong, L., and Guo, S. (2004). Trend test and change-point detection for the annual discharge series of the Yangtze River at the Yichang hydrological station/Test de tendance et détection de rupture appliqués aux séries de débit annuel du fleuve Yangtze à la station hydrologique de Yichang. *Hydrological Sci. J.* 49, 99–112. doi:10.1623/hysj.49.1.99.53998

Yang, S. L., Xu, K. H., Milliman, J. D., Yang, H. F., and Wu, C. S. (2015). Decline of Yangtze River Water and Sediment Discharge: Impact from Natural and Anthropogenic Changes. *Sci. Rep.* 5, 12581. doi:10.1038/srep12581

Yao, Y. H., Zhang, B. P., Ma, X. D., et al. (2006). Large-scale Hydroelectric Projects and Mountain Development on the Upper Yangtze River. *Mountain Res. Development [J]* 26, 109–114. doi:10.1659/0276-4741(2006)26[109:LHPAMD]2.0.CO;2

Ye, L., Zhou, J., Zeng, X., and Tayyab, M. (2015). *Hydrological Mann-Kendal Multivariate Trends Analysis in the Upper Yangtze River Basin. J. Geo. Environ. Prot.* 3, 34–39. doi:10.4236/gep.2015.310006

Ye, Y. T., Liang, L. L., Gong, J. G., et al. (2014). Spatial-temporal Evolution of Precipitation Structure in the Upper Reaches of the Yangtze River Basin (In Chinese). *Adv. Water Sci. [J]* 25 (2), 164–171.

Yu, S.-P., Yang, J.-S., Liu, G.-M., Yao, R.-J., and Wang, X.-P. (2012). Multiple Time Scale Characteristics of Rainfall and its Impact on Soil Salinization in the Typical Easily Salinized Area in Huang-Huai-Hai Plain, China. *Stoch Environ. Res. Risk Assess.* 26, 983–992. doi:10.1007/s00477-012-0557-1

Yue, S., Pilon, P., Phinney, B., and Cavadias, G. (2002). The Influence of Autocorrelation on the Ability to Detect Trend in Hydrological Series. *Hydrol. Process.* 16, 1807–1829. doi:10.1002/hyp.1095

Zhang, Q., Liu, C., Xu, C.-Y., Xu, Y., and Jiang, T. (2006). Observed Trends of Annual Maximum Water Level and Streamflow during Past 130 Years in the Yangtze River basin, China. *J. Hydrol.* 324, 255–265. doi:10.1016/j.jhydrol.2005.09.023

Zhang, Q., Xu, C.-Y., and Chen, Y. D. (2010). Wavelet-based Characterization of Water Level Behaviors in the Pearl River Estuary, China. *Stoch Environ. Res. Risk Assess.* 24, 81–92. doi:10.1007/s00477-008-0302-y

Zhang, X., Vincent, L. A., Hogg, W. D., and Niitsoo, A. (2000). Temperature and Precipitation Trends in Canada during the 20th century. *Atmosphere-Ocean* 38, 395–429. doi:10.1080/07055900.2000.9649654

Zolina, O., Simmer, C., Gulev, S. K., and Kollet, S. (2010). Changing Structure of European Precipitation: Longer Wet Periods Leading to More Abundant Rainfalls. *Geophys. Res. Lett.* 37, a–n. doi:10.1029/2010gl042468

Conflict of Interest: Authors ZT and HZ were employed by the company China Yangtze Power Co., Ltd., and XB was employed by the company Jiangsu Water Source Co., Ltd.

The remaining authors declare that the research was conducted in the absence of any commercial or financial relationships that could be construed as a potential conflict of interest.

frontiers in Environmental Science

ORIGINAL RESEARCH
published: 14 June 2021
doi: 10.3389/fenvs.2021.672295

Dual Effects of Synoptic Weather Patterns and Urbanization on Summer Diurnal Temperature Range in an Urban Agglomeration of East China

Min Guo[1], Minxuan Zhang[1], Hong Wang[1], Linlin Wang[2], Shuhong Liu[1], Lian Zong[1], Yanhao Zhang[1] and Yubin Li[1]*

[1]Collaborative Innovation Centre on Forecast and Evaluation of Meteorological Disasters, School of Atmospheric Physics, Nanjing University of Information Science and Technology, Nanjing, China, [2]State Key Laboratory of Atmospheric Boundary Layer Physics and Atmospheric Chemistry (LAPC), Institute of Atmospheric Physics, Chinese Academy of Sciences, Beijing, China

OPEN ACCESS

Edited by:
Qingxiang Li,
Sun Yat-Sen University, China

Reviewed by:
Jiachuan Yang,
Hong Kong University of Science and Technology, China
Jinming Feng,
Institute of Atmospheric Physics, Chinese Academy of Sciences (CAS), China

***Correspondence:**
Linlin Wang
linlinwang@mail.iap.ac.cn

Specialty section:
This article was submitted to Interdisciplinary Climate Studies, a section of the journal Frontiers in Environmental Science

Received: *25 February 2021*
Accepted: *25 May 2021*
Published: *14 June 2021*

Citation:
Guo M, Zhang M, Wang H, Wang L, Liu S, Zong L, Zhang Y and Li Y (2021) Dual Effects of Synoptic Weather Patterns and Urbanization on Summer Diurnal Temperature Range in an Urban Agglomeration of East China. Front. Environ. Sci. 9:672295. doi: 10.3389/fenvs.2021.672295

Previous studies on the impact of urbanization on the diurnal temperature range (DTR) have mainly concentrated on the intra-seasonal and interannual–decadal scales, while relatively fewer studies have considered synoptic scales. In particular, the modulation of DTR by different synoptic weather patterns (SWPs) is not yet fully understood. Taking the urban agglomeration of the Yangtze River Delta region (YRDUA) in eastern China as an example, and by using random forest machine learning and objective weather classification methods, this paper analyzes the characteristics of DTR and its urban–rural differences (DTR_{U-R}) in summer from 2013 to 2016, based on surface meteorological observations, satellite remote sensing, and reanalysis data. Ultimately, the influences of urbanization-related factors and different large-scale SWPs on DTR and DTR_{U-R} are explored. Results show that YRDUA is controlled by four SWPs in the 850-hPa geopotential height field in summer, and the DTRs in three sub-regions are significantly different under the four SWPs, indicating that they play a role in regulating the DTR in YRDUA. In terms of the average DTR for each SWP, the southern sub-region of the YRDUA is the highest, followed by the northern sub-region, and the middle sub-region is the lowest, which is most significantly affected by high-level urbanization and high anthropogenic heat emission. The DTR_{U-R} is negative and differs under the four different SWPs with variation in sunshine and rainfall. The difference in anthropogenic heat flux between urban and rural areas is one of the potentially important urbanization-related drivers for DTR_{U-R}. Our findings help towards furthering our understanding of the response of DTR in urban agglomerations to different SWPs via the modulation of local meteorological conditions.

Keywords: diurnal temperature range, urbanization, synoptic weather pattern, random forests, Yangtze River Delta region

INTRODUCTION

Diurnal temperature range (DTR) is the difference between the maximum surface air temperature and the minimum surface air temperature in a whole day, which can reflect the global and regional characteristics of temperature change (Easterling, 1997; Braganza et al., 2004; Vose et al., 2005), and has an important impact on human health (Kan et al., 2007; Lim et al., 2012; Yang et al., 2013; Zhang et al., 2018) and crop yield (Lobell, 2007; Tao et al., 2008). Indeed, DTR has become an important indicator of climate change and the human living environment (Easterling et al., 2000).

In the past century, the global average temperature has been rising, with an asymmetrical trend of change in the maximum and minimum temperature. The rising trend of minimum temperature is higher than that of maximum temperature, which leads to a decline in the global DTR (Sun et al., 2019). The intensification of urbanization across the globe has also contributed to the decline in DTR since the 1950s (Gallo et al., 1996; Kalnay and Cai, 2003; Feddema 2005; Mohan and Kandya, 2015). This is mainly because the underlying impervious surfaces of cities increases the nighttime temperature by absorbing a large amount of energy in the daytime and releasing it at night (Forster and Solomon, 2003; Zhou et al., 2007; Yang et al., 2020a; Zong et al., 2021). At the same time, due to the radiative cooling effect of aerosol pollution over cities, the daytime temperature decreases (Zheng et al., 2018; Yang et al., 2020b), and ultimately the DTR decreases in cities owing to the asymmetry in the changes of maximum and minimum temperature.

With its developed economy and dense human population, the level of urbanization in the Yangtze River Delta region is the heighest in China. Under such rapid urbanization, the distance between urban areas is shrinking, which greatly changes the original natural state and the regional-scale ecological environment, intensifies the risk of high-temperature heat waves in summer (Luo and Lau, 2018, 2019), and seriously endangers the public health and production of the region (Chen et al., 2018; Yang Y. et al., 2013; Yang X. et al., 2017, 2019). The rapid urbanization of the Yangtze River Delta region also has an important impact on its DTR (Hua et al., 2006; Chen and Chen, 2007; Liu et al., 1995-2000; Wang et al., 2012; Shen et al., 2014). Through the effect of urbanization on the maximum temperature, the DTR also shows a significant decreasing trend (Shen et al., 2014). In the past 40 years, the extreme values of maximum temperature and minimum temperature in big cities were greater than those in small towns, and the number of days with a low DTR was more than those in small towns (Hua et al., 2006; Qi et al., 2019). Taking Shanghai as an example, in the past 130 years, its DTR has shown a significant decreasing trend, with the DTR decreasing by 0.15°C per decade, and urbanization has had a significant impact on this trend (Zhou et al., 2012). In general, the change in DTR is directly affected by the asymmetry of the change in the maximum and minimum temperature, and the influencing factors can be mainly divided into natural factors (radiation, sunshine duration, precipitation, atmospheric circulation, etc.) and human factors (urbanization-related land-use change, anthropogenic heat release, aerosol pollution, etc.) (Dai et al., 1999; Liu et al., 2016; Sun et al., 2019; Xue et al., 2019; Yang et al., 2020b). Existing research on the variation in the DTR in the Yangtze River Delta region mainly focuses on the intra-seasonal scale (Dong and Huang, 2015; Yang et al., 2020a) and the interannual–decadal scale (Hua et al., 2006; Chen and Chen, 2007; Liu et al., 1995-2000; Wang et al., 2012; Shen et al., 2014), with the synoptic scale relatively less well studied. In particular, the regulatory effects of different synoptic weather patterns (SWPs) on DTR variation and the urban–rural differences in DTR (DTR_{U-R}) in the Yangtze River Delta region remain unclear.

Therefore, taking the urban agglomeration of the Yangtze River Delta (YRDUA) in eastern China as an example, this paper studies the influence of circulation patterns at different synoptic scales on the DTR in the region, and explores the factors driving the variation in DTR on the synoptic scale. Section *Data and Methods* describes the data and methods used in this study. Section *Results and Discussion* examines the difference in DTR between urban and rural areas and the influence of synoptic circulation on DTR_{U-R}. In this section, we also discuss the factors influencing the DTR of YRDUA and how weather patterns affect local meteorological elements to change the DTR_{U-R}. Conclusions are provided in Section *Conclusion*.

DATA AND METHODS

Data

This paper employs surface meteorological observation data in the form of daily maximum surface air temperature (T_{max}), daily minimum surface air temperature (T_{min}), sunshine duration (SSD), and precipitation on the daily and 8-days-average scales. Covering 148 stations in the Yangtze River Delta region during June, July and August from 2013 to 2016, the data were provided by the China Meteorological Data Service Center (http://Data.cma.cn/en). The DTR is the difference between T_{max} and T_{min}.

Additionally, daily and 8-days-average daytime land surface temperature, nighttime land surface temperature, and Normalized Difference Vegetation Index (NDVI) were obtained from MODIS remote sensing land surface temperature data with a spatial resolution of 1 km (https://lpdaac.usgs.gov); anthropogenic heat flux (AHF) data in the Yangtze River Delta region were retrieved from NOAA satellite nighttime light information (http://ngdc.NOAA.gov/eog/dmsp/downloadV4composites.html) noting that the error in the AHF results is generally within 12% (Chen and Shi, 2012; Chen et al., 2012, 2014, 2015, 2016); and specific humidity, air pressure, and horizontal and vertical wind speed data were obtained from the fifth generation European Centre for Medium-Range Weather Forecasts reanalysis (ERA5), which has a high spatiotemporal resolution (0.25° × 0.25, hourly; https://cds.climate.copernicus.eu/cdsapp#!/home). The built up area data are from the 30m resolution dataset of China's urban impervious surfaces (derived from https://zenodo.org/record/4034161#.YFXn29y-uUk) (Kuang et al., 2000-2018).

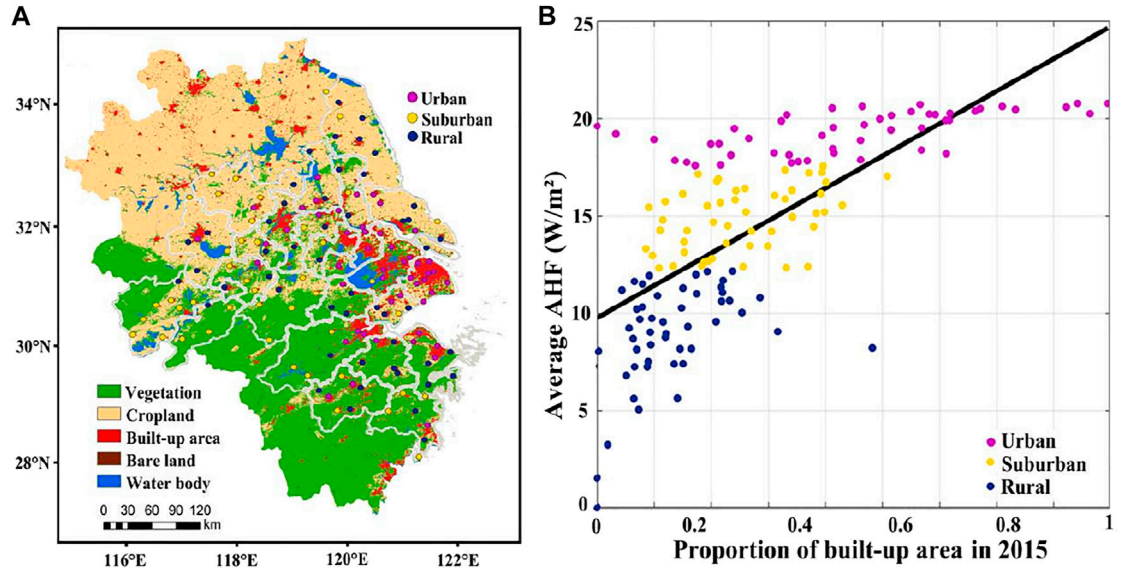

FIGURE 1 | (A) Spatial distribution of built-up area in summer 2015 in the Yangtze River Delta region and classification of urban and rural stations. **(B)** Correlation between anthropogenic heat flux and built-up area in 2015.

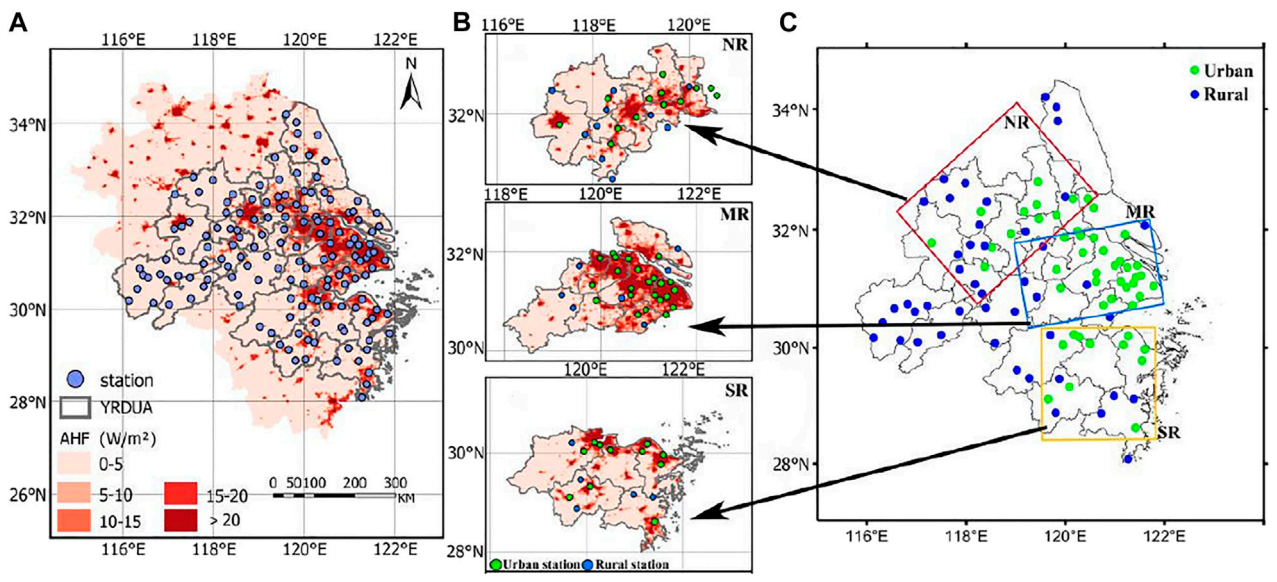

FIGURE 2 | (A) Spatial distribution of anthropogenic heat in summer 2016 in the Yangtze River Delta region. **(B)** Average anthropogenic heat flux (W/m^2) distribution within 5 km around stations in three sub-regions of YRDUA. **(C)** Three sub-regions of YRDUA and the classification of urban and rural stations.

Methods

Division and Matching of Urban and Rural Stations

Since the measurement of surface air temperature is taken at the height of 2m, according to previous studies (Cai, 2008; Yang et al., 2013; Shi et al., 2015; Shi et al., 2021; Yang et al., 2020), the maximum impact of anthropogenic heat on meteorological observations around the station usually does not exceed 5 km under advection and turbulence transport conditions. Thus, we chose 5 km as the radius of the buffer zone to capture the effects of urbanization on air temperature. Firstly, we took the built-up area (i.e., impervious surface area) as background in **Figure 1**, showing that the spatial distribution of anthropogenic heat flux corresponds well with actual distribution of the land covers (**Figure 1**). Anthropogenic heat flux is closely related to the change in built-up area around the stations (**Figure 1B**). Therefore, anthropogenic heat flux can be considered to

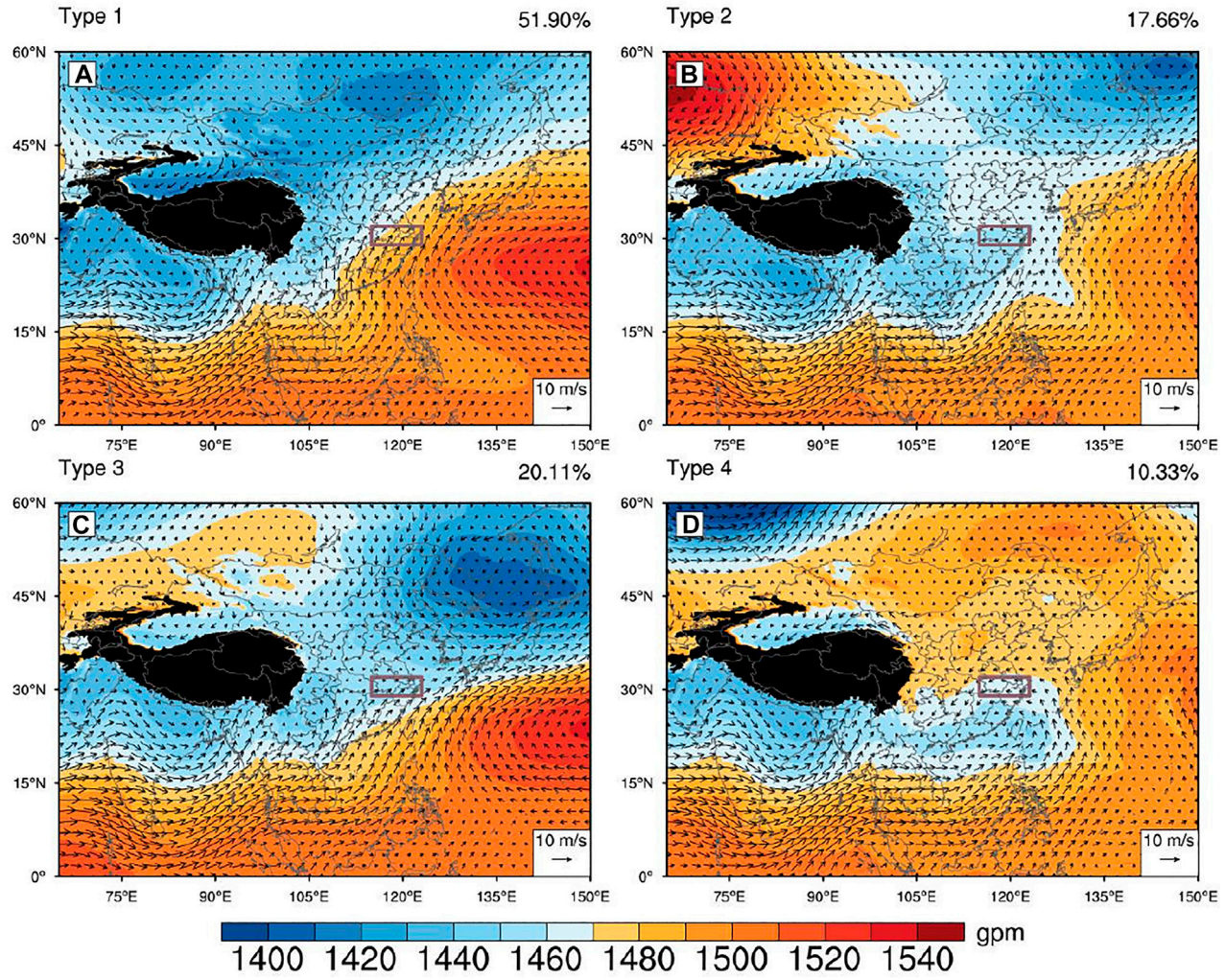

FIGURE 3 | The 850-hPa geopotential height field and wind field for four Synoptic Weather Patterns (SWPs): **(A)** Type 1, **(B)** Type 2, **(C)** Type 3, and **(D)** Type 4. The purple box indicates the YRDUA region.

reliably reflect the effects of both anthropogenic emissions and land-use change related to latent heat flux and sensible heat flux (Jiang et al., 2019; Chen et al., 2020). Therefore, classified the stations by the mean anthropogenic heat fluxes around all the stations. **Figure 2A** shows the spatial distribution of anthropogenic heat in the Yangtze River Delta region in 2016. It can be seen that high anthropogenic heat is mainly distributed in the YRDUA region. Therefore, we further calculated the average AHF within 5 km around each station in the YRDUA region (**Figure 2B**), and then, based on the correlation between anthropogenic heat and the built-up area, the average anthropogenic heat within 5 km of the 148 stations was sorted from high to low to distinguish urban and rural reference stations; that is, the first third of stations with a high anthropogenic heat value are regarded as urban stations, and the last third as rural reference stations (**Figure 2B,C**). Finally, based on the local pattern of precipitation, the difference in sunshine with latitude, and the level of urbanization of different regions, this paper divides the YRDUA region into three sub-regions—the northern plain and hilly region (NR), the central urban agglomeration region (MR), and the southern mountainous region (SR) (**Figures 2B,C**). Then we further calculated the diurnal temperature range difference (DTR_{u-r}) between the city stationand one or more nearby rural reference stations in each sub-region in order to discuss the influence of urbanization on the DTR (**Figure 2C**).

Random Forest Model

The random forest (RF) model is currently a popular and highly flexible machine learning algorithm. The basic unit of the RF model is a decision tree. Compared with traditional statistical methods, RF has a better fitting effect on nonlinear data, and can analyze the importance of variables. The specific steps of the RF model construction process are as follows (Zeng et al., 2020): 1) In the

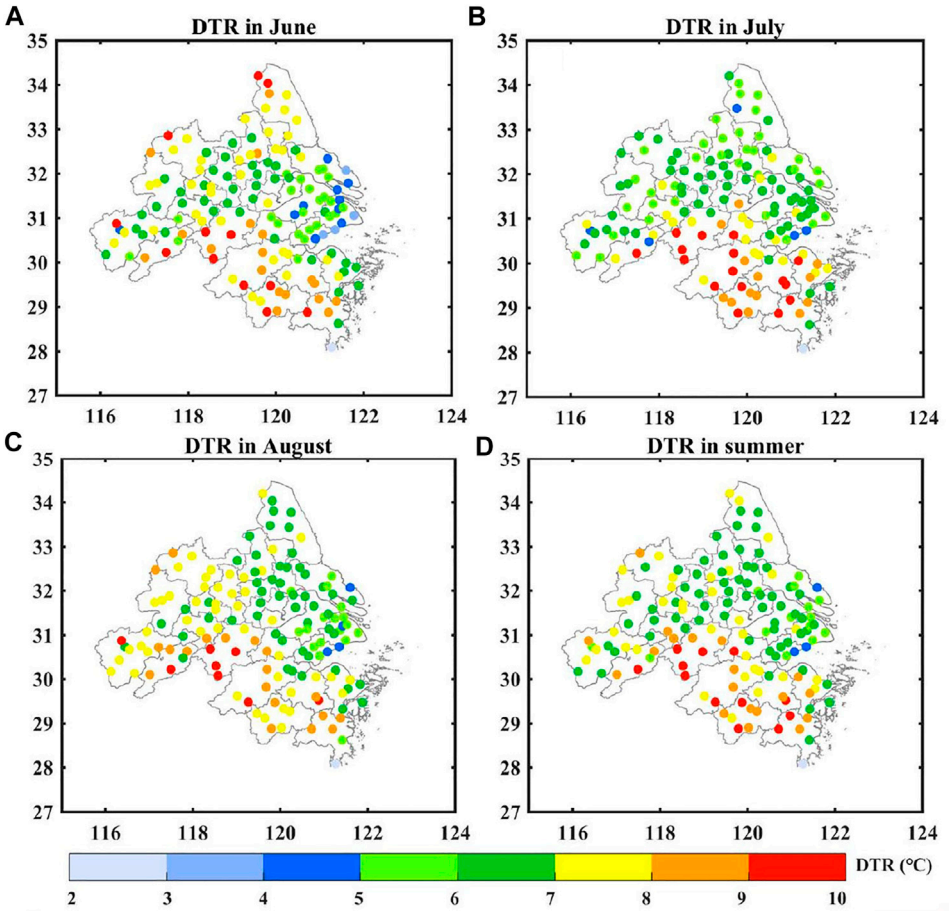

FIGURE 4 | Spatial distribution of the mean Diurnal Temperature Range (DTR) in the urban agglomeration of the Yangtze River Delta region in summer: **(A)** June, **(B)** July, **(C)** August, and **(D)** June–August.

TABLE 1 | Statistics of the DTR in three YRDUA sub-regions in June, July and August.

Subregion	Mode (°C) (Jun/Jul/Aug)	Median (°C) (Jun/Jul/Aug)	Mean (°C) (Jun/Jul/Aug)	Skewness (Jun/Jul/Aug)	Kurtosis (Jun/Jul/Aug)
NR	6.9/6.6/6.7	7.3/7.3/7.2	7.3/7.4/7.5	0.2/0.6/1.1	−0.4/1.3/2.3
MR	5.7/6.8/7.5	6.4/7.1/6.6	6.4/7.4/6.8	0.2/0.5/0.9	−0.1/0.5/2.1
SR	7.8/8.8/7.9	7.4/8.5/7.6	7.5/8.7/7.8	0.3/0.2/0.5	0.02/−0.2/0.8

N total samples, *n* times of replacement are randomly selected, n new training sets are obtained, and the unextracted part constitutes "out-of-bag" (OOB) data; 2) Each training set generates a decision tree, each node of the decision tree selects mtry from the independent variables, and branches grow according to the principle of minimum node impurity; 3) Repeat step (2) *n* times to obtain *n* decision trees to form a random forest; 4) The result of the random forest is the result obtained by the simple averaging method for each decision tree, and the prediction accuracy is determined by the average OOB of each decision tree.

Based on the RF model, we obtain the DTR difference between urban and rural areas and explore and analyze the importance of each factor influencing the DTR_{U-R}. We validated the RF model using a 10-fold cross validation (CV) method to repeatedly estimate the expected model performance based on each subset of training data in general during prediction (Wang H. et al., 2019; Yang X. et al., 2019; Zeng et al., 2020). The method of 10-fold CV involved cutting the sample into 10 subsets, reserving one subset for testing the accuracy of the model, and using the other nine subsets for training the model. This CV was repeated 10 times until every subset was guaranteed to have been used once for testing. The average value of the 10-fold CV results was taken to obtain a final prediction result. The coefficient of determination (R^2) and root-mean-square error (RMSE) were

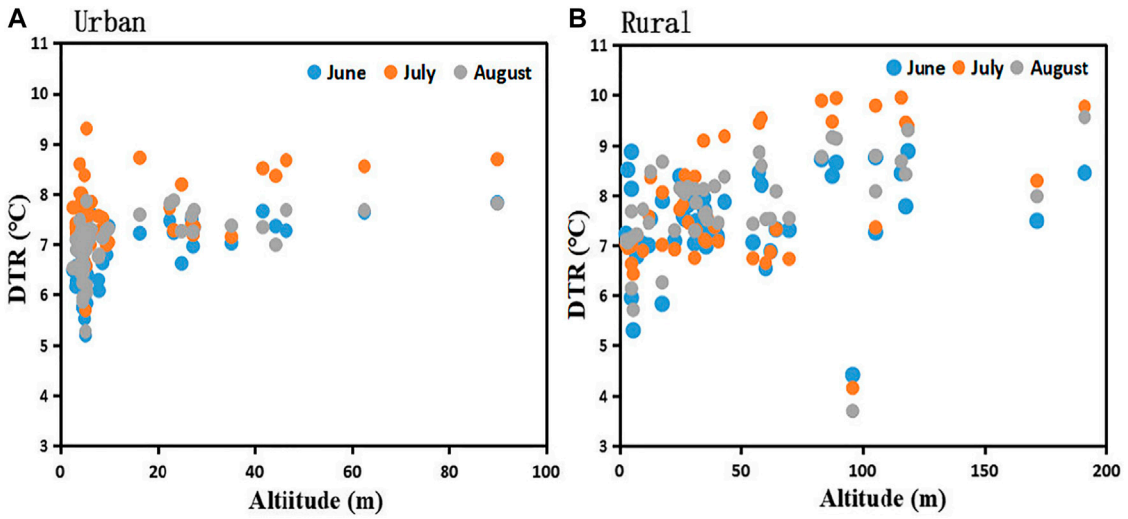

FIGURE 5 | Seasonal variation of the DTR at **(A)** urban and **(B)** rural stations in the urban agglomeration of the Yangtze River Delta region.

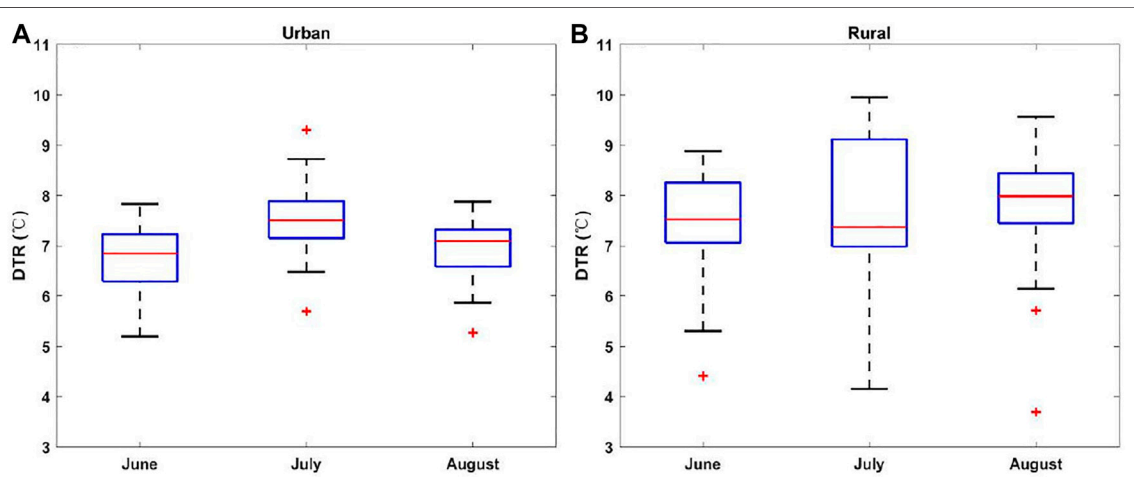

FIGURE 6 | Boxplots of the DTR of **(A)** urban and **(B)** rural stations in the urban agglomeration of the Yangtze River Delta region from June to August.

used to jointly assess the predictive performance of the 10-fold CV approach.

Finally, variance importance analysis was conducted to determine the contribution of each variable; that is, the "Mean Decrease Accuracy" (%IncMSE) and "Mean Decrease Gini" (IncNodePurity) (sorted in descending order from top to bottom) of attributes were used. A higher value of %IncMSE or IncNodePurity indicates a more important input variable.

Classification of Synoptic Weather Patterns

In this paper, T-mode principal component analysis (T-PCA) is used for the classification of SWPs, which is a computer-based objective mathematical method (Huth et al., 2008; Miao et al., 2017, 2019). It can reproduce the preset dominant SWPs without relying on the preset parameters (Ning et al., 2018; Ning et al., 2019; Yang et al., 2021). The T-PCA analysis module of the COST733 software (http://cost733.met.no/) developed by the European Scientific and Technical Research Cooperation, was used to classify the daily synoptic circulation patterns based on the 850 hPa geopotential height field. The cost733class program is a FORTRAN software package consisting of several modules for classification, evaluation and comparison of weather and circulation patterns. First, the weather data are spatially standardized and split into 10 subsets by T-PCA. Then the principal components (PCs) of weather information are estimated by applying singular value decomposition, and the PC score for each subset can be calculated after oblique rotation. Finally, the resultant subset with the highest sum will be selected

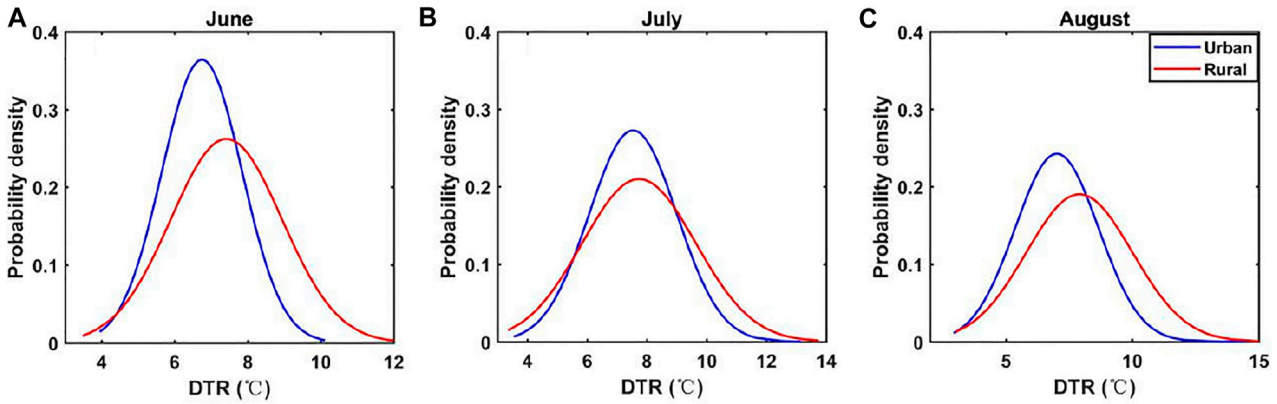

FIGURE 7 | Probability density distributions of DTR at urban and rural stations in the urban agglomeration of the Yangtze River Delta region in **(A)** June, **(B)** July, and **(C)** August.

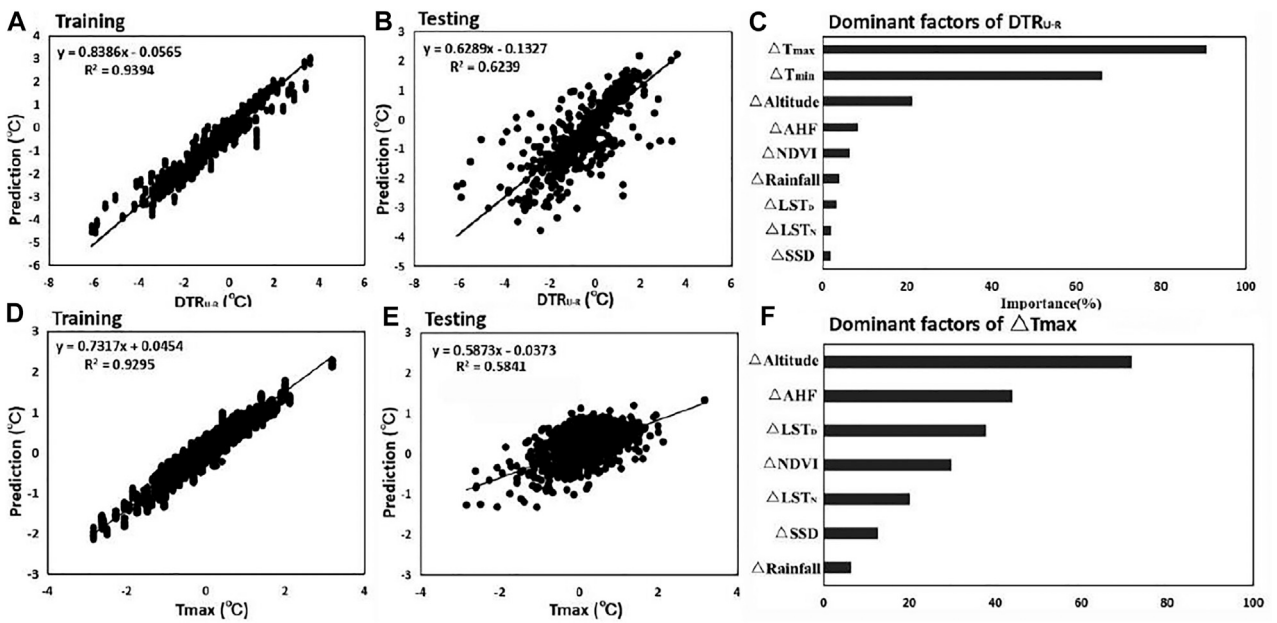

FIGURE 8 | The DTR_{U-R} **(A)** training value and **(B)** testing value and the importance of **(C)** DTR_{U-R} impact factors, and the $\triangle T_{max}$ **(D)** training value and **(E)** testing value and the importance of **(F)** $\triangle T_{max}$ impact factors, of the RF model.

by comparing 10 subsets according to contingency tables, and its types can be output as well (Philipp et al., 2014; Miao et al., 2017). To assess the performance of synoptic classification and determine the number of classes, the explained cluster variance (ECV) was selected in this study (Hoffmann and Heinke SchlüNzen, 2013; Philipp et al., 2014; Ning et al., 2019). The purpose of using this method is to analyze the differences in the characteristics of the DTR and its main driving factors between urban and rural areas under different SWPs.

Four SWPs were obtained through objective classification of the 850-hPa geopotential height field and wind field in June, July and August from 2013 to 2016. **Figure 3** shows the different patterns of the 850-hPa geopotential height field and wind field. Type 1 is southeastern subtropical high pressure (frequency 51.90%), in which the Yangtze River Delta region is located in the northwest of the subtropical high pressure, the weather system frequency is the highest, and the dominant wind is southwesterly. Type 2 is western low pressure (frequency 17.66%), in which there is a weak low pressure in the west of the Yangtze River Delta region and the dominant wind is easterly. Type 3 is controlled by wind shear in the west (frequency: 20.11%), and the dominant wind is southwesterly and northwesterly. Type 4 is southern low pressure (frequency:

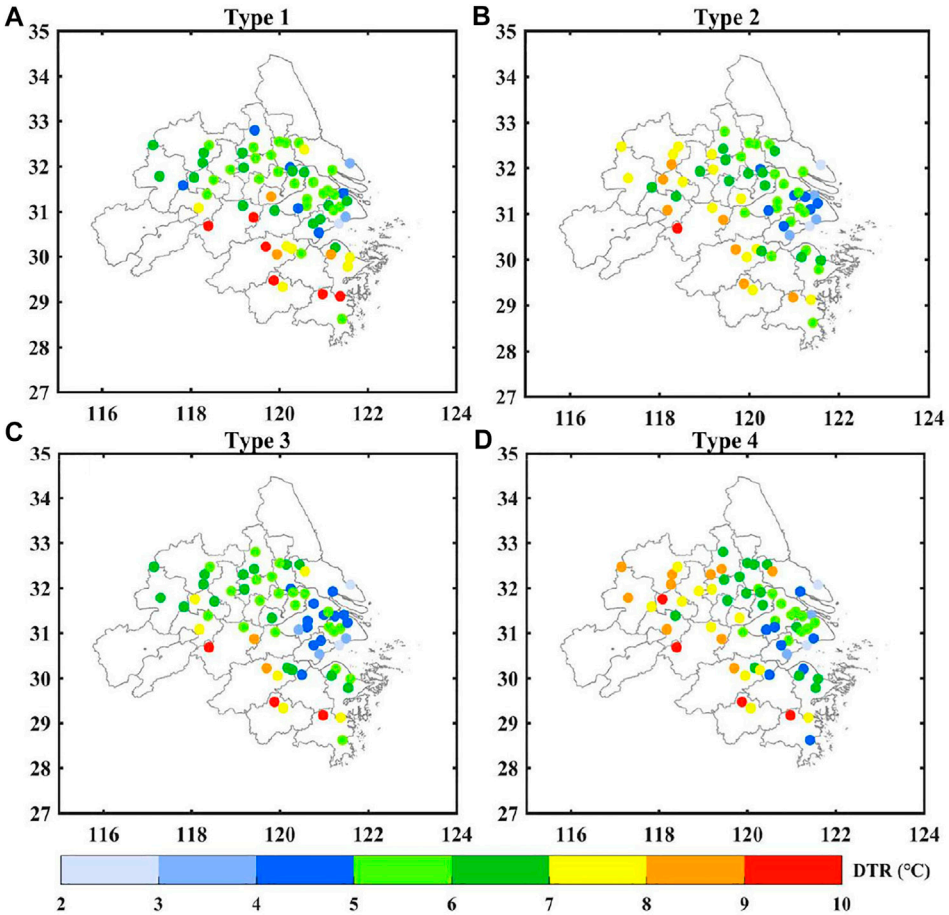

FIGURE 9 | Spatial distribution of mean DTR in the YRDUA region: **(A)** Type 1; **(B)** Type 2; **(C)** Type 3; and **(D)** Type 4.

10.35%), in which the Yangtze River Delta region is located at the top of the low pressure, the dominant wind is easterly, and the occurrence frequency of the weather system is the lowest.

RESULTS AND DISCUSSION

Urban–Rural Differences in Diurnal Temperature Range at the Monthly Scale

Figure 4 shows the spatial distribution of DTR in YRDUA in summer, showing obvious intra-seasonal variation and significant sub-regional differences. Accordingly, **Table 1** shows the mode, median, mean, skewness, and kurtosis of DTR in June, July, and August. On the whole, the DTR in the MR sub-region (with its high density of urban areas) is relatively low (most concentrated at 3–9°C), which is related to the rapid development of urbanization in this sub-region. The monthly mean DTR is significantly higher in July (7.4°C) than in June (6.4°C) and August (6.8°C). The DTR in the mountainous SR sub-region is relatively high (about 6–10°C), which also shows intra-seasonal variation, and the average DTR value is 7.5, 8.7 and 7.8°C in June, July, and August, respectively. While the DTR distribution in the NR sub-region is similar (about 6–9°C) from June to August, i.e., the average DTR value is 7.3°C in June, 7.4°C in July, and 7.5°C in August.

Figure 5 further shows the monthly variation of the summer monthly mean DTR of urban and rural stations in the YRDUA. The DTR of urban stations is the highest in July, ranging from 7 to 10°C, while the DTR in June and August is similar, ranging from 5 to 8°C. The monthly average DTRs of rural reference stations are similar, and there is no obvious seasonal variation. The DTR of rural stations range from 5 to 10°C during June–August.

Figure 6 shows boxplots of the DTR difference between urban and rural stations in the YRDUA region from June to August, showing that the DTR of urban stations in June, July and August is more concentrated than that of rural stations. As can be seen from **Figure 6**, the DTR of urban stations in July is concentrated within 7–8°C, which is basically a normal distribution, and the mean value of DTR is higher than that of June and August. The DTR of urban stations in June and August is concentrated within 6.5–7°C, in which there are small anomalies and large abnormal anomalies in July, and small anomalies in August. Overall, the peak DTR for urban stations occurs in July. The DTR of rural stations in June and August is relatively concentrated, and the

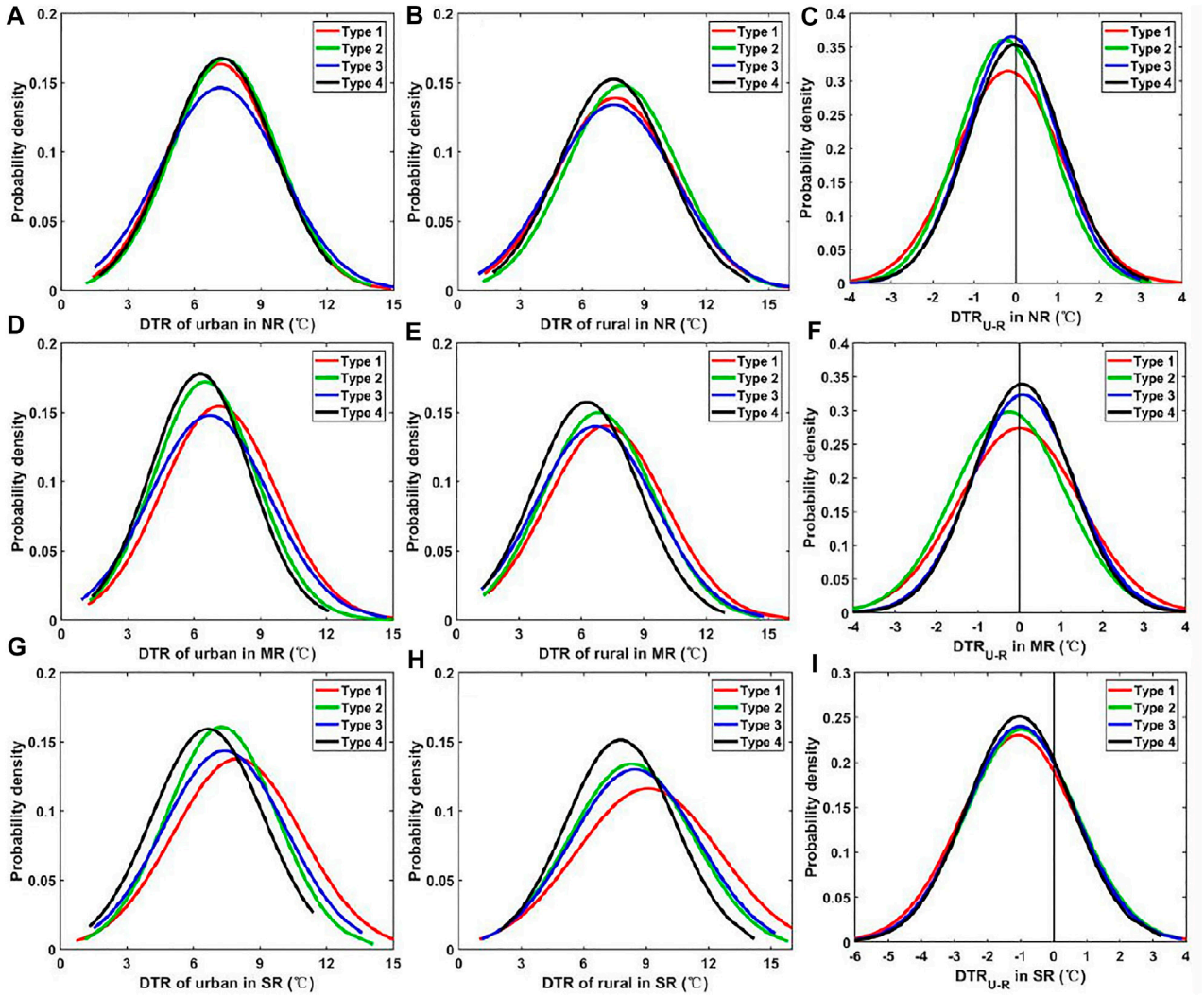

FIGURE 10 | Probability density distributions of the DTR in **(A,D,G)** urban and **(B,E,H)** rural areas, and **(C,F,I)** their difference (DTR_{U-R}), under four SWPs in NR, MR and SR, respectively.

DTR in August is basically a normal distribution, among which the DTR in July is relatively high and the value is concentrated within 7.5–9°C. Small anomalies appear in June and August at rural stations.

The probability density distributions of DTR for urban and rural stations in June, July and August are shown in **Figure 7** In June, the peak value of DTR for urban stations is about 6.5°C, and that of rural stations is about 7.5°C. In July, the peak values of DTR for urban and rural stations are around 7.5–8°C. In August, the distribution of urban DTR is concentrated at 7°C, and the peak distribution of DTR for rural stations is concentrated at 8°C. In general, the DTR of urban stations is lower than that of rural stations, which indicates that urbanization influences the decrease in DTR. Due to the development of urbanization, the concentrations of aerosols produced by human activities have increased greatly. Aerosols scatter and absorb solar radiation in the daytime, making the maximum temperature drop, while they weaken the upward longwave radiation on the surface and increase the minimum temperature at night, which leads to the decrease in DTR at urban stations (Dai et al., 1999; Zhang et al., 2011; Zheng et al., 2018; Yang et al., 2020b).

Urbanization Drivers

In order to explore what is the first dominant factor for DTR_{U-R}, $\triangle T_{max}$ or $\triangle T_{min}$, we calculated nine factor differences between urban and rural stations (**Figures 8A–C**), including the average DTR and T_{max}, T_{min}, the average surface temperature in the day (LST_D), the surface temperature at night (LST_N), anthropogenic heat emission, the NDVI within a 5-km range of meteorological observation stations, altitude, rainfall, and SSD at the 8-days scale. These nine factors of difference between urban and rural areas were the independent variables, and DTR_{U-R} the dependent variable, when building the RF machine learning model, and the output was the importance of factors affecting DTR_{U-R}. The

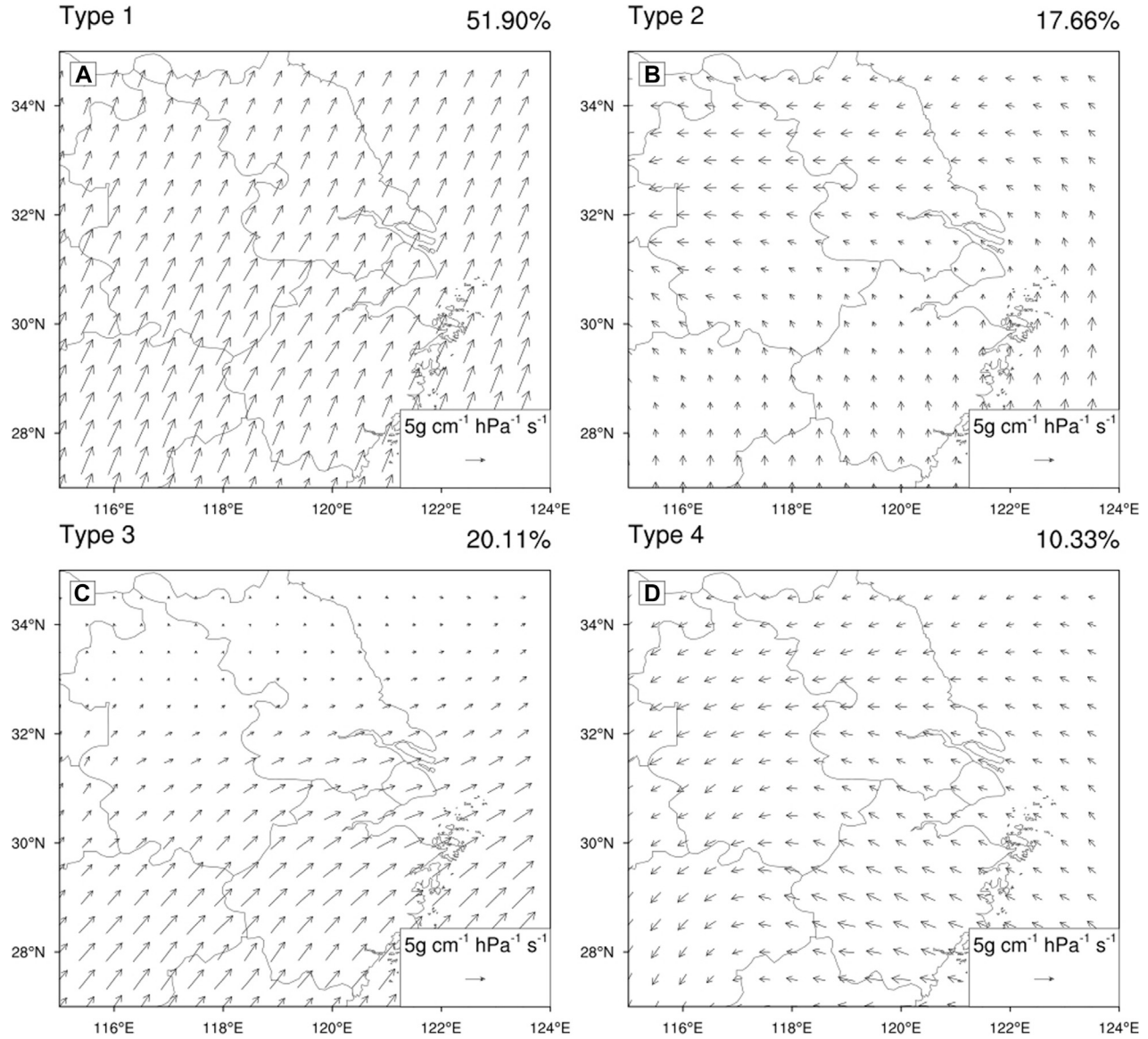

FIGURE 11 | The 850-hPa water vapor flux (WVF = Vxq/g, where q is specific humidity, g is gravitational acceleration, and V is horizonal wind; vectors; see scale arrow in the bottom right in units of 5 $gcm^{-1}hPa^{-1}s^{-1}$) under four SWPs: **(A)** Type 1; **(B)** Type 2; **(C)** Type 3; and **(D)** Type 4.

results show that the change of DTR_{U-R} is T_{max}–driven type in the urban agglomeration of the Yangtze River Delta region (**Figure 8C**). So, we further employed the RF model to check the drivers of $\triangle T_{max}$ (**Figures 8D–F**), that is, T_{max} was selected as the dependent variable, and $\triangle LST_D$, $\triangle LST_N$, $\triangle$AHF, $\triangle$NDVI, $\triangle$Altitude, $\triangle$rainfall, and $\triangle$SSD as independent variables. In addition to the direct retrieval of solar radiation, SSD also includes the influence of aerosols, cloud cover, and precipitation on the daily global solar radiation (Wang K. et al., 2012, Wang Y. et al., 2012, 2013; Zeng et al., 2020).

The RF model was not only used to reveal the possible factors related to the difference in DTR between urban and rural stations, but also to evaluate the relative importance and contribution of these factors. Firstly, 10-fold CV was used to test the reliability of the RF model. **Figures 8A,B,D,E** show the model training and validation of DTR_{U-R} and $\triangle T_{max}$. It can be seen that the results of RF training and testing are good, i.e., the R^2 value of the traning and testing of DTR_{U-R} is 0.94 and 0.62, respectively, and the R^2 value of training and the testing of $\triangle T_{max}$ is 0.93 and 0.58, respectively, indicating that the RF model is reasonable and reliable for analyzing the impact factors of DTR_{U-R}.

Further analysis of the RF model results provides the order of importance of the factors affecting DTR_{U-R}. As shown in **Figure 8C**, $\triangle T_{max}$ is more important to DTR_{U-R} than $\triangle T_{min}$, implying that the comprehensive effect of urbanization (changed land use and soil water content) and aerosol pollution (changed

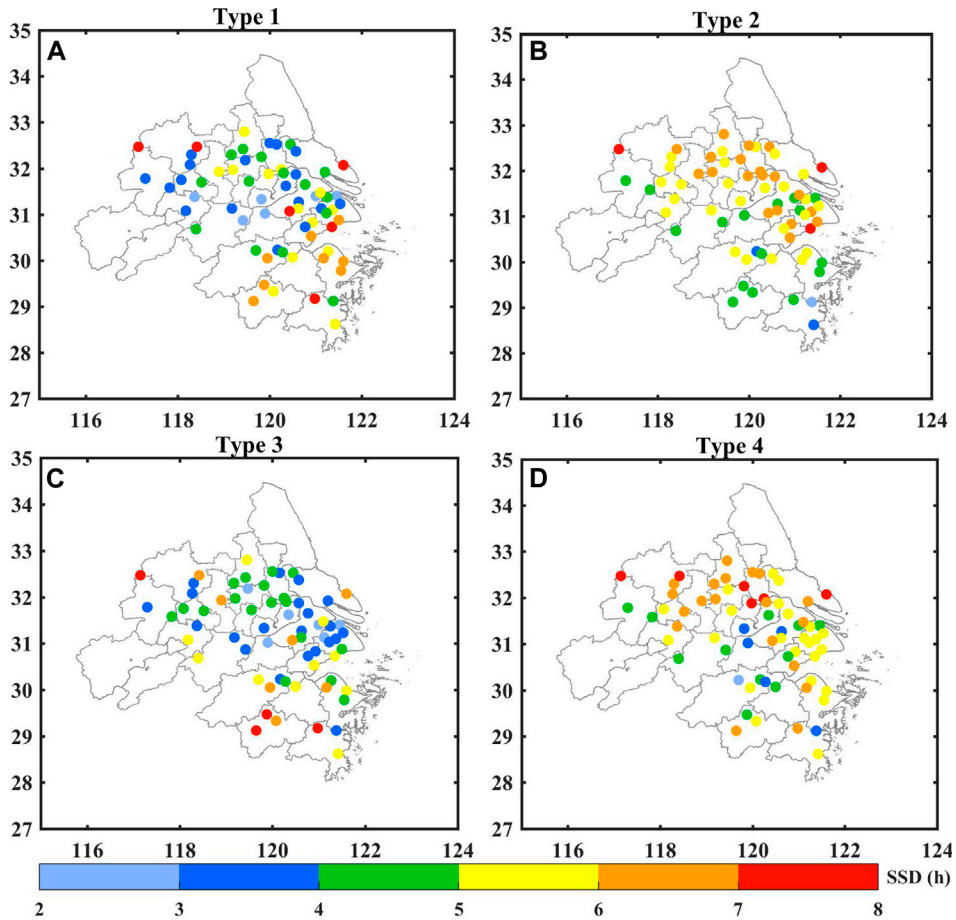

FIGURE 12 | As in **Figure 9** but for mean Sunshine Duration (SSD).

solar radiation and cloud fraction) has a more obvious impact on daytime air temperature in urban areas, relative to rural areas (Dai et al., 1999; Sun et al., 2019; Yang et al., 2020b). The development of urbanization results in elevated concentrations of the aerosols produced by human activities, which leads to increased cloud cover (Wang K. et al., 2012, Wang Y. et al., 2012, 2013; Yang et al., 2020b; Zeng et al., 2020). The existence of aerosols and clouds can have an impact on solar radiation. Aerosols and cloud can reduce daytime incoming shortwave radiation at the surface and trap more upward longwave radiation from the surface and emit more downward longwave radiation to warm the near-surface atmosphere during nighttime. Relative to clean days, this radiation effect will easily lead to a smaller (larger) T_{max} (T_{min}) during pollution days, leading to a smaller DTR over urban areas. These are consistent with previous studies (Dai et al., 1999; Zhang et al., 2011; Zheng et al., 2018; Yang et al., 2020b), and so the variation trend of DTR_{U-R} also increases. However, due to different regional environments, the thermal environment around meteorological stations will also be different, such as the difference in land-use types, vegetation coverage, etc. The most important environmental factors in this regard are Altitude, AHF, and NDVI, followed by rainfall, SSD, LST_N and LST_D,. Urban–rural differences of AHF play an important role in the magnitude of DTR_{U-R} (Wang K. et al., 2012, Wang Y., et al., 2012, 2013; Zeng et al., 2020). The development of urbanization will also change the DTR by changing the nature of the urban underlying surface. Gallo et al. (1996) pointed out that different vegetation coverage around meteorological stations will cause different DTRs, and the DTRs of farms and towns are larger than those of cities. In conclusion, the difference in AHF is one of the potentially important driving factor of urbanization for DTR_{U-R}. In general, the $\triangle T_{max}$, $\triangle$Altitude, $\triangle$AHF, $\triangle$NDVI, $\triangle$LSTD, $\triangle$LSTN between urban and rural areas are almost unchanged, which are more important relative to the various $\triangle$SSD and $\triangle$rainfall between urban and rural areas. This is because $\triangle$SSD and $\triangle$rainfall are also modulated by various synoptic patterns in urban and rural areas.

Urban–Rural Differences in DTR Under Different Synoptic Weather Patterns

To better compare the DTR at urban stations with rural stations, we have excluded the suburban stations from the below analysis.

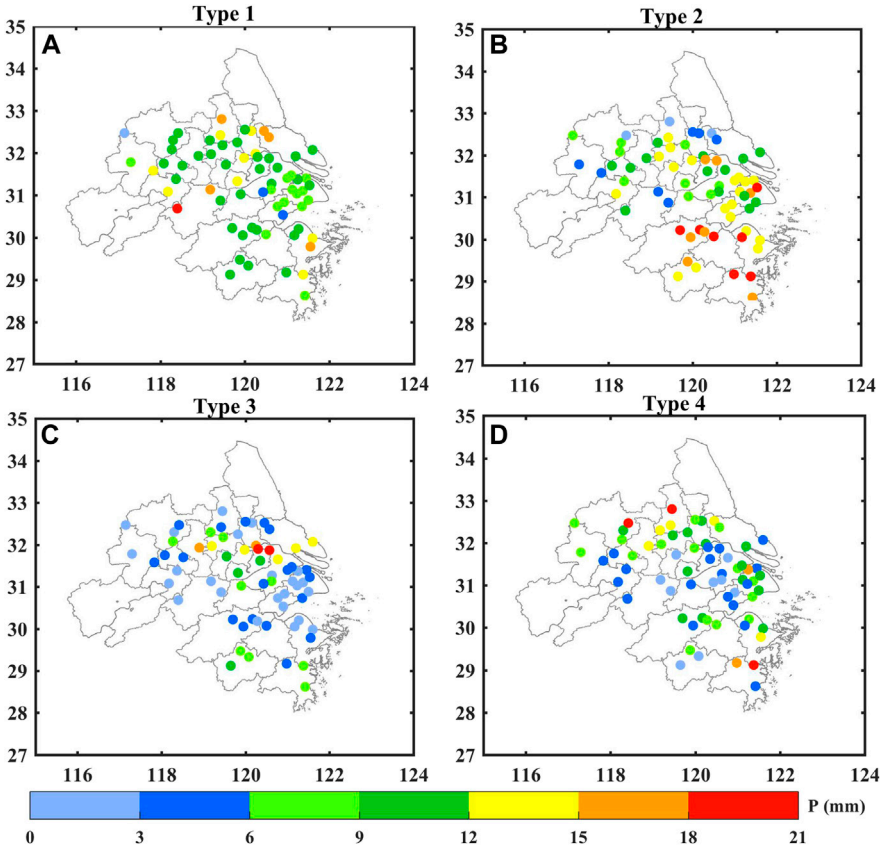

FIGURE 13 | As in **Figure 9** but for mean precipitation.

Figure 9 shows the spatial distributions of mean DTR under the four synoptic circulation patterns. In general, under these four weather patterns, the DTR in the southern region is the highest, followed by the northern region, and the DTR in the central region is the lowest (ranging from 2 to 6°C), mainly because the central-region DTR is most significantly affected by urbanization. Specifically, the DTR in the three sub-regions of YRDUA is greatly affected by the synoptic circulation, and the DTRs under the four SWPs are significantly different. For example, the DTR in the northern region is high under type 4 but low under type 1, in the central urban agglomeration it is high under type 1 and low under type 3, while in the southern region it is high under type 1 and low under type 2.

The probability density distributions of DTR for urban and rural stations in the three sub-regions under the four SWPs are shown in **Figures 10A,B,D,E,G,H**. In NR, the DTR peak distributions of urban stations are concentrated at about 7–8°C under the four weather patterns. Meanwhile, the peak distributions of rural stations are also concentrated at about 7–8°C under type 1, 3 and 4, whereas under type 2 it is about 8–9°C. In MR, the DTR peak distributions of urban and rural stations are concentrated at about 6–8°C under the four weather patterns. In SR, the peak values of DTR for urban stations are concentrated at about 6–8°C, and that of rural stations are concentrated at about 7–8°C under type 2, 3 and 4, while that of urban stations at about 8–9°C and rural stations at about 9–10°C under type 1. In order to further compare the influence of weather systems on the difference in DTR between urban and rural areas, the probability density distributions of DTR_{U-R} under different weather patterns were statistically analyzed (**Figures 10C,F,I**). The results show that the probability density distribution of DTR_{U-R} under the four weather types tends to be negative on the whole, and the peak values are concentrated within −1–0°C. The absolute value of the peak value of DTR_{U-R} in NR and MR under the four weather patterns follow the order Type 2 > Type 1 > Type 3 > Type 4. It can be concluded that the difference in DTR between urban and rural areas in NR and MR under Type 4 is relatively small, while that under Type 2 is the largest. But the absolute values of the peak value of DTR_{U-R} in SR under the four weather patterns are similar and higher than that of in NR and MR. However, the DTR also is regulated by meteorological conditions (precipitation and SSD) under different SWPs, which is further analyzed below.

Roles of Synoptic Weather Patterns

Local meteorological factors are closely related to SWPs. The increase in global precipitation is one of the reasons for the downward trend in global DTR, but the relationship between

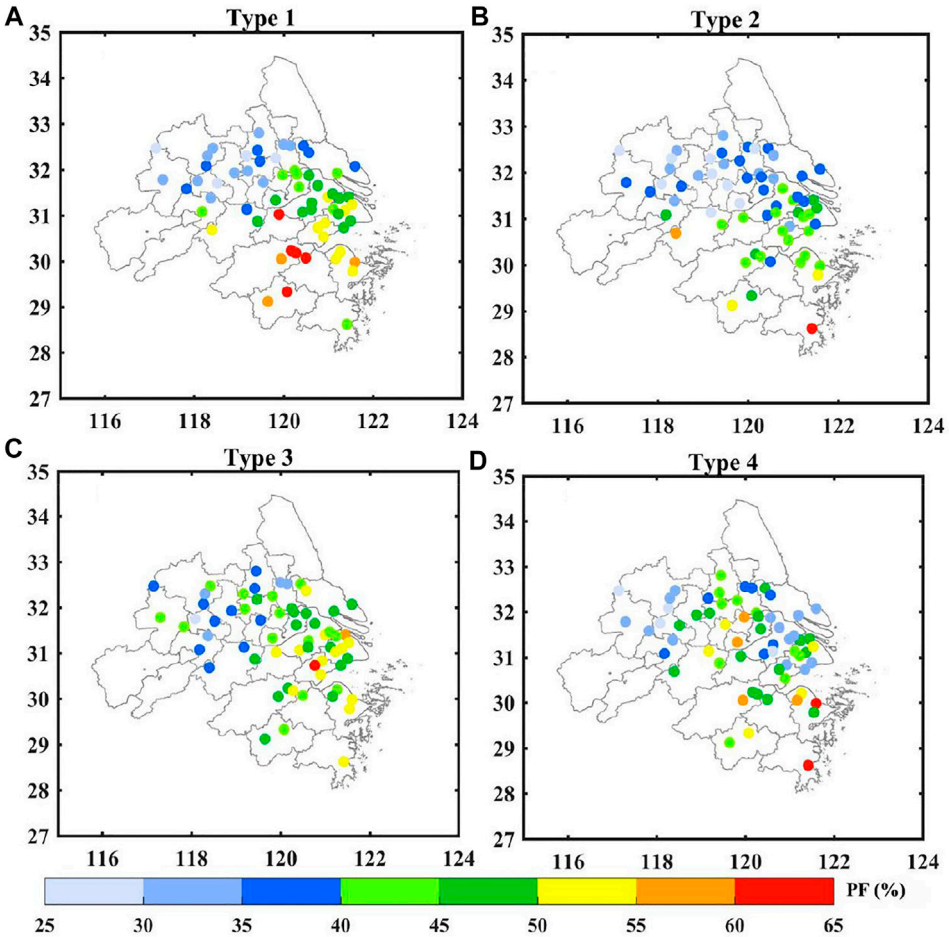

FIGURE 14 | As in **Figure 9** but for mean precipitation frequency (PF = D_P/D_T×100%, where D_P is the number of days of precipitation, and D_T is total number of days).

precipitation and DTR is more based on the good correlation between precipitation, cloud cover, and soil water content (Dai et al., 1997, 1998, 1999; Sun et al., 2019). Cloud cover and soil water content mainly lead to a decrease in DTR by decreasing the T_{max}. Therefore, increased cloud cover and precipitation will slow down the rising trend of T_{max} and have relatively little effect on T_{min} (Dai et al., 1999), which is consistent with our RF model results showing that the urban–rural difference in T_{max} is most important to DTR_{U-R}.

Cloud cover and soil water content are closely related to water vapor flux in summer, so **Figure 11** shows the 850-hPa water vapor flux in the urban agglomeration of the YRDUA region. Combined with the classification results (**Figure 3**), we found that, under the type 1 synoptic circulation, the YRDUA is affected by the southeastern subtropical high pressure, and the southwest has strong water vapor transport, large water vapor flux, and more precipitation. The water vapor under type 2 synoptic circulation comes from the south, and the water vapor flux is small. Type 3 water vapor mainly comes from the southwest, and the water vapor flux is large in the south of YRDUA, but small in the north. The water vapor of type 4 comes from the southeast ocean area, and the water vapor flux is small.

The SSD reflects the influence of cloud cover and precipitation on the daily total solar radiation, so the variation of DTR can be discussed through the influence of SSD and precipitation on temperature. **Figures 12**, **13** show the average distribution of sunshine duration and local precipitation under the four SWPs. Due to the difference in the synoptic circulation situation and water vapor flux, there are obvious differences in local precipitation and sunshine duration under the four SWPs. Specifically, compared with **Figure 9** and **Figure 11**, less precipitation and longer SSD favor a larger DTR in most sub-regions, e.g., the NR sub-region under type 2, the MR sub-region under type 4, and the SR sub-region under types 1, 3 and 4,. Meanwhile, more precipitation and shorter SSD induce a smaller DTR, e.g., in the NR sub-region under type 1, the MR sub-region under type 1, and the SR sub-region under type 2.

Because urbanization has increased extreme precipitation, we further quantified the precipitation frequency (PF) (**Figure 14**). Compared with **Figure 13**, precipitation under type 1 and 2 is

large, but the PF is small, which indicates that urban extreme precipitation is more significant under type 1 and 2, especially in the central urban agglomeration under type 2. Combined with **Figure 10**, the difference in DTR between urban and rural areas is the most significant under type 2. Due to the impervious nature of the urban underlying surface, the soil moisture increases when precipitation occurs, while soil moisture increases the releases of surface latent heat and slows down the rise in temperature during the day (Dai et al., 1999), which also reduce the urban DTR and increase the urban–rural DTR differences. This also indicates that precipitation plays an important role in the impact of urbanization on DTR.

CONCLUSION

Through objective weather classification and machine learning modeling, this paper analyzes the difference characteristics and influencing factors of DTR and DTR_{U-R} in YRDUA under different SWPs (according to the differences in the climate background and underlying surface properties). The main conclusions are as follows:

The YRDUA region is mainly controlled by four SWPs in the 850-hPa geopotential height field. The average values of DTR under each SWP exhibit obvious sub-regional differences in space: the southern subregion is the highest, followed by the northern subregion, and the middle subregion is the lowest. The lower DTR in the middle sub-region is mainly affected by its high levels of urbanization and anthropogenic heat emissions. The average DTR in the three sub-regions of YRDUA present significant differences in DTR under the four SWPs, indicating that SWPs play a greater role in regulating the DTR in YRDUA. In general, the DTR of urban stations is smaller than that of rural stations under all four SWPs, and the urban–rural difference in AHF is one of the potentially important urbanization-related driver affecting DTR_{U-R}. The order of the absolute value of the DTR_{U-R} peak in NR and MR under the four SWPs is as follows: type 2 > type 1 > type 3 > type 4. In particular, affected by urban extreme precipitation, the DTR under Type 2 is the largest, while the absolute values of the peak DTR_{U-R} in SR under the four weather patterns are similar and higher than that of in NR and MR. The present work provides evidence that the complex features of levels of urbanization and atmospheric circulation patterns on synoptic scales can modulate the daily variations of DTR. This study's findings help towards furthering our understanding of the response of DTR in an urban agglomeration to different SWPs via the modulation of local meteorological conditions (e.g., precipitation, SSD, etc.).

Overall, whilst the present paper discusses the dual impact of urbanization factors and SWPs on DTR_{U-R} on the synoptic scale, the influence of changes in the occurrence frequencies of different SWPs at the interannual scale on the long-term trend of DTR requires further exploration.

DATA AVAILABILITY STATEMENT

The data analyzed in this study is subject to the following licenses/restrictions: The data were provided by the China Meteorological Data Service Center. Requests to access these datasets should be directed to All MODIS data can be downloaded from https://lpdaac.usgs.gov. Surface meteorological data can be collected from the China Meteorological Data Service Center (http://data.cma.cn/en).

AUTHOR CONTRIBUTIONS

MG: Conceptualization, Data curation, Formal analysis, Writing—original draft preparation, Writing—Reviewing and Editing; MZ: Data curation; HW: Methodology, Formal analysis, Writing—original draft preparation; LW: Conceptualization, Formal analysis, Writing—original draft preparation; SL: Methodology; LZ: Methodology, Writing—Reviewing and Editing; YZ: Data curation; YL: Methodology.

FUNDING

This study is supported by National Key Research and Development Program of China (2016YFC0203300), the National Natural Science Foundation of China (42061134009 and 42075072) and Innovation and Entrepreneurship Training Program for College Students of Nanjing University of Information Science and Technology.

REFERENCES

Braganza, K., Karoly, D. J., and Arblaster, J. M. (2004). Diurnal Temperature Range as an index of Global Climate Change during the Twentieth century. *Geophys. Res. Lett.* 31, a–n. doi:10.1029/2004GL019998

Cai, X. H. (2008). Footprint Analysis in Micrometeorology and its Extended Applications. *Chin. J. Atmos. Sci.* 32, 123–132. doi:10.3878/j.issn.1006-9895

Chen, B., and Shi, G. Y. (2012). Estimation of the Distribution of Global Anthropogenic Heat Flux. *Atmos. Oceanic Sci. Lett.* 5, 108–112. doi:10.1080/16742834.2012.11446974

Chen, B., Dong, L., Liu, X., Shi, G. Y., Chen, L., Nakajima, T., et al. (2016). Exploring the Possible Effect of Anthropogenic Heat Release Due to Global Energy Consumption upon Global Climate: a Climate Model Study. *Int. J. Climatol.* 36, 4790–4796. doi:10.1002/joc.4669

Chen, B., Dong, L., Shi, G., Li, L.-J., and Chen, L.-F. (2014). Anthropogenic Heat Release: Estimation of Global Distribution and Possible Climate Effect. *J. Meteorol. Soc. Jpn.* 92A, 157–165. doi:10.2151/jmsj.2014-a10

Chen, B., Shi, G., Wang, B., Zhao, J., and Tan, S. (2012). Estimation of the Anthropogenic Heat Release Distribution in China from 1992 to 2009. *Acta Meteorol. Sin* 26 (4), 507–515. doi:10.1007/s-13351-012-0409-y10.1007/s13351-012-0409-y

Chen, B., Zhao, J.-Q., Chen, L.-F., and Shi, G.-Y. (2015). Reply to the Comments of F. Fujibe on "Anthropogenic Heat Release: Estimation of Global Distribution and Possible Climate Effect" by Chen, B. et al. *J. Meteorol. Soc. Jpn.* 93 (4), 505–508. doi:10.2151/jmsj.2015-028

Chen, G., Wang, D., Wang, Q., Li, Y., Wang, X., Hang, J., et al. (2020). Scaled Outdoor Experimental Studies of Urban thermal Environment in Street canyon Models with Various Aspect Ratios and thermal Storage. *Sci. Total Environ.* 726, 138147. doi:10.1016/j.scitotenv.2020.138147

Chen, Q., Ding, M., Yang, X., Hu, K., and Qi, J. (2018). Spatially Explicit Assessment of Heat Health Risk by Using Multi-Sensor Remote Sensing Images and Socioeconomic Data in Yangtze River Delta, China. *Int. J. Health Geogr.* 17, 15. doi:10.1186/s12942-018-0135-y

Chen, Tiexi., and Chen, Xing. (2007). Variation of Diurnal Temperature Range in China in the Past 50 Years. *Plateau Meteorology* 26 (1), 150–157. [in Chinese, with English summary].

Dai, A., Fung, I. Y ., and Del Genio, A. D. (1997). Surface Observedglobal Land Precipitation Variations during 1900ns. *during* 10, 2943943cip. doi:10.1175/1520-0442(1997)010<2943:soglpv>2.0.co;2

Dai, A., Trenberth, K. E., and Karl, T. R. (1999). Effects of Clouds, Soil Moisture, Precipitation, and Water Vapor on Diurnal Temperature Range. *J. Clim.* 12 (8), 2451–2473. doi:10.1175/1520-0442(1999)012<2451:eocsmp>2.0.co;2

Dai, A., Trenberth, K. E., and Karl, T. R. (1998). Global Variations in Droughts and Wet Spells: 1900-1995. *Geophys. Res. Lett.* 25, 3367–3370. doi:10.1029/98gl52511

Dong, D., and Huang, G. (2015). Relationship Between Altitude and Variation Characteristics of the Maximum Temperature, Minimum Temperature, and Diurnal Temperature Range in China. *Chinese J. Atmos. Sci.* 39 (5), 1011–1024. [in Chinese, with English summary]. doi:10.3878/j.issn.1006-9895.1501.14291

Easterling, D. R., Evans, J. L., Groisman, P. Y., Karl, T. R., Kunkel, K. E., and Ambenje, P. (2000). Observed Variability and Trends in Extreme Climate Events: A Brief Review*. *Bull. Amer. Meteorol. Soc.* 81 (3), 417–425. doi:10.1175/1520-0477(2000)081<0417:ovatie>2.3.co;2

Easterling, D. R. (1997). Maximum and Minimum Temperature Trends for the globe. *Science* 277 (5324), 364–367. doi:10.1126/science.277.5324.364

Feddema, J. J. (2005). The Importance of Land-Cover Change in Simulating Future Climates. *Science* 310 (5754), 1674–1678. doi:10.1126/science.1118160

Forster, P. M. d. F., and Solomon, S. (2003). Observations of a "Weekend Effect" in Diurnal Temperature Range. *Proc. Natl. Acad. Sci.* 100 (20), 11225–11230. doi:10.1073/pnas.2034034100

Gallo, K. P., Easterling, D. R., and Peterson, T. C. (1996). The Influence of Land Use/land Cover on Climatological Values of the Diurnal Temperature Range. *J. Clim.* 9 (11), 2941–2944. doi:10.1175/1520-0442(1996)009<2941:tioluc>2.0.co;2

Hoffmann, P., and Schlünzen, K. H. (2013). Weather Pattern Classification to Represent the Urban Heat Island in Present and Future Climate. *J. Appl. Meteorol. Climatol.* 52 (12), 2699–2714. doi:10.1175/JAMC-D-12-065.1

Hua, L.-J., Ma, Z.-G., and Zeng, Z.-M. (2006). The Comparative Analysis of the Changes of Extreme Temperature and Extreme Diurnal Temperature Range of Large Cities and Small Towns in Eastern China. *Chin. J. Atmos. Sci. (in Chinese)* 30 (1), 80–92. doi:10.3878/j.issn.1006-9895.2006.01.07

Huth, R., Beck, C., Philipp, A., Demuzere, M., Ustrnul, Z., Cahynová, M., et al. (2008). Classifications of Atmospheric Circulation Patterns. *Ann. N. Y. Acad. Sci.* 1146, 105–152. doi:10.1196/annals.1446.019

Jiang, S., Lee, X., Wang, J., and Wang, K. (2019). Amplified Urban Heat Islands during Heat Wave Periods. *J. Geophys. Res. Atmos.* 124, 7797–7812. doi:10.1029/2018JD030230

Kalnay, E., and Cai, M. (2003). Impact of Urbanization and Land-Use Change on Climate. *Nature* 423 (6939), 528–531. doi:10.1038/nature01675

Kan, H., London, S. J., Chen, H., Song, G., Chen, G., Jiang, L., et al. (2007). Diurnal Temperature Range and Daily Mortality in Shanghai, China. *Environ. Res.* 103, 424–431. doi:10.1016/j.envres.2006.11.009

Kuang, W., Zhang, S., Li, X., and Lu, D. (2000–2018). A 30 M Resolution Dataset of China's Urban Impervious Surface Area and green Space, 2000-2018. *Earth Syst. Sci. Data* 13, 63–82. doi:10.5194/essd-13-63-2021

Lim, Y.-H., Hong, Y.-C., and Kim, H. (2012). Effects of Diurnal Temperature Range on Cardiovascular and Respiratory Hospital Admissions in Korea. *Sci. Total Environ.* 417-418, 55–60. doi:10.1016/j.scitotenv.2011.12.048

Liu, B., Xu, M., Henderson, M., Qi, Y., and Li, Y. (1955–2000). Taking China's Temperature: Daily Range, Warming Trends, and Regional Variations. *J. Clim.* 17 (22), 4453–4462. doi:10.1175/3230.1

Liu, L., Li, Z., Yang, X., Gong, H., Li, C., and Xiong, A. (2016). The Long-Term Trend in the Diurnal Temperature Range over Asia and its Natural and Anthropogenic Causes. *J. Geophys. Res. Atmos.* 121, 3519–3533. doi:10.1002/2015JD024549

Lobell, D. B. (2007). Changes in Diurnal Temperature Range and National Cereal Yields. *Agric. For. meteorology* 145 (3-4), 229–238. doi:10.1016/j.agrformet.2007.05.002

Luo, M., and Lau, N.-C. (2018). Increasing Heat Stress in Urban Areas of Eastern China: Acceleration by Urbanization. *Geophys. Res. Lett.* 45 (23), 13060–13069. doi:10.1029/2018gl080306

Luo, M., and Lau, N.-C. (2019). Urban Expansion and Drying Climate in an Urban Agglomeration of east China. *Geophys. Res. Lett.* 46 (2), 6868–6877. doi:10.1029/2019gl082736

Miao, Y., Guo, J., Liu, S., Liu, H., Li, Z., Zhang, W., et al. (2017). Classification of Summertime Synoptic Patterns in Beijing and Their Associations with Boundary Layer Structure Affecting Aerosol Pollution. *Atmos. Chem. Phys.* 17 (4), 3097–3110. doi:10.5194/acp-17-3097-2017

Miao, Y., Liu, S., and Huang, S. (2019). Synoptic Pattern and Planetary Boundary Layer Structure Associated with Aerosol Pollution during winter in Beijing, China. *Sci. Total Environ.* 682, 464–474. doi:10.1016/j.scitotenv.2019.05.199

Mohan, M., and Kandya, A. (2015). Impact of Urbanization and Land-Use/land-Cover Change on Diurnal Temperature Range: A Case Study of Tropical Urban Airshed of India Using Remote Sensing Data. *Sci. Total Environ.* 506-507, 453–465. doi:10.1016/j.scitotenv.2014.11.006

Ning, G., Wang, S., Yim, S. H. L., Li, J., Hu, Y., Shang, Z., et al. (2018). Impact of Low-Pressure Systems on winter Heavy Air Pollution in the Northwest Sichuan Basin, China. *Atmos. Chem. Phys.* 18 (18), 13601–13615. doi:10.5194/acp-18-13601-2018

Ning, G., Yim, S. H. L., Wang, S., Duan, B., Nie, C., Yang, X., et al. (2019). Synergistic Effects of Synoptic Weather Patterns and Topography on Air Quality: a Case of the Sichuan Basin of China. *Clim. Dyn.* 53 (11), 6729–6744. doi:10.1007/s00382-019-04954-3

Philipp, A., Beck, C., Esteban, P., Krennert, T., Lochbihler, K., Spyros, P., et al. (2014). COST733CLASS v1.2 User guide. Available at: www.researchgate.net/publication/269335894_COST733CLASS_v12_User_guide.

Qi, Qinghua., Cai, Rongshuo., and Guo, Haixia. (2019). The Climatological Features and Peculiarities of Temperature over Eastern China. *Scientia Geographica Sinica (in Chinese)* 39 (08), 1340–1350. doi:10.13249/j.cnki.sgs.2019.08.016

Shen, X., Liu, B., Li, G., Wu, Z., Jin, Y., Yu, P., et al. (2014). Spatiotemporal Change of Diurnal Temperature Range and its Relationship with sunshine Duration and Precipitation in china. *J. Geophys. Res. Atmos.* 119 (23), 163–213. doi:10.1002/2014jd022326

Shi, T., Huang, Y., Sun, D., Lu, G., and Yang, Y. (2021). A New Method for Correcting Urbanization-Induced Bias in Surface Air Temperature Observations: Insights from Comparative Site-Relocation Data. *Front. Environ. Sci.* 9, 625418. doi:10.3389/fenvs.2021.625418

Shi, T., Huang, Y., Wang, H., Shi, C.-E., and Yang, Y.-J. (2015). Influence of Urbanization on the thermal Environment of Meteorological Station: Satellite-Observed Evidence. *Adv. Clim. Change Res.* 6, 7–15. doi:10.1016/j.accre.2015.07.001

Sun, X., Ren, G., You, Q., Ren, Y., Xu, W., Xue, X., et al. (2019). Global Diurnal Temperature Range (DTR) Changes since 1901. *Clim. Dyn.* 52, 3343–3356. doi:10.1007/s00382-018-4329-6

Tao, F., Yokozawa, M., Liu, J., and Zhang, Z. (2008). Climate-crop Yield Relationships at Provincial Scales in China and the Impacts of Recent Climate Trends. *Clim. Res.* 38 (1), 83–94. doi:10.3354/cr00771

Vose, R. S., Easterling, D. R., and Gleason, B. (2005). Maximum and Minimum Temperature Trends for the globe: an Update through 2004. *Geophys. Res. Lett.* 32, L23822. doi:10.1029/2005GL024379

Wang, H., Li, J., Gao, Z., Yim, S. H., Shen, H., Ho, H. C., et al. (2019). High-Spatial-Resolution Population Exposure to PM2.5 Pollution Based on Multi-Satellite Retrievals: A Case Study of Seasonal Variation in the Yangtze River Delta, China in 2013. *Remote Sensing* 11, 2724. doi:10.3390/rs11232724

Wang, K., Ye, H., Chen, F., Xiong, Y., and Wang, C. (2012). Urbanization Effect on the Diurnal Temperature Range: Different Roles under Solar Dimming and Brightening*. *J. Clim.* 25 (3), 1022–1027. doi:10.1175/jcli-d-10-05030.1

Wang, Y., Yang, Y., Han, S., Wang, Q., and Zhang, J. (2013). Sunshine Dimming and Brightening in Chinese Cities (1955-2011) Was Driven by Air Pollution rather Than Clouds. *Clim. Res.* 56 (1), 11–20. doi:10.3354/cr01139

Wang, Y., Yang, Y., Zhao, N., Liu, C., and Wang, Q. (2012). The Magnitude of the Effect of Air Pollution on sunshine Hours in China. *J. Geophys. Res.* 117, a–n. doi:10.1029/2011jd016753

Xue, W., Guo, J., Zhang, Y., Zhou, S., Wang, Y., Miao, Y., et al. (2019). Declining Diurnal Temperature Range in the North China Plain Related to Environmental Changes. *Clim. Dyn.* 52 (9–10), 6109–6119. doi:10.1007/s00382-018-4505-8

Yang, J., Liu, H.-Z., Ou, C.-Q., Lin, G.-Z., Zhou, Q., Shen, G.-C., et al. (2013). Global Climate Change: Impact of Diurnal Temperature Range on Mortality in Guangzhou, China. *Environ. Pollut.* 175, 131–136. doi:10.1016/j.envpol.2012.12.021

Yang, X., Ruby Leung, L., Zhao, N., Zhao, C., Qian, Y., Hu, K., et al. (2017). Contribution of Urbanization to the Increase of Extreme Heat Events in an Urban Agglomeration in east China. *Geophys. Res. Lett.* 44, 6940–6950. doi:10.1002/2017GL074084

Yang, X., Ye, T., Zhao, N., Chen, Q., Yue, W., Qi, J., et al. (2019). Population Mapping with Multisensor Remote Sensing Images and Point-Of-Interest Data. *Remote Sensing* 11, 574. doi:10.3390/rs11050574

Yang, Y.-J., Wu, B.-W., Shi, C.-e., Zhang, J.-H., Li, Y.-B., Tang, W.-A., et al. (2013). Impacts of Urbanization and Station-Relocation on Surface Air Temperature Series in Anhui Province, China. *Pure Appl. Geophys.* 170 (11), 1969–1983. doi:10.1007/s00024-012-0619-9

Yang, Y., Wang, Rui., Chen, Fengjiao., Liu, Chao., Bi, Xueyan., and Huang, Meng. (2021). Synoptic Weather Patterns Modulate the Frequency, Type and Vertical Structure of Summer Precipitation over Eastern China: A Perspective from GPM Observations. *Atmos. Res.* 249, 05342. doi:10.1016/j.atmosres.2020.105342,

Yang, Y., Zhang, M., Li, Q., Chen, B., Gao, Z., Ning, G., et al. (2020a). Modulations of Surface thermal Environment and Agricultural Activity on Intraseasonal Variations of Summer Diurnal Temperature Range in the Yangtze River Delta of China. *Sci. Total Environ.*, 736. 139445. doi:10.1016/j.scitotenv.2020.139445

Yang, Y., Zheng, Z., Yim, S. Y. L., Roth, M., Ren, G., Gao, Z., et al. (2020b). PM 2.5 Pollution Modulates Wintertime Urban Heat Island Intensity in the Beijing-Tianjin-Hebei Megalopolis, China. *Geophys. Res. Lett.* 47 (1). doi:10.1029/2019gl084288

Zeng, Z., Wang, Z., Gui, K., Yan, X., Gao, M., Luo, M., et al. (2020). Daily Global Solar Radiation in China Estimated from High-Density Meteorological Observations: A Random Forest Model Framework. *Earth Space ScienceEarth Space Sci.* 7. doi:10.1029/2019EA001058

Zhang, L., Ren, G. Y., Liu, J., Zhou, Y. Q., Ren, Y. Y., Zhang, A. Y., et al. (2011). Urban Effect on Trends of Extreme Temperature Indices at Beijing Meteorological Station. *Chin. J Geophys (in Chinese)* 54 (5), 1150–1159. doi:10.3969/j.issn.0001-5733.2011.05.002

Zhang, Y., Peng, M., Wang, L., and Yu, C. (2018). Association of Diurnal Temperature Range with Daily Mortality in England and Wales: A Nationwide Time-Series Study. *Sci. Total Environ.* 619-620, 291–300. doi:10.1016/j.scitotenv.2017.11.056

Zheng, Z., Ren, G., Wang, H., Dou, J., Gao, Z., Duan, C., et al. (2018). Relationship between Fine-Particle Pollution and the Urban Heat Island in Beijing, China: Observational Evidence. *Boundary-layer Meteorol.* 169, 93–113. doi:10.1007/s10546-018-0362-6

Zhou, L., Dickinson, R. E., Tian, Y., Vose, R. S., and Dai, Y. (2007). Impact of Vegetation Removal and Soil Aridation on Diurnal Temperature Range in a Semiarid Region: Application to the Sahel. *Proc. Natl. Acad. Sci.* 104 (46), 17937–17942. doi:10.1073/pnas.0700290104

Zhou, Y., Shi, J., and Sun, G. (2012). Changes of Diurnal Temperature Range and its Influencing Factors from 1873 to 2009 in Shanghai. *J. Meteorology Environ. (in Chinese)* 28 (01), 24–30.

Zong, L., Liu, S., Yang, Y., Ren, G., Yu, M., Zhang, Y., et al. (2021). Synergistic Influence of Local Climate Zones and Wind Speeds on Urban Heat Island and Heat Waves in Beijing. *Front. Earth Sci.* doi:10.3389/feart.2021.673786

Conflict of Interest: The authors declare that the research was conducted in the absence of any commercial or financial relationships that could be construed as a potential conflict of interest.

frontiers in Environmental Science

ORIGINAL RESEARCH
published: 16 June 2021
doi: 10.3389/fenvs.2021.656639

Whether the CMIP5 Models Can Reproduce the Long-Range Correlation of Daily Precipitation?

*Tianyun Dong[1], Shanshan Zhao[2,3], Ying Mei[1], Xiaoqiang Xie[1], Shiquan Wan[4] and Wenping He[1,2]**

[1]School of Atmospheric Sciences, and Key Laboratory of Tropical Atmosphere-Ocean System (Sun Yat-sen University), Ministry of Education, and Southern Marine Science and Engineering Guangdong Laboratory, Zhuhai, China, [2]Collaborative Innovation Center on Forecast and Evaluation of Meteorological Disasters, Nanjing University of Information Sciences and Technology, Nanjing, China, [3]National Climate Center, China Meteorological Administration, Beijing, China, [4]Yangzhou Meteorological Office, Yangzhou, China

In this study, we investigated the performance of nine CMIP5 models for global daily precipitation by comparing with NCEP data from 1960 to 2005 based on the detrended fluctuation analysis (DFA) method. We found that NCEP daily precipitation exhibits long-range correlation (LRC) characteristics in most regions of the world. The LRC of daily precipitation over the central of North American continent is the strongest in summer, while the LRC of precipitation is the weakest for the equatorial central Pacific Ocean. The zonal average scaling exponents of NCEP daily precipitation are smaller in middle and high latitudes than those in the tropics. The scaling exponents are above 0.9 over the tropical middle and east Pacific Ocean for the year and four seasons. Most CMIP5 models can capture the characteristic that zonal mean scaling exponents of daily precipitation reach the peak in the tropics, and then decrease rapidly with the latitude increasing. The zonal mean scaling exponents simulated by CMCC-CMS, GFDL-ESM2G and IPSL-CM5A-MR show consistencies with those of NCEP, while BCC_CSM1.1(m) and FGOALS-g2 cannot capture the seasonal variations of daily precipitation's LRC. The biases of scaling exponents between CMIP5 models and NCEP are smaller in the high latitudes, and even less than the absolute value of 0.05 in some regions, including Arctic Ocean, Siberian, Southern Ocean and Antarctic. However, for Western Africa, Eastern Africa, Tropical Eastern Pacific and Northern South America, the simulated biases of scaling exponents are greater than the absolute value of 0.05 for the year and all four seasons. In general, the spatial biases of LRC simulated by GFDL-ESM2G, HadGEM2-AO and INM-CM4 are relatively small, which indicating that the LRC characteristics of daily precipitation are well simulated by these models.

Keywords: detrended fluctuation analysis, CMIP5, daily precipitation, scaling exponent, long-range correlation

OPEN ACCESS

Edited by:
Qingxiang Li,
Sun Yat-Sen University, China

Reviewed by:
Shujuan Hu,
Lanzhou University, China
Ruiqiang Ding,
Beijing Normal University, China

****Correspondence:***
Wenping He
wenping_he@163.com

Specialty section:
This article was submitted to Interdisciplinary Climate Studies, a section of the journal Frontiers in Environmental Science

Received: *21 January 2021*
Accepted: *27 May 2021*
Published: *16 June 2021*

Citation:
Dong T, Zhao S, Mei Y, Xie X, Wan S and He W (2021) Whether the CMIP5 Models Can Reproduce the Long-Range Correlation of Daily Precipitation? Front. Environ. Sci. 9:656639. doi: 10.3389/fenvs.2021.656639

INTRODUCTION

Precipitation changes not only affect the global hydrographic cycle (Trenberth, 2011; Ma and Zhou, 2015), but also play an essential role for human societal and economic development (Wang et al., 2012; IPCC, 2013; Zhang et al., 2018; Chen et al., 2020). Global climate models are widely used to reproduce the current climate and project future climate change (Zhou and Yu, 2006; Xu and Xu,

TABLE 1 | Details of the nine CMIP5 climate models.

Modeling center	Nation	Institution	Model information	
			Model name	Atmosphere resolution
BCC	China	Beijing Climate Center, China Meteorological Administration	BCC_CSM1.1(m)	T106 (~1.125 × 1.125°) L26
CMCC	Italy	Centro Euro-Mediterraneo per I Cambiamenti Climatici	CMCC-CMS	T63 (~1.875 × 1.865°) L95
CNRM-CERFACS	France	Center National de Recherches Meteorologiques/Center Europeen de Recherche et Formation Avancees en Calcul Scientifique	CNRM-CM5	TL127 (~1.4 × 1.4°) L31
LASG	China	Institue of Atmospheric Physics Chinese Academy of Sciences	FGOALS-g2	(~2.81 × 1.66°) L26
GFDL	United States	NOAA Geophysical Fluid Dynamics Laboratory	GFDL-ESM2G	M45 (~2 × 2.5°) L24
INM	Russia	Institute for Numerical Mathematics	INM-CM4	(~1.5 × 2.0°) L21
IPSL	France	Institute Pierre-Simon Laplace	IPSL-CM5A-MR	LMDZ4 (~1.2587 × 2.5°)
MOHC	United Kingdom	Met Office Hadley Center	HadGEM2-AO	T63 (~1.875 × 1.865°) L38
MPI-M	Germany	Max Planck Institute for Meteorology	MPI-ESM-MR	T63 (~1.875 × 1.865°) L47

TABLE 2 | Names and coordinates for 34 regions in the world.

Region name	Abbreviation	Coordinates	
		Longitude	Latitude
Tropical West Pacific	TWP	110–170°E	20°S–20°N
Tropical Central Pacific	TCP	170°E–125°W	20°S–20°N
Tropical Eastern Pacific	TEP	125°W–75°W	20°S–20°N
North Pacific Ocean	NPO	120°E–120°W	20–70°N
South Pacific Ocean	SPO	140°E–70°W	60–20°S
Northern South America	NSA	170°E–125°W	20°S–20°N
Southern South America	SSA	75–40°W	60–20°S
Southern Africa	SAF	10–40°E	35–10°S
Eastern Africa	EAF	20–50°E	10°S–20°N
North Africa	NAF	20°W–65°E	20–30°N
Western Africa	WAF	20°W–20°E	10°S–20°N
Tropical Indian Ocean	TIO	40–120°E	20°S–20°N
South Indian Ocean	SIO	15–140°E	60–20°S
Australia	AUS	110–155°E	40–10°S
South Atlantic Ocean	SAO	65°W–15°E	60–20°S
Tropical Atlantic Ocean	TAO	70°W–10°E	20°S–20°N
North Atlantic Ocean	NAO	90°W–0°	20–60°N
Mexio	MEX	115–80°W	10–30°N
Central North America	CNA	105–85°W	30–50°N
Eastern North America	ENA	85–60°W	20–50°N
Western North America	WNA	130–105°W	30–60°N
Alaska	ALA	170–105°W	60–70°N
Greenland	GRL	105–10°W	50–80°N
Mediterranean	MED	10°W–40°E	30–50°N
Central Asia	CAS	40–75°E	30–50°N
Tibetan	TIB	75–100°E	30–50°N
East Asia	EAS	100–145°E	20–50°N
South Asia	SAS	65–100°E	5–30°N
Southeast Asia	SEA	90–155°E	10°S–20°N
Siberian	SIB	40°E–180°E	50–70°N
Northern Europe	NEU	10°W–40°E	50–75°N
Arctic Ocean	AO	0°–180°W	60–90°N
Southern Ocean	SO	0–180°W	80–60°S
Antarctic	ANT	0–180°W	90–60°S

2012; Knutson et al., 2013; Kumar et al., 2013; Jiang et al., 2015; Dong et al., 2018; He et al., 2019). It's crucial to evaluate and investigate the models' performance in simulating daily precipitation for developing adaptation strategies to reduce uncertainties of projecting precipitation in the future (Jiang et al., 2007; Jiang et al., 2009; Wang and Chen, 2013; Li et al., 2015; Li et al., 2018; Lin et al., 2019).

The Coupled Model Intercomparison Project Phase 5 (CMIP5) includes more comprehensive global climate models enabling researchers to address many scientific questions (Taylor et al., 2012). At present, assessment methods for different models' performance are transforming from traditional qualitative methods to quantitative methods (Sillmann et al., 2013; Jiang et al., 2016; Li et al., 2017). A lot of studies evaluate models based on some traditional statistical methods, such as linear trend analysis (Guo et al., 2013; Dong et al., 2018), the spatial correlation coefficients (Zhao et al., 2014; Tian et al., 2015), the standard deviation (STD) (Yang et al., 2014), signal-to-noise ratio (SNR) (Peng et al., 2019) and so on. However, these evaluation methods cannot reproduce the inner dynamical characteristics of climate system. Therefore, a nonlinear method, long-range correlation (LRC) is needed to understand the intrinsic dynamical characteristics of climate system (Koscielny-Bunde et al., 1998; Malamud and Turcotte 1999; Fu et al., 2016; He et al., 2016; Zhao et al., 2017).

The LRC method is characterized by a timescale and shows the scaling law of an autocorrelation function (Peng et al., 1994; Bunde et al., 2005). For a random system, it is uncorrelated in both temporal and spatial evolution, so the scaling exponent of its time series is 0.5. However, for the climate system, which is a nonlinear complex system with multi-scale interactions, the persistence of external forcing and transmission of energy and information between different subsystems make it no longer isolated. Moreover, the large scale system will have a continuous impact on the small scale system, which makes its time evolution nonrandom. Therefore, its previous state will have a strong or weak impact on its future evolution, which is the LRC revealed in this paper. The value of LRC reflects the strength of nonlinear interaction between different subsystems, and to some extent,

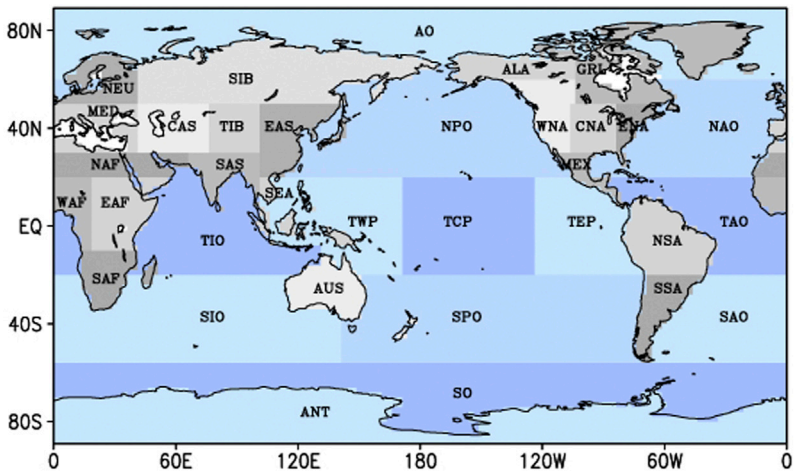

FIGURE 1 | Divisions of the world.

it reflects the internal dynamic characteristics of climate system (Bunde and Havlin., 2002; Lennartz and Bunde 2011; Yuan et al., 2015). For example, the LRC in equatorial Pacific is larger than that in land, which shows relatively strong interaction between ocean and atmosphere (Yeo and Kim, 2014). Therefore, we try to address the question about whether the CMIP5 models can reproduce the LRC of daily precipitation. It is very important and urgent to consider the LRC besides the traditional statistical methods.

The detrended fluctuation analysis (DFA) is a useful tool to estimate the LRC for assessing models' simulate performance (Kantelhardt et al., 2001; Kantelhardt et al., 2002; Blender and Fraedrich, 2003; Kumar et al., 2013; Zhao and He, 2014; Zhao and He, 2015; He and Zhao, 2017). Govindan et al. (2002) found that seven models failed to reproduce the LRC of temperature. Kumar et al. (2013) assessed the performance of 19 CMIP5 models based on long-term persistence and concluded that these models show poor performance in the long-term persistence of precipitation, however, they show better performance in temperature. Different models show different performance in the LRC of climatic variables. Most continents exhibit the long-range correlation of temperature in global coupled general circulation models (Rybski et al., 2008). Daily precipitation also shows long-range correlation both for the Beijing Climate Center Climate System Model [BCC_CSM1.1(m)] and observational data in China (Zhao and He, 2015). The LRC is present in many aspects of climate system, such as air temperature (Du et al., 2013; Yuan et al., 2015; Koscielny-Bunde, et al., 1998; Talkner and Weber, 2000), precipitation (Kantelhardt et al., 2006; Zhao and He, 2015; He and Zhao, 2017), sea surface temperature (Zhang and Zhao, 2015), geopotential height (Tsonis et al., 1999), extreme climate events (Feng et al., 2009) and so on. Therefore, in terms of the LRC of climate system, it is an effective way to assess CMIP5 models' performance in global daily precipitation. Based on this, we will have a deeper understanding for intrinsic dynamical characteristics of the climate system and make contributions to improve models' development.

The remainder of this paper is organized as follows. The data sets and DFA method are introduced in *Methods and Data*. *Results* presents the features of the LRC for the year and four seasons based on NCEP and CMIP5 data. Moreover, the spatial differences of LRC from different regions are shown in *Results*. Finally, a summary and discussion are given in *Discussion and Conclusion*.

METHODS AND DATA

Data

The global daily precipitation datasets used in this study are composed of reanalysis data from the National Centers for Environmental Prediction and National Center for Atmospheric Research (NCEP) (Kalnay et al., 1996). The performance of NCEP reanalysis dataset has been assessed based on LRC characteristics (He and Zhao, 2017; Zhao et al., 2017), which are similar to the results of the observation. So we can use NCEP dataset as the benchmark to evaluate CMIP5 models' LRC characteristic of daily precipitation.

The simulated daily precipitation data is retrieved from the Earth System Grid (ESG) data portal for nine CMIP5 models (https://esgf-node.llnl.gov/search/cmip5/) (Taylor et al., 2012), which are from historical experiments. Only one realization of each model is analyzed. The more detailed information of each model is listed in **Table 1**. The horizontal resolution is different in different models. In order to facilitate model intercomparison and validation against observation, the inverse distance weighting method is used to regrid the model outputs to 2.5° × 2.5° grid. Considering the length of time series both for reanalyzed and simulated data, we chose 1960–2005 as the study period.

To reveal the geographical heterogeneity of DFA for the daily precipitation in the world, we divided the global world into 34 regions, including 12 ocean basins and 22 sub-continental land regions (**Table 2** and **Figure 1**). The 22 sub-continental regions are defined based on Giorgi (2002), and the 12 ocean basins are modified based on Chan and Wu (2015). We calculated the area-averaged LRC in each region for NCEP and model data, then the differences between NCEP and CMIP5 models are compared.

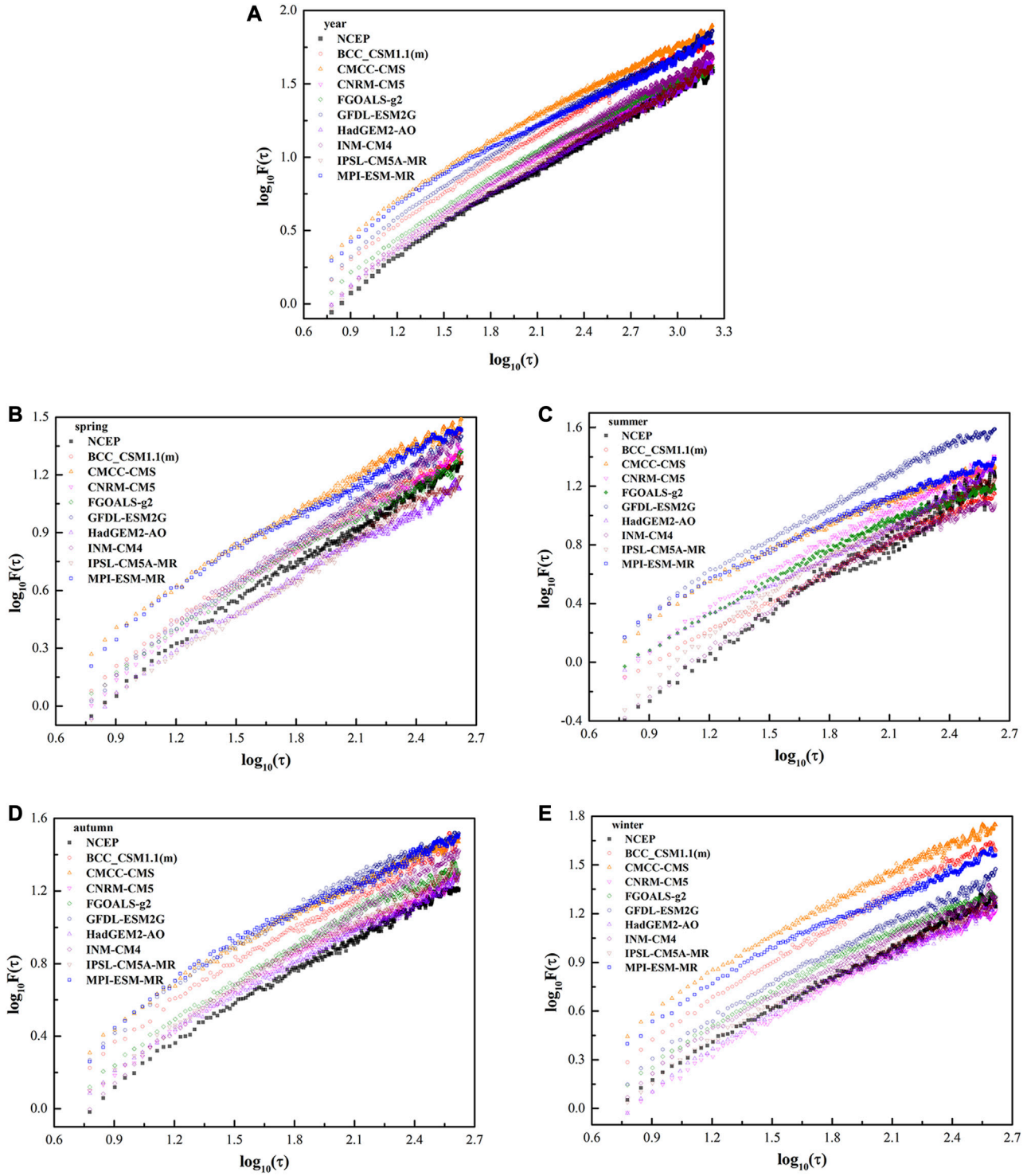

FIGURE 2 | The DFA2 results of daily precipitation from NCEP and CMIP5 models at the point of (110°W, 35°N) for **(A)** year, **(B)** spring, **(C)** summer, **(D)** autumn, and **(E)** winter.

Method

The DFA method is often used to estimate the LRC of time series and an index of power law exponent, namely scaling exponent, can be used to quantitatively quantify the strength of LRC, which could be obtained by DFA (Peng et al., 1994; Bunde and Havlin, 2002; Bunde et al., 2005). DFA has been extensively applied to investigate LRC in climate variability (Talkner and Weber, 2000; Kantelhardt et al., 2006; Gan et al.,

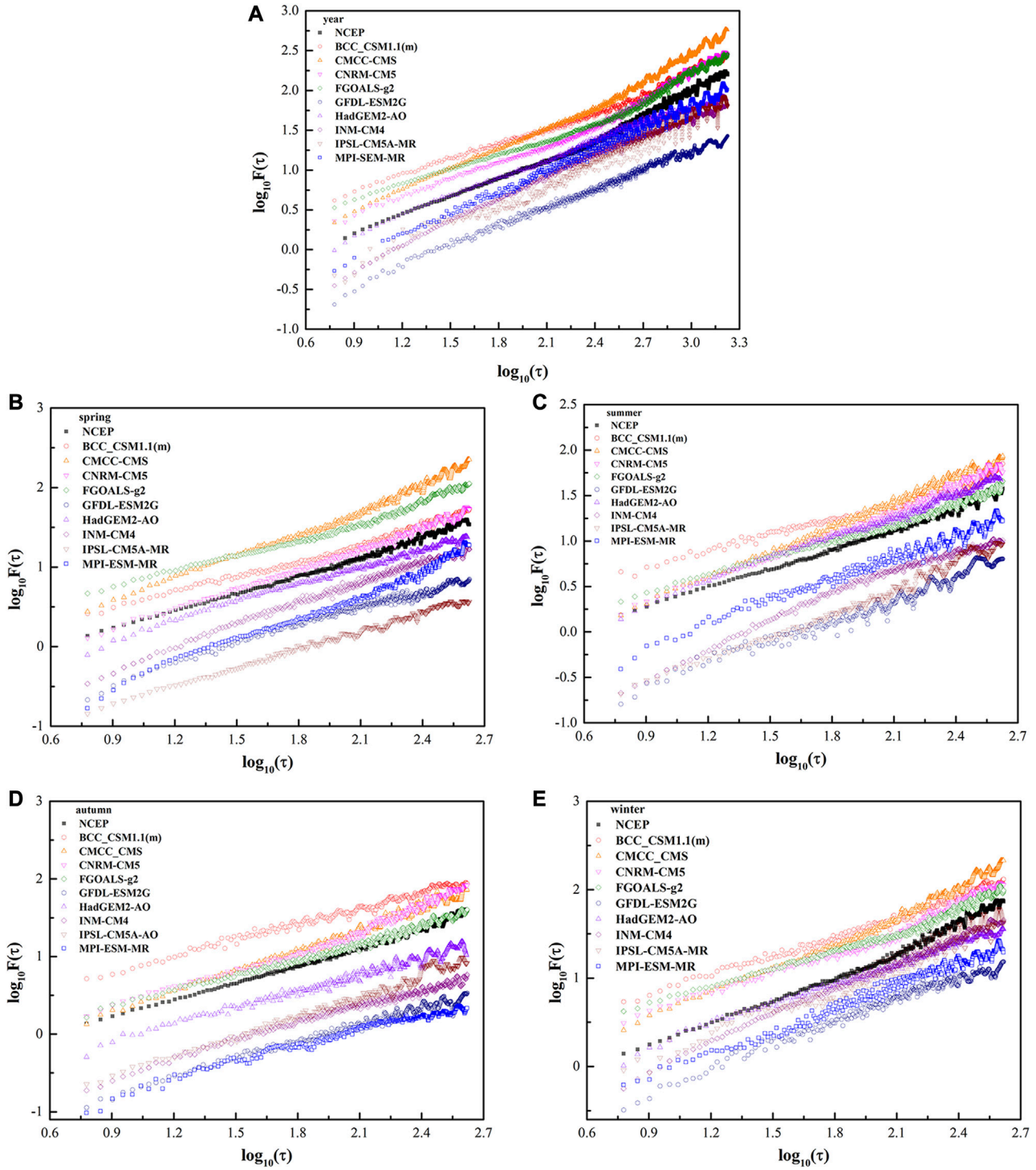

FIGURE 3 | The DFA2 exponents of daily precipitation obtained from NCEP and CMIP5 models at **(A)** point of (110°W, 35°N), **(B)** point of (175°W, 0°) for year and all four seasons.

2007; Jiang et al., 2015). For a giving time series, {X*i*, i = 1, 2, . . ., N}, the departures of X_i is calculated to eliminate the periodic seasonal trends in the climate system.

$$x_i = X_i - \overline{X_i} \quad (1)$$

In this study, $\overline{X_i}$ is the daily mean value for each calendar date i. For example, $\overline{X_i}$ in 1st January can be obtained by averaging

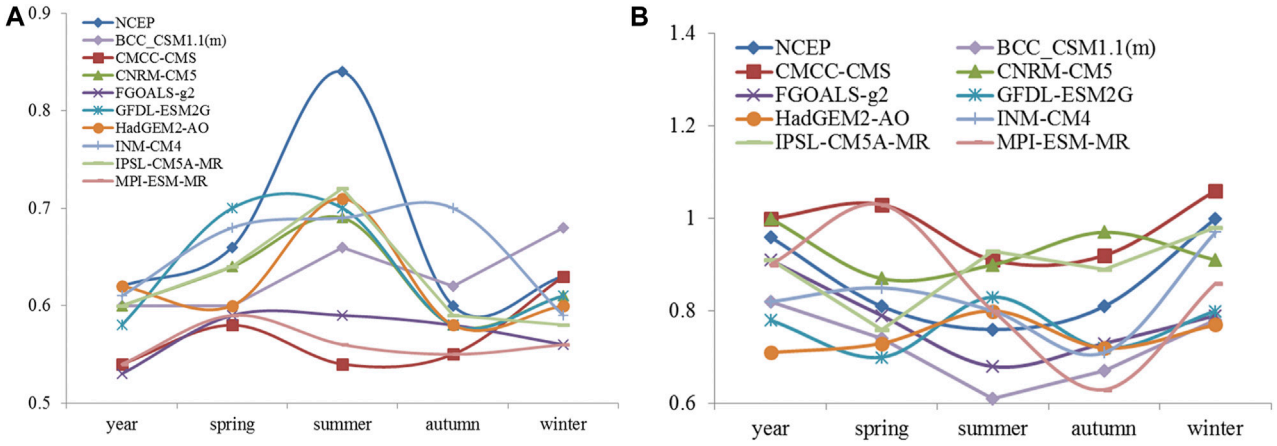

FIGURE 4 | The same as **Figure 2**, but for the point of (175°W, 0°).

the daily temperature on 1st January of all years in the records. Then, cumulative sum $y(k)$ of the time series $x(i)$ is calculated (**Eq. 2**), which is called profile.

$$y(k) = \sum_{i=1}^{k} x_i, k = 1, 2, \ldots, N \quad (2)$$

Next, the profile $y(k)$ is divided into $n = \text{int}(N/\tau)$ non-overlapping segments of equal length τ. In each segment, we apply a polynomial function, $y_\tau(k)$, to fit the local trend. For order l of DFA (DFA1 if $l = 1$, DFA2 if $l = 2$, etc.), the l-order polynomial function should be used for the fitting. Thus, profile $y(k)$ is detrended by subtracting the local trend $y_\tau(k)$ in each segment, and the fluctuation function $(F(\tau))$ of each segment is calculated by

$$F(\tau) = \sqrt{\frac{1}{n\tau}\sum_{k=1}^{n\tau}\left[y(k) - y_\tau(k)\right]^2} \quad (3)$$

Typically, $F(\tau)$ will increase with the segment length τ. A linear relationship on a log-log plot indicates the presence of the power law. In this case, fluctuations functions can be characterized by a scaling exponent a.

$$F(\tau) \sim \tau^{\alpha} \quad (4)$$

If $0.5<a<1$, the time series $\{Xi, i = 1, 2, \ldots, N\}$ is long range correlation. If $a = 0.5$, the time series is uncorrelated. If $0<a<0.5$, the series $\{X_i\}$ has anti-persistent correlation. In this study, the DFA2 method is used to estimate the scaling exponent in a time series.

RESULTS

The LRC Characteristics of Daily Precipitation Based on NCEP and CMIP5 Models

Two grid points in the central of North American continent (110°W, 35°N) and the equatorial central Pacific Ocean (175°W, 0°) are randomly selected as examples to show the detailed information of precipitation's LRC on land and ocean, respectively. The scaling exponent of NCEP daily precipitation is 0.62 (typical LRC characteristic) at the point of North American continent. The daily precipitation simulated by all nine CMIP5 models exhibits the LRC characteristic (**Figure 2A**). The scaling exponents of CMCC-CMS, FGOALS-g2 and MPI-ESM-MR range from 0.5 to 0.55, while the scaling exponents for the other models are close to 0.62 at the grid point (110°W, 35°N) (**Figure 3A**). In spring, the scaling exponent of NCEP precipitation is 0.66 at this point. Except for CMCC-CMS, FGOALS-g2 and MPI-ESM-MR, the other models show greater scaling exponents than 0.59, and even the value for GFDL-ESM2G is 0.7 (**Figures 2B**, **3A**). In summer, the LRC of NCEP daily precipitation at this point is the strongest, and the scaling exponent reaches 0.84. Except for CMCC-CMS, FGOALS-g2 and MPI-ESM-MR, the other models' scaling exponents are greater than 0.6. In autumn, the scaling exponent of NCEP precipitation is 0.6, which is the smallest among four seasons (**Figure 3A**). The scaling exponents of CMCC-CMS and MPI-ESM-MR are smaller (0.55), while that of INM-CM is the largest (0.7) among nine models. In winter, the scaling exponent for daily precipitation of NCEP is 0.63. Except for BCC_CSM1.1(m), the LRC value of most CMIP5 models are underestimated.

In general, the scaling exponent of NCEP daily precipitation at the central of North American continent (110°W, 35°N) is the biggest in summer and the smallest in autumn (**Figures 2**, **3A**). The seasonal variations of scaling exponents simulated by CNRM-CM5, GFDL-ESM2G, HadGEM2-AO and IPSL-CM5A-MR are similar to those of NCEP. These four models can capture the main characteristics that the scaling exponents are the largest in summer and the smallest in autumn, while the seasonal differences of scaling exponents simulated by the other models are various.

At the grid point (175°W, 0°) of the equatorial central Pacific Ocean, the scaling exponent of NCEP precipitation is 0.96 for the whole year, and the values simulated by nine CMIP5 models range from 0.71 to 1.0 (**Figure 4A**). In spring, the scaling exponent of NCEP precipitation is 0.81. The scaling exponents of daily precipitation simulated by CMCC-CMS and MPI-ESM-

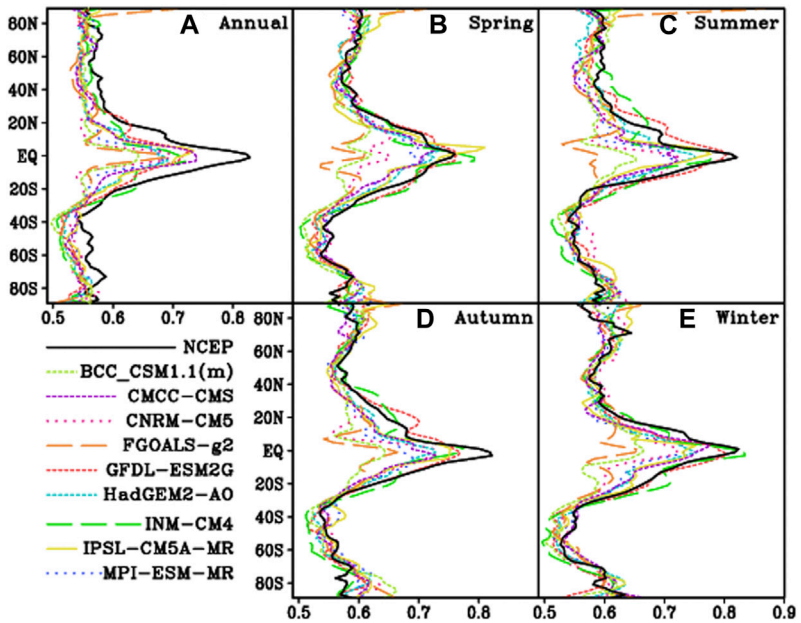

FIGURE 5 | Zonal distribution of daily precipitation's scaling exponents obtained from NCEP and nine CMIP5 models for **(A)** year; **(B)** spring; **(C)** summer; **(D)** autumn; **(E)** winter.

MR are both 1.03, while the values of the other models are closer to NCEP (**Figure 4B**). The scaling exponent of NCEP precipitation in summer is 0.76, which is slightly lower than that in spring. Except for BCC_CSM1.1(m) and FGOALS-g2, the scaling exponents of the other models are greater than 0.7, among which CMCC-CMS, CNRM-CM5 and IPSL-CM5A-MR are greater than 0.9 (**Figures 3B**, **4C**). The scaling exponent of NCEP in autumn is 0.76, which is the same as that in spring. For the results of models, the scaling exponents of BCC_CSM1.1(m) and MPI-ESM-MR are less than 0.7, while those of CMCC-CMS and CNRM-CM5 are greater than 0.9 (**Figures 3B**, **4D**). In winter, the scaling exponent of NCEP precipitation is 1.0. The scaling exponents of CMCC-CMS, CNRM-CM5, INM-CM4 and IPSL-CM5A-MR are close to 1.0 value, meanwhile, CMCC-CMS shows the biggest scaling exponent among nine models, which is 1.06 (**Figures 3B**, **4E**).

We also calculated the median values of the scaling exponents for year and four seasons (Figure is not shown). The median values of the scaling exponents' biases throughout the year range from −0.04 to −0.02, and most of them are closer to zero. From the 5% and 95% ranking values, GFDL-ESM2G and HadGEM2-AO show smaller biases band, FGOALS-g2 shows bigger biases band. The differences of scaling exponents of global daily precipitation simulated by models are smaller in spring than those of other seasons.

Generally, the scaling exponents of daily precipitation in the equatorial central Pacific Ocean are the smallest in summer, followed by spring and autumn. While for winter and the whole year, the scaling exponents fluctuate around the value of 1.0 (**Figure 3B**). The seasonal differences of scaling exponents simulated by BCC_CSM1.1(m), CMCC-CMS and FGOALS-g2 are smaller than the other models in summer.

The Spatial Distribution of LRC for nine CMIP5 Models' Daily Precipitation

The zonal average scaling exponents of NCEP daily precipitation are smaller in middle and high latitudes (**Figure 5A**). The zonal mean scaling exponents decrease rapidly from the equator to middle latitudes and decrease to about 0.6 near 30°S and 30°N. Subsequently, the reduction rate slows down and the zonal average scaling exponents range from 0.5 to 0.6 in the high latitude regions. The scaling exponents of daily precipitation simulated by CMIP5 models also show similar characteristics, the zonal average scaling exponents are smaller in middle and high latitudes. However, the scaling exponents of CMIP5 models' daily precipitation are underestimated, especially in the tropics. The zonal mean scaling exponents simulated by CMCC-CMS, GFDL-ESM2G and IPSL-CM5A-MR are closer to those of NCEP, while BCC_CSM1.1(m) and FGOALS-g2 show relatively poor performance.

In spring, the zonal mean scaling exponents of NCEP are larger in the northern hemisphere than those in the southern hemisphere, and reach a peak value more than 0.7 in the equatorial region (**Figure 5B**). The zonal average scaling exponents in the northern hemisphere vary slightly from extratropical areas to high latitudes. In the southern hemisphere, the zonal average scaling exponents reach the minimum near 40°S, and then increase to 0.6 with the increase of latitudes. The zonal mean scaling exponents simulated by most models in the mid-latitude region are

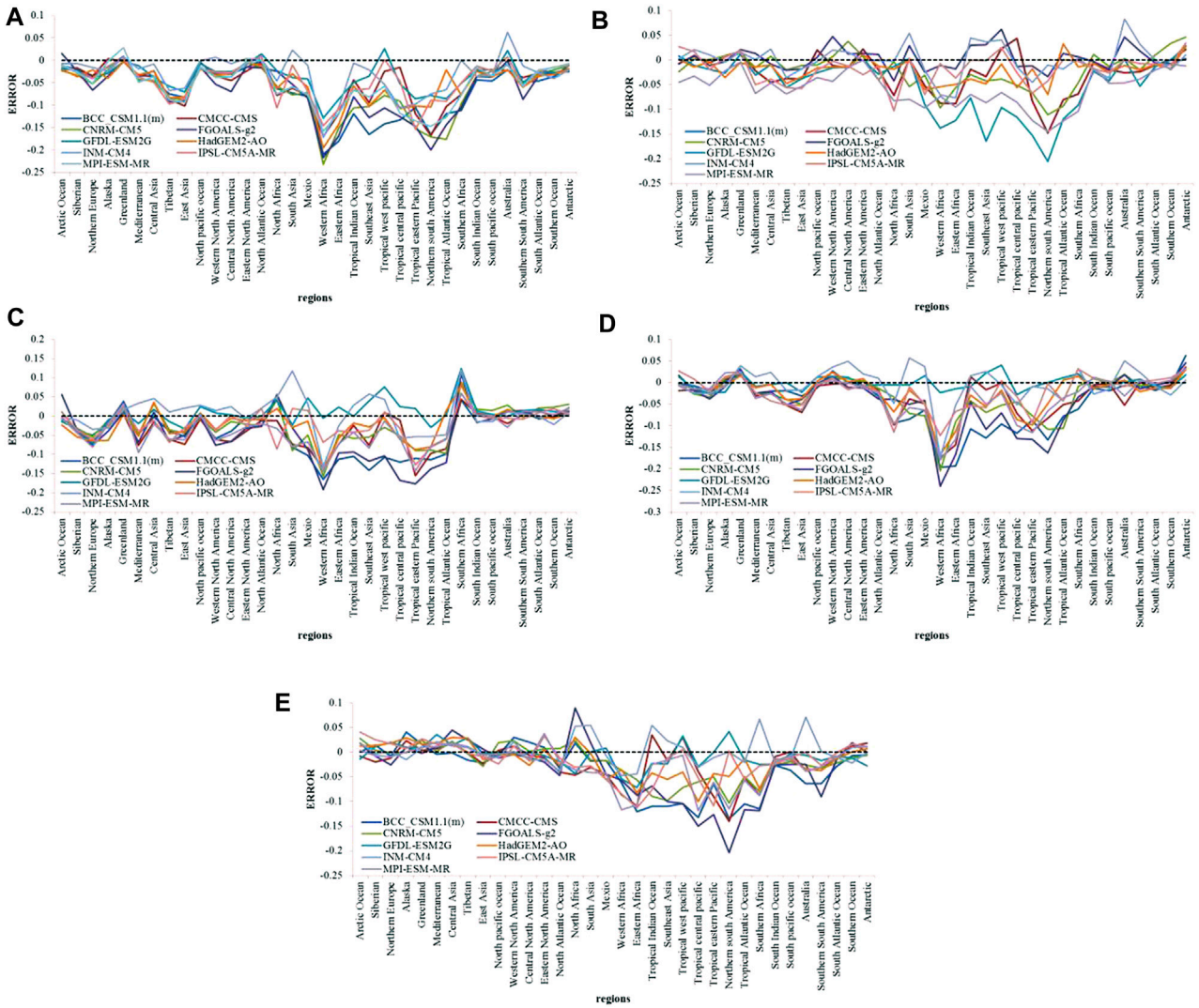

FIGURE 6 | The biases of the region average scaling exponents between CMIP5 models and NCEP for **(A)** year; **(B)** spring; **(C)** summer; **(D)** autumn; **(E)** winter.

closer to those of NCEP, while the differences simulated by BCC_CSM1.1(m), CNRM-CM5, FGOALS-g2 are greater in the tropical region. The zonal mean scaling exponents of daily precipitation simulated by CMIP5 models are generally smaller than those of NCEP in low and middle latitudes. Seasonal characteristics in summer and autumn are similar to those in spring (**Figures 5C,D**). INM-CM4 performs worse at the middle latitudes in summer. In winter, the scaling exponents of NCEP daily precipitation reach the minimum near 60°S in the southern hemisphere, and then increase rapidly (**Figure 5E**).

In conclusion, most CMIP5 models can capture the characteristic that zonal mean scaling exponents of daily precipitation reach the peak in the tropics, and then decrease rapidly with the latitude increasing. Among nine CMIP5 models, the zonal mean scaling exponents simulated by CMCC-CMS, GFDL-ESM2G and IPSL-CM5A-MR are similar to those of NCEP, while BCC_CSM1.1(m) and FGOALS-g2 cannot capture the feature of seasonal variations.

According to the annual average scaling exponents of daily precipitation in each region, the differences between CMIP5 models and NCEP are generally no more than the absolute value of 0.25. In addition, the differences are larger in the middle and low latitudes (**Figure 6A**). In AO, SIB, ALA, GRL, MED, CAS, NPO, ENA, NAO, SIO, SPO, SAO, SO and ANT regions, the differences of scaling exponents between CMIP5 models and NCEP are less than the absolute value of 0.05. While the scaling exponent biases are greater than the absolute value of 0.05 in TIB, EAS, EAF, TEP and NSA.

In spring, the differences of scaling exponents between NCEP and CMIP5 models are less than the absolute value of 0.05 in most of the world, while the differences are greater in tropical areas (**Figure 6B**). In MEX, WAF, EAF, TEP, NSA, TAO, more than half of the models show the absolute value of biases more

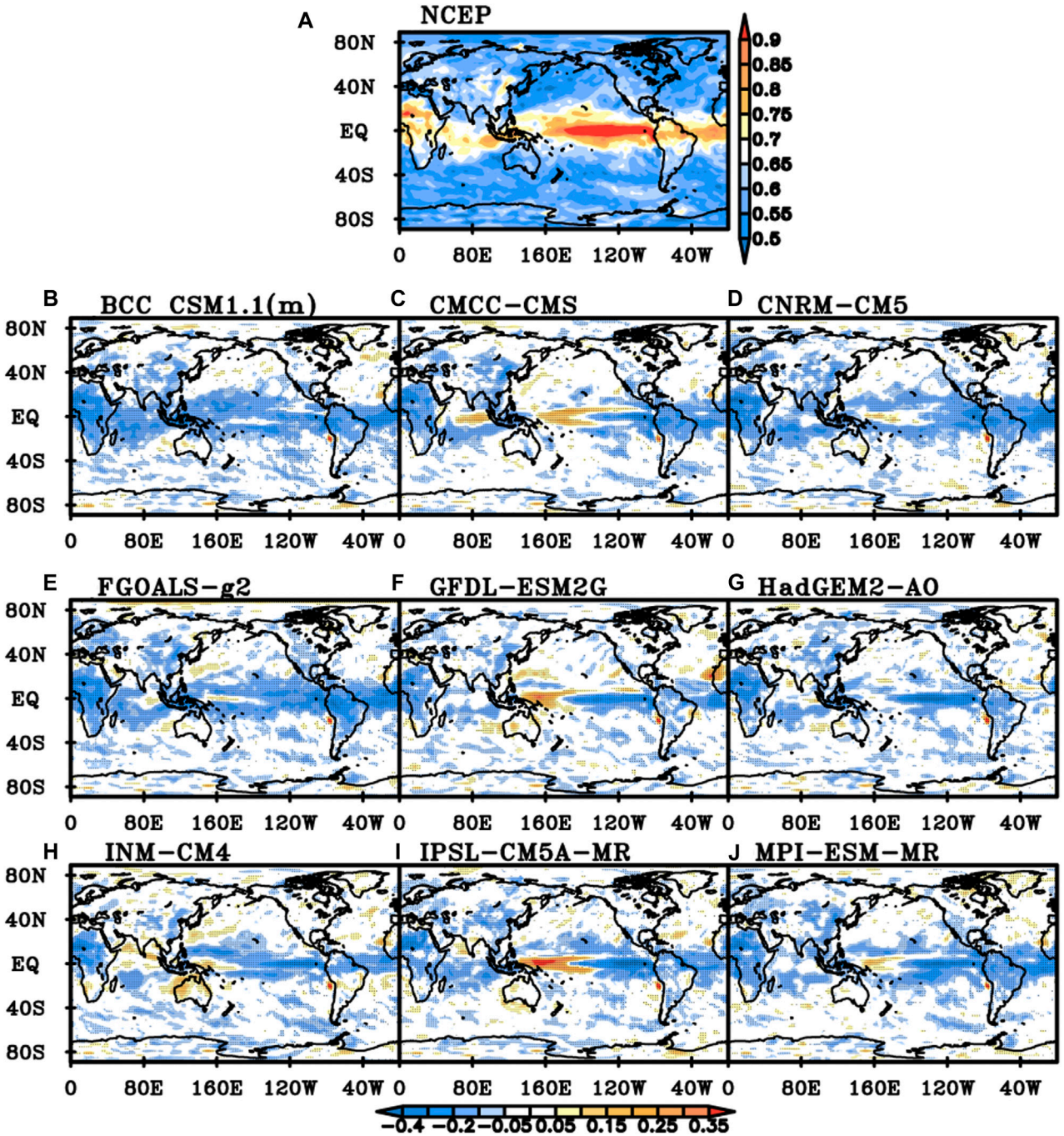

FIGURE 7 | Scaling exponents of NCEP daily precipitation and differences between NCEP and nine CMIP5 models for annual average. **(A)** NCEP daily precipitation, **(B)** BCC_CSM1.1(m), **(C)** CMCC-CMS, **(D)** CNRM-CM5, **(E)** FGOALS-g2, **(F)** GFDL-ESM2G, **(G)** HadGEM2-AO, **(H)** INM-CM4, **(I)** IPSL-CM5A-MR, **(J)** MPI-ESM-MR (Black dot represents the difference is significant at a significance level of 0.05).

than 0.05. In summer, models performs relatively well in the middle and high latitudes of the southern hemisphere. In SIO, SPO, AUS, SSA, SAO, SO, ANT, AOGRL, CASNPO, ENA and NAO, the absolute value of biases simulated by CMIP5 models are less than 0.05. In WAF, EAF, NEU, SAS, SEA, TCP, TEP, NSA, TAO, SAF, there are more than half of models, which show the absolute value of differences greater than 0.05 (**Figure 6C**). In autumn, the absolute value of the model's biases are less than 0.05 in the most extratropical areas, while the absolute value of more than half of simulated models' biases are greater than 0.05 in WAF, EAF, SEA and TEP areas (**Figure 6D**). In winter, the absolute value of the CMIP5

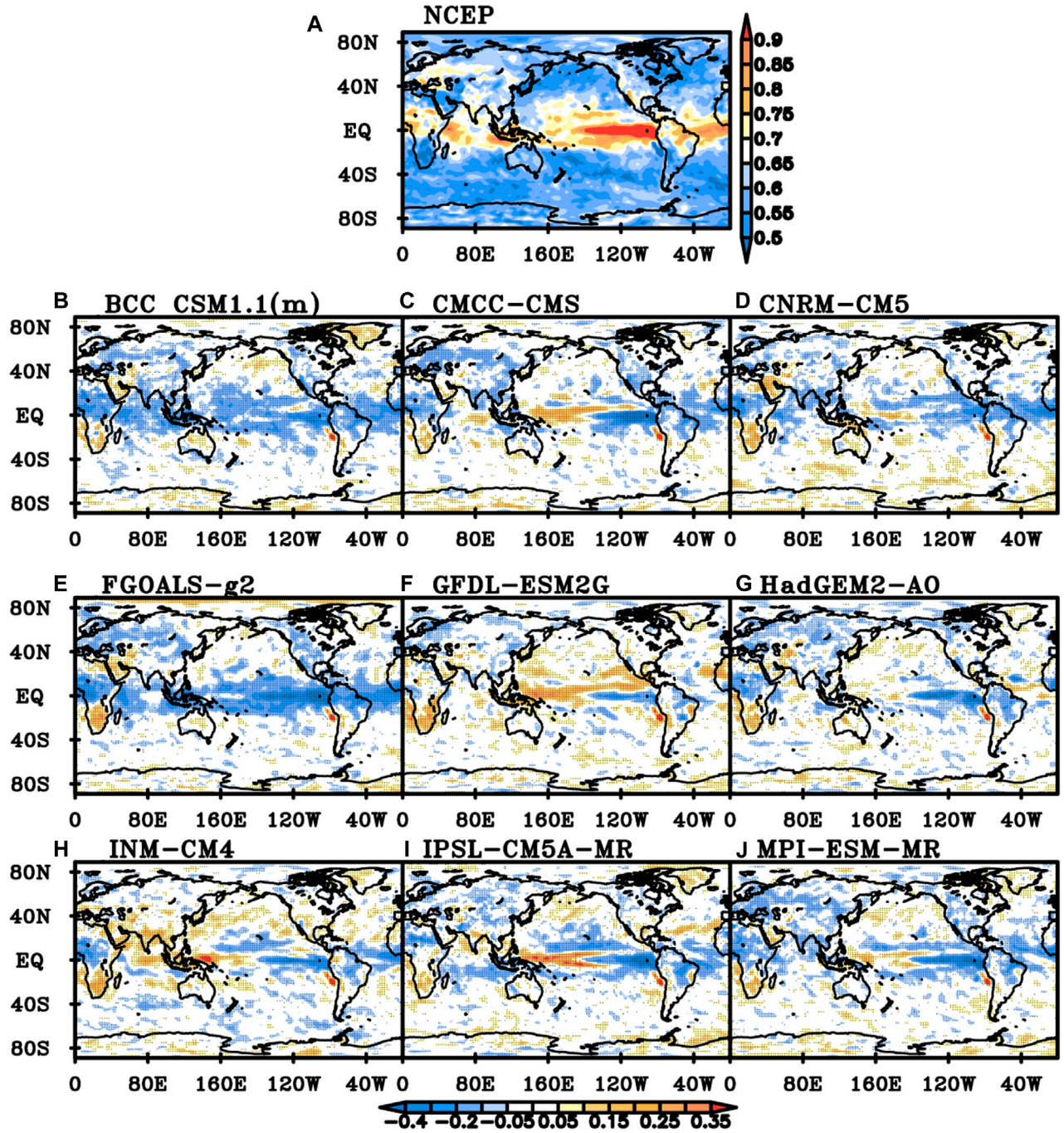

FIGURE 8 | The same as **Figure 7**, but for summer.

models' simulated biases are less than 0.05 in most parts of the northern hemisphere and middle and high latitudes in the southern hemisphere. In WAF, EAF, TIO, TCP, TEP, NSA and SAF areas, there are more than half of the models' absolute value of biases greater than 0.05 (**Figure 6E**).

The global daily precipitation of NCEP shows LRC characteristic in most parts of the world. The scaling exponents are generally range from 0.65 to 0.9 in tropical areas and even above 0.9 in the tropical middle and east Pacific Ocean, which are significant at a significance level of 0.05 (**Figure 7A**). Compared with NCEP data, the scaling exponents simulated by most models are smaller in the tropics. Seven models overestimate the LRC in the equatorial western Pacific except for BCC_CSM1.1(m) and HadGEM2-AO. There are larger biases in Northwest Africa, while smaller biases in the extratropical areas for most models. Overall, the biases of

GFDL-ESM2G, INM-CM4 and HadGEM2-AO are relatively small. For seasonal variations, global spatial distributions of scaling exponents obtained by NCEP data are similar to those of annual mean distributions. Taking summer as an example, the scaling exponents of NCEP precipitation in the tropics and most regions of Eurasia are above 0.65, and the values in the equatorial Middle East and Pacific are above 0.9, which are significant at a significance level of 0.05 (**Figure 8**). Compared with NCEP, the scaling exponents of BCC_CSM1.1(m), CNRM-CM5, FGOALS-g2 and MPI-ESM-MR are smaller in the tropics, most of Eurasia and North America. The scaling exponents of CMCC-CMS and INM-CM4 in the tropical western Pacific and Indian Ocean are bigger than those in other tropical regions. The scaling exponents obtained by GFDL-ESM2G and HadGEM2-AO show similar spatial distribution to that of NCEP precipitation in most of the world, except for the equatorial eastern Pacific. In other seasons, the performance of nine CMIP5 models also varies in different regions, and the biases' distribution of higher values and lower values are similar to those in summer. Generally, the biases of precipitation's scaling exponents simulated by GFDL-ESM2G, HadGEM2-AO and INM-CM4 are relatively small, which means the inner dynamical characteristics of climate systems are well simulated by these models.

DISCUSSION AND CONCLUSION

Based on the DFA method, this paper evaluates the performance of nine CMIP5 models for global daily precipitation from 1960 to 2005. The DFA results of NCEP daily precipitation present long-term correlation characteristics in most regions of the world. The scaling exponents of precipitation in the central part of North America are the largest in summer. The seasonal variations of daily precipitation's scaling exponents simulated by CNRM-CM5, GFDL-ESM2G, HadGEM2-AO and IPSL-CM5A-MR are similar to those of NCEP, which can capture the characteristics that scaling exponents are the biggest in summer and the smallest in autumn. The scaling exponents of precipitation in the equatorial central Pacific are the smallest in summer, indicating the LRC in this region is the weakest in summer. Moreover, the scaling exponents in winter are around 1.0 value.

The zonal average scaling exponents of NCEP daily precipitation are smaller in middle and high latitudes. In spring, the zonal mean scaling exponents of NCEP are larger in the northern hemisphere than those in the southern hemisphere. The zonal average scaling exponents in the northern hemisphere vary slightly with the latitudes increasing and the scaling exponents are around 0.6. In the southern hemisphere, the zonal average scaling exponents reach the minimum near 40°S, and then increase to 0.6 with the increase of latitudes. Seasonal characteristics in summer and autumn are similar to those in spring. In winter, the scaling exponents of NCEP reach the minimum near 60°S in the southern hemisphere and then increase rapidly. Most CMIP5 models can capture the characteristics that zonal mean scaling exponents of daily precipitation reach the peak in the tropics and then decrease rapidly with the latitudes increasing. The zonal mean scaling exponents simulated by CMCC-CMS, GFDL-ESM2G and IPSL-CM5A-MR are similar to those of NCEP, while BCC_CSM1.1(m) and FGOALS-g2 cannot capture this feature of seasonal variations.

The global daily precipitation of NCEP shows LRC in most parts of the world, in which the scaling exponents are generally bigger and above 0.9 over the tropical middle and east Pacific Ocean for the year and four seasons. The differences between models and NCEP are larger in the middle and low latitudes. In AO, SIB, SO and ANT regions, the differences of scaling exponents' absolute value between CMIP5 models and NCEP are less than 0.05. While in WAF, EAF, TEP and NSA, the absolute value of scaling exponents' biases are greater than 0.05 for the year and all four seasons. The biases of GFDL-ESM2G, HadGEM2-AO and INM-CM4 are relatively small, which means that the dynamical characteristics of climate systems are well simulated by these models.

The present study provides a reference for different CMIP5 models' performance in simulating the LRC of global daily precipitation. Comparing the individual models for certain regions reveals that most CMIP5 models can capture the dynamical characteristics of climate system, while there are inter-model differences in various regions. Therefore, appropriate models should be selected according to different research regions.

DATA AVAILABILITY STATEMENT

The datasets presented in this study can be found in online repositories. Further inquiries can be directed to the corresponding author.

AUTHOR CONTRIBUTIONS

TD: Draft paper. Approve the final edition of the paper to be published WH: Make important revisions to the paper. Provide overall thinking. Approve the final edition of the paper to be published SZ, YM, XX, and SW offered the suggestion. All authors contributed to the article and approved the submitted version.

FUNDING

This work was funded by National Key R&D Program of China (2016YFA0602703), the National Natural Science Foundation of China (Grant Nos. 41775092, 41975086, 41905063, and 91644225), the Fundamental Research Funds for the Central Universities (Grant No. 20lgzd06), and Guangdong Basic and Applied Basic Research Foundation (No. 2021A1515011428).

REFERENCES

Blender, R., and Fraedrich, K. (2003). Long Time Memory in Global Warming Simulations. *Geophys. Res. Lett.* 30, 1769–1722. doi:10.1029/2003GL017666

Bunde, A., Eichner, J. F., Kantelhardt, J. F., and Havlin, S. (2005). Long-Term Memory: A Natural Mechanism for the Clustering of Extreme Events and Anomalous Residual Times in Climate Records. *Phys. Rev. Lett.* 94, 048701. doi:10.1103/PysRevLett.94.048701

Bunde, A., and Havlin, S. (2002). Power-law Persistence in the Atmosphere and in the Oceans. *Physica A: Stat. Mech. its Appl.* 314, 15–24. doi:10.1016/s0378-437102)01050-6

Chan, D., and Wu, Q. (2015). Attributing Observed SST Trends and Subcontinental Land Warming to Anthropogenic Forcing during 1979-2005. *J. Clim.* 28, 3152–3170. doi:10.1175/JCLI-D-14-00253.1

Chen, Z., Zhou, T., Zhang, W., Li, P., and Zhao, S. (2020). Projected Changes in the Annual Range of Precipitation under Stabilized 1.5°C and 2.0°C Warming Futures. *Earth's Future* 8, e2019EF001435. doi:10.1029/2019EF001435

Dong, T.-Y., Dong, W.-J., Guo, Y., Chou, J.-M., Yang, S.-L., Tian, D., et al. (2018). Future Temperature Changes over the Critical Belt and Road Region Based on CMIP5 Models. *Adv. Clim. Change Res.* 9 (1), 57–65. doi:10.1016/j.accre.2018.01.003

Du, H., Wu, Z., Li, M., Jin, Y., Zong, S., and Meng, X. (2013). Characteristics of Extreme Daily Minimum and Maximum Temperature over Northeast China, 1961-2009. *Theor. Appl. Climatol.* 111, 161–171. doi:10.1007/s00704-012-0649-3

Feng, G. L., Gong, Z. Q., Hou, W., Wang, Q. G., and Zhi, R. (2009). Long-range Correlation of Extreme Events in Meteorological Field (In Chinese). *Acta Phys. Sin.* 58 (4), 2853–2861. doi:10.3321/j.issn:1000-3290.2009.04.115

Fu, Z., Shi, L., Xie, F., and Piao, L. (2016). Nonlinear Features of Northern Annular Mode Variability. *Physica A: Stat. Mech. its Appl.* 449, 390–394. doi:10.1016/j.physa.2016.01.014

Gan, Z., Yan, Y., and Qi, Y. (2007). Scaling Analysis of the Sea Surface Temperature Anomaly in the South China Sea. *J. Atmos. Ocean. Tech.* 24, 681–687. doi:10.1175/JTECH1981.1

Giorgi, F. (2002). Variability and Trends of Sub-continental Scale Surface Climate in the Twentieth century. Part I: Observations. *Clim. Dyn.* 18, 675–691. doi:10.1007/s00382-001-0204-x

Govindan, R. B., Vyushin, D., Bunde, A., Brenner, S., Havlin, S., and Schellnhuber, H.-J. (2002). Global Climate Models Violate Scaling of the Observed Atmospheric Variability. *Phys. Rev. Lett.* 89, 028501–028504. doi:10.1103/PhysRevLett.89.028501

Guo, Y., Dong, W. J., Ren, F. M., Zhao, Z. C., Huang, J. B., et al. (2013). Surface Air Temperature Simulations over China with CMIP5 and CMIP3. *Adv. Clim. Chang. Res.* 4, 145–152. doi:10.3724/SP.J.1248.2013.145

He, W.P., and Zhao, S.S. (2018). Assessment of the Quality of NCEP-2 and CFSR Reanalysis Daily Temperature in China Based on Long-Range Correlation. *Clim. Dyn.* 50, 493–505. doi:10.1007/s00382-017-3622-0

He, W.P., Zhao, S.S., Wu, Q., Jiang, Y.D., and Wan, S. Q. (2019). Simulating Evaluation and Projection of the Climate Zones over China by CMIP5 Models. *Clim. Dyn.* 52 (5), 2597–2612. doi:10.1007/s00382-018-4410-1

He, W. P., Zhao, S. S., Liu, Q. Q., Jiang, Y. D., and Deng, B. S. (2016). Long-range correlation in the drought and flood index from 1470 to 2000 in eastern China. *Int. J. Climatol.* 36, 16761685. doi:10.1002/joc.4450

IPCC (2013). *Climate Change 2013: The Physical Science Basis. Contribution of Working Group I to the Fifth Assessment Report of the Intergovernmental Panel on Climate Change*. Cambridge and New York: Cambridge University Press. http://www.ipcc.ch/report/ar5/wg1/.

Jiang, D., Tian, Z., and Lang, X. (2016). Reliability of Climate Models for China through the IPCC Third to Fifth Assessment Reports. *Int. J. Climatol.* 36, 1114–1133. doi:10.1002/joc.4406

Jiang, L., Li, N., Fu, Z., and Zhang, J. (2015). Long-range Correlation Behaviors for the 0-cm Average Ground Surface Temperature and Average Air Temperature over China. *Theor. Appl. Climatol.* 119, 25–31. doi:10.1007/s00704-013-1080-0

Jiang, Z. H., Chen, W. L., Song, J., and Wang, J. (2009). Projection and Evaluation of the Precipitation Extremes Indices over China Based on Seven IPCC AR4 Coupled Climate Models (In Chinese). *Chin. J. Atmos. Sci.* 33, 109–120. doi:10.3878/j.issn.1006-9895.2009.01.10

Jiang, Z. H., Ding, Y. G., and Chen, W. L. (2007). Projection of Precipitation Extremes for the 21st Century over China (In Chinese). *Adv. Clim. Chang. Res.* 3, 202–207.

Jiang, Z., Li, W., Xu, J., and Li, L. (2015). Extreme Precipitation Indices over China in CMIP5 Models. Part I: Model Evaluation. *J. Clim.* 28 (21), 8603–8619. doi:10.1175/JCLI-D-15-0099.1

Kalnay, E., Kanamitsu, M., Kistler, R., Collins, W., Deaven, D., Gandin, L., et al. (1996). The NCEP/NCAR 40-Year Reanalysis Project. *Bull. Amer. Meteorol. Soc.* 77, 437–471. doi:10.1175/1520-0477(1996)077<0437:tnyrp>2.0.co;2

Kantelhardt, J. W., Koscielny-Bunde, E., Rego, H. H. A., Havlin, S., and Bunde, A. (2001). Detecting Long-Range Correlations with Detrended Fluctuation Analysis. *Physica A: Stat. Mech. its Appl.* 295, 441–454. doi:10.1016/s0378-4371(01)00144-3

Kantelhardt, J. W., Koscielny-Bunde, E., Rybski, D., Braun, P., Bunde, A., and Havlin, S. (2006). Long-term Persistence and Multifractality of Precipitation and River Runoff Records. *J. Geophys. Res.* 111, D01106. doi:10.1029/2005JD005881

Kantelhardt, J. W., Zschiegner, S. A., Koscielny-Bunde, E., Havlin, S., Bunde, A., and Stanley, H. E. (2002). Multifractal Detrended Fluctuation Analysis of Nonstationary Time Series. *Physica A: Stat. Mech. its Appl.* 316, 87–114. doi:10.1016/S0378-4371(02)01383-3

Knutson, T. R., Zeng, F., and Wittenberg, A. T. (2013). Multimodel Assessment of Regional Surface Temperature Trends: CMIP3 and CMIP5 Twentieth-Century Simulations. *J. Clim.* 26, 8709–8743. doi:10.1175/JCLI-D-12-00567.1

Koscielny-Bunde, E., Roman, H. E., Bunde, A., Havlin, S., and Schellnhuber, H. J. (1998). Long-range Power-Law Correlations in Local Daily Temperature Fluctuation. *Philosophical Mag. B* 77, 1331–1340. doi:10.1080/13642819808205026

Kumar, S., Merwade, V., Kinter, J. L., and Niyogi, D. (2013). Evaluation of Temperature and Precipitation Trends and Long-Term Persistence in CMIP5 Twentieth-century Climate Simulations. *J. Clim.* 26, 4168–4185. doi:10.1175/JCLI-D-12-00259.1

Lennartz, S., and Bunde, A. (2011). Distribution of Natural Trends in Long-Term Correlated Records: A Scaling Approach. *Phys. Rev. E* 84, 021129. doi:10.1103/PhysRevE.84.021129

Li, C., Zwiers, F., Zhang, X., and Li, G. (2019). How Much Information Is Required to Well Constrain Local Estimates of Future Precipitation Extremes? *Earth's Future* 7, 11–24. doi:10.1029/2018ef001001

Li, Q., Zhang, L., Xu, W., Zhou, T., Wang, J., Zhai, P., et al. (2017). Comparisons of Time Series of Annual Mean Surface Air Temperature for China since the 1900s: Observations, Model Simulations, and Extended Reanalysis. *Bull. Amer. Meteorol. Soc.* 98, 699–711. doi:10.1175/BAMS-D-16-0092.1

Li, W., Jiang, Z. H., Xu, J., and Li, L. (2015). Extreme Precipitation Indices over China in CMIP5 Models, Part I: Model Evaluation. *J. Clim.* 28, 8603–8617. doi:10.1175/JCLI-D-15-0099.11

Lin, L., Gettelman, A., Xu, Y., Wu, C., Wang, Z., Rosenbloom, N., et al. (2019). CAM6 Simulation of Mean and Extreme Precipitation over Asia: Sensitivity to Upgraded Physical Parameterizations and Higher Horizontal Resolution. *Geosci. Model. Dev.* 12, 3773–3793. doi:10.5194/gmd-12-3773-2019

Ma, S., and Zhou, T. (2015). Precipitation Changes in Wet and Dry Seasons over the 20th century Simulated by Two Versions of the FGOALS Model. *Adv. Atmos. Sci.* 32 (6), 839–854. doi:10.1007/s00376-014-4136-x

Malamud, B. D., and Turcotte, D. L. (1999). Self-affine Time Series: I. Generation and Analyses. *Adv. Geophys.* 40, 1–90. doi:10.1016/S0065-2687(08)60293-9

Peng, C.-K., Buldyrev, S. V., Havlin, S., Simons, M., Stanley, H. E., and Goldberger, A. L. (1994). Mosaic Organization of DNA Nucleotides. *Phys. Rev. E* 49, 1685–1689. doi:10.1103/PhysRevE.49.1685

Peng, D., Zhou, T., Zhang, L., Zhang, W., and Chen, X. (2019). Observationally Constrained Projection of the Reduced Intensification of Extreme Climate Events in Central Asia from 0.5 °C Less Global Warming. *Clim. Dyn.* 54, 543–560. doi:10.1007/s00382-019-05014-6

Rybski, D., Bunde, A., and von Storch, H. (2008). Long-term Memory in 1000-year Simulated Temperature Records. *J. Geophys. Res.* 113, D02106. doi:10.1029/2007JD008568

Sillmann, J., Kharin, V. V., Zhang, X., Zwiers, F. W., and Bronaugh, D. (2013). Climate Extremes Indices in the CMIP5 Multimodel Ensemble: Part 1. Model Evaluation in the Present Climate. *J. Geophys. Res. Atmos.* 118, 1716–1733. doi:10.1002/jgrd.50203

Talkner, P., and Weber, R. O. (2000). Power Spectrum and Detrended Fluctuation Analysis: Application to Daily Temperatures. *Phys. Rev. E* 62, 150–160. doi:10.1103/PhysRevE.62.150

Taylor, K. E., Stouffer, R. J., and Meehl, G. A. (2012). An Overview of CMIP5 and the experiment Design. *B. Am. Meteorol. Soc.* 93, 485–498. doi:10.1175/BAMS-D-11-00094.1

Tian, D., Guo, Y., and Dong, W. (2015). Future Changes and Uncertainties in Temperature and Precipitation over China Based on CMIP5 Models. *Adv. Atmos. Sci.* 32, 487–496. doi:10.1007/s00376-014-4102-7

Trenberth, K. (2011). Changes in Precipitation with Climate Change. *Clim. Res.* 47 (1), 123–138. doi:10.3354/cr00953

Tsonis, A. A., Roebber, P. J., and Elsner, J. B. (1999). Long-range Correlations in the Extratropical Atmospheric Circulation: Origins and Implications. *J. Clim.* 12, 1534–1541. doi:10.1175/1520-0442(1999)012<1534:lrcite>2.0.co;2

Wang, B., Liu, J., Kim, H.-J., Webster, P. J., and Yim, S.-Y. (2012). Recent Change of the Global Monsoon Precipitation (1979-2008). *Clim. Dyn.* 39 (5), 1123–1135. doi:10.1007/s00382-011-1,266-z

Wang, L., and Chen, W. (2013). A CMIP5 Multimodel Projection of Future Temperature, Precipitation, and Climatological Drought in China. *Int. J. Climatol.* 34, 2059–2078. doi:10.1002/joc.3822

Xu, Y., and Xu, C. H. (2012). Preliminary Assessment of Simulations of Climate Changes over China by CMIP5 Multi Models. *Atmos. Oceanic Sci.* 5, 489–494. doi:10.1080/16742834.2012.11447041

Yang, S., Feng, J., Dong, W., and Chou, J. (2014). Analyses of Extreme Climate Events over China Based on CMIP5 Historical and Future Simulations. *Adv. Atmos. Sci.* 31, 1209–1220. doi:10.1007/s00376-014-3119-2

Yeo, S.-R., and Kim, K.-Y. (2014). Global Warming, Low-Frequency Variability, and Biennial Oscillation: an Attempt to Understand the Physical Mechanisms Driving Major Enso Events. *Clim. Dyn.* 43 (3-4), 771–786. doi:10.1007/s00382-013-1862-1

Yuan, N., Ding, M., Huang, Y., Fu, Z., Xoplaki, E., and Luterbacher, J. (2015). On the Long-Term Climate Memory in the Surface Air Temperature Records over Antarctica: a Nonnegligible Factor for Trend Evaluation. *J. Clim.* 28, 5922–5934. doi:10.1175/JCLI-D-14-00733.1

Zhang, W. F., and Zhao, Q. (2015). Asymmetric Long-Term Persistence Analysis in Sea Surface Temperature Anomaly. *Physica A: Stat. Mech. its Appl.* 428, 314–318. doi:10.1016/j.physa.2015.01.081

Zhang, W., Zhou, T., Zou, L., Zhang, L., and Chen, X. (2018). Reduced Exposure to Extreme Precipitation from 0.5 °C Less Warming in Global Land Monsoon Regions. *Nat. Commun.* 9 (1), 3153. doi:10.1038/s41467-018-05633-3

Zhao, S., and He, W. (2015). Evaluation of the Performance of the Beijing Climate Centre Climate System Model 1.1(m) to Simulate Precipitation across China Based on Long-Range Correlation Characteristics. *J. Geophys. Res. Atmos.* 120, 12576–12588. doi:10.1002/2015JD024059

Zhao, S., He, W., and Jiang, Y. (2017). Evaluation of NCEP-2 and CFSR Reanalysis Seasonal Temperature Data in China Using Detrended Fluctuation Analysis. *Int. J. Climatol.* 38, 252–263. doi:10.1002/joc.5173

Zhao, S. S., and He, W. P. (2014). Performance Evaluation of Chinese Air Temperature Simulated by Beijing Climate Center Climate System Model on the Basis of the Long-Range Correlation (In Chinese). *Acta Phys. Sin.* 63, 209201. doi:10.7498/aps.63.209201

Zhao, S. S., and He, W. P. (2015). Performance Evaluation of the Simulated Daily Average Temperature Series in Four Seasons in China by Beijing Climate System Model (In Chinese). *Acta Phys. Sin.* 64, 049201. doi:10.7498/aps.64.049201

Zhao, T., Chen, L., and Ma, Z. (2014). Simulation of Historical and Projected Climate Change in Arid and Semiarid Areas by CMIP5 Models. *Chin. Sci. Bull.* 59, 412–429. doi:10.1007/s11434-013-0003-x

Zhou, T., and Yu, R. (2006). Twentieth-century Surface Air Temperature over China and the globe Simulated by Coupled Climate Models. *J. Clim.* 19, 5843–5858. doi:10.1175/JCLI3952.1

Conflict of Interest: The authors declare that the research was conducted in the absence of any commercial or financial relationships that could be construed as a potential conflict of interest.

Advantages of publishing in Frontiers

OPEN ACCESS
Articles are free to read for greatest visibility and readership

FAST PUBLICATION
Around 90 days from submission to decision

HIGH QUALITY PEER-REVIEW
Rigorous, collaborative, and constructive peer-review

TRANSPARENT PEER-REVIEW
Editors and reviewers acknowledged by name on published articles

Frontiers
Avenue du Tribunal-Fédéral 34
1005 Lausanne | Switzerland

Visit us: www.frontiersin.org
Contact us: frontiersin.org/about/contact

REPRODUCIBILITY OF RESEARCH
Support open data and methods to enhance research reproducibility

DIGITAL PUBLISHING
Articles designed for optimal readership across devices

FOLLOW US
@frontiersin

IMPACT METRICS
Advanced article metrics track visibility across digital media

EXTENSIVE PROMOTION
Marketing and promotion of impactful research

LOOP RESEARCH NETWORK
Our network increases your article's readership